14th Carolus Magnus Summer School on Plasma and Fusion Energy Physics

20 September – 1 October 2021

Editor: Dirk Reiser (Scientific Secretary CMSS 2021)

Energie & Umwelt / Energy & Environment
Band / Volume 568
ISBN 978-3-95806-613-7

Mitglied der Helmholtz-Gemeinschaft

JÜLICH
Forschungszentrum

Schriften des Forschungszentrums Jülich
Reihe Energie & Umwelt / Energy & Environment Band / Volume 568

Forschungszentrum Jülich GmbH
Institut für Energie- und Klimaforschung
Plasmaphysik (IEK-4)

14th Carolus Magnus Summer School on Plasma and Fusion Energy Physics

20 September – 1 October 2021

Editor: Dirk Reiser (Scientific Secretary CMSS 2021)

Schriften des Forschungszentrums Jülich
Reihe Energie & Umwelt / Energy & Environment Band / Volume 568

ISSN 1866-1793 ISBN 978-3-95806-613-7

Bibliografische Information der Deutschen Nationalbibliothek.
Die Deutsche Nationalbibliothek verzeichnet diese Publikation in der
Deutschen Nationalbibliografie; detaillierte Bibliografische Daten
sind im Internet über http://dnb.d-nb.de abrufbar.

Herausgeber und Vertrieb: Forschungszentrum Jülich GmbH
Zentralbibliothek, Verlag
52425 Jülich
Tel.: +49 2461 61-5368
Fax: +49 2461 61-6103
zb-publikation@fz-juelich.de
www.fz-juelich.de/zb

Umschlaggestaltung: Grafische Medien, Forschungszentrum Jülich GmbH

Druck: Grafische Medien, Forschungszentrum Jülich GmbH

Schriften des Forschungszentrums Jülich
Reihe Energie & Umwelt / Energy & Environment, Band / Volume 568

ISSN 1866-1793
ISBN 978-3-95806-613-7

Vollständig frei verfügbar über das Publikationsportal des Forschungszentrums Jülich (JuSER)
unter www.fz-juelich.de/zb/openaccess.

PREFACE

The 14th edition of the Carolus Magnus Summer School on Plasma and Fusion Energy Physics took place from 20 September to 1 October 2021. The biennial Carolus Magnus Summer School (http://www.carolusmagnus.net/) is organised by the Trilateral Euregio Cluster (TEC), a partnership between fusion institutions from Euregio: the Laboratory for Plasma Physics of the Royal Military Academy (ERM/KMS) in Brussels (Belgium), the Belgian Nuclear Research Centre (SCK·CEN) in Mol (Belgium), the Dutch Institute for Fundamental Energy Research (DIFFER) in Eindhoven (The Netherlands) and the Forschungszentrum Jülich (FZJ) (Germany). All these institutes are also members of the EUROfusion Consortium, which supports and funds fusion research activities on behalf of the European Commission's Euratom programme. Due to the Covid-19 pandemics, the 14th edition of the Carolus Magnus Summer School, originally scheduled to take place in Bad Honnef, Germany in September 2020, was first postponed and then organised as a virtual event, hosted by Forschungszentrum Jülich.

The first Carolus Magnus Summer School took place in Vaals, The Netherlands, in 1993 and was one of the first initiatives of the neighbouring fusion institutions from Belgium, Germany and The Netherlands for a coherent science and research programme, which later in 1995 resulted in the formation of the Trilateral Euregio Cluster. The following editions of Carolus Magnus Summer School were then organised by TEC: Aachen (Germany) in 1995, Spa (Belgium) in 1997, Maastricht (The Netherlands) in 1999, Bad Honnef (Germany) in 2001, Brussels (Belgium) in 2003, Mechelen (The Netherlands) in 2005, Bad Honnef (Germany) in 2007, Herbeumont-sur-Semois (Belgium) in 2009, Weert (The Netherlands) in 2011, Bad Honnef (Germany) in 2013, Leuven (Belgium) in 2015 and Weert (The Netherlands) in 2018.

The Carolus Magnus Summer School is named after the well-known emperor Charlemagne (or Charles the Great, Latin: Carolus Magnus) (747 - 814), who united the majority of western and central Europe and became the first recognised emperor to rule from western Europe since the fall of the Western Roman Empire. During his reign, schools and education were introduced in most of Western Europe. Charlemagne ruled from his imperial capital city of Aachen, nowadays one of the prominent cities in Euregio, approximately 30 km away from Jülich. The logo of the Carolus Magnus Summer School shows a silhouette of an equestrian statuette of Charlemagne, exhibited in the Louvre Museum in Paris. The blue logo background depicts the territory of the organising countries: Belgium, The Netherlands and the German state North Rhine-Westphalia.

An educational event organised via internet has obvious drawbacks, first of all, the lack of personal and social interaction between students and lecturers, whether during the lectures or in the convivial evening atmosphere. Being confronted with the restrictions of the Covid-19 pandemics in early 2020 causing the postponement of the Carolus Magnus Summer School, the Programme Committee and the local organisers immediately started elaborating possible solutions for the event in 2021. We aimed at providing an online event with a maximum possible level of interaction and involvement. That is when the ideas of the pre-recorded students' presentations, breakout rooms for the interaction between lecturers and students and students among themselves, virtual lab tours and our most popular quiz with questions based on the content of the last session lectures were born. The quiz rounds helped us tracking the attendance, which was one of the criteria for issuing the Certificates of Participation, and added a flavour of competition between the students throughout the full 10-day course.

Besides all the drawbacks, there are also a few advantages of a virtual event. For example, this kind of organisation saves money, so that we were able to waive the participation fee for this edition of the Carolus Magnus Summer School. Thanks to the virtual format, it was much easier for students from distant countries like Mexico, Costa Rica, Egypt, India and China to attend this Carolus Magnus Summer School. The result was a record number of participants: 90 young scientists and engineers from 25 countries attended the 2021 edition of the Carolus Magnus Summer School, underlining its popularity among events teaching the basics and advances of plasma and fusion energy physics.

For the second time after 2015, the Proceedings of the Carolus Magnus Summer School were published in the open access format and are available for everyone to download. We thank the FZJ Publishing House for providing this service. If you would like to use the material from these Proceedings for your own publications or presentations, we would like to ask you to properly cite the corresponding manuscript using its persistent web id beginning with "http://hdl.handle.net/...", which you will find on the corresponding web page of the FZJ publishing house.

Last but not least, I personally would like to thank all lecturers for providing excellent lectures, the participants for their enormous interest in our event and the time they spent with us during these 10 days and nights (different time zones!), the members of the Programme Committee: Kristel Crombé (ERM/KMS), Yevgen Kazakov (ERM/KMS), Dmitry Terentyev (SCK·CEN), Hugo de Blank (DIFFER) and Dirk Reiser (FZJ). Dirk as the Scientific Secretary and me as the Chair comprised the compact circle of local organisers of this Carolus Magnus Summer School. On behalf of all of you reading these Proceedings, I would like to thank the authors for providing the manuscripts and Dirk as the Editor for setting-up this compilation.

Arkadi Kreter

Chair of the 14th Carolus Magnus Summer School
on Plasma and Fusion Energy Physics

Forschungszentrum Jülich GmbH,
Institut für Energie- und Klimaforschung - Plasmaphysik,
Partner of the Trilateral Euregio Cluster (TEC),
52425 Jülich, Germany

14th Carolus Magnus Summer School
on Plasma and Fusion Energy Physics

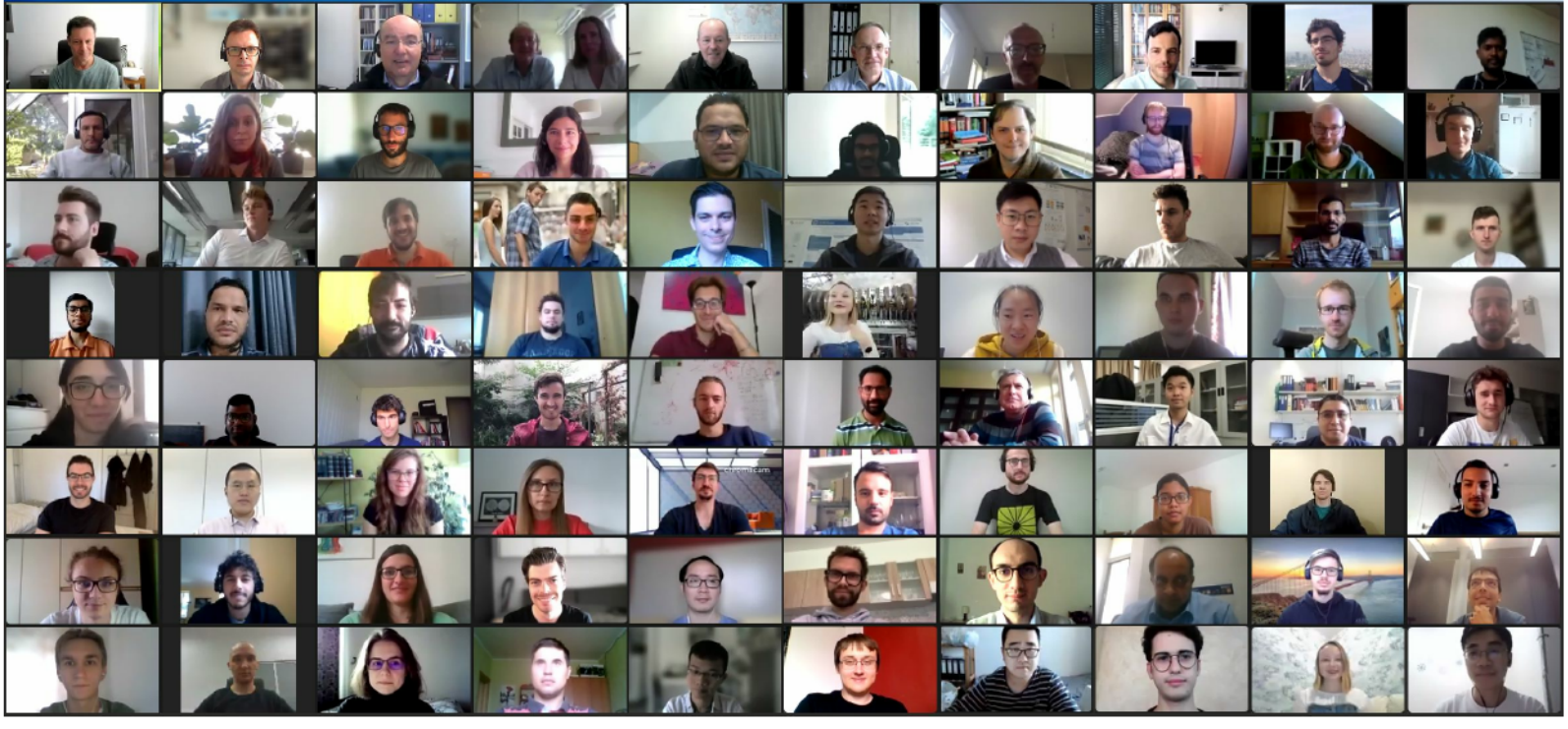

Topics of the 14th Carolus Magnus Summer School

Fusion energy (FE)

- Energy resources and prospects for fusion
- Status and outlook of fusion research
- Thermonuclear burn criteria
- Deuterium-tritium fusion experiments
- Scaling and extrapolation to reactors
- ITER and DEMO
- Reactor safety

Confinement concepts (CC)

- Magnetic fields and plasmas
- Tokamaks
- Stellarators
- Operational limits
- Transport barriers
- Degraded and improved confinement
- Control of plasma discharge

Theory and modelling of fusion plasma (TM)

- Guiding center motion
- Plasma equilibrium
- Kinetic and gyro-kinetic descriptions of plasmas
- Macroscopic description of plasmas
- Ideal and resistive MHD instabilities
- Micro-instabilities
- Classical and neoclassical transport
- Anomalous transport, turbulence and fluctuations
- Transport codes

Plasma heating, current drive and fast particle physics (HC)

- Neutral beam injection
- Propagation and absorption of waves in confined plasmas
- Wave heating (ECRH, ICRH)
- Current drive
- Energetic particle driven instabilities

Diagnostics and data analysis (DD)

- Fusion plasma diagnostics
- Microwave diagnostics
- Optical emission spectroscopy
- Fusion product diagnostics
- Methods of surface analysis
- Methods of data analysis

Plasma wall interaction (PW)

- Transport processes in the plasma edge
- Erosion and deposition mechanisms in fusion plasmas
- Fusion ash removal and impurities
- Neutral particles and recycling
- Radiation phenomena
- Stochastic boundary plasmas
- Limiter and divertor concepts

Fusion reactor materials (FM)

- Basics of material science
- Plasma facing, structural and functional materials and components
- Degradation of material properties and effects of neutrons
- Fuel retention in wall materials
- Wall conditioning
- Laboratory experiments to study plasma material interaction

List of Lectures of the 14th Carolus Magnus Summer School

Lecture ID	Lecturer's name	First name	Affiliation	Lecture title
FE-1	Ongena	Jef	ERM/KMS	Energy for future centuries: prospects for fusion
FE-2	Jaspers	Roger	TU Eindhoven	Thermonuclear burn criteria
FE-3	Biel	Wolfgang	FZJ	Status and outlook of fusion research
FE-4	Garcia	Jeronimo	CEA	Deuterium-tritium (DT) experiments on JET
FE-5	Massaut	Vincent	SCK•CEN	Nuclear aspects of a fusion power plant: constraints and challenges
FE-6	Pitts	Richard	ITER Org	ITER status and challenges
FE-7	Ongena	Jef	ERM/KMS	The big step from ITER to DEMO
CC-1	Van Schoor	Michael	ERM/KMS	Fusion machines (1)
CC-2	Van Schoor	Michael	ERM/KMS	Fusion machines (2)
CC-3	Ongena	Jef	ERM/KMS	Confinement in tokamaks
CC-4	Koslowski	Rudi	FZJ	Operational limits and limiting instabilities in tokamak machines
CC-5	Hartmann	Dirk	IPP Greifswald	Stellarators (1)
CC-6	Hartmann	Dirk	IPP Greifswald	Stellarators (2)
CC-7	Citrin	Jonathan	DIFFER	Degraded confinement and turbulence in tokamaks (1)
CC-8	Citrin	Jonathan	DIFFER	Degraded confinement and turbulence in tokamaks (2)
CC-9	de Baar	Marco	DIFFER	Flying a tokamak
CC-10	Vergote	Maarten	ERM/KMS	Radial electric fields and transport barriers
TM-1	de Blank	Hugo	DIFFER	Guiding center motion (1)
TM-2	de Blank	Hugo	DIFFER	Guiding center motion (2)
TM-3	Proll	Josefine	TU Eindhoven	Classical and neoclassical transport in magnetized plasmas (1)
TM-4	Proll	Josefine	TU Eindhoven	Classical and neoclassical transport in magnetized plasmas (2)
TM-5	de Blank	Hugo	DIFFER	Plasma equilibrium in tokamaks
TM-6	de Blank	Hugo	DIFFER	MHD instabilities in tokamaks
TM-7	Wilson	Howard	U York	Neoclassical tearing modes
TM-8	Wilson	Howard	U York	Edge localized modes in tokamaks
TM-9	Poedts	Stefaan	KU Leuven	Kinetic plasma theory
TM-10	Pucci	Francesco	KU Leuven	Kinetic plasma simulation
TM-11	Reiser	Dirk	FZJ	Introduction to drift wave turbulence models (1)
TM-12	Reiser	Dirk	FZJ	Introduction to drift wave turbulence models (2)
HC-1	Kazakov	Yevgen	ERM/KMS	Plasma heating
HC-2	Louche	Fabrice	ERM/KMS	Coupling of ion cyclotron waves to plasma
HC-3	Dumortier	Pierre	ERM/KMS	Antenna design and matching issues
HC-4	Lerche	Ernesto	ERM/KMS	Ion cyclotron, lower hybrid and Alfvén wave heating methods
HC-5	Lerche	Ernesto	ERM/KMS	Kinetic theory of plasma waves (1)
HC-6	Van Eester	Dirk	ERM/KMS	Kinetic theory of plasma waves (2)
HC-7	Van Eester	Dirk	ERM/KMS	Numerical modeling of particle heating and diffusion
HC-8	Westerhof	Egbert	DIFFER	Electron cyclotron waves
HC-9	Westerhof	Egbert	DIFFER	Non-inductive current drive
HC-10	Sharapov	Sergei	CCFE	Energetic particle driven instabilities: theory and experiment
DD-1	Jaspers	Roger	TU Eindhoven	Overview of fusion plasma diagnostics
DD-2	Brezinsek	Sebastijan	FZJ	In-situ plasma wall interaction diagnostics
DD-3	Kreter	Arkadi	FZJ	Diagnostics for plasma material interaction studies
DD-4	van Berkel	Matthijs	DIFFER	Data-driven analysis for physics and control of fusion plasmas using perturbative experiments
DD-5	Krämer-Flecken	Andreas	FZJ	Microwave diagnostics
DD-6	Kiptily	Vasily	CCFE	Fusion product diagnostics
PW-1	Unterberg	Bernhard	FZJ	Transport processes in the plasma edge (1)
PW-2	Unterberg	Bernhard	FZJ	Transport processes in the plasma edge (2)
PW-3	Wiesen	Sven	FZJ	Impurity transport and radiation
PW-4	Matveev	Dmitry	FZJ	Erosion and deposition mechanisms in fusion plasmas (1)
PW-5	Matveev	Dmitry	FZJ	Erosion and deposition mechanisms in fusion plasmas (2)
PW-6	Borodin	Dmitry	FZJ	Recycling and transport of neutrals (1)
PW-7	Borodin	Dmitry	FZJ	Recycling and transport of neutrals (2)
PW-8	Liang	Yunfeng	FZJ	Stochastic boundary plasmas
PW-9	Brezinsek	Sebastijan	FZJ	Plasma wall interaction in all metal tokamaks
FM-1	Terentyev	Dmitry	SCK•CEN	Basics of material science (1)
FM-2	Terentyev	Dmitry	SCK•CEN	Basics of material science (2)
FM-3	Morgan	Tom	DIFFER	Laboratory experiments to study plasma material interaction
FM-4	Linsmeier	Christian	FZJ	Beryllium and mixed materials: Surface compounds and hydrogen retention
FM-5	Coenen	Jan	FZJ	Tungsten and advanced materials for fusion applications
FM-6	Wirtz	Marius	FZJ	High heat flux performance of plasma facing components
FM-7	Rubel	Marek	KTH Stockholm	Structural and functional materials in fusion reactors
EV-1	Donné	Tony	EUROfusion	EUROfusion

Manuscripts of Lectures - Table of Contents

OPERATIONAL LIMITS AND LIMITING INSTABILITIES IN TOKAMAK MACHINES

H. R. Koslowski

Forschungszentrum Jülich GmbH, Institut für Energie- und Klimaforschung - Plasmaphysik, Partner of the Trilateral Euregio Cluster (TEC), 52425 Jülich, Germany

ABSTRACT

The optimisation of the fusion output power in a tokamak device of given size and magnetic field requires to maximise the fusion triple product $nT\tau_E$. The parameter space for safe, reliable, and stable operation of a tokamak is limited by various constraints. Operational limits of tokamak devices originate from violation of magnetohydrodynamic stability criteria or excessive radiation from impurity ions in the plasma. Exceeding the boundaries of stable operation may either result in a deterioration of plasma confinement, or even lead to the uncontrolled disruptive termination of the discharge.

I. INTRODUCTION

The need to optimise the tokamak operation in order to get a sufficient fusion yield is the main motivating force to explore and understand operational limits. As a starting point, a quite general 0-dimensional consideration of a fusion power generating machine will be presented. The thermonuclear power density (i.e. released power per volume) in a D-T plasma is

$$p_{\mathrm{DT}} = n_{\mathrm{D}} n_{\mathrm{T}} \langle \sigma v \rangle \epsilon_{\mathrm{DT}}, \tag{1}$$

where n_{D} and n_{T} are the densities of D and T nuclei, $\langle \sigma v \rangle$ is the rate coefficient of the fusion reaction, and $\epsilon_{\mathrm{DT}} = 17.6\,\mathrm{MeV}$ is the released energy per fusion reaction. The fusion power density has a maximum when the concentrations of both, D and T ions, are each 50% of the total ion density. In the temperature range between 10 keV and 20 keV the rate coefficient scales within a few % proportional to the square of the temperature, $\langle \sigma v \rangle \propto T^2$. Using the definition of the plasma beta, the ratio between kinetic plasma pressure, p, and magnetic field pressure, $\beta = 2\mu_0 p/B^2$, substituting quantities in equation 1, and integrating over the plasma volume yields the fusion power

$$P_{\mathrm{fus}} \propto p^2 V \propto \beta^2 B^4 V. \tag{2}$$

This relation shows that the achievable fusion power of a tokamak device strongly depends on the magnetic field and the machine size, but there is a considerable dependence on the plasma pressure, i.e. the way in which the machine is operated. One path to increase the fusion power output of a machine is to build a larger device with a higher magnetic field. Beside the fact that especially increasing the size of the machine will increase the cost, there are technological limits. The magnetic field can not be increased arbitrarily because the required superconducting coils only allow a maximum field and superconductivity gets lost at magnetic field strengths above a critical field H_{c}. Another route to performance optimisation opens due to the dependence of the fusion power on the square of the plasma pressure. Appropriate means to tailor the discharge and increase the pressure at a given magnetic field are required.

The most common operational scenario of a tokamak machine nowadays (and foreseen as base operational mode on ITER) is the so-called ELMy H-mode (*high confinement mode*). This is a plasma regime (only observed in tokamaks with a poloidal divertor) where a transport barrier at the plasma edge builds up, steepens the plasma profiles, and leads to an increase of the stored energy in the plasma [1]. The energy confinement time, $\tau_{\mathrm{E,th}}$, of H-mode plasmas has been well documented in numerous experiments on many divertor tokamaks and a scaling law based on engineering quantities has been derived [2]:

$$\tau_{\mathrm{E,th}} \propto I_{\mathrm{p}}^{0.93} B_{\mathrm{t}}^{0.15} P^{-0.69} n_{\mathrm{e}}^{0.41} M^{0.19} R^{1.97} \epsilon^{0.58} \kappa^{0.78} \tag{3}$$

(I_{p} plasma current, B_{t} toroidal magnetic field, P heating power, n_{e} line averaged electron density, M isotope mass, R major tokamak radius, $\epsilon = a/R$ inverse aspect ratio, a minor tokamak radius, κ plasma elongation). Without going in too much detail[1], it can be seen again that increasing machine size, plasma current, or density have a beneficial effect on the confinement. In addition, the plasma elongation has a strong influence on the confinement quality.

The equations above indicate which plasma parameters have to be maximised in order to achieve best plasma performance in a tokamak machine of given size and magnetic field. However, there are only a few actuators for external control of plasma param-

[1] For a detailed discussion of this scaling law see "Heating, Confinement and Extrapolation to Reactors", these proceedings.

eters. The density can be controlled by adjusting the gas fuelling into the plasma. The plasma current is controlled by adjusting the loop voltage through the flux change in the primary winding of the transformer. The plasma temperature can be regulated by auxiliary heating systems, e.g. neutral beam heating or wave heating in the ion cyclotron, electron cyclotron, and lower hybrid range of frequencies. As a side effect (or in some situations deliberately wanted) the plasma heating methods can drive localised currents in the plasma. This feature can be utilised to increase plasma stability or to access a certain confinement mode of the plasma.

All actions and attempts to optimise the fusion power output are constraint by operational boundaries, i.e. the plasma density cannot be increased infinitely but has to be kept below the so-called density limit. The plasma current cannot be increased above a critical value without excitation of magnetohydrodynamic (MHD) instabilities. In the worst case the violation of operational limits leads to a disruption of the discharge, which is a sudden breakdown of the plasma current and a release of the stored energy in the plasma to the first wall of the tokamak. The severity of operational limits can be categorised into *soft limits*, which result in a deterioration of confinement and a related reduction of fusion power, and *hard limits*, which eventually lead to a disruption with potentially harmful impact on the integrity of the machine.

The mechanisms leading to a deterioration of confinement or initiating a plasma disruption have to be studied in detail in order to devise strategies to avoid touching on operational limits, stabilise an instability once it occurs, or completely prevent disruptions to happen.

II. OPERATIONAL PARAMETER SPACE OF A TOKAMAK: THE HUGILL DIAGRAM

An overview on the operational space of a specific tokamak machine is usually given in form of the so-called *Hugill diagram* [3]. Figure 1 shows such a plot for the TEXTOR tokamak[2] The Hugill diagram is a plot of the inverse safety factor at the plasma boundary, $1/q_a$, versus the Murakami number, $n_e R/B_t$ [4]. Because in a cylindrical approximation the edge safety factor[3] can be written as

$$q_a = 5a^2 B_t/(RI_p). \quad (4)$$

The inverse of the edge safety factor is proportional to the plasma current I_p. Therefore, the Hugill diagram

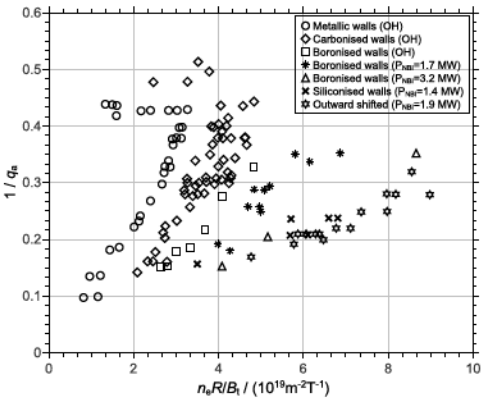

Figure 1: Hugill diagram for the TEXTOR tokamak.

can be seen as a plot of the plasma current versus the line averaged plasma density (scaled by machine size).

The operational space of the TEXTOR tokamak is shown in figure 1. The data have been collected during several years and cover various experimental campaigns with different methods of wall conditioning and ohmic as well as neutral beam injection heated scenarios [5, 6]. Careful inspection of this diagram reveals the existence of three operational boundaries.

At first one notices the absence of data points above an inverse edge safety factor of 0.5, i.e. $q_a < 2$. When the edge safety factor falls below 2 the $m = 2, n = 1$ external kink mode gets destabilised [7]. This mode grows to a large amplitude[4]. Eventually the plasma will end up in a disruption.

A second operational limit manifests itself by the absence of data points in the lower right of the diagram. For a given plasma current (which corresponds to a specific $1/q_a$ value) there exists a maximum electron density. This is an empirical boundary which is not as sharply defined as the $q_a > 2$ limit discussed before. The Hugill diagram shows that the maximum density depends on the first wall surface material of the tokamak, and on the applied heating power. Especially the improvement of wall conditioning techniques led to an increase of tokamak performance which can be attributed to cleaner plasmas with a lower effective charge, Z_{eff} [8]. There is an obvious link of the achievable density with the pureness of the plasma, or in other words, the plasma can sustain a higher density when there are less impurity ions in the plasma. Impurity ions cause an increased energy loss of the plasma which increases with density up to the critical point when the radiated power equals the heating power. It can be seen in figure

[2]The TEXTOR tokamak was located in the Forschungszentrum Jülich and has been in operation for 30 years until 2013. See O. Neubauer et al., *Fusion Sci. Technol.* **47** 76 (2005) for a description of the machine.

[3]The edge safety factor is infinite in a poloidal X-point divertor configuration. In those cases the safety factor q_{95} of the flux surface encompassing 95% of poloidal flux is used synonymously.

[4]Mode amplitude is the radial magnetic field component, but in this context the displacement of flux surfaces is used synonymously.

1 that discharges with neutral beam heating can be stably operated at higher density.

A third limit is not very obvious but results in a lack of data points at very low electron densities, i.e. close to the left axis of figure 1. Due to the toroidal loop voltage the electrons in the plasma experience an accelerating force. Under normal conditions the electric force is balanced by the friction force resulting from collisions. Because friction scales $\propto n_e v^{-2}$ there is a critical velocity upon which an electron is continuously accelerated and *runs away*. The Maxwellian distribution function develops a non-thermal tail. The plasma operation under these conditions has to be avoided because runaway electrons (RE) will be accelerated up to several MeV of energy and the RE beams can carry a substantial amount of energy which, when released to the first wall, may cause serious damage to the machine.

III. RADIATION LIMITS

Tokamak plasmas always contain a certain amount of impurity ions. These ions originate either from the material of the surrounding walls and are released by sputtering, or impurities are deliberately introduced in the discharge for the purpose to cool the plasma edge or divertor region in order to control plasma surface interaction. The presence of these impurity ions results in an increase of the radiation from the plasma which brings about the possibility of radiation driven instabilities.

A. Radiation Mechanisms

In a tokamak plasma different sources for radiation losses are present. The power radiated by *bremsstrahlung* due to electron-ion collisions (free-free) or recombination (free-bound) scales like

$$P_{\mathrm{br}} \propto Z^2\, n_e\, n_Z\, T_e^{1/2}, \tag{5}$$

where Z is the ion charge state[5], n_e and n_Z are the densities of electrons and ions in charge state Z, and T_e denotes the electron temperature. For normal tokamak operational conditions this power loss can be easily balanced by the plasma heating systems.

A more substantial power loss is due to *electron cyclotron radiation*:

$$P_c = e^4/(3\pi\epsilon_0 m_e^3 c^3)\; B^2\, n_e\, T_e, \tag{6}$$

where e is the elementary charge, ϵ_0 the permeability of free space, m_e the electron mass, and c the velocity of light. The power radiated by electron cyclotron emission can become quite large, but it is not of concern because the plasma is optically thick at the fundamental frequency and the emitted power is immediately re-absorbed. Loss of a small fraction of radiated power can occur at the harmonic frequencies where the plasma in not optically thick.

[5] Due to the strong dependence on the effective charge number, the standard Z_{eff} diagnostic of a tokamak is the measurement of the visible bremsstrahlung.

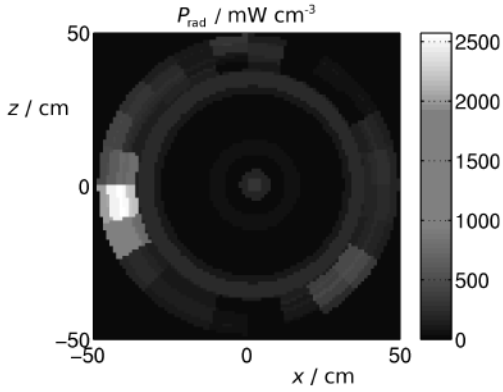

Figure 2: Asymmetric plasma radiation after onset of a MARFE in TEXTOR.

Most important source of radiative power loss are impurity ions. They lead to an increase of bremsstrahlung losses (see equation 5) and additionally emit *line radiation* with a power density given by

$$P_{\mathrm{R}} = L(T_e)\, n_e\, n_{\mathrm{I}}, \tag{7}$$

where $L(T_e)$ is the cooling rate[6] [9] for a specific impurity and n_{I} gives the impurity density. It is important to note that the cooling rates increase when the temperature drops, i.e. $\mathrm{d}L_{T_e}/\mathrm{d}T_e < 0$.

B. Density Limit

The density limit in tokamaks is actually a radiation limit. When the elctron density is increased at constant pressure (i.e. without increasing the heating power), the electron temperature drops. This leads to an increase of the radiative power loss due to the above mentioned shape of the cooling rate curves. The density limit is reached when the radiative power equals the total heating power which is the sum of ohmic and auxiliary heating powers:

$$P_{\mathrm{rad}} = P_{\mathrm{heat}} = P_{\mathrm{OH}} + P_{\mathrm{aux}}. \tag{8}$$

The critical density scales like [10]

$$n_e^{\mathrm{crit}} \propto (P_{\mathrm{heat}}/(Z_{\mathrm{eff}} - 1))^{1/2}. \tag{9}$$

Low effective charge and high heating power can effectively increase the density limit. This can be seen as well in the Hugill diagram figure 1 where with the progress in wall conditioning (carbonisation, boronisation) and with increased heating power higher densities were accessible.

[6] Other authors refer to this quantity as radiation parameter or radiation function.

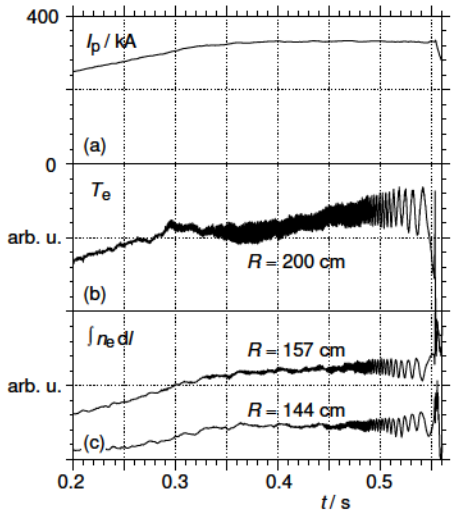

Figure 3: $m = 2, n = 1$ disruption precursor mode.

Present-day tokamaks with metal walls and/or state-of the art wall cleaning methods and sufficient heating power installed would allow for a rather high density limit. Unfortunately, it turns out that the radiative density limit is not dominated by a symmetric radiation belt following equation 9, but is determined by a variety of other mechanisms [11]. Particle transport at the edge, plasma detachment and recycling phenomena leading to plasma cooling are key elements and exhibit a complex interplay. One important and rather common phenomenon in this context is the appearance of the so-called MARFE[7] [12]. In a situation with local plasma cooling the characteristic shape of the cooling rate curves leads to a self amplifying *condensation* process most often resulting in a radiation collapse. The requirement of pressure balance results in a local, cold and very dense plasma, the MARFE. Figure 2 shows a tomographic reconstruction of the poloidal radiation distribution during a MARFE. The appearance of the MARFE is strongly correlated with the recycling flux from the plasma edge [13]. Reducing this particle flux by moving the plasma away from the surrounding walls allows for higher densities (see points labelled *outward shifted* in figure 1). The data from many tokamaks has been analysed in detail [11] and a surprisingly simple scaling law, named the *Greenwald limit*, has been derived:

$$\overline{n}_G = \kappa \overline{j}, \tag{10}$$

with n_G the maximum line-averaged density in units of $10^{20}\,\mathrm{m}^{-3}$, κ the elongation of the poloidal plasma cross section, and $\overline{j}$ the poloidal average of the current density in units of MAm^{-2}. Despite its simplicity, this simple formula has been found to well approximate the density limit in a variety of tokamaks of different size.

[7]The acronym MARFE stands for *Multifacetted Asymmetric Radiation From the Edge*.

C. Impurity Accumulation

Nowadays tokamak are more and more equipped with limiters and divertor tiles made of high-Z materials like tungsten due to their high melting temperatures and low sputtering rates. When off-normal events lead to increased thermal and particle loads high-Z material may be eroded and released to the plasma where it is transported toward the plasma centre. The strong radiation causes local cooling and flat or even hollow temperature profiles. Because the electrical conductivity scales $\sigma \propto f(Z_{\mathrm{eff}})T_e^{3/2}$ with temperature a decreases of the central plasma current follows and enforces the temperature decay and further accumulation of the high-Z impurity in the plasma centre.

IV. BETA LIMIT

In the introduction it has been shown that the increase of toroidal beta

$$\beta_t = 2\mu_0\langle p\rangle / B_t^2, \tag{11}$$

where $\langle p\rangle$ is the volume averaged plasma pressure, is a rational way to increase fusion performance and make best use of the applied toroidal magnetic field B_t. This gives rise to the question, how large the plasma pressure can get before eventually MHD instabilities become destabilised.

A. The Ideal Beta Limit

The maximum plasma pressure which can be confined by a given magnetic field has been calculated by Troyon [14]. In his calculations he considered stability against (i) the Mercier criterion [15], (ii) ballooning modes, and (iii) the $n = 1$ free-boundary kink mode. It has been found that the latter determines the upper limit on beta. For circular plasma cross section a simple scaling law for the poloidal beta[8] has been derived:

$$\beta_p^{\max} = 0.14\,(R/a)\,q_a. \tag{12}$$

More general, the maximim beta β_m for a given configuration[9] can be written as

$$\beta_m = g\frac{I}{aB_t} \tag{13}$$

where g is called the *Troyon factor* and a value of $g = 2.8$ is commonly referred to as the *Troyon limit*. The quantity

$$\beta_N = \frac{\beta}{I/(aB_t)} \tag{14}$$

[8]Same as toroidal beta in equation 11 but toroidal field is replaced by poloidal field B_p.

[9]Here configuration means plasma shape.

is called normalised beta. The stability limit can then be simply expressed as $\beta_N \leq g$. It turns out that the Troyon factor depends on the shape of the current density profile and can be approximated in many cases by $g = 4l_i$, where l_i is the internal inductance of the plasma.

B. Resistive Wall Modes

A special operational mode of tokamaks, the so-called advanced scenario, makes use of an elevated q-profile, a broad current density distribution, and steep pressure gradients which lead to a large bootstrap current fraction. In this scenario the external kink mode plays the limiting role. The mode can be stabilised by a close fitting conducting wall which will allow to achieve a somewhat higher maximum beta value. Due to the conducting wall the growth rate of the external kink is reduced to the inverse of the resistive time constant of the wall. Depending on the properties of the stabilising wall, the achievable beta is in the range

$$\beta^{\mathrm{no-wall}} < \beta < \beta^{\mathrm{ideal-wall}}. \tag{15}$$

In this context the beta limit is called the *resistive wall mode* (RWM) limit. Stabilisation of the RWM is proposed via two different mechanisms: (i) dissipation of the free energy of the mode by fast plasma rotation, and (ii) active feedback control to cancel the RWM field by a set of saddle coils mounted inside the vacuum vessel [16].

C. (Neoclassical) Tearing Modes[10]

In contrast to kink modes which are driven by the plasma pressure, a class of modes named *tearing modes* are driven by the radial gradient of the plasma current. These modes, when destabilised, form so-called magnetic islands which are radially and poloidally localised regions where reconnection of magnetic field lines occurs and the magnetic topology is changed. The growth of tearing modes depends on the tearing parameter Δ' defined as

$$\Delta'(w) = \frac{1}{B_r}\frac{\partial B_r}{\partial r}\bigg|_{r_s-w/2}^{r_s+w/2}, \tag{16}$$

where w is the island width and r_s is the radius of the rational surface where the mode grows [17]. A positive Δ' will destabilise the mode. The growth rate depends on the resistivity η of the plasma and is approximately given by

$$\frac{\mathrm{d}w}{\mathrm{d}t} \simeq \frac{\eta}{2\mu_0}\Delta'(w). \tag{17}$$

Tearing modes can grow to rather large size with a radial width up to 10%-20% of the minor plasma radius. An example of a tearing mode is shown in figure 3. Here the plasma current (a), the electron temperature at about half radius (b), and two interferometer chords (c) are shown. The time traces of T_e and n_e measurements show a characteristic modulation which results from the flattening of the plasma profiles across the island[11] and the diamagnetic drift motion. It can be seen in the figure that the island rotation frequency slows down when the island size gets larger.

A common observation in almost all tokamaks is that the ideal beta limit can only be reached transiently but that the stationary achievable beta values are lower [18]. This behaviour has been found to be caused by the onset of a $m = 3, n = 2$ or $m = 2, n = 1$ tearing modes. Importantly, the Δ' parameter of these modes is negative, i.e. the modes should be stable. These modes have been named *neoclassical tearing modes* (NTM) and their growth can be described by a generalised Rutherford equation [18]. Additional to the tearing parameter this equation contains two pressure driven contributions. One term is destabilising and originates from the loss of bootstrap current due to the pressure profile flattening in the island. The second term is assumed to be stabilising and results from a polarisation current within the island. Neoclassical tearing modes are usually a soft limitation, i.e. the discharge does not disrupt but the confinement gets deteriorated. Plasma disruptions are possible in case the $m = 2, n = 1$ neoclassical tearing mode gets unstable. A widely investigated method for stabilisation of NTMs is to replace the missing bootstrap current in the island by non-inductively driven current using ECRH wave injection or lower hybrid current drive[12] [19, 20].

V. THE CURRENT LIMIT

The q_a-limit

$$q_a > 2 \tag{18}$$

has been already mentioned when discussing the Hugill diagram (figure 1). This is a hard limitation and decreasing q_a below 2 will unavoidably end up with a disruption. Because the density increases with plasma current, increasing the current is an easy way to achieve better confinement, as can be seen by the proportionality of the energy confinement time with plasma current in equation 3. The main implication of the q_a-limit is, that there exists a maximum sustainable plasma current for a given toroidal magnetic field. But even at q_a values above 2 but close to 2 the plasma may be already affected by MHD stability issues due to the growth of the $m = 2, n = 1$ tearing mode. There is no simple criterion to decide whether

[10] This section is just for completeness and kept rather concise, the much more detailed article on "Neoclassical Tearing Modes" can be found elsewhere in these proceedings.

[11] Magnetic islands are commonly referred as O-points of the mode, whereas the crossing of the island separatrix between O-points is labelled the X-point.

[12] See E. Westerhof's article on "Non-inductive Current Drive" in these proceedings.

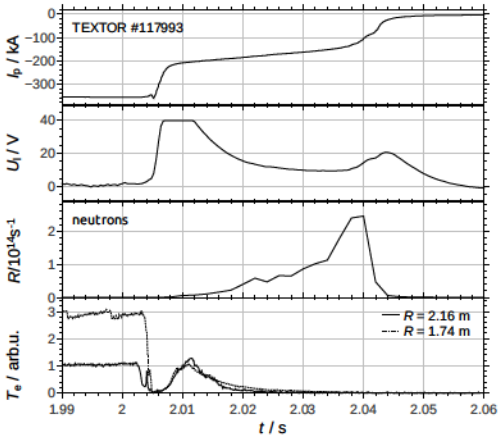

Figure 4: Plasma disruption with RE plateau. Traces from top to bottom are (i) plasma current, (ii) loop voltage (maesurement is saturated), (iii) neutron rate, and (iv) electron temperature (centre and edge).

this mode will become unstable because the shape of the current density profile, the plasma pressure, plasma rotation, and the proximity to a conducting wall influence the stability. As a rule of thumb one can say, that the excitation of the $m = 2, n = 1$ mode becomes more likely the lower the edge safety factor q_a is. Most plasma scenarios today operate with q_a values of 3 or larger.

VI. LOCKED MODES AND ERROR FIELDS

MHD perturbations like kink or tearing modes are usually frozen in the plasma fluid according to Alfvén's theorem. As a consequence modes rotate due to drifts or momentum input by neutral particle injection. A growing mode in the plasma will experience friction caused by induced eddy currents in the wall and slow down the plasma rotation. Eventually the mode can lock to the wall and the rotation in the tokamak frame stands still. The growth rate of the mode after locking is determined by the resistivity of the tokamak first wall and much larger than in the rotating state. In many cases mode locking is observed to be a precursor to a disruption. The slowing down and locking leading to fast mode growth and disruption can be seen in figure 3. Here a disruption starts at $t = 0.552\,\mathrm{s}$ shortly after the mode stopped and a fast growth (see T_e signal) set in.

A common source for the excitation of locked modes are intrinsic error fields. These fields can arise from small alignment errors of the coils systems. Already low error field amplitudes of the order $B_r/B_t \approx 10^{-4}$ (B_r is the radial component of the error field) have been found sufficient to excite locked $n = 1$ modes. An error field of this size is expected on ITER due to small coil misalignments [21].

The critical mode amplitude for mode excitation has been investigated in a variety of tokamaks and a power law scaling expression has been derived [22]:

$$B_r/B_t \propto n_e^{\alpha_n} B_t^{\alpha_B} q_{95}^{\alpha_q} R^{\alpha_R}. \qquad (19)$$

The exponents α_x show a rather large scatter between the data from individual machines, good agreement has been found only for α_n which is about 1, i.e. the threshold for excitation of error field driven modes increases linearly with plasma density. α_B is always negative, implying that acceptable error field levels become even smaller at larger machines.

Plasma rotation generally increases the threshold for mode excitation. Momentum input which adds to the diamagnetic drift will act stabilising. However, when the fluid rotation is compensated by external momentum input the error field threshold shows a minimum at a certain rotation speed [23].

VII. VERTICAL STABILITY

A circular shaped plasma is stable with respect to vertical displacements if the field index

$$n = -\frac{R}{B_v}\frac{\mathrm{d}B_v}{\mathrm{d}R}, \qquad (20)$$

where B_v is the vertical component of the total magnetic field, is larger than zero [7]. Vertical elongation κ has a positive effect on the confinement (see equation 3) and most of the tokamaks are operated with elongated plasma shape. However, a drawback is that the plasma column becomes unstable with respect to vertical displacements. The growth rate of this vertical displacement event (VDE) depends on plasma elongation and can become rather large. A loss of control will result in a vertical movement of the the plasma which will either touch the divertor (which is normally installed at the bottom of the torus) or armour tiles at the top. Large heat loads and halo currents[13] may occur before the plasma current eventually disrupts. The growth rate of the VDE can be decreased by a close fitting conducting wall (similar to RWM stabilisation). Experiments on the Swiss tokamak TCV have shown that growth rates of several $1000\,\mathrm{s}^{-1}$ could be feedback stabilised [24].

VIII. DISRUPTIONS

A disruption is a fast decay of the plasma current as a consequence of a severe plasma instability, an operational limit, or a loss of plasma control. The evolution of a disruption can be divided into several stages

[13] Halo currents arise when the plasma column touches the wall and a fraction of the plasma current flows partly in the wall.

[10]. An initiating event causes an unstable state, often accompanied by changes of the current density distribution. Precursor like mode oscillations appear next before the actual disruption starts. There are two distinct phases: (i) the thermal quench (TQ) during which the temperature profile collapses and the stored plasma energy is released to the surrounding walls, and (ii) the current quench (CQ) during which the plasma current decays very fast and the magnetic energy is released. REs with energies up to several MeV can be generated during the CQ because the tokamak loop voltage rises due to Lenz's law.

Disruptions pose a threat to the integrity of a tokamak because they could result in (i) radiative and convective heat loads on plasma facing components which may cause melting or evaporation, (ii) strong $j \times B$ forces on the vacuum vessel due to induced eddy currents and halo currents, and (iii) a beam of high energetic electrons which can carry a significant fraction of the plasma current and may cause severe damage when hitting plasma facing components.

Disruption studies are at high urgency for ITER [21] and methods for reliable early detection, avoidance, and mitigation need to be developed.

A. Runaway Electrons

REs are generated when the friction force due to collisions gets smaller than the electric force caused by the toroidal loop voltage. A relativistic calculation of the critical electric field required for electrons to run away yields

$$E_{\mathrm{crit}} = \frac{n_{\mathrm{e}} e^3 \ln\Lambda}{4\pi\epsilon_0^2 m_{\mathrm{e}} c^2} \qquad (21)$$

where $\ln\Lambda$ is the Coulomb logarithm, e and m_{e} charge and mass of an electron, and c the speed of light. For normal tokamak conditions the electric field is less than the critical electric field, so no REs are generated. At very low density the loop voltage is large enough to produce REs. These conditions are at the left edge of the Hugill diagram (figure 1). Although in a strict sense the generation of REs is no operational limit, tokamak operation at these conditions is usually avoided because of the potential damage they may cause.

Once there is a population of energetic electrons an avalanche-like process due to small angle collisions with thermal electrons sets in [25]. This secondary generation process will be dominant on large tokamaks.

B. Disruption Avoidance

The optimum approach to solve the disruption problem would be to avoid any disruption happening. This requires a reliable way to detect the very early stage of a disruption, e.g. a precursor, and some actuators to rectify whatever went wrong and to regain plasma control. The application of neural networks for early detection of disruptions is under investigation and shows good progress [26]. For certain classes of disruptions a direct detection of a precursor mode and the use of neutral beam injection in order to enhance plasma rotation and stabilise the mode has proven to be successful [27].

C. Disruption Mitigation

The situation that a disruption cannot be avoided may arise. In this case a way to deliberately shut down the plasma discharge and to ameliorate the consequences of a disruption is required. The shutdown procedure has to be designed in a way which keeps $j \times B$ forces on vessel and coil systems within acceptable limits, dissipates the plasma stored thermal and magnetic energies in a way which does not lead to localised overheating of plasma facing components, and prevents that a part of the plasma current is transformed into REs. The energy balance for a disruption is as follows:

$$W_{\mathrm{th}} + W_{\mathrm{mag}} = W_{\mathrm{rad}} + W_{\mathrm{coupled}} + W_{\mathrm{conv}}\ (+W_{\mathrm{RE}}) \qquad (22)$$

The thermal plasma energy W_{th} and the magnetic energy W_{mag} are converted into radiated energy W_{rad} (this is preferred because radiation is distributed on a large wall surface), the energy W_{coupled} which is coupled via the mutual inductances into the tokamak coil systems, W_{conv} is the energy which is convected by plasma wall contact, and W_{RE} the energy carried by the RE electrons. Especially the latter two components result in small wetted areas and large local heat loads. Various disruption mitigation methods have been proposed: (i) A fast controlled ramp-down of the plasma current seems to be a good solution but is not always possible. It needs a rather large warning time, and the plasma density (and radiation) may not decrease with the required rate thus provoking a density limit disruption. (ii) *Massive gas injection* [28] using specially designed fast valves is another promising method to deliberately induce a radiation collapse. (iii) Injection of so-called *killer pellets*[14] or *shattered pellets*[15] in order to force the plasma into a radiation limit disruption. The latter method is presently under investigation on several tokamaks and has been chosen for the disruption mitigation system on ITER [29].

IX. SUMMARY

The operational limits of a tokamak machine arise from a variety of different physical mechanisms. The density limit is actually defined by the balance between plasma radiation and heating power. Clean plasmas and good wall conditioning together with sufficient heating power can assure stable operation close to this limit. A limitation on the maximum plasma

[14] Similar to frozen hydrogen fuelling pellets but made of neon or argon.

[15] Nobel gas pellets of large size shot against a solid target which disaggregates the pellets before entry into the plasma.

current at a given toroidal field results from the MHD stability properties of the $m = 2, n = 1$ mode. The generation of runaway electrons constrains the operation at low density. The ideal beta limit originates from pressure driven $n = 1$ kink instabilities. Very important is the so-called *practical beta limit* which is due to the excitation of neoclassical tearing modes and constitutes the most frequent limitation to plasma performance. Disruptions can cause damage to the machine and pose the most severe problem on large tokamaks requiring an adequate mitigation method.

REFERENCES

1. F. Wagner et al., "Regime of Improved Confinement and High Beta in Neutral-Beam-Heated Divertor Discharges of the ASDEX Tokamak", *Phys. Rev. Lett.*, **49**, 1408 (1982).
2. ITER Physics Expert Groups on Confinement and Transport and Confinement Modelling and Database, "Chapter 2: Plasma confinement and transport", *Nucl. Fusion*, **39**, 2175-2249 (1999).
3. S. J. Fielding et al., "High-Density Discharges with Gettered Torus Walls in DITE", *Nucl. Fusion* **17** 1382 (1977).
4. M. Murakami et al., "Some Observations on Maximum Densities in Tokamak Experiments", *Nucl. Fusion* **16** 347 (1976).
5. G. Waidmann et al., "Density Limits and Evolution of Disruptions in Ohmic TEXTOR Plasmas", *Nucl. Fusion*, **32**, 645 (1992).
6. J. Rapp et al., "Scaling of Density Limits with Respect to Global and Edge Parameters in TEXTOR-94", in Proc. 26th EPS Conf. on Contr. Fusion and Plasma Physics, Maastricht, *ECA* **23J**, 665 (1999).
7. J. A. Wesson, "Hydrodynamic Stability of Tokamaks", *Nucl. Fusion*, **18**, 87 (1978).
8. J. Winter, "Wall conditioning in fusion devices and its influence on plasma performance", *Plasma Phys. Control. Fusion*, **38**, 1503 (1999).
9. D. E. Post et al., "Steady-state radiative cooling rates for low-density high-temperature plasmas", *At. Data Nucl. Data Tables*, **20**, 397 (1977).
10. F. C. Schüller, "Disruptions in Tokamaks", *Plasma Phys. Control. Fusion*, **37**, A135 (1995).
11. M. Greenwald, "Density Limits in Toroidal Plasmas", *Plasma Phys. Control. Fusion*, **44**, R27 (2002).
12. B. Lipschultz, "Review of MARFE Phenomena in Tokamaks", *J. Nucl. Mater.*, **145-147**, 15 (1987).
13. P. C. de Vries et al., "Influence of Recycling on the Density Limit in TEXTOR-94", *Phys. Rev. Lett.* **80**, 3519 (1998).
14. F. Troyon et al., "MHD-Limits to Plasma Confinement", *Plasma Phys. Control. Fusion*, **26**, 209 (1984).
15. C. Mercier, "A necessary condition for hydromagnetic stability of plasma with axial symmetry", *Nucl. Fusion* **1** 47 (1960).
16. M. S. Chu and M. Okabayashi, "Stabilisation of the external kink and the resistive wall mode", *Plasma Phys. Control. Fusion*, **52**, 123001 (2010).
17. H. P. Furth et al., "Tearing mode in the cylindrical tokamak" *Phys. Fluids*, **16**, 1054 (1973).
18. O. Sauter et al., "Beta Limits in Long-Pulse Tokamak Discharges", *Phys. Plasmas*, **4**, 1654 (1997).
19. H. Zohm et al., "Experiments on Neoclassical Tearing Mode Stabilisation by ECCD in ASDEX-Upgrade", *Nucl. Fusion*, **39**, 577 (1999).
20. C. D. Warrick et al., "Complete Stabilisation of Neoclassical Tearing Modes with Lower Hybrid Current Drive on COMPASS-D", *Phys. Rev. Lett.*, **85**, 574 (2000).
21. T. Hender et al., "MHD Stability, Operational Limits and Disruptions" (Chapter 3 in "Progress in the ITER Physics Base"), *Nucl. Fusion*, **47**, S128 (2007).
22. R. J. Buttery et al., "Error field mode studies on JET, COMPASS-D and DIII-D, and implications for ITER", *Nucl. Fusion*, **39**, 1827 (1999).
23. H. R. Koslowski et al., "Dependence of the Threshold for Perturbation Field Generated m/n = 2/1 Tearing Modes on the Plasma Fluid Rotation", *Nucl. Fusion*, **46**, L1 (2006).
24. F. Hofmann et al., "Vertical Position Control in TCV: Comparison of Model Predictions with Experimental Results", *Nucl. Fusion*, **40**, 767 (2000).
25. R. Jaspers et al., "Disruption Generated Runaway Electrons in TEXTOR and ITER", *Nucl. Fusion*, **36**, 367 (1996).
26. G. Pautasso et al., "Prediction and mitigation of disruptions in ASDEX Upgrade", *J. Nucl. Mater.*, **290-293**, 1045 (2001).
27. A. Krämer-Flecken et al., "Heterodyne ECE Diagnostic in the Mode Detection and Disruption Avoidance at TEXTOR", *Nucl. Fusion*, **43**, 1437 (2003).
28. D. G. Whyte et al., "Disruption mitigation with high-pressure noble gas injection", *J. Nucl. Mater.*, **313-316**, 1239 (2003).
29. M. Lehnen et al., "R&D for Reliable Disruption Mitigation in ITER", *27th IAEA Fusion Energy Conference*, EX/P7-12 (2018).

DIAGNOSTICS FOR PLASMA-MATERIAL INTERACTION STUDIES

A. Kreter

Forschungszentrum Jülich GmbH, Institut für Energie- und Klimaforschung,
Partner of the Trilateral Euregio Cluster (TEC), 52425 Jülich, Germany

ABSTRACT

The manuscript is accompanying the corresponding lecture at the 14th Carolus Magnus Summer School on Plasma and Fusion Energy Physics. The contribution is focused on surface analysis and erosion-deposition diagnostics frequently applied in the fusion relevant research on plasma-material interaction. The definitions of real-time, in-situ, in-vacuo and ex-situ diagnostics are given. The working principles of the following surface analysis tools are described and examples of their applications are given: thermal desorption spectrometry (TDS); scanning electron microscopy (SEM) including the option of focused ion beam (FIB); ion beam analysis (IBA) methods of nuclear reaction analysis (NRA) and Rutherford back-scattering (RBS); and secondary ion mass spectrometry (SIMS). Two methods of erosion-deposition measurements are introduced: quartz microbalance (QMB) and marker techniques.

I. INTRODUCTION

The availability of the fusion reactor is crucial for its economic operation and is to a large extent determined by plasma material interaction (PMI). There are two main PMI issues limiting the availability of the reactor: the lifetime of the wall components and the operational safety. The first wall will suffer from heat loads and particle bombardment, causing erosion of materials and limiting the lifetime of the first wall components. The safety issues are connected to the restrictions on the amount of radioactive tritium and dust stored in the reactor vacuum vessel.

PMI studies in both large-scale, at close-to-reactor conditions, and lab-scale, at well-defined conditions, devices are necessary for a better understanding of the background processes, refined predictions for the reactor and finding solutions to critical issues [1,2]. Therefore, the methods to determine PMI related values, i.e. material erosion and deposition and fuel retention, are important experimental tools in the fusion research.

There are numerous surface analysis techniques analysing the physical and chemical properties of the material surface. E.g. an overview table in the book by G.A. Somorjai [3] lists 60 "most frequently used surface characterization techniques". In this paper, only a fraction of the techniques, which are most relevant to the PMI research, are covered, along with the methods for studying erosion and deposition of the wall materials.

II. DEFINITIONS OF REAL-TIME, IN-SITU, IN-VACUO AND EX-SITU

Material samples can be analysed in different ways concerning the temporal and spatial scale of analysis. The following nomenclature has been established for the description of different methods, here listed in order of the time point of their application or data availability: "real-time", "in-situ", "in-vacuo" and "ex-situ" ("post-mortem").

The real-time techniques deliver the data during the investigated process. They are frequently used for the real-time, or feedback, control of the process. Usually, less complex, robust methods are applied real-time for the control purposes.

In-situ (lat.: "in position") methods are, similarly to the real-time ones, applied during the investigated process, e.g. during the plasma exposure of a material sample. However, the data analysis often requires additional efforts after the actual experiment, e.g. for the conversion of the raw diagnostics data to the meaningful data describing the particular PMI process. Therefore, the data of the in-situ measurements typically becomes available after the experiment. Nevertheless the in-situ data often provides valuable insights in the temporal evolution of the investigated process. In-situ methods of PMI including optical emission spectroscopy are the topic of a different lecture.

In-vacuo (lat.: "in vacuum") methods are applied after the investigated process, e.g. after the plasma exposure of a material sample, but before the exposure of samples to air. Typically they are conducted in the same vacuum chamber. Plasma-exposed surfaces are often chemically activated, exposure to air changes the chemical state of the surface, e.g. by oxidation. Therefore, it is favourable to analyse the sample surface in-vacuo.

Ex-situ (lat.: "out of position") methods are applied after the investigated process and after the exposure to air. In some cases the influence of air is minimised by the use of sealable enclosures, called "desiccators", which are pumped down or filled with inert gas, for the sample storage and transport. However, it cannot be excluded, that the sample surface changes its characteristics between the exposure and the ex-situ analysis. "Post-mortem" (lat.: "after death") is a term equivalent to "ex-situ".

It is usually quite challenging to install and

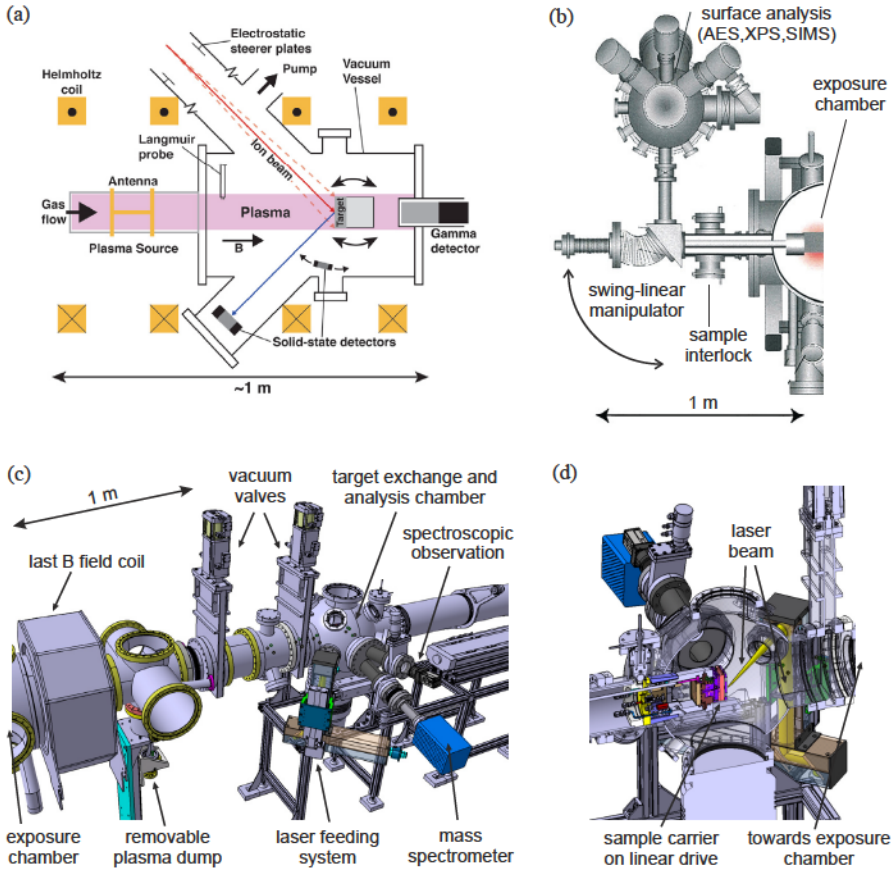

Figure 1. (a) In-situ ion beam analysis in DIONISOS [4]; (b) in-vacuo analysis station of PISCES-B [5]; (c) PSI-2 target exchange and analysis chamber with a laser feeding system for in-vacuo analysis; (d) cross-section of the opposite side of the PSI-2 target exchange and analysis chamber including an illustration of a sample exposed to a laser beam [6].

operate a diagnostic for in-situ or in-vacuo surface analyses. However, the largely increased value of the data with respect to the ex-situ methods and the technical progress in the analysis tools make the use of these techniques more popular. Despite their advantages, in-situ and in-vacuo analysis solutions have a significant downside of high complexity and costs. Therefore, most PMI experiments still rely on the ex-situ surface analysis techniques. Another reason for the predominant use of ex-situ is that the material samples can be transported to various laboratories specializing in particular analysis techniques, thus increasing the versatility and quality of analyses.

One example of in-situ analysis in the DIONISOS plasma facility [4] at MIT, USA is given in figure 1(a). Here, an ion beam accelerator is used for the ion beam analysis simultaneously during the plasma exposure, providing insight on the dynamics of PMI processes. Figure 1(b) shows the in-vacuo surface analysis station of PISCES-B [5]. The samples are extracted from the target station, after termination of the plasma discharge, by a swing-linear manipulator and inserted in the surface analysis station, where Auger electron spectroscopy (AES), X-ray photoelectron spectroscopy (XPS) and secondary ion mass spectrometry (SIMS) techniques can be applied. For the PSI-2 device [6], the application of the laser based techniques including LID and LIBS is envisaged for in-vacuo surface characterization in the target exchange and analysis chamber (figure 1(c,d)). The sample carrier can be retracted after the exposure to plasma by a linear manipulator to the target exchange and analysis chamber, where it can be analysed by the laser based techniques. Mass spectrometry can be used for measurement of the desorbed deuterium, and a 2D optical spectroscopy system can be applied to detect the light intensity at a wavelength corresponding to a certain element on the surface. The plasma operation in PSI-2 can be continued with the retracted sample carrier using a removable plasma dump. The vacuum

valves separate the exposure and the analysis regions of the vessel.

III. SURFACE ANALYSIS TECHNIQUES

III.A THERMAL DESORPTION SPECTROMETRY (TDS)

Thermal desorption spectrometry (TDS) is a frequently applied technique for the analysis of the gas, i.e. hydrogen isotopes, retention in samples. The gas is retained in various trapping sites in the material. By heating up of the sample the gas atoms escape the traps, diffuse to the sample surface and are released from the sample. In a TDS apparatus (figure 2(a)), the samples are heated in a compact vacuum chamber by a surrounding furnace. The ramp rate of temperature is defined by the power of the furnace feedback controlled by the thermocouple measurements at the sample inside the vacuum chamber. Therefore, the technique is also often referred to as temperature programmed desorption (TPD). Partial pressures of different gas components are measured by a residual gas analyser (RGA), which is calibrated for the relevant masses by calibrating leaks. Typical temperature ramp rates are 0.1 K/s – 10 K/s. A faster ramp results in a higher signal but a lower temperature resolution in comparison with a slower ramp. The typical heaters which are used for TDS are infrared lamp or resistive furnace.

Figure 2(b) shows an example of thermal desorption spectra of mass 4 (deuterium D_2) for carbon fibre composite (CFC) samples exposed to PISCES-A deuterium plasma at different sample temperatures [7]. The peaks correspond to different trapping sites of D in CFC. The distribution of deuterium in the sample bulk and a finite diffusion time out of the sample during the heating ramp lead to the peak broadening. The integral of the curve gives the total amount of deuterium in the sample released as D_2 molecules. Various methods are available to analyse the TD spectra, including sophisticated numerical codes describing the transport of solute gases in solids such as TMAP [8] and CRDS [9].

Laser induced desorption (LID) is a method in which a laser is used to heat up samples. The method can be seen as TDS with an extremely fast (~1-10 ms) heating ramp. In this mode, the temperature resolution of the desorbed signal is completely lost, only the total amount can be measured. However, the method is fast and can be applied with a lateral resolution along the sample surface, e.g. to obtain a 2D mapping of the gas retention.

III.B SCANNING ELECTRON MICROSCOPY (SEM) AND FOCUSED ION BEAM (FIB)

Scanning electron microscopy (SEM) is an electron beam based method of the surface analysis. The incident e-beam of ~1-30 kV is scanned across the surface and causes emission of secondary electrons (SE mode of operation) and backscattered electrons (BSE mode of operation) (figure 3(a)).

The SE mode is the most frequently used operation mode of SEM. It provides the surface topology by measuring the intensity of secondary electrons, which is a function of the angle between the surface and the detector. The imaging is provided by the rastering (scanning) of the e-beam along the surface. Figure 3 (b) shows an example of an SEM image taken in the SE mode.

The BSE mode provides the information on the elemental composition of the surface. It uses the fact that the intensity of backscattered electrons is a function of atomic mass of the scattering element. Heavy elements on the surface correspond to a bright part of the image, while light elements result in a dark part of the image (figure 3(c)).

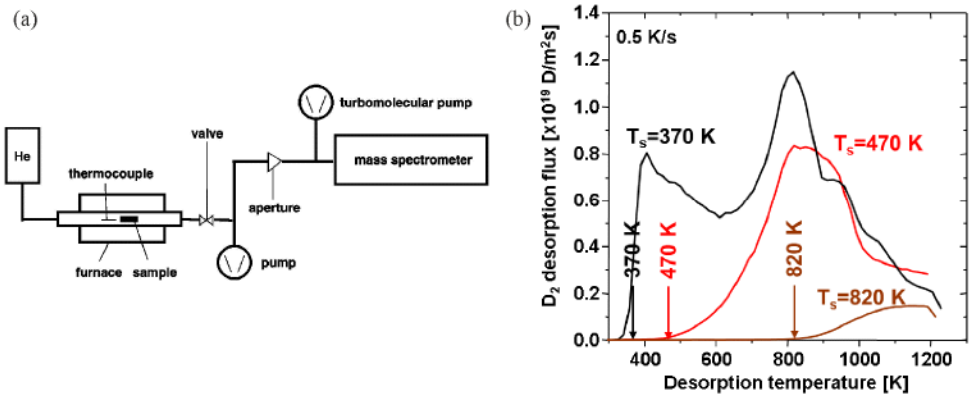

Figure 2. (a) Scheme of TDS system; (b) examples of spectra from thermal desorption. Temperatures at which the samples were exposed to deuterium plasma are indicated.

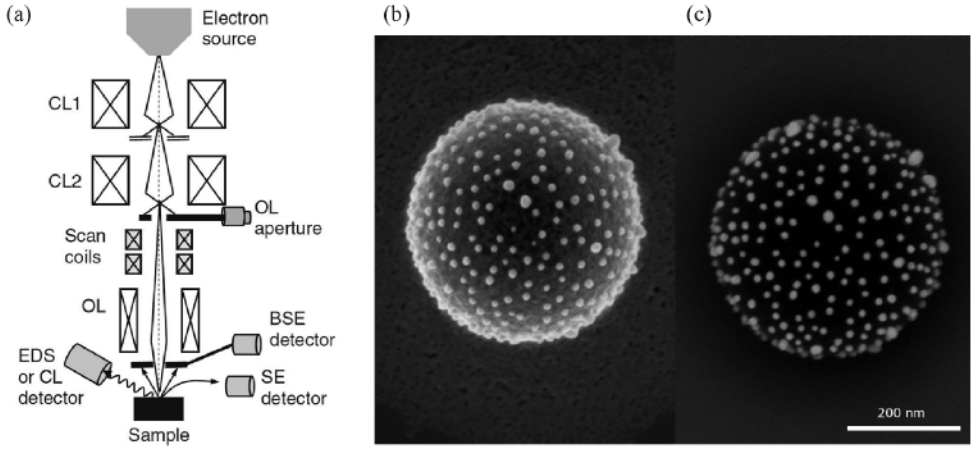

Figure 3. (a) Scheme of a SEM apparatus [10]; examples of (b) SE and (c) BSE operational modes of a SEM system: gold nanoparticles on polystyrol sphere. The SE image provides surface topography, while the BSE image gives material contrast [11].

The focused ion beam (FIB) technique is used for the nano-machining of the surface, e.g. surface cross-sectioning or preparation of small specimens. After the FIB treatment the surface is typically analysed by SEM. In a FIB instrument, an ion beam, typically Ga^+, is rastered over the sample causing well controlled sputtering. Figure 4 shows a scheme of the application of FIB for the surface cross-sectioning with the subsequent SEM analysis, as well as SEM images of the surface topology and cross-section of a nano-structured tungsten surface, also known as tungsten fuzz.

III.C ION BEAM ANALYSIS (IBA): NUCLEAR REACTION ANALYSIS (NRA) AND RUTHERFORD BACK-SCATTERING (RBS)

Ion beam analysis (IBA) techniques rely on a high energy (~1 MeV) ion beam produced, e.g., by a tandem accelerator. Several beam lines for different experiments are usually attached to the accelerator. In the example of the in-situ surface analysis given in figure1(a), the linear plasma device DIONISOS is attached to one of the beam lines delivering the ion beam from the accelerator. There are numerous IBA techniques available, with nuclear reaction analysis and Rutherford back-scattering being the most frequently used in the fusion related PMI research.

For nuclear reaction analysis (NRA), a ^3He beam in a range of energies 1-6 MeV is usually used, because ^3He reacts with many fusion relevant materials. The frequently used nuclear reactions with ^3He are: D (^3He,p) ^4He, ^{12}C (^3He,p) ^{14}N, ^{13}C (^3He,p) ^{15}N, ^9Be (^3He,p) ^{11}B and ^{11}B (^3He,p) ^{13}C, all of them having protons as one of the reaction product. The detection of further elements using other beams, i.e. H, D and Li, and reactions is possible. Figure 5(a) shows a measurement scheme of NRA.

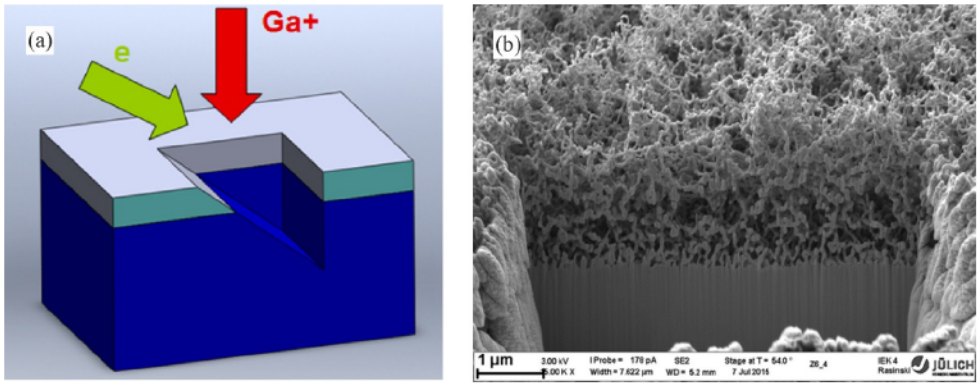

Figure 4. (a) Scheme of FIB application [12]; (b) SEM image of a FIB cross section for nano-structured surface of a tungsten sample exposed to He plasma, also known as tungsten fuzz [13].

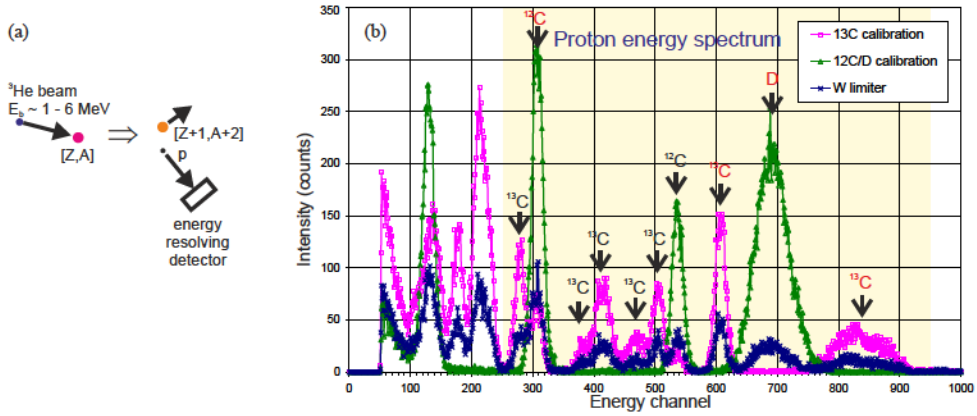

Figure 5. (a) Measurements scheme of NRA and (b) examples of NRA spectra for carbon-deuterium co-deposition layer on a tungsten test limiter after a $^{13}CH_4$ tracer injection experiment in TEXTOR as well as ^{12}C/D and ^{13}C reference samples [15]. Peaks from reactions which were used for the analysis are marked red.

The method can determine the absolute amount of material in a maximal analysis depth of ~1-10 μm, depending on the material and the ion beam energy. It has a moderate sensitivity of ~10^{15} atoms/cm^2. The amount of the material can be determined by a cross-calibration with a sample with a known amount of material, or by using available reaction cross-section. Most of the PMI relevant reactions are incorporated in the IBA data analysis software SIMNRA [14]. A typical lateral resolution of ~1 mm, corresponding to the beam diameter, can be reduced down to ~10 μm using the μ-NRA technique. NRA has a poor depth resolution, which can be improved by the use of beams of different energies and therefore different probing depths for the same sample. Figure 5(b) shows examples of NRA spectra for ^{12}C/D and ^{13}C reference samples and from a mixed ^{12}C/^{13}C/D layer deposited on a tungsten test limiter in the tokamak TEXTOR [15].

For Rutherford back-scattering (RBS), a ^{4}He beam in a range of energies 1-6 MeV is usually used. A ^{3}He beam can also be used, thus RBS and NRA measurements can be combined. However, the market price of ^{3}He gas is significantly higher than of ^{4}He. Figure 6 shows a scheme of the RBS technique and an example of RBS spectrum. The energy of backscattered beam particles is $E_R = K(m_b, m_s, \theta, d) \times E_b$, where the kinematic factor K is a function of the beam particle mass m_b, scattering particle mass m_s, scattering angle θ and depth d and E_b is the beam energy. The method provides quantitative depth profiles of elements on the sample surface. The maximal analysis depth is typically ~5 μm. The technique has a high sensitivity ~10^{12} atoms/cm^2. The latera resolution is of ~1 mm (beam diameter), similarly to NRA. RBS suffers from a pure discrimination of heavy elements with similar masses and has a limited applicability for mixed material layers and high-Z substrates.

III.D SECONDARY ION MASS SPECTROMETRY (SIMS)

Secondary ion mass spectrometry (SIMS) utilises ion probing beams in a range of energies of ~1-30 keV. The primary beam causes the emission of secondary ions from the sample, which are then analysed by a mass spectrometer delivering information on the elemental surface composition. Figure 7(a) shows the scheme of a SIMS apparatus. It usually incorporates at least two primary ion beam sources, e.g. an oxygen primary ion beam for probing of electropositive surface constituents and a caesium primary ion beam for electronegative elements.

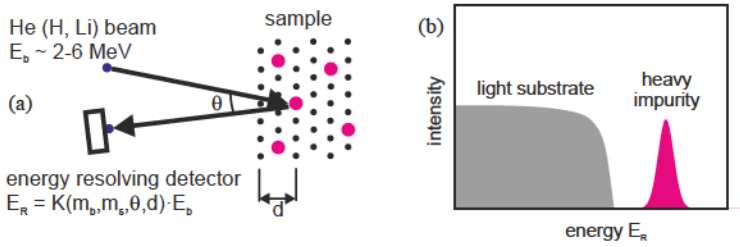

Figure 6. (a) Measurements scheme of RBS and (b) typical RBS energy spectrum for a heavy impurity on a light substrate.

In some SIMS devices, an additional ion beam is used for the surface sputtering to obtain a high quality depth profiling. The method has a high lateral resolution of ~100 nm - 1 μm. The modern SIMS devices, especially those equipped with a time-of-flight (TOF) mass spectrometer, have a high mass resolution and are able to resolve different molecular fragments. One drawback of the method is that only sputtered ion are analysed. The neutrals, which are the majority of sputtered particles, get lost. The process of the production of secondary ions is complex. Therefore, SIMS typically delivers qualitative but not quantitative information on the material composition. If the depth profiling is applied, the sputtering rate of the SIMS apparatus can be calibrated by measuring the depth of the SIMS crater by a surface profilometer.

Figure 7(b) shows an example of the SIMS depth profiling of a mixed layer deposited on a collector probe during a full experimental campaign in the tokamak TEXTOR [17]. The SIMS measurement was stopped when the signals dropped by a factor of two, corresponding to the bottom of the layer. Then the crater depth of 1.1 μm was measured by a stylus profilometer, thus, the sputtering rate of SIMS was obtained. The layer consists mainly of carbon from the normal plasma operation, with carbon being the main plasma impurity in TEXTOR, and boron from the boronisation wall conditioning. Seven boronisations were performed during the experimental campaign, which is reflected in the SIMS depth profiling.

IV. MEASUREMENTS OF EROSION AND DEPOSITION

IV.A QUARTZ MICROBALANCE (QMB)

The quartz microbalance (QMB) technique uses the fact that the quartz (SiO_2) crystals have a resonant frequency changing with their mass. Quartz crystal microbalance (QCM) is a different notation for the technique. For commercially available quartz crystals for QMB, the resonant frequency is usually a few MHz, decreasing when gaining mass with a rate of ~10 08 g/Hz, thus providing a high mass sensitivity corresponding to about one monolayer of deposition on the quartz surface. Electronics measuring the crystal frequency have to be placed close to the detector, which increases the complexity of the QMB application in fusion devices. Another drawback is the sensitivity of the resonant frequency on the surrounding temperature. In fusion devices the particle flux is typically accompanied by a significant heat flux. Therefore, the influence of temperature on the QMB signal has to be monitored. It is often done by a second, reference, quartz, which is placed close to the first, measuring quartz. The reference quartz has similar temperature as the measuring one, but is mechanically covered to prevent any deposition on it and to keep its initial mass. Thus, the reference quartz has only the temperature response and can therefore be used for the temperature compensation of the measuring quartz.

The piezoelectric constant of quartz drops sharply for temperatures >300°C and reaches zero at the Curie point of 573°C. Therefore, QMB systems are typically installed in remote areas of a fusion device, where the heat flux is low. Material eroded from plasma facing components under the plasma impact is transported to remote areas where it is collected by QMB systems. Therefore, although actually measuring deposition, QMB systems are used as in-situ erosion monitors of the plasma facing components.

Figure 8 shows the scheme of QMB application in a plasma device as well as photographs of commercially available QMB systems [18] and of a

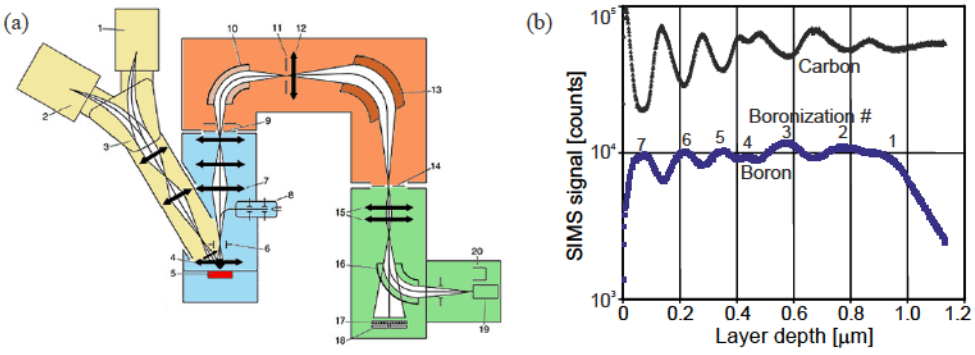

Figure 7. (a) Scheme of a SIMS apparatus: (yellow) primary ion column consisting of (1) and (2) ion sources, (3) primary beam mass filter, (4) immersion lens, (blue) secondary ion extraction system consisting of (5) specimen, (6) dynamic transfer system, (7) transfer optical system, (8) electron flood gun, (orange) mass spectrometer consisting of (9) entrance slit, field aperture, (10) electrostatic analyser, (11) energy slit, (12) spectrometer lens, (13) electromagnet, (14) exit slit, (green) detection system consisting of (15) projection lenses, (16) electrostatic sensor, (17) and (18) ion detectors and (19) Faraday cup [16]; (b) SIMS depth profile of a layer deposited on a collector probe installed for one experimental campaign in TEXTOR showing anti-correlated signals of carbon from the tokamak operation and boron from the boronizations [17].

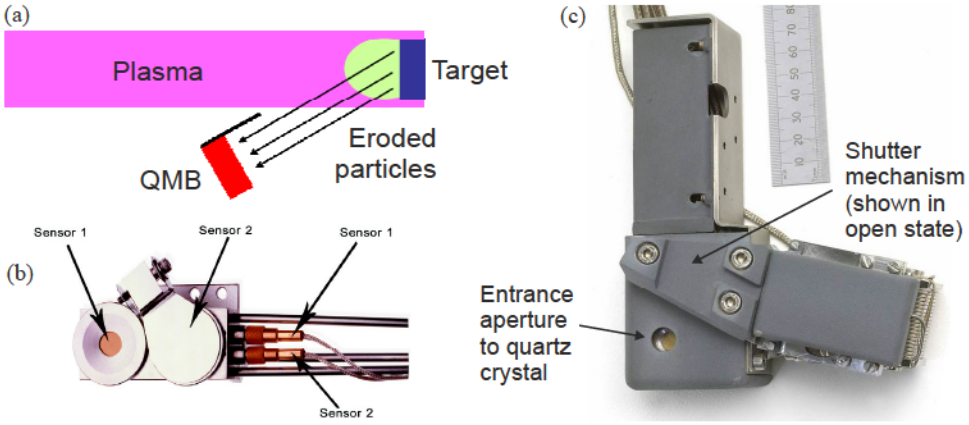

Figure 8. (a) Measurement scheme of QMB; (b) commercial dual QMB sensor [18]; (c) QMB diagnostic used at JET is protected by a graphite cover against heat loads [19,20].

QMB system for the in-situ application in the tokamak JET [19,20].

IV.B APPLICATION OF MARKER TILES

There are numerous methods which can quantify the amount of deposition on a certain sample or a tokamak wall tile. It is significantly more complicated to measure the erosion, something which is absent. A well-established method is marker techniques. Markers have to be prepared on samples or wall tiles in advance, before their exposure. The wall components equipped with markers are also called "smart tiles". Typically the installation of "smart tiles" at the wall needs the air vent of the vessel, which is done between experimental campaigns. Therefore, unlike the in-situ QMB method, the marker technique is campaign-averaged. Markers can be e.g. well-defined layers of material deposited on a substrate in a combination suitable for the applied surface analysis techniques. The marker layers are characterised before and after the exposure. The difference is then the amount of eroded material. Techniques like RBS or SIMS are often used for the marker characterisation.

Another approach of markers is the application of reference points on the sample surface which are not subjected to erosion. The reference points can be e.g. recessed grooves or pits, which bottom is shaded from the eroding plasma flux. Figure 9(a) shows a marker tile of the main toroidal limiter in TEXTOR made of isotropic graphite, which was used to determine the erosion-deposition pattern over the full tokamak campaign [21]. 3 × 10 drill recessions were used as the reference points. It was found out by SIMS that up to several µm of deposition was accumulated in the recessions during the experimental campaign. It was taken into account when comparing the surface profiles measured by the optical surface profilometry before and after the exposure (figure 9(b)). A full erosion-deposition pattern of the tile surface was reconstructed by combining the surface profiles across the recessions done in both toroidal and poloidal directions (figure 9(c)).

REFERENCES

[1] Ch. Linsmeier et al, *Material testing facilities and programs for plasma-facing component testing*, Nucl. Fusion **57** (2017) 092012.

[2] A. Kreter, *Reactor-relevant plasma-material interaction studies in linear plasma devices*, Fusion Sci. Technol. **59** (2011) 51.

[3] G.A. Somorjai, *Introduction to Surface Chemistry and Catalysis*, published by John Wiley & Sons, ISBN 978-0471031925 (1994).

[4] G.M. Wright et al., *An experiment on the dynamics of ion implantation and sputtering of surfaces*, Rev. Sci. Instrum. **85** (2014) 023503.

[5] R.P. Doerner, M.J. Baldwin and K. Schmid, *The influence of a beryllium containing plasma on the evolution of a mixed-material surface*, Phys. Scr. **T111** (2004) 75.

[6] A. Kreter et al., *Linear plasma device PSI-2 for plasma-material interaction studies*, Fusion Sci. Technol. **68** (2015) 8.

[7] A. Kreter et al, *Fuel retention in carbon materials under ITER-relevant mixed species plasma conditions*, Phys. Scr. **T138** (2009) 014012

[8] G.R. Longhurst, *TMAP7 User Manual*, Idaho National Laboratory, INEEL/EXT-04-02352 (2008).

[9] M. Oberkofler, M. Reinelt, Ch. Linsmeier, *Retention and release mechanisms of deuterium implanted into beryllium*, Nucl. Instrum. Meth. B **269** (2011) 1266.

[10] *Low Voltage Electron Microscopy: Principles and Applications*, Editors: D.C. Bell, N. Erdman,

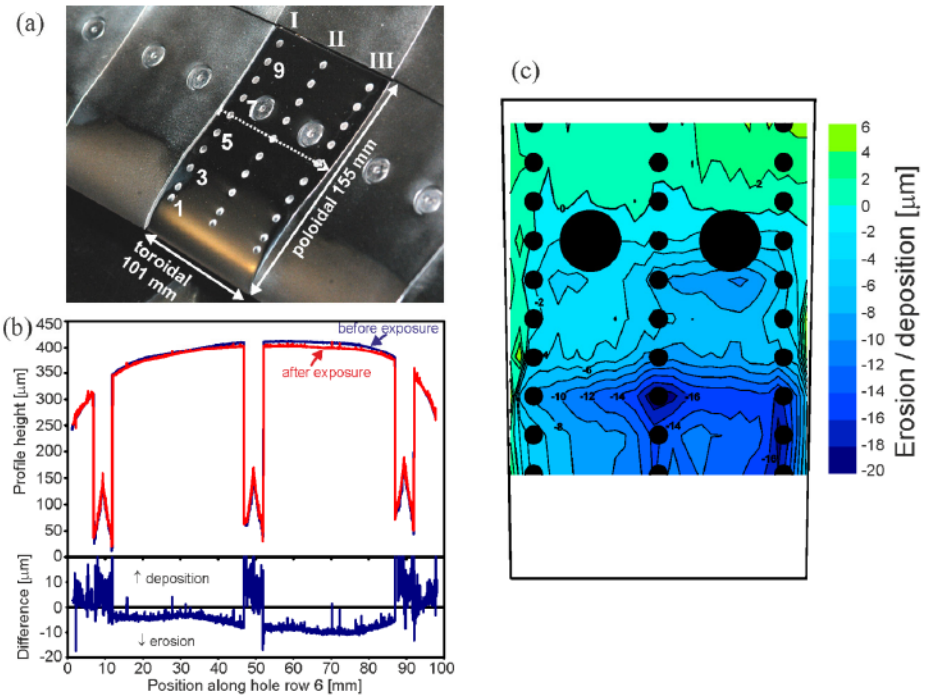

Figure 9. (a) View of the special limiter tile in TEXTOR after the exposure for one experimental campaign [21]. The dimensions of the tile and the positions of the marker holes are indicated. The dotted line represents the position and the direction of the X axis in (b); (b) surface height profile measured by optical profilometry before and after the exposure; (c) 2D reconstruction of the erosion and deposition pattern of the limiter tile. Negative values represent erosion, positive values deposition.

published by John Wiley & Sons, ISBN: 9781119971115 (2013), DOI: 10.1002/9781118498514.

[11] Carl Zeiss Microscopy GmbH, *ZEISS Gemini Optics - High Resolution Images On Real World Samples*, EN_42_050_016, CZ 05-2015, http://www.zeiss.com/geminisem.

[12] M. Rasinski, private communication.

[13] M. Wirtz et al, *Influence of helium induced nanostructures on the thermal shock performance of tungsten*, Nuclear Materials and Energy **9** (2016) 177.

[14] M. Mayer, *SIMNRA User's Guide*, Report IPP 9/113, Max-Planck-Institut für Plasmaphysik, Garching, Germany (1997).

[15] A. Kreter et al, *Investigation of carbon transport by $^{13}CH_4$ injection through graphite and tungsten test limiters in TEXTOR*, Plasma Phys. Control. Fusion **48** (2006) 1401.

[16] J.W. Valley et al., *4-Ion Microprobe Analysis of Oxygen, Carbon, and Hydrogen Isotope Ratios*, Reviews in Econ. Geology **7** (1998) 73.

[17] A. Kreter et al., *Long-term carbon transport and fuel retention in gaps of the main toroidal limiter in TEXTOR*, J. Nucl. Mater. **438** (2013) S746.

[18] INFICON, *Front Load Dual Sensor*, cibe23a1-a, http://www.inficon.com.

[19] H.G. Esser et al., *Effect of plasma configuration on carbon migration measured in the inner divertor of JET using quartz microbalance*, J. Nucl. Mater. **337-339** (2005) 84.

[20] A. Kreter et al., *Nonlinear impact of edge localized modes on carbon erosion in the divertor of the JET tokamak*, Phys. Rev. Lett. **102** (2009) 045007.

[21] A. Kreter et al., *Long-term erosion and deposition studies of the main graphite limiter in TEXTOR*, Phys. Scr. **T128** (2007) 35.

MICROWAVE AND FAR INFRA-RED DIAGNOSTICS

A. Krämer-Flecken
Institut für Energie und Klimaforschung / Plasmaphysik, Forschungszentrum Jülich
D-52425, Jülich, Germany

I. INTRODUCTION

The measurement of plasma quantities is a difficult task since the plasma cannot be treated like *normal* material. The properties of a plasma with an electron density $\leq 1 \times 10^{20}\,\mathrm{m}^{-3}$ and temperatures up to several keV asks for sophisticated probes. Any measurement of plasma quantities with solid probes will yield interactions with the plasma and cause a perturbation of the measured quantity. Inside a hot plasma those methods are not applicable, since they cause a contamination which, on the long run, ends in a disruption of the plasma. Therefore it is necessary to use optical properties as refraction and reflection as tool for plasma diagnostic. Plasmas in fusion experiments are transparent when looked with human eyes. However, choosing the right wavelength where refraction effects are large, plasma properties can be accessed. The propagation of millimetre and sub millimetre waves in a plasma is quite sensitive to refraction and reflection. In addition those waves are less demanding regarding their installation requirements on fusion facilities either tokamak or stellerator due to the little space requirements. Microwave radiation can easily be guided in wave guides, either oversized or fundamental ones, which can be bend around corners and which widens the application range. Furthermore due to the rapid growing application in telecommunication, active as well as passive microwave components have become less expensive and more powerful.
Refraction and reflection allows to obtain information on the plasma density, when actively probed by microwaves. An other way of diagnosing a hot plasma is the measurement of the emitted radiation in the microwave range. With both methods main plasma parameters as the electron density and the electron temperature can be measured quite accurate and reliable. However, also the measurement of fluctuations in density and temperature and the determination of the plasma current density are possible with sophisticated microwave diagnostics. Using more than one observation location and performing cross correlation analysis yields information on the propagation of the plasma and the properties of turbulent structures can be achieved under certain assumptions. Those measurements contribute a lot on the understanding of turbulent transport and the interaction of different scales from microscopic (*turbulence*) to macroscopic (*flows*).
In the following section the propagation of electro magnetic waves in a plasma is reviewed. Sections III to VI are devoted to different diagnostic techniques. Section VII gives an outlook on future applications.

II. THE DISPERSION RELATION FOR THE PROPAGATION IN PLASMAS

Starting point is the *Appleton-Hartree* equation [1] which relates the refractive index N to the probing frequency ω.

$$\begin{aligned} N^2 &= 1 - \frac{A \cdot (1-A)}{1 - A - 1/2B^2 sin^2\theta \pm C} \qquad (1)\\ A &= \frac{\omega_{pe}^2}{\omega^2} \quad ; \quad B = \frac{\omega_{ce}}{\omega} \\ C &= \left[\left(1/2B^2 sin^2\theta\right)^2 + (1-A)^2 B^2 cos^2\theta \right]^{1/2} \end{aligned}$$

Here ω_{pe} denotes the plasma frequency and ω_{ce} the cyclotron frequency:

$$\omega_{pe} = \sqrt{\frac{n_e e^2}{\epsilon_0 m_e}}; \quad \omega_{ce} = \frac{eB}{m_e \gamma} \qquad (2)$$

γ takes into account relativistic effects, e denotes the electron charge, m_e the electron mass, n_e is the electron density and B the local magnetic field. The angle θ in Eq. 1 denotes the angle between the wave vector and the magnetic field. In the case $\theta = 0$ the propagation is parallel to the magnetic field. For $\theta = \pi/2$ we have a perpendicular propagation. In this case two solutions for the refractive index are possible, depending on whether the electric field vector of the wave **E** is parallel to the magnetic field (*O-Mode*) or perpendicular (*X-Mode*). The refractive index for both cases is given in equ. 3.

$$\begin{aligned} O-Mode \qquad N_O^2 &= 1 - \frac{\omega_{pe}^2}{\omega^2} \qquad (3)\\ X-Mode \qquad N_X^2 &= 1 - \frac{\omega_{pe}^2\left(\omega^2 - \omega_{pe}^2\right)}{\omega^2\left(\omega^2 - \omega_{pe}^2 - \omega_{ce}^2\right)} \end{aligned}$$

All microwave diagnostics studying the propagation of millimetre waves are based on these equations, regardless of being applied in fusion plasmas, telecommunication, surface inspection or climate research.

III. INTERFEROMETRY

A standard tool for measuring the electron density n_e within a plasma is an interferometer. In this case we have the refractive index for *X-Mode* which is investigated with the additional assumption that $\omega_{ce}/\omega \ll 1$, neglecting the effects of the magnetic field. The measurement of the electron density is done by comparing the phase change of two wave trains, one travelling through the plasma, and another travelling through vacuum or air and which is used as reference. The phase change for a given wave number k and frequency is given by:

$$\Delta\Phi = \int (k_{plasma} - k_0) dl = \int (N-1)\frac{\omega}{c} dl \qquad (4)$$

The above equation can be rewritten with the use of the critical electron density n_c at the cut-off layer where $N = 0$. From Eq. 2 we achieve the critical density as

$$n_c = \frac{\epsilon_0 m_e \omega^2}{e^2} \qquad (5)$$

yielding for the phase change:

$$\begin{aligned} \Delta\Phi &= \frac{\omega}{c} \int \left(\sqrt{1 - \frac{n_e}{n_c}} - 1 \right) dl \\ &\approx \frac{\omega}{2cn_c} \cdot \int n_e dl \end{aligned} \qquad (6)$$

Here, it has been assumed that $n_e \ll n_c$, truncating the expansion of the square root expression after the first term. Such a phase change can be measured by an interferometer.
Several types of interferometers exist. Two arm interferometer like *Michelson Interferometer* or *Mach-Zehnder Interferometer* (fig. 1) and multiple beam in-

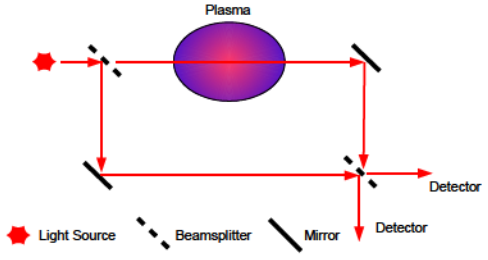

Figure 1: Schematic view of a Mach-Zehnder Interferometer

The major difference between the Michelson- and the Mach-Zehnder-Interferometer is the fact that the reference as well as the plasma path are only passed once in the Mach-Zehnder set-up. Two major drawbacks of all those types of interferometer are:

- The ambiguity of phase changes for $\Delta\Phi = n \cdot \pi$
- Amplitude variations due to refraction or absorption of the beam

To overcome those problems the frequency of the reference wave is shifted with a rotating grating. The detector will mix the two incoming frequencies from the plasma path ω_1 and the reference path ω_2 and yield an intermediate frequency $\Delta\omega_0 = \omega_1 - \omega_2$ and its higher harmonics. Such a detection scheme is called a heterodyne receiver. An additional phase change due to the plasma yield $\Delta\omega = \Delta\omega_0 + d\Phi/dt$. This allows a distinction between positive and negative phase changes.
To allow for interferometric measurements of n_e the following conditions have to be fulfilled.

- Sufficient power level for splitting the beam into radial separated chords and enough to detect at the same time 1 % modulation in density with a time resolution $\leq 100\,\mu s$
- No cut-offs or resonances in the plasma for the desired frequency deduced by the maximum n_e which can be achieved
- Small angular deviation of the beam ($\alpha \leq 10\,\text{mrad}$)

An interferometer-polarimeter of Mach-Zehnder type [2] using a HCN-laser operating at a frequency of 800 GHz was installed at TEXTOR (see fig. 2) where the signals are detected by pyroelectric detectors. As can be seen from Eq. 6 the interferometric phase shift is integrated along the line of sight yielding line averaged densities. However, of importance is the local electron density and its profile. To fulfil an accurate calculation of the local density from the phase shift, tomographic methods have to be used. The phase shift has to be measured within a poloidal cross section of the tokamak with several chords at different radial position. Therefore assumption about the shape and symmetry of the plasma have to be made. With an inversion procedure (Abel-Inversion) a density profile is calculated.
A draw back of the previous mentioned short wavelength is the sensitivity to vibrations of the interferometer frame. Already small vibrations yield a disturbance of the path length and therefore an error in the phase measurement. To overcome this problems (i) the optics has to be mounted in a rigid frame or (ii) two different wavelength should be used. The shorter wavelength measures the disturbance of the diagnostic and the longer wavelength measures the refractive effects due to the plasma. From the geometrical point of view a multi chord interferometer is best suited for devices with circular plasma cross section. In D-shaped plasma only a few chords can be realized, mainly due to the restricted access from the top of the vessel. In this case other diagnostics are needed to calculate the required density profiles.

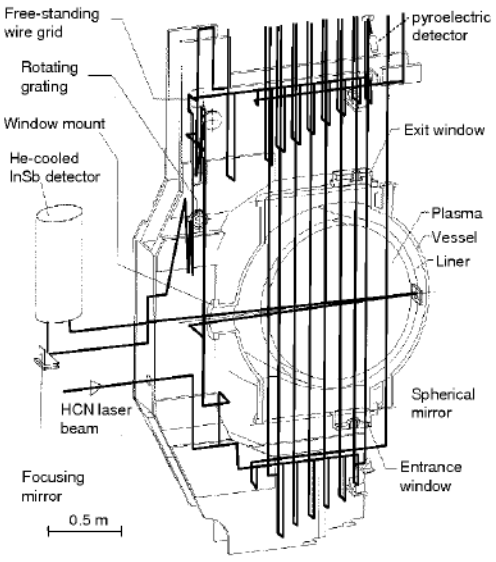

Figure 2: Schematic view of the nine channel HCN-interferometer-polarimeter as it was installed at TEXTOR. The thick lines show the optical path of the nine vertical, the horizontal and the reference channels.

A. Dispersion Interferometry

The main draw back of a Mach-Zehnder or Fabry-Perot interferometer is the sensitivity to vibrations, specially for large devices like ITER and DEMO. This drawback can be overcome by using a second interferometer with a different wavelength and operated at the same path as the first one. or by using a dispersion interferometer [3, 4] which is not sensitive to phase changes due to vibrations. Probing and reference path use the same geometrical path but at different frequencies. Therefore a non linear crystal is used which generates the 2^{nd} harmonic of the incoming frequency. Both waves at 1^{st} and 2^{nd} harmonic propagate through the plasma. After passing the plasma a second non linear crystal generates the 2^{nd} harmonic of the incoming frequency with the phase information due to passing the plasma. after eliminating the 1^{st} harmonic in a frequency selective filter the interferometer pattern of the two 2^{nd} harmonic frequencies is detected by a photo detector (see fig. 3). The phase difference is the difference between twice the phase of the fundamental frequency and the phase of the 2^{nd} harmonic travelling through the plasma an can be expressed by:

$$\Delta\Phi = \frac{\omega}{c}\int \left[N(\omega) - N(2\omega)\right]dl \qquad (7)$$

With the equation for the refractive index N_O the phase change can be written as:

$$\Delta\Phi = \frac{3e^2}{8\pi\epsilon_0 m_e c^2}\lambda < n_e l > \qquad (8)$$

with λ being the probing wavelength and $< n_e l >$ the line integrated density. It should be noted that $\Delta\Phi$ increases with the used wave length. In most systems the incoming laser light is reflected at a mirror in the vessel. Due to material erosion and deposition such mirrors show a degradation of reflectivity. A compromise for the used wave length is found in CO_2-Laser at 28.3 THz corresponding to $\lambda = 10.6\,\mu$m. Such a system is installed e.g. at LHD [5] for density control. It has a temporal resolution of 300 µs and a sensitivity of $< n_e l >_{min} \leq 3 \times 10^{17}\,\mathrm{m}^{-2}$. Also at W7-X a dispersion interferometer is installed to measure the line averaged density in the plasma [6]

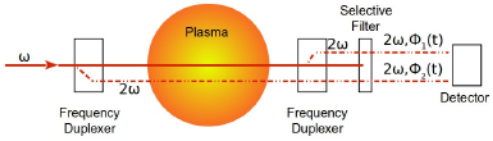

Figure 3: Principle scheme of a dispersion interferometer from [7].

IV. POLARIMETRY

In a tokamak the estimation of the current profile is of importance because the magnetic configuration is a superposition of toroidal and poloidal magnetic field. The latter is caused by the plasma current. Due to the magnetic field the refractive index is different for the two circular components of a linear polarized incident wave. In the case of a plasma current, generating a poloidal magnetic field, the interferometer-polarimeter set-up shown in fig. 2 is sensitive to the parallel component of the poloidal magnetic field [2]. For a propagation of the wave parallel ($\theta = 0^o$) to the magnetic field component, the refractive index can be achieved from Eq. 1 retaining only first order terms in B, then we get:

$$N^2_{X,O} \approx 1 - A \pm AB cos\theta \qquad (9)$$

The difference in N causes a different propagation speed of the O- and X-mode wave, which causes a rotation of the electric field vector of a linearly polarized wave (*Faraday Rotation*). This is a rotation of the polarization plane. The phase change along the propagation direction (z-axis) is given by:

$$\Delta\Phi = \frac{\omega}{c}\left(N_X - N_O\right) z \qquad (10)$$

The Faraday rotation angle α depends only on Bdl and n_e. It can be expressed by the measured phase

change and making use of Eq. 9 where only the first order terms in ω_{ce}/ω are considered.

$$\begin{aligned}\alpha &= \frac{\Delta\Phi}{2} = \frac{e}{2\,m_e\,c}\int \frac{n_e\,\mathbf{B}\cdot\mathbf{dl}}{n_e\,(1\,-\,n_e/n_c)^{1/2}} \\ &\approx \frac{e}{2\,m_e\,c}\int \frac{1}{n_c}\cdot n_e\mathbf{B}\cdot\mathbf{dl} \qquad (11)\end{aligned}$$

This last approximation is valid if the ratio of electron density to critical density (n_c) is less than one. With the measurement of α the poloidal magnetic field can be estimated. The approximation is only depending on n_c which itself is a function of the used wavelength and the magnetic field, so that a numerical approach can be expressed by

$$\begin{aligned}\alpha\,[degree/cm] &= 1.5\times10^{-17}\,\lambda^2\,[mm] \\ &\times\ n_e\,[cm^{-3}]\ B\,[Gauss] \qquad (12)\end{aligned}$$

After the measurement of the poloidal magnetic field at different radial positions the plasma current profile $j(r)$ as well as the q-profile can be estimated.

V. REFLECTOMETRY

In contrast to interferometry reflectometry measures the reflected signal of a probing microwave (ω_{ref}) from a cut-off layer (R_{co}) corresponding to a cut-off frequency (ω_{co}) in the plasma. The propagation time and the phase of the reflected wave contains information on the position of the cut-off layer and information on the density fluctuations [8]. At R_{co} the refractive index is $N_{O,X} = 0$. Beside the frequency the cut-off position depends on the polarization as well (e.g. selected by the orientation of the launching and receiving antenna). The phase change can be calculated by Eq. 13,

$$\Phi = \frac{2\omega}{c}\int_{R_{edge}}^{R_{co}} N_{X,O}(R,\omega)dR - \frac{\pi}{2} \qquad (13)$$

where c denotes the speed of light and $N_{X,O}$ the refractive index for *X*- or *O-mode* polarization as deduced from Eq. 3. At the R_{co} a phase jump of $\pi/2$ will take place. Reflectometry can be done in *O-Mode* and *X-Mode*, respectively. In case of *X-Mode* reflectometry N_X is a function of the magnetic field and it has the advantage that $n_e(r) = 0$ at $\omega_{co} = \omega_{ce}$ which offers a stable initialization condition for the measurement of density profiles. In contrast to *O-mode* reflectometry which needs a monotonic increasing density profile to access all radii, *X-mode* reflectometry covers a larger radial range. Furthermore the smaller wave length yield a smaller radial errorbar of the measurement. Concerning its accuracy the radial resolution depends on the density scale length and the fluctuation level. Reflectometry is therefore a good tool for plasma density profile measurements in the gradient region and for density fluctuation (turbulence) measurements. As in interferometry where the two signals are compared to get the phase difference in reflectometry the reflected signal is compared to a signal which travels a well known delay line to obtain the phase information.
An overview on the diagnostic potential of the reflectometry can be found in [9].

A. Density Profiles

The determination of the density profile was somewhat difficult in the past due to the large sweep times of the available microwave generators. The sweep time of the generators should be less or equal the life time of the fluctuation which is in the order of 10-20 µs. Today's technique allows a sweep time less than $2\mu s$ using hyperabrupt varactor tuned oscillators (HTO) [10, 11, 12, 13]. In this case the fluctuations can be considered as frozen during one sweep of the oscillator. For profile measurements both polarizations can be used. Independent from the polarization the net time delay (τ) is given by:

$$\tau(f) = \frac{d\Phi}{d\omega} = f_B(\frac{df}{dt})^{-1} \qquad (14)$$

Here f_B denotes the beat frequency of the reference and the reflected wave and $d\Phi/d\omega(f)$ denote the group delay. It is essential to know the linear frequency response on the the generator voltage, because it causes uncertainties in the estimation of the time delay. The density profile is reconstructed from an initialization procedure. Furthermore the sampling rate for such a system should be large, so that the fluctuations can be treated as frozen. In today set-ups a sampling frequency up to 50 MHz and more is necessary to have a good frequency resolution of the beat frequency during one sweep. In fig. 4 the set-up of an instrument designed for stellarator W-7X is shown [14]. The instrument is planned for the measurement of the electron density profile in front of the ICRH antenna. To improve the coupling of the ion cyclotron waves the knowledge of the density profile in front of the antenna is necessary. The profile reflectometer consists of two frequency bands E (60 GHz to 90 GHz) and W (75 GHz to 110 GHz). The VCO frequency is controlled by a signal generator (Red Pitaya). The signals are modulated by a single side band modulator before multiplexing and launching into the plasma. The reflected signal is mixed with the reference signal coming from a delay line (DL).

B. Turbulence and Rotation Measurements

With one launching and receiving antenna information on the phase fluctuation can be retrieved from reflectometry. This can be related to density fluctuations as long as the phase fluctuation are small and not saturated. However, at the plasma edge the

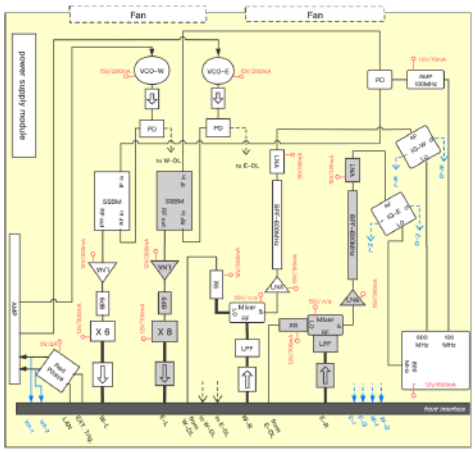

Figure 4: Principle scheme of the density profile reflectometer

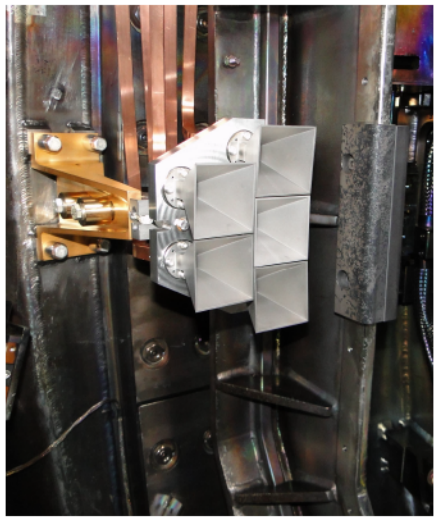

Figure 5: Photograph of the installed correlation reflectometry antenna at AUG. The middle antenna in the right column launches the microwave and the surrounding antenna measure the reflected signal.

turbulence level becomes large and small angle scattering effects disturb the measurement. It makes the estimation of the turbulence level more complicated and sometimes even impossible.

The use of more than one receiving antenna surrounding the launcher allows the calculation of cross correlation as function of the toroidal and poloidal separation of antennae. The so called Correlation Reflectometry (CR) is often used to measure turbulence properties. An example of the antenna head for the Correlation Reflectometry at AUG is shown in fig. 5. Correlation reflectometry is sensitive to long wavelength turbulent structures with wave numbers $k_\perp \leq 3\,\mathrm{cm}^{-1}$ [15]. Correlations can be achieved by (i) an array of antennae measuring at toroidally and/or poloidally separated positions or (ii) by two reflectometers operating at different frequencies to obtain radial information on the turbulence structure and on the radial transport. A combination of both methods is possible as well. Using antennae arrays poloidally or toroidally separated and aiming on a common focal point yields further information on the poloidal or toroidal structure of the turbulence, e.g. poloidal correlation length ($\lambda_\perp$) and decorrelation time (τ_{dc}). However, the propagation time Δt between receiving antenna must fulfil the condition $\Delta t = \Delta s / v_\perp \leq \tau_{dc}$, where Δs is the distance between the correlated antennae. In fig. 6 an example from poloidal CR shows the complex amplitude and cross phase spectra deduced from the quadrature detectors.

From the complex amplitude spectrum different types of fluctuations can be recognized. Most pronounced are broad band fluctuations (BB)and the quasi coherent modes at low and high frequency (QC LF and QC HF). The different propagation velocities of the quasi coherent mode are obvious from the different slopes in the cross phase spectrum. For signals from poloidal separated antennae the angular velocity (Ω_{turb}) of the turbulence is measured from the cross phase (Φ) between the signals from two or more antennae [16].

$$\Omega = \frac{2\pi\ \alpha}{d\Phi/df}, \tag{15}$$

where α is the angle between the antennae. With the assumption that the additional phase velocity of the turbulence is small compared to the poloidal plasma velocity $\Omega_{turb} \approx \ \Omega_{E\times B}$ is valid. This allows to estimate the radial electric field E_r from the measured turbulence rotation. With $v_{turb} = \Omega_{turb} \cdot r_c$, where r_c is the radius of the reflection point the radial electric field is calculated as $E_r = v_{turb} \cdot B$. This gives the possibility to compare the measure E_r from reflectometry with neoclassical calculation which is important for to deduce the influence of anomalous transport.

In case of a high sampling rate of the reflected reflectometry signal it is also possible to analyse velocity oscillations. Such oscillations go along with the existence of zonal flows and geodesic acoustic modes. In this cases the velocity oscillations introduce an additional velocity shear which could reduce turbulent transport.

In a paper by A. Krämer-Flecken et al. [17] it has been demonstrated that poloidally and toroidally separated antennae allow the determination of the inclination angle of the magnetic field line at r_c. The projection of the distance of different antennae combinations on the direction of $v_\perp, B_\perp$ (see fig. 7) yield different values for delay time Δt. With the assump-

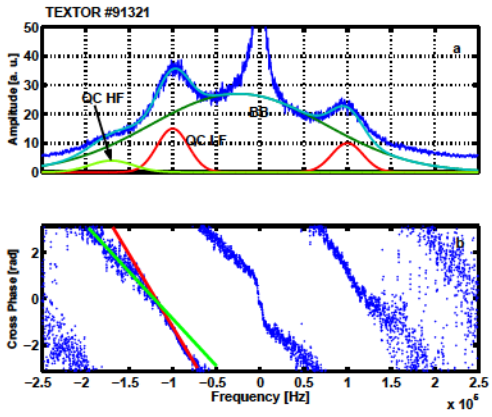

Figure 6: (a) Amplitude spectrum obtained from reflectometry showing the different fluctuation components. (b) The different propagation velocities are determined from the slopes in the cross phase spectrum.

tion of a constant $v_\perp$ the ratio of the measured delay time is proportional to the magnetic pitch angle.

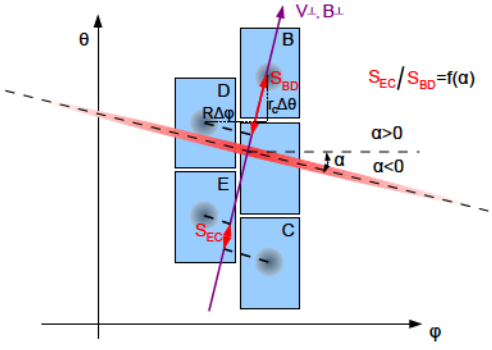

Figure 7: Schematic view of an antennae array. It shows the projection on the $v_\perp$ axis for combinations BD and EC.

Correlation reflectometers are installed at different devices. The first one was installed at T-10 [18]. A similar system was operated at TEXTOR [16]. More recent applications of correlation reflectometry can be found at AUG [19] and the stellarator W7-X [20].

An alternative method to deduce plasma velocity is the Doppler reflectometry [21]. Here the plasma velocity is deduced from the Doppler shift of the receiving microwave. Instead of measuring the 0^{th} order reflection which is used in standard reflectometry higher order diffraction is used for Doppler reflectometry (see fig. 8). In most cases a tilted antenna (not perpendicular to the flux surface) is used for the launching and receiving microwave. In this case the tilting angle is adjusted to measure the -1^{st} order of diffraction and a monostatic antenna arrangement is sufficient. Such an set up is sensitive to different wave number values ($k_\perp$) depending on the tilt angle. Selecting the tilt angle of the antenna allows to measure a certain wave number. This is the major advantage of Doppler reflectometry: measurement of turbulence at different wave numbers to obtain a wave number spectrum. The relation between the measured wave number and the tilt angle is given by:

$$k_\perp = 2k_0 \sin \alpha_{tilt} \tag{16}$$

Here k_0 is the wave number of the probing microwave in vacuum. If the reflection layer in the plasma is propagating with a velocity $v_\perp$, a frequency shift of $\Delta\omega = -v_\perp \cdot k_\perp$ is observed. As for CR, Doppler reflectometry is able to deduce the radial electric field when the phase velocity of the turbulence can be neglected. Doppler reflectometry extents the measurement of turbulence properties to higher $k_\perp$ values and opens the window to electron temperature gradient driven turbulence. In case several Doppler reflectometry systems are operated at different frequencies cross correlation analysis can provide information on radial wavelength of the turbulence as well. Doppler

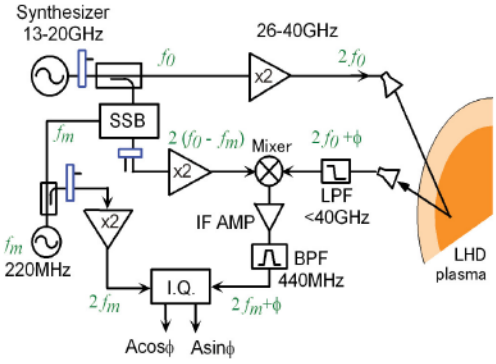

Figure 8: Principle of Doppler reflectometry as installed at LHD. Figure taken from [22]

reflectometry is installed on mostly every fusion device in the world. It has become a working horse for the estimation of rotation and E_r-profiles [23].
Of interest is the measurement of the turbulence or wave number spectrum at the same radial position and time. This asks for the launch of a frequency at different tilt angles. Such non-mechanical steering antenna can cover for small frequency variations a range of $-20°$ to $20°$. The phased array antenna (PAA) is developed at the University Stuttgart [24]. A first application of the PAA has taken place at W7-X [25] together with a Doppler reflectometer set-up. Another diagnostic mainly to study the small scale fluctuations is the upper hybrid resonance (UHR)

scattering [26, 27]. The principle relies on the backscattering of a launched X-mode microwave at the UHR. After mixing the local and the time delayed received waves a spectrum is obtained. The amplitude of the spectral components depends on the time delay between the launched and the received wave and allows to estimate the wave number of density fluctuations. At the UHR also a conversion from X- to O-mode takes place. The backscattered O-mode component contains information on magnetic fluctuations. If the receiving X-mode antennae is replaced by a O-mode sensitive horn it is in principle possible to measure magnetic fluctuations as well.
A major draw back of the discussed different reflectometer system is that the measurement takes place at one radial position only at one time. To obtain more information along the radius the simultaneous probing of many frequencies is necessary. the comb reflectometer is able to launch a collection of different frequencies into the plasma. In principle the antenna front end can be the same as for the Correlation and Doppler reflectometry. Only the frequency generator has to be replaced by a frequency comb. Such a first comb reflectometer in Ka-band (24 GHz to 40 GHz) has been installed at Large Helical Device (LHD) [28]. The steps between the single frequencies was set to 410 MHz and the frequency spectrum ranges from 0 GHz to 20 GHz. With a $\times 2$ the frequencies are covering the Ka-band. As an antenna set-up the standard Doppler reflectometry set-up was used. The detection of the signal becomes more complicated because for every single frequency of the comb a detection circuit is necessary which needs a splitter in the microwave path. As a consequence the power after the splitter drops down. Recently a design for a variable frequency comb reflectometer was proposed for ASDEX Upgrade [29]

VI. ECE DIAGNOSTIC

In this section the properties of the radiation emitted by the plasma are investigated. A review on the theoretical aspects of the propagation of microwave radiation in a plasma can be found in [30].
The radiation results from gyrating electrons at a frequency ω_{ce},

$$\omega_{ce} = \frac{e \cdot B}{m_e \cdot \gamma} \tag{17}$$

where γ is the relativistic mass factor. Due to relativistic effects the radiation is emitted also in higher harmonics of ω_{ce}. Having a spatial varying toroidal magnetic field as in a tokamak where $B_t \propto 1/R$ a relation between the emitted frequency and the location within the plasma is possible. In the case of a Maxwellian energy distribution of the electrons the intensity of the emitted radiation can be related to the temperature. The emitted frequency spectrum can be described by Planck's equation. In a fusion plasma $\hbar\omega \ll kT_e$ is fulfilled and the Rayleigh-Jeans approximation can be used.

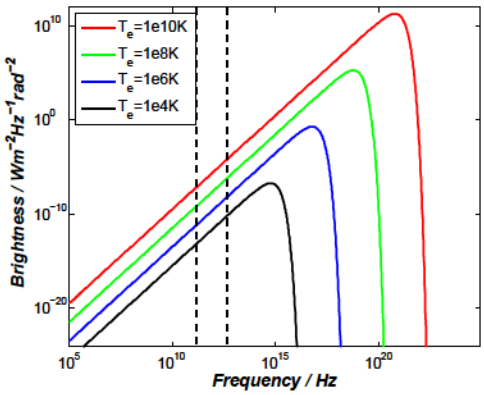

Figure 9: Brightness as function of frequency. The region of cyclotron frequencies used for T_e-measurements is indicated by dashed lines

$$I(\omega) = B(\omega) = \frac{\omega^2 \cdot T_e}{8 \cdot \pi^3 \cdot c^2} \tag{18}$$

Shown in fig. 9 are the brightness curves for 4 different temperatures. It is clearly seen that the region of the cyclotron frequencies is governed by the Rayleigh-Jeans approximation which depends linear on T_e. The measurement of the intensity of the emitted frequency alone is not sufficient. Also the transport of the radiation from its point of emission across the plasma to the observing antenna has to be taken into account. The transport of the radiation is described by

$$\frac{dI}{ds} = j(\omega) - I \cdot \alpha(\omega) \tag{19}$$

where s is the ray path and α the absorption coefficient and j the emissivity which are itself a functions of the frequency. The differential equation can be integrated yielding

$$I(s_2) = I(s_1) \cdot e^{-\tau_{21}} + \frac{j}{\alpha} \cdot [1 - e^{-\tau_{21}}], \quad \tau_{21} = \tau_2 - \tau_1 \tag{20}$$

where τ is the optical depth defined by:

$$\tau = \int \alpha(\omega) ds \tag{21}$$

The absorption coefficient is itself a function of local plasma parameters as n_e, T_e, the polarization of the wave (e.g. *X- or O-Mode*) and the harmonic number. With respects to cut-off's a suitable measurement of the electron temperature is performed for X-mode perpendicular propagation $\theta = 90^o$. In this case τ can be calculated from a WKB approach as outlined in paper by Bornatici [30].

For optical thick plasmas ($\tau \gg 1$) the first term on the right side of Eq. 20 becomes small, yielding:

$$T_e^{rad} = \frac{\omega^2 \cdot T_e}{8 \cdot \pi^3 \cdot c^2} \cdot \left(1 - e^{-\tau}\right) \tag{22}$$

As mentioned above, the propagation of electron cyclotron radiation in a plasma is limited by resonances and cut-off's. To find those positions we start from the *Appleton-Hartree relation* (Eq. 1) again. As already known from the first section the refractive index decides about cut-off and absorption frequencies for the propagation in *X-Mode*. Cut-offs and resonances are depending on the local B- and n_e-values. For $N^2 = 0$ a cut-off will reflect the wave. If $N^2 = \infty$ a resonance will absorb the wave. As can be seen from the Eq. 3 for *X-Mode* propagation perpendicular to the magnetic field we get the following equation for cut-off,

$$\omega_{CO1,2} = \sqrt{\frac{\left(2\omega_{pe}^2 + \omega_{ce}^2\right)}{2} \pm \sqrt{\frac{\left(2\omega_{pe}^2 + \omega_{ce}^2\right)^2}{4} - \omega_{pe}^4}} \tag{23}$$

and for resonances in the plasma we get:

$$\omega = \omega_{pe} \tag{24}$$

$$\omega = \sqrt{\omega_{pe}^2 + \omega_{ce}^2} \tag{25}$$

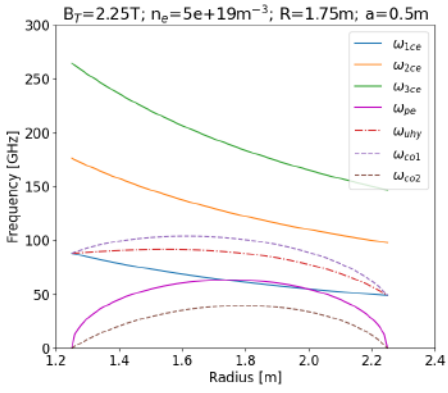

Figure 10: Cut-offs and resonances for a parabolic n_e-profile and $B_t = 2.25\,\mathrm{T}$ and $n_e^{max} = 5 \times 10^{19}\,\mathrm{m}^{-3}$ and $R_0 = 1.75\,\mathrm{m}$. Furthermore the first three harmonics of the electron cyclotron frequency are shown

From fig. 10 it becomes clear that the 1^{st} harmonic can not be used for ECE-measurements since $\omega_{ce} \leq \omega_{pe}$ for $1.8 \leq R \leq 2\,\mathrm{m}$. But as long as the n_e is small enough the 2^{nd} harmonic is very well suited to measure the electron temperature. However for an increased density the cut-off frequency ω_{co1} overcomes the 2^{nd} harmonic. Already when the local n_e reaches $80 - 85\%$ of the cut-off density the 2^{nd} harmonic intensity drops, because of the divergence of the antenna beam [31]. In this case the 3^{rd} harmonic must be used. Disadvantage of this method is that the plasma is not optical thick for the 3^{rd} harmonic. Also multiple reflections of the radiation due to the plasma facing walls have to be taken into account. Therefore the first term in Eq. 20 is not zero and reflections from the wall have to be taken into account. The reflection coefficient ρ of the wall is material depending. For a wall covered by graphite tiles $\rho = 0.7$ is achieved [32]. The equation for the estimation of the temperature has to be modified

$$T_e^{rad} = \frac{\omega^2 \cdot T_e}{8 \cdot \pi^3 \cdot c^2} \cdot \frac{\left(1 - e^{-\tau}\right)}{1 - \rho \cdot e^{-\tau}} \tag{26}$$

This method needs the knowledge of the local electron density and temperature when calculating the optical depth. The measurement of T_e from 3^{rd} harmonic is restricted to a small frequency range mostly in the plasma core. At the plasma edge of the outboard side of the plasma an overlap of where the frequency range of 2^{nd} and 3^{rd} harmonic takes place (see fig. 10) and a mixture of both harmonics will be measured and yield wrong T_e-values.

The technique to measure the emission of the 2^{nd} harmonic is not simple. As can be seen from fig. 9, the power ranges from several nW to µW. The radiation measurement at frequencies above $f = 70\,\mathrm{GHz}$ is difficult since the amplifier in this frequency range are noisy and the total amplification of the signal has to be around 80 dB, due to the low input power. To overcome this problem heterodyne radiometers are used for the measurement of T_e. They use a local oscillator for down conversion of the input frequency. As local oscillators Gunn-diodes made of GaAs are used because they are stable in frequency and have long lifetime compared with other microwave sources. The incoming RF-frequency is mixed with the frequency of the local oscillator, yielding an intermediate frequency (IF). The IF will pass a narrow filter with $\Delta f = 100 - 200 MHz$. This filter is responsible for the radial resolution of the radiometer. The noise temperature of such a radiometer is below $T_{sys} \leq 1000\,\mathrm{K}$. Unfortunately it is not possible to sweep the Gunn-diode over a large frequency range with constant output power therefore a broad-band mixer is used which covers the region from 2 GHz to 10 GHz. With a multiplexer and additional narrow bandpass filters T_e can be measured at several frequencies using only one LO-oscillator.This kind of radiometer has in general a higher noise temperature of $T_{sys} \approx 4000\,\mathrm{K}$. A typical example of a modern ECE diagnostic is shown in fig. 11. The system is installed at Tore Supra [33] and is operated with 4 local oscillators. The mixer cover a frequency range of 2 GHz to 18 GHz and after the mixer the signal is filtered and splits into 8 channels each. In total 32 radial positions can be measured with the system.

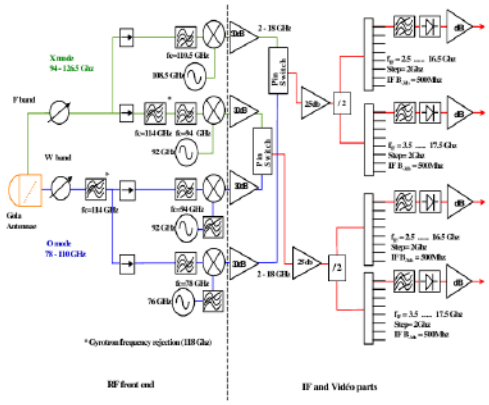

Figure 11: Set up of an ECE system at Tore Supra. The black dashed line shows the separation between the high frequency and the IF part.

Furthermore the investigations towards 2-dimensional images (poloidal cross section) from the plasma in the range of microwave frequencies needs advanced antennae technique. Without a probing beam and a detector array in covering the 2^{nd} harmonic cyclotron frequencies small scale structures in T_e can be resolved. However, the same optical set-up can also be used for the mircowave imaging reflectometry (MIR) as shown in fig. 12. In this case a probing frequency is launced in the plasma and the receivers have to be replaced by those covering the O-mode cut-off frequencies. With such a diagnostic an image of the density fluctuations on a flux surface can be achieved. A successful MIR set-up is installed at the Korean tokamak KSTAR [34]. The system has in total 16 channels with a poloidal spacing of 2.3 mm for the measuremet of density fluctuations. First experiments using ECE imaging are successful implemented at AUG [35]. Recent investigations of synthetic aperture microwave imaging for passive and active operation have been started at MAST [36]. The system operates with a time resolution of 10 µs and records images at 16 different frequencies. With such a system propagation as well as the pitch angle of turbulence can be studied.

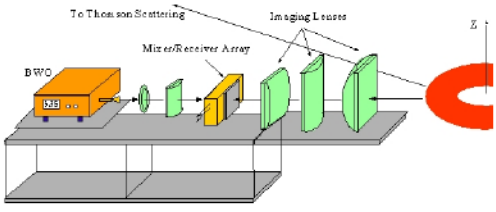

Figure 12: Set up of an MIR imaging system at TEXTOR.

A draw back of all microwave imaging diagnostics is the space needed for the installation. In all cases a large port window in necessary to launch radiation into and collect radiation from the plasma.

Beside heterodyne radiometer Michelson-interferometer or a grated polychromator are used to measure T_e. The Michelson-Interferometer is mostly used to measure the emitted microwave radiation over a large frequency range (e.g. 1^{st} -4^{th} harmonic). This is done by a vibrational or pneumatically mirror in the device, allowing a scan over a large frequency range within $\approx$ 10 ms. Since the power transferred to detector is very small the detector noise has to be reduced as much as possible by cooling with liquid helium.

Applications of Michelson-interferometer are found on several devices. It can be used to measure non Maxwellian components in the spectrum from comparison of comparison of the intensity of different harmonics [37]. Due to the long scan time a Michelson-interferometer is not well suited to measure temporal and spatial resolved electron temperature in the plasma. However, it can be used to measure the level of stray radiation in produced by electron cyclotron heating in a plasma [38].

VII. AN OUTLOOK TO FUTURE APPLICATIONS

What are the main directions in the development of microwave diagnostics? The rapid increase in the development of microwave components for the automotive sector will make standard reflectometry diagnostics for today devices smaller and more cheap. Already today the development of monolithic microwave integrated circuits (MMIC) allows to integrated a full W-band radar sensor in a matchbox, includibg several amplification stages as well as the mixer. This kind of sensors, developed by Fraunhofer for Applied Solid State Physics are applied in industry for precise distance measurements in dusty environments or as landing aid for helicopters. A draw back at the moment is te small output power. Keep in mind that microwave diagnostic components in fusion are normally several 10^{th} meters away from the plasma and cause large attenuation. Together with smaller antennae correlation measurements of turbulence structures could be realised easier.

Beside the more technical oriented development new diagnostic ideas show up as the measurement of the local magnetic field from the pitch angle or equivalent to measure the ellipticity of the reflected beam cross-section (the axis is aligned with the magnetic field) using coherent detection techniques with two orthogonal components [39].But also for the next generation of fusion devices microwave diagnostics will play an important role. Due to the robustness with respect of high heat loads, erosion of material they will play

a major role for the control of thermonuclear reactor as ITER and DEMO [40].

REFERENCES

1. Ian H Hutchinson. Principles of plasma diagnostics. *Plasma Physics and Controlled Fusion*, 44(12):2603, 2002.
2. H.R Koslowski and H. Soltwisch. Electron density and q profile measurements with the far-ir interferometer-polarimeter on the textor tokamak. *Fusion Engineering and Design*, 3435:143–150, 1997.
3. Frederic A Hopf, Akira Tomita, and G Al-Jumaily. Second-harmonic interferometers. *Optics letters*, 5(9):386–388, 1980.
4. VP Drachev, Yu I Krasnikov, and PA Bagryansky. Dispersion interferometer for controlled fusion devices. *Review of scientific instruments*, 64(4):1010–1013, 1993.
5. T Akiyama, K Kawahata, R Yasuhara, S Okajima, and K Nakayama. Dispersion interferometer for large helical device. *Journal of Instrumentation*, 7(01):C01055, 2012.
6. J. Knauer, P. Kornejew, H. Trimino Mora, M. Hirsch, and A. Werner \etal. A new dispersion interferometer for the stellarator Wendelstein 7-X. page P4.017. 43rd European Physical Society Conf. on Plasma Physics (Leuven, Belgium), 2016.
7. PA Bagryansky, AD Khilchenko, AN Kvashnin, AA Lizunov, RV Voskoboynikov, AL Solomakhin, HR Koslowski, and TEXTOR team. Dispersion interferometer based on a co 2 laser for textor and burning plasma experiments. *Review of Scientific Instruments*, 77(5):053501, 2006.
8. R Nazikian, GJ Kramer, and E Valeo. A tutorial on the basic principles of microwave reflectometry applied to fluctuation measurements in fusion plasmas. *Physics of Plasmas*, 8(5):1840–1855, 2001.
9. GD Conway. Microwave reflectometry for fusion plasma diagnosis. *Nuclear Fusion*, 46:S665–S669, 2006.
10. A Silva, ME Manso, L Cupido, M Albrecht, F Serra, P Varela, J Santos, S Vergamota, F Eusébio, J Fernandes, et al. Ultrafast broadband frequency modulation of a continuous wave reflectometry system to measure density profiles on asdex upgrade. *Review of Scientific Instruments*, 67(12):4138–4145, 1996.
11. T Tokuzawa, A Mase, N Oyama, A Itakura, and T Tamano. Ultrafast broadband frequency-modulation reflectometer for density profile measurements in gamma 10. *Review of scientific instruments*, 68(1):443–445, 1997.
12. Ph Moreau, F Clairet, JM Chareau, M Paume, and C Laviron. Ultrafast frequency sweep heterodyne reflectometer on the tore supra tokamak. *Review of Scientific Instruments*, 71(1):74–81, 2000.
13. F. Clairet, C. Bottereau, A. Medvedeva, D. Molina, G. D. Conway, A. Silva, and U. Stroth. 1 s broadband frequency sweeping reflectometry for plasma density and fluctuation profile measurements. *Review of Scientific Instruments*, 88(11):113506, November 2017. Publisher: American Institute of Physics.
14. X.Han, A.Krämer-Flecken, J.Ongena, O.Neubauer, B.Schweer, and A. \etal. Development of a dual band x-mode reflectometer for the density profile measurement at the icrf antenna in W7-X. 14th International Reflectometry Workshop for Fusion Plasma Diagnostics (IRW14) (Lausanne, Swiss), 2019.
15. S Soldatov, A Krämer-Flecken, and CN Klimov. Investigation of the poloidal spectral resolution of o-mode reflectometry with two-dimensional full-wave modeling. *Fusion engineering and design*, 84(1):64–71, 2009.
16. A Krämer-Flecken, V Dreval, S Soldatov, A Rogister, V Vershkov, et al. Turbulence studies with means of reflectometry at textor. *Nuclear fusion*, 44(11):1143, 2004.
17. A Krämer-Flecken, S Soldatov, B Vowinkel, and P Müller. Correlation reflectometry at textor. *Review of scientific instruments*, 81(11):113502, 2010.
18. VA Vershkov, VV Dreval, and SV Soldatov. A three-wave heterodyne correlation reflectometer developed in the t-10 tokamak. *Review of scientific instruments*, 70(3):1700–1709, 1999.
19. D Prisiazhniuk, G D Conway, A Krmer-Flecken, U Stroth, and the ASDEX Upgrade Team. Density fluctuation correlation measurements in ASDEX Upgrade using poloidal and radial correlation reflectometry. *Plasma Physics and Controlled Fusion*, 60(7):075003, July 2018.
20. A. Krämer-Flecken, T. Windisch, W. Behr, G. Czymek, and P. Drews et al. Investigation of turbulence rotation in limiter plasmas at W7-X with newly installed poloidal correlation reflectometer. *Nuclear Fusion*, 57(6):066023, 2017.
21. M Hirsch, E Holzhauer, J Baldzuhn, B Kurzan, and B Scott. Doppler reflectometry for the investigation of propagating density perturbations. *Plasma physics and controlled fusion*, 43(12):1641, 2001.
22. T. Tokuzawa, A. Ejiri, K. Kawahata, K. Tanaka, I. Yamada, M. Yoshinuma, K. Ida, and

C. Suzuki. Microwave Doppler reflectometer system in LHD. *Review of Scientific Instruments*, 83(10):10E322, July 2012. Publisher: American Institute of Physics.

23. GD Conway, J Schirmer, S Klenge, W Suttrop, E Holzhauer, et al. Plasma rotation profile measurements using doppler reflectometry. *Plasma Physics and Controlled Fusion*, 46(6):951, 2004.
24. S. Wolf. *A phased array antenna for Doppler reflectometry in ASDEX Upgrade*. PhD Thesis, University Stuttgart, 2016.
25. T. Windisch, S. Wolf, G. M. Weir, S. A. Bozhenkov, H. Damm, G. Fuchert, O. Grulke, M. Hirsch, W. Kasparek, T. Klinger, C. Lechte, E. Pasch, B. Plaum, E. A. Scott, and W7-X Team. Phased array Doppler reflectometry at Wendelstein 7-X. *The Review of Scientific Instruments*, 89(10):10H115, October 2018.
26. I Fidone. Enhanced incoherent scattering at the upper-hybrid resonance. i. cold plasma theory. *The Physics of Fluids*, 16(10):1680–1684, 1973.
27. DG Bulyiginskiy, AD Gurchenko, EZ Gusakov, VV Korkin, MM Larionov, KM Novik, Yu V Petrov, A Yu Popov, AN Saveliev, VL Selenin, et al. Radar upper hybrid resonance scattering diagnostics of small-scale fluctuations and waves in tokamak plasmas. *Physics of Plasmas*, 8(5):2224–2231, 2001.
28. Tokihiko Tokuzawa, Shigeru Inagaki, Akira Ejiri, Ryota Soga, Ichihiro Yamada, Shin Kubo, Mikiro Yoshinuma, Katsumi Ida, Chihiro Suzuki, Kenji Tanaka, Tsuyoshi Akiyama, Naohiro Kasuya, Kimitaka Itoh, Kiyomasa Watanabe, Hiroshi Yamada, Kazuo Kawahata, and LHD Experiment Group. *Ka*-band Microwave Frequency Comb Doppler Reflectometer System for the Large Helical Device. *Plasma and Fusion Research*, 9:1402149–1402149, 2014.
29. T. HAPPEL, W. KASPAREK, P. HENNEQUIN, K. HFLER, and C. HONOR and. Design of a variable frequency comb reflectometer system for the ASDEX Upgrade tokamak. *Plasma Science and Technology*, 22(6):064002, March 2020. Publisher: IOP Publishing.
30. M Bornatici. Theory of electron cyclotron absorption of magnetized plasmas. *Plasma Physics*, 24(6):629, 1982.
31. WHM Clark. The precision of electron cyclotron emission measurements from dite tokamak. *Plasma physics*, 25(12):1501, 1983.
32. Tony Donne and Toon Verhoeven. *Ec-10: Proceedings Of The 10th Joint Workshop On Electron Cyclotron Emission And Electron Cyclotron Resonance*. World Scientific, 1998.
33. JL Ségui, D Molina, G Giruzzi, M Goniche, G Huysmans, P Maget, M Ottaviani, and Tore Supra Team. An upgraded 32-channel heterodyne electron cyclotron emission radiometer on tore supra. *Review of scientific instruments*, 76(12):123501, 2005.
34. W. Lee, I. Hong, J. Leem, M. Kim, Y. Nam, G. S. Yun, H. K. Park, Y. G. Kim, K. W. Kim, C. W. Domier, and N. C. Luhmann. Microwave imaging reflectometry for KSTAR. *Journal of Instrumentation*, 7(01):C01070–C01070, January 2012. Publisher: IOP Publishing.
35. I. G. J. Classen, J. E. Boom, W. Suttrop, E. Schmid, B. Tobias, C. W. Domier, N. C. Luhmann, A. J. H. Donn, R. J. E. Jaspers, P. C. de Vries, H. K. Park, T. Munsat, M. Garca-Muoz, and P. A. Schneider. 2d electron cyclotron emission imaging at asdex upgrade (invited). *Review of Scientific Instruments*, 81(10):10D929, 2010.
36. Vladimir F Shevchenko, Roddy GL Vann, Simon J Freethy, and Billy K Huang. Synthetic aperture microwave imaging with active probing for fusion plasma diagnostics. *Journal of Instrumentation*, 7(10):P10016, 2012.
37. Yong Liu, Stefan Schmuck, Hailin Zhao, John Fessey, Paul Trimble, Xiang Liu, Zeying Zhu, Qing Zang, and Liqun Hu. A Michelson Interferometer for Electron Cyclotron Emission Measurements on EAST. *Plasma Science and Technology*, 18(12):1148–1154, November 2016. Publisher: IOP Publishing.
38. Johan W. Oosterbeek, Neha Chaudhary, Matthias Hirsch, Udo Hfel, and Robert C. Wolf. Assessment of ECH stray radiation levels at the W7-X Michelson Interferometer and Profile Reflectometer. *EPJ Web of Conferences*, 203:03010, 2019. Publisher: EDP Sciences.
39. A Stegmeir, GD Conway, E Poli, and E Strumberger. Analysis of the iter low field side reflectometer employing the beam tracing method. *Fusion engineering and design*, 86(12):2928–2942, 2011.
40. F. A. Volpe. Prospects for a dominantly microwave-diagnosed magnetically confined fusion reactor. *Journal of Instrumentation*, 12(01):C01094–C01094, January 2017. Publisher: IOP Publishing.

LABORATORY EXPERIMENTS TO STUDY PLASMA MATERIAL INTERACTIONS

T.W. Morgan
DIFFER- Dutch Institute for Fundamental Energy Research,
De Zaale 20, 5612 AJ Eindhoven, The Netherlands

ABSTRACT

Laboratory experiments are a key tool to investigate plasma material interactions for future devices like ITER and DEMO in a controlled and flexible manner. They give the ability to determine valuable data with a well regulated parameter space and are essential to model and project the expected wall performance and evolution for these systems. This paper gives an overview of the needs and capabilities of laboratory-scale devices, focusing particularly on linear plasma devices, their operation and future developments.

I. THE NEED FOR LABORATORY EXPERIMENTS TO STUDY PMI

A key constraint on the size and performance of fusion reactors of the future such as ITER [1] or DEMO [2] is the interactions that take place between the extremely high heat and particle loads expelled from the plasma and the wall materials which make up the solid boundary of the containing vacuum vessel. These conditions place strict limits on the choice of material for the wall and the design of plasma facing components (PFCs) in order to maximise power transfer to coolant while minimizing material loss into the plasma and loss of fuel ions retained in the wall. At the same time plasma material interactions (PMI) set limits on the total power which can cross the separatrix and consequently the total fusion power generated for a given size of machine [3], the power which arrives at the divertor surface and the temperature of the divertor plasma [4]. Overall careful control of the interaction of the plasma with the wall has been vital in the continual advancement in fusion power output over the last several decades. For example, the development of wall conditioning techniques enabled high temperature plasma conditions and better confinement times to be achieved [5]. The invention of the divertor transposed PMI to a region more distant from the confined plasma region and enabled an H-mode with high levels of detachment with suppressed erosion [6]. The use of Li as a wall conditioning coating in TFTR led to record fusion power outputs during so-called "supershots" [7]. Understanding the interaction between plasma and material has therefore been vital to the maturation of nuclear fusion as a technology. While a great deal has of course been learnt from experiments in confinement devices, the development of understanding of PMI in tokamaks and stellarators is hampered by several issues:

1. The ability to exchange wall materials is typically limited within a given experimental campaign, which typically lasts months at a time.
2. During this time period many different plasma conditions are typically achieved, leading to a complex time history for the material.
3. Time for dedicated PMI studies is limited due to other demands on the available experimental time.
4. Diagnostic access of the wall area of interest is usually difficult due to the limited views via ports and the competing demands for diagnosis of the plasma.
5. Understanding of the loading conditions can be challenging due to the geometry of the plasma, limited diagnostic coverage, and imperfect control of the desired experimental conditions.

The advantages of such confinement device experiments are that the conditions are by definition relevant to the device, and that investigations which rely on the nature of the confinement device such as transport around the toroidal extent of the machine or how impurities from the wall influence the core plasma are able to be investigated. Several excellent dedicated modules exist for the study of PMI in-situ, such as DIMES in the DIII-D tokamak [8] and the DIM-II manipulator in ASDEX-Upgrade [9]. However, in these cases the latter three points listed above still apply. By contrast, laboratory experiments to investigate PMI possess the following advantages:

1. The PMI can be investigated in a controlled situation where single or multiple parameters can easily be varied independently and repeatably.
2. Because of this simplified situation it is easier to make and validate model-based predictions.
3. Exchange and comparison of samples is typically faster and easier.

4. Diagnostic coverage is typically more comprehensive and diagnostic access is much easier.

5. Because it is a dedicated PMI experiment more time can be devoted to studying a particular issue.

6. Typically the operational cost of such a laboratory scale experiment is much lower than confinement devices due to their relative simplicity.

Another limitation for experiments in current day confinement devices is that they increasingly do not represent the PMI conditions that can be expected in ITER and in fusion reactors beyond that. This includes:

- Very high heat and particle fluxes which leads to much more challenging performance conditions for the PFC design to avoid unacceptable damage.

- Much higher duty cycle, leading to much higher total particle fluences to the wall, as well as fatigue cycling effects.

- Much higher neutron loads and neutron fluences than current day devices, leading to very large displacement per atom (dpa) levels and significant transmutation, generally resulting in a degradation of thermomechanical properties and thermal diffusivity.

- Synergistic effects of the above three points.

Here laboratory devices can make a significant contribution by more closely recreating one or more of these points, enabling the systematic investigation of materials undergoing these sorts of loading conditions.

II. TYPES OF LABORATORY DEVICES

Many different types of laboratory devices have been used to investigate various aspects of fusion-relevant material performance. These can be subdivided into plasma and non-plasma loading devices. Examples of the latter include electron guns such as JUDITH-II [10], IDTF [11] or FE-200 [12]; neutral beam test facilities such as GLADIS [13] or ion beam accelerators. These types of experimental devices are typically dedicated to investigating one type of effect. For example electron beams can well simulate the expected steady-state and transient loading conditions in fusion confinement devices [14–16], while ion beams can be used to carry out investigations of sputtering yields [17] or deuterium blistering [18] in a highly controlled manner.

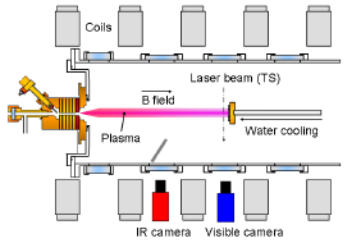

Figure 1: Schematic of Pilot-PSI as an example of a linear plasma device [20].

In this paper we will focus on (non-confinement based) plasma loading devices. These are predominantly linear plasma devices (LPDs), but also include plasma guns such as QSPA [19]. These are more typically used to investigate multiple effects simultaneously, and to identify the synergies between them. For example the influence of high heat loads and plasma loading at high fluxes can be simultaneously achieved. This brings the exposure conditions much closer to those expected in ITER or DEMO and accelerates the development of solutions for the design of these devices.

A wide number of different designs of linear plasma devices exist, with a variety of sources, magnetic field topologies, vacuum systems and target designs, however LPDs can be seen to consist generally of a few main components. Contained at one end of a cylindrical vacuum vessel, a plasma source generates a low electron temperature plasma of typically 1-10 eV and diameter 1-10 cm. This is confined and guided by a series of magnetic coils to a target region where materials of interest are investigated (figure 1). Typically this magnetic field is generated in steady-state, enabling high fluences of plasma to be achieved, however pulsed magnetic fields of a few seconds like Pilot-PSI have been used to quickly generate a short high-flux plasma instead [21]. An array of ports allow diagnostics such as Langmuir probes, visible spectroscopy or infrared thermography to be used to quantify the plasma and target parameters. The main parameters of interest of a number of LPDs which are employed in PMI research worldwide are given in table 1.

Three main types of plasma sources are employed in LPD's to reach high flux conditions ($> 10^{22}$ (m^{-2} s^{-1})). The earliest employed (since the 1980's for fusion research) in this type of device are DC arc plasma generators, of which there are sub-sorts such as Reflex Arcs, Cusp Arcs or Cylindrical Arcs. These all work on broadly similar principles. A lanthanum hexaboride (LaB_6) cathode is heated to a high temperature (around 1900 K) in the presence of a working gas at a pressure of a few Pa. LaB_6 has a low work func-

Property	PISCES-A	PISCES-B	NAGDIS-II	PSI-2	Magnum-PSI	MAGPIE	Proto-MPEX
Country	USA	USA	Japan	Germany	The Netherlands	Australia	USA
Source type	Reflex Arc	Reflex Arc	Cusp Arc	Cylindrical Arc	Cascaded Arc	Helicon	Helicon
B-field strength (T)	0.1	0.04	0.25	0.1	0.01-2.5	0.2	1.0
Electron temperature T_e (eV)	3-20	3.50	0.1-10	1-40	0.1-7	3-5	1-20
Electron density n_e (m^{-3})	10^{16-19}	10^{17-19}	10^{18-20}	10^{16-19}	10^{18-21}	10^{18-19}	10^{18-20}
Particle flux Γ (m^{-2} s^{-1})	$10^{21} - 3 \cdot 10^{22}$	10^{20-23}	10^{21-23}	10^{20-23}	10^{22-25}	10^{22-23}	10^{22-24}
Beam diameter (cm)	5	5	2	6	1-2	6	8
Ion Energy (bias) (eV)	10-200	10-300	10-200	10-300	1-120	1-300	1-20
References	[28]	[23]	[24]	[29]	[30]	[31]	[32]

Table 1: Table of selected current linear plasma devices producing high flux plasma ($> 10^{22}$ (m^{-2} s^{-1}))

Property	JULE-PSI (projected)	MPEX (projected)	UPP (projected)	LiMeS-PSI (projected)
Country	Germany	USA	The Netherlands	The Netherlands
Source type	Cylindrical arc	Helicon	Cascaded Arc	Cascaded Arc
B-field strength (T)	0.1	1-2	0.2	1.5
Electron temperature T_e (eV)	1-20	1-25	1-5	1-5
Electron density n_e (m^{-3})	10^{17-19}	$4 - 6 \cdot 10^{19}$	$10^{18}6 - 5 \cdot 10^{19}$	10^{18-20}
Particle flux Γ (m^{-2} s^{-1})	10^{21-23}	10^{22-24}	10^{22-23}	10^{22-24}
Beam diameter (cm)	6-15	10	1-2	1-2
Ion Energy (bias) (eV)	1-300	1-25	1-100	1-100
Unique features	Be, neutron irradiated and T exposed samples	Be, neutron irradiated and T exposed samples	Operando ion beam analysis	Flowing liquid metal with active cooling
References	[33]	[32]		

Table 2: Table of selected new LPDs currently planned or under construction.

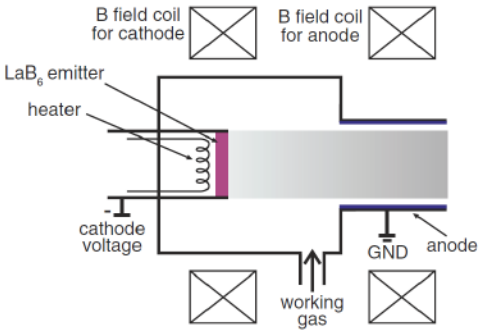

Figure 2: Schematic of a DC arc plasma generator of the reflex arc type [34]

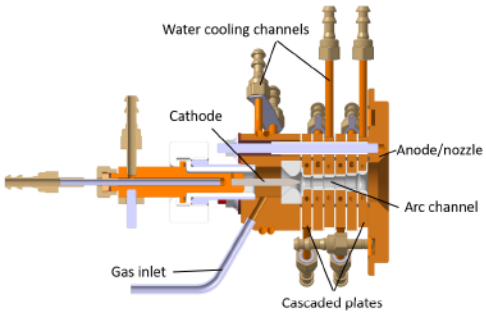

Figure 3: Schematic of a DC cascaded arc source

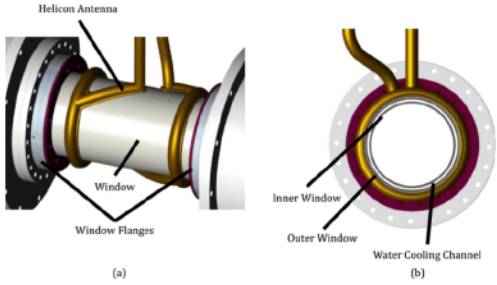

Figure 4: Schematic of helicon source mounted to window in MPEX [39]

tion of around 2.5 eV and therefore thermionically emits a high current of electrons at this temperature. Typically the anode of the system is grounded and a negative potential applied to the cathode. If the magnetic field lines are arranged such that the field lines intersect directly with the anode, such as occurs in PSI-2 [22], this has the advantage that it burns with high stability and is easy to ignite, but most of the power is converted in the periphery region, leading to a hollow density and temperature profile. In reflex and cusp arcs, such as are used in PISCES-B [23] and NAGDIS-II [24] the magnetic field lines are arranged so that the electrons can only reach the anode via cross-field transport (figure 2). Instead they are reflected between the negatively charged cathode and target. Because this requires cross-field transport to ignite and sustain the arc, these devices typically operate at low magnetic field strengths of 0.2 T or less. Other examples of this type of LPD include DiPS (Korea) [25], TPE (USA) [26], MP^2 (Korea) [25] and STEP (China) [27].

A second more recent type of LPD emerged in the 2000's and employs Cascaded Arc plasma discharges (figure 3). Unlike the previously mentioned arcs this type operates at significantly higher pressure ($10^3 - 10^5$ Pa), producing a high plasma density (10^{20-21} m^{-3}). In this case the arc is struck from thermionic emission from a lanthanated or thoriated tungsten cathode with a sharp tip rather than a wide LaB_6 surface. The walls of the discharge channel are electrically isolated from one another, leading to a gradual step-down in potential which avoids direct arcing through the gas which flows through the channel. A very large pressure decrease as the plasma enters the vacuum chamber accelerates the plasma to supersonic speeds, and a shock front forms a few cm downstream as the plasma expands and slows again. If no magnetic field were applied the plasma would freely expand, leading to cooling and recombination to take place. By applying the external magnetic field losses to the anode are reduced to cross-field transport which strongly increases the plasma density and permits extra Ohmic heating of the plasma to take place. The advantages of this type of source are that a high density plasma is created which is more relevant for fusion reactors, and due to the high plasma collisionality the ions and electrons are equilibrated with each other. A challenge is to avoid recombination of the plasma due to its low temperature and the relatively high neutral background pressure due to high gas throughput and low ionization efficiency. To reduce this differential pumping is used in Magnum-PSI to limit the plasma-neutral interactions which lowers the pressure in the final chamber to below 1 Pa [35]. Other LPDs which employ this type of source include Pilot-PSI (the Netherlands) [21], CIMPLE-PSI (India), [36], DUT-PSI (China) [37] and CRAFT (China) [38].

In the last decade Helicon plasma sources have also started to be employed in LPDs for fusion research (figure 4). Unlike the previous two sources which operate in DC, these are RF sources which use an antenna to generate an oscillating electric field. This accelerates and heats electrons which then leads to an ionized plasma being formed. Helicon waves are of relatively low frequency, lying between the lower hybrid and ion plasma frequencies, and are

named for the spiralling natuer of their waveforms [40]. Unlike in inductively coupled plasmas, the exciting wave propagates into the plasma, which allows more global plasma generation by comparison [41]. Helicon sources do not have internal electrodes and so reduce the introduction of impurities in the plasma, and can generate high temperature and density plasmas, however they can be complicated to couple to the plasma and generate a large amount of heating to the windows [39]. LPDs which employ this type of source include DIONISOS (USA) [42], MAGPIE (Australia)[31], HPPX (China) [43] and Proto-MPEX (USA) [39].

III. FUTURE DEVELOPMENTS IN LINEAR PLASMA DEVICES

When considering the future development of PFCs for future fusion reactors, several aspects take on increasing importance. Here LPDs can offer dedicated facilities which contribute towards understanding of these new challenges:

1. Neutron irradiation of PFCs will be of much greater importance in creating volumetric damage in PFCs (around 3 dpa per full power year [44]), which will lead to strong degradation in material properties.

2. The duty cycle of a reactor like DEMO will be much greater even than ITER while fluxes to the wall will be similar or greater. This leads to extremely high plasma fluences and large numbers of loading cycles over the PFC lifetime.

3. To help handle these challenges alternative approaches to materials such as advanced tungsten alloys or liquid metal PFCs are under investigation and need to be investigated under the correct experimental loading conditions.

4. Combinations between the several different types of loading effects (ions, electrons, neutrons, photons, heating) may likely give rise to synergistic surface modifications and damage evolution over time.

Some of these items are already addressed to some extent with current day LPDs. For example, Magnum-PSI has demonstrated the ability to reach fluences of up to 10^{30} m^{-2}, which is equivalent to around one year of ITER Fusion Power Operation [45]. However, for several aspects new devices are under development to specifically address these challenges. Here we will touch on a selection of these currently either under construction or planned.

Neutron irradiation and how this affects the PMI and PFC lifetime are key challenges and a huge step change for materials compared to current day devices.

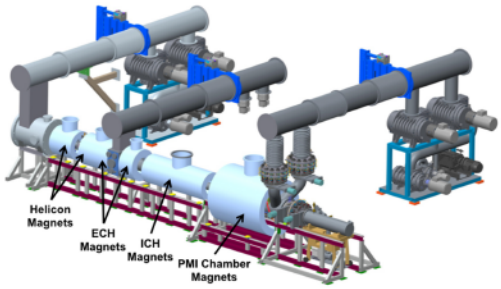

Figure 5: Schematic of the MPEX device design overview [46]

Two devices, MPEX and JULE-PSI, are in particular under development to address this problem.

JULE-PSI is currently planned to be built at Forschungszentrum Jülich in Germany and is designed as a LPD which will operate similarly to PSI-2 [33]. The machine will be placed in a hot cell and will be capable of handling pre-irradiated samples, as well as samples made of toxic materials such as beryllium. It will connect to a target exchange and analysis chamber equipped with laser diagnostics which can identify material composition and amount of fuel trapped.

MPEX is a machine currently being designed at Oak Ridge National Lab (ORNL), USA (figure 5) [39, 46]. A prototype device, Proto-MPEX, has been developed at ORNL to test the source and heating concepts and has been able to demonstrate the viability of the new approach [32]. This machine uses a combination of a helicon source with electron and ion heating sections via electron Berstein waves and ion cyclotron heating respectively [47]. This enables the energy of the ions and electrons to be separately controlled and for the conduction limited regime of heat transport to be reached in the plasma column [39]. This brings it closer to simulating the scrape-off layer of large fusion devices, unlike most LPDs where convective transport dominates. MPEX is designed to operate in steady-state with high flux and high fluence capabilities, and will also be housed in a hot-cell to enable it to handle neutron irradiated materials. The target station is envisaged to run on rails to allow it to move to a separate analysis location.

Two new devices are also under development at DIFFER in the Netherlands: LiMeS-PSI and Upgraded Pilot-PSI (UPP). These are designed to address points 3 and 4 above respectively. LiMeS-PSI is designed as a dedicated test stand for liquid-metal based PFCs (figure 6). Liquid metal based PFCs are attractive as a future option for fusion reactors for a variety of reasons, such as self-healing surfaces and resilience against off-normal events like Edge Localized Modes or disruptions [48]. LiMeS-PSI is designed to handle large scale mock-ups (up to 30 cm long) with

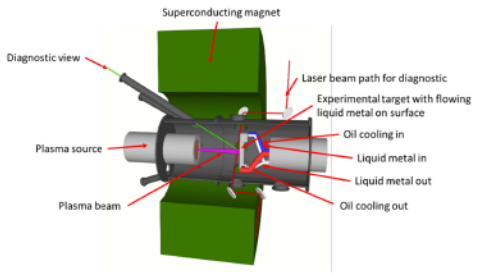

Figure 6: Conceptual design of the LiMeS-PSI linear plasma device

flowing liquid metal surfaces. Additionally it will utilize high temperature coolant to keep the liquid metal molten, and is designed to enable the development of this technology to a higher maturity level.

UPP is designed as a linear plasma device similar to Magnum-PSI, also with a cascaded arc plasma source, but with lower field (0.2 T) copper coils. To increase the flux the target is placed close to the target and large pumps positioned downstream to lower the background pressure to a few Pa. An ion beam is coupled to the vacuum vessel such that ion beam analysis such as Nuclear Reaction Analysis (NRA), Rutherford Backscattering Spectroscopy (RBS) or Elastic Recoil Detection Analysis (ERDA) can be carried out simultaneously with the plasma exposure. Unlike other LPDs which have such *operando* ion beam analysis capabilities such as DIONISOS [42] or PS-DIBA [49], this should combine this with high flux plasma exposure, which should more closely recreate the expected divertor conditions and achieve high fluences.

These and other developments should help to close the gap between our current knowledge based on current confinement and laboratory experimental devices and our understanding of what will occur in a fusion reactor. This will provide confidence in extrapolating to this larger scale as a result of these laboratory-scale experiments.

IV. ACKNOWLEDGEMENTS

I would like to thank Gerard van Rooij for his input in preparing this paper.

V. *

REFERENCES

[1]K. Ikeda, "Progress in the ITER Physics Basis", Nuclear Fusion **47**, 10.1088/0029-5515/47/6/E01 (2007).

[2]G. Federici et al., "Overview of EU DEMO design and R&D activities", Fusion Engineering and Design **89**, 882–889 (2014).

[3]D. Maisonnier et al., "Power plant conceptual studies in Europe", Nuclear Fusion **47**, 1524–1532 (2007).

[4]A. Loarte et al., "Chapter 4: power and particle control", Nuclear Fusion **47**, S203–S263 (2007).

[5]J. Winter, "Wall conditioning in fusion devices and its influence on plasma performance", Plasma Physics and Controlled Fusion **38**, 1503–1542 (1996).

[6]O. Gruber et al., "Observation of continuous divertor detachment in h-mode discharges in asdex upgrade", Phys. Rev. Lett. **74**, 4217–4220 (1995).

[7]D. Mansfield et al., "Observations concerning the injection of a lithium aerosol into the edge of TFTR discharges", Nuclear Fusion **41**, 1823–1834 (2001).

[8]C. Wong et al., "Divertor materials evaluation system at DIII-D", Journal of Nuclear Materials **196-198**, Plasma-Surface Interactions in Controlled Fusion Devices, 871–875 (1992).

[9]A. Herrmann, N. Jaksic, P. Leitenstern, H. Greuner, K. Krieger, P. De Marné, M. Oberkofler, V. Rohde, and G. Schall, "A large divertor manipulator for ASDEX Upgrade", Fusion Engineering and Design **98-99**, 1496–1499 (2015).

[10]P. Majerus, R. Duwe, T. Hirai, W. Kühnlein, J. Linke, and M. Rödig, "The new electron beam test facility JUDITH II for high heat flux experiments on plasma facing components", Fusion Engineering and Design **75-79**, Proceedings of the 23rd Symposium of Fusion Technology, 365–369 (2005).

[11]V. Kuznetsov et al., "Status of the IDTF high-heat-flux test facility", Fusion Engineering and Design **89**, Proceedings of the 11th International Symposium on Fusion Nuclear Technology-11 (ISFNT-11) Barcelona, Spain, 15-20 September, 2013, 955–959 (2014).

[12]I. Bobin-Vastra, F. Escourbiac, M. Merola, and P. Lorenzetto, "Activity of the European high heat flux test facility: FE200", Fusion Engineering and Design **75-79**, Proceedings of the 23rd Symposium of Fusion Technology, 357–363 (2005).

[13]H. Greuner, B. Boeswirth, J. Boscary, and P. McNeely, "High heat flux facility GLADIS: operational characteristics and results of W7-X pre-series target tests", Journal of Nuclear Materials **367-370**, Proceedings of the Twelfth International Conference on Fusion Reactor Materials (ICFRM-12), 1444–1448 (2007).

[14]J. Linke, F. Escourbiac, I. Mazul, R. Nygren, M. Rödig, J. Schlosser, and S. Suzuki, "High heat flux testing of plasma facing materials and components – Status and perspectives for ITER related activities", Journal of Nuclear Materials **367-370**, 1422–1431 (2007).

[15]T. Loewenhoff, J. Linke, G. Pintsuk, and C. Thomser, "Tungsten and CFC degradation under combined high cycle transient and steady state heat loads", Fusion Engineering and Design **87**, 1201–1205 (2012).

[16]M. Wirtz, J. Linke, T. Loewenhoff, G. Pintsuk, and I. Uytdenhouwen, "Transient heat load challenges for plasma-facing materials during long-term operation", Nuclear Materials and Energy **12**, 148–155 (2017).

[17]R. Behrisch and W. Eckstein, *Sputtering by particle bombardment*, Vol. 110 (Springer, Berlin, 2007), pp. 1–507.

[18]W. M. Shu, "High-dome blisters formed by deuterium-induced local superplasticity", Applied Physics Letters **92**, 1–4 (2008).

[19]A. Zhitlukhin et al., "Effects of ELMs on ITER divertor armour materials", Journal of Nuclear Materials **363-365**, Plasma-Surface Interactions-17, 301–307 (2007).

[20]G. De Temmerman, J. Daniels, K. Bystrov, M. van den Berg, and J. Zielinski, "Melt-layer motion and droplet ejection under divertor-relevant plasma conditions", Nuclear Fusion **53**, 023008 (2013).

[21]G. van Rooij, V. Veremiyenko, W. Goedheer, B. de Groot, A. Kleyn, P. Smeets, and T. Versloot, "Extreme hydrogen plasma densities achieved in a linear plasma generator", Applied Physics Letters **90**, 121501 (2007).

[22]D. Naujoks, G. Fussmann, and H. Meyer, "I(U)-characteristics of the plasma generator psi-1: experiment and theory", Contributions to Plasma Physics **38**, 127–133 (1998).

[23]Y. Hirooka et al., "A new plasma-surface interactions research facility: PISCES-B and first materials erosion experiments on bulk-boronized graphite", Journal of Vacuum Science Technology A **8**, 1790–1797 (1990).

[24]N. Ohno et al., "Static and dynamic behaviour of plasma detachment in the divertor simulator experiment NAGDIS-II", Nuclear Fusion **41**, 1055–1065 (2001).

[25]K.-S. Chung et al., "Plasma-wall interaction facilities in Korea", Fusion Science and Technology **63**, 16–20 (2013).

[26]M. Shimada, C. N. Taylor, R. J. Pawelko, L. C. Cadwallader, and B. J. Merrill, "Tritium Plasma Experiment Upgrade and improvement of surface diagnostic capabilities at STAR facility for enhancing tritium and nuclear PMI sciences", Fusion Science and Technology **71**, 310–315 (2017).

[27]G.-H. Lu et al., "Development and optimization of STEP—a Linear Plasma Device for plasma-material interaction studies", Fusion Science and Technology **71**, 177–186 (2017).

[28]D. Goebel, G. Campbell, and R. Conn, "Plasma surface interaction experimental facility (PISCES) for materials and edge physics studies", Journal of Nuclear Materials **121**, 277–282 (1984).

[29]A. Kreter, C. Brandt, A. Huber, S. Kraus, S. Möller, M. Reinhart, B. Schweer, G. Sergienko, and B. Unterberg, "Linear plasma device PSI-2 for plasma-material interaction studies", Fusion Science and Technology **68**, 8–14 (2015).

[30]H. van Eck et al., "High-fluence and high-flux performance characteristics of the superconducting Magnum-PSI linear plasma facility", Fusion Engineering and Design **142**, 26–32 (2019).

[31]B. D. Blackwell, J. F. Caneses, C. M. Samuell, J. Wach, J. Howard, and C. Corr, "Design and characterization of the magnetized plasma interaction experiment (MAGPIE): a new source for plasma–material interaction studies", Plasma Sources Science and Technology **21**, 055033 (2012).

[32]J. Rapp et al., "Latest results from Proto-MPEX and the future plans for MPEX", Fusion Science and Technology **75**, 654–663 (2019).

[33]B. Unterberg et al., "New linear plasma devices in the Trilateral Euregio Cluster for an integrated approach to plasma surface interactions in fusion reactors", Fusion Engineering and Design **86**, Proceedings of the 26th Symposium of Fusion Technology (SOFT-26), 1797–1800 (2011).

[34]C. Linsmeier, B. Unterberg, J. Coenen, R. Doerner, H. Greuner, A. Kreter, J. Linke, and H. Maier, "Material testing facilities and programs for plasma-facing component testing", Nuclear Fusion **57**, 092012 (2017).

[35]H. J. Van Eck, W. R. Koppers, G. J. Van Rooij, W. J. Goedheer, R. Engeln, D. C. Schram, N. J. Cardozo, and A. W. Kleyn, "Modeling and experiments on differential pumping in linear plasma generators operating at high gas flows", Journal of Applied Physics **105**, 063307 (2009).

[36]M. Kakati et al., "Design, development and recent experiments of the CIMPLE-PSI device", Nuclear Fusion **59**, 112008 (2019).

[37]Y. Wang, C. Li, J. Shi, X. Wu, and H. Ding, "Measurement of electron density and electron temperature of a cascaded arc plasma using laser thomson scattering compared to an optical emission spectroscopic approach", Plasma Science and Technology **19**, 115403 (2017).

[38]X. Yuan et al., "Particle flux characteristics of a compact high-field cascaded arc plasma device", Plasma Science and Technology (2021).

[39]J. Rapp et al., "The development of the Material Plasma Exposure Experiment", IEEE Transactions on Plasma Science **44**, 3456–3464 (2016).

[40]F. F. Chen, "Helicon discharges and sources: a review", Plasma Sources Science and Technology **24**, 014001 (2015).

[41]S. Shinohara, "Helicon high-density plasma sources: physics and applications", Advances in Physics: X **3**, 1420424 (2018).

[42]G. Wright, D. Whyte, B. Lipschultz, R. Doerner, and J. Kulpin, "Dynamics of hydrogenic retention in molybdenum: first results from DIONISOS", Journal of Nuclear Materials **363-365**, Plasma-Surface Interactions-17, 977–983 (2007).

[43]P. Lan-Lan, Z. Xin-Jun, and Y. Hua, "Numerical analysis of helicon plasma power deposition on Helicon Physics Prototype eXperiment", AIP Conference Proceedings **2254**, 060002 (2020).

[44]M. Gilbert, S. Dudarev, D. Nguyen-Manh, S. Zheng, L. Packer, and J.-C. Sublet, "Neutron-induced dpa, transmutations, gas production, and helium embrittlement of fusion materials", Journal of Nuclear Materials **442**, Fifteenth International Conference on Fusion Reactor Materials, S755–S760 (2013).

[45]T. W. Morgan, M. Balden, T. Schwarz-Selinger, Y. Li, T. H. Loewenhoff, M. Wirtz, S. Brezinsek, and G. D. Temmerman, "ITER monoblock performance under lifetime loading conditions in Magnum-PSI", Physica Scripta **T171**, 014065 (2020).

[46]J. Rapp et al., "Developing the science and technology for the Material Plasma Exposure eXperiment", Nuclear Fusion **57**, 116001 (2017).

[47]J. B. O. Caughman et al., "Plasma source development for fusion-relevant material testing", Journal of Vacuum Science & Technology A **35**, 03E114 (2017).

[48]T. W. Morgan, P. Rindt, G. G. Van Eden, V. Kvon, M. A. Jaworksi, and N. J. Lopes Cardozo, "Liquid metals as a divertor plasma facing material explored using the Pilot-PSI and Magnum- PSI linear devices", Plasma Phys. Control. Fusion **60**, `10.1088/1361-6587/aa86cd` (2018).

[49]M. Yamagiwa et al., "In situmeasurement of hydrogen isotope retention using a high heat flux plasma generator with ion beam analysis", Physica Scripta **T145**, 014032 (2011).

TUNGSTEN AS A PLASMA FACING COMPONENT AND DEVELOPMENT OF ADVANCED MATERIALS FOR FUSION

J.W.Coenen

Forschungszentrum Jülich GmbH, Institut für Energie- und Klimaforschung - Plasmaphysik
52425 Juelich, Germany

ABSTRACT

For the realization of fusion energy especially materials questions pose a significant challenge already today. Heat, particle and neutron loads pose a significant problem to material lifetime when extrapolating to DEMO [1, 2] the first stage prototype fusion reactor [3–5] considered to be the next step after ITER towards realizing fusion [6].

From a historic point of view the material mix used for the first wall of a fusion reactor has continually evolved, from original steel vessels to carbon and other low-Z materials like beryllium to tungsten as the primary candidate for a reactor first wall armour and divertor material.

For Materials considered for Fusion Applications a highly integrated approach is necessary. Resilience against neutron damage, good power exhaust, as well as oxidation resistance during accidental air ingress are design relevant issues when deciding on new materials or improving upon baseline materials. Neutron induced effects e.g. transmutation adding to embrittlement, retention, and changes to thermo-mechanical properties, are crucial to material performance.

For many of the issues faced tungsten was considered the solution. Recent progress [7] has however shown that new advanced tungsten or material grades maybe required. Here we present a summary of the issues as given in [8] with a focus on new materials developments.

In particular safety relevant components such as the first wall and the divertor of the reactor can benefit from introducing new approaches such as composites or new alloys into the discussion. Cracking, oxidation as well as fuel management are driving safety issues when deciding for new materials. Considering in all this also the neutron induced effects such as transmutation, embrittlement and after-heat and activation is essential. A component approach taking into account all aspects is required.

I. BOUNDARY CONDITIONS

When considering a future fusion power-plant multiple interlinked issues need to be evaluated (fig. 1). Some of the main problems a future reactor is faced with are linked to the materials exposed to the fusion environment and their lifetime considerations. Already from fig. 1 one can see that at the far branches of the tree multiple times the following issues arise, cooling media, neutron flux and neutron damage, ion impact and sputtering as well as heat loads and transient events.

Figure 1: Materials Issues for fusion - incomplete

In the following a subset of those conditions can be evaluated only and so far only for the relatively well known conditions of the next step devices e.g. DEMO [2].

The devices called DEMO is so far considered to be the nearest-term reactor design that has the capability to produce electricity and is viewed as single step between ITER and a commercial fusion plant. Currently, no conceptual design exists apart from early studies [3,5]. A design has not been formally selected, and detailed operational requirements are not yet available [9]. For discussion purposes it is simple to assume a reactor with the fusion power of 2GW and a wall area of $1200m^2$.

$$P_{exaust} = P_H + P_\alpha \sim 450MW \quad (1)$$

$$P_n = 1600MW/1200m^2 (\sim (40dpa/5fpy) \quad (2)$$

$$P_R = 225MW/1200m^2 \quad (3)$$

$$P_P = 225MW/1200m^2 \qquad (4)$$

This means an average of $1.5MW/m^2$ on the first wall with $\sim 1.3MW$ coming from neutrons, typically $10-20MW/m^2$ on the divertor and not yet any transient loads taken into account. This machine is already significantly different in size and performance from the next step device, ITER. Main differences include significant power and hence neutron production ($1dpa \sim 5 \times 10^{25} n/m^2$), Tritium self sufficiency, high availability and duty cycle as well as a pulse length of hours rather than minutes. In addition, safety regulation will be more stringent both for operation and also for maintainability and component exchange [9]. A reactor might even go beyond, e.g. steady state operation.

II. PWI CONSIDERATIONS

Several issues related to materials used in its construction of a future fusion reactor need still to be tackled. Among those are the issues related to the first wall and divertor surfaces, their power handling capabilities and lifetime. For the next generation device, ITER, a solution based on actively cooled tungsten (W) components has been developed for the divertor, while beryllium will be used on the first wall [10]. The cooling medium will be water as is also considered for high heat load components in DEMO [9]. In contrast to a reactor where high wall temperature ($> 300°$ C) facilitate energy production ITER W components are only operated at 70° C and hence in the brittle regime.

For the first wall of a fusion reactor unique challenges on materials in extreme environments require advanced features in areas ranging from mechanical strength to thermal properties. The main challenges include wall lifetime, erosion, fuel management and overall safety. For the lifetime of the wall material, considerations of erosion, thermal fatigue as well as transient heat loading are crucial as typically 10^9 (30Hz) transients, so called ELMs, are to be expected during one full power year of operation.

Tungsten is the main candidate material for the first wall of a fusion reactor as it is resilient against erosion (Fig. 2), has the highest melting point of any metal and shows rather benign behavior under neutron irradiation as well as low tritium retention. Erosion of the first wall and the divertor will require a significant armor thickness or short exchange intervals, while high-power transients need strong mitigation efficiency to prevent damage to the plasma facing components (PFCs) [13].

One issue that is related to the wall erosion is the fusion performance of the fusion device and hence the amount of tolerable impurities. For tungsten only minute amounts can be tolerated when considering

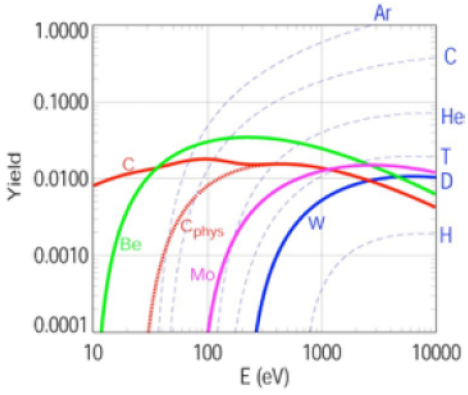

Figure 2: Sputtering yields for C, Mo, Be and W bombarded with D ions [11]. For C, chemical erosion enhances the yield at low energies and yields. For W, impurity sputtering, such as Ar ions, dominates. Based on [11, 12]

the burn conditions of the plasma and cooling provide by tungsten radiating in the plasma. In [14] the analysis given for only helium as on of the impurities shows that 10^{-4} W atoms per deuterium atom can be enough to extinguish the fusion performance.

For the next step devices, e.g. DEMO, or a future fusion reactor the limits on power-exhaust, availability and lifetime are quite stringent. Radiation effects including neutron embrittlement may limit actively cooled W components in DEMO to about 3-5 MW/m^2 due to the diminished thermal conductivity or the need to replace CuCrZr with Steels [15]. Quite extensive studies and materials programs [1, 16–18] have already been performed hence it is assumed that the boundary conditions [15] be fulfilled for the materials are in many cases above the technical feasibility limits as they are understood today.

- High divertor power handling, i.e., ability to withstand power loads larger than $10\,MW/m^2$. here especially the choice of coolant is critical. Water cooling will be required to allow sufficient exhaust efficienvy
- The radiation damage for the divertor is predicted to be close to 3 dpa/fpy. For copper if chosen the value varies between 3 and 5 dpa / fpy (full power year)
- It is assumed that despite the radiation damage erosion is the dominant lifetime determining factor.
- Even when starting up DEMO in phases a final blanket should be capable of lasting up to 50 dpa.

In the following we will however try to concentrate on three groups of issues [9, 15]

- Power exhaust and energy production: The first wall blanket exhausts the power and hence must be operated at elevated temperatures to allow for efficient energy conversion. Here a material must be chosen with a suitable operational window and sufficient exhaust capability. The cooling medium for high temperature operation can be crucial.

- Mitigate material degradation due to neutrons and reduce radioactive waste: One can select materials that allow high temperature operation, mitigate effect of operational degradation such as embrittlement and neutron effects linked to transmutation.

- Tritium self-sufficiency and safety: 22 kg/year of tritium are required for a 2GW plasma operated at 20% availability, this means $\sim$ 85% [15] of the in-vessel surface must be covered by a breeding blanket and the loss of tritium without ability to recover needs to be minimized. Accident scenarios need to be considered e.g. loss of coolant and air ingress are among the possible scenarios.

Tritium retention in plasma-facing components (PFCs) due to plasma wall interactions is one of the most critical safety issues for ITER and future fusion devices. For carbon based PFCs the co-deposition of fuel with re-deposited carbon has been identified as the main retention mechanism (fig. 3).

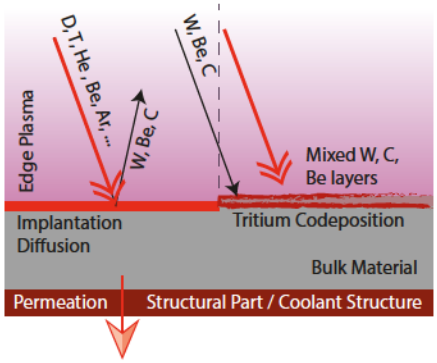

Figure 3: Fuel retetention and permeation issues under plasma exposure conditions

This retention grows linearly with particle fluence and can reach such large amounts that carbon is omitted in the activated phase of ITER and future reactors [12]. Instead, tungsten is foreseen as PFC material in the divertor of ITER and is the most promising candidate for PFCs in future reactors. Fuel retention behaviour of tungsten is subject to present studies. It was shown that by replacing CFC with W in the Joint European Torus (JET) the retention e.g. can be significantly reduced [19] as predicted (Fig. 4).

An issue that however remains is the potential for diffusion of hydrogen into the material. In the breeding blankets especially the interaction of tritium with Reduced Activation Ferritic Martensitic (RAFM) steels, e.g. EUROFER-97, can be crucial to minimise fuel retention or loss.

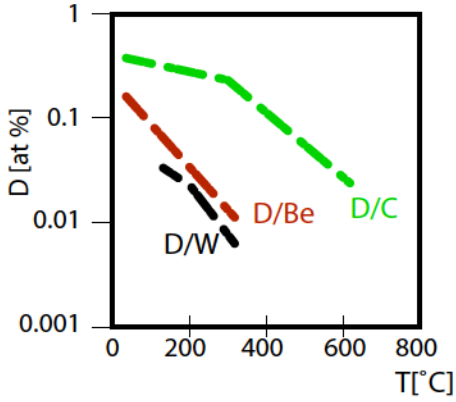

Figure 4: Estimate of retained deuterium concentration in C, Be and W deposits under codeposition conditions. (Sketch based on [12])

III. MATERIAL ISSUES FOR TUNGSTEN

In the following sections several issues are described that arise from the above depicted boundary conditions. As an example the divertor lifetime is considered as the desired parameter. Typically there are three main avenues of damage to the material of the divertor. Either high heat-loads cause melting, cracking or recrystallisation or neutrons impact the actual microstructure of the material. Surfaces are damage by ions impacting and causing both surface morphology changes or erosion. Fig. 5 depicts hence one approach to solving at least some of the problems. Choosing Tungsten (W) as the main wall material suppresses sputtering due to the high atomic mass in contrast to the sputtering ions. Tungsten also has a rather high thermal conductivity (Cu: $\sim$ 390 W/(mK) W: $\sim$ 173 W/(mK) Mo: $\sim$ 138 W/(mK) Steel: $\sim$ 17 W/(mK) and can hence facility higher heat exhaust than e.g. steel, for tungsten also the high melting point is beneficial. Thermal properties however are intrinsically linked to potential transmutation and irradiation processes. In addition it is know that tungsten has a rather low hydrogen solubility and hence facilitates low retention under fusion conditions [19]. Tungsten is however inherently brittle and does show catastrophic oxidation behaviour at elevated temperatures.

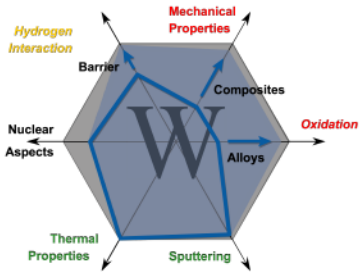

Figure 5: Tungsten as a first wall material

As shown in fig. 5 one can not always fine tune all material properties at once with one approach, but multiple issues might have to be improved, thus later maybe a component can be built that can tackle all issues.

A. Operational Window

Based on the assumption that W is the option so far to be used as the surface layer the reactor PFCs already quite basic assumptions can be made when picking the operational window and thickness of such components.

The lower operating temperature limit in metal alloys is mainly determined by radiation embrittlement (decrease in fracture toughness), which is generally most pronounced for irradiation temperatures below $\sim 0.3T_{melt}$, where T_{melt} is the melting temperature (Tungsten $\sim 3300K$) [20]. The upper operating temperature limit is determined by one of four factors, all of which become more pronounced with increasing exposure time such as thermal creep (grain boundary sliding or matrix diffusional creep), high temperature helium embrittlement of grain boundaries, cavity swelling (particularly important for Cu alloys), and coolant compatibility such as corrosion issues.

If the PFCs surface is operated at 1100 ° C as optimal for W [21] and copper is chosen together with water as part of the coolant solution the thickness is automatically determined (5) with κ the heat conductivity)

$$q = \frac{T_{surface} - T_{cool}}{d_1/\kappa_1 + d_2/\kappa_2} \tag{5}$$

This means that the maximum heat-exhaust is determined by the heat conduction, the potential for recrystallization and the ductile to brittle transition behavior of the material. Here new material options are required to allow a larger operational window, by overcoming the limiting factor, keeping in mind that a maximized heat conduction is crucial (e.g. Steel). For transient events the limits can even be more stringent when considering the limited penetration depth of a given heat-pulse fig. 6(b) and its maximum surface temperature rise (egn. (6)) with κ the heat

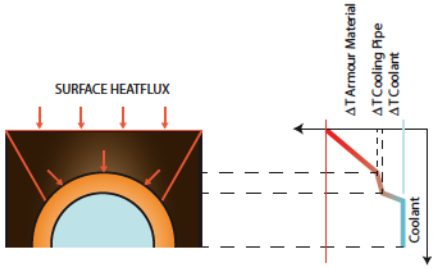

(a) Steady state heat flux in a conventional monoblock like structure

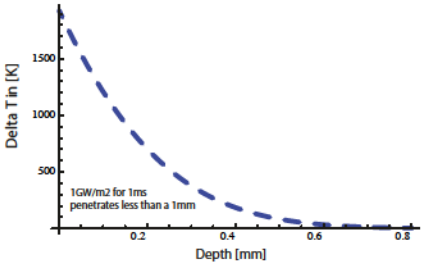

(b) Heat flux penetration (in tungsten) from 1GW, 1ms event

Figure 6: Power-exhaust - Issues arising from steady state and transients

conductivity, ρ the density and c the heat capacity). Active cooling for fast transients is meaningless because of the small penetration depth.

$$\Delta T^{\infty}_{surface}(t) = \frac{q_s}{\sqrt{\kappa\rho c}\cdot\sqrt{\pi}}\sqrt{\Delta t} \tag{6}$$

From assumptions related to unmitigated ELMs at 1 GW/m^2 for 1ms [13] already a temperature rise of 1500K is achieved in only the top 1 mm. Cracking or melting is difficult to prevent here. Irreparable damage has to be avoided at any cost. Even higher thermal wall loads caused by so called disruptions, sudden and uncontrolled loss of the plasma with deposition of the energy on the wall. Assuming that 50% of the thermal energy are radiated during thermal quench of the plasma and with a limited inhomogeneity in toroidal and poloidal direction respectively the thermal disruption loads are always much above the crack limit [22] even-though below the melt limit. Variation of the torus geometry (aspect ratio) provides only moderate reduction of loads.

B. Evolution of Thermal Properties

In addition to the above mentioned issues fig. 7 shows that the fusion environment can also drastically change some of the set assumptions. Already a small amount of transmutation can have a significant influence on the power-exhaust. When calculating the thermal conductivity based on $\kappa \cdot \rho = L \cdot T$ with κ

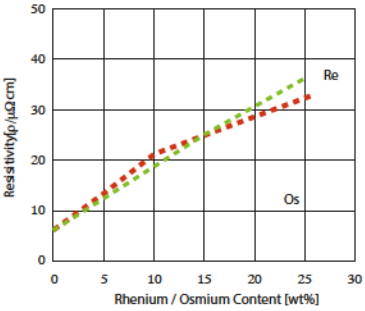

(a) Electrical resistivity of W containing various amounts of Re or Os. The red line and green line stand for W-xRe and W-xOs respectively [23]

Figure 7: Change of electrical and thermal properties of tungsten under neutron irradiation and transmutation

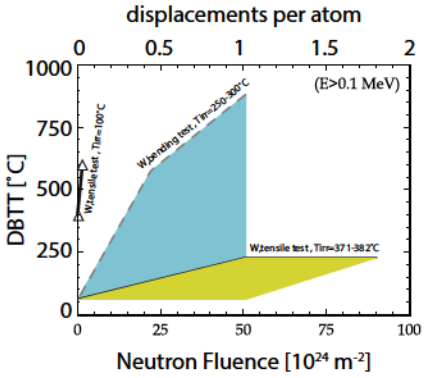

Figure 8: DBTT dependence after neutron irradiation based on [26]

the thermal conductivity, ρ the resistivity and L the Lorentz number with a value of $3.2 \times 10^{-8} W\Omega K^{-2}$ for tungsten one can estimated that κ drops 60% already at 5wt% or Re or Os. From previous work [24] one can determine that especially at lower temperatures κ drops significantly (30%). In any case one does depend on stable and predictable material properties even under radiation - or a detailed knowledge of the time dependent evolution to determine lifetime and performance of components.

C. Embrittlement

Conventional high performance materials offer high strength and stiffness combined with low density hence weight. However, a fundamental limitation of the current approach is the inherent brittleness of tungsten. As seen above cracking hence brittle behavior can be a limiting factor when operating any PFC in a tokamak [22]. For the fusion environment the additional problem becomes operational embrittlement. An issue related to embrittlement is certainly the recrystallization of tungsten. at temperatures of 1400K only mere hours are required to complete recrystallize the material [25].

Fig. 8 shows that already at moderate neutron fluence corresponding to 1 dpa the DBTT of tungsten moves up to almost 900° C. If in addition recyrstallisation takes place (fig. 8) almost no structural load can be given to the tungsten component at temperatures of a few hundred degrees. For a typical mono-block [13, 24] a tungsten thickness of 6mm on top of the CuCrZr cooling pipe would mean, based on simple estimations (egn. 5) that only the top part of a exposed mono-block would be in the allowed temperature range [21]. This means for a water-cooled solution tungsten is normally a brittle hence only a functional part, suppressing e.g. erosion and allowing for high operational temperatures. Failure is usually sudden and catastrophic, with no significant damage or warning and little residual load-carrying capacity if any. Structures that satisfy a visual inspection may fail suddenly at loads much lower than expected. Cracking is usually avoided for PFCs and certainly for structural components.

D. Activation & Transmutation

An issue that especially for complex components with multiple material and alloying components can be quite crucial is the recyclability and activation under neutron irradiation. As fusion is typically considered a technology with minimal or now longterm nuclear waste [26] tungsten and e.g. special steel grades [27] have optimized radiation performance with respect to low activation, e.g. molybdenum and aluminium are avoided as they produce long term activation products [26, 28]

Based on a study provided in [5, 28] with a neutron flux at the first wall of $\sim 1.0^{15} ncm^{-2} s^{-1}$ one can estimate the activation of materials after a 5 year period. For materials exposed in the divertor a factor 10 lower neutron rate is expected in the area of the high heat flux exposure due to geometrical reasons [9].

Fig. 9 shows the values of an assumed component containing W, Cr, Cu and Er, representing e.g. a typical mono-block with small interlayers and a copper cooling structure. Already here it is clear that the shielded hands on radiation level can not be achieved after 100 years when using copper cooling at the first wall. Mitigation of these effects need to be considered by utilizing non or low activation materials. e.g. replacing copper for the first wall and removing Er or Al oxides in favor of Ytrria.

IV. NEW MATERIAL OPTIONS

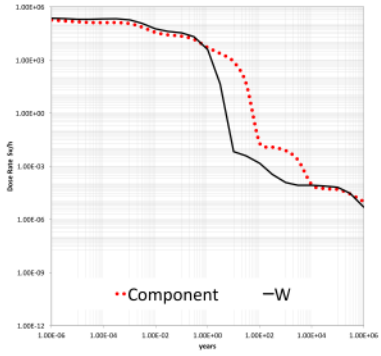

Figure 9: The activation of tungsten (first wall) is shown in comparison to a component (W 79.7wt%, Er 0.6wt%, Cr 12.1wt%, Cu 7.5%) for the first wall can be estimated as an upper bound (based on [28]). Divertor components in general are less prone to activation. Shielded hands-on level: $2\,mSv/h$, Hands-On Level: $10\,\mu Sv/h$

In [29] most of the problems for future fusion materials have been set out with links to the established roadmaps and assessments for fusion materials in existence at that time. Below a short summary is given to show the development of materials and the systematic efforts undertaken as part of the material program at Forschungszentrum Jülich GmbH.

Materials programs as given in [1,16–18,30] have already shown that the boundary conditions [15] to be be fulfilled for the materials in a future reactor are in many cases above the currently understood technical boundaries [31].

For the next step devices, e.g. DEMO [9,15,32–35], or a future fusion reactor including CFETR [36] the limits on power exhaust, availability and lifetime are even more demanding, as conventional monoblocks are allowing for $10MW/m^2$ [13,37] and transmutation and radiation damage can quickly diminish the thermal conductivity to 50% [23,38]. Radiation effects including neutron embrittlement [39] do limit actively cooled W components in DEMO to about 3-5 MW/m^2 due to the diminished thermal conductivity and the need to replace CuCrZr with Steels with their low thermal conductivity [15,40].

Quite extensive studies and materials programs [1, 16–18] have already been performed. Based on these it is assumed that the boundary conditions [15,32] to be fulfilled for the materials are in many cases above the technical feasibility limits as they are understood today. Here, also new design criteria are needed [32,41–43]

In the following we will however try to concentrate on three groups of issues and related new material classes

- Tungsten Armour on the first wall: Accident scenarios need to be considered e.g. loss-of-coolant and air ingr ess (Smart - W Alloys section).
- First wall Armour Joints - Choose appropriate technologies for first wall Materials Joints of W - and Steels (Functionally Graded Materials section).
- High Heat Flux Materials: Effects of material degradation due to neutrons and high temperatures - generally embrittlement needs to be taken into account (W-Composites).
- Tritium self-sufficiency and safety: loss of Tritium must be minimised (Permeation Barriers section).

New material for fusion are being considered worldwide and include also new Copper Materials and Copper Composites [44, 45], tungsten heavy alloy and ductile phase toughened tungsten [46–48] as well as advanced manufacturing methods for even more advanced material concepts [49,50].

A. W - Alloys

As mentioned above W is the most promising candidate materials for the first wall. However, in case of a loss-of-coolant accident (LOCA), the temperature of the first wall armour made of W could rise up to 1450 K - due to nuclear after heat as shown in figure 10 [3,4]. In combination with influx of air, a break of vacuum or coolant, water, significant amounts of tungsten oxides WO_3 can be formed, which can be mobilized by sublimation at temperatures of about 1170 K. At the highest predicted temperatures of around 1450 K a sublimation rate of 300kg/h is calculated assuming a $1000m^2$ of first wall surface [51].

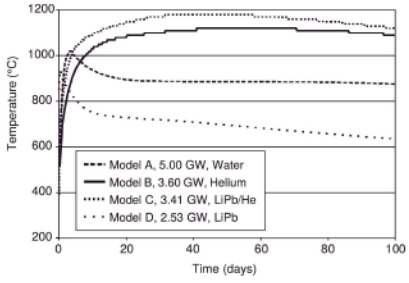

Figure 10: Calculated temperature profiles after an accident with a total loss of all coolant, (Reproduced with permission [3] Copyright 2007 EFDA , IOP , [4]. Copyright 2006 EFDA, ELSEVIER)

In case of a reactor LOCA normally less than 50% of the elements typically found in the aerosols

(like Ag, Re, W,...) are actually released into the environment [52].

In order to suppress the release of W oxides tungsten-based alloys containing vitrifying components seem feasible, as they can be processed to thick protective coatings with reasonable thermal conductivity, e.g. by plasma spraying with subsequent densification as already demonstrated for titanium and tantalum coatings [53]. To suppress the release of W-oxides W-based self-passivating alloy were proposed by Koch et al. [17,54,55].

As shown in figure 11 a stable oxide scale would be formed in contrast to a volatile layer of W-oxides. The crucial part of the materials development is now to establish what alloying elements can be used and are possible when also considering bulk production.

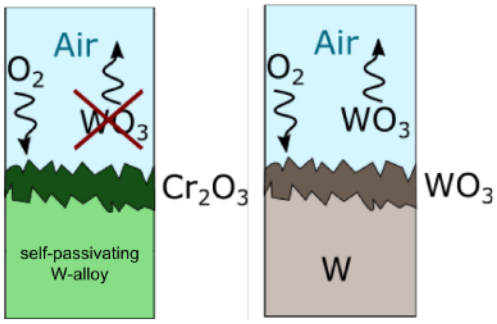

Figure 11: Self-passivation (l) compared to oxidation (r).

W-Si alloys showed good self-passivation properties by forming a SiO_2 film at the surface [54]. A compound of W-Si-Cr showed an even further reduction of the oxidation rate by a factor of 10^4 at 1273 K. However, the formation of brittle tungsten silicides was identified as unfeasible for mass production. In a next step W-Cr-Ti was utilised and showed as well good oxidation suppression [55].

Intensive studies on oxidation behaviour, manufacturing and mechanical properties were performed for both W-Cr-Si [56] and W-Cr-Ti [57–60] and compared in [61,62].

Enhanced erosion of light elements during regular reactor operation is not expected to be of concern as preferential sputtering of alloying elements leads to rapid depletion of the first atomic layers and leaves a pure W surface facing the plasma as per the given different sputtering yields. [11,63]. Subsequently, the tungsten layer suppresses further erosion, hence utilising its beneficial properties.

In the course of joint studies a new composition was proposed W-Cr-Y [51,64] based on existing results from [65]. Yttrium (Y) has the benefit of being a low activation material and shows high thermal stability as described above. As before model-systems were produced by means of magnetron sputtering and tested with respect to the oxidation behaviour.

So far, the most promising alloy systems feature chromium (Cr) as a passivating element as well as small amounts of yttrium as an active element improving the oxidation resistance.

Y enhances the Cr transport towards component surface during oxidation; it adds to the stability of the oxide layer and supports the formation of a continuously growing, well-adhering and dense Cr_2O_3 scale [51].

In figure 12 one of the main achievements is shown, the production of and oxidation study on - FAST produced, Bulk - W-Cr-Y samples [66].

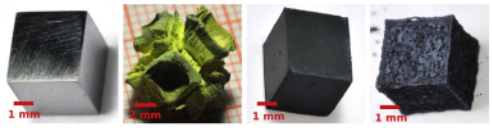

Figure 12: Photographs of the samples. (a) W-Cr-Y alloy before oxidation , after grinding. An identical pure W sample is not shown as it looks identical. (b) Pure W sample after 10h of oxidation in synthetic air at 1273K. (c) Optimized W-Cr-Y alloy after 44 h of oxidation in synthetic air at 1273 K. (d) W-Cr-Y alloy after 467 h of oxidation in synthetic air at 1273 K [66].

In [66] it is stated that to achieve full passive safety it is required that the alloy maintains the protective oxide layer for several weeks to suppress sublimation.Thus studies for passivation of up to 467h were performed as shown in figure 12. Crucially identified was also the quantification not only of oxidation / mass gain but direct measurement of the sublimation of the oxides [66,67].

It was shown that WCrY-systems can suppress the oxidation rate significantly compared to that of pure W and have a much better performance then previous systems like W-Cr-Ti [64,68–74].

I

B. W - Composites

To overcome the intrinsic brittleness and mechanical issues when using W as armour, a W fibre-reinforced W composite material (W_f/W), incorporating extrinsic toughening mechanisms can be used as shown in figure 13.

Various production routes are available when considering components based on W_f/W composites, either Chemical Vapor Deposition (CVD) [75,76] or powder metallurgical processes like Field Assisted Sintering (FAST) [77,78] and Hot Isostatic Pressing (HIP) [79–82] are available. As presented in [81] pressureless sintering of W_f/W was unsuccessful, as additional external pressure during sintering of W_f/W

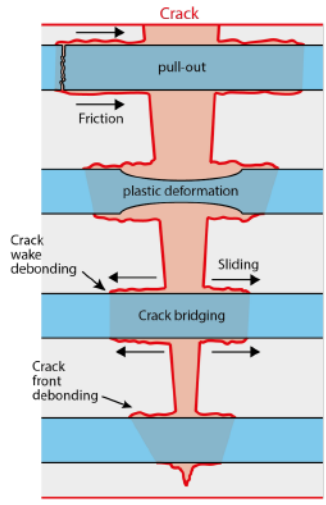

Figure 13: A selection of energy dissipation mechanisms in a fiber-composite material. Pullout of fibers, pull-out of matrix elements, crack deflection at the interface, crack bridging by fibers, crack meandering at the interface as well as plastic deformation of fibers.

is required to get a dense and crack-free sample. The proof of principle for CVD & PM W_f/W has been achieved and was presented in multiple publications [79, 82–86]. In the following a short overview on the basic mechanisms and achievements will be given based on the Powder Metallurgical (PM) production route as described in [79, 82, 87–90]

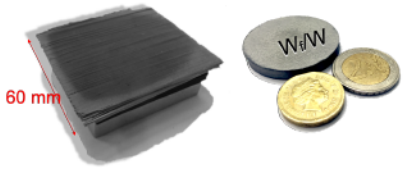

Figure 14: CVD W_f/W (l) PM W_f/W (r)

Typical Samples of CVD & PM W_f/W are shown in figure 14 where usual sizes are in the range of 40 mm x 40 mm x 5 mm or slightly larger for the CVD route.

Potassium doped W-fibres with 150 μm diameter and 2.4 mm length (OSRAM), together with pure W-powders (OSRAM) (average particle size 5 μm) were used as raw materials.These wires have been extensively characterised as to allow meaningfull extrapolations [91–96]. Potassium doped W-wires will retain their ductility even at elevated temperatures (above 1500 K) [83]. All pseudo-ductility mechanisms will thus remain activated [81, 82, 84].

Properties of the fibres will degrade however due to various influences e.g. by impurities during fabrication, high-temperatures or neutron irradiation during operation [26, 97]. In [98] it was found that all fibre samples categorised as brittle exhibit an increased C content compared to the fibres categorised as ductile.

All samples which are found to behave brittle have a C content of 0.0586 wt:% compared to the ductile samples with lower then 0.0013 wt%. This was later also found in the W_f/W samples and found to be related to the carbon distribution in the samples [86, 99].

The short fibres used in this PM version of W_f/W are shown in Fig. 15. Yttria is used as the interface material in order to allow the energy dissipation mechanisms to become active. Without the interface fibre and matrix would simple sinter together. Yttria is an ideal candidate as the interface material for the W_f/W composite due to its several advanced properties: good thermal and chemical stability, high mechanical strength and hardness [81, 87].

Studies to understand the pull out of fibres include modeling [100].

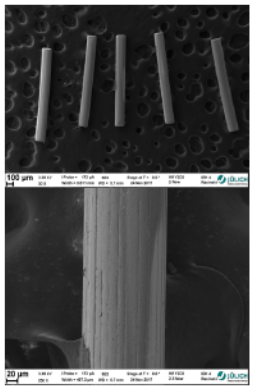

Figure 15: Short W-fibres coated by 2.5 μ Yttria interface

For the developed powder-metallurgical production of W_f/W the homogenous introduction of powder between the fibres is required for good material properties, hence short fibres are used in contrast to e.g. woven preforms [101, 102] or parallel long fibres as used in the CVD process route [75, 76].

The process gives rise to pressure and high temperatures on the interface and can thus cause a thin interface to dissipate [103–105]. Here 2.5 μm thick yttria is applied for a viable interface similar to the work given in [82].The fibres and powders are mixed homogeneously before sintering, in order to produce a W_f/W sample with a random fibre distribution and orientation. A density of $\sim$ 94% was achieved after applying the sintering process at 2173 K (4 min) and

60 MPa (heating rate 200 K/min) [81, 82]. In most production cases a fibre-volume-fraction of 30% was used. However variations thereof are used to understand the influence of interface fibre and matrix.

One of the crucial issues is to maintain as much of the properties [106] of the constituents even after exposing the material to the production cycle and the fusion environment. This allows for better extrinsic toughening and pseudo-ductile behaviour. Here, mainly the weak interface and the strength of the fibre is important [106]. As the material should dissipate as much energy as possible it is hoped to at least start with the inclusion of ductile fibres. Even if the fibres loose their ductility the pull-out of fibres and the crack deflection can still deliver some pseudo-ductility for a viable material option. In the following we will describe that one aspect of the production needs to be controlled with particular care to minimise the degradation of the material properties of the fibres.

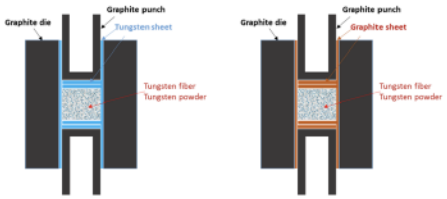

Figure 16: Two FAST procedures are employed to facilitate understanding of carbon diffusion on the final material properties (a) Tungsten foil as diffusion barrier, (b) graphite sheets for lubrication

One of the major improvements of the PM W_f/W samples established in the course of these studies was the role which the impurity content can play. In [86,99] it was established that depending on the production mechanisms of the PM W_f/W, namely the choice of the die material, the properties do change from fibres becoming brittle to remaining ductile after production. In figure 16 a sketch of the two different FAST procedures used is given. In one case the powder and die are separated by a graphite foil while in the other case a thin tungsten foil is used. Based on FAST samples with 20 and 40 mm diameter and a height of 5 mm were produced as shown in Fig. 14.

Typical tests for the materials include 3- or 4-point bending tests but also more advanced non destructive tests [107,108]. From the bending test samples as given e.g. in figure 17 one can clearly see fracture surfaces and thus the mechanisms at work required for pseudo-ductile behavior (cf. Fig. 13).

For both PM W_f/W as well as CVD W_f/W upscaling is crucial for further applications, thus the development of larger scale material samples, mockups [109] and their tests is an important part of the

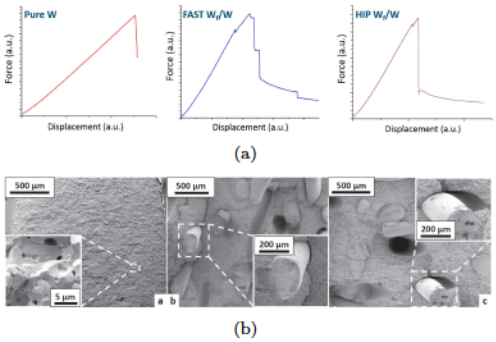

Figure 17: In (a) force displacement curves in (a.u.) are given to compare the reletive behavior of pure tungsten, FAST and HIP W_f/W, (b) gives the fracture surfaces in which the different energy dissipating mechanisms can be identified.

W_f/W development. For the PM W_f/W upscaling is related to the application of FAST on larger scale material samples and thus relatively straight forward. For the CVD route multipel complications arise. From previous work including [101] as well as modeling [110] it is known that the choice of preform as well as deposition or infiltration process is crucial. Should one choose a layer-wise deposition process [75, 76, 84] for the production of the W_f/W composite the CVD parameters need to be chosen carefully [101, 110] to allow full densification. The temperature as well as partial pressures are the rate determining properties.

In order to overcome the limitations of a layer-wise deposition a continuous process was developed. For this process a tungsten weave is continually rolled onto a copper tube and coated in-situ with the W-Matrix. In general it can be said that up-scaling is the next big challenge for all types of W_f/W.

As a final remark on W_f/W it also needs to be said that studies related to PWI are essential when applying new materials in the fusion environment thus the influence of the interface - fibre - matrix complex needs to be studied. The interfaces in the material and at the material surface can potentially influence fuel retention and erosion behaviour significantly [111]. Yttria among other characteristics is also used as a permeation barrier (see below).

C. W - Steel Joints

Having discussed tungsten as the main candidate for the PFMs of a fusion reactor the joint to the underlying cooling structure or wall structure in general is crucial. From the differing thermal expansion coefficients for the different materials (copper $\sim 16.5\mu$m/(mK), tungsten: $\sim 4.5\mu$m/(mK), stainless steel: $\sim 12\mu$m/(mK)) it is clear that a mature solution of joining them needs to be established. Ther-

mally induced stresses and strains may either spontaneously or in the long term yield pre-mature failure of the FW component requiring feasible ways to reduce the loads [112, 113]. Here especially the high neutron capture cross section and long cooling down time of tungsten, required before maintenance, is limiting tungsten armour at the first wall to a thin layer in the order of a few mm [114].

As example systems for such armour layers the development of functionally graded materials (FGMs) between W as the PFM and the structural material, typically Steel (EUROFER97), can be considered. As depicted in [115] FGMs are promising candidates for interlayers between components of two different materials especially when considering applications such as the blanket modules of a DEMO [9, 116] or even a helium cooled tungsten divertor with low to medium heat-flux (1-5MW/m^2) for which the heat conductivity of EUROFER-97 may be sufficient.

For the production of W-Steel FGMs typically powder-metallurgical routes are considered. Here atmospheric and vacuum plasma spraying [117, 118], as well as resistive sintering technologies [119, 120] are relevant techniques.However, all current methods have problems with the formation of cracks or inter-metallic phases (Fe7W6, Fe2W) due to extended high temperature exposure of the W-Steel mixtures.

A new and unique production route for W-Steel FGMs is being considered. The main new feature is the ultra fast sintering technique in addition to mechanical alloying allowing for the suppression of the brittle inter-metallic phases.

The main focus of the activity is to establish if and how FGMs can be superior or comparable to classical joints. Here modelling, and production methods are considered together [121–123]. In addition to the Ultra fast sintered FGMs [124] also Atmospheric Plasma Spraying (APS) produced FGMs are being studied [125].

From modelling it was concluded:

- An FGM is ideally composed of 10 sublayers. Considering manufacturing aspects, three layers are however a good compromise still keeping plastic deformations in the component at a minimum.

- FGM thickness depends on the thermal loads expected. For lower heat loads, the stress-redistributing performance improves with thicker FGMs

Electro discharge sintering (EDS) is a uniquely short sintering technique [126] that was first used for the fabrication of Fe/W composites in [124]. EDS combines characteristics of spark plasma sintering (SPS) and capacitor discharge welding. After mechanical alloying of the Fe and W powders consolidation takes place within seconds. The structure of the powders

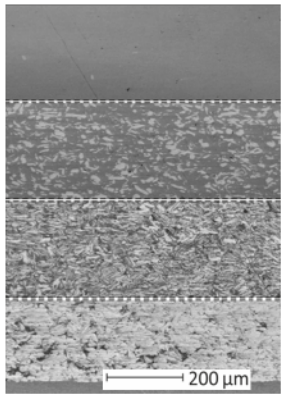

Figure 18: Microstructure of FGM produce via electro discharge sintering. Top to bottom 100% Fe, 75% Fe, 50% Fe, 25% Fe.

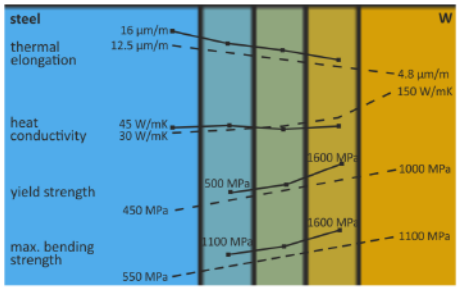

Figure 19: Rough sketch of thermo-mechanical properties of W/Iron FGMs based on [121, 124].

is typically stratified allowing for low or no production of inter-metallics. The resulting properties of the FGM are summarised in figure 19 and are in line with rule of mixture predictions.

In summary:

- Fe/W composites, shows little porosity and a fine distribution of Fe and W volumes.
- With increasing W fraction, the Fe/W composites show a linear decrease of the coefficient of thermal expansion.
- Albeit defects like porosity and elemental interfaces, thermal conductivity of all composites is still above that of Fe/ Steel.
- The mechanical parameters, e.g. yield-strength, show an increase with increasing W fraction.

The work is currently moving towards utilising EUROFER powders to produce even more relevant model-systems.

D. Permeation Barriers

One of the most prominent issues for fusion is fuel retention and management. Deuterium and Tritium are the two hydrogen isotopes used. Tritium is a rare and radioactive isotope of hydrogen, and as such decays with a half life of roughly 12 years. Naturally occurring Tritium is extremely rare on Earth. The atmosphere has only trace amounts, formed by the interaction of its gases with cosmic rays. It can be produced by irradiating lithium metal or lithium-bearing ceramic pebbles in a nuclear reactor.

For fusion applications both the availability and safety aspects are important. The first one in order to maximise fuel efficiency and the later in order to minimise environmental impact. In order to reduce fuel loss and maximise inherent safety, Tritium accumulation into reactor walls and permeation through walls have to be prevented. Therefore, the development of Tritium permeation barriers (TPB) is crucial for safe reactor operation [127–129].

For a viable power plant permeation barrier with a permeation reduction factor in the range of 50-500 is necessary [127, 128]. In general, the layers applied as Tritium permeation barriers have to feature high thermal and chemical stability in a reducing atmosphere. A lot of thin ceramic coatings, e.g. $Er_2O_3$and Y_2O_3, fulfil these requirements [130, 131]. In the last decades, $Al_2O_3$and Er_2O_3 are among a large basket of material suitable as permeation barriers [132, 133] however many of them show issues with respect to production and especially with stability under activation and activation itself.

Recently, Y_2O_3 is being considered as an ideal candidate for Tritium permeation barrier material, because of its favourably low activation behaviour [134]. Studies on Yttria production, coating as well as the analysis of the permeation behaviour have been the corner stone of the activity. Based on a magnetron sputtering deposition process developed for Y_2O_3 [87] studies on the permeation behaviour of Yttria have lead to a significant breakthrough in the permeation reduction factor (PRF) as well as the understanding of the underlying microstructure.

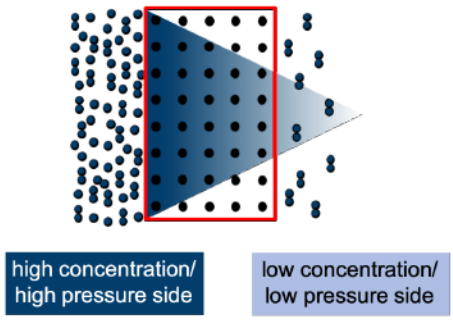

Figure 20: Schematic view of experimental setup for permeation rate determination.

For the determination of the permeation reduction factor a setup containing the sample between a high (HPV) and a low pressure volume (LPV) is used as depicted schematically in figure 20. By varying pressure and temperature during the experiments the various dependencies of the permeation process can be elucidated as described e.g. in [135]. Typically the permeation process can be described as a combination of a surface or diffusion limited process, depending on surface properties and of the systems used.

For the initial studies Y_2O_3 is deposited on both sides of mirror polished Eurofer97 steel substrates [136]. Before coating the samples the substrate is cleaned by the magnetron plasma at lower energies. Then, additionally oxygen is injected into the chamber, and an yttrium metal target (Kurt J. Lesker Company) is sputtered.

Due to the reaction of gas with metal ions an Y_2O_3 thin film is formed. After the deposition the roughly 1 μm thin films are annealed at 550 °C for 16 h in a vacuum furnace at a pressure to achieve the stable cubic phase structure of the Y_2O_3 system. For further studies three different deposition modes were used. The hot metallic mode with substrate surface heating during the deposition process, the cold metallic mode without this surface heating, and the reacted mode also without this surface heating. Due to the higher resistance of the oxidized target, the deposition voltage in the reacted mode (< 100 V) is lower than in the hot metallic mode (> 300 V) [135]. Dependent on the mode used the mismatch of the Coefficient of Thermal Expansion (CTE) between Steel and Oxide Ceramic can lead to cracking. In order to reduce the surface temperature differences be-

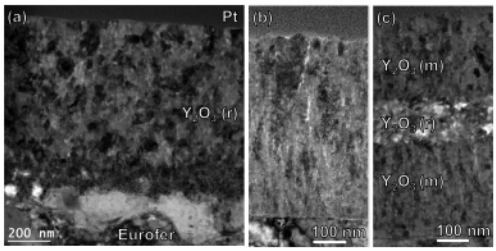

Figure 21: TEM images of the Y_2O_3 thin film cross sections after the permeation measurements of the reacted mode (a), the hot metallic mode (b), and the layer system (c) on Eurofer. Pt is coated on the top of each thin film. (b and c).

tween the deposition process and the subsequent experiments, the substrate surfaces are heated up to $\sim$ 300° C for hot metallic mode.

In figure 21 the three main types of microstructures produced are indicated and also related to their respective production process. a) and b) are mainly governed by the difference between (hot) metallic mode and reactive mode and c) is also indicating the option of a layered system [135].

When considering the different coatings one of the main outcomes of the studies can be summarised as follows.

The PRF varies clearly with the microstructure of the coating in the order of up to a factor of 100 [135]. Due to the difference in the coating process, control of the microstructure can be achieved e.g. hot metallic vs reacted mode (figure 21). The thin films grow in the reacted deposition mode in an equiaxed grain structure and in the hot metallic mode in a columnar grain structure. In the layer system both grain structures can be found as one layer is based on the hot metallic the other on the reacted mode. Annealing at 550 °C for 15 h, leads to all samples showing the Y_2O_3 stoichiometry. This annealing step is essential to achieve the cubic phase of Y_2O_3.

For the three different samples one can essentially identify a decrease in grain boundary densities in the permeation direction from highest to lowest: reacted mode, layer system, and hot metallic mode - this is essentially also the trend for the permeation flux. Consequently, the grain boundary diffusion through the Y_2O_3 thin films is preferred compared to bulk diffusion. For the reacted mode a PRF of 24 and for the hot metallic mode a PRF of 1100 is determined. In addition to Tritium permeation barriers also the permeation behaviour through pure steel and EUROFER97 samples was measured [137]. In both cases, Eurofer97 and 316L, the permeation behaviour is diffusion limited. The permeation through the 316L Steel is about a factor of ten smaller when compared to EUROFER97. This is relevant in particular for consideration in ITER operation as no permeation barriers are so far considered.

For studies of other candidate materials references related to an intensive collaboration with a Japanese group are given. Here particularly erbia is considered below [138–153].

V. SUMMARY AND OUTLOOK

Considering all the above mentioned issues when using materials in a fusion reactor environment a highly integrated approach is required. The lifetime of PFCs and joints due to erosion, creep, thermal cycling, embrittlement needs to be compatible with steady state operation and short maintenance intervals.Thermal properties of composites and components have to be at least similar to bulk materials when enhanced properties in terms of strength are not to hinder the maximization of operational performance. Damage resilient materials can here facilitate small, thin components and hence higher exhaust capabilities. The components need to be compatible with the aim of tritium breeding and self-sufficiency and hence mitigate tritium retention and loss.

In summary it can be said that based on the presented work new operational space can be gained by making tungsten more resilient to failure modes by utilising a composite approach and allowing for passive safety by controlling potential oxidation behaviours by means of new tungsten alloys. The later is relevant in particular for the first wall and blanket area of a future fusion reactor while the composites due to their enhanced ductility, while retaining pure tungsten thermal properties is typically considered for the load bearing components in the divertor.

In general material for fusion need to be considered in an integrated approach, thus joints and functional layers need to be included in any component design, this is where FGMs as well as permeation barriers play an integral party to make plasma facing components viable for application. In future the materials research related to fusion, will extend the activities with respect to industrial upscaling and component production and testing. Here the focus will be the applicability in the medium to long term for a European Demo to be constructed in the 2040s. Material testing of those components will then be performed analogous to the activities described in [154] that successfully lead to the use and qualification of bulk baseline tungsten materials in ITER.

VI. ACKNOWLEDGEMENTS

In particular I would like to thank all people involved in preparing this manuscript which are mainly the authors of works cited in [7]

REFERENCES

1. D. Stork et al. Assessment of the EU R&D programme on DEMO structural and high-heat flux materials, final report of the materials assessment group,. Technical Report EFDA(12)52/7.2, EFDA, December 2012.

2. R.P. Wenninger, M. Bernert, T. Eich, E. Fable, G. Federici, A. Kallenbach, A. Loarte, C. Lowry, D. McDonald, R. Neu, T. Puetterich, P. Schneider, B. Sieglin, G. Strohmayer, F. Reimold, and M. Wischmeier. DEMo divertor limitations during and in between elms. *Nuclear Fusion*, 54(11):114003, 2014.

3. D. Maisonnier, D. Campbell, I. Cook, L. Di Pace, L. Giancarli, J. Hayward, A. Li Puma, M. Medrano, P. Norajitra, M. Roccella, P. Sardain, M.Q. Tran, and D. Ward. Power plant conceptual studies in Europe. *Nuclear Fusion*, 47(11):1524, 2007.

4. David Maisonnier, Iau Cook, Sardain Pierre, Boccaccini Lorenzo, Di Pace Luigi, Giancarli Luciano, Norajitra Prachai, and Pizzuto Aldo. DEMO and fusion power plant conceptual studies in Europe. *Fusion Engineering and Design*, 81(8-4):1123–1130, 2006. ISFNT-7.

5. D. Maisonnier, I. Cook, P. Sardain, R. Andreani, L. Di Pace, M. Forrest, L. Giancarli, S. Hermsmeyer, P. Norajitra, N. Taylor, and D. Ward. A conceptual study of commercial fusion power plants. Final Report of the European Fusion Power Plant Conceptual Study (PPCS) EFDA(05)-27/4.10, EFDA, 2005. EFDA(05)-27/4.10.

6. F. Romanelli. *Fusion Electricity A roadmap to the realisation of fusion energy.* European Fusion Development Agreement, EFDA, 2012. ISBN 978-3-00-040720-8.

7. J. W. Coenen. Fusion materials development at forschungszentrum juelich. *Advanced Engineering Materials*, mar 2020.

8. J.W. Coenen. *TUNGSTEN AS A PLASMA FACING COMPONENT AND DEVELOPMENT OF ADVANCED MATERIALS FOR FUSION*, chapter MA-1, pages 250–259. Forschungszentrum Jülich GmbH, 2015. 12th Carolus Magnus Summer School on Plasma and Fusion Energy Physics Leuven (Belgium), August 24 - September 4 2015 Online-Publikation 468 Seiten; ISBN 978-3-95806-107-1;.

9. G. Federici, G. Giruzzi, C. Lowry, R. Kemp, D. Ward, R. Wenninger, and H. Zohm. Eu DEMo design and r and d studies. In *Fusion Engineering (SOFE), 2013 IEEE 25th Symposium on*, pages 1–8, June 2013.

10. R.A. Pitts, S. Carpentier, F. Escourbiac, T. Hirai, V. Komarov, A.S. Kukushkin, S. Lisgo, A. Loarte, M. Merola, R. Mitteau, A.R. Raffray, M. Shimada, and P.C. Stangeby. Physics basis and design of the ITER plasma-facing components. *Journal of Nuclear Materials*, 415(1 SUPPL):S957–S964, 2011.

11. W. Eckstein, C. Garcia-Rosales, J. Roth, and W. Ottenberger. Sputtering data. Report IPP 9/82, Max-Planck-Instut fuer Plasmaphysik, 1993.

12. Joachim Roth, E. Tsitrone, A. Loarte, Th. Loarer, G. Counsell, R. Neu, V. Philipps, S. Brezinsek, M. Lehnen, P. Coad, Ch. Grisolia, K. Schmid, K. Krieger, A. Kallenbach, B. Lipschultz, R. Doerner, R. Causey, V. Alimov, W. Shu, O. Ogorodnikova, A. Kirschner, G. Federici, and A. Kukushkin. Recent analysis of key plasma wall interactions issues for {ITER}. *Journal of Nuclear Materials*, 390, 391(0):1–9, 2009. PSI-18.

13. R.A. Pitts, S. Carpentier, F. Escourbiac, T. Hirai, V. Komarov, S. Lisgo, A.S. Kukushkin, A. Loarte, M. Merola, A. Sashala Naik, R. Mitteau, M. Sugihara, B. Bazylev, and P.C. Stangeby. A full tungsten divertor for ITEr: physics issues and design status. *Journal of Nuclear Materials*, 438:S48, 2013.

14. T. Puetterich, R. Neu, R. Dux, A.D. Whiteford, M.G. O'Mullane, H.P. Summers, and the ASDEX Upgrade Team. Calculation and experimental test of the cooling factor of tungsten. *Nuclear Fusion*, 50(2):025012, 2010.

15. Ch. Bachmann. Initial DEMo tokamak design configuration studies. In *http://www.soft2014.eu*, volume 98-99, page 1423–1426, http://www.soft2014.eu, October 2014.

16. D. Stork, P. Agostini, J.L. Boutard, D. Buckthorpe, E. Diegele, S.L. Dudarev, C. English, G. Federici, M.R. Gilbert, S. Gonzalez, A. Ibarra, C. Linsmeier, A. Li Puma, G. Marbach, P.F. Morris, L.W. Packer, B.l Raj, M. Rieth, M.Q. Tran, D.J. Ward, and S.J. Zinkle. Developing structural, high-heat flux and plasma facing materials for a near-term DEMO fusion power plant: The eu assessment. *Journal of Nuclear Materials*, 455(1-3):277–291, 2014.

17. M. Rieth, S.L. Dudarev, S.M. Gonzalez De Vicente, J. Aktaa, T. Ahlgren, S. Antusch, D.E.J. Armstrong, M. Balden, N. Baluc, M.-F. Barthe, W.W. Basuki, M. Battabyal, C.S. Becquart, D. Blagoeva, H. Boldyryeva,

J. Brinkmann, M. Celino, L. Ciupinski, J.B. Correia, A. De Backer, C. Domain, E. Gaganidze, C. Garcia-Rosales, J. Gibson, M.R. Gilbert, S. Giusepponi, B. Gludovatz, H. Greuner, K. Heinola, T. Hoeschen, A. Hoffmann, N. Holstein, F. Koch, W. Krauss, H. Li, S. Lindig, J. Linke, C. Linsmeier, P. Lopez-Ruiz, H. Maier, J. Matejicek, T.P. Mishra, M. Muhammed, A. Munoz, M. Muzyk, K. Nordlund, D. Nguyen-Manh, J. Opschoor, N. Ordas, T. Palacios, G. Pintsuk, R. Pippan, J. Reiser, J. Riesch, S.G. Roberts, L. Romaner, M. Rosinski, M. Sanchez, W. Schulmeyer, H. Traxler, A. Urena, J.G. Van Der Laan, L. Veleva, S. Wahlberg, M. Walter, T. Weber, T. Weitkamp, S. Wurster, M.A. Yar, J.H. You, and A. Zivelonghi. A brief summary of the progress on the EFDA tungsten materials program. *Journal of Nuclear Materials*, 442(1-3 SUPPL.1):173–180, 2013.

18. Jens Reiser and Michael Rieth. Optimization and limitations of known DEMO divertor concepts. *Fusion Engineering and Design*, 87(5 - 6):718–721, 2012.

19. S. Brezinsek, T. Loarer, V. Philipps, H.G. Esser, S. Gruenhagen, R. Smith, R. Felton, J. Banks, P. Belo, A. Boboc, J. Bucalossi, M. Clever, J.W. Coenen, I. Coffey, S. Devaux, D. Douai, M. Freisinger, D. Frigione, M. Groth, A. Huber, J. Hobirk, S. Jachmich, S. Knipe, K. Krieger, U. Kruezi, S. Marsen, G.F. Matthews, A.G. Meigs, F. Nave, I. Nunes, R. Neu, J. Roth, M.F. Stamp, S. Vartanian, U. Samm, and JET EFDA contributors. Fuel retention studies with the ITEr-like wall in jet. *Nuclear Fusion*, 53(8):083023, 2013.

20. Y. Igitkhanov, B. Bazylev, and R. Fetzer. The quantification of the key physics parameters for the DEMo fusion power reactor and analysis of the reactor relevant physics issues. KIT Scientific Reports 7661, KIT, 2015.

21. S.J Zinkle and N.M Ghoniem. Operating temperature windows for fusion reactor structural materials. *Fusion Engineering and Design*, 51(0):55–71, 2000.

22. J. Linke, T. Loewenhoff, V. Massaut, G. Pintsuk, G. Ritz, M. Roedig, A. Schmidt, C. Thomser, I. Uytdenhouwen, V. Vasechko, and M. Wirtz. Performance of different tungsten grades under transient thermal loads. *Nuclear Fusion*, 51(7):073017, 2011.

23. T. Tanno, A. Hasegawa, J.C. He, M. Fujiwara, M. Satou, S. Nogami, K. Abe, and T. Shishido. Effects of transmutation elements on the microstructural evolution and electrical resistivity of neutron-irradiated tungsten. *Journal of Nuclear Materials*, 386-388(0):218–221, 2009. ICFRM-13.

24. J. Linke. High heat flux performance of plasma facing materials and components under service conditions in future fusion reactors. *Fusion Science And Technology*, 53(2T):278–287, 2008.

25. Frank Goodwin, Sivaraman Guruswamy, KarlU. Kainer, Catrin Kammer, Wolfram Knabl, Alfred Koethe, Gerhard Leichtfried, Guenther Schlamp, Roland Stickler, and Hans Warlimont. Metals. In Werner Martienssen and Hans Warlimont, editors, *Springer Handbook of Condensed Matter and Materials Data*, pages 161–430. Springer Berlin Heidelberg, 2005.

26. H Bolt, V Barabash, G Federici, J Linke, A Loarte, J Roth, and K Sato. Plasma facing and high heat flux materials - needs for ITER and beyond. *Journal of Nuclear Materials*, 307, Part 1(0):43–52, 2002.

27. R. Lindau, A. Moeslang, M. Rieth, M. Klimiankou, E. Materna-Morris, A. Alamo, A.-A. F. Tavassoli, C. Cayron, A.-M. Lancha, P. Fernandez, N. Baluc, R. Schaeublin, E. Diegele, G. Filacchioni, J.W. Rensman, B.v.d. Schaaf, E. Lucon, and W. Dietz. Present development status of {EUROFER} and ods-eurofer for application in blanket concepts. *Fusion Engineering and Design*, 75-79(0):989–996, 2005. SOFT-23.

28. R.A. Forrest, A. Tabasso, C. Danani, S. Jakhar, and A.K. Shaw. Handbook of activation data calculated using easy-2007. UKAEA FUS 552, EURATOM/UKAEA Fusion Association, March 2009.

29. JW Coenen, S Antusch, M Aumann, W Biel, J Du, J Engels, S Heuer, A Houben, T Hoeschen, B Jasper, et al. Materials for DEMO and reactor applications—boundary conditions and new concepts. *Physica Scripta*, 2016(T167):014002, dec 2016.

30. Y. Ueda, K. Schmid, M. Balden, W. Coenen J., T. Loewenhoff, A. Ito, A. Hasegawa, c. Hardie, M. Porton, and M. Gilbert. Baseline high heat flux and plasma facing materials for fusion. *Nuclear Fusion*, 57(9):092006, jun 2017.

31. J.H. You, E. Visca, Ch. Bachmann, T. Barrett, F. Crescenzi, M. Fursdon, H. Greuner, D. Guilhem, P. Languille, M. Li, S. McIntosh, A.V. Mueller, J. Reiser, M. Richou, and M. Rieth. European DEMO divertor target: Operational requirements and material-design interface. *Nuclear Materials and Energy*, 9:171–176, dec 2016.

32. J.H. You, E. Visca, T. Barrett, B. Böswirth, F. Crescenzi, F. Domptail, M. Fursdon, F. Gallay, B-E. Ghidersa, H. Greuner, M. Li, A.v.

Müller, J. Reiser, M. Richou, S. Roccella, and Ch. Vorpahl. European divertor target concepts for DEMO: Design rationales and high heat flux performance. *Nuclear Materials and Energy*, 16:1–11, aug 2018.

33. Nobuyuki Asakura, Kazuo Hoshino, Hiroyasu Utoh, Youji Someya, Satoshi Suzuki, Christian Bachmann, Holger Reimerdes, Ronald Wenninger, Hironobu Kudo, Shinsuke Tokunaga, Yuki Homma, Yoshiteru Sakamoto, Ryoji Hiwatari, Kenji Tobita, Jeong-Ha You, Gianfranco Federici, Koichiro Ezato, Yohji Seki, Yoshio Ueda, and Noriyasu Ohno. Plasma exhaust and divertor studies in japan and europe broader approach, DEMO design activity. *Fusion Engineering and Design*, 136:1214–1220, nov 2018.

34. Kenji Tobita, Nobuyuki Asakura, Ryoji Hiwatari, Youji Someya, Hiroyasu Utoh, Kazunari Katayama, Arata Nishimura, Yoshiteru Sakamoto, Yuki Homma, Hironobu Kudo, Yuya Miyoshi, Makoto Nakamura, Shunsuke Tokunaga, and Akira Aoki and. Design strategy and recent design activity on japan's DEMO. *Fusion Science and Technology*, 72(4):537–545, sep 2017.

35. Kunihiko Okano, Ryuta Kasada, Yasushi Ikebe, Yasutomo Ishii, Kyoko Oba, Mieko Kashiwagi, Ryuichi Sakamoto, Naoki Sawa, Hidenobu Takenaga, Arata Nishimura, Masaru Fukuie, Shinsuke Fujioka, Yoshio Ueda, and Tsuyoshi Akiyama. An action plan of japan toward development of demo reactor. *Fusion Engineering and Design*, 136:183–189, nov 2018.

36. Jiangang Li, Guangnan Luo, Rui Ding, Damao Yao, Junling Chen, Lei Cao, Jiansheng Hu, and Qiang Li and. Plasma facing components for the experimental advanced superconducting tokamak and CFETR. *Physica Scripta*, T159:014001, apr 2014.

37. R.A. Pitts, X. Bonnin, F. Escourbiac, H. Frerichs, J.P. Gunn, T. Hirai, A.S. Kukushkin, E. Kaveeva, M.A. Miller, D. Moulton, V. Rozhansky, I. Senichenkov, E. Sytova, O. Schmitz, P.C. Stangeby, G. De Temmerman, I. Veselova, and S. Wiesen. Physics basis for the first ITER tungsten divertor. *Nuclear Materials and Energy*, 20:100696, aug 2019.

38. M Fujitsuka, B Tsuchiya, I Mutoh, T Tanabe, and T Shikama. Effect of neutron irradiation on thermal diffusivity of tungsten–rhenium alloys. *Journal of Nuclear Materials*, 283-287:1148–1151, dec 2000.

39. I Uytdenhouwen, T Schwarz-Selinger, JW Coenen, and M Wirtz. Mechanical and microstructural changes in tungsten due to irradiation damage. *Physica Scripta*, 2016(T167):014007, jan 2016.

40. J.-H. You. Damage and fatigue crack growth of eurofer steel first wall mock-up under cyclic heat flux loads. part 2: Finite element analysis of damage evolution. *Fusion Engineering and Design*, 89(4):294–301, 2014.

41. J.H.a You, G.b Mazzone, E.b Visca, C.c Bachmann, E.d Autissier, T.e Barrett, V.b Cocilovo, F.b Crescenzi, P.K.f Domalapally, D.b Dongiovanni, S.g Entler, G.c Federici, P.b Frosi, M.e Fursdon, H.a Greuner, D.e Hancock, D.i Marzullo, S.e McIntosh, A.V.a Mueller, M.T.b Porfiri, G.b Ramogida, J.h Reiser, M.d Richou, M.h Rieth, A.b Rydzy, R.b Villari, and V.h Widak. Conceptual design studies for the european demo divertor: Rationale and first results. *Fusion Engineering and Design*, 109-111(PartB):1598–1603, 2016. cited By 0.

42. J.H.a You, E.d Visca, C.b Bachmann, T.c Barrett, F.d Crescenzi, M.c Fursdon, H.a Greuner, D.f Guilhem, P.f Languille, M.a Li, S.c McIntosh, A.V.a Mueller, J.e Reiser, M.f Richou, and M.e Rieth. European demo divertor target: Operational requirements and material-design interface. *Nuclear Materials and Energy*, 9:171–176, 2016. cited By 0.

43. Michael Gorley, Eberhard Diegele, Sergei Dudarev, and Gerald Pintsuk. Materials engineering and design for fusion—towards DEMO design criteria. *Fusion Engineering and Design*, 136:298–303, nov 2018.

44. Steven J Zinkle. Applicability of copper alloys for DEMo high heat flux components. *Physica Scripta*, 2016(T167):014004, 2016.

45. A.v. Muller, D. Ewert, A. Galatanu, M. Milwich, R. Neu, J.Y. Pastor, U. Siefken, E. Tejado, and J.H. You. Melt infiltrated tungsten–copper composites as advanced heat sink materials for plasma facing components of future nuclear fusion devices. *Fusion Engineering and Design*, 124:455–459, nov 2017.

46. C. H. Henager et al. Ductile-phase toughened tungsten for plasma-facing materials in fusionreactors. *International Journal of Powder Metallurgy*, 2017.

47. Ba Nghiep Nguyen, Charles H. Henager, Nicole R. Overman, and Richard J. Kurtz. A multiscale microstructural approach to ductile-phase toughened tungsten for plasma-facing materials. *Journal of Nuclear Materials*, 508:371–384, sep 2018.

48. R. Neu, H. Maier, M. Balden, R. Dux, S. Elgeti, H. Gietl, H. Greuner, A. Herrmann, T. Höschen, M. Li, V. Rohde, D. Ruprecht, B. Sieglin, and I. Zammuto. Results on the use of tungsten heavy alloys in the divertor of ASDEX upgrade. *Journal of Nuclear Materials*, 511:567–573, dec 2018.

49. Richard E. Nygren, Ryan R. Dehoff, Dennis L. Youchison, Yutai Katoh, Y. Morris Wang, Charles M. Spadaccini, Charles H. Henager, P. Randall Schunk, David M. Keicher, R. Allen Roach, Mark F. Smith, and Dean A. Buchenauer. Advanced manufacturing—a transformative enabling capability for fusion. *Fusion Engineering and Design*, 136:1007–1011, nov 2018.

50. A. v. Müller, G. Schlick, R. Neu, C. Anstätt, T. Klimkait, J. Lee, B. Pascher, M. Schmitt, and C. Seidel. Additive manufacturing of pure tungsten by means of selective laser beam melting with substrate preheating temperatures up to 1000degc. *Nuclear Materials and Energy*, 19:184–188, may 2019.

51. T . Wegener, A. Litnovsky, J. Brinkmann, F. Koch, and Ch. Linsmeier. Development of yttrium-containing self-passivating tungsten alloys for future fusion power plant. *Nuclear Materials and Energy*, 9:394–398, dec 2016. ICFRM Conference 2015.

52. M. Schwarz, G. Hache, and P. von der Hardt. PHEBUS FP: a severe accident research programme for current and advanced light water reactors. *Nuclear Engineering and Design*, 187(1):47–69, jan 1999.

53. T. Kinos, S.L. Chen, P. Siitonen, and P. Kettunen. Densification of plasma-sprayed titanium and tantalum coatings. *Journal of Thermal Spray Technology*, 5(4):439–444, 1996.

54. F. Koch and H. Bolt. Self passivating W-based alloys as plasma facing material for nuclear fusion. *Physica Scripta T*, T128:100–105, mar 2007.

55. F Koch, J Brinkmann, S Lindig, T P Mishra, and Ch Linsmeier. Oxidation behaviour of silicon-free tungsten alloys for use as the first wall material. *Physica Scripta*, 2011(T145):014019, 2011.

56. P. Lopez-Ruiz, F. Koch, N. Ordas, S. Lindig, and C. Garcia-Rosales. Manufacturing of self-passivating w-cr-si alloys by mechanical alloying and hip. *Fusion Engineering and Design*, 86(9-11):1719–1723, 2011. cited By 22.

57. E. Joffrin. The effects of ion irradiation on the micromechanical fracture strength and hardness of a self-passivating tungsten alloy. *Journal of Nuclear Materials*, 486:34–43, 2017. cited By 3.

58. C. García-Rosales, P. López-Ruiz, S. Alvarez-Martín, A. Calvo, N. Ordás, F. Koch, and J. Brinkmann. Oxidation behaviour of bulk w-cr-ti alloys prepared by mechanical alloying and HIPing. *Fusion Engineering and Design*, 89(7-8):1611–1616, oct 2014.

59. P. Lopez-Ruiz, N. Ordas, S. Lindig, F. Koch, I. Iturriza, and C. Garcia-Rosales. Self-passivating bulk tungsten-based alloys manufactured by powder metallurgy. volume T145, 2011. cited By 22.

60. M.T. Lessmann, A. Calvo, C.D. Hardie, M. Porton, N. OrdÃ¡s, C. GarcÃa-Rosales, and P.M. Mummery. Fracture strength testing of a self-passivating tungsten alloy at the micrometre scale. *Philosophical Magazine*, 96(32-34):3570–3585, 2016. cited By 0.

61. P. Lopez-Ruiz, N. Ordas, I. Iturriza, M. Walter, E. Gaganidze, S. Lindig, F. Koch, and C. Garcia-Rosales. Powder metallurgical processing of self-passivating tungsten alloys for fusion first wall application. *Journal of Nuclear Materials*, 442(1-3 SUPPL.1):S219–S224, 2013. cited By 29.

62. P. Lopez-Ruiz, N. Ordas, I. Iturriza, F. Koch, S. Lindig, M. Walter, and C. Garcia-Rosales. Self-passivating tungsten based alloys obtained by hip for application in fusion reactors beyond iter (demo). volume 4, 2012. cited By 0.

63. W. Eckstein et al. Atomic and plasma-material interaction data for fusion,. *Atomic and Plasma-Material Interaction Data for Fusion,IAEA*, (7b), 2001. Vienna.

64. A Litnovsky, T Wegener, F Klein, Ch Linsmeier, M Rasinski, A Kreter, X Tan, J Schmitz, J W Coenen, Y Mao, J Gonzalez-Julian, and M Bram. New oxidation-resistant tungsten alloys for use in the nuclear fusion reactors. *Physica Scripta*, T170:014012, sep 2017.

65. Suresh Telu, Rahul Mitra, and Shyamal Kumar Pabi. Effect of y2o3 Addition on oxidation behavior of w-cr alloys. *Metallurgical and Materials Transactions A*, 46(12):1–11, oct 2015.

66. Felix Klein, Tobias Wegener, Andrey Litnovsky, Marcin Rasinski, Xiaoyue Tan, Janina Schmitz, Christian Linsmeier, Jan Coenen, Hongchu Du, Joachim Mayer, and Uwe Breuer. On oxidation resistance mechanisms at 1273 k of tungsten-based alloys containing chromium and yttria. *Metals*, 8(7):488, jun 2018.

67. Felix Klein, Andrey Litnovsky, Tobias Wegener, Xiaoyue Tan, Jesus Gonzalez-Julian, Marcin Rasinski, Janina Schmitz, Christian Linsmeier, Martin Bram, and Jan Willem Coenen. Sublimation of advanced tungsten alloys under demo relevant accidental conditions. *Fusion Engineering and Design*, 2019.

68. A. Litnovsky, T. Wegener, F. Klein, Ch. Linsmeier, M. Rasinski, A. Kreter, B. Unterberg, J.W. Coenen, H. Du, J. Mayer, C. Garcia-Rosales, A. Calvo, and N. Ordas. Smart tungsten alloys as a material for the first wall of a future fusion power plant. *Nuclear Fusion*, 57(6):066020, apr 2017.

69. A Litnovsky, T Wegener, F Klein, Ch Linsmeier, M Rasinski, A Kreter, X Tan, J Schmitz, Y Mao, J W Coenen, M Bram, and J Gonzalez-Julian. Advanced smart tungsten alloys for a future fusion power plant. *Plasma Physics and Controlled Fusion*, 59(6):064003, apr 2017.

70. Tobias Wegener, Felix Klein, Andrey Litnovsky, Marcin Rasinski, Jens Brinkmann, Freimut Koch, and Christian Linsmeier. Development and analyses of self-passivating tungsten alloys for DEMO accidental conditions. *Fusion Engineering and Design*, mar 2017.

71. A. Litnovsky, T. Wegener, F. Klein, C. Linsmeier, M. Rasinski, A. Kreter, X. Tan, J. Schmitz, Y. Mao, J.W. Coenen, M. Bram, and J. Gonzalez-Julian. Advanced smart tungsten alloys for a future fusion power plant. *Plasma Physics and Controlled Fusion*, 59(6), 2017. cited By 10.

72. A. Litnovsky, T. Wegener, F. Klein, C. Linsmeier, M. Rasinski, A. Kreter, B. Unterberg, J.W. Coenen, H. Du, J. Mayer, C. Garcia-Rosales, A. Calvo, and N. Ordas. Smart tungsten alloys as a material for the first wall of a future fusion power plant. *Nuclear Fusion*, 57(6), 2017. cited By 14.

73. A. Litnovsky, F. Klein, J. Schmitz, T. Wegener, Ch. Linsmeier, M.R. Gilbert, M. Rasinski, A. Kreter, X. Tan, Y. Mao, J.W. Coenen, M. Bram, and J. Gonzalez-Julian. Smart first wall materials for intrinsic safety of a fusion power plant. *Fusion Engineering and Design*, apr 2018.

74. A. Litnovsky, F. Klein, J. Schmitz, T. Wegener, C. Linsmeier, M.R. Gilbert, M. Rasinski, A. Kreter, X. Tan, Y. Mao, J.W. Coenen, M. Bram, and J. Gonzalez-Julian. Smart first wall materials for intrinsic safety of a fusion power plant. *Fusion Engineering and Design*, 136:878–882, 2018. cited By 4.

75. J. Riesch, J.-Y. Buffiere, T. Hoeschen, M. di Michiel, M. Scheel, Ch. Linsmeier, and J.-H. You. In situ synchrotron tomography estimation of toughening effect by semi-ductile fibre reinforcement in a tungsten-fibre-reinforced tungsten composite system. *Acta Materialia*, 61(19):7060–7071, 2013.

76. J Riesch, T Hoeschen, Ch Linsmeier, S Wurster, and J-H You. Enhanced toughness and stable crack propagation in a novel tungsten fibre-reinforced tungsten composite produced by chemical vapour infiltration. *Physica Scripta*, 2014(T159):014031, 2014.

77. M. Hubert et al. The absence of plasma in "spark plasma sintering". *J. Appl. Phys.*, 104(3):033305, 2008.

78. Y. Mao, J. W. Coenen, J. Riesch, S. Sistla, C. Chen, Y. Wu, L. Raumann, R. Neu, C. Linsmeier, and C. Broeckmann. Spark plasma sintering produced w-fiber-reinforced tungsten composites. In *Spark Plasma Sintering of Materials*. Springer International Publishing, 2019.

79. B. Jasper, S. Schoenen, J. Du, T. Hoeschen, F. Koch, Ch. Linsmeier, R. Neu, J. Riesch, A. Terra, and J.W. Coenen. Behavior of tungsten fiber-reinforced tungsten based on single fiber push-out study. *Nuclear Materials and Energy*, 9:416–421, dec 2016.

80. Bruno Jasper, Jan W Coenen, Johann Riesch, Till Höschen, Martin Bram, and Christian Linsmeier. Powder metallurgical tungsten fiber-reinforced tungsten. *Materials Science Forum*, 825:125–133, 2015.

81. J.W. Coenen, J. Riesch, J-H You, M. Rieth, G. Pintsuk, H. Gietl, B. Jasper, F. Klein, A. Litnovsky, Y. Mao, et al. Advanced materials for a damage resilient divertor concept for DEMO: Powder-metallurgical tungsten-fibre reinforced tungsten. *Fusion Engineering and Design*, 124:964–968, dec 2017.

82. Y Mao, J W Coenen, J Riesch, S Sistla, J Almanstötter, B Jasper, A Terra, T Höschen, H Gietl, M Bram, J Gonzalez-Julian, Ch Linsmeier, and C Broeckmann. Development and characterization of powder metallurgically produced discontinuous tungsten fiber reinforced tungsten composites. *Physica Scripta*, T170:014005, aug 2017.

83. J. Riesch, M. Aumann, J.W. Coenen, H. Gietl, G. Holzner, T. Hoeschen, P. Huber, M. Li, Ch. Linsmeier, and R. Neu. Chemically deposited tungsten fibre-reinforced tungsten – the way to a mock-up for divertor applications. *Nuclear Materials and Energy*, 9:75–83, may 2016.

84. J Riesch, Y Han, J Almanstötter, JW Coenen, T Höschen, B Jasper, P Zhao, Ch Linsmeier, and R Neu. Development of tungsten fibre-reinforced tungsten composites towards their use in DEMO—potassium doped tungsten wire. *Physica Scripta*, T167(T167):014006, jan 2016.

85. H Gietl, J Riesch, JW Coenen, T Höschen, Ch Linsmeier, and R Neu. Tensile deformation behavior of tungsten fibre-reinforced tungsten composite specimens in as-fabricated state. *Fusion Engineering and Design*, 124:396–400, mar 2017.

86. J.W. Coenen, Y. Mao, S. Sistla, J. Riesch, T. Hoeschen, Ch. Broeckmann, R. Neu, and Ch. Linsmeier. Improved pseudo-ductile behavior of powder metallurgical tungsten short fiber-reinforced tungsten (wf / w). *Nuclear Materials and Energy*, 15:214–219, may 2018.

87. Y Mao, J Engels, A Houben, M Rasinski, J Steffens, A Terra, Ch Linsmeier, and JW Coenen. The influence of annealing on yttrium oxide thin film deposited by reactive magnetron sputtering: Process and microstructure. *Nuclear Materials and Energy*, 10:1–8, jan 2017.

88. Y. Mao, J.W. Coenen, J. Riesch, S. Sistla, J. Almanstötter, J. Reiser, A. Terra, C. Chen, Y. Wu, L. Raumann, T. Höschen, H. Gietl, R. Neu, Ch. Linsmeier, and C. Broeckmann. Fracture behavior of random distributed short tungsten fiber-reinforced tungsten composites. *Nuclear Fusion*, 59(8):086034, jul 2019.

89. Yiran Mao, Jan W. Coenen, Johann Riesch, Sree Sistla, Jürgen Almanstötter, Alexis Terra, Chang Chen, Yucheng Wu, Leonard Raumann, Till Höschen, Hanns Gietl, Rudolf Neu, Christoph Broeckmann, and Christian Linsmeier. Fiber volume fraction influence on randomly distributed short fiber tungsten fiber reinforced tungsten composites. *Advanced Engineering Materials*, mar 2020.

90. Y Mao, J W Coenen, S Sistla, X Tan, J Riesch, L Raumann, D Schwalenberg, T Höschen, C Chen, Y Wu, C Broeckmann, and Ch Linsmeier. Development of tungsten fiber-reinforced tungsten with a porous matrix. *Physica Scripta*, T171:014030, jan 2020.

91. D. Terentyev, J. Riesch, S. Lebediev, T. Khvan, A. Zinovev, M. Rasiński, A. Dubinko, and J.W. Coenen. Plastic deformation of recrystallized tungsten-potassium wires: Constitutive deformation law in the temperature range 22-600c. *International Journal of Refractory Metals and Hard Materials*, 73:38–45, jun 2018.

92. D. Terentyev, J. Riesch, S. Lebediev, T. Khvan, A. Dubinko, and A. Bakaeva. Strength and deformation mechanism of tungsten wires exposed to high temperature annealing: Impact of potassium doping. *International Journal of Refractory Metals and Hard Materials*, 76:226–233, nov 2018.

93. D Terentyev, J Riesch, S Lebediev, A Bakaeva, and JW Coenen. Mechanical properties of as-fabricated and 2300degc annealed tungsten wire tested up to 600degc. *International Journal of Refractory Metals and Hard Materials*, 66:127–134, mar 2017.

94. P. Zhao, J. Riesch, T. Hoeschen, J. Almanstoetter, M. Balden, J.W. Coenen, W. Himml, W. Pantleon, U. Toussaint, and R. Neu. Microstructure, mechanical behaviour and fracture of pure tungsten wire after different heat treatments. *International Journal of Refractory Metals and Hard Materials*, 68:29–40, November 2017.

95. J Riesch, A Feichtmayer, M Fuhr, J Almanstötter, J W Coenen, H Gietl, T Höschen, Ch Linsmeier, and R Neu. Tensile behaviour of drawn tungsten wire used in tungsten fibre-reinforced tungsten composites. *Physica Scripta*, T170:014032, oct 2017.

96. J Riesch, J Almanstoetter, J W Coenen, M Fuhr, H Gietl, Y Han, T. Hoeschen, Ch Linsmeier, N Travitzky, P Zhao, and R Neu. Properties of drawn w wire used as high performance fibre in tungsten fibre-reinforced tungsten composite. *IOP Conference Series: Materials Science and Engineering*, 139:012043, jul 2016.

97. Xunxiang Hu, Takaaki Koyanagi, Makoto Fukuda, NAP Kiran Kumar, Lance L Snead, Brian D Wirth, and Yutai Katoh. Irradiation hardening of pure tungsten exposed to neutron irradiation. *Journal of Nuclear Materials*, 480:235–243, nov 2016.

98. A. von Mueller. "The effects of heat treatment on the mechanical properties of high-strength tungsten fibres for plasma-facing component composite material applications". *To be published in NME*, 2017. ICFRM - 18 International Conference on Fusion Reactor Materials.

99. Y. Mao, C. Chen, J.W. Coenen, J. Riesch, S. Sistla, J. Almanstötter, A. Terra, Y. Wu, L. Raumann, T. Höschen, H. Gietl, R. Neu, Ch. Linsmeier, and Ch. Broeckmann. On the nature of carbon embrittlement of tungsten fibers during powder metallurgical processes. *Fusion Engineering and Design*, 145:18–22, aug 2019.

100. Stephan Schönen, Bruno Jasper, Jan Willem Coenen, Juan Du, Till Höschen, Johann Riesch, Ghaleb Natour, Rudolf Neu, and Christian Linsmeier. Insight into single-fiber push-out test of tungsten fiber-reinforced tungsten. *Composite Interfaces*, 26(2):1–20, 2019.

101. H Gietl, A v Müller, JW Coenen, M Decius, D Ewert, T Höschen, Ph Huber, M Milwich, J Riesch, and R Neu. Textile preforms for tungsten fibre-reinforced composites. *Journal of Composite Materials*, 52(28):002199831877114, apr 2018.

102. H. Gietl, J. Riesch, J.W. Coenen, T. Höschen, and R. Neu. Production of tungsten-fibre reinforced tungsten composites by a novel continuous chemical vapour deposition process. *Fusion Engineering and Design*, 146:1426–1430, apr 2019.

103. Cecile S Bonifacio, Troy B Holland, and Klaus van Benthem. Evidence of surface cleaning during electric field assisted sintering. *Scripta Materialia*, 69(11):769–772, 2013.

104. Cecile S Bonifacio, Troy B Holland, and Klaus van Benthem. Time-dependent dielectric breakdown of surface oxides during electric-field-assisted sintering. *Acta Materialia*, 63:140–149, 2014.

105. Joanna R Groza and Antonios Zavaliangos. Sintering activation by external electrical field. *Materials Science and Engineering: A*, 287(2):171–177, 2000.

106. Y. Mao, J.W. Coenen, J. Riesch, S. Sistla, J. Almanstötter, B. Jasper, A. Terra, T. Höschen, H. Gietl, Ch. Linsmeier, and C. Broeckmann. Influence of the interface strength on the mechanical properties of discontinuous tungsten fiber-reinforced tungsten composites produced by field assisted sintering technology. *Composites Part A: Applied Science and Manufacturing*, 107:342–353, apr 2018.

107. H. T. Lee, S. Ando, J. W. Coenen, Y. Mao, J. Riesch, and Y. Ueda. Micro- and macro- elastic properties of tungsten fiber-reinforced tungsten composites probed by nano-indentation and laser ultrasonics. *Nuclear Materials and Energy*, 19:262–266, May 2019.

108. H T Lee, S Ando, J W Coenen, Y Mao, J Riesch, H Gietl, R Kasada, Y Hamaji, K Ibano, and Y Ueda. Longitudinal and shear wave velocities in pure tungsten and tungsten fiber-reinforced tungsten composites. *Physica Scripta*, T170:014024, oct 2017.

109. J.W. Coenen, Y. Mao, S. Sistla, A.v. Müller, G. Pintsuk, M. Wirtz, J. Riesch, T. Hoeschen, A. Terra, J.-H. You, H. Greuner, A. Kreter, Ch. Broeckmann, R. Neu, and Ch. Linsmeier. Materials development for new high heat-flux component mock-ups for DEMO. *Fusion Engineering and Design*, 146:1431–1436, feb 2019.

110. L. Raumann, J.W. Coenen, J. Riesch, Y. Mao, H. Gietl, T. Höschen, Ch. Linsmeier, and O. Guillon. Modeling and validation of chemical vapor deposition of tungsten for tungsten fiber reinforced tungsten composites. *Surface and Coatings Technology*, 381:124745, jan 2020.

111. J. W. Coenen, M. Berger, M.J. Demkowicz, D. Matveev, A. Manhard, R. Neu, J. Riesch, B. Unterberg, M. Wirtz, and C. Linsmeier. Plasma-wall interaction of advanced materials. *Nuclear Materials and Energy*, 12:307–312, aug 2017.

112. J.M. Missiaen, J.J. Raharijaona, A. Antoni, C. Pascal, M. Richou, and P. Magaud. Design of a w/steel functionally graded material for plasma facing components of DEMO. *Journal of Nuclear Materials*, 416(3):262–269, sep 2011.

113. Widodo Widjaja Basuki and Jarir Aktaa. Investigation on the diffusion bonding of tungsten and EUROFER97. *Journal of Nuclear Materials*, 417(1-3):524–527, oct 2011.

114. N.P. Taylor and R. Pampin. Activation properties of tungsten as a first wall protection in fusion power plants. *Fusion Engineering and Design*, 81(8,14):1333–1338, 2006. Proceedings of the Seventh International Symposium on Fusion Nuclear Technology.

115. J. Aktaa, W.W. Basuki, T. Weber, P. Norajitra, W. Krauss, and J. Konys. Manufacturing and joining technologies for helium cooled divertors. *Fusion Engineering and Design*, 89(7,8):913–920, 2014. ISFNT-11.

116. H. Greuner, H. Bolt, B. Boeswirth, S. Lindig, W. Kuhnlein, T. Huber, K. Sato, and S. Suzuki. Vacuum plasma-sprayed tungsten on {EUROFER} and 316l: Results of characterisation and thermal loading tests. *Fusion Engineering and Design*, 75,79(0):333–338, 2005. Proceedings of the 23rd Symposium of Fusion Technology {SOFT} 23.

117. T. Weber, M. Stüber, S. Ulrich, R. Vaßen, W.W. Basuki, J. Lohmiller, W. Sittel, and J. Aktaa. Functionally graded vacuum plasma sprayed and magnetron sputtered tungsten/EUROFER97 interlayers for joints in helium-cooled divertor components. *Journal of Nuclear Materials*, 436(1-3):29–39, may 2013.

118. Zhangjian Zhou, Shuangquan Guo, Shuxiang Song, Weizhi Yao, and Changchun Ge. The development and prospect of fabrication of w based plasma facing component by atmospheric plasma spraying. *Fusion Engineering and Design*, 86(9-11):1625–1629, oct 2011.

119. Widodo Widjaja Basuki and Jarir Aktaa. Diffusion bonding between w and EUROFER97 using v interlayer. *Journal of Nuclear Materials*, 429(1-3):335–340, oct 2012.

120. Thomas Weber. *Entwicklung und Optimierung von gradierten Wolfram/EUROFER97-Verbindungen für Divertorkomponenten*. Karlsruher Institut für Technologie, 2014.

121. S. Heuer, Th. Weber, G. Pintsuk, J.W. Coenen, J. Matejicek, and Ch. Linsmeier. Aiming at understanding thermo-mechanical loads in the first wall of DEMO: Stress–strain evolution in a eurofer-tungsten test component featuring a functionally graded interlayer. *Fusion Engineering and Design*, 135:141–153, oct 2018.

122. S Van den Kerkhof, M Blommaert, J W Coenen, S Heuer, and M Baelmans. Investigating the potential of FGMs through numerical minimization of thermal stresses. *Physica Scripta*, T171:014001, jan 2020.

123. S Heuer, J W Coenen, G Pintsuk, J Matějíček, M Vilémová, and Ch Linsmeier. Overview of challenges and developments in joining tungsten and steel for future fusion reactors. *Physica Scripta*, T171:014028, jan 2020.

124. S. Heuer, T. Lienig, A. Mohr, Th. Weber, G. Pintsuk, J.W. Coenen, F. Gormann, W. Theisen, and Ch. Linsmeier. Ultra-fast sintered functionally graded fe/w composites for the first wall of future fusion reactors. *Composites Part B: Engineering*, 164:205–214, may 2019.

125. S. Heuer, J. Matejicek, M. Vilemova, M. Kollerm, K. Illkova, J. Veverka, Th. Weber, G. Pintsuk, J. W. Coenen, and C. Linsmeier. Atmospheric plasma spraying of functionally graded steel/tungsten layers for the first wall of future fusion reactors. *Surface and Coatings Technology*, 366:170–178, May 2019.

126. Philipp Schuette. *Aufbau einer Kurzzeitsinteranlage zur Herstellung verschleissbestaendiger Verbundwerkstoffe*. doctoralthesis, Ruhr-Universitaet Bochum, Universitaetsbibliothek, 2013.

127. Hirofumi Nakamura, Shinji Sakurai, Satoshi Suzuki, Takumi Hayashi, Mikio Enoeda, and Kenji Tobita. Case study on tritium inventory in the fusion DEMO plant at JAERI. *Fusion Engineering and Design*, 81(8-14):1339–1345, feb 2006.

128. Fabrizio Franza, LV Boccaccini, Andrea Ciampichetti, and Massimo Zucchetti. Tritium transport analysis in hcpb DEMo blanket with the fus-tpc code. *Fusion Engineering and Design*, 88(9):2444–2447, 2013.

129. D. Demange, L.V. Boccaccini, F. Franza, A. Santucci, S. Tosti, and R. Wagner. Tritium management and anti-permeation strategies for three different breeding blanket options foreseen for the european power plant physics and technology demonstration reactor study. *Fusion Engineering and Design*, 89(7-8):1219–1222, oct 2014.

130. D Levchuk, F Koch, H Maier, and H Bolt. Gas-driven deuterium permeation through Al2O3 coated samples. *Physica Scripta*, 2004(T108):119, 2004.

131. Takumi Chikada, Akihiro Suzuki, Zhenyu Yao, Denis Levchuk, Hans Maier, Takayuki Terai, and Takeo Muroga. Deuterium permeation behavior of erbium oxide coating on austenitic, ferritic, and ferritic/martensitic steels. *Fusion Engineering and Design*, 84(2,Àì6):590–592, 2009. Proceeding of the 25th Symposium on Fusion Technology (SOFT-25).

132. G.W Hollenberg, E.P Simonen, G Kalinin, and A Terlain. Tritium/hydrogen barrier development. *Fusion Engineering and Design*, 28(0):190–208, 1995. Proceedings of the Third International Symposium on Fusion Nuclear Technology.

133. R.A. Causey, R.A. Karnesky, and C. San Marchi. 4.16 - tritium barriers and tritium diffusion in fusion reactors. In Rudy J.M. Konings, editor, *Comprehensive Nuclear Materials*, pages 511–549. Elsevier, Oxford, 2012.

134. Mark R Gilbert, Jean-Christophe Sublet, and Robin A Forrest. Handbook of activation, transmutation, and radiation damage properties of the elements simulated using fispact-ii & tendl-2014; magnetic fusion plants. *Rep. CCFE*, 2015.

135. J. Engels, A. Houben, P. Hansen, M. Rasinski, and Ch. Linsmeier. Influence of the grain structure of yttria thin films on the hydrogen isotope permeation. *International Journal of Hydrogen Energy*, 43(51):22976–22985, dec 2018.

136. J. Engels, A. Houben, M. Rasinski, and Ch. Linsmeier. Hydrogen saturation and permeation barrier performance of yttrium oxide coatings. *Fusion Engineering and Design*, feb 2016. Poster Soft 2016(P3.180).

137. A. Houben, J. Engels, M. Rasiński, and Ch. Linsmeier. Comparison of the hydrogen permeation through fusion relevant steels and the influence of oxidized and rough surfaces. *Nuclear Materials and Energy*, 19:55–58, may 2019.

138. T. Chikada, H. Fujita, J. Engels, A. Houben, J. Mochizuki, S. Horikoshi, M. Matsunaga, M. Tokitani, Y. Hishinuma, S. Kondo, K. Yabuuchi, T. Schwarz-Selinger, T. Terai, and Y. Oya. Deuterium permeation behavior and its iron-ion irradiation effect in yttrium oxide coating deposited by magnetron sputtering. *Journal of Nuclear Materials*, 511:560–566, 2018. cited By 2.

139. T. Chikada, H. Fujita, M. Matsunaga, S. Horikoshi, J. Mochizuki, C. Hu, F. Koch, M. Tokitani, Y. Hishinuma, K. Yabuuchi, and Y. Oya. Deuterium permeation behavior in iron-irradiated erbium oxide coating. *Fusion Engineering and Design*, 124:915–918, 2017. cited By 5.

140. T. Chikada, H. Fujita, M. Tokitani, Y. Hishinuma, T. Terai, and Y. Oya. Deuterium permeation through monoclinic erbium oxide coating. *Fusion Engineering and Design*, 133:121–124, 2018. cited By 3.

141. T. Chikada, K. Kimura, J. Mochizuki, S. Horikoshi, M. Matsunaga, H. Fujita, K. Okitsu, T. Tanaka, Y. Hishinuma, Y. Sakamoto, Y. Someya, and H. Nakamura. Surface oxidation effect on deuterium permeation in reduced activation ferritic/martensitic steel f82h for demo application. *Fusion Engineering and Design*, 2018. cited By 0.

142. T. Chikada, M. Matsunaga, S. Horikoshi, J. Mochizuki, H. Fujita, Y. Hishinuma, K. Isobe, T. Hayashi, T. Terai, and Y. Oya. Fabrication technology development and characterization of tritium permeation barriers by a liquid phase method. *Fusion Engineering and Design*, 136:215–218, 2018. cited By 3.

143. T. Chikada, S. Naitoh, A. Suzuki, T. Terai, T. Tanaka, and T. Muroga. Deuterium permeation through erbium oxide coatings on rafm steels by a dip-coating technique. *Journal of Nuclear Materials*, 442(1-3):533–537, 2013. cited By 18.

144. T. Chikada, M. Shimada, R.J. Pawelko, T. Terai, and T. Muroga. Tritium permeation experiments using reduced activation ferritic/martensitic steel tube and erbium oxide coating. *Fusion Engineering and Design*, 89(7-8):1402–1405, 2014. cited By 16.

145. T. Chikada, A. Suzuki, C. Adelhelm, T. Terai, and T. Muroga. Surface behaviour in deuterium permeation through erbium oxide coatings. *Nuclear Fusion*, 51(6), 2011. cited By 40.

146. T. Chikada, A. Suzuki, T. Kobayashi, H. Maier, T. Terai, and T. Muroga. Microstructure change and deuterium permeation behavior of erbium oxide coating. *Journal of Nuclear Materials*, 417(1-3):1241–1244, 2011. cited By 50.

147. T. Chikada, A. Suzuki, T. Kobayashi, Z. Yao, D. Levchuk, H. Maier, T. Terai, and T. Muroga. Thermal influence on erbium oxide coating for tritium permeation barrier. *Fusion Science and Technology*, 56(1):309–313, 2009. cited By 15.

148. T. Chikada, A. Suzuki, F. Koch, H. Maier, T. Terai, and T. Muroga. Fabrication and deuterium permeation properties of erbia-metal multilayer coatings. *Journal of Nuclear Materials*, 442(1-3 SUPPL.1):S592–S596, 2013. cited By 13.

149. T. Chikada, A. Suzuki, H. Maier, T. Terai, and T. Muroga. Modeling of tritium permeation through erbium oxide coatings. *Fusion Science and Technology*, 60(1):389–393, 2011. cited By 17.

150. T. Chikada, A. Suzuki, T. Tanaka, T. Terai, and T. Muroga. Microstructure control and deuterium permeability of erbium oxide coating on ferritic/martensitic steels by metal-organic decomposition. *Fusion Engineering and Design*, 85(7-9):1537–1541, 2010. cited By 37.

151. T. Chikada, A. Suzuki, and T. Terai. Deuterium permeation and thermal behaviors of amorphous silicon carbide coatings on steels. *Fusion Engineering and Design*, 86(9-11):2192–2195, 2011. cited By 19.

152. T. Chikada, A. Suzuki, T. Terai, T. Muroga, and F. Koch. Compatibility of erbium oxide coating with liquid lithium-lead alloy and corrosion protection effect of iron layer. *Fusion Engineering and Design*, 88(6-8):640–643, 2013. cited By 12.

153. T. Chikada, A. Suzuki, Z. Yao, D. Levchuk, H. Maier, T. Terai, and T. Muroga. Deuterium permeation behavior of erbium oxide coating on austenitic, ferritic, and ferritic/martensitic steels. *Fusion Engineering and Design*, 84(2-6):590–592, 2009. cited By 61.

154. Jochen Linke, Juan Du, Thorsten Loewenhoff, Gerald Pintsuk, Benjamin Spilker, Isabel Steudel, and Marius Wirtz. Challenges for plasma-facing components in nuclear fusion. *Matter and Radiation at Extremes*, 4(5):056201, sep 2019.

STRUCTURAL AND FUNCTIONAL MATERIALS IN FUSION REACTORS: ISSUES RELATED TO TRITIUM, RADIOACTIVITY AND RADIATION-INDUCED EFFECTS

M. Rubel

KTH Royal Institute of Technology, School of Electrical Engineering and Computer Science, Dept. of Fusion Plasma Physics, Teknikringen 31, 100 44 Stockholm, Sweden

ABSTRACT

A concise overview is given on materials applied in fusion technology. The influence of plasma operation on the behaviour of reactor components and diagnostic systems is discussed with emphasis on effects caused by fast particles reaching the reactor wall. Issues related to primary and induced radioactivity are reviewed: tritium inventory and transmutation. Tritium breeding in the reactor blanket, separation of hydrogen isotopes and safety aspects in handling radioactively contaminated components are also included.

I. INTRODUCTION

The ultimate goal of fusion research is to construct and operate an energy generating system. In a controlled fusion reactor the temperature gradients between the plasma and the surrounding wall will probably be the greatest in the Universe and, the operation will be associated with intense nuclear radiation. Therefore, the technology for next-step devices presents challenges not encountered in present-day machines. This includes development and construction of components capable of reliable performance in highly radioactive environment.

The assessment of radioactivity level and lifetime of materials and components (multi-material structures) are the driving forces in studies of plasma-material interactions in controlled fusion devices [1,2]. They are essential for economy and safety of a reactor-class machine operated with a 50:50 mixture of deuterium and tritium (D-T). Secondly, radioactivity-related effects and power handling by plasma-facing components (PFC) are universal for all confinement schemes, either magnetic or inertial, realised for energy generating systems. A broad overview of power handling by the reactor first wall has been presented by Loarte [3] and Linke [4]. This paper deals with radioactivity aspects of the fusion process and their influence on the reactor structure and plasma-facing materials and components (PFMC). In this work, first basic requirements for plasma-facing and other reactor materials are presented. This is followed by a description of radioactivity sources in a fusion reactor. Afterwards tritium inventory, tritium breeding and radiation effects are discussed. The work is concluded with remarks on safety issues associated with handling components in radioactive environment. Finally, crucial topics to be tackled in future research of fusion reactor materials (FRM) are addressed.

II. REACTOR STRUCTURE AND MATERIALS

The next-step fusion machine is ITER being under construction in Cadarache, France. The objectives of ITER science and technology programme include: (a) extended burn time; (b) achievement of a self-sustained thermonuclear burn; (c) safe operation of a reactor-like device; (d) testing of components under reactor-like conditions and (e) testing of tritium breeding modules (TBM) [5,6]. These steps are essential for construction of power-generating systems in the future. In brief, a reactor is composed of a support structure, a cryostat housing super-conducting magnets and a vacuum vessel with the first wall being an integrated blanket. The blanket includes structural materials, a neutron absorber and high-heat flux (HHF) components: plasma-facing armour and heat sink.

Energy leaves plasma in the form of electromagnetic radiation and kinetic energy of particles. Plasma-surrounding wall is irradiated by ions, charge-exchange neutrals, electrons, neutrons and photons originating from nuclear (γ) and electronic processes (X, UV). All of them modify material properties, from the very surface to the bulk. Therefore, blanket materials must be compatible with ultra-high vacuum, magneto-hydro dynamics, neutron irradiation, handling of high heat loads and the coolant media. In a consequence, there are stringent requirements regarding properties of PFMC: high thermal conductivity, reliable thermo-mechanical properties and resilience to thermal shocks, low activation by neutrons and resistance to radiation damage, low accumulation of hydrogen isotopes (fuel inventory) accompanied by low chemical affinity to hydrogen in order to avoid chemical erosion leading to the formation of volatile compounds. High affinity to oxygen towards formation of stable and non-volatile oxides is also important for gettering oxygen impurity species from the plasma. Properties of no single element, compound or alloy can satisfy all points from that list. Only a few candidate materials for PFC have been seriously considered: carbon fibre composites (CFC), beryllium (Be) and tungsten (W). Behaviour of these elements under plasma conditions, i.e. particle bombardment and high heat flux deposition, is very different [1-4]. Therefore, their originally planned distribution in ITER wall was following: beryllium on the main chamber wall; tungsten on the divertor dome and upper vertical target, while CFC on the lower

vertical target where the greatest power loads are deposited [5]. The operation with such a material mix had never been done in any device, while problems with respective elements were known. For instance, thermal shocks and high power loads are excellently handled by carbon composites, but C erosion by hydrogen fluxes leads to the formation of hydrocarbons and, as described in Chapter IV, to unacceptable levels of fuel inventory [6,7]. In year 2004 a reconstruction of wall components in the Joint European Torus (JET) tokamak was decided in order to test operation with an all-metal PFC: ITER-Like Wall (JET-ILW) Project: beryllium in the main chamber wall (limiters and inner wall cladding) and the tungsten divertor [8]. The JET operation with the carbon wall (JET-C) was finished in October 2009. The installation of the metal wall was completed in May 2011. Photographs in Fig. 1 show in-vessel components and distribution of wall materials (a) and, a section of the bulk W divertor (b). Scientific objectives of the ILW project and challenges in the design and construction of components have been presented by Matthews [8,9] and Mertens [10], while plasma-wall interactions in a full metal machine have been reviewed by Matthews in [11]. A successful operation of JET-ILW lead to decision to start the ITER operation from Day-1 with the tungsten divertor [12].

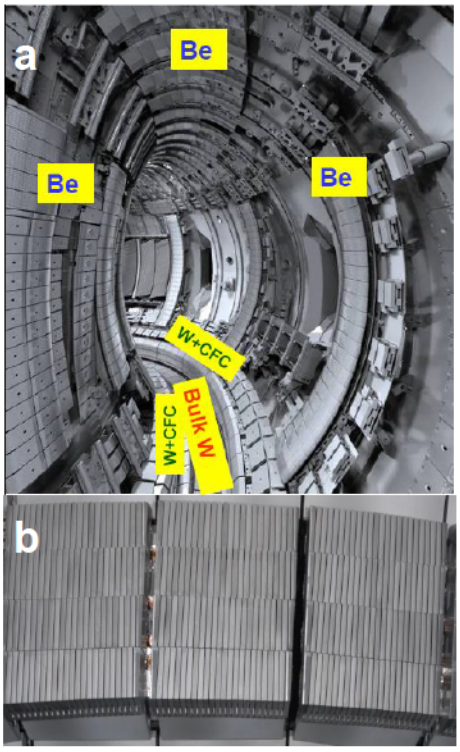

Figure 1: Toroidal view inside the JET vessel with the ITER-Like Wall (a) and a toroidal section of the tungsten load bearing plate in the divertor.

The list of candidate structural materials for the blanket comprises mainly steel (e.g. 316L(N)), Eurofer alloy, vanadium-titanium alloys (V-Ti, V-Ti-Si, V-Ti-Cr) and silicon carbide composites [13]. Major requirements emphasise mechanical strength and low activation by neutrons. Low activation and increased resistance to radiation damage are also crucial for functional materials: ceramic insulators and components of in-vessel diagnostic such as optical fibres, cables, mirrors and windows [14,15].

The intention of this paper is to highlight the field of FRM and physics underlying their behaviour in radioactive environment, but not to give an extensive account on all ever-considered candidate materials and all kinds of radiation-induced effects. The most important processes affecting material properties will be discussed in more detail in Chapter V.

III. SOURCES OF RADIOACTIVITY

All primary and induced radioactivity in controlled fusion devices is associated with the substrates and products of the fusion process: tritium in the D – T fuel and a consequent production of high energy neutrons:

$$D + T \rightarrow \alpha\ (3.5\ MeV) + n\ (14.1\ MeV) \quad (1)$$

$$D + D \rightarrow T\ (1.01\ MeV) + H\ (3.03\ MeV) \quad (2)$$

$$D + D \rightarrow {}^{3}He\ (0.82\ MeV) + n\ (2.45\ MeV) \quad (3).$$

A branching ratio of reactions (2) and (3) is around one. Tritium (symbol: T, t or ^{3}H) is a low-energy β^- emitter:

$$^{3}H\ (\beta^-) \rightarrow {}^{3}He\ (18.59\ keV,\ t_{1/2} = 12.32\ years) \quad (4).$$

Resulting radioactivity of 1 g of tritium equals to 9652 Ci (3.571×10^{14} Bq). Safety requirements limit the in-vessel inventory to the total of 700 g T. If this level would be overcome, a clean-up of the vessel would become necessary in order to reduce the radioactivity. Processes leading to the accumulation of tritium and methods of tritium removal will be discussed in the next chapter. *In-situ* induced radioactivity attributed to nuclear transmutation by fast neutrons passing the plasma-facing and structural materials of the blanket will be presented in Chapter V.

IV. IMPACT OF EROSION & RE-DEPOSITION ON FUEL INVENTORY AND DUST GENERATION

The term "fuel inventory" denotes accumulation and long-term retention of fuel in all in-vessel components, either those facing the plasma directly or located in remote (shadowed) areas such as water cooled louvers in the divertor structure [1,6,7] or other parts of pumping ducts. This applies to all hydrogen isotopes and has several detrimental effects on the reactor operation. There are several pathways leading to the accumulation of fuel in reactor components:

i. direct implantation in the PFC surface region,
ii. T production by neutron-induced transmutation,

iii. diffusion and migration into the bulk,
iv. co-deposition process.

Neutron-assisted production of T will be treated in the next chapter. The process of in-depth fuel migration into CFC and other carbon-based materials is still under investigation in order to assess its impact on the overall inventory [16-18]. There is a consensus that the process of co-deposition is decisive for the in-vessel fuel accumulation.

Co-deposition is defined as re-deposition of eroded and then transported material (i.e. plasma impurities) together with fuel species. Material eroded from one location of the reactor wall is re-deposited in another place, unless it is pumped-out [19]. The most serious consequence of co-deposition is the formation of mixed-material layers which may contain vast amounts of fuel. The process that has been studied most extensively in devices with carbon walls is directly related to the pronounced erosion (physical and chemical) of carbon by hydrogen plasma and the resultant formation of various hydrocarbon species. They are characterised by different sticking coefficients to solid surfaces [20]. Those of a high sticking co-efficient are easily deposited and form amorphous carbonaceous (a:C-H) films retaining from a few to about 50 % atomic percent of hydrogen isotopes [6,21]. As measured in various tokamaks, the growth rate of such films is usually between 1.5 and 12 nm/s. When this number is scaled-up to a full year of plasma operation co-deposited layer of a thickness from 4.7 cm to 38 cm would be formed, respectively. This indicates the scale of the problem arising from the carbon erosion, its re-deposition and fuel inventory. The retention of radioactive tritium causes the most severe problems because methods are still to be developed to accomplish the efficient release of fuel and/or decomposition and removal of co-deposits in order to ensure safe and economical reactor operation. A range of concepts has been proposed and tested in laboratories [22-25] and, also inside tokamaks [26-28]. The operation of JET-ILW has clearly shown that the elimination carbon PFC (i.e. the direct C source) reduced carbon fluxes by 10-15 times in comparison to JET-C [29]. Also the thickness of co-deposited layers and fuel inventory [30,31] have decrease significantly thus proving advantages of operation with metal walls [32].

Fig. 2(a) shows a limiter tile exposed at the TEXTOR tokamak (carbon wall) for a few operation hours. One can distinguish two regions: a shiny and smoothly looking erosion zone and a deposition zone covered with a peeling-off (flaking) deposit. Images in Fig.2 (b) and (c) show two basic micro-structures of co-deposited films stratified (laminar) and granular, respectively [21,33]. The layers shown here are 30-50 micrometers thick, but the formation of much thicker deposits (1 mm) was also found on the neutraliser plates of the belt pump limiter at TEXTOR [33]. Fig. 3 and 4 show respectively the outer divertor plates and test mirrors from the inner divertor of JET-C and JET-ILW.

These results clearly demonstrate a significant decrease of deposition in operation with the metal wall. Smaller deposition has a direct impact on the dust generation in a reactor. Thick deposits are very brittle, easily disintegrate hence the fuel-rich dust is produced. The amount of dust in the reactor must be strictly controlled as it poses danger of ignition and steam reaction in the case of accidental massive air or cooling water leak into the vacuum vessel. Dust generation mechanism, motion in plasma and morphology of particulates has been intensively studied [34-37]. The amount of dust dropped after the change of the wall: from over 200 g in the last JET-C campaign to around 1 g in JET-ILW [30,38,39]. This result provides a very positive message for ITER, especially that the amount of loose metal dust (Be-rich deposits or metal droplets) constitute only a small fraction of that total amount of 1 g.

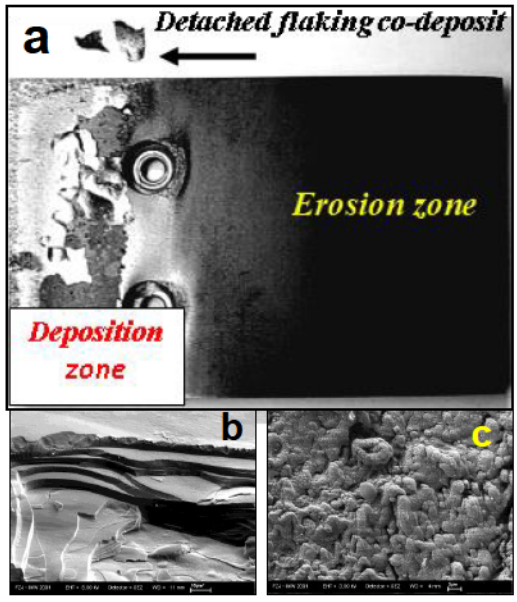

Figure 2: Limiter tile exposed at the TEXTOR tokamak (a); stratified (b) and granular (c) co-deposits.

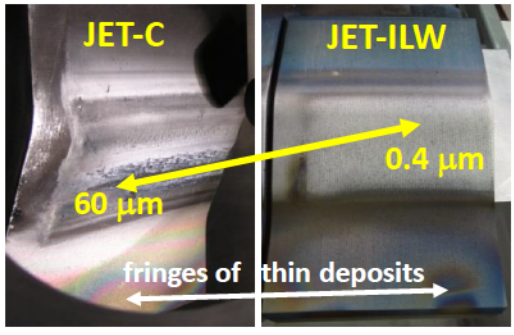

Figure 3: Comparison of deposition on the divertor tiles in JET-C (thick) and JET-ILW (thin layers).

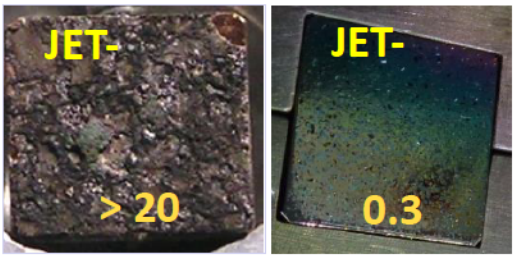

Figure 4: Comparison of deposition on test mirrors from the inner divertor of JET-C [40] and JET-ILW [31].

The estimated fuelling rate of the ITER plasma is around 54 g of T per 400 s pulse. From this amount approximately only 1 g will be burnt in the D–T fusion, whereas the remaining majority must be pumped out and returned to the tritium plant (the plant is discussed in Chapter VII). However, the pumped-out fraction will depend on the long-term tritium retention in co-deposits. Predictions have been made for the cumulative tritium retention in co-deposited carbon films until the safety limit for in-vessel inventory (700 g) is reached and a clean-up must be performed [41]. Based on the experience gathered after the full D–T operation in JET-C and on scenarios modelled by computer codes for erosion and re-deposition the clean-up would be necessary after 30-40 (JET equivalent at full carbon wall) to 350-400 ITER pulses (inventory 2 g/pulse with carbon tiles only in the strike zone in the divertor). In a full metal surrounding the limit of 700 g would be after thousands of discharges [42]. The operation of JET-ILW with deuterium fuelling confirms small retention [11,43]. New results are expected in 2021-22 after completion of the full D-T operation [44,45].

Even with positive results indicating the low retention rate with a metal wall, the development of the fuel clean-up methods is not abandoned. In the past, several methods of T removal and vessel clean-up were tested at TFTR and JET following full D–T campaigns [22,26]: tokamak discharges in D_2 fuelled plasma, H and He glow discharge cleaning, venting with oxygen. Tokamak discharges and hydrogen glow aim at the D–T and H–T isotope exchange. Helium glow sputters away isotopes from the surface layer. Ventilation with air leads to the formation of tritiated water. While the T removal from the main chamber (PFC) could be deemed reasonable effective, the removal rate from remote areas, where the thickest tritiated co-deposits were formed, was poor. Peeled-off flakes were removed by vacuum cleaning. Several other methods for tritium and co-deposit removal have been proposed and tested under laboratory conditions. They are based on chemical decomposition (H and He glow plasma with water vapour [23], O_2-He glow [27]), pulsed irradiation [24,25] or mechanical treatment of surfaces with co-deposits [46]. Irradiation with a laser [25] or a flash lamps [30] stimulates desorption of H isotopes and disintegration of co-deposits. However, the side effect of the deposit removal and disintegration is the formation of dust particulates. Another challenge is related to development of an efficient method to remove co-deposits from gaps between tiles and grooves of castellation [47]. The issue is important because all plasma-facing components in ITER will be castellated and the number of narrow grooves will be over one million. Taking into account a variety of co-deposit structures and their location in the reactor, a combination of techniques must be applied. An overview of methods has been presented by Counsell [41]. Some of those procedures will still be useful with metal PFC. The toolbox with methods is enlarged by ion and electron cyclotron wall conditioning (ICWC and ECWC), as detailed in [48-50]. Experiments are in the TOMAS facility dedicated to the development of techniques, and in tokamaks. Comprehensive full-scale *in-situ* tests are to be continued in large tokamaks to assess global efficiency of fuel removal.

V. RADIATION-INDUCED EFFECTS

Properties of reactor materials and components are modified by fast neutrons and ionising radiation: γ, X and UV. The neutron flux to the wall of ITER will be of the order of 5×10^{17} m^{-2} s^{-1}. Energy carried by 14 MeV neutrons must be converted in the blanket into heat and tritium breeding. The blanket acts as a neutron absorber and T-breeder [51,52]. Its additional important role is the protection of the vacuum vessel and super-conducting coils from neutron irradiation. Neutrons, on their way through the armour and structural components of the blanket, cause volumetric radiation damage and chemical modification leading to the change and deterioration of material properties. The major neutron-induced effects in solids are: structural damage (displacement) [53,54] and nuclear transmutation [55]. These are very closely inter-related processes and they affect all types of materials. Some specific effects are induced by fast photons in ceramic insulators.

The measure of damage to a crystalline matter caused by bombardment with energetic particles is expressed in terms of "displacement per atom" (dpa), i.e. the number of times each atom is dislodged by radiation from its place in the crystal. In other words, 1 dpa is equivalent to displacing all atoms once from their lattice sites. The cross-section for processes of neutron displacement damage is generally in the range from 1 to 10 barns ($1b = 10^{-28}$ m^2). Damage depends on the fluence (total dose) and, in some cases, also on the neutron flux. For instance, in carbon, beryllium or ceramic materials 1 dpa is produced by a neutron dose of around 1×10^{25} m^{-2}. Volumetric damage leads to the formation of dislocations, interstitials, voids and vacancies in the crystal lattice. This results from the direct knock-on of atoms and/or ions from their sites. Knock-on atoms of sufficiently high energy may produce further displacements by cascades. Dislocation is defined as a line, plane or region in which there is a discontinuity in the regularity of the lattice. Voids and vacancies are the empty spaces formed by shifting the atoms from their

original sites. In the end effect materials volume is changed due to swelling (metals, ceramics) or shrinkage (CFC). 1 dpa typically results in 1 % volume change. This in turn, leads to the significant drop in thermal conductivity, even by 70% from the original value [56]. Swelling of a metal crystal changes drastically its mechanical properties causing hardening and resultant increased brittleness (embrittlement). The extent of damage is reduced at elevated temperatures due to annealing. However, for obvious reasons the temperature of in-vessel materials and components cannot be increased indefinitely. Therefore, efforts in irradiation tests are focused on the definition of operation limits, i.e. dose and temperature.

The processes described above apply also to all insulating ceramics applied as important components of heating and current drive and diagnostic systems exposed directly to neutron fluxes: feed-through assemblies, magnetic pick-up coils, mineral insulated cables, bolometers, pressure gauges, thermocouples, other temperature sensors, optical fibres, laser diodes, detectors, windows, mirrors, etc [15,57]. For insulators the requirements are more stringent than for metallic materials because it is necessary to maintain not only their mechanical performance but also sensitive physical properties such as insulation and optical transmission. These properties are influenced by neutrons and photons due to radiation-induced or radiation-enhanced:

i. conductivity (excitation of electrons into a conduction band),
ii. electrical degradation (increased electrical conductivity),
iii. absorption (light transmission loss),
iv. electromotive force (induced voltage between the centre and outer conductors of a mineral insulated cable),
v. radiation-enhanced diffusion (for instance increased tritium mobility in ceramic windows).

To ensure reliable performance of insulated devices further testing and development of radiation-hard materials must be carried out. The list of ceramic materials include Al, Mg, Si, Be oxides, nitrides (Si_3N_4), natural and CVD-diamonds, mica and ferroelectrics.

The second fundamental radiation-induced effect is transmutation defined as the change in a nucleus structure leading to the formation of different isotope(s) or element(s) induced by bombarding the nucleus with particles or photons. In the case of photons, the process goes *via* the Compton effect. The efficiency of transmutation, as for all nuclear reactions, depends on the cross-section of a given nuclear process. Basically, neutron-induced transmutation can be divided into three categories dependent on the reaction products:

i. formation of gaseous species such as hydrogen isotopes and helium: (n,p), (n,np), (n,d), (n,t) (n,α), (n,nα),
ii. gamma radiation: (n,γ), (n,n'γ)
iii. neutron breeding: (n,2n), (n,3n).

One may easily notice that the first-group processes lead to the formation of hydrogen isotopes (H,D,T) or helium. Gases accumulated in the crystal lattice form bubbles and blisters. Bubbles are formed not only in the surface layer but also in the bulk. This increases brittleness. When the pressure of the accumulated gas overcomes a certain limit, blisters explode leading to the exfoliation (example is shown in Fig. 5).

An important consequence of nuclear reactions is simultaneous formation of other (than H and He) transmutation products modifying material properties. The problem associated with such impurities becomes particularly serious following high-dose irradiation. Secondly, some of those transmutation products are radioactive isotopes. Basic physics underlying the transmutation cannot be overcome and the only way to minimize its effects is to use low-activation materials, i.e. materials containing elements of low cross-section for transmutation or elements whose transmutation products are either non-radioactive or isotopes of short lifetime. It is clear that products and related radioactivity (i.e. energy spectrum and lifetime) strongly depend on the initial composition of the irradiated material. It also implies that not only major constituents must undergo low activation but also the quantity and quality of admixtures and impurities must be strictly controlled. For instance, while major constituents of a low activation vanadium alloys (V-3Ti-1Si) transmute to isotopes of short lifetime, the presence of nickel impurities transmuted to ^{60}Co leads to a long-term activation ($t_{1/2}$ ^{60}Co = 5.27 years). In conclusion, fabrication of low activation and high purity FRM is essential.

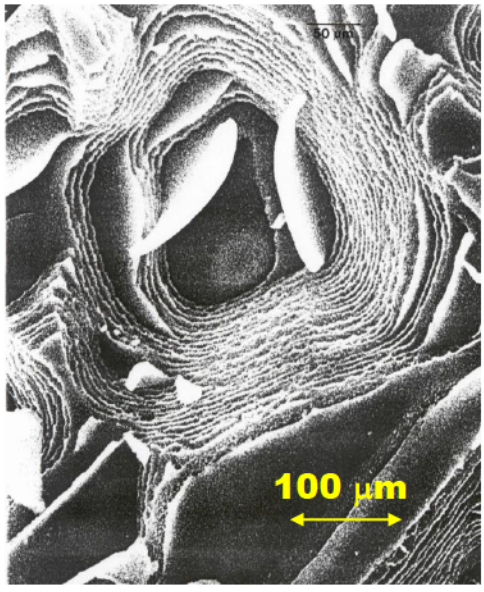

Figure 5: Exfoliation of metal following high dose irradiation.

VI. TRITIUM BREEDING IN THE BLANKET

As already pointed out, the conversion of neutron energy to heat and T-breeding takes place in the absorber part of the blanket. The role of the blanket is also to shield superconducting magnets (niobium-tin Nb_3Sn and/or niobium-titanium Nb-Ti) against neutrons and gamma radiation [58]. Several test tritium breeding blanket modules (TBM) are planned to be installed in ITER. The aim of TBM implementation in ITER is to test their performance and verify technology for DEMO, i.e. for a prototype of a power-generating fusion reactor. The modules are composed of structural (i.e. containment and coolant loop made of EUROFER) and functional materials (i.e. breeder). Two basic coolants have been considered: water and high-pressure helium [59]. Figure 6 shows a scheme of helium-cooled blanket being developed for DEMO.

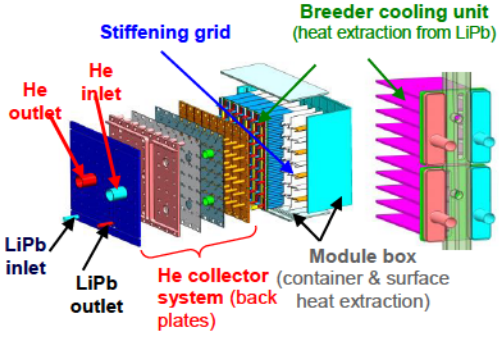

Figure 6: Schematic view of a helium-cooled blanket module to be operated with liquid lithium-lead developed for DEMO. *Source: EFDA.*

Lithium is an efficient breeder. Therefore, it is a constituent of all candidate materials considered for the absorber. Lithium has two stable isotopes ^6Li and ^7Li with natural abundance of 7.5% and 92.5%, respectively:

$$^6Li + n \rightarrow \alpha + T + 4.78\ MeV \quad (5)$$
$$^7Li + n \rightarrow \alpha + T + n' - 2.47\ MeV \quad (6).$$

These reactions are essential for tritium production because that isotope must be produced on site. Several ceramics have been tested: Li_2ZrO_3, Li_8ZrO_6, Li_2TiO_3, $LiAlO_2$, Li_2SiO_3 and Li_4SiO_4 [60]. The other candidates are lithium oxide (Li_2O), Li17-Pb liquid alloy (eutectic) and 2LiF-BeF_2 mixture called Flibe, Li_2BeF_4. To increase the amount of neutrons for T breeding, beryllium is added as a neutron multiplier:

$$^9Be + n \rightarrow 2\alpha + 2n' \qquad (E_{th} = 2.7\ MeV) \quad (7).$$

However, other side reactions with low cross-sections also occur thus leading to the production of tritium and helium and, eventually, to accumulation of tritium in He bubbles in Be:

$$^9Be + n \rightarrow \alpha + {}^6He \qquad (E_{th} = 0.67\ MeV) \quad (8)$$
$$^6He\ (\beta^-) \rightarrow {}^6Li \qquad (3.508\ MeV,\ t_{1/2} = 0.807\ s) \quad (9)$$

$$^9Be + n \rightarrow {}^7Li + T - 10.40\ MeV \qquad (E_{th} = 11.6\ MeV) \quad (10),$$

where E_{th} is the threshold energy. Then, ^6Li and ^7Li are transmuted to tritium in processes (5) and (6), respectively. Taking into account all these pathways of T generation from lithium, the overall fusion process reads:

$$\mathbf{D + Li \rightarrow 2\alpha + Energy} \quad (11),$$

showing that the energy production cycle is based on easily achievable reactants found in nature in inexhaustible supply: deuterium extracted from sea water (~33.3 g D/m^3) and lithium extracted from sea water or obtained from common minerals such as lepidolite, petalite, spodumene and amblygonite.

VII. TRITIUM PLANT

Tritium breeded in the blanket and that pumped-out from the torus (non-used fuel and released from the wall by cleaning methods) must be handled in the tritium plant before it can be used for plasma fuelling. Tritiated species occur in the form of gas molecules (I_2, where I denotes a mixture of hydrogen isotopes), hydrocarbons (C_xI_y) and water (I_2O). The separation methods comprise cryogenic distillation, condensation, electrolysis, diffusion via Pd membranes, catalytic processes: oxidation of C_xI_y, decomposition of I_2O and C_xI_y and vapour stage exchange:

$$CO + I_2O \leftrightarrow CO_2 + I_2 \quad [\text{water gas shift}] \quad (12)$$
$$CI_4 + I_2O \leftrightarrow CO + 3I_2 \quad [\text{steam reforming}] \quad (13)$$
$$CI_4 \leftrightarrow C + 2I_2 \quad [\text{methane cracking}] \quad (14).$$

Fig. 7 shows a schematic flow diagram in an isotope separation facility [61]. This example is based on the Tritium Separation Test Assembly, TSTA, operated until 1997 in Los Alamos NL, New Mexico, USA. Details of the ITER fuel cycle have been recently presented by Mardoch [62].

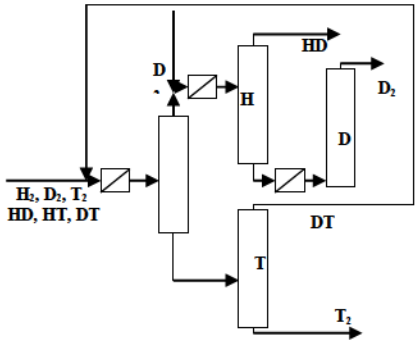

Figure 7: A schematic flow diagram of tritiated gases in an isotope separation station (ISS).

All tritium for introduction to the torus (freshly supplied to the reactor site and that leaving the ISS) must be stored in uranium or Co-Zr beds at low temperature. This is to ensure precise dosing and to avoid

uncontrolled release of the radioactive gas. Also deuterium for the gas introduction system is stored in U-beds. The discharge of pure gases from the beds is realised at elevated temperature of about 450 °C [26].

VIII. SAFETY ASPECTS AND HANDLING OF REACTOR COMPONENTS

Already the D–D phase of the ITER operation will activate components to the level unacceptable for manned intervention in the reactor vessel. Radioactivity will be significantly increased in the D – T phase. Additionally, the use of beryllium (health hazard) on the entire wall of the main chamber imposes strict precautions for in-vessel operation during shut-down periods. Therefore, like in other branches of nuclear industry, the design and construction of all in-vessel components of a fusion reactor is fully compatible with remote handling by robotic arms. The major role of these programmed (trained) devices is in installation, exchange and repair of PFC, blanket, divertor modules and in-vessel diagnostics. Fig. 8 shows a robotic arm used in the JET tokamak. The technology was developed for handling components following the full D–T campaign [26,63]. All replacements of the JET divertor structure and installation of diagnostic tools are performed by these means. Remote handling technology at JET has been further developed to meet requirements in installation of beryllium and tungsten components for the ILW project. This has comprised a design and construction of new robots capable of handling and installing components of up to 100 kg [9,10].

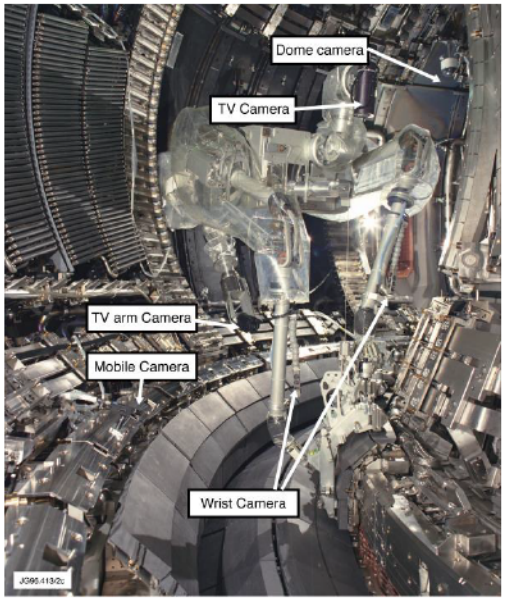

Figure 8: A remotely controlled robotic arm at JET: restructuring of the divertor configuration (1998).

IX. FUTURE STUDIES OF FUSION REACTOR MATERIALS

The list of most important issues to be tackled on the way towards the reactor construction includes:

i) further development of low-activation and radiation-hard materials and components of high purity,

ii) development of efficient techniques for tritium removal or elimination of carbon as material for PFC in order to reduce inventory related to the co-deposition,

iii) testing of materials and components under high-flux irradiation with 14 MeV neutrons.

The last point requires a construction of an efficient test facility capable of simulating the neutron energy spectrum of a D–T fusion reactor. Sufficient intensity of the n-flux and the irradiation volume of at least 500 cm^3 are indispensable for testing samples of candidate materials up to a full lifetime of anticipated use in a reactor (e.g. DEMO), i.e. over 80 dpa. A conceptual design of the facility has been completed. Engineering validation and engineering design activity (EVEDA) phase will soon begin and it should be followed by decisions regarding the site for the facility and work schedule. The project is called IFMIF: International Fusion Material Irradiation Facility [64-66]. The facility shown schematically in Fig. 9 is an intense neutron source based on an accelerator-driven generation of neutrons by deuterium–lithium reactions: $^{7}Li(d,2n)^{7}Be$, $^{6}Li(d,n)^{7}Be$ [67-69]. Deuterons in the range of 30 - 40 MeV are to be produced by means of two continuous-wave linear accelerators. Interaction of deuterons in a flowing lithium target would lead to production of neutrons with the energy spectrum peaking at around 14 MeV. The neutron generation rate of some 10^{17} n s^{-1} would result in a flux of some 10^{19} m^{-2} s^{-1} at the rear side of the target. Therefore, displacement damage and transmutation products (He) in the irradiated material would match the neutron-induced effects anticipated in the fusion reactor environment. Fig. 10 shows a scheme of the IFMIF test assembly and target chambers.

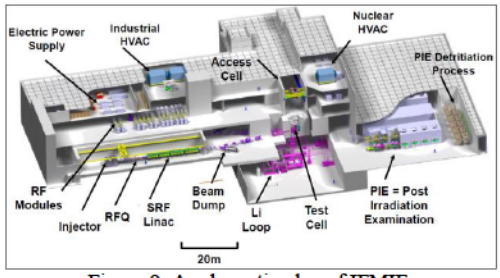

Figure 9: A schematic plan of IFMIF.
RFQ: Radio frequency quadrupole; SRF Linac: superconducting radio frequency linear accelerator; HVAC: Heating–Ventilation –Air Conditioning.

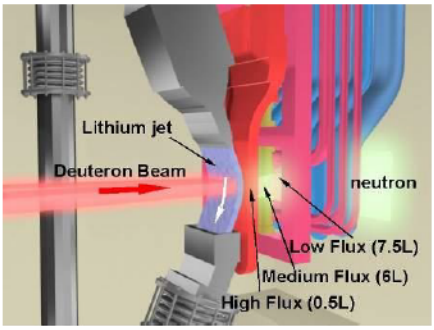

Figure 10: IFMIF: liquid lithium target and characteristics of target chambers.

X. CONCLUDING REMARKS

The above mentioned aspects of material science are necessary and important to accomplish the ultimate goal of fusion research, i.e. the construction of a power generating system. Development and intense testing of materials and components, will play a crucial role in and for the operation of ITER and DEMO machines. Having in mind scientific and technical challenges associated with the project, all efforts are to be made to ensure the best possible material selection for a reactor-class machine. Fusion, if realised under terrestrial conditions, offers inexhaustible energy supply free of CO_2 emission. However, a reactor is a nuclear device and radioactive aspects of fusion will undergo intense public scrutiny. For that reason, proper testing and validation of material and component performance is essential. Based on the best of our present knowledge we have to use and to develop tools, methods and materials best fitted for the steady-steady reactor operation. International co-operation established around ITER is an important step on the way towards commercial fusion.

The lecture has addressed not only problems and future challenges but also achievements in technology of FRM. With the present-day experience and background from many fields of science and technology we know "*what*" and "*why*" may happen with materials in a hostile fusion environment. This, in turn, allows definition of actions "*how*" to deal with problems and reach solutions. It certainly still requires substantial funding but also a lot of invention. In that sense, fusion-related material research is an attractive and long-term field for a generation of young scientists and nuclear engineers.

REFERENCES

1. G. Federici et al., "Plasma-Material Interactions in Current Tokamaks and their Implications for Next Step Fusion Reactors", *Nucl. Fusion,* **41**, 1967 (2001).
2. W. O. Hofer and J. Roth (Eds), *Physical Processes of the Interaction of Fusion Plasmas with Solids,* Academic Press, New York (1996).
3. D. Naujoks, "Plasma-Material Interactions in Controlled Fusion", Springer Series in Atomic, Optical and Plasma Physics, Springer, 2006.
4. J. Linke, "Plasma Facing Materials and Components Future Fusion Devices: Development, Characterisation and Performance under Fusion Specific Loading Conditions", *Phys. Scr.,* **T123**, 45 (2006).
5. Progress in the ITER Physics Basis, *Nucl. Fusion,* **47** (2007) (also: www.iter.org).
6. J. P. Coad et al., "The Amount and Distribution of Deuterium Retained in the JET Divertor after the C and Be Phases", *J. Nucl. Mater,*. **241-243**, 408 (1997).
7. M. Rubel et al., "Beryllium and Carbon Films in JET following D-T Operation", *J. Nucl. Mater*., **313-316**, 323 (2003).
8. G. F. Matthews et al. "Overview of the ITER-Like Wall Project", *Phys. Scr.,* **T128**, 137 (2007).
9. G.F. Matthews et al., "The JET ITER-Like Wall – Status and Experimental programme", *Phys. Scr*., **T145**, 014001 (2011).
10. Ph. Mertens at al., "Detailed Design of a Solid Tungsten Divertor at JET", *Phys. Scr*., **T145**, 014002 (2011).
11. G.F. Matthews, "Plasma Operation with an All Metal First Wall: Comparison of an ITER-Like Wall and a Carbon Wall in JET", *J. Nucl. Mater*., **438**, S2 (2013).
12. R.A. Pitts et al., "A Full Tungsten Divertor for ITER: Physics Issues and Design Status", *J. Nucl. Mater.,* **438**, S48 (2013).
13. E. E. Bloom, "The Challenge of Developing Structural Materials for Fusion Power Systems", *J. Nucl. Mater*., **258-263**, 7 (1998).
14. T. Yano et al, "Physical Property Change of Neutron Irradiated CVD-diamond, Silicon and Silicon Carbide", *J. Nucl. Mater.,* **307-311**, 1102 (2002).
15. M. Decréton, T. Shikama and E. Hodgson, "Performance of Functional Materials and Components in a Fusion Reactor: the Issue of Radiation Effects in Ceramics and Glass Materials for Diagnostics", *J. Nucl. Mater.,* **329-333**, 125 (2004).
16. B. Emmoth, M. Rubel and E. Franconi, "Deep Penetration of Deuterium in Carbon-Based Substrates", *Nucl. Fusion,* **30**, 1140 (1990).
17. V. K. Alimov and J. Roth, "Hydrogen isotope retention in plasma-facing materials: review of recent experimental results", *Phys. Scr.,* **T128**, 6 (2007).

18. A. Kreter et al., "Deuterium Retention in Different Carbon Materials Exposed at TEXTOR*", J. Physics Conf. Series,* **100**, 062024 (2008).
19. V. Philipps et al., "Erosion and Re-deposition of Wall Material in Controlled Fusion Devices", *Vacuum,* **67**, 399 (2002).
20. A. von Keudell et al., "Surface Loss Probabilities of Hydrocarbon Radicals on Amorphous Hydrogenated Carbon Film Surfaces", *Nucl. Fusion,* **39**, 1451 (1999).
21. M. Rubel et al., "Analysis and Oxidation of Thick Deposits on TEXTOR Plasma Facing Components", *J. Nucl. Mater.,* **266-269**, 1185 (1999).
22. C.H. Skinner et al., "Plasma Wall Interaction and Tritium Retention in TFTR", *J. Nucl. Mater.,* **241-243**, 214 (1997).
23. B. Landkammer et al.,"Erosion of Thin Hydrogenated Carbon Films in Oxygen, Oxygen/Hydrogen and Water Plasmas", *J. Nucl. Mater*. **264**, 148 (1999).
24. C. H. Skinner et al., "Thermal Response of Tritiated Co-deposits from JET and TFTR to Transient Heat Pulses", *Phys. Scr.,* **T103**, 34 (2003).
25. D. Ivanova et al., "Laser-based and Thermal Methods for Fuel Removal and Cleaning of Plasma-Facing Components", *J. Nucl. Mater.,* **415**, S801 (2011).
26. D. Stork (Ed.), *Technical Aspects of Deuterium-Tritium Operation at JET*, (special issue) *Fusion Eng. Des.,* **47**, (1999).
27. M. Rubel et al., "Fuel Removal from Plasma-Facing Components by Oxidation-Assisted Technique. An Overview of surface morphology after oxidation", *J. Nucl. Mater*., **363-365**, 877 (2007).
28. A. Widdowson et al., "Efficacy of photon cleaning of JET divertor tiles" *J. Nucl. Mater.,* **363-365**, 341 (2007).
29. S. Brezinsek et al., "Beryllium Migration in JET ITER-Like Wall Plasmas", *Nucl. Fusion*, **55** 063021 (2015).
30. A. Widdowson et al., "Material Migration Pattern and Overview of First Surface Analysis of the JET ITER-Like Wall", *Phys. Scr.*, **T159**, 014010 (2014).
31. Sunwoo Moon et al., "First Mirror Test in JET for ITER: Complete Overview after Three ILW Campaigns", *Nucl. Mater. Energy,* **19**, 59 (2019).
32. S. Brezinsek et al., "Plasma Wall Interaction in All Metal Tokamaks, *These Proceedings,* 2021.
33. M. Rubel et al., "Thick Co-Deposits and Dust in Controlled Fusion Devices with Carbon Walls: Fuel Inventory and Growth Rate of Co-Deposited Layers", *Phys. Scr*., **T103**, 20 (2003).
34. M. Rubel et al., "Dust Particles in Controlled Fusion Devices", *Nucl. Fusion,* **41**, 1087 (2001).
35. J. Winter and G. Gebauer, "Dust in Magnetic Confinement Devices and its Impact on Plasma Operation", *J. Nucl. Mater.,* **266-269,** 228 (1999).
36. V. Rohde et al., "Dust Investigations at ASDEX Upgrade"*Phys. Scr.,* **T138**, 014024 (2009).
37. D. Ivanova et al., "Survey of Dust Formed in the TEXTOR Tokamak: Structure and Fuel Retention", *Phys. Scr.,* **T138**, 014025 (2009).
38. M. Rubel et al., "Dust Generation in Tokamaks: Overview of Beryllium and Tungsten Dust Characterisation in JET with the ITER-Like Wall", *Fusion Eng. Design*, **136**, 579 (2018).
39. E. Fortuna-Zalesna et al., "Fine Metal Dust Particles on the Wall Probes from JET-ILW", *Phys. Scr*., **T170**, 014038 (2017).
40. M. Rubel et al., "An Overview of a Comprehensive First Mirror Test for ITER at JET", *J. Nucl. Mater*., **390-391**, 1066 (2009).
41. G. Counsell et al., "Tritium Retention in Next Step Devices and Requirement for Mitigation and Tritium Removal Techniques*", Plasma Phys. Control. Fusion,* **48**, B189 (2006).
42. J. Roth et al., "Recent Analysis of Key Plasma Wall Interactions Issues for ITER", *J. Nucl. Mater.,* **390-391**, 1 (2009).
43. T. Loarer et al., "Comparison of Long-Term Retention in JET between Carbon and the ITER-Like Wall", *J. Nucl. Mater.,* **438** S108 (2013)
44. E. Joffrin and JET Contributors, "Overview of the JET Preparation for Deuterium-Tritium Operation with the ITER-Like Wall", *Nucl. Fusion*, **59**, 112021 (2019).
45. J. Mailloux and JET Contributors, "Overview of JET Results for Optimising ITER Operation", *Nucl. Fusion*, in press (2021).
46. G. Counsell and C.H. Wu, "In-situ Detection and Removal of Carbon Debris – a Challenge for the Next Step Fusion Device", *Phys. Scr.,* **T91**, 70 (2001).
47. M. Rubel et al., "Overview of Co-deposition and Fuel Inventory in Castellated Divertor Structures at JET", *J. Nucl. Mater.,* **367-370**, 1432 (2007).
48. D. Douai et al., "Wall Conditioning for ITER: Current Experimental and Modelling Activities", *J. Nucl. Mater*., **463**, 150 (2015)
49. T. Wauters et al., "Wall Conditioning in Fusion Devices with Superconducting Coils", *Plasma Phys. Control. Fusion*, **62**, 034002 (2020),
50. A. Goriaev et al., "The Upgraded TOMAS device: A Toroidal Plasma Facility for Wall Conditioning, Plasma Production, and Plasma-Surface Interactions", *Rev. Sci. Instrum*., **92** 0233506 (2021)
51. T. Tanabe (Ed.), *Tritium: Fuel of Fusion Reactors,* Springer, Japan, 2017.

52. M. Rubel, "Fusion Neutrons: Impact on Wall Materials and Components of Diagnostic Systems", *J. Fusion Energy*, **38**, 315 (2019).

53. R. A. Johnson and A. N. Orlov (Eds*), Physics of Radiation Effects in Crystals, Modern Problems in Condensed Matter Sciences*, Vol. 13, Noth-Holland, Amsterdam (1986).

54. H. Ullmaier, *Contributions to High-Temperature Plasma Physics*, K. H. Spatschek and J. Ulenbusch (Eds), Chap. 3, p. 201, Akademie Verlag, Berlin (1994).

55. H. S. Plendl (Ed.), *Nuclear Transmutation Methods and Technologies,* North-Holland, Amsterdam 1998. (also : www.chemistrycoach.com/nuclearchem.htm)

56. T. D. Burchell, "Radiation Damage in Carbon-Carbon Composites", *Phys. Scr.,* **T64**, 17 (1996).

57. Ph. Maquet et al., "Development of ITER Diagnostic Window Assemblies", *Fusion Eng. Design*, **88**, 2841 (2013).

58. L. Giancarli et al., "Breeding Blanket Modules Testing in ITER: An International Programme on the Way to DEMO", *Fusion Eng. Design,* **81**, 393 (2006).

59. Y. Poitevin et al., "The Test Blanket Modules Project in Europe", *Fusion Eng. Design,* **82**, 2164 (2007).

60. A. R. Raffray et al., "Breeding Blanket Concepts for Fusion and Material Requirements", *J. Nucl. Mater.*, **307-311**, 21(2002).

61. J. L. Anderson and P. LaMarche, "Tritium Activities in the United States", *Fusion Technol.,* **28**, (1995) 479.

62. D.K. Murdoch et al., "ITER Fuel Cycle Development", *Fusion Sci. Technol*., **48**, 3 (2005).

63. A. Rolfe, "Remote Handling on Fusion Experiments", *Fusion Eng. Design,* **36**, 91 (1997).

64. A. Möslang et al., "Suitability and Feasibility of the International Fusion Materials Irradiation Facility (IFMIF) for Fusion Materials Studies", *Nucl. Fusion*, **40**, 619 (2000) 619.

65. J. Knaster et al., "Overview of IFMIF/EVEDA Project", *Nucl. Fusion* **57**, 102016 (2017).

66. H. Kondo et al., "IFMIF/EVEDA Lithium Test Loop: Design and Fabrication Technology of Target Assembly as a Key Component", *Nucl. Fusion* **51**, 123008 (2011).

67. J. Knaster et al., "IFMIF, the European–Japanese Efforts under the Broader Approach Agreement Towards a Li(d, xn) Neutron Source: Current Status and Future Options", *Nucl. Mater. Energy* **9**, 46 (2016).

68. J. Knaster, T. Kanemura, K. Kondo, "Assessment of the Evaporation and Condensation Phenomena of Lithium during the Operation of a Li(d, xn) Fusion Relevant Neutron Source", *Heliyon,* **2**, e00199 (2016).

69. H. Kondo et al., "Validation of Liquid Lithium Target Stability for an Intense Neutron Source", *Nucl. Fusion,* **57**, 066008 (2017).

THE COUPLING OF ION CYCLOTRON WAVES TO PLASMAS

F. Louche

Laboratory for Plasma Physics - ERM/KMS, Belgian "EUROfusion Consortium" Member, Renaissancelaan 30 Avenue de la Renaissance, B-1000 Brussels, Belgium

ABSTRACT

This lecture addresses, on the basis of elementary and intuitive treatments, the process of coupling of electromagnetic power to plasma. We focus on the process of coupling a vacuum wave to plasma waves in the edge plasma region in the Ion Cyclotron Range of Frequencies (ICRF). From the properties of the plasma waves at the edge of the plasma, where the cold plasma approximation can be used, we infer the necessary conditions for good coupling and good absorption. In particular the importance of the launcher geometry on the radiation spectrum of the antenna is underlined. We also discuss recent experimental results and we show how particular issues such as impurity production during heating can be alleviated. In the final section we introduce how the principle of travelling waves antennas and comblines can be applied in the ICRF.

I. INTRODUCTION

The principle of wave heating is similar for all schemes and is sketched in Fig.1. The electromagnetic energy is produced by a generator and sent to the machine area via transmission lines constituted of coaxial lines at low frequency and waveguides at higher frequency. At very high frequency optical transmission is also possible. Some matching circuitry has to be incorporated in the transmission system in order to prevent the reflected power to come back to the generator. The transmission line is connected to some launching structure (antenna, waveguide,...) that will couple the power inside the machine's vacuum chamber. The vacuum wave that exists inside the launching structure and at the very edge of the plasma is then converted to a plasma wave that transports electromagnetic energy to some region inside the plasma where it will be absorbed. This is the region where the resonant process occurs. This process accelerates the population of particles that is in resonance with the wave, usually a small fraction of the plasma particles. A slightly or strongly non-maxwellian resonant population builds up against the restoring force of collisions between this population and the remainder of the plasma. It is through the latter collisional process that the bulk of the plasma is heated up.

The concept of "coupling" as it will be treated here concerns essentially the coupling of vacuum electromagnetic power to plasma waves. Even if this cannot be completely disentangled from the other processes (absorption, thermalization, ...), we will mainly consider here the physics of the system "launcher-vacuum-plasma edge". The detailed physics of the resonant absorption is discussed in [1, 2] while the thermalization is studied in [3]. In this paper, we shall not describe the technical parts of the launching systems, i.e. generators, transmission lines, matching systems (see [4]). Let us first start with the elementary wave theory.

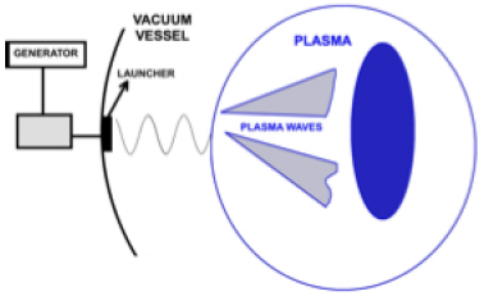

Figure 1: Principle of heating by plasma waves

II. WAVE PROPAGATION IN A PLASMA

The study of plasma waves is a very broad subject and we will limit ourselves to to the cold-plasma approximation [5] which is mostly sufficient to describe the basic propagation properties of the waves used in plasma heating. Interested readers should consult references [6, 7] for an exhaustive description of plasma waves.

We consider a plasma immersed in a static magnetic induction field $\vec{B_0}$. If the wave is considered as a first-order perturbation with a harmonic space-time dependence $\sim \exp\left[-i(\omega t - \vec{k}\cdot\vec{x})\right]$ then the cold-plasma dispersion relation can be written [6]:

$$\mathbf{D}\cdot\vec{E} = \vec{k}\times\left(\vec{k}\times\vec{E}\right) + \frac{\omega^2}{c^2}\boldsymbol{\varepsilon}\cdot\vec{E} = 0 \qquad (1)$$

where $\vec{k}$ is the wave vector, $\vec{E}$ is the wave electric field, ω is the generator angular frequency and c is the speed of light. It is sometimes useful to work instead with the refractive index vector $\vec{n} = \vec{k}/k_0$ where $k_0 = \omega/c$ is the vacuum wave vector. The components of the cold-plasma dielectric tensor $\boldsymbol{\varepsilon}$ are given by [6]:

$$\boldsymbol{\varepsilon} = \begin{pmatrix} \varepsilon_\perp & i\varepsilon_{xy} & 0 \\ -i\varepsilon_{xy} & \varepsilon_\perp & 0 \\ 0 & 0 & \varepsilon_\parallel \end{pmatrix} \text{ with } \begin{aligned} \varepsilon_\perp &= 1 - \sum_s \frac{\omega_{ps}^2}{\omega^2 - \omega_{cs}^2} \\ \varepsilon_{xy} &= \sum_s \frac{\omega_{ps}^2 \Omega_{cs}}{(\Omega_{cs}^2 - \omega^2)\omega} \\ \varepsilon_\parallel &= 1 - \sum_s \frac{\omega_{ps}^2}{\omega^2} \end{aligned} \quad (2)$$

The wave equation is an algebraic homogeneous system of 3 equations for the 3 cartesian components of the electric field. It will have a non vanishing solution if and only if the determinant of **D** is zero. This defines the dispersion relation, an implicit relation between the generator frequency, the parallel and perpendicular components of the refractive index vector $\vec{n_\perp}$ and $n_\parallel$, and the plasma properties (encoded in the dielectric tensor). The dispersion equation solution determines all the wave modes which can propagate in the plasma for a given plasma model. If the static magnetic induction $\vec{B_0}$ is taken along the z-direction of a cartesian frame, then, because of the isotropy in the plane parallel to $\vec{B_0}$, the direction of the perpendicular component of the wave vector $\vec{k_\perp}$ is irrelevant and can be arbitrarily chosen as x-direction. The dispersion equation is then expressed as a bi-quadratic equation in $n_\perp = |\vec{n_\perp}|$:

$$\begin{vmatrix} \varepsilon_\perp - {n_\parallel}^2 & i\varepsilon_{xy} & n_\perp n_\parallel \\ -i\varepsilon_{xy} & \varepsilon_\perp - {n_\perp}^2 - {n_\parallel}^2 & 0 \\ n_\perp n_\parallel & 0 & \varepsilon_\parallel - {n_\perp}^2 \end{vmatrix} = 0 \quad (3)$$

We shall generally express its solution as ${k_\perp}^2 = \kappa(k_\parallel, \omega)$ because $k_\parallel$ is generally fixed by the launcher structure. The two roots are often called fast and slow waves respectively. Their behaviour will be studied in details in [1, 8] for the various ranges of frequencies. For our purpose we simply need to underline that at some frequencies (corresponding to specific locations in the plasma) "something can happen" ! First, the dielectric tensor becomes singular each time $\omega = \omega_{cs}$. This means that the particle current becomes infinite for a finite electric field (*wave-particle resonances*). The other special frequencies are those for which ${k_\perp}^2 \to \infty$ and appear when $\varepsilon_\perp = 0$. We speak about *wave resonances*.

III. COUPLING THEORY IN THE I.C.R.F.

A. Dispersion curves in the I.C.R.F.

In the ICRF, or below, $\varepsilon_\parallel$ is much larger than the other elements such that the dispersion equation reduces to the top left 2X2 determinant (3). This approximation corresponds to the zero electron mass limit and leaves only one wave (the fast wave) in the dispersion. A typical set dispersion curves for a JET plasma can be seen in figure 2. In the ICRH the slow wave is evanescent almost everywhere in the plasma bulk, and practically the zero electron mass limit is equivalent to neglecting the parallel component of the electric field. This can be forced by setting up a screen in front of the launcher.

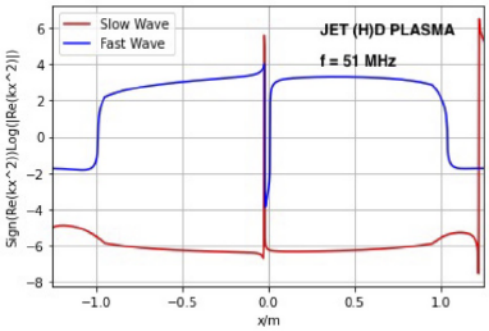

Figure 2: Dispersion curves for a typical JET plasma with parabolic density profile. Frequency is 51 MHz.

The results presented in figure 2 are from one single value of $k_\parallel$=8 m^{-1} typical of dipole phasing operation in JET. It is important to underline that if $k_\parallel$ becomes significantly smaller than the vacuum wave vector amplitude k_0, the fast wave dispersion curve near the edge locally matches the slow wave curve just before the lower hybrid resonance, which means the two wave modes are likely to exchange energy before the slow wave damps on the electrons. Consequently level of edge heating can increase which is a concern for the efficient heating of the plasma. Therefore values such that $|k_\parallel|^2 \leq |k_0|^2$ are preferably avoided.

B. Types of launcher and coupling

The simplest case is that of electron cyclotron waves in large machines. In this case, the wavelength of the vacuum wave $\lambda = 2\pi/k_0$ is very small as compared to the plasma cross-section. The wave is launched as a propagating wave pencil that will progressively convert to a plasma wave. Because of the smallness of the wavelength, the boundary conditions at the conducting wall of the machine, as well as on the launching structure, play no explicit role. The wave can be accurately described in the geometric optics limit and the only boundary conditions that matter are the initial launching angle and reflections at the wall, if any [8]. If the vacuum wavelength becomes comparable to the antenna structure, the scale length of variations of edge plasma parameters or the plasma radius, the launcher environment and the plasma will affect the coupling process and a full boundary-value problem has to be solved to describe it. Such is usu-

ally the case of Alfvén wave, ion cyclotron, or lower hybrid wave launchers in medium or large-size machines [1]. But this may also be the case of electron cyclotron launchers in low-field, small machines.

The most natural way to couple energy in the ICRF is to excite the fast wave, i.e. to excite a vacuum wave characterized by an electric field with a similar E_y polarization. This can be done by generating a modulated magnetic field parallel to the static magnetic field B_0 induced by a poloidal RF current j_y flowing on a vertical stripline. This concept, called "loop antenna", or "strap", is widely used in ICRF antennas.

We shall now introduce coupling theory, on the basis of the simplest model. More sophisticated theories rest on similar principles but include more of a realistic geometry.

C. Coupling model

We consider the simplest case of an antenna facing a large plasma such that the plasma looks nearly uniform in the toroidal (z) and poloidal (y) directions (Fig.3). In the radial direction x the plasma is usually non-uniform, and this is taken into account in standard coupling models, but here, in order to simplify the algebra, we consider a step model. The density is zero for $x < 0$ and constant density for x positive. The influence of a realistic density profile was studied in [9]: the cut-off position and the density gradient were shown to have a primary importance in the assessment of an antenna coupling capabilities, but these considerations are out of the scope of the present introduction. We assume that the absorption is good and hence, there is no reflected wave. This is the so-called single-pass approximation. In addition, we shall also assume that the system is invariant in the y-direction (which implies in particular that the antenna is infinite) and neglect propagation in the y-direction ($k_y = 0$). Next, we have to choose a model for the plasma waves. To be specific, we choose the case of coupling in the ion cyclotron frequency range (ICRF). The slow wave being evanescent in the plasma bulk, we shall consider only coupling to the fast magnetosonic wave (FW). As the FW equations will be needed later on, we first derive them, starting from the cold wave theory.

C.1 The fast magnetosonic wave equation

We write the full cold-plasma dispersion relation in terms of the parallel ($n_\parallel = n \sin\theta$) and perpendicular ($n_\perp = N \cos\theta$) components of the refractive index

$$n_\parallel = \frac{k_\parallel}{k_0}; n_\perp = \frac{-i}{k_0}\frac{d}{dx} \tag{4}$$

We keep to $n_\perp$ its operator meaning because x is the direction of inhomogeneity. In the parallel direction, the plasma is homogeneous and we use the Fourier

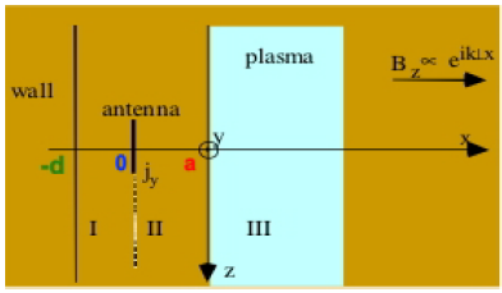

Figure 3: 2-D slab coupling model. The plasma is uniform in the y (poloidal) and z (toroidal) directions. The width of the antenna is $2w_z$, the distance between the antenna and the plasma is a and the distance between the antenna and the wall is d.

transformed form. The dispersion equation (3) derived previously can be used and we take the zero electron mass limit to uncoupling the FW. This limit implies that the parallel electric field cannot penetrate the plasma, i.e. that the evanescence length of the slow wave is zero. Eq. (1) can be recast to

$$k_{\perp,FW}{}^2 E_y = -i\left(\frac{d}{dx} + \mu k_y\right)(\omega B_z) \tag{5a}$$

$$k_{\perp,FW}{}^2 E_x = -\left(k_y + \mu\frac{d}{dx}\right)(\omega B_z) \tag{5b}$$

$$i\omega B_z = \frac{d}{dx}E_y - ik_y E_x \tag{5c}$$

with $\mu = \epsilon_{xy}k_0{}^2/u$, $u = k_0{}^2\varepsilon_\perp - k_\parallel{}^2$ and $k_{\perp,FW}{}^2 = u\left(1-\mu^2\right)$. The other components of the FW field follow from Maxwell's equation $i\omega\vec{B} = \vec{\nabla}\times\vec{E}$ (with $E_z = 0$):

$$B_x = \frac{-k_\parallel}{\omega}E_y; \quad B_y = \frac{k_\parallel}{\omega}E_x \tag{6}$$

Finally, taking the limit $k_y \to 0$ and eliminating B_z from (5a)-(5c), we obtain the FW equation:

$$\frac{d^2E_y}{dx^2} + k_{\perp,FW}{}^2 E_y = 0 \tag{7}$$

C.2 The Plasma surface impedance

For a uniform plasma, the wave equation (7) has constant coefficient and the solutions are simply exponential. The single-pass approximation allows us to impose at $z \to \infty$ a *radiating boundary condition* and the wave solution in the plasma can be written:

$$E_y = C_{III}\exp\left(ik_{\perp,FW}x\right) \tag{8}$$

where C_{III} is a constant (relative to region III in Fig. 3) to be determined. Eq. (6) then gives the longitudinal magnetic induction field field component:

$$B_z = \frac{k_{\perp,FW}}{\omega}E_y \tag{9}$$

The field in the plasma is thus known up to a multiplicative constant. Tangential field components being continuous at the plasma-vacuum interface (II-III), their ratio is also continuous. This quantity is known as the *surface impedance* of the plasma Z_S

$$Z_S = \frac{E_y}{\omega B_z} = \frac{1}{k_{\perp,FW}} \tag{10}$$

We express the continuity of this quantity at $x = 0$ as

$$[[Z_S]]_0 = Z_S(0_+) - Z_S(0_-) = 0 \tag{11}$$

In the general case where all field components are to be considered, the equivalent of (10) is a vector relation and $\mathbf{Z}_S$ is the surface impedance matrix:

$$\begin{pmatrix} E_y \\ E_z \end{pmatrix} = \mathbf{Z}_S \begin{pmatrix} \omega B_y \\ \omega B_z \end{pmatrix} \tag{12}$$

C.3 Fields in the vacuum region I-II

Equipped with this boundary condition, the vacuum problem can be solved on its own. The plasma properties will enter its solution only via the quantity Z_S and the vacuum solution is therefore formally independent of the particular plasma model considered. The general electromagnetic field in vacuum can be decomposed into its TE (transverse electric) and TM (transverse magnetic) parts with respect to a given direction, here z. Maxwell's equations then appear in the form:

$$\begin{pmatrix} B_x \\ E_y \end{pmatrix} = \frac{1}{{k_0}^2 - {k_\parallel}^2} \begin{pmatrix} -i\omega/c^2 & ik_\parallel \\ ik_\parallel & -i\omega \end{pmatrix} \begin{pmatrix} ik_y E_z \\ dB_z/dx \end{pmatrix} \tag{13a}$$

$$\begin{pmatrix} E_x \\ B_y \end{pmatrix} = \frac{1}{{k_0}^2 - {k_\parallel}^2} \begin{pmatrix} -i\omega & ik_\parallel \\ -ik_\parallel & i\omega/c^2 \end{pmatrix} \begin{pmatrix} -ik_y B_z \\ dE_z/dx \end{pmatrix} \tag{13b}$$

$$\frac{d^2}{dx^2} \begin{pmatrix} E_z \\ B_z \end{pmatrix} = \left({k_y}^2 + {k_\parallel}^2 - {k_0}^2\right) \begin{pmatrix} E_z \\ B_z \end{pmatrix} \tag{14}$$

From this it can be seen that the problem can be solved independently for E_z and B_z. The TM part of the field, which has a longitudinal (along z) $\vec{E}$ component does not couple to the plasma waves because $E_z = 0$ in the plasma (see section II). Therefore, for the simplified problem considered here, we can retain the TE mode alone and ignore the field components deriving from E_z.The solution for the two vacuum regions is elementary:

$$\text{Region I:} \quad B_z = A_I \cosh k_\parallel x + B_I \sinh k_\parallel x \tag{15a}$$

$$\text{Region II:} \quad B_z = A_{II} \cosh k_\parallel x + B_{II} \sinh k_\parallel x \tag{15b}$$

where the A's and the B's are constants to be determined by the following boundary conditions:

- At the metallic wall $x = -d$: $E_y = 0$ (16a)
- The antenna is represented by an infinitely thin current sheet of finite width w and infinite length. This gives rise to a jump condition on the tangential magnetic field: $[[B_z]]_0 = -\mu_0 j_y$ (16b)
- and a continuity condition $[[E_y]]_0 = 0$ (16c)
- At the plasma surface, $x = 0$: $[[Z_s]]_a = 0$ (16d)

These conditions are sufficient to determine the 4 constants in (15a) and (15b). In particular, this gives the relation between all field components and their source, the current density at the antenna j_y [10].

There is one additional condition, the continuity of E_y (or B_z) at $x = a$ that was not necessary to solve the vacuum problem. It can be used to determine C_{III} in Eq. (8) as all field quantities in the vacuum region are now known.

C.4 Poynting's theorem and antenna radiation

Let us consider in the vacuum region I-II an arbitrary volume containing the antenna. Starting from Maxwell's equations, one can easily write down Poynting's theorem [11] from which we get the complex radiated power in region II for an antenna current $\vec{j_A}$:

$$P = -\frac{1}{2} \int_V \vec{E} \cdot \vec{j_A} dV \tag{17}$$

On the r.h.s. appears the work done by the electric field on the antenna current. Strictly speaking, it should be zero because the antenna is a metallic conductor on which the tangential electric field should vanish. It is non-zero because the current distribution on the antenna has been *assumed* rather than self-consistently computed. This is known as the *induced e.m.f. method*. Though it may appear rough, this method usually gives good results if the assumed current is a reasonable guess of the exact one. In more sophisticated computations [12], the current distribution on the antenna is self-consistently determined.
A theory completely similar to the above one can be done for waveguide [12] or aperture launchers. In these cases, the incoming wave field distribution on the aperture is given and the field reflected by the plasma and surrounding structures is the result of the computation. Alternatively, the above formalism can be applied without changes if the aperture boundary condition is expressed as an equivalent current density [13].
It is to be observed that the quantity on the r.h.s. of Eq.(17) has both a real and an imaginary part. The real part is the power radiated by the antenna, while the imaginary part is related to the reactive properties of the antenna, as we will see. We can compute the former for our simplified model. First

we rewrite Poyntings theorem (17) in terms of the $k_\parallel$ field spectrum using Parseval's relation:

$$P = -\frac{1}{2}\int_V E_y j_y{}^* dV = -\frac{1}{4\pi}\int_{-\infty}^{\infty} E_y(k_\parallel) j_y(k_\parallel) dk_\parallel \tag{18}$$

The Fourier spectrum of the electric field $E_y(k_\parallel)$ is evaluated in region II, in front of the strap ($x = 0$) and is given by:

$$E_y(k_\parallel) = \omega\mu_0(g_2 - ih_2) j_y(k_\parallel) \tag{19a}$$

with

$$g_2 - ih_2 = \frac{i\sinh k_\parallel d}{k_\parallel}\frac{\sinh k_\parallel a - iZ_S\cosh k_\parallel a}{\sinh k_\parallel(a+d) - iZ_S\cosh k_\parallel(a+d)} \tag{19b}$$

The antenna radiation spectrum can be obtained from the Poynting theorem and taking the real part of it

$$\Re(P) = -\frac{\omega\mu_0}{4\pi}\int_V g_2 \left|j_y\right|^2 dk_\parallel \tag{20}$$

If we take the limit $d \to \infty$

$$\Re(P) \sim -\frac{\omega\mu_0}{4\pi}\int_V \frac{k_\perp}{{k_\perp}^2 + {k_\parallel}^2} e^{-2|k_\parallel|a} \left|j_y\right|^2 dk_\parallel \tag{21}$$

This expression highlights one of the fundamental challenges of low frequency wave heating, namely the fact that ingoing waves undergo a strong *evanescence* in the vacuum layer between the antenna and the plasma and are furthermore confronted on their path to the plasma bulk with brutal *refractive index change*, leading to a strong reflection at plasma vacuum interface. The $k_\parallel$ spectrum of a given launcher is mostly determined by the geometry of the launcher. For a simple radiating strap of width w it is given by $k_\parallel \sim \pi/w$. Therefore the radiated power will decay as $\exp(-2\pi a/w)$. This provides a simple rule to estimate the evanescence of the field launched by the antenna in vacuum. If the launcher is made of an array of identical elements spaced by $L_z < w$ in the toroidal direction and excited with a phase difference $\Delta\Phi$, then the typical parallel wave vector must be taken as $k_\parallel a = \Delta\Phi/L_z$. Evanescence will then be stronger than in the previous case of an unphased structure. One could think that working with an antenna spectrum peaking at $k_\parallel = 0$ (monopole phasing) could solve this problem. Actually realistic plasma surface spectra displays large contributions occurring for $k_\parallel < k_0$, but they are due to coaxial & surface modes [14]. The coaxial modes correspond to TEM/z or TE/z electromagnetic waves propagating between the tokamak wall and the plasma column, which plays the role of a lossy metal wall. These modes lead to power deposition in the SOL and wall region.

C.5 Antenna coupling properties

As mentioned above the structure of the antenna modelled in the present exercise is basically that of a strip-line, i.e. a conductor running above an infinite conducting plane. The field in such a strip line is known to have a TEM (transverse electro-magnetic) structure, like a coaxial transmission line. A TEM field has the property that the electric and magnetic field structure in the transmission line cross-section is the same as that respectively of the electrostatic and magnetostatic field it can sustain. Therefore, the antenna properties can be computed in the electrostatic and magnetostatic limits and used as in transmission line theory. We shall recast the results obtained above in terms of strip line characteristics. This formalism is often used in practice to represent properties of real ICRF antennas, which structure is indeed close to that of strip lines. The radiation impedance Z_A of the antenna can be obtained by equating the power flow to the same expression for a transmission line:

$$-\frac{1}{2}\int_V \vec{E}\cdot\vec{j_A} dV = \frac{1}{2}(R + iX) I^2 \tag{22}$$

where I is the total current flowing on the antenna, R and $X = -\omega L$ being respectively the specific input resistance and reactance of the line, and L being the specific inductance. From the spectral form of Poynting's theorem (17) we obtain:

$$\frac{1}{2}(R - i\omega L) I^2 = -\frac{1}{4\pi}\int_{-\infty}^{\infty} E_y(k_\parallel) j_A(k_\parallel) dk_\parallel \tag{23}$$

The previous equality constitutes the definition of the two quantities R and L in the present antenna model. The plasma enters their definition only through the functions g_2 and h_2 (19b). No equivalent capacitance C appears in Eq.(23) because we have dropped the TM part of the field. It can however easily be obtained by solving the TM vacuum field equations with the boundary condition $E_y = 0$ at the plasma $x = 0$. The three constants R, L, C completely determine the properties of the transmission-line equivalent to the antenna [15, 10] and are of primary interest for the design of the transmission and matching system [4].

C.6 Radiated field

Using the additional boundary condition at the plasma-vacuum interface, i.e. continuity of E_y, the field in the plasma can also be computed and used to determine the properties of the radiated far field [16]. In Fig. 4, the far field Poynting flux distribution over constant phase surfaces is shown for a phased antenna array in an ITER-like plasma. As the Poynting flux is the RF power flux, this shows how phasing, by sending the power at different parallel wave numbers sends it in different spatial directions as well.

C.7 State of the art

The theory presented in the previous sections is as we said simple: it neglects feeders, poloidal antenna

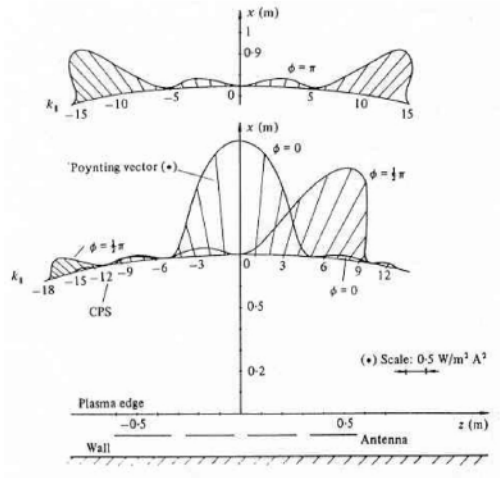

Figure 4: Distribution of the Poynting vector in the far-field region for three different phase differences Φ between successive straps of a 4-strap antenna array. From [16].

inhomogeneity and plasma density profile. These limitations were assessed in [10, 17] notably, and it appears that such a simple model can fairly reproduce most of the coupling properties of more realistic antenna models. Nevertheless the rigorous self-consistent solution of the full boundary-values problem is a formidable task that can only be tackled with numerical codes. A review of the early development of sophisticated coupling codes can be found in the review [18]. More recently in the 3D code TOPICA [13] detailed current distributions are now computed over all antenna parts for imported CAD geometries. The fast ANTITER II code [19] computes the Fourier expanded field distribution in front of of the antenna box, while an expansion in orthogonal modes is computed inside the antenna box. In a similar way to what was presented in section III-C, the continuity of the tangential fields at the interface between these media, called the "aperture" is imposed and the expansions are matched to give the full solution. Unlike TOPICA which requires substantial computer resources, ANTITER II runs on a home computer and provides results in a few minutes. In parallel to the development of these plasma coupling codes, sophisticated commercial codes have been used to compute and optimise the reactive properties of antennas in vacuum or in the presence of a dielectric [20, 21, 22]. In this process, it was shown that an adequately chosen dielectric can to some extent simulate coupling to a plasma [20]. Antenna models in the ICRF have been compared with success to experimental results in a number of cases [23, 24, 25, 26] and are used to predict the performance of ITER antennas [21, 22, 27].

D. The coupling/heating challenge

The previous results have notably underlined the evanescence of the vacuum wave which increases with increasing $k_{\|}$. On the other hand there is a large evidence that the heating efficiency (or absortivity) in the plasma increases when the dominant $k_{\|}$ in the antenna radiation spectrum increases. This latter effect was notably observed on TEXTOR [28] and JET [29]. A summary of experimental results with JET A2 heating scenarios can be seen on figure 5 where the opposite trends of heating efficiency and coupling as a function of the dominant $k_{\|}$ are clearly visible. A detailed explanation of the almost linear variation of the efficiency with the dominant $k_{\|}$ is beyond the scope of this lecture. Nevertheless it must be taken into account when antennas arrays are designed and phasing operations are being considered: the overall performance of an antenna system depends on a compromise to produce waves with low $k_{\|}$ to ensure good coupling, but also high $k_{\|}$ to ensure good ICRF heating.

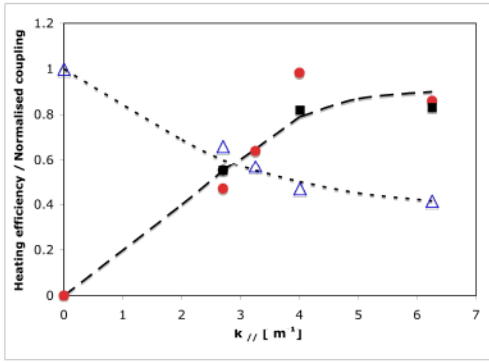

Figure 5: Heating efficiency and coupling from JET's A2 antennas as a function of dominant $k_{\|}$. From [30].

IV. RECENT EXPERIMENTAL RESULTS

The interaction between ICRF waves and the edge of the plasma is a complex domain: we know that the edge plasma profile and in particular the location of the cut-off density layer directly determines the evanescence width and then the coupling efficiency. But many other processes can occur where the heating itself influences the profile. This is beyond the scope of the present note, but the interested reader will find a detailed review in [31].

Impurity production during ICRH has been correlated with an increase of plasma-wall interactions in situations of low coupling and absorption of the RF waves. In [28] it was notably demonstrated that passing from monopole phasing to π phasing operation of

the two-strap antenna in TEXTOR could decrease the impurity production, and this was attributed to the optimisation of the absorption expected in dipole phasing. In a more recent work [29] the level of impurities (Ni) was monitored during ICRF discharges in JET, showing a direct correlation between the level of RF power launched with the A2 antennas. By varying the relative phasing of the straps the fraction of Ni produced could be significantly reduced for $0\pi\pi0$ phasing, giving a dominant $k_{\|} \simeq 4\text{m}^{-1}$. The formation of RF-enhanced sheath is the mechanism being currently considered as the main responsible for the production of impurities during ICRH. The higher level of parallel electric fields in the SOL during lower coupling situations and the corresponding increase of sputtered impurities from the plasma facing components is in agreement with the experimental observations.

Recent experiments performed at JET also demonstrated the importance of localized plasma gas injection in order to optimize plasma coupling [32, 33]. The increase of the density in front of the antenna is shown to move the location of the cut-off density closer to the launcher and therefore to directly reduce the width of the evanescence region.

V. THE CONCEPT OF TRAVELLING WAVE ANTENNA FOR ICRH

Typical antenna systems in modern machines where high power densities are required are plugged-in systems inserted in specific ports in the main metallic vessel. This strongly limit the design flexibility, and then limits the selectivity of the wave number spectrum. For a machine like DEMO where the plasma conditions are such that a low coupling is expected, antenna optimisation is needed more than ever. The concept of a travelling wave antenna brings an elegant method to maximise the radiated power, while providing good directivity and load resilience.

If we assume that the space available for the antenna is not a limitation, let us consider number n_s of infinitely thin straps equally spaced by a distance S_z (see Figure 6). If the current amplitude on each strap is I_A and the phase difference between two consecutive straps is $\Delta\Phi$, the Fourier spectrum of the total current density is given by

$$J_y = n_s I_A \sum_p \sin(\xi_p)/\xi_p \tag{24a}$$

with

$$\xi_p = 0.5 n_s S_z \left[k_{\|} - (\Delta\Phi - p2\pi)/S_z\right]. \tag{24b}$$

Due to the strong decrease effect of the resistive part of the spectrum for increasing $k_{\|}$, only the first peak at $k_{\|0} = \Delta\Phi/S_z$ will contribute to the radiated power. Consequently, a specific central $k_{\|0}$ can

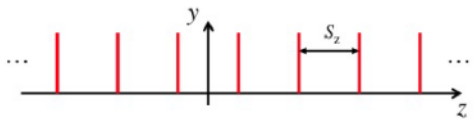

Figure 6: Array of straps with spacing S_z, from [34]

be selected by carefully choosing the phase difference $\Delta\Phi$. Also, by integrating the current spectrum in the whole $k_{\|}$ domain, we have

$$P_{rad} \sim n_s/S_z. \tag{25}$$

This scaling is confirmed by more realistic computations with ANTITER II [34] where the finite strap width is taken into account, and demonstrates that increasing the number of straps allows to linearly increase the radiated power.

In practice the total control on the radiated spectrum would require to individually feed each strap, which could pose technical issues (intrusions in the reactor vessel). Therefore practical solutions must be found:

1. *Travelling wave along a resonant strap array* [34]: an array of short-circuited straps tuned by an external capacitor at a given frequency f_0 is considered. Only the first strap is fed by the generator (input power P_{in}), and the currents propagate from strap to strap by mutual coupling. Each strap n individually radiates a power $P_n = P_1 \exp -2n\alpha$ into the plasma, where α is the imaginary part of the phase difference $\Delta\Phi$. The power leaving the array is then $P_{out} = P_{in} - \Sigma_n P_n$, and is negligible when the loading resistance is sufficiently large. The last strap can be terminated by a dummy load with a characteristic impedance equal to the so-called "iterative impedance" of the array [35], which makes the system load-resilient.

2. *360° configuration with periodic feeding* [36]: a continuous distributed array all around the machine fed by periodically placed generators.

3. *Resonant rings in 360° configuration* [34, 36]: multiple resonant arrays are mounted in a resonant ring.

The latter solution provides the most advantages: best selective excitation spectrum, load resilience, and simplicity. The concept needs to be tested experimentally in a fusion-relevant environment, and, at the time of writing the present text, implementation in the WEST tokamak is being discussed. An ICRH system based on travelling waves antenna for DEMO is proposed and analysed in [37]: modeling shows that the system can couple 50 MW with voltages up to 25-30 kV, for an unfavourable low density profile. This

design will require an iterative procedure to align the RF performance with the thermo-mechanical requirements of the blanket where the antenna is located.

REFERENCES

1. E. Lerche, "Ion cyclotron, lower hybrid and Alfvén wave heating", *These Proc.*
2. D. Van Eester & E. Lerche, "Kinetic Theory of Plasma Waves", *These Proc.*
3. D. Van Eester, "Fast Particle Heating (NBI) & Modelling particle heating and current drive in tokamaks", *These Proc.*
4. P. Dumortier, "Antenna Design and Matching Issues", *These Proc.*
5. Y. Kazakov, "Heating the Plasma", *These Proc.*
6. T.H. Stix, "Waves in plasmas", AIP New York (1992).
7. D.G. Swanson, "Plasmas Waves", American Institute of Physics (1989).
8. E. Westerhof, "Electron Cyclotron Resonance Heating", *These Proc.*
9. A. Messiaen & R. Weynants, "ICRH antenna coupling physics and optimum plasma edge density profile. Application to ITER", *Plasma Phys. Contr. Fus.* **53** (2010) 085020
10. A. M. Messiaen *et al.*, "Theoretical aspects of the coupling properties of ICRH antennae", in "Heating in toroidal plasmas", Commission of the European Communities, Vol. I (1982), 243
11. J.D. Jackson, "Classical Electrodynamics" 2nd Ed., J. Wiley & Sons (1975)
12. R. Koch, "A global solution of the ICRH problem based on the combined use of a planar coupling model and hot-plasma ray-tracing in tokamak geometry", *Computer Phys. Comm.*, **40** (1986), 1
13. V. Lancellotti *et al*, "TOPICA: an accurate and efficient numerical tool for analysis and design of ICRH antennas", *Nucl. Fusion* **46** (2006), S476
14. A. M. Messiaen *et al.*, "Analysis of the plasma edge radiation by ICRH antenna", Proc. 4th International Symp. on Heating in Toroidal Plasmas, Vol. I (1984), 315
15. R.R. Weynants *et al.*, "ICRH antenna design and coupling optimisation studies", in "Heating in toroidal plasmas", Commission of the European Communities, Vol. I (1980), 487
16. R. Koch *et al.*, "An asymptotic analysis of the radiation pattern of ion cyclotron resonance heating antennas", *J. Plasma Phys.* **32** (1984), 291
17. V.P. Bhatnagar *et al.*, "A 3-D Analysis of the Coupling Characteristics of ICRH Antennae", *Nucl. Fusion* **22** (1982) 280
18. R. Koch *et al.*,"Progress in RF Theory: a sketch of recent evolution in selected areas", *J. Plasma Phys.* **40** (1998), A141
19. A. Messiaen *et al.*, "Performance of the ITER ICRH system as expected from TOPICA and ANTITER II modelling", *Nucl. Fusion* **50** (2010), 025026
20. P. Lamalle *et al.*, "Recent developments in ICRF antenna modelling ", *Nucl. Fusion*, **46** (2006), 432-443
21. F. Louche *et al.*, "Eigenmode analysis of the ITER ICRF antenna plug and electrical solution to the grounding of the antenna", *Nucl. Fusion* **49** (2009) 065025
22. F. Louche *et al.*, "3D electromagnetic optimization of the front face of the ITER ICRF antenna", *Nucl. Fusion* **51** (2011), 103002
23. R. Koch *et al.*, "A Comparison Between ICRF Theory and Experiment", *Plasma Phys. Contr. Fus.*, **30** (1988), 1559
24. P. Descamps *et al.*, "Global Modes Excitation in TEXTOR and Comparison with Theory", *Plasma Phys. Contr. Fus.*, **33** (1991), 1109
25. M.D. Carter *et al.*, "Three Dimensional Modelling of ICRF Launchers for Fusion Devices", *Nucl. Fusion* **36** (1996), 209
26. D. Milanesio *et al.*, "Analysis of the Tore Supra ICRF antenna in TOPICA RF antenna code", *Plasma Phys. Contr. Fus.*, **39** (2009), 405-419
27. D. Milanesio & R. Maggiora, "ITER ICRF antenna analysis and optimisation using the TOPICA code", *Nucl. Fusion* **50** (2010), 025007
28. A. Messiaen *et al.*, "Effect of Antenna Phasing and Wall Conditioning on ICRH in TEXTOR", *Plasma Phys. Control. Fusion*, **31**, 921-939 (1989)
29. A. Czarnecka *et al.*, "Impurity production from the ion cyclotron resonance heating antennas in JET", Plasma Phys. Control. Fusion **54**(2012) 074013 (13pp)
30. R. R. Weynants, "ICRF Review: from ERASMUS to ITER", *Radio Frequency Power in Plasmas*, AIP Conference Proceedings **1187** 3 (2009)

31. J-M Noterdaeme & G. Van Oost, "The interaction between waves in the ion cyclotron range of frequencies and the plasma boundary", *Plasma Phys. and Control. Fusion* **35** (1993) 1481-1511

32. E. Lerche *et al.*, "Impact of localized gas injection on ICRF coupling and SOL parameters in JET-ILW H-mode plasmas", *J. Nucl. Mater.* **463** (2015) 634-639

33. P. Jacquet *et al.* "Maximisation of ICRF power by SOL density tailoring with local gas injection", *Nucl. Fusion* **56** (2016) 046001 (14pp)

34. R. Ragona & A. Messiaen, "Conceptual study of an ICRH travelling-wave antenna system for low coupling conditions as expected in DEMO", *Nucl. Fusion* **56** (2016) 076009 (18pp)

35. A. Messiaen & R. Ragona, "Modeling of the Travelling Wave Antenna in view of the ICRF heating of DEMO", *EPJ Web of Conferences* **157**, 03033 (2017)

36. R. Ragona & A. Messiaen, "Study of a distributed ICRF antenna system in DEMO", *EPJ Web of Conferences* **157**, 03044 (2017)

37. R. Ragona *et al.*, "A travelling wave array system as solution for the ion cyclotron resonance frequencies heating of DEMO", *Nucl. Fusion* **60** (2020), 016027

THE ION CYCLOTRON, LOWER HYBRID AND ALFVEN WAVE HEATING METHODS

R. Koch, E. Lerche, D. Van Eester

Laboratory for Plasma Physics
Ecole Royale Militaire - Koninklijke Militaire School
B-1000 Brussels, Belgium

ABSTRACT

This lecture covers the practical features and experimental results of the three heating methods. The emphasis is on ion cyclotron heating. First, we briefly come back to the main non-collisional heating mechanisms and to the particular features of the quasilinear coefficient in the ion cyclotron range of frequencies (ICRF). The specific case of the ion-ion hybrid resonance is treated, as well as the polarisation issue and minority heating scheme. The various ICRF scenarios are reviewed. The experimental applications of ion cyclotron resonance heating (ICRH) systems are outlined. Then, the lower hybrid and Alfvén wave heating and current drive experimental results are covered more briefly. Where applicable, the prospects for ITER are commented.

I. ION CYCLOTRON HEATING

I.A. Introduction

Before going in further details of heating mechanisms, it is important to recapitulate the order of magnitude of the different quantities characterising the plasma and the RF. A table of plasma parameters (Table 1), typical of moderate plasma performance in a machine like JET, was given earlier[1]. Two important parameters that characterise the collisionality of the plasma are to be added to complete the picture: the ion an electron collision frequencies: $\nu_e \approx 10$kHz, $\nu_i \approx 100$Hz. A JET-type machine is characterised by the following parameters:
$R_0 = 3$m, $2\pi R_0 \approx 20$m; $a_p = 1.5$m, $2\pi a_p = 10$m.
In the light of these numbers, one sees that the time for a cyclotron gyration is extremely short: 10ps for an electron, 40ns for an ion. During this single gyration, the electron travels 0.4mm in the toroidal direction and the ion 2cm. It takes 1μs to an electron to complete a toroidal turn around the machine, 40μs to an ion. During this turn, an electron has performed 50,000 cyclotron gyrations, an ion 1,000. This means that gyro motion is an extremely fast process as compared to transit times across any macroscopic area. Equivalently, the gyro radii of electrons (0.05mm) and of ions (3mm) are small as compared to plasma size. The plasma is nearly non-collisional: the electron mean free path is 3km and the ion one 5km, or, respectively, 150 and 250 toroidal revolutions.

The following parameters are typical of an ICRF system:

- frequency: f ≈ 10-100 MHz
- Power: 2 MW/antenna strap
- Voltage: 10-50 kV at the antenna
- Antenna current: $I_A \approx$ 1 kA
- Central conductor: width ≈ 0.2m, length ≈ 1m, distance to the plasma 5cm, to the wall 20cm
- Typical RF electric field: 20kV/m
- Typical RF magnetic induction: 10^{-3}T

ICRF antennas are quite often built as boxes enclosing one or several *central conductors* to whom the high voltage is applied. Such a central conductor is also called a *strap*. The maximum voltage that could be applied to an antenna operating in a tokamak, in the presence of plasma, lies around 45kV. The ratio of voltage to current and the power coupling capability of an antenna are determined by the geometry of the antenna and the plasma edge properties[1]. The electric field at the antenna is easily evaluated by dividing the input voltage by the antenna length. This is valid for the field component polarised along the antenna; other field components can be much higher in the vicinity of the antenna feeding point. Except for possible focusing effects, the field inside the plasma is lower than at the antenna, because $k_\perp |E|^2$ is nearly constant and $k_\perp$ is roughly proportional to $\sqrt{n}$. The typical RF magnetic field is easily computed using ampere's law: $2\pi dH = I_A$ where d is typical of the distance over which the magnetic field can spread. These electrostatic- and magnetostatic-type estimates have a meaning due to the fact that the vacuum wavelength is large as compared to the antenna dimensions:
$\lambda_0 = c/f \approx 10$ m (30 MHz).

I.B. Linearity

These numbers show that the RF causes only a small perturbation of the particle trajectory. First, the RF magnetic field is much smaller than the static one:
$B_{RF} \approx 10^{-3}$ T « $B_0 \approx 3$ T.
Second, the RF electric field ≈ 20 kV/m is also much smaller than the v×B field associated with the ion's (and even more electron's) thermal motion: $V_{ti} \times B_0 \approx 1.5$MV/m.
Third, we shall show below that the perturbation of the parallel motion is also small. Let us write the equation of motion of a particle in the RF field, decomposing the motion into an unperturbed (thermal) part labelled 0 and a perturbed part: $\mathbf{v} \rightarrow \mathbf{v}_0 + \mathbf{v}$

$$m\left(\frac{d\mathbf{v}_0}{dt} + \frac{d\mathbf{v}}{dt}\right) = Ze(\mathbf{E} + \mathbf{v}_0 \times \mathbf{B}_0 + \mathbf{v}_0 \times \mathbf{B} + \mathbf{v} \times \mathbf{B}_0 + \mathbf{v} \times \mathbf{B}) \quad (1)$$

Subtracting the unperturbed part of this equation

$$m\frac{d\mathbf{v}_0}{dt} = Ze\,\mathbf{v}_0 \times \mathbf{B}_0 \quad (2)$$

which describes the unperturbed cyclotron motion leaves us with the perturbed part of the equation of motion.

$$m\frac{d\mathbf{v}}{dt} = Ze(\mathbf{E} + \mathbf{v}_0 \times \mathbf{B} + \mathbf{v} \times \mathbf{B}_0 + \mathbf{v} \times \mathbf{B}) \quad (3)$$

In the r.h.s parenthesis the last term is clearly negligible as compared to the 3rd one. We thus arrive at the following equation, which is linear in the perturbed field amplitude:

$$m\frac{d\mathbf{v}}{dt} = Ze(\mathbf{E} + \mathbf{v}_0 \times \mathbf{B} + \mathbf{v} \times \mathbf{B}_0) \quad (4)$$

Finally, we can estimate the correction to the parallel uniform motion due to the RF field. Taking the parallel component of Eq.(3) and $d/dt \approx \omega_{ci}$, we get for an ion

$$m\,\omega_c v_{//} = Ze[E_{//} + (\mathbf{v}_0 \times \mathbf{B})_{//}] \quad (5)$$

or, in order of magnitude

$$v_{//} \approx \left|\frac{E_{//}}{B_0}\right| \quad \text{or} \quad \approx V_{ti}\left|\frac{B_{RF}}{B_0}\right| \quad (6)$$

Thus, in any case the RF-induced particle quiver velocity is small as compared to the thermal (unperturbed) ion velocity. In summary, the corrections to the particle's trajectory due to the RF field are indeed small, and the linearisation is justified.

Although Eq.(4) is linear in the fields, it is not at all linear for the unknowns **r** and **v**. Indeed, the electric field depends non-linearly on the particle position **r**. However, we have seen that the RF fields only cause small perturbations to the particle trajectories. Therefore, we can neglect these small deviations in the evaluation of the electromagnetic field at the particle location and write

$$\mathbf{E}(\mathbf{r}) \approx \mathbf{E}(\mathbf{r}_0); \quad \mathbf{B}(\mathbf{r}) \approx \mathbf{B}(\mathbf{r}_0) \quad (7)$$

with $d\mathbf{r}_0/dt = \mathbf{v}_0$ and $\mathbf{v}_0$ is the solution of the unperturbed equation of motion Eq.(2). Then the equation determining the velocity perturbation is

$$m\frac{d\mathbf{v}}{dt} = Ze[\mathbf{v} \times \mathbf{B}_0 + \mathbf{E}(\mathbf{r}_0) + \mathbf{v}_0 \times \mathbf{B}(\mathbf{r}_0)] \quad (8)$$

This is now a linear equation that can be solved explicitly if the unpertubed trajectories ($\mathbf{r}_0$, $\mathbf{v}_0$) are known explicitly. The next step in the solution of the problem is to decompose the zero-th order motion into a guiding centre motion $\mathbf{r}_G$ and a gyromotion $\boldsymbol{\rho}$:

$$\mathbf{r}_0 = \mathbf{r}_G + \boldsymbol{\rho} \quad (9)$$

and to expand around the guiding centre motion:

$$\mathbf{E}(\mathbf{r}_0) = \sum_{n=0}^{\infty} \frac{\left[(\boldsymbol{\rho}.\nabla)^n \mathbf{E}\right]_{\mathbf{r}_0 - \mathbf{r}_G}}{n!} \quad (10)$$

This procedure is known as the *small Larmor radius expansion*. In general geometry this development can become quite heavy[2], but in straight geometry, it can be performed explicitly. In the latter case (uniform plasma), the decomposition of the motion, Eq.(9) is exact and the expansion Eq.(10) can be expressed in terms of Bessel functions, see Eq.(13, 16) of ref.[3]. Like in the case of Landau damping[1], the explicit integration of the linearised equation of motion Eq.(8) can, in some cases, lead to secular solutions, corresponding to resonant denominators in Fourier space[4]. The same denominators are found back under the velocity integral in the expression of the full hot conductivity tensor[3], leading to the general resonance condition

$$\omega - n\omega_c - k_{//}v_{//} = 0; \quad n = 0, \pm 1, \pm 2, \ldots \quad (11)$$

I.C. The cyclotron absorption mechanisms

I.C.1 Resonances due to non-rotating fields

If we look at the n=0 contribution to the conductivity tensor Eq.(20) in ref.[3], we see that only the lower right 2×2 part of the S_n matrix is non-zero. For a uniform electric field ($k_\perp \mathbf{E} = \partial\mathbf{E}/\partial x = 0$), only the zz term survives. It correspond to resonant parallel acceleration by the parallel electric field, i.e. to Landau damping. The three other terms require, at least, a gradient of the electric field ($\partial\mathbf{E}/\partial x \neq 0$). By computing the expression $\mathbf{E}^*.\boldsymbol{\sigma}.\mathbf{E}$, (proportional to the absorbed wave power) for the case where only E_y is present, it is easy to see that this quantity is proportional to $(k_\perp E_y)^2 = (\omega B_z)^2$
If we assume E_y to be linear, we thus have a case of acceleration by a uniform B_z field propagating in the z direction with $\omega = k_{//}v_{//}$. We have seen[1] that the resonance mechanism in this case is *transit time magnetic pumping* (TTMP). More detail about this and about the interplay between Landau damping and TTMP in the case both E_y and E_z differ from zero, can be found in the book of Stix[5].

Landau damping and TTMP are not important mechanisms for the ions in the ICRF because $k_{//}V_{th}$ is usually much smaller than $\omega \approx \omega_{ci}$, as can be seen from Table 1 and $k_{//}$ estimates[1]. For the electrons, on the

contrary, they are the only damping mechanisms in this frequency range. As they correspond to parallel acceleration, they are of primary importance for the fast wave *current drive* applications.

I.C.2. Resonances due to the left-handed component of the field.

This is the case where the wave has the same handedness as the ions and the resonances correspond to $n>0$ in Eq.(11). If $n=1$, we have the case of the fundamental cyclotron resonance, which was discussed already[1]:

$$\omega = \omega_c + k_{//} v_{//} \qquad (12)$$

Because the Doppler shift $k_{//}v_{//}$ is small, this requires that the operating frequency be rather close to the ion cyclotron frequency. Looking at the expression of S_n in ref.[3], we see that such a resonance can be caused by a uniform field ($k_\perp \mathbf{E}=\partial \mathbf{E}/\partial x=0$). On the contrary, for second harmonic damping ($n=2$) to exist, the same expression shows that a gradient of the electric field is required. Similarly, higher harmonic damping requires the existence of non-vanishing higher derivatives of the electric field.

While it is easy to imagine how the fundamental cyclotron resonance works, it is much harder to visualise the reason why a particle rotating at the frequency ω_c can resonate with a wave that is rotating at twice this frequency! In order to understand how this happens it is useful to come back first to the fundamental resonance and look at the simpler situation where the wave propagates (or is non-uniform) in the x-direction while the E-field is polarised in the y-direction. The principle is shown on top of Fig.1. The particle travels from left to right and at the initial moment $t=0$, I assume that the electric force is in phase with the particle velocity. After a quarter period, if the field oscillates at the cyclotron frequency, $\omega=\omega_c$, the field is zero, after half a period it is negative, etc. Therefore, either the force is in phase with the particle motion, or it is zero and over one cyclotron period, the particle experiences a net acceleration in the direction of its motion. If, with the same uniform field distribution, the field varies at twice the cyclotron frequency $\omega=2\omega_c$, after a quarter period, it has changed sign, points in the negative y direction and is perpendicular to the particle's velocity. After half a cyclotron period, its phase has varied of 2π, it is again positive, points out of the paper in the direction opposite to the particle's velocity and so on. Hence, over a cyclotron period, the average force exerted on the particle is zero, there is no net acceleration and no resonance. However, if the field varies linearly in space, as shown on the bottom of Fig.1, at the same time as it alternates sign, the particle moves from one side of the gradient to the other, therefore keeping in phase with the electric force and experiencing a net acceleration over one period, as shown.

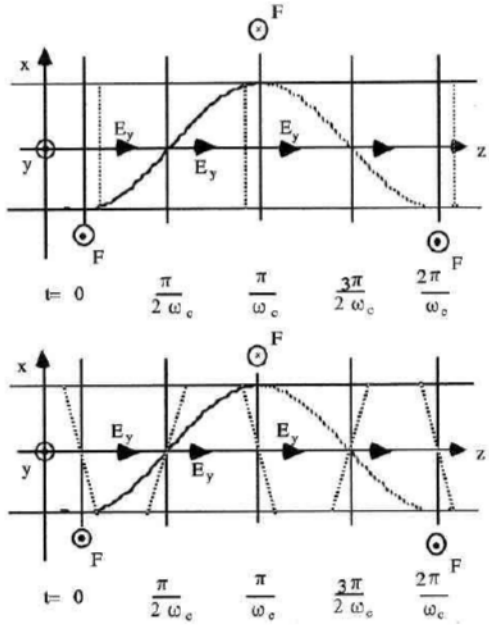

Fig. 1. Mechanism of the fundamental (top) and second harmonic (bottom) resonance. The ion moves in the z-direction and the projection of its helical motion on the (x,z) plane is shown: solid line, above the plane; dotted line, below. The electric field distribution along x is shown at quarter periods of the cyclotron frequency. The direction of the electric force F at the particle's position is also indicated.

It is therefore the interplay between the field periodicity and the sampling of the field non-uniformity by the particle that allows resonance at the cyclotron harmonics.

I.C.3. Resonances due to the right-handed component of the field.

This type of resonance, corresponding to $n<0$, is somewhat counter-intuitive as the field rotates in the direction opposite to the particle. However the resonance condition shows that, in order to come into resonance, the particle must have a very large velocity:

$$v_{//} = \frac{\omega + |n|\omega_c}{k_{//}} >> V_{ti} \qquad (13)$$

One can then understand the resonance process as follows. Let us start with a particle with zero parallel velocity and a right-hand polarised field at frequency ω slightly larger than ω_{ci} and positive phase velocity $\omega/k_{//}>0$. The particle sees the field rotating slightly faster than itself, in the opposite direction. Then if the particle starts to move at a speed $v_{//}>0$, in the reference frame moving at the same

velocity, the field is now rotating at the slightly lower frequency $\omega'=\omega-k_{//}v_{//}$. If $v_{//}$ is large enough, this frequency may equal ω_{ci} but the ion and the field are rotating in opposite directions. Then, if the particle's velocity becomes much larger, the field may become stationary $\omega-k_{//}v_{//}=0$: the particle is gyrating in a stationary field. This cannot give rise to a resonance. If $v_{//}$ is still increased, $\omega-k_{//}v_{//}<0$ and the wave field will start to rotate in the left-handed direction. Still increasing the particle's velocity, we can come to the situation where $\omega-k_{//}v_{//}=-\omega_{ci}$ which means that the field is left-hand polarised and rotating at the cyclotron frequency, thereby causing resonant acceleration. This absorption mechanism is generally negligible for particles belonging to the thermal population in the plasma. However, for the much faster particles belonging to a high-energy tail, either created by the RF itself, or by NBI or for α-particles, this mechanism may not be negligible at all. Even more so, as we shall see, as the right-hand field component tends to dominate in the fast wave, in the vicinity of resonances.

I.C.4. Quasilinear diffusion coefficient

Ion cyclotron heating tends to create high-energy tails in the distribution function of the heated particles. For heating at the n-th cyclotron harmonic, the diffusion coefficient is of the form:

$$D \propto \left|J_{n-1}E_+ + J_{n+1}E_-\right|^2 \approx \left|J_{n-1}\left(\frac{k_\perp v_\perp}{\omega_c}\right)\right|^2 \left|E_+\right|^2 \qquad (14)$$

where E_+ and E_- are, respectively, the left-hand and right-hand components of the electric field:

$$E_+ = \frac{1}{2}(E_x + iE_y); \quad E_- = \frac{1}{2}(E_x - iE_y) \qquad (15)$$

One notices the presence of a right hand component contribution in the diffusion coefficient. For not too fast particles in the FW field, this contribution is negligible because the argument of the Bessel functions is small. This is not necessarily the case for fast ions. In the case of the thermal population, one can take only the first term of the power series expansion of the Bessel functions, and we get:

- Fundamental: $D \propto K\left|E_+\right|^2$ with K a constant (16.1)
- Second harmonic: $D \propto \left|\frac{k_\perp v_\perp}{\omega_c}\right|^2 \left|E_+\right|^2$ (16.2)
- n-th harmonic: $D \propto \left|\frac{k_\perp v_\perp}{\omega_c}\right|^{2(n-1)} \left|E_+\right|^2$ (16.3)

A first conclusion to be drawn from these expressions is that, as $k_\perp r_L$ is a small quantity, the diffusion coefficient (hence the strength of the heating) strongly decreases with the harmonic number. Second, fundamental heating pushes all particles with the same strength irrespective of their velocity: the diffusion coefficient is independent of velocity. On the contrary, harmonic heating tends to accelerate more the faster particles. A consequence of this last observation is that harmonic heating tends to create tails at higher energy than fundamental heating. In the same vein, harmonic heating tends to interact more with faster particles like beams or alphas.

I.D. The FW dispersion and polarisation

The FW equation was given in section II.C of ref.[1]. We shall now specialise the expressions of the dielectric tensor components[3] to the ICRF where

$$\omega \approx \omega_{ci} \ll \omega_{pi} \ll \omega_{pe}, \omega_{ce}, \qquad (17)$$

We obtain

$$S = 1 - \frac{\omega_{pe}^2}{\omega^2 - \omega_{ce}^2} - \sum_i \frac{\omega_{pi}^2}{\omega^2 - \omega_{ci}^2} \approx - \sum_i \frac{\omega_{pi}^2}{\omega^2 - \omega_{ci}^2} \qquad (18)$$

$$\begin{aligned} D &= \frac{\omega_{ce}}{\omega}\frac{\omega_{pe}^2}{\omega^2 - \omega_{ce}^2} + \sum_i \frac{\omega_{ci}}{\omega}\frac{\omega_{pi}^2}{\omega^2 - \omega_{ci}^2} \\ &\approx \frac{\omega_{pe}^2}{-\omega\omega_{ce}} + \sum_i \frac{\omega_{ci}}{\omega}\frac{\omega_{pi}^2}{\omega^2 - \omega_{ci}^2} = \sum_i \frac{\omega}{\omega_{ci}}\frac{\omega_{pi}^2}{\omega^2 - \omega_{ci}^2} \end{aligned} \qquad (19)$$

The first line of Eq.(12) of ref.[1] gives the relation linking E_x and E_y and can be used to compute the ratio of the left- to right-hand components of the electric field:

$$\left|\frac{E_x + iE_y}{E_x - iE_y}\right| = \left|\frac{D + (S - N_{//}^2)}{D - (S - N_{//}^2)}\right| \qquad (20)$$

Let us now consider the case of a single ion species. Eqs.(18-19) become

$$S \approx - \frac{\omega_{pi}^2}{\omega^2 - \omega_{ci}^2} \; ; \quad D \approx - \frac{\omega}{\omega_{ci}} S \qquad (21)$$

and

$$\left|\frac{E_x + iE_y}{E_x - iE_y}\right| \approx \left|\frac{1 - \frac{\omega}{\omega_{ci}} - N_{//}^2/S}{1 + \frac{\omega}{\omega_{ci}} - N_{//}^2/S}\right| \approx \left|\frac{\omega - \omega_{ci}}{\omega + \omega_{ci}}\right| \qquad (22)$$

The last approximate equality follows from

$$N_{//}^2/S \approx \frac{N_{//}^2(\omega_{ci}^2 - \omega^2)}{\omega_{pi}^2} << 1 \qquad (23)$$

The striking feature of the result Eq.(22) is that, at cyclotron resonance $\omega=\omega_{ci}$, in a plasma with only one ion species i, the left-hand polarised component of the wave vanishes. Thus the cyclotron resonance mechanism cannot work because the resonant wave component is absent! Incidentally, this shows explicitly why there is no singularity of the fast wave propagation at the cyclotron frequency[3]: the resonant wave component is blocked by the resonance and all the power is transferred to the other component. This dramatic result can be avoided by heating a small amount of ions of one species in a plasma with ions of another species. This is called the *minority heating* scenario. Consider, for example a plasma of deuterium with a minority of hydrogen. Then the wave polarisation is

determined by the majority component while the wave frequency is the cyclotron frequency of hydrogen. Inserting $\omega=\omega_{cH}=2\omega_{cD}$ in Eq.(22) yields

$$\left|\frac{E_x+iE_y}{E_x-iE_y}\right| \approx \left|\frac{\omega-\omega_{cD}}{\omega+\omega_{cD}}\right| = \left|\frac{2\omega_{cD}-\omega_{cD}}{2\omega_{cD}+\omega_{cD}}\right| = \frac{1}{3} \qquad (24.1)$$

This is the most widely used minority heating scenario, denoted D-(H) to indicate that a minority of H is heated in a majority D plasma. This concept of heating a given species in a mixture can be extended to other mixtures. For example in a reactor, one can heat D at the fundamental in a D-T mixture. Then, for not too large D concentration, the ratio of polarisations is:

$$\left|\frac{E_x+iE_y}{E_x-iE_y}\right| \approx \left|\frac{\omega_{cD}-\omega_{cT}}{\omega_{cD}+\omega_{cT}}\right| = \frac{1}{5} \qquad (24.2)$$

This explanation has the advantage of simplicity and to some extent gives a good picture of reality. The shrewd reader would however notice by working out himself the complete polarisation expression for a mixture of ions that even in this case the left-handed polarisation vanishes at each cyclotron harmonic! The final explanation can only be obtained by taking hot-plasma (absorption) effects[3] into consideration and noting that in a mixture the wave left-handed component has a significant magnitude over a much wider region around the cyclotron harmonic than in the single-ion case. This is of course particularly evident when only a small minority is considered. This allows non-collisional damping at Doppler-shifted frequencies to remain efficient over a much wider range as compared to the single-ion case.

Another way to avoid the polarisation problem is to work at harmonics of the cyclotron frequency. Then

$$\left|\frac{E_x+iE_y}{E_x-iE_y}\right| \approx \left|\frac{n\omega_{ci}-\omega_{ci}}{n\omega_{ci}+\omega_{ci}}\right| = \frac{n-1}{n+1} \qquad (24.3)$$

however, as we saw in Eq.(16.3), the damping strength strongly decreases with harmonic number.

I.E. The ion-ion hybrid resonance

Let us now consider, like in ref.[3], the case of a 50%-50% mixture of D and T.

$$n_D = n_T = n_e/2 \qquad (25)$$

Then, taking into account the fact that $\omega_{cD}=\omega_{cH}/2$ and $\omega_{cT}=\omega_{cH}/3$, and defining

$$\omega_{pH}=\sqrt{2}\,\omega_{pD}=\sqrt{3}\,\omega_{pT} \qquad (26)$$

we can recast the expressions for S and D, Eq.(18-19) as

$$S=\frac{2\omega_{pH}^2}{\omega_{cH}^2-4\omega^2}+\frac{3\omega_{pH}^2}{\omega_{cH}^2-9\omega^2}=\frac{5\omega_{pH}^2(\omega_{cH}^2-6\omega^2)}{(\omega_{cH}^2-4\omega^2)(\omega_{cH}^2-9\omega^2)} \qquad (26.1)$$

$$D=\frac{\omega}{\omega_{cH}}\left[\frac{4\omega_{pH}^2}{\omega_{cH}^2-4\omega^2}+\frac{9\omega_{pH}^2}{\omega_{cH}^2-9\omega^2}\right] \qquad (26.2)$$

Eq.(26.1) clearly shows that S will vanish -which is the condition of wave resonance for perpendicular propagation[3]- when $\omega_{cH}=\sqrt{6}\omega$. This is the ion-ion hybrid resonance condition for a 50%-50% D-T plasma. One can likewise obtain this resonance condition from the FW wavevector Eq.(14.2) of ref.[1], for the case of purely perpendicular propagation ($k_{//}=0$):

$$k_{\perp FW}^2=k_0^2S-\frac{(k_0^2D)^2}{k_0^2S}=k_0^2\frac{5\omega_{pH}^2}{\omega_{cH}^2}\frac{(\omega_{cH}^2-5.76\omega^2)}{(\omega_{cH}^2-6\omega^2)} \qquad (27)$$

Note that the general ($k_{//}\neq 0$) resonance condition of the FW is

$$k_0^2S-k_{//}^2=0 \qquad (28)$$

and is *not* one of the general resonances $A=0$ discussed in ref.[3]. In fact, it does not exist in the full cold-plasma dispersion relation, where a conversion between the FW and the slow wave (Eq.(62) of ref.[3]) takes place instead of a resonance. The FW resonance Eq.(28) arises because of the neglect of the slow wave.

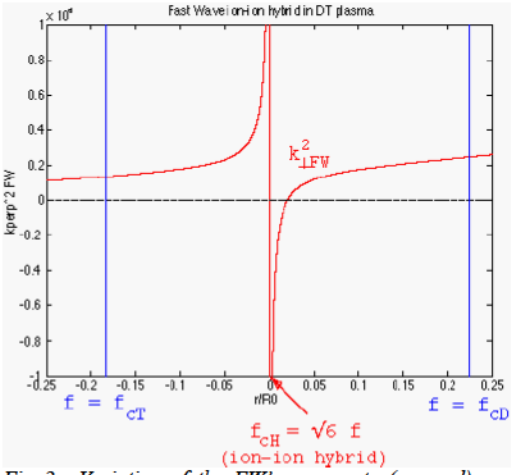

Fig. 2. Variation of the FW's wavevector(squared) over the plasma cross-section. The plasma density is assumed uniform. The ion-ion hybrid is located in the centre x=0.

We are now in a position to show that the model equation Eq.(38) of ref.[1] is a reasonable simplified resonance model. For the specific case of the ion-ion hybrid, and using Eq.(27) for simplicity, we shall also be able to show how to determine which sign to use in Eq.(43) of ref.[1]. In a tokamak, the toroidal magnetic field decreases as $1/R$, R the major radius. Accordingly, the FW's wavevector varies across the plasma. Such a variation is

shown in Fig.2, in the vicinity of the ion-ion hybrid resonance and assuming that the plasma density is constant for simplicity. Let us define the resonance location as $R=R_0$ and

$$\omega_{cH0}^2 = 6\omega^2; \quad \omega_{cH} = \frac{\omega_{cH0}R_0}{R} = \frac{\omega_{cH0}R_0}{R_0+x} \tag{29}$$

With these definitions, we can re-write the resonant denominator

$$\omega_{cH}^2 - 6\omega^2 = \frac{\omega_{cH0}^2 R_0^2}{(R_0+x)^2} - 6(\omega + i\nu)^2 \tag{30}$$

where we have introduced a small imaginary part to the frequency, in agreement with the causality rule[3]. In the vicinity of the resonance ($x/R \ll 1$),

$$\omega_{cH}^2 - 6\omega^2 \approx -\frac{12\omega^2}{R_0}\left(x + \frac{i\nu}{\omega}R_0\right) \tag{31.1}$$

$$k_{\perp FW}^2 \approx -\frac{k_0^2\omega_{pH}^2}{60\omega^2}\frac{R_0}{(x+i\frac{\nu}{\omega}R_0)} \tag{31.2}$$

This proves our statements, as the singularity is indeed $1/x$ and the pole is slightly *below* the real x-axis. It is thus circled clockwise while performing the x-integration in Eq.(42) of ref.[1], which implies that the negative sign has to be taken in Eq.(43) of ref.[1], and that, given the sign in the r.h.s. of Eq.(31.2), the wave energy is indeed absorbed – rather than emitted- at the crossing of the resonance.

I.F. Scenarios

In present-day machines, the most usual scenario is fundamental heating of a hydrogen minority in a D plasma, or D-(H). Other mixtures have been tried successfully, like D-(^{3}He), or even *heavy minority scenarios* like H-(D), H-(^{3}He). Second and third harmonic heating, like $f=2f_{cH}$ or $f=3f_{cD}$, have been used, either as a majority or as a minority scenario. Mode conversion heating was proven to heat efficiently electrons, and FW current drive based on Landau-TTMP damping has been shown to follow theoretical expectations. In D-T plasmas, nearly all possible scenarios have been tested, T-(D), D-(T), second harmonic T, mixed $f=2f_{cT}$ and fundamental minority ^{3}He, D-T-(^{3}He) and even mode conversion. Finally, let us note that direct ion Bernstein wave launch experiments have also been performed, with limited success in terms of power coupling, but inducing in some cases poloidal rotation and transport barrier formation. A good survey of these experiments, together with a large number of references is given in ref.[6].

I.G. Database and applications

High power ICRH systems have been installed in a large number of machines. A maximum power of 22MW was coupled to the plasma in JET[7]. ICRH power was injected in various sorts of plasmas, including L-mode, ELM-free and ELMy H-mode, RI-mode[8]. In D-T, a record steady-state fusion Q performance (Q=0.22) was achieved with ICRH alone in JET[9]. At the occasion of the compilation of transport databases for ITER, it was noted that no significant differences in heating efficiency can be observed between the RF (ICRH and ECRH) subset and the rest of the database[10]. Although it is generally the case that the heating efficiency is equivalent for all auxiliary heating methods, there are cases where differences are observed. They are usually interpreted as resulting either from differences in power deposition profile or from a different impact on confinement. As an example of the latter, the choice of heating method – H/D co/counter NBI / ICRH-D-injection, can have definite impact on the achievement and quality of the RI-mode on TEXTOR[11].

Like in the case of NBI, the neutron production rate furnishes an indirect measurement of the tail created by the RF. Comparisons with theoretical predictions indicate that the tail formation process is fairly well understood[12]. Fast ion energy content[13] and direct tail measurements[14] provide similar indications. Other comparisons have addressed the question of ion/electron power partition and power deposition profile[15,16]. The interaction of ICRH with beam-injected fast-ions was also investigated, in particular in relation with third harmonic heating and RF-induced fast particle diffusion[17]. Good agreement with theoretical predictions was observed. FW electron current drive has been tested in DIII-D and Tore-Supra, showing good agreement with the expected T_e-scaling[6]. Minority-ion current drive, by flattening or steeping the current density profile allowed control of the sawtooth frequency[18]. ICRF systems have recently found new applications in the field of plasma production in presence of a static magnetic field. The plasmas produced in this way could be used for efficient wall conditioning or for start-up assistance[11,19,20].

An ICRF system has been designed for ITER[6], which would couple 50MW through three ports. A rather large voltage is required (42kV) because the coupling is relatively low due to the large distance between the antenna and the plasma.

II. LOWER HYBRID HEATING

In the lower hybrid (LH) heating domain, two waves coexist: the fast and the slow wave. For $N_{//}=0$, they are uncoupled and evanescent and only the FW exhibits a

resonance at the LH. If $N_{//}$ is increased (up to $N_{//} \approx 1$), both waves become propagating at the edge but merge some distance inside the plasma (confluence). Further in, both are evanescent (complex conjugate $k_\perp^2$) and the central part of the plasma is not accessible to the waves from the edge. It is only when the *accessibility condition* Eq.(65) of ref.[3], is satisfied that the two waves uncouple and propagate both inside the plasma. The accessibility condition implies that the launcher must be designed such as to launch waves with a parallel wavelength shorter than

$$\lambda_{//} = c/(N_c f) \qquad (32)$$

This is obtained by using an array of phased waveguides called the *grill*[21].

The original concept of LH heating is to launch the slow wave (SW) at a frequency below the central value of the LH resonance. The SW then propagates up to the LH resonance and is absorbed there. It however became apparent from experiments that usually the wave tended to be absorbed by electron Landau damping before having reached the resonance. This is largely due to the cone propagation effect[3]. Indeed, the wave rays tend align to the magnetic field as the wave propagates inwards, eventually becoming exactly parallel at the LH resonance. Accordingly, the waves tend to circle around the plasma centre and to damp there. This efficient electron absorption is now exploited and recent LH heating experiments operate at frequencies above the central LH frequency, so that there is no longer a wave resonance inside the plasma and all the power goes to electrons. With an asymmetric $N_{//}$ spectrum, LH heating is used as a current drive method. The cone behaviour is responsible for the main problem in applying LH to reactor-size machines, namely that the LH wave energy tends to propagate peripherally around the plasma and to deposit its energy away from the plasma centre. More precise information about the location where the power is deposited in toroidal geometry can be obtained using ray-tracing techniques[22].

LH was first used as a heating method. The corresponding experimental results have been nicely summarised in a plot showing the different heating regimes in FT[23]. At low density, LH waves heat electrons. As the density is increased, electron heating fades away and ion heating sets in, creating ion tails. At still higher density, ion heating also decreases and disappears while parametric decay activity sets in. The different damping mechanisms of LH waves and the interpretation problems of experimental results, such as the spectral gap problem, are described in the book by Cairns[24]. Presently, the main application of LH is non-inductive current drive; it constitutes today the best, experimentally proven, current drive method. In large hot plasmas like ITER or reactors, the LH waves can usually not reach the centre. Accordingly, LH in ITER[25] is mainly seen as a tool for controlling the current profile by off-axis current drive in advanced scenarios[26]. It can also be used for saving volt-seconds in the ramp-up phase of the plasma current.

III. ALFVEN WAVE HEATING

In the Alfvén wave domain, two types of cold-plasma waves can propagate[3],

$\omega = k_{//} c_A$ the shear Alfvén wave (SW) (33.1)

$\omega = k\, c_A$ the compressional Alfvén wave (FW) (33.2)

The first of these relations implies that the shear Alfvén wave can propagate only along the field lines.

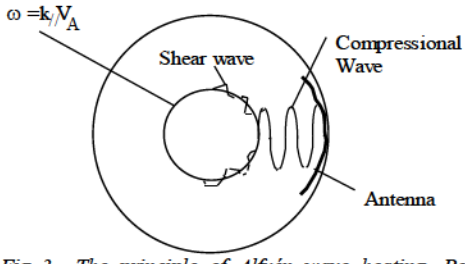

Fig. 3. The principle of Alfvén wave heating. Poloidal cross-section of the tokamak.

In an inhomogeneous plasma there is only one surface, close to a magnetic surface, where for a given $N_{//}$ the shear wave dispersion relation Eq.(33.1) is satisfied. So, the shear Alfvén wave can propagate only on that surface, as shown on Fig.3: it is trapped on that surface. Therefore, the idea is to launch from the outside the compressional Alfvén wave, which can propagate in all directions and reach the Alfvén resonance. Once the power is coupled to the shear wave, it stays on the magnetic surface and dissipates there. Note that the wavelength of the compressional wave is of the order of 1m. This means that, for 1m wide or narrower antennas, most of the wave spectrum will be evanescent with an evanescence length of the order of the antenna size[1].

From the experimental point of view the most extensive experiments and analysis of Alfvén wave heating have been performed on the TCA tokamak[27] (R_0=0.6m). Although antenna coupling and general wave behaviour appeared to be in agreement with the theory, generally speaking little plasma heating was observed while the main effect of the RF was a large density increase, sometimes interpreted as an increase in the particle confinement time. In view of these disappointing results there have been few attempts to apply Alfvén wave heating to large tokamaks and this method is usually not mentioned for the heating of

ITER or reactors. However, there has been some renewed interest in this field as the conversion to the kinetic Alfvén wave may induce poloidal shear flows, and possibly generate transport barriers[28].

IV. FURTHER READING

An excellent introductory overview of the different wave heating methods is given by Cairns[24]. A very complete work on plasma waves is that of Stix[5]. Brambilla[29] reviews the same subject with finer detail and a more direct view toward practical applications. In particular, many dispersion relation features are discussed in detail.

REFERENCES

1. R. KOCH, "The coupling of electromagnetic power to plasmas" *These Proc.*
2. P. LAMALLE, "Kinetic theory of plasma waves: Part III Inhomogeneous plasma" *These Proc.*
3. E. WESTERHOF, "Kinetic theory of plasma waves: Part II Homogeneous plasma" *These Proc.*
4. R. KOCH, "Heating by Waves in the Ion Cyclotron Frequency Range", *Transactions of Fusion Technology*, 33, 227, (1998)
5. T.H. STIX,"Waves in plasmas", AIP New York (1992).
6. ITER team, *et al*., "ITER Physics basis", *Nucl. Fus.* 39(1999)
7. V.P.BHATNAGAR, *et al*., "ICRF Heating and Synergistic LH and Fast-Wave current Drive in JET", *9th Top. Conf. on Radio Freq. Power in Plasmas, Charleston* 115, (1991)
8. J.P.H.E. ONGENA, "Extrapolation to reactors", *These Proc*
9. J. JACQUINOT & The JET Team, "Deuterium-tritium operation in magnetic confinement experiment: results and underlying physics", *Plasma Phys. Contr. Fus.* 41, A13,(1999)
10. K. THOMSEN, *et al*., "ITER H-mode confinement database update", *Nucl. Fus.* 34, 131, (1994).
11. R. KOCH, *et al*., "Progress on TEXTOR-94: Radiative-Improved-Mode and Radio-Frequency plasma production in the Ion Cyclotron Range", Proc. VI Ukrainian Conf. and School on Plasma Phys. and Contr. Fus., Alushta 1, 70,(1998)
12. L.-G. ERIKSSON, *et al*., "Theoretical analysis of ICRF heating in JET DT plasmas", ICPP & 25th EPS Conf. on Contr. Fus. and Plasma Phys., Prague, Europhysics Conf. Abstracts 22C, 1186, (1998)
13. L.-G. ERIKSSON, *et al*., "Comparison of Time Dependent Simulations with Experiments in Ion Cyclotron Heated Plasmas", *Nucl. Fus*., 33, 1037, (1993)
14. D.F.H. START, *et al*., "ICRF Results in D-T Plasmas in JET and TFTR and Implications for ITER", *Plasma Phys. Contr. Fus*., 40, A87, (1998)
15. R. KOCH *et al.*, "A Comparison Between ICRF Theory and Experiment", *Plasma Phys. Contr. Fus*., 30, 1559, (1988).
16. M.PORKOLAB, *et al*., "Recent Progress in ICRF Physics", *Plasma Phys. Contr. Fus*., 40, A35,(1998)
17. R. KOCH *et al.*, "Interaction of ICRF Waves with Fast Particles on TEXTOR", *Plasma Phys. Contr. Fus*., 37, A291, (1995).
18. V.P.BHATNAGAR, *et al*., "Local Magnetic Shear Control in a Tokamak via Fast Wave Minority Ion Current Drive: Theory and Experiments in JET", *Nucl. Fus.,* 34, 1579, (1994)
19. R. KOCH *et al.*, "Low loop voltage start-up of the TEXTOR-94 plasma with ICRF and/or NBI assistance", 26th EPS Conf. on Contr. Fus. & Plasma Phys., Maastricht, (1999)
20. A. LYSSOIVAN *et al.*, "ICRF Plasma Production in TORE SUPRA: Analysis of Antenna Coupling and Plasma Properties", ibid.
21. A. EKEDAHL, *et al*., "Conditioning and high power operation of the lower hybrid current drive launcher in JET" *Report* JET- P(97)19 (1997)
22. M. BRAMBILLA, "Ray tracing of lower hybrid and ion cyclotron waves", *Computer Phys. Reports* 4, 71 (1986).
23. F. ALLADIO *et al.*, "Lower hybrid heating experiments on FT", in Proc. *4th Int. Symp. Heating in Toroidal Plasmas, (Roma), Ed. Knoepfel H., Sindoni E.* 1, 546 (1984).
24. R.A. CAIRNS, "Radiofrequency heating of plasmas", Adam Hilger, IOP (1991).
25. P. FROISSARD, *et al.*, "Lower hybrid wave injection system", NET report EUR FU/XII-218/113/98 (1998)
26. D. MOREAU *et al.*, "ITER operation scenarios involving current profile control", NET report EUR FU/XII-218/112/98 (1998)
27. G. BESSON *et al.*, "A review of Alfvén waves heating", *Plasma Phys Contr. Fus.* 28, 1291 (1986).
28. G. AMARANTE SECUNDO, *et al.*, " Calculation of Alfvén wave driving forces, plasma flow, and current drive in the TCABR tokamak", *26th EPS Conf. on Contr. Fus. Plasma Phys., Maastricht,* (1999)P3.092
29. M. BRAMBILLA, "Kinetic Theory of Plasma Waves – Homogeneous Plasmas", *Clarendon Press Oxford* (1998).

KINETIC THEORY OF PLASMA WAVES

D. Van Eester and E. Lerche
Laboratorium voor Plasmafysica - Laboratoire de Physique des Plasmas
EUROfusion Consortium member
Koninklijke Militaire School - Ecole Royale Militaire
Trilateral Euregio Cluster, Renaissancelaan 30 - B1000 Brussels - Belgium
Tel.: (32 2) 44 14 134, Fax.: (32 2) 735 24 21, e-mail: d.van.eester@fz-juelich.de & ealerche@msn.com

ABSTRACT

In the present paper a very brief introduction is provided to the theory of kinetic waves relevant to the description of wave heating in fusion machines and focussing mostly on radio frequency or ion cyclotron resonance frequency waves in tokamaks. The text starts by sketching the basic philosophy underlying the standardly adopted methods, describing the interaction of a single particle with a given wave and the assumptions typically made to arrive at a trustworthy description of the energy exchange, and ends by discussing some of the subtleties of the modeling of wave-particle interaction in inhomogeneous magnetized plasmas. None of the topics will be treated in full detail. Hence, by no means, this text is meant to be all-inclusive. Rather, it aims at providing a framework that should allow understanding what are the difficulties involved, leaving out the detailed derivation of the expressions as well as subtleties such as relativistic corrections. The interested reader is referred to the provided references - and the references given therein - for more in depth information.

I. INTRODUCTION

The interaction between charged particles and electromagnetic waves can be looked at from 2 vantage points: From the point of view of the waves 'plasma heating' is a process by which they lose energy. The relevant equation to describe this is the wave equation, derived from Maxwell's equations. From the point of view of the particles the same process is viewed as a gain of energy. The relevant equation to describe this second interpretation of the same physical phenomenon is the Fokker-Planck equation, derived starting from the kinetic equation of state. A proper description of the phenomena requires that these 2 aspects are described on the same footing, which is not at all straightforward and which only starts to be done now that powerful computers are increasingly available.

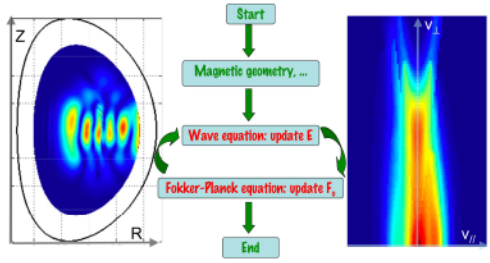

Figure 1: Wave-particle interaction: wave point of view (left: fast dynamics) vs. particle point of view (right; slow - net - dynamics) and scheme for modeling both aspects self-consistently. The wave field (left) is plotted in a toroidal cut of a tokamak, the RF heated ion distribution (right) is plotted in terms of the velocity components at the low field side crossing of the equatorial plane for a prescribed radial position.

The kinetic description of waves in plasmas typically starts from the equation

$$\frac{df}{dt} = C + S - L \tag{1}$$

in which f is the distribution function of the charged particles being studied, and the right hand side describes how the distribution equation evolves under the influence of collisions the particles undergo, and of particle injection (S=source) and particle loss (L). In the high frequency domain and for a sufficiently strong magnetic field, the left hand side is dominated by processes on a vastly different time scale than that of the net effect of collisional interaction and particle loss or gain. Hence on the fastest time scale of the problem the right hand side is negligibly small and can be neglected to a first approximation. The above equation then simply states that the number of particles is conserved in phase space: Particles can move about and gain or lose energy - which causes a stretching or squeezing of the

volume in which a given number of particles resided at a given initial time - but the number of particles in the stretched phase-space volume is always conserved.

II. BASIC PHILOSOPHY [1-11]

II.A. General Formulation

In general, the orbits of particles immersed in electromagnetic fields are not integrable i.e. their motion cannot be described in terms of constants of the motion but is stochastic and thus ergodically covering parts of phase space. On top of that, charged particles in motion constitute a current themselves and thus influence the electromagnetic fields in the fusion machine. Hence, the RF plasma current needs to be carefully accounted for when solving Maxwell's equations. Describing the impact of the charged particles on the fields and the back reaction of the fields on the particles involves the challenging task of solving a set of coupled nonlinear equations in 6 independent variables in phase space. As the temporal and spatial scales cover a range of many orders of magnitude (ion cyclotron motion involves frequencies in the radio frequency - megaHertz - domain while net collisional interaction occurs on a time scale of hundreds of milliseconds in a tokamak such as JET, or seconds in ITER; the macroscopic dimensions of such fusion machines is several meters, while the ion Larmor radius ρ is of the order of a few millimeters) making simplifications is a necessity. The drawback of the wide range of scales is thereby turned into an advantage, allowing to set apart phenomena and tackling processes happening on drastically different scales separately.

It is instructive to have an idea of the relative magnitudes of various relevant quantities to understand why the 'quasi-linear' approach and other commonly made approximations make sense. For typical JET parameters in a D majority plasma (temperature of $5keV$, density of $5 \times 10^{19} m^{-3}$, magnetic field $3T$, major radius of $3m$ and minor radius of $1m$), the ion cyclotron frequency of the D ions is $23MHz$ and the electron cyclotron frequency is $80GHz$, the ion thermal velocity is $5 \times 10^5 m/s$ so the typical ion Larmor radius is $3mm$, the electron thermal velocity $3 \times 10^7 m/s$ so the electron gyroradius is $0.05mm$, the ion collision frequency is $100Hz$ and the electron collision frequency is $10kHz$. For typical RF waves of several MW with electric field values of $50kV/m$ close to the antennas, the RF magnetic field is $5 \times 10^{-3} T$ and the RF magnetic contribution to the Lorentz acceleration $|\vec{v} \times \vec{B}_{RF}| = 2.5kV/m$.

Hence the ions travel around the torus in about $4 \times 10^{-5} s$. The cyclotron ('gyro') period τ_g is much shorter than the transit ('bounce' & 'drift') time $\tau_{b,d}$, which itself is much smaller than the collision time τ_c, making it senseful to describe the cyclotron motion as much faster than the bounce/transit motion, itself typically much faster than the collision time and rendering a collisionless description senseful. The scaling $\tau_g << \tau_{b,d} << \tau_c$ is crucial for the customary models. In particular, the 'slower' phenomena are assumed to be constant on the faster time scale while the faster - oscillatory - phenomena are treated as being beyond their transient state, all quantities merely varying as a function of time as $exp[i\omega t]$, where ω is the frequency at which the external wave launchers are operated. The particle motion is essentially imposed by the confining magnetic field, the RF field being a small - be it fast - perturbation and the RF electric field effect dominating that of the magnetic field. Finally, the Larmor radius is commonly much smaller than the equilibrium quantity gradients, this giving rise to the so-called drift approximation and locally making a quasi-homogeneous description senseful. In particular $\rho / L_{B_o} << 1$ where ρ is the Larmor radius and L_{B_o} is a typical scalelength of the variation of the confining magnetic field.

To understand the basic physics of the impact of the RF electric field on a test particle, we locally solve the equation of motion and then use the result to evaluate the net energy a charged particle can gain or lose in a rapidly varying electric field along the trajectory it is forced to follow by the fusion machine's strong static confining magnetic field. We start from a homogeneous plasma, straight magnetic field line analysis and gradually include other effects.

Because the magnetic field is imposing a clear asymmetry in the dynamics along as opposed to perpendicular to the magnetic field lines, the discussion of the wave-particle interaction is most easily described with reference to the direction along $\vec{e}_{//} = \vec{B}_o / B_o$ and 2 independent directions perpendicular to the static magnetic field $\vec{B}_o$. Neglecting the equilibrium electric field related to the ohmic circuit, the solution of the equation of motion of a charged particle immersed in a homogeneous, static magnetic field can be written as $v_{\perp,1} = v_\perp cos\phi$, $v_{\perp,2} = v_\perp sin\phi$ where $\phi = \phi_o - \Omega(t - t_o)$ while $v_{//} = ct$, with $\Omega = qB_o/m$ (B_o the confining field, q the charge and m the mass of the species) the cyclotron frequency, which can further be integrated to get the particle position: $x_{\perp,1} = x_{\perp,1,GC} - \rho sin\phi$, $x_{\perp,2} = x_{\perp,2,GC} + \rho cos\phi$ in which the Larmor radius is given by $\rho = v_\perp / \Omega$ and 'GC' refers to the guiding centre position. Assuming the electric field is a plane wave characterized by a wave vector $\vec{k}$, defining ψ as the angle between $\vec{k}$ and $\vec{e}_{\perp,1}$ ($k_{\perp,1} = k_\perp cos\psi$, $k_{\perp,2} = k_\perp sin\psi$), the work the electric field does on a particle can be written

$$q\vec{E}.\vec{v} = q \sum_{N=-\infty}^{N=+\infty} L_N exp[-N\phi] \qquad (2)$$

in which

$$L_N = [\frac{v_\perp}{2}(E_- J_{N+1} e^{i\psi} + E_+ J_{N-1} e^{-i\psi})$$

$$+E_{//} v_{//} J_N] e^{iN\psi}$$

is the Kennel-Engelmann operator [17] and where the electric field is evaluated at the guiding center $\vec{x}_{GC} = [x_{\perp,1} + \rho sin\phi]\vec{e}_{\perp,1} + [x_{\perp,2} - \rho cos\phi]\vec{e}_{\perp,2} + [v_{//}(t-t_o)]\vec{e}_{//}$ rather than at the particle position and in which the argument of the Bessel functions is $k_\perp \rho$; E_+ rotates in the same sense of the gyro-motion of the ions, E_- in that of the electrons. In doing so the most rapidly varying contribution (the cyclotron oscillation) is conveniently isolated from all slower contributions. Figure 2 illustrates that using the guiding center position rather than the particle position as the reference position makes the bookkeeping much simpler when studying heating: In the particle frame, integration over a reference volume entails integrating over all orbits with various speeds and guiding centers that are intersecting the reference volume. When particles are in coherent motion with a wave and are periodically exchanging energy with it, this exchange is not considered to be 'heating' although the energy streaming into the reference volume in $\vec{x}$ will increase at some times and decrease at others. In the guiding center $\vec{x}_{GC}$ frame the picture is much clearer, simpler and more symmetrical, as there is no leaking of particles into or out of reference volumes. On top of that, the fastest evolution has been separated out, a non-negligible advantage when searching for equations that will need to be solved numerically as it implies a significant speed-up of the computations. Finally, as will be seen later, expressing the fields in terms of guiding center coordinates allows interfacing to the Fokker-Planck equation describing the net impact of the fields on the particles (rather than the impact of the particle motion on the fields) in a natural way, allowing to make wave and particle equations more easily compatible. From the equation of motion one readily finds that the change of the particle energy is $\dot{\epsilon} = \frac{d\epsilon}{dt} = q\vec{E}.\vec{v}$ which, using the above found expression, can be written more explicitly as

$$\dot{\epsilon} = q \sum_{-\infty}^{+\infty} L_N(\vec{E}_{GC}(t_o)) exp[i(N\Omega + k_{//} v_{//} - \omega)(t - t_o)].$$

For most frequencies ω the right hand side is periodic and hence the energy transfer between the electric field and the particles is merely oscillating around an average value but no net acceleration is taking place. At the Doppler shifted cyclotron resonances $\omega = N\Omega + k_{//} v_{//}$ the exponential time dependent factor associated to a specific cyclotron harmonic N on the right hand side is constant and hence - in spite of all other terms still oscillating as a function of time - there is a net energy transfer.

Net heating takes place when $N\Omega + k_{//} v_{//} = \omega$, in which the Doppler shift term $k_{//} v_{//}$ is usually a correction to $N\Omega$, except when $N = 0$ in which case it is crucial. In the radio frequency domain (tens of MHz) and for typical magnetic field strengths of current-day magnetic fusion machines (a few Tesla), the resonance condition for the ions can easily be satisfied for $N \neq 0$ i.e. they undergo cyclotron heating, while that of the electrons requires $N = 0$ i.e. they feel the Cerenkov effect. As a consequence, ions and electrons react very differently to waves driven at frequencies in the ion cyclotron frequency range: For not too energetic particles, the argument $k_\perp \rho$ of the Bessel function is small so that $J_0 \approx 1$ and $J_M << 1$ when $M \neq 0$. Hence, the ions are mainly accelerated in the *perpendicular* direction by the perpendicular components of the electric field - modest energy ions mainly by E_+, high energy ions by both E_+ and E_- - while the contribution of the parallel electric field has a minor impact on them; on the other hand, the parallel electric field gives the electrons a net pull in the *parallel* direction (Landau damping). Cerenkov interaction equally involves the perpendicular electric field components, an effect known as transit time magnetic pumping (TTMP). Whereas Landau damping causes parallel acceleration and is present even when the electric field is spatially uniform, TTMP affects the perpendicular energy and requires inhomogeneity of the field. An elegant discussion of the wave-particle interaction can be found in [12].

Since collisons are infrequent but non-absent, it is customary to interpret the frequency ω in the resonant denominator as a complex quantity with a very small, positive imaginary part $i\nu$, ν loosely being interpreted as the collision frequency that would appear in the particle equation of motion if collisions would be accounted for in a simple way. Mathematically, this gives a recipe for how to encircle the poles at the resonances to ensure causality. The contribution of the energy from events in the far past ($t_o \to -\infty$) is then absent and only the end contribution of the time integral at time t survives. The need for the elimination of the far past history is of particular interest to ensure there is net heating. It will be discussed separately later.

II.B. The Quasilinear Approach: The RF Perturbed Distribution and the Quasilinear Diffusion Operator

The time evolution equation (1) is rewritten making use of the fact the confining magnetic field is much larger than the fastly varying purely oscillatory electromagnetic perturbation, driven at the antenna frequency ω i.e. proportional to $\propto exp[i\omega t]$: Both the distribution itself and the Lorentz force are separated into a large term only involving slowly varying quantities (referred

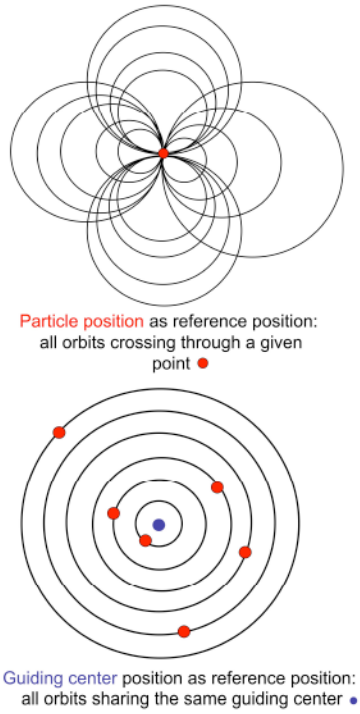

Figure 2: Cyclotron motion as seen in the particle (top) and guiding centre (bottom) reference frame.

to with a subscript 'o'), and a small but rapidly varying contribution (related to the driven RF fields):

$$\frac{df}{dt} = \frac{df}{dt}|_o + \frac{df}{dt}|_{RF} =$$

$$\frac{dF_o}{dt}|_o + \frac{dF_o}{dt}|_{RF} + \frac{df_{RF}}{dt}|_o + \frac{df_{RF}}{dt}|_{RF} = C + S - L$$

with $\frac{d}{dt}|_o = \frac{\partial}{\partial t} + \vec{v}.\nabla_{\vec{x}} + \frac{q}{m}[\vec{E}_o + \vec{v} \times \vec{B}_o].\nabla_{\vec{v}}$ and $\frac{d}{dt}|_{RF} = \vec{a}_{RF}.\nabla_{\vec{v}} = \frac{q}{m}[\vec{E}_{RF} + \vec{v} \times \vec{B}_{RF}].\nabla_{\vec{v}}$, F_o the slowly varying and f_{RF} the rapidly varying distribution function. The first, zero order term in the above only varies on the slowest time scale, the next 2 terms are first order corrections which oscillate at frequency ω, while the most rapidly varying terms in the last, second order term contains factors that oscillate at frequency 2ω. Since F_o only depends on the constants of the motion, $\frac{dF_o}{dt}|_o$ can be simplified to $\frac{\partial F_o}{\partial t}$. The 2 linear terms yield an expression for the RF perturbed distribution i.e. for the evolution on the fast time scale, known as the Vlasov equation:

$$\vec{a}_{RF}.\nabla_{\vec{v}}F_o + \frac{df_{RF}}{dt}|_o = 0$$

i.e.

$$f_{RF} = -\int_{orbit}^{t} dt' \vec{a}_{RF}.\nabla_{\vec{v}}F_o \qquad (3)$$

which can be inserted in the fourth term of the evolution equation. Averaging $< ... >$ the 4 terms over a full oscillation period for all oscillatory aspects of the motion and the driven response, yields an equation for the slow time variation, known as the Fokker-Planck equation. The first term stays untouched, the second and third term as well as the oscillatory parts of the fourth term vanish while a constant, second order contribution survives. This yields

$$\frac{\partial F_o}{\partial t} =< C > + < S > - < L > + < Q > \qquad (4)$$

in which $< Q >=< \nabla_{\vec{v}}.\vec{a}^*_{RF} \int_{orbit}^{t} dt' \vec{a}_{RF}.\nabla_{\vec{v}}F_o >$ is the quasi-linear diffusion operator, acting on the slowly varying distribution function.

II.C. The Wave Equation & the Conductivity Tensor

Combining Maxwell's equations for the evolution of the electric field and the magnetic field, and assuming the waves are driven at a frequency ω, the wave equation can be written in terms of the electric field $\vec{E}$ only,

$$\nabla \times \nabla \times \vec{E} - k_o^2 \vec{E} = i\omega\mu_o[\vec{J}_{antenna} + \vec{J}_{plasma}], \qquad (5)$$

in which $k_o = \omega/c$ with c the speed of light. The fields are excited by the current density $\vec{J}_{antenna}$ flowing on the antennas typically located close to the edge of the plasma. The plasma current $\vec{J}_{plasma}$ is composed of the contributions from the various plasma constituants s, $\vec{J}_{plasma} = \sum_s q_\alpha \int d\vec{v}\vec{v} f_{RF,s}$, and is fully defined when the perturbed distributions of all species are known. Strictly, the plasma current contains an ohmic contribution ($\vec{J}_{plasma} = \vec{J}_{ohmic} + \vec{J}_{RF}$) aside from the fast-varying RF contribution. It has been neglected in the present text.

An elegant way to solve the wave equation is relying on variational techniques, by multiplying the equation with a test function vector and integrating over the volume of interest. Performing partial integration to remove the highest order derivatives from $\vec{E}$ not only allows to chose lower order base functions for a given desired numerical accuracy when solving the equation, it also allows to obtain a more symmetrical formulation in which the test function vector $\vec{F}$ and the electric field $\vec{E}$ play a similar role. The resulting equation is

$$\int d\vec{x}[k_o^2 \vec{F}^*.\vec{E} - (\nabla \times \vec{F})^*.(\nabla \times \vec{E})] + W =$$

$$-[\int_{surface} d\vec{S}.\vec{F}^* \times \nabla \times \vec{E} + i\omega\mu_o \int d\vec{x}\vec{F}^*.\vec{J}_{antenna}]$$

with $W/[i\omega\mu_o] = \int d\vec{x}\vec{F}^*.\vec{J}_{RF} = q\int d\vec{x}d\vec{v}\vec{F}^*.\vec{v}f_{RF}$. The surface term needs to vanish at the metallic wall to ensure no electromagnetic flux leaks away. A supplementary advantage of this formulation is that it readily yields the associated energy conservation theorem when substituting the test function vector by the electric field (see further for the expression for the absorbed power density shared by the wave and particle descriptions). The perturbed current density $\vec{J}_{plasma}$ and the electric field $\vec{E}$ are related by the conductivity tensor $\vec{\vec{\sigma}}$: In Fourier space $\vec{J}_{plasma,\vec{k}'} = \vec{\vec{\sigma}}_{\vec{k}',\vec{k}}.\vec{E}_{\vec{k}}$ which is closely related to the dielectric tensor $\vec{\vec{K}} = \vec{\vec{1}} + i\omega\mu_o\vec{\vec{\sigma}}$.

For a plasma in thermal equilibrium, the term $q\vec{F}^*.\vec{v}f_{RF}$ can be written more explicitly as $-q\vec{F}^*.\vec{v}\int^t dt' q\vec{E}.\vec{v}\frac{F_o}{kT}$ in which the last factor can be shifted in front of the particle history integral since the slowly varying distribution only depends on the constants of the motion. One gets

$$W = \omega\mu_o q^2 2\pi \int d\vec{x}dv_\perp dv_{//} v_\perp \frac{F_o}{kT}\sum_N \frac{L_N(\vec{F})^* L_N(\vec{E})}{N\Omega + k_{//}v_{//} - \omega} \tag{6}$$

Isolating the various contributions from the test function vector and the electric field in this expression yields an expression for the conductivity tensor.

The velocity space integrals in Eq. (6) can be performed to yield a compact expression for the dielectric response in a Maxwellian plasma. The integral over the *parallel* velocity yields the Fried-Conte plasma dispersion function $Z(\zeta)$, which - aside from the hot plasma corrections to the wave propagation - describes the process of collisionless damping. The argument of the Fried-Conte function is $\zeta = \frac{\omega - N\Omega}{k_{//}v_{th}}$. Figure 3 depicts this function for $Im(\zeta) \to 0^+$. The real part asymptotically approaches the cold plasma limit $Re[Z] \approx -1/\zeta$, but bends the resonant crossing from $+\infty$ to $-\infty$ at $\zeta = 0$ into a smooth transition behaving like $Re[Z] \approx -2\zeta$. The imaginary part is a Gaussian. Physically its width is determined by the scalelength over which the cyclotron frequency Ω varies, and the factors contributing to the Doppler shift, namely the parallel wave number $k_{//}$ and the thermal velocity v_{th}. Away from the cold plasma resonance damping fades away quickly while the reactive part stays significant much further from $\zeta = 0$.

As long as $k_\perp\rho << 1$ is satisfied, the Bessel functions can easily be approached by their truncated Taylor series expansion and the perpendicular integrals can easily be integrated. Retaining *all* finite Larmor radius effects yields modified Bessel functions (see e.g. [3]). Although the perpendicular (cyclotron gyration) dynamics seems more daunting than the parallel dynamics, it is the latter that is most challenging: In strong magnetic fields, the cyclotron motion moves the particle only a small distance - the Larmor radius ρ - away from the guiding center, hence equilibrium quantities typically vary little between the particle and the guiding center positions. But the guiding centers themselves often sample large regions of the machine since their motion is only restricted by the magnetic field topology. Taylor series expansions are routinely used for the perpendicular dynamics but have to be used with care for the parallel dynamics.

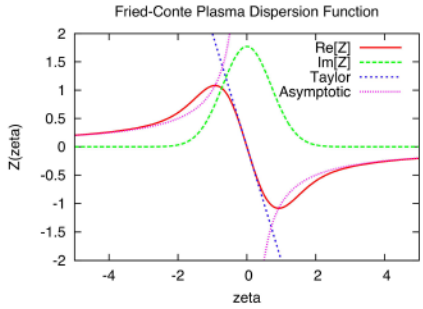

Figure 3: The Fried-Conte plasma dispersion function and its leading order Taylor and asymptotic series representation.

Expressions have also been derived to account for arbitrary F_o (see e.g.[7]). The Fried-Conte function is now replaced by other (in general numerically evaluated) functions. For a sufficiently refined velocity grid, the distribution function can locally be approximated with bi-linear functions and the partial integral can be evaluated analytically, yielding a logarithmic contribution. Upon crossing the resonance, the logarithm picks up a 'switch-on kick' imaginary contribution: It is the delta function contribution at the pole of the original integrand that represents the discontinuous Heaviside step energy 'kick' when picking up the energy due to crossing the resonance. The kick shows up in the uniform plasma description as a resonance crossing in velocity space. In non-uniform plasmas the kick can just as well be described by integrating along the orbit.

II.D. The Cold Plasma Limit

To get a feeling of how drastically a plasma changes the wave characteristics of the electromagnetic waves that exist in vacuum, it is already sufficient to simply consider the cold plasma limit. This may seem a drastic oversimplification but since $k_\perp\rho$ is small when the temperature is low, the cold plasma limit yields a reasonable description of the fate of the waves launched from RF antennas, to the obvious exception of the collisionless damping processes themselves which are an

inherently kinetic - as opposed to fluid - effect.

Although it is sufficient to take the asymptotic limit $Z(\zeta) \rightarrow -1/\zeta$ and $J_0(k_\perp \rho) \rightarrow 1$, while $J_M \rightarrow 0$ for Bessel function with order $M > 1$ to retrieve the cold plasma limit, it is much easier to directly rederive the conductivity tensor starting from the solutions of the equation of motion. Using the Stix notation [3], the cold plasma dielectric tensor can be written

$$\vec{\vec{K}}.\vec{E} = \begin{pmatrix} S & -iD & 0 \\ iD & S & 0 \\ 0 & 0 & P \end{pmatrix} . \begin{pmatrix} E_{\perp,1} \\ E_{\perp,2} \\ E_{//} \end{pmatrix}$$

in which $S = (R+L)/2$, $D = (R-L)/2$, with

$$R = 1 - \sum_s \omega_{p,s}^2/\omega(\omega + \Omega_s),$$

$$L = 1 - \sum_s \omega_{p,s}^2/\omega(\omega - \Omega_s)$$

$$P = 1 - \sum_s \omega_{p,s}^2/\omega^2$$

where the sum is on the various types of species s the plasma is constituted of and ω_p is the plasma frequency.

II.E. Dispersion Equation Roots

Waves in a cold plasma are electromagnetic in character i.e. their energy is carried purely by the Poynting flux. When the plasma density goes to zero, their dispersion roots join the vacuum roots $k_\perp^2 = k_o^2 - k_{//}^2$. With respect to $\vec{B}_o$, one of the 2 cold plasma roots is essentially transverse electric, and the other essentially transverse magnetic in character. Referring to the group (energy propagation) velocity, the former is known as a 'fast' wave while the other is a 'slow' wave. The former allows to carry wave power across magnetic surfaces and is the preferred candidate to heat the plasma core in the ion cyclotron domain, while the latter tends to propagate along magnetic surfaces. Finite temperature effects add kinetic corrections to these modes, and introduce supplementary wave branches. For not too energetic particles, the dielectric tensor is usually truncated at second order effects in the Larmor radius. This results in a supplementary mode appearing in the dispersion equation: the (first) Bernstein wave. This wave is essentially electrostatic in nature i.e. its energy is carried by particles in coherent motion with the wave, while its Poynting flux is negligible. Figure 4 shows a dispersion plot of the fast wave exciting the Berstein wave at the place where the decoupled cold plasma fast wave has a resonance ($S = k_{//}^2$). This being very close to the ion-ion hybrid layer ($S = 0$) since $k_{//}^2 << |S|$ in sufficiently dense plasmas, the mode conversion layer is often labeled as the ion-ion hybrid layer.

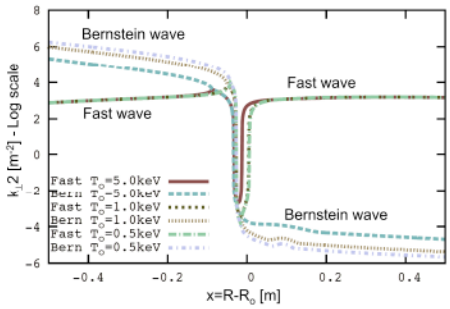

Figure 4: Fast and (first) ion Bernstein wave dispersion equation roots for 3 different central temperatures using a dielectric description retaining all finite Larmor radius corrections. Note that the fast wave root hardly changes while the Bernstein wave root - a root absent in a cold plasma description - depends sensitively on the temperature.

Strictly speaking, the Berstein wave cannot be described by a dispersion resulting from a truncated Taylor series expansion in $k_\perp \rho$ since $k_{\perp,Bern}\rho$ is of order 1, although such a model does correctly locate the places where the fast wave excites it for up to second cyclotron harmonic terms. At higher frequencies and/or for more energetic particles, the customary truncation of the dielectric tensor is not even rigorous for the fast wave anymore. Hence, higher order finite Larmor radius terms have to be retained. A hot plasma supports an infinity of hot plasma modes, adding supplementary Bernstein modes. Whether they actually play a role depends on whether or not they are excited. Increasing the frequency while keeping the magnetic field fixed brings higher harmonics into the plasma. Higher Bernstein wave modes can be excited but the fast and Bernstein waves are gradually more decoupled at higher frequencies.

II.F. The Fokker-Planck Equation [17-23]

Electromagnetic waves cannot directly be observed experimentally so their behavior is indirectly studied through e.g. the response of temperature and density to sudden changes in the externally launched power level (see e.g. [22]). On the other hand, multiple diagnostics exist to monitor aspects of fast particle populations present in the plasma and to cross-check against theoretical predictions.

As briefly discussed before, when all fast scale dynamics are removed from the description by averaging over all oscillatory aspects of the motion and driven response, the Fokker-Planck equation (4) results. Whereas the wave equation is commonly tackled by integrating

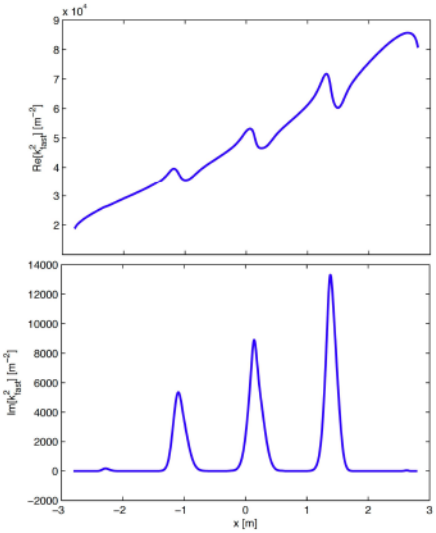

Figure 5: Fast wave dispersion root at $f = 300MHz$ and $k_{//,o} = 5/m$ in a $D-T-(\alpha)-(D_{NBI})$ DEMO plasma; $B_o = 5.74T$. The top curve shows the real part of the fast wave root; the bottom plot depicts the imaginary part in which ion cyclotron heating at the 6th, 7th and 8th harmonic is observed.

over velocity space so that the independent variables are spatial coordinates, the Fokker-Planck equation is necessarily solved in terms of constants of the motion. The distribution function of a given plasma species represented in terms of the constants of the motion (e.g. energy, magnetic moment) is, by definition, the same along the trajectory. However, because of the magnetic field inhomogeneity, the same distribution expressed in terms of its local velocity components $(v_\perp, v_{//})$ looks different depending on the location one looks at it (see Fig.6). Hence, interpretation of experimental data requires careful analysis: As diagnostics focus on different aspects of a same distribution, they may seemingly contradict but in truth corroborate one another.

The Coulomb collision operator for a uniform plasma is known. A convenient, symmetrical form is due to Landau (see e.g. [1, 2, 18]):

$$\sum_s C(F_{oa}, F_{os}) = \nabla_{\vec{v}} \cdot \sum_s \vec{S}_C^{a/s}$$

$$\vec{S}_C^{a/s} = \frac{q_a^2 q_s^2 ln\Gamma^{a/s}}{8\pi\epsilon_o^2 m_a} \int d\vec{v}' \frac{u^2\vec{\vec{1}} - \vec{u}\vec{u}}{u^3} [\frac{F_{oa}}{m_s}\frac{\partial F_{os}}{\partial \vec{v}'} - \frac{F_{os}}{m_a}\frac{\partial F_{oa}}{\partial \vec{v}}]$$

in which 'a' refers to the species under examination and the sum is over all species 's' in the plasma; $\vec{u}$ is the relative velocity $\vec{v} - \vec{v}'$. Since the species of type 'a' is one of the species in the sum, the collision operator is a non-linear integro-differential operator. *If* the species 'a' is a small minority, its selfcollisions can be neglected and the Fokker-Planck equation becomes a linear equation in F_{oa}, but if it is one of the main constituants the nonlinear collision operator has to be retained.

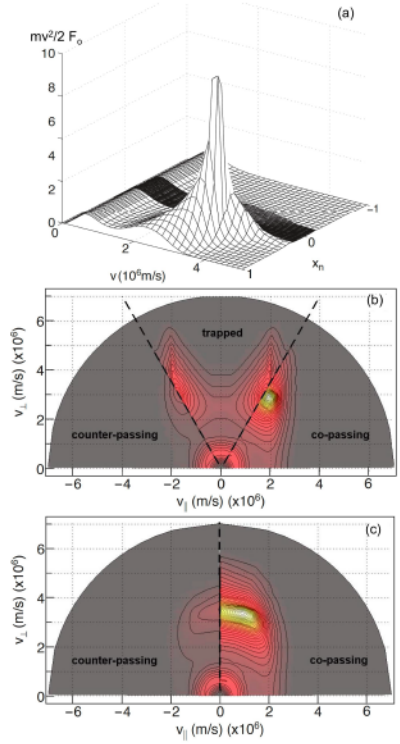

Figure 6: 3 representations of the *same* RF heated beam distribution energy density $\frac{mv^2}{2}F_o$: (a) as a function of the constants of the motion velocity v and (normalized) magnetic moment x_n, and as a function of $(v_\perp, v_{//})$ at (b) the low field side midplane and (c) the high field side midplane (see [23]).

Again, analytical expressions are available for the case the distribution function of the species 's' is Maxwellian, in which case the collision operator can be written in terms of the error function. In case F_{os} is isotropical, the integrals that need to be evaluated reduce to 1-dimensional integrals and in the fully anisotropical case the operator acting on F_{oa} can be written in terms of the Rosenbluth potentials. The step from the uniform plasma collision operator C to the operator $< C >$ averaged over all fast aspects of the motion is a nontrivial step, the fully rigorous treat-

ment of which is still awaited.

In view of the fact that the various species interact with each other collisionally, and that several types of species can simultaneously be heated by electromagnetic waves, a series of coupled Fokker-Planck equations rather than a single one should be solved. This can be done iteratively, taking the distributions obtained in the previous iteration to compute the collision operator in the current step. Provided convergence is reached, this allows accounting for the non-linear collision operator without making use of a non-linear system solver. Figure 7 shows a simplified 1-dimensional case in which it was assumed that all distributions are isotropic. It depicts an ITER example for the conditions foreseen for wave heating of the $D-T$ plasma during the activated phase of operation of the machine: the majority of T ions is heated at its second harmonic cyclotron layer, while a minority of ^3He is simultaneously heated at its fundamental cyclotron resonance to help cranking up the fusion reactivity; unavoidably, the electrons are heated by Landau and TTMP damping.

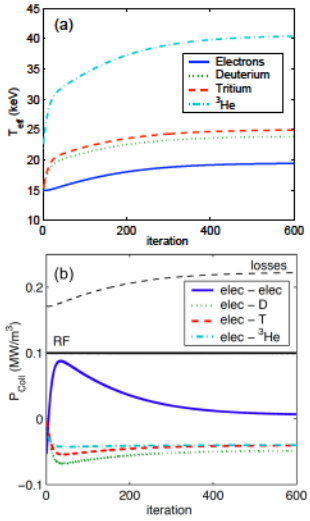

Figure 7: ITER $D-T-(^3He)$ heating: (a) Effective temperatures and (b) electron power balance.

II.G. A Note on Selfconsistency

A rigorous treatment requires that the Fokker-Planck (FP) and wave (W) equations are solved simultaneously and on the same footing. Their intimate connection is exemplified by the 2 expressions of the absorbed power density:

$$P_{abs,FP} = \frac{\partial}{\partial t}[\int d\vec{v}d\vec{x}\epsilon F_o]|_{RF} = \int d\vec{v}d\vec{x}\epsilon\frac{\partial F_o}{\partial t}|_{RF} =$$

$$\frac{1}{2}Re\int d\vec{v}d\vec{x}\epsilon\nabla_{\vec{v}}.\vec{a}^*_{RF}\int_{-\infty}^{t}dt'\vec{a}_{RF}.\nabla_{\vec{v}}F_o$$

$$= \frac{q}{2}Re\int d\vec{v}d\vec{x}\vec{E}^*.\vec{v}f_{RF} = \frac{q}{2}Re\int d\vec{x}\vec{E}^*.\vec{J}_{RF} = P_{abs,W}$$

in which $P_{abs,FP}$ is the RF power density written in the way it is used in the Fokker-Planck equation (with ϵ the energy, and $\frac{\partial F_o}{\partial t}|_{RF}$ the RF diffusion operator, and $P_{abs,W}$ the RF power density as written in the wave equation, involving the RF perturbed current density $\vec{J}_{RF}$ and f_{RF} the perturbed distribution function; $\vec{a}_{RF} = \frac{q}{m}[\vec{E}_{RF} + \vec{v}\times\vec{B}_{RF}]$ is the Lorentz force acceleration/decelaration caused by the small but rapidly varying electromagnetic field driven at frequency ω. Formally writing down the above expression is immediate. To come up with practical expressions for the coefficients to be used in the wave and Fokker-Planck equations is less trivial, at least when the equations are truly treated on the same footing i.e. when the 2 problems posed in 6-dimensional phase space are solved removing 3 of the 6 independent variables to arrive at an equation in the remaining 3 variables using the *same* approximations for both equations. Getting the proper coefficients requires integrating (a) on the velocity space variables to obtain the dielectric response coefficients needed in the wave equation and (b) on the gyro, bounce and drift motions to find an expression for the quasi-linear diffusion operator. Ideally, the same elementary 'building blocks' are used and the relevant integrations are performed on them.

III. SOME ASPECTS OF NONUNIFORM PLASMA MODELING

III.A. Mode Coupling [38-51]

Before commenting on the particular issues brought about by the impact of the plasma inhomogeneities on the orbits of the particles and the challenges this leads to when trying to write down a rigorous expression for the dielectric response, a simplified problem is looked at first, namely that of the wave propagation in a tokamak in absence of a poloidal field i.e. where the guiding center orbits are assumed to simply being given by $\varphi(t) = \varphi(t_o) + v_{//}(t-t_o)$. Starting from Eq. (6), but retaining the full wave spectrum and toroidal curvature while assuming that the various species are Maxwellian and that the toroidal angle as well as the distance from midplane are ignorable variables (allowing to isolate individual n toroidal modes and k_Z) yields

$$W = \omega\mu_o(2\pi)^3\int dRRdv_{\perp}dv_{//}v_{\perp}\frac{F_o}{kT}$$

$$\sum_N \frac{[\int k_{R'}L_N(\vec{F})]^*[\int k_R L_N(\vec{E})]}{N\Omega + k_{//}v_{//} - \omega}$$

which is fully symmetrical w.r.t. the test function vector $\vec{F}$ and the electric field $\vec{E}$, guaranteeing a positive definite power density for a plasma in thermal equilibrium. To arrive at a practical expression one of the following 2 approaches is used:

- Assuming that $k_\perp \rho << 1$ so that the Bessel functions in the Kennel-Engelmann expressions can be approximated by a truncated Taylor series expansion around the origin, which upon realizing that

$$\frac{d^m}{dR^m}\vec{E}(R) = \int dk_R (ik_R)^m exp[ik_R R]\vec{E}_{k_R}$$

  allows to write down an expression for the dielectric response W and the purely electromagnetic (curl) term to be used in the Galerkin form of the wave equation; it is customary to truncate the Taylor series at terms of second order in $k_\perp \rho$. Removing the differential operators from the test function vector components $\vec{F}$ by partial integrations allows to find the corresponding expression for the dielectric tensor, and the so obtained surface terms immediately provide the expression for the kinetic flux [38].

- In reality, $k_\perp \rho << 1$ is not satisfied for all modes that the plasma supports and thus that assumption should not be made if such modes are excited. Bernstein modes are finite temperature modes for which $k_\perp \rho \approx 1$ and even the cold plasma slow mode violates the smallness condition. Hence *if* short wavelength branches are excited - either directly at the plasma edge or at ion-ion hybrid layers [3] - a more rigorous treatment is needed to ensure the predicted fate of the shorter wavelength modes is correctly described. The easiest way to do this is to rewrite the Fourier integrals as discrete sums and to use locally constant base functions $[H(k_R - k_{R,i})][H(k_{R,i+1} - k_R)]$. The Galerkin form of the wave equation is hereby transformed into a system of linear equations allowing to find the electric field Fourier components in the discretized Fourier space.

Figure 8 shows an example of the integration of the 1D integrodifferential wave equation. The top figure depicts the perpendicular wave components. An incoming fast wave carries energy into the region of interest from the right. At the ion-ion hybrid layer at $R \approx 3m$ mode conversion to the Bernstein wave takes place, although part of the fast wave energy simply tunnels through the confluence layers and makes it to the high field side (left on the plot) as a fast wave. Note that the Bernstein wave is efficiently absorbed, its amplitude having shrunk again to zero about $0.3m$ towards

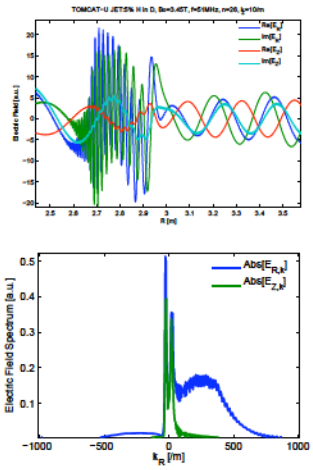

Figure 8: Bernstein wave excitation by the fast magnetosonic wave at the ion-ion hybrid layer: electric field components (top) and Fourier spectrum (bottom).

the high field side. The bottom figure shows the corresponding k_R Fourier spectrum of the perpendicular electric field. The Bernstein wave is a backward, electrostatic wave transporting its energy via the kinetic rather than the Poynting flux: Its main field component is the component in the direction of the background gradient, and for a leftward propagating wave that carries energy from the confluence layer towards the high field side it is the $k_R > 0$ spectrum that is significantly nonzero. The 2 peaks in the low k_R part of the spectrum correspond to the incoming fast wave (highest amplitude for $k_R < 0$ as the fast wave is a forward wave carrying energy in the same direction as the phase velocity) and the reflected wave (somewhat smaller peak, and in the $k_R > 0$ region since the reflected wave necessarily carries less energy that the incoming wave).

In two dimensions poloidal as well as radial mode coupling occurs. Figure 9 gives an example of 2D wave equation modeling in which the geometry and the poloidal magnetic field has been accounted for. In this ITER example the short wavelength modes are not excited.

III.B. Orbit topology [24-32]

The motion of a charged particle in an axisymmetrical tokamak is characterized by 3 constants of the motion and by 3 periodic aspects of the motion. The 3 constants of the motion often used are the energy $\epsilon = \frac{mv^2}{2}$, the magnetic moment $\mu = \frac{mv_\perp^2}{2B_o}$ and the toroidal angular momentum $P_\varphi = mRv_\varphi - q\Psi/2\pi$ (φ is the toroidal angle, q the charge and Ψ the poloidal magnetic flux)

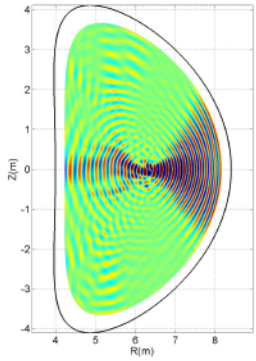

Figure 9: Poloidal electric field component for the RF heating scenario foreseen for the activated ITER phase; 3% ^3He in a balanced $D-T$ plasma, f=53MHz and $B_o = 5.3T$.

but suitable other sets of 3 independent functions of the customary 3 can equally well be used. In order of decreasing oscillation frequency, the 3 oscillatory aspects are the cyclotron motion, the bounce motion and the toroidal drift motion. Figure 10 gives a schematic view of the various oscillatory aspects of the motion for a trapped particle in a tokamak.

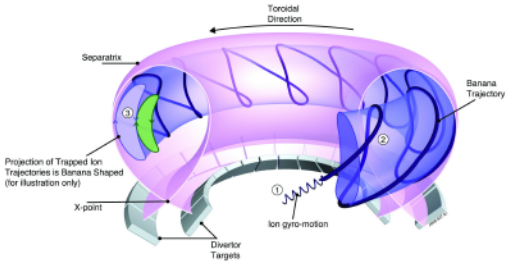

Figure 10: Schematic representation of the particle orbits in a tokamak (JET-EFDA figure JG05.537-4).

Even on a single particle level, adding the poloidal field to the description vastly changes the complexity of the wave-particle interaction problem since the guiding center orbits are now no longer on $R = ct$ surfaces but have become poloidally closed loops. Rather than sampling a unique value of the confining magnetic field, the guiding centers sample regions of varying toroidal field strength. Whereas in a uniform plasma a particle either is 'in resonance' or 'out of resonance' at all times, the resonances in inhomogeneous plasmas are localized i.e. the resonance condition is satisfied only locally at some positions along the orbit. The phase factor $exp[i(N\Omega + k_{//}v_{//} - \omega)(t - t_o)]$ in the earlier mentioned evolution equation for the particle energy is now generalized to an integral over $\vec{k}$ space of terms of the form $exp[i\Theta(t)]$ in which $\Theta = -N\phi + \vec{k}(t).\vec{x}_{GC}(t) - \omega t$. In the neighbourhood of the resonance the phase in the exponential can be approximated by a truncated Taylor series expansion, $\Theta(t) \approx \Theta(t_o) + \dot{\Theta}(t_o)(t - t_o) + \frac{1}{2}\ddot{\Theta}(t_o)(t - t_o)^2 + \frac{1}{3!}\dddot{\Theta}(t_o)(t - t_o)^3$. The corresponding exponential factor generally oscillates very quickly so that its integral does not accumulate a net contribution. Close to stationary phase points ($\dot{\Theta} = 0$) the phase variation slows down and the integral picks up a finite contribution. Figure 11 depicts the relevant integral for a regular stationary phase point ($\ddot{\Theta} \neq 0$) and for a higher order stationary phase point ($\ddot{\Theta} = 0$). The former is representative for a standard resonance crossing while the latter is representative for a resonance at a turning point of the orbit, where 2 resonances merge (strictly, the higher order stationary phase point is a bit separated from the turning point: $v_{//} = 0$ does not coincide with $v_\theta = 0$). The linear line corresponding to the uniform plasma case for which the particle always stays in resonance is indicated as well.

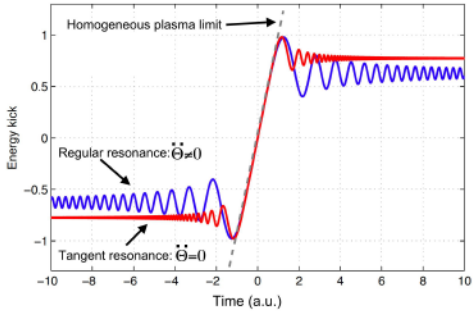

Figure 11: The energy kick felt by the particle along the orbit for resonance at a regular point ($\ddot{\Theta} \neq 0$) and at a tangent resonance point ($\ddot{\Theta} = 0$).

In spite of the fact that energetic ions have guiding center orbits that deviate significantly from magnetic surfaces, the difference between the toroidal angular momentum P_φ and the poloidal flux function Ψ is often neglected ('zero drift' or 'zero banana width' approximation). Aside from the fact that this is an acceptable approximation in large enough machines or for low enough temperatures, the main motivation for this approximation is that it hugely simplifies the equations while keeping poloidal mode coupling and particle trapping/detrapping, two of the most important inhomogeneity effects, intact. Since the dielectric response written earlier was using the electric field at the guiding

center rather than the particle position and since guiding centers stay on magnetic surfaces in the zero drift approximation, the parallel gradient can be written as an *algebraic* rather than as a differential operator when expressing the various quantities in terms of their (discrete) toroidal and poloidal Fourier series expansions:

$$\nabla_{//} = \frac{cos\alpha}{|\partial\vec{x}/\partial\varphi|}\frac{\partial}{\partial\varphi} + \frac{sin\alpha}{|\partial\vec{x}/\partial\theta|}\frac{\partial}{\partial\theta}$$

$$= cos\alpha\frac{in_{tor}}{R} + sin\alpha\frac{im_{pol}}{|\partial\vec{x}/\partial\theta|} = ik_{//}$$

for each individual poloidal mode m_{pol} and toroidal mode n_{tor}; α is the angle between the total magnetic field and the toroidal direction. The denominator resulting from the particle history integral is now no longer a constant and net resonant interaction only takes place at the poloidal angle that satisfies $N\Omega + k_{//}v_{//} = \omega$ in which the cyclotron frequency, the parallel wave number and the parallel velocity now all vary along the orbit. Although the density and temperature are constant along the zero-drift guiding center trajectory, poloidal mode coupling takes place because of the magnetic field and geometrical inhomogeneity the guiding center experiences along its orbit. This has one mild and one more important consequence:

- The mild consequence is that the perpendicular differential operator in the expression L_N due to Kennel-Engelmann requires retaining the differential character in both independent perpendicular directions. The resulting expressions yield a double sum over poloidal modes, and differential operators in the direction perpendicular to the magnetic surfaces. For heating scenarios in which short wavelength branches are excited, a proper description of the poloidal coupling requires accounting for a very large number of poloidal modes and couplings, and a large number of radial grid points. In an axisymmetrical tokamak there is no toroidal coupling and thus a single sum on the toroidal mode spectrum remains; in a real tokamak - in which magnetic ripple occurs since a discrete number of toroidal magnetic field coils are installed - and in a stellarator, also the toroidal modes are coupled. Even in the zero drift limit, solving the wave equation in 2 or 3 dimensions requires powerful computers.
- Whereas the previous section involves supplementary bookkeeping but is not truly posing a problem, the fact that the parallel mode number appears in the resonant denominator gives rise to a fundamental problem: Whereas expression (6) is fully symmetrical in the test function vector $\vec{F}$ and the electric field $\vec{E}$ and guarantees positive definite and purely resonant absorption for Maxwellian distributions, which is what is physically expected, the now obtained expressions are symmetrical for what concerns the perpendicular operator but are asymmetrical for what concerns the parallel dynamics. As long as $k_{//}$ is modest (as is typically the case for the fast wave), this is of little consequence. But for short wavelength branches, positive definite absorption for Maxwellian distributions is no longer guaranteed. A rigorous cure for that flaw requires a much more sophisticated model, as will be discussed in the next section.

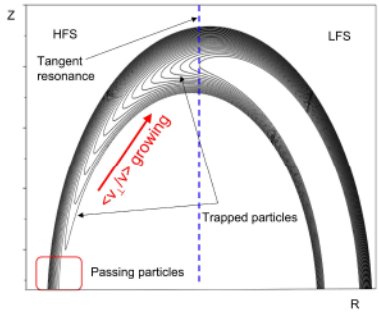

Figure 12: Schematic representation of the impact of cyclotron heating on a charged particle in a tokamak: The perpendicular energy of the particle gradually increases. Initially passing particles become trapped, their banana tip shifting towards the low field side when $v_\perp$ gradually grows. The interaction of the particle with the wave stops when the orbit no longer cuts the resonance. Just prior to that happening, 2 resonances merge, giving rise to efficient heating at the tangent resonance.

It was mentioned earlier that for not too energetic ions the Doppler shift term $k_{//}v_{//}$ in the resonance condition $N\Omega + k_{//}v_{//} = \omega$ is a small correction to the cyclotron term. As the corresponding distribution is only significant in a restricted region of velocity space, it implies that the region where cyclotron interaction takes place is restricted in space as well: $\delta R/R \approx \delta(k_{//}v_{//})/\omega$. Although the electrons are equally resonantly interacting with the field, the resonance condition is much less stringent on them since $k_{//}v_{//} = \omega$ is commonly satisfied in a wide region because of the modest steepness of the temperature profile. Consequently, it is fairly straightforward in the ion cyclotron frequency domain to ensure ion heating can only take places at a predetermined location but it is less evident to avoid the often unwanted electron heating. In big, hot and dense machines such as ITER RF waves have already lost a non-negligible fraction of their energy by electron Landau and TTMP damping before arriving at the cyclotron layer.

III.C. Bounce Motion, Tangent Resonance, ...

Two approaches are commonly used to derive the wave equation (and in particular to find a suitable expression for the RF perturbed distribution function f_{RF}) and the Fokker-Planck equation (and in particular the quasilinear diffusion operator $< Q >$). One is the very intuitive approach in which the governing Lorentz force can readily be recognized in the expressions and for which the link with straight magnetic field line uniform plasm theory is direct (see e.g. [26, 44, 43]). The other is more formal but more general and allows to benefit from the action-angle (Hamiltonian) formalism (see e.g. [33, 35, 36, 30]).

Practical expressions proposed by various authors tend to differ somewhat since different variables are chosen and different approximations are made. For wave equation studies (focussing on the fast dynamics), the trajectory integral is most intuitive and therefore most frequently adopted but for Fokker-Planck equation, the details of the fast dynamics are only indirectly relevant and all has to be expressed in terms of constants of the motion, hence tending to be closer to the action-angle technique which elegantly allows to retain the slow time scale physics while integrating away the fast phenomena by suitable averages over the various relevant oscillation periods. Kaufman showed, however, that the Hamiltonian description can equally be used to describe the fast scale physics. More importantly still, he stressed that a rigorous description of both aspects of the wave-particle interaction requires making the *same* approximations in both equations if one wants to describe the physics self-consistently. If applied rigorously, the path integral and action-angle methods are fully equivalent; for a somewhat more detailed discussion, see [34]. However, and in spite of Kaufman's visionary paper and presently available powerful computers, a fully rigorous description of the plasma heating process by electromagnetic waves is still awaited and a fully selfconsistent description based on a sufficiently rigorous footing is a project still to be tackled ...

The drift approximation and quasilinear approach make sense because of the vastly different time and spatial scales to describe the wave-particle interaction by first computing the zero order motion in absence of the rapid but small perturbation, and to account for the corrections relying on perturbation theory. In an axisymmetric tokamak in absence of perturbations, the particle motion can be described in terms of 3 constants of the motion $\vec{\Lambda}$ and 3 angles $\vec{\Phi}$ that describe the periodic aspects of the particle motion. Kaufman proposed to rely on action-angle variables but in the literature a wide variety of constants of the motion was successfully used. In contrast, the choice of the angles as used in the Hamiltonian theory is much more appealing than any other choice since these angles vary *linearly* with time and thus time history integrals become trivial: Formally, the integrals are like those appearing in the uniform plasma case since - once functions only involving constants of the motion have been pulled out of time history integrals (since $\frac{d}{dt}|_o = \frac{\partial}{\partial t} + \vec{\omega}.\frac{\partial}{\partial \Phi}$ e.g. $f_{RF} = -\int dt' \vec{a}_{RF}.\nabla_{\vec{v}} F_o$ can simply be written as $f_{RF} = -\frac{\partial F_o}{\partial \vec{\Lambda}}.\int dt' \dot{\vec{\Lambda}}$), the rapidly varying phase factor denoting all 4 oscillatory aspects of the driven response and particle motion is of the form $\vec{m}.\vec{\Phi}(t) - \omega t$ in which $\vec{\Phi}(t) = \vec{\Phi}(t_o) + \vec{\omega}(t - t_o)$ and the gyro, bounce and toroidal drift frequencies $\vec{\omega} = (\omega_g, \omega_b, \omega_d)$ are only depending on the constants of the motion $\vec{\Lambda}$; the corresponding mode numbers are $\vec{\tilde{m}} = (m_g = -N, m_b, m_d = n_{tor})$ in which the bounce mode number m_b should not be confused with the poloidal mode number m_{pol} but the other 2 mode numbers correspond to the cyclotron mode and the toroidal mode numbers. And so time history integrals simply yield factors of the form $.../[\vec{\tilde{m}}.\vec{\omega} - \omega]$ i.e. prescribe that waves and particles resonantly interact when the resonance condition $\vec{\tilde{m}}.\vec{\omega} = \omega$ (ω being the generator frequency) is satisfied.

A major simplification of the algebra comes from the identity $\vec{a}_{RF} = \frac{i}{\omega m}[\frac{d}{dt}\nabla_{\vec{v}} - \nabla_{\vec{x}}]q\vec{E}.\vec{v}$ (see e.g. [5]) since it allows to write the various contributions of which the time history integrals needs to be found to come up with an appropriate expression for the dielectric response of the plasma to a rapidly oscillating electromagnetic wave in terms of $\dot{\epsilon} = q\vec{E}.\vec{v}$. For example

$$f_{RF} = \sum_{j=1}^{3} \frac{i}{\omega m}\frac{\partial F_o}{\partial \Lambda_j}[-q\vec{E}.\nabla_{\vec{v}}\Lambda_j + \int^t dt' D_{\Lambda_j}\dot{\epsilon}]$$

in which $D_{G}... = \frac{d}{dt}[\nabla_{\vec{v}} G.\nabla_{\vec{v}}...] + \nabla_{\vec{v}} G.\nabla_{\vec{x}}...$, hereby essentially reducing the algebraic work to be done to describe the impact of an arbitrary distribution function $F_o(\vec{\Lambda})$ to the work needed for the case of an isotropic distribution. For a Maxwellian distribution, it can easily be shown that the net absorption of wave energy by a particle population is positive definite and that the interaction is resonant in nature:

$$\sum_{\vec{\tilde{m}},\, \vec{\tilde{m}}'} < q\vec{E}.\vec{v}|^*_{\vec{\tilde{m}}'} \int_{\infty}^{t} dt' q\vec{E}.\vec{v}|_{\vec{\tilde{m}}} >= \sum_{\vec{\tilde{m}}} \frac{|q\vec{E}.\vec{v}|_{\vec{\tilde{m}}}|^2}{i[\vec{\tilde{m}}.\vec{\omega} - \omega]}.$$

Making use of generating functions for the transformation between canonical variables and applying them to the action-angle $(\vec{J}, \vec{\Phi})$ variables proposed by Kaufman, one finds $D_{J_i} = m\frac{\partial}{\partial \Phi_i}$ where m is the mass of the examined type of particles [34]. Whereas the toroidal angular momentum P_φ and the magnetic moment μ are natural variables to use in the computations, the third Kaufman action - related to the surface enclosed by the poloidal closed drift orbit - is not very practical. Replacing it by the energy ϵ allows to find a compact operator to generalize the expression found for a

Maxwellian distribution to that for an arbitrary distribution $F_o(\vec{\Lambda})$: $\frac{\partial F_o}{\partial \Lambda_1} \rightarrow \frac{\partial}{\partial \Lambda_1} + N\frac{\partial}{\partial \Lambda_2} + n_{tor}\frac{\partial}{\partial \Lambda_3}$ when $\vec{\Lambda} = (\frac{\epsilon}{\omega}, -\frac{mv_{//}^2}{2\Omega}, P_\varphi = mRv_\varphi - \frac{q\Psi}{2\pi})$ where Ψ is the poloidal magnetic flux.

Of course, although the Hamiltonian method offers an elegant framework to do the required evaluations, its simplicity is somewhat misleading:

- The Fourier transformation of the work $q\vec{E}.\vec{v}$ done by the electric field on the particles, written down only *formally* in Kaufman's paper is where the full complexity of the acceleration and deceleration of particles on their orbits through an inhomogeneous static magnetic field will show up. Happily, the vast difference in time response time of the various aspects of the motion allows to rely on asymptotic techniques to perform this step. First, the Fourier analysis is performed *at a fixed time*, and then the integrals along the orbits are evaluated. The Fourier transform of $q\vec{E}.\vec{v}$ is

$$q\vec{E}.\vec{v}|_{\tilde{\vec{m}}}(\vec{\Lambda}) = \frac{1}{(2\pi)^3}\int d\vec{\Phi} q\vec{E}.\vec{v} exp[-i\tilde{\vec{m}}.\vec{\Phi}].$$

  Formally writing the electric field in terms of its $\vec{k}$ spectrum so that, analogously to the uniform plasma Eq. (2), the phase of $q\vec{E}.\vec{v}$ is $\vec{k}.\vec{x}_{GC} - N\phi - \omega t$ (GC=guiding center), it can readily be seen that the stationary phase points of the $\tilde{\vec{m}}$ Fourier component are given by the condition $\vec{k}.\vec{v}_{GC} + N\Omega = \tilde{\vec{m}}.\vec{\omega}$ so that the global resonance condition $\tilde{\vec{m}}.\vec{\omega} = \omega$ can be rewritten as $\vec{k}.\vec{v}_{GC} + N\Omega = \omega$, which reduces to the familiar resonance condition $k_{//}v_{//} + N\Omega = \omega$ of the uniform plasma (and more in particular $\rho/L_{B_o} = 0$ i.e. driftless) limit. It is not a trivial task to rigorously account for the drift orbit effects since perpendicular corrections not only have to be added to the generalized Kennel-Engelmann operator but they now enter the resonance condition as well.

- A supplementary difficulty comes from the fact that there are many thousands of bounce modes that need to be evaluated to describe wave-particle interaction accounting for the plasma inhomogeneity rigorously. This amounts to a significant increase of the computation time required to solve the equations.

III.D. Decorrelation, Superadiabaticity [33-37,52-55]

It was discussed earlier that the work $q\vec{E}.\vec{v}$ the electric field does on a charged particle is an oscillatory function of time i.e. can be written as a sum of terms proportional to a phase factor $exp[i\Theta(t)]$. As the guiding center orbits in the drift approximation are closed poloidally (at least for an axisymmetrical tokamak), the particles cross every poloidal position many times every second (bounce frequency). Most of the contributions to the work are oscillatory in nature and cancel out when integrated over all fast time scales (gyro-, poloidal bounce and toroidal drift motion), yielding a zero net effect. Only the resonant contributions possibly give rise to a finite effect. That even these do not cancel on average, is not as evident as it may seem at first sight: In general, the number of cycles the work goes through in between 2 successive transits is not an integer number and thus the phase change is not a multiple of 2π so the average work done over a longer period of time is the sum of 'energy kicks' with the same amplitude *but* at different phase. Assuming that the phase difference between 2 successive transits modulo 2π is $\Delta\Theta$, it can readily be seen that for every particular phase at a given crossing, there is another crossing in a not too distant past that more or less cancels out the present contribution since $\Delta\Theta$ attains any value between 0 and 2π with equal probability. And so, even if the particle gets an energy kick every time it crosses the resonance, the net effect of many crossings (typically a few thousand per second for standard ion temperatures in typical working conditions) is still zero ... *Unless* something breaks the pure periodicity and makes the particles somehow 'forget' about their encounters in the far past so that rather than a very large number of crossings being relevant, only the most recent ones are. Collionality does exactly that.

Let us consider the simplest possible 'Krook' collision operator $C(f) = \nu f$, where ν is the dominant collision frequency for the species considered, to discuss the principle: Whereas the fast dynamics of the wave-particle interaction is typically described by the Vlasov equation, a somewhat more careful examination of the evolution equation we started from shows that collisionality can strictly *not* be omitted when describing the fast time scale: the collision operator C in that original equation acts on the full distribution $f = F_o + f_{RF}$ and not only on the slowly varying part F_o. Hence the Vlasov equation should be extended to contain a small but nonzero contribution, reflecting the rare but non-absent collisions the particles undergo along their unperturbed orbits: $\frac{d}{dt}|_o f_{RF} + \vec{a}_{RF}.\nabla F_o = C(f_{RF})$. Writing the time derivative along the trajectory in terms of the constants of the motion $\vec{\Lambda}$ and the angles $\vec{\Phi}$ and assuming that the perturbed distribution can be written as the product of a term *only* involving slow dynamics and a term involving fast dynamics i.e. $f_{RF} = H(\vec{\Lambda}, t)\tilde{f}(\vec{\Lambda}, \vec{\Phi}, t)$, the fast and slow dynamics can be isolated: $[H\frac{d}{dt}|_o\tilde{f} + \vec{a}_{RF}.\nabla_{\vec{v}}F_o]/\tilde{f} = [-\frac{\partial}{\partial t}H + \nu H]$. Since the right hand side of this expression only contains slow dynamics (no fast period response), one can formally write that both sides of this equation indepen-

dently have to be equal to a slowly varying function, $G = G(\vec{\Lambda}, t)$ which is negligibly small on the fast dynamics time scale, $G \approx 0$. It follows that the factor H can to good approximation be evaluated explicitly: $H \propto exp(\nu t)$. And so the Vlasov equation is supplemented with a 'switch-off' or 'phase memory loss' factor: $f = -\int_{-\infty}^{t} dt' H^{-1} \vec{a}_{RF}.\nabla F_o$ which - in view of the result found for H consistent with the Krook collision operator - is simply equivalent to the 'causality rule' which prescribes the frequency ω in the driven time response factor $exp(i\omega t)$ and the resonant denominator $(N\Omega + k_{//}v_{//} - \omega$ in the uniform plasma expression, or $\vec{\omega}.\vec{\tilde{m}} - \omega$ in its drift approximation generalisation) to be replaced by $\omega + i\nu$. Whereas the collisional contribution is very small, it plays a crucial role in the evaluation of the time history integral when integrating over many crossings through a given point on the closed bounce orbit: It constitutes the 'memory loss' factor ensuring that a finite net contribution is obtained for the resonant contributions to the work done by the driven electric field on the particles.

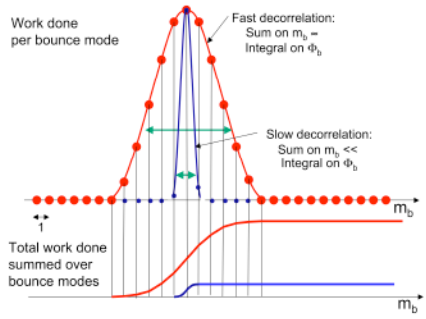

Figure 13: Schematic representation of the importance of decorrelation.

Why this is crucial and how it works can readily be seen in Fig. 13: due to the periodic nature of the bounce motion, the sum of the contributions over all bounce modes is only equivalent to the corresponding integral over (the stationary phase position) bounce angles *if* the collisional broadening of the resonance is wide enough. This brings out a subtle point in the analysis of the wave-particle interaction: Because of the large difference between the bounce and the gyrofrequency ($\omega_b << \omega_g$), it takes thousands of bounce modes to rigorously account for the magnetic field inhomogeneity i.e. the corresponding stationary phase points where the resonant interaction predominantly takes place ($\dot{\Theta}$=0) are very closely spaced. Yet the discrete sum on the bounce modes *cannot* justifiably be replaced by a bounce integral unless the decorrelation time is short enough i.e. the collision frequency *large* enough. And so the very different time scale on which the gyro and bounce motions occur is crucial to restore the 'quasi-homogeneous' nature of localized resonances, while the decorrelation needs to be sufficiently *fast* to ensure that a net interaction takes place at these resonance locations when averaging over all the faster processes. In view of the typical collision frequencies in hot plasmas, collisions at first sight cannot cause a fast enough decorrelation to guarantee RF heating to have a net effect.

Fully accounting for the actual collision operator in the right hand side of the 'generalised' Vlasov equation is not at all a trivial task. Kasilov [53] did the exercise of examining more realistic collision operators and found that the 'switch-off' factor H can to first approximation be taken to be $H = exp[(t/\tau)^n]$ where $n = 3$ for Cerenkov interaction (Landau damping and transit time magnetic pumping) and $n = 5$ for cyclotron damping. He found that the decorrelation times τ are significantly *shorter* than the collison times $1/\nu$, implying that particles 'lose' memory of their phase quickly enough for RF heating to be efficient in magnetic fusion devices. Although the details of the impact of the various decorrelation functions differs, the net effect is the same: the 'kick' particles receive when crossing the resonance is similar (see Fig. 14).

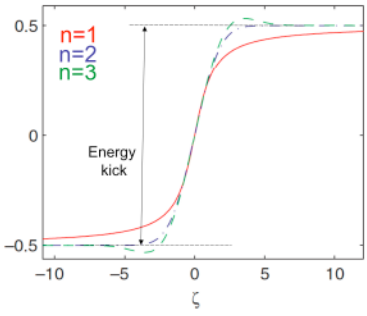

Figure 14: Integrated decorrelation functions for $n = 1, 2, 3$; $\zeta = \tau(\vec{\tilde{m}}.\vec{\omega} - \omega)$ with τ the decorrelation time.

While for thermal particles it is thought that the details of the actual decorrelation are not too relevant (to the important exception of what happens near tangent resonance points where two closely spaced resonance points merge into a single one), for too energetic particles, however, the collisions may still be too unfrequent so that their net effective absorption is reduced. This regime is known as 'superadiabaticity'.

Not only collisions cause a randomization of the phase. Because of the non-integrability of the full (as

opposed to GC) orbits and the non-linearity of the problem, stochastization takes place even if collisions would be absent when launching RF waves of a few MW in fusion relevant plasmas. The rich spectrum of modes, each contributing to the full wave-particle interaction and giving rise to fast phase variations of the total work done on the particles, is likely to trigger sufficient decorrelation.

IV. END NOTE

With the dawn of powerful parallel computers, the degree of realism that can be reached when modeling the interaction of particles and waves in hot, magnetized, inhomogeneous plasmas contained in magnetic fusion experimental reactors is gradually increasing. Various techniques are available to highlight the study of specific aspects of the interaction. Even so, the problem to be tackled is challenging and a number of aspects are only starting to be touched upon.

One aspect of importance in the context of wave-particle interaction is the description of the opposite of wave heating, namely the onset of instabilities triggered by particle distributions: In present-day wave and Fokker-Planck descriptions, it is implicitly assumed that the RF fields are never powerful enough to make the factor $\frac{\partial F_o}{\partial \Lambda_1} + N\frac{\partial F_o}{\partial \Lambda_2} + n\frac{\partial F_o}{\partial \Lambda_3}$ that appears in the perturbed distribution f_{RF} and hence in the expression for $< Q >$ change sign, while experimentally it is well known that MHD modes can be triggered when RF heating is efficient.

Another - even more essential - aspect is the rigorous accounting of the bounce spectrum ensuring that the dielectric response is properly described, without artificially giving rise to damping that has to be rejected on physical grounds: While only the rigorous application of the procedure proposed by Kaufman guarantees the causality to be respected for all modes the plasma supports, no models based on this procedure are yet available.

V. A COMMENT ON THE LIST OF REFERENCES

Although most authors in the reference list comment on various subtopics treated in this text - making a clean separation impossible - the papers most relevant to read up on the general treatment have references [1-11], the wave equation is somewhat more the focus in [12-16] while the Fokker-Planck aspects are the main subject in [17-23]. Details on the orbit topology and its role in describing the wave-particle interaction can be found in [24-32]. The action-angle formalism is discussed in [33-37]. Comments on how to solve the relevant set of equations - with a focus on accounting for the realistic geometry - are given in [38-51] while the role of decorrelation is the key subject in [52-55].

VI. ACKNOWLEDGMENT

The authors gladly thank Dr. P.U. Lamalle for the material he provided for this lecture.

REFERENCES

1. B. WEYSSOW, *Kinetic Theory*, these summer school proceedings
2. R. BALESCU, *Transport Processes in Plasmas*, North-Holland, Amsterdam (1988)
3. T.H. STIX, *Waves in Plasmas*, AIP, New York (1992)
4. B.D. FRIED and S.D CONTE, *The Plasma Dispersion Function*, Academic, New York (1961)
5. L.D. LANDAU & E.M LIFSCHITZ, *Course of Theoretical Physics*, Pergamon, Oxford (1960)
6. R. KOCH, Phys. Lett. A **157**, 399 (1991)
7. D. VAN EESTER, Plasma Phys. Contr. Fusion **35**, 1309-1319 (1993)
8. D. VAN EESTER, Journal Plasma Phys. **54** 1, pp. 31-58 (1995)
9. D. VAN EESTER, Journal Plasma Phys. **60** 3, pp. 627-671 (1998)
10. D. VAN EESTER, Journal Plasma Phys. **65** 5, pp. 407-452 (2001)
11. D. VAN EESTER, Plasma Phys. Contr. Fusion **47** 5, pp. 459-481 (2005)
12. R. KOCH, *Ion cyclotron, lower hybrid and Alfven wave heating*, these summer school proceedings
13. E. WESTERHOF, *Electron cyclotron waves*, these summer school proceedings
14. P.U. LAMALLE, Phys. Lett. A **175**, pp. 45-52 (1993)
15. P.U. LAMALLE, *Non-local theoretical generalisation and tridimensional numerical study of the coupling of an ICRH antenna to a tokamak plasmas*, LPP-ERM/KMS Laboratory Report 101, Brussels (1994)
16. P.U. LAMALLE, Plasma Phys. Contr. Fusion **39**, 1409 (1997)

17. C.F. KENNEL and F. ENGELMANN, Phys. Fluids **9**, 2377 (1966)

18. C.F.F. KARNEY, Computer Physics Reports 4, North-Holland, Amsterdam, 1986 pp 183-244

19. J.D. GAFFEY, J. Plasma Phys. **16** 149 (1976)

20. R. KOCH, *Fast particle heating*, these summer school proceedings

21. E. WESTERHOF, *Current Drive*, these summer school proceedings

22. E. LERCHE et al., Plasma Phys. Contr. Fusion **50** 035003 (2008)

23. E. LERCHE et al., Plasma Phys. Contr. Fusion **51** 044006 (2009)

24. H. DE BLANK, *Guiding center motion*, these summer school proceedings

25. H. DE BLANK, *Plasma equilibrium in tokamaks*, these summer school proceedings

26. I.B. BERNSTEIN et al., Phys. Fluids **24**, 108 (1981)

27. V.S. BELIKOV and Y. I. KOLESNICHENKO, Plasma Phys. **24** 61 (1982)

28. V.S. BELIKOV and Y. I. KOLESNICHENKO, Plasma Phys. Contr. Fusion **36** 1703 (1994)

29. J. HEDIN, *Ion Cyclotron Heating in Toroidal Plasmas*, Ph.D. thesis, Royal Institute of Technology, Stockholm (2001)

30. J. HEDIN et al., Nucl. Fusion **42**, pp. 527-540 (2002)

31. P.U. LAMALLE, Plasma Phys. Contr. Fusion **40**, 465-479 (1998)

32. P.U. LAMALLE, Plasma Phys. Contr. Fusion **48**, 433-477 (2006)

33. A.N. KAUFMAN, Phys. Fluids **15** pp. 1063-1069 (1972)

34. D. VAN EESTER, Plasma Phys. Contr. Fusion **41**, L23 (1999)

35. A. BECOULET et al., Phys. Fluids B **3**, pp. 137-150 (1991)

36. A. BECOULET et al., Phys. Plasmas **1**, pp. 2908-2925 (1994)

37. H.E. MYNICK, Nucl. Fusion **30** 357 (1990)

38. D. VAN EESTER et al., Plasma Phys. Contr. Fusion **40**, 1949-1975 (1998)

39. L. VILLARD et al., Comput. Phys. Rep. **4**, 95 (1986)

40. D. SMITHE et al., Phys. Rev. Lett. **60** 801 (1988)

41. O. SAUTER, *Nonlocal Analyses of Electrostatic and Electromagnetic Waves in Hot, Magnetized, Nonuniform, Bounded Plasmas*, LRP-457/92, Ecole Polytechnique Fédérale de Lausanne (1992)

42. M. BRAMBILLA, Nucl. Fusion **34**, 1121 (1994)

43. M. BRAMBILLA, Plasma Phys. Contr. Fusion **41**, 1 (1999)

44. E.F. JAEGER et al., Phys. Plasmas **8** 1573 (2001)

45. E.F. JAEGER et al., Phys. Plasmas **13**, 056101 (2006)

46. J.C. WRIGHT et al., Phys. Plasmas **11**, 2473 (2004)

47. D.B. BATCHELOR, *Integrated Simulation of Fusion Plasmas*, Physics Today, **02/05**, 35 (2005)

48. J. CARLSSON et al., Nucl. Fusion **37**, 719 (1997)

49. J. CARLSON, *ICRH Heating and Current Drive in Tokamaks*, Ph.D. thesis, Royal Institute of Technology ISBN 97-7107-237-7 (1998)

50. T. HELLSTEN et al., Nucl. Fusion **44**, pp. 892-908 (2004)

51. M. DIRICKX and B. WEYSSOW, J. Plasma Phys. **59** 211 (1998)

52. D. FAULCONER and R. LIBOFF, Phys. Fluids **15** 1831 (1972)

53. S.V. KASILOV et al., Nucl. Fusion **30** 2467 (1990)

54. D. VAN EESTER et al., Phys. Letters A, **218**, pp. 70-79 (1996)

55. Y. LOUIS, *Etude analytique et numérique de la réponse diélectrique non-locale d'un plasma de tokamak à une perturbation radiofréquence, tenant compte de la toroidicité et de la décorrelation*, PhD thesis, Université Libre de Bruxelles, LPP-ERM/KMS Report 103 (1995)

MODELING PARTICLE HEATING AND CURRENT DRIVE IN FUSION MACHINES: BRIEF OVERVIEW OF ADOPTED TECHNIQUES

D. Van Eester
Laboratorium voor Plasmafysica - Laboratoire de Physique des Plasmas
EUROfusion Consortium member
Koninklijke Militaire School - Ecole Royale Militaire
Trilateral Euregio Cluster, Renaissancelaan 30 - B1000 Brussels - Belgium
Tel.: (32 2) 44 14 134, fax.: (32 2) 735 24 21, e-mail: d.van.eester@fz-juelich.de

ABSTRACT

A brief overview is given of the techniques adopted for modeling plasma heating and current drive as well as the associated particle diffusion. Weaknesses and strengths of each method are highlighted; references are provided for those seeking further information.

I. INTRODUCTION: THE BASIC EQUATIONS

Plasma heating by virtue of RF (radio frequency) waves can be looked at from two complementary points of view. From the wave's viewpoint plasma heating is a loss process. Solving the relevant wave equation, $\nabla \times \nabla \times \vec{E}/k_o^2 = \mathbf{K}.\vec{E} + i\vec{J}_a/\omega\epsilon_o = \vec{E} + i[\vec{J}_a + \vec{J}_p]/\omega\epsilon_o$ reveals where and to which particles the wave energy is lost. Here, $\vec{E}$ is the electric field, $\mathbf{K}$ is the dielectric tensor, ω is the driver frequency, and $\vec{J}_a$ and $\vec{J}_p$ are the antenna and plasma current densities. From the particle's point of view, plasma heating is the process of being accelerated or decelerated by an electric field. The net diffusion of particles resulting from this is described by the Fokker-Planck equation, $\frac{\partial F_o}{\partial t} = Q + C + S - L$ in which F_o is the distribution function, Q is the RF quasilinear diffusion term, C represents the effect of the Coulomb collisions, S is a source and L a loss term. Solving the coupled wave + Fokker-Planck equations involves tackling a 6-dimensional problem. Two - equivalent - approaches have been proposed to achieve this: the trajectory integral technique and the Hamiltonian formalism [1]. The key is to rewrite both equations in terms of shared "building blocks" describing the interaction of a particular wave component with a guiding center orbit. In absence of an external electric field, the orbits can be expressed in terms of 3 independent constants of the motion $\vec{\Lambda}$ and 3 angles $\vec{\Phi}$ (which - think of Hamiltonian action-angle variables - vary linearly with time and describe the rapid oscillatory aspects of the motion i.e. the poloidal bounce, the toroidal drift and the cyclotron motions). When wave power is injected, the $\vec{\Lambda}$ are no longer constant as a function of time. The coefficients of the Fokker-Planck equation require removing all fast time scale effects i.e. filtering out all oscillatory motion. Evaluating the dielectric response in the wave equation involves integrating over the velocity space coordinates. This can either be done recasting the wave equation in a form directly amenable for non-local treatment [2] or it can be done by writing down a local expression for the dielectric tensor (see e.g. [3, 4]). Since the wave and Fokker-Planck equations describe 2 aspects of the same physics, they should be solved as a coupled system of equations (see e.g. [5] and the references therein). Because of the complexity involved, they are, however, solved separately in most applications.

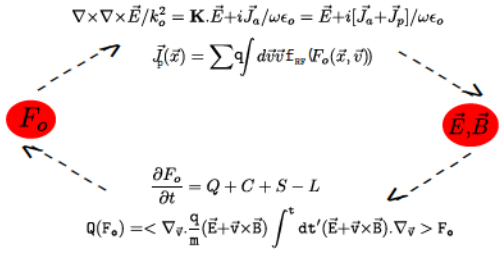

Figure 1: Schematic representation of self-consistent treatment of particle heating by electromagnetic waves.

II. WAVE DYNAMICS AND RAY TRACING

Lacking powerful computers allowing to solve the underlying equations truthfully, plasma heating was historically studied by making simplifications. The geometric optics or ray tracing method is a typical example. Its appealing simplicity results from the fact that

it decouples the coexisting branches of the dispersion equation and traces their characteristics independently. As it traces the evolution of a wave, it is a powerful technique for getting insight in the details of the wave-particle interaction. Ray tracing is based on the WKB assumption that the electric field of propagative waves can be written in the form

$$\vec{E} \propto exp[\sum_{n=0}^{\infty} \delta^{n-1} S_n(\vec{x})] \quad (1)$$

where δ is a small parameter and the S_n vary slowly as a function of $\vec{x}$. Consider the simple 1-dimensional equation

$$\mathsf{E}'' + k^2(x)\mathsf{E} = 0 \quad (2)$$

where E is some electric field component and $' = d/dx$. When k^2 is constant, E describes plane waves propagating in the x-direction: $\mathsf{E} = \mathsf{E}_o exp[\pm ikx]$. When k varies slowly as a function of x, a solution of the above wave equation in the form of the proposed WKB expression can be sought. Assuming k is of order $1/\delta$ and grouping the terms of like order in δ results in a system of equations for the S_n [6]:

$$(S_o'/\delta)^2 + k^2(x) = 0; 2S_o'S_1' + S_o'' = 0 \quad (3)$$

$$2S_o'S_n' + S_{n-1}'' + \sum_{j=1}^{n-1} S_j'S_{n-j}' = 0; n \geq 2 \quad (4)$$

Solving the first 2 equations above yields $\mathsf{E}_\pm \propto exp[\pm i \int dx k(x)]/k^{1/2}$. The WKB version of the conservation law associated with Eq.(1) can be written $(lnP)' = -2Im(k)$ where $P = Im(\mathsf{E} * \mathsf{E}') = Re(k)|\mathsf{E}|^2$.

Reinserting Eqs.(3-5) into Eq.(1) shows that the WKB solution is a good approximation if $|3/4(k'/k)^2 - 1/2k''/k| << |k^2|$ i.e. that the WKB ordering is justified when short wavelength waves are studied but that it breaks down near cutoffs ($k = 0$) and resonances or confluences ($k' = \infty$).

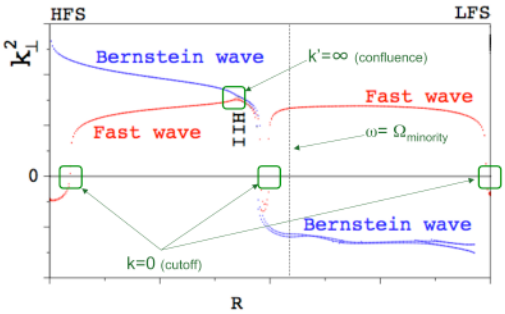

Figure 2: Dispersion plot with locations at which WKB breaks down.

Ray tracing is the multidimensional equivalent of the above scheme. Using the geometric optics definition $\vec{k} = \nabla\psi$ of the wave vector (ψ being the wave phase), the lowest order equation is the Fourier transformed wave equation for a homogeneous medium,

$$\mathbf{G}.\vec{E}_o = \vec{k} \times \vec{k} \times \vec{E}_o + k_o^2 \mathbf{K}.\vec{E}_o = \vec{0}. \quad (5)$$

Nontrivial solutions exist when the dispersion equation $D = det(\mathbf{G}) = 0$ is satisfied. The different dispersion equation roots and their eigenvectors correspond to the different decoupled waves the plasma supports. The evolution of these waves is visualized via the method of characteristics. The characteristics or rays, by definition, are given by the equations

$$d\vec{x}/d\tau = -\partial D/\partial \vec{k}; d\vec{k}/d\tau = +\partial D/\partial \vec{x} \quad (6)$$

where τ is a variable that changes monotonically along the rays. When the dispersion is satisfied in one point on a ray, it is satisfied in all others ($\delta D = 0$). The variable τ can be linked to the physical time t through the transformation $dt = \partial D/\partial\omega d\tau$. The ray equations then become

$$d\vec{x}/dt = \partial\omega/\partial\vec{k}; d\vec{k}/dt = +[\partial D/\partial\vec{x}]/[\partial D/\partial\omega] \quad (7)$$

The first equation states that the ray's velocity is the energy propagation or group velocity $\vec{v}_g = \partial\omega/\partial\vec{k}$ and the second shows how the wave vector changes as a result of the background variations sensed by the ray. The ray equations can, strictly spoken, only be adopted when the plasma is lossless: as soon as dissipation is present, D is complex so the ray path is no longer a real trajectory. To overcome this problem the damping is assumed to be weak such that the anti-Hermitian part $\mathbf{K}^A$ of the dielectric tensor is of order δ compared to the Hermitian part $\mathbf{K}^H$ which allows to replace D by D^H in the above equation. A power transport equation, $dlnP/dt = [dlnP/d\vec{x}].[d\vec{x}/dt] = -2Im(\vec{k}).\vec{v}_g$, generalization of the earlier mentioned conservation law, is added to the system (see e.g. [7]).

The WKB approximation is very useful when the wavelength of the waves is short w.r.t. the machine size. The fact that it breaks down near cutoffs, confluences and resonances is, however, a drawback limiting the ray tracing method's applicability. To overcome such problems one can try to solve the wave equation without making any a-priori assumptions on the dependence of $\vec{E}$ on $\vec{x}$. In the next two sections we discuss how differential equations or partial differential equations can be solved by transforming them into algebraic ones.

III. THE FINITE DIFFERENCE METHOD

Of all methods to tackle partial differential equations, the finite difference approach is probably the one

that is most easily implemented. It is frequently used, both for studying wave and particle dynamics. It consists in replacing the partial differential operators in the equation and the boundary conditions by their finite difference counterparts. Doing so at each of the inner grid points and imposing the boundary conditions at the edge points, the differential problem is hereby reduced to an algebraic one that can be solved using standard matrix algebra techniques. Because the finite difference formulae only involve a small number of values of the unknown function(s) at neighbouring points, the matrices of the algebraic system are sparse. Dedicated algorithms accounting for this allow to save CPU time. Finite difference expressions for the various operators can be taken "off the shelf" (see e.g. [8]) or be auto-constructed from the truncated Taylor series expansion

$$G \approx \sum_{n=0}^{N} \frac{\hat{G}_n (x - x_o)^n}{n!} = \sum_{j=0}^{N} \alpha_j G(x_j) \qquad (8)$$

where x_o is the point for which the N-point difference scheme is constructed, and the coefficient $\hat{G}_n$ can be identified with the n-th derivative of G at x_o if $n \to \infty$ and if x is sufficiently close to x_o. The values of the function at x_o and at N neighboring grid points are used to write down a linear system of $N+1$ equations for finite difference approximations of up to the first N derivatives at x_o. Non-uniform grids are automatically accommodated for but the best performance for a given number of points is obtained using a uniform grid centered on x_o. Invoking more neighbors allows eliminating lower order contributions in the expansion: The 2-point forward scheme for the first derivative is of first order. Including the backward contribution allows to compensate the first order contribution and results in a second order accurate scheme. Doing the same for the next neighbors yields the third order scheme $(G_{-2} - 8G_{-1} + 8G_{+1} - G_{+2})/12\Delta x$ for the first derivative, etc.

III.A. Stability of finite difference schemes

Lacking sufficiently general theorems, stability analysis of a numerical scheme is often done by trial and error. The diffusion equation $\Delta\psi(\vec{x}, t) = \partial\psi/\partial t$ can be solved analytically and is sufficiently simple to perform the stability analysis for various finite difference schemes. Let us start from the 1-D version and impose Dirichlet conditions $\psi = 0$ at $x = 0$ and $x = 1$, and $\psi = \psi_o(x)$ at $t = 0$. Through Fourier analysis one finds $\psi = \sum_{k=1}^{\infty} \alpha_k exp[-k^2 t] sin[kx]$, the Fourier coefficients α_k in which are those of ψ_o. Note that high k-modes disappear fast from the exact solution when time advances. Morton and Mayers [9] examined the numerical stability of various finite difference schemes for this equation by adopting a uniform grid in both $x = j\Delta x$ and $t = n\Delta t$, and introducing the "amplification factor" λ to study the evolution of the numerically obtained kth Fourier mode, $\psi_j^n = \lambda^n exp[ikj\Delta x]$. For the explicit forward scheme $\psi_j^{n+1} = \psi_j^n + \nu\delta_x^2\psi^n$ in which $\nu = \Delta t/\Delta x^2$ and $\delta_x^2\psi^n = \psi_{j+1}^n - 2\psi_j^n + \psi_{j-1}^n$, one finds $\lambda = 1 - 4\nu sin^2 k\Delta x/2$. Hence, when $\nu > 0.5$ this solution numerically grows in time, although the true solution does not! The fastest growing mode is characterized by a phase jump of π in between successive grid points. It eventually dominates the numerical solution. As the spatial grid scale is determined by the spatially fastest varying modes in the differential system, one is forced to make sufficiently small steps in time to avoid these unphysically growing solutions. To avoid having to take too small time steps, implicit rather than explicit schemes are adopted. Replacing the forward difference by a backward difference in the above we obtain the scheme

$$-\nu\psi_{j-1}^{n+1} + (1 + 2\nu)\psi_j^{n+1} - \nu\psi_{j+1}^{n+1} = \psi_j^n \qquad (9)$$

In contrast to the forward scheme, time stepping now requires the inversion of a matrix. This extra amount of work pays off, however: one finds that λ is now of the form $\lambda = 1/[1 + 4\nu sin^2 k\Delta x/2]$. Since $0 \leq |\lambda| \leq 1$ for any ν, this scheme is unconditionally stable.

The above two schemes either use 3 points at the previous time level, or 3 at the new time level. A straighforward generalisation consists in using all 6 of these points i.e. in adopting the scheme $\psi_j^{n+1} - \psi_j^n = \nu[\theta\delta_x^2\psi^{n+1} + (1-\theta)\delta_n^2\psi^n]$ which is known as the θ-method. This scheme is conditionally stable if $\theta < 1/2$ and unconditionally stable if $1/2 \leq \theta < 1$. The first regime imposes that $\nu \leq 0.5/(1 - 2\theta)$ while ν is unconstrained for the second. Whereas the difference scheme is usually of first order in time, the scheme is second order accurate both in position and time when $\theta = 1/2$. This particular scheme is due to Crank and Nicolson.

III.B. Practical example

Applying a finite difference scheme to the time dependent Fokker-Planck equation yields a system of the form

$$\partial\vec{X}/\partial t = \mathbf{A}.\vec{X} - \vec{b} \qquad (10)$$

in which the contributions not involving F_o are grouped in the source term $\vec{b}$ and the values of F_o at the grid points are stored in $\vec{X}$. When adopting the Crank-Nicolson method, the algebraic system takes the form

$$\vec{X}(t + \Delta t/2) = \mathbf{C}^{-1}.\vec{d}; \mathbf{C}{=}\mathbf{1} - \Delta t/2\mathbf{A}; \qquad (11)$$

$$\vec{d} = [1 + \Delta t/2\mathbf{A}].\vec{X}(t - \Delta t/2) - \Delta t\vec{b} \qquad (12)$$

If $\mathbf{A}$ is time independent, the $\mathbf{C}$ matrix can be inverted once and for all. The "source" $\vec{d}$ has to be updated at

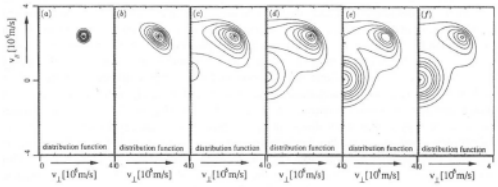

Figure 3: Time evolution of a beam population from the moment the particle source is switched on up to when the stationary state is reached, at which time the beam consists of a Maxwellian sub-population and a non-thermal sub-population centered on the source.

each time step, independent of the actual source term $\vec{b}$ being independent of time or not.

IV. THE FINITE ELEMENT METHOD

IV.A. Variational techniques

Requiring somewhat more preparation and bookkeeping than the finite difference method but allowing a better control on the overall numerical error, the finite element method is probably the most robust numerical technique for solving differential or integro-differential problems. To discuss this technique, we will again focus on Eq.(2). The finite element technique relies on a variational principle [10, 11]. Consider the functional

$$I(\mathrm{E}) = \int_{x_1}^{x_2} dx[-\mathrm{E}'^2 + k^2\mathrm{E}^2] + \hat{S} \quad (13)$$

$$\hat{S} = A_2\mathrm{E}^2(x_2) + B_2\mathrm{E}(x_2) - A_1\mathrm{E}^2(x_1) - B_1\mathrm{E}(x_1) \quad (14)$$

Allowing for a small variation of E, one observes that the linear perturbation of the functional is stationary for the function E obeying Eq.(2) and satisfying the boundary conditions $\mathrm{E}'(x_{1,2}) = A_{1,2}\mathrm{E}(x_{1,2}) + B_{1,2}/2$.

The Ritz approach to solve the equation consists in writing E in terms of a set of base functions $\mathrm{E}(x) = \sum_{j=1}^{J} c_j\Theta_j(x)$ and imposing I to be stationary for all j: $\partial I/\partial c_j = 0$. Provided the integrals involving the base functions can be evaluated, this reduces the problem of integrating the wave equation to solving the (linear) system for the c_j. Although base functions allowing to evaluate the integrals over the full domain exist (see section V), one often prefers to subdivide the interval $[x_1, x_2]$ into a large number N of sub-regions and to use low order polynomials with restricted range such that the integrals can be approximated e.g. using the integration method of Gauss [8]. When J base functions are considered in each interval, a total of NJ linear equations for the NJ unknown coefficients is obtained by imposing all stationarity conditions. In case the grid is so dense that coefficients of the original equation hardly vary in a single finite element, their variation can be omitted altogether and the integrals only involving base functions can then be done once and for all.

The Ritz approach seems cumbersome as prior to actually solving the equation, one first needs to find the functional I and derive the stationarity conditions. These 2 steps can be omitted when adopting the Galerkin approach, which consists of multiplying the differential equation with each of the base functions Θ_j, and integrating over the domain of interest. The resulting system is again a linear system that can be solved to find the c_j. The disadvantage of this strong approach is that the Θ_j need to have meaningful nth derivatives for an nth order equation. Lower order polynomial base functions can be chosen when tackling the problem in its weak form i.e. after removal of the highest order E-derivative terms from the integrand by performing partial integrations. Imposing the boundary conditions via the surface term, one readily finds that the weak Galerkin approach is equivalent to the Ritz approach.

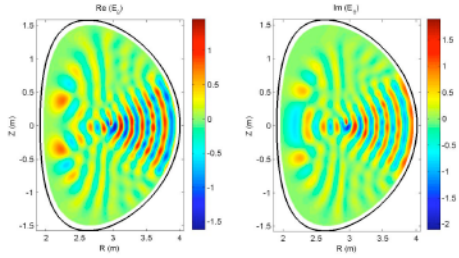

Figure 4: RF wave pattern for (H)-D heating at 3.45T and 51MHZ in JET, computed using finite elements on a 2-D mesh of triangles. The RF field propagates from the antenna on the low field side to the core, where it is damped near the central H cyclotron layer.

IV.B. Natural vs. essential boundary conditions

Natural boundary conditions can directly be derived from the weak variational form of the equation. The strong form is obtained by multiplying the equation by a sufficiently smooth test function G and integrating it over a finite interval. Partial integration is used to remove higher order derivatives from the unknown function and "transfer" them to derivatives of the test function. For a 1D differential equation of order n, $n/2$ derivatives can be removed from the unknown. The surface terms arising from these partial integrations involve the test function itself as well as its higher order derivatives up to $n/2-1$. Choosing a test function

with only 1 nonzero mth derivative ($0 \leq m \leq n/2-1$) at one of the two edges provides a set of $n/2$ "natural" boundary conditions at each edge, corresponding to "fluxes" entering or leaving the domain of interest. Imposing these at the two edges provides the exact number n of boundary conditions to uniquely define the solution (see e.g. [12]). Natural boundary conditions are intimately connected with the equation. Deriving the natural boundary conditions of the Laplace equation in the domain ($x_1 \leq x \leq x_2, y_1 \leq y \leq y_2, z_1 \leq z \leq z_2$) by multiplying the equation by a test function G, integrating over the volume, performing a partial integration and identifying $G = 1$, one finds

$$\int dydz \frac{\partial \psi}{\partial x}|_{x_1}^{x_2} + \int dxdz \frac{\partial \psi}{\partial y}|_{y_1}^{y_2} + \int dxdy \frac{\partial \psi}{\partial z}|_{z_1}^{z_2} = 0 \tag{15}$$

imposing that the imposed Neumann boundary conditions should be consistent with the equations i.e. that they must guarantee that the net influx balances the net outflux, no losses being present.

Boundary conditions imposed on lower order ($< n/2$) derivatives cannot be derived from the equation itself, and cannot be imposed via the surface term. To impose such conditions another procedure is required. One common solution is to choose the base functions in such a way that the conditions in question are automatically fulfilled. Because of their more basic nature, the second type of boundary conditions is known as "essential" conditions.

To solve a differential equation, we transformed it into a linear system. When the original equation is an integro-differential instead of a differential equation, exactly the same method can be used, the only difference being that also integrals of products of base functions and not just derivatives appear inside the variational integral. In that case, the linear system is generally not sparse.

IV.C. Numerical pollution

The finite element technique relies on the local approximation of the solution of an equation by a sum of simple base functions. Aside from truncation errors which automatically creep into the system, such approximations can lead to numerical pollution i.e. to the excitation of modes lacking a physical counterpart. The vacuum wave equation

$$(k_{//}^2 - k_o^2)E_x + ik_{//}E_z' = 0 \tag{16}$$

$$(k_{//}^2 - k_o^2)E_y - E_y" = 0 \tag{17}$$

$$ik_{//}E_x' - k_o^2 E_z - E_z" = 0 \tag{18}$$

suffices to demonstrate this effect [13]. In the above, it can be noted that E_x plays a different role than E_y or E_z: the highest order derivative of E_x appearing in the system is one order lower than that for E_y and E_z. Knowing that the exact solutions of the vacuum wave equation are proportional to $exp[ik_x x]$ where $k_x^2 = k_o^2 - k_{//}^2$ we make the ansatz $\vec{E}(\vec{x}) = \sum_j exp[ik_x x_j]\vec{\eta}_j$ where the x_j are the grid points and $\vec{\eta}_j$ the vectors of base functions. The discretized dispersion equation is the condition for having nontrivial solutions. Adopting the obtained equation for linear base functions, Sauter demonstrated that the physical root is well approximated by two of the numerical dispersion roots when the grid is sufficiently refined (small enough $k_x \Delta x$) but that the agreement is less good when $k_x \Delta x$ well exceeds 1. A third, purely numerical, root further spoils the solution. Reminding that E_x is differentiated one time less in the wave equation, Sauter subsequently considered constants for E_x while using linear functions for E_y and E_z. Although one expects intuitively that such cruder procedure would lead to less accurate results, he demonstrated that - quite on the contrary - the solution is now no longer polluted. One might hope that the spectral pollution problem automatically resolves itself when a more refined description (higher order polynomials as base functions) is used. It turns out that this is not the case. One finds exactly the same problem when using higher order polynomials for all components. Again, pollution can be removed choosing polynomials for E_x which have 1 degree of freedom less than those taken for E_y and E_z. Adding finite Larmor radius (temperature) effects to the wave equation destroys the special role E_x plays and eliminates this particular problem of pollution.

IV.D. Grid refinement techniques

One of the peculiarities of finite elements is that is allows squeezing and stretching local finite elements, which enables describing phenomena with vastly different length scales accurately by merely reshuffling the adopted grid but without touching the structure of the local equations. Hence, rather than opting for a more complete set of base functions enabling to capture more dynamics on a fixed grid but increasing the number of local 'projection' equations, code developers often prefer to refine the grid at locations where it is needed while keeping the base functions as simple as possible. This guarantees that CPU memory is optimally used: at every location the adopted grid is just fine enough to reach the desired accuracy level, but regions not requiring a fine grid are not densely populated with grid points. Various grid refinement techniques are available in the literature, and more often than not grid generating software can be found on the www. One of the classical techniques of grid refinement is the so-called 'red-triangle/green-triangle' technique [14] adopted when subdividing the domain of interest for a 2-D problem into a set of triangles. When local

gradients are too steep inside a triangle (e.g. the triangle with black thick lines in Fig. 5), it is subdivided into 4 child-triangles born when dividing each of the 3 sides of the parent-triangle in 2 and connecting these 3 midpoints. If refinement in a neighboring triangle is required as well, the same technique is applied there while if no refinement is needed, the midpoint of the side is just connected to the opposite triangle corner (green triangle) to ensure the topology of the mesh is not changed.

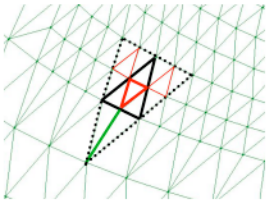

Figure 5: 'Red-green triangle' grid refinement scheme. Thick solid line: 'parent' triangle, subdivided into 4 child-triangles. Dotted lines: neighbor triangles with 'red' or 'green' subdivisions.

V. SPECTRAL METHODS: DIRECT FOURIER REPRESENTATION

As the set of exponential functions $exp(ikx)$ is complete, any (sufficiently continuous) function of the variable x can uniquely be represented by its k-spectrum. In a finite domain $[x_o, x_o + L_x]$, the coordinate x can then be related to the angular variable $\theta = 2\pi x/L_x$ and the spectrum of modes m is discrete. Although any function can be represented using the exponential set with a global error that is arbitrarily small, the spectrum of non-periodic functions decays so slowly as a function of m that one can wonder if the spectral method is the appropriate tool for tackling problems involving such functions. At the edge discontinuities the series will never converge, although taking enough terms allows to find the correct value up to very close to the edge (Gibbs phenomenon). When all functions are periodic, the Gibbs phenomenon is absent and spectral representation is more appropriate. Consider again Eq.(2), $d^2\psi/d\theta^2 + M^2(\theta)\psi = 0$, for convenience rewritten in terms of the angular variable θ. Finding the Fourier spectrum of M^2, $M^2(\theta) = \sum_{l=-\infty}^{+\infty} M_l^2 exp[im\theta]$, and projecting on the exponential base yields

$$-m^2\psi_m + \sum_{l=-\infty}^{+\infty} M_l^2 \psi_{m-l} = 0 \qquad (19)$$

for each m in the spectrum. Truncating the spectrum of the coefficient M^2 yields a sparse but infinite set of non-trivial equations to be solved simultaneously. For large $|m|$ ($m^2 >> M_l^2$), the first term dominates the others, guaranteeing the Fourier series of ψ is convergent and justifying to truncate the spectrum. Through M^2, the physics of the problem dictates the minimal number of modes to be retained in the truncated spectrum: For the simple case of a constant M^2, the above equation prescribes that ψ_m must be zero unless $m^2 = M^2$. More generally, this filtering makes that part of the physics is not captured by the model if the spectrum is truncated at a too low m-value (see also in the next section). A practical example is the treatment of electron (Landau + TTMP) damping in the ion cyclotron range of frequencies: the damping strength being proportional to the square of the local perpendicular wave number $k_\perp$, this damping is underestimated by a model that does not properly resolve the Bernstein wave mode, a mode for which $k_\perp$ is of the order of the inverse of the ion Larmor radius.

The spectral representation is commonly used for numerical applications posed in finite domains but is, by its nature, best suited to be adopted in wave problems. A spectral method in periodic variables is often combined with a finite element representation in the non-periodic variables.

The SciDAC project [15] gave a major thrust to RF modeling in the USA. Thanks to powerful computers and the adoption of Fourier techniques, wave problems have been solved that were off-limits before: Brambilla's TORIC has been upgraded to enable accounting for up to 10^4 poloidal modes simultaneously so that the fate of short wavelength branches can now be examined in detail (see e.g. [16]), and Jaeger's integro-differential AORSA code now solves the wave equation both for Maxwellian as for non-Maxwellian populations (see e.g. [17]).

VI. FAST FOURIER TRANSFORM & ALIASING

The spectral method relies on the fact that the Fourier spectra of the coefficients of the equation are known. In general the coefficients are known locally, but the spectrum is not. Finding the poloidal spectrum of functions needed to solve the 2-D or 3-D wave equation in tokamak geometry can be done relying on the smallness of the minor radius a_p w.r.t. to the major radius R_o, by writing out the various terms explicitly up to a given order in the inverse aspect ratio a_p/R_o. This procedure soon becomes cumbersome, however, and since a_p is not so small w.r.t. R_o, many terms in the development should be retained for a reasonable approximation. In practice, the Fourier components

$F_m = \frac{1}{2\pi}\int_0^{2\pi} d\theta exp[-im\theta]f(\theta)$ of any needed quantity f are most often evaluated numerically. Adopting a uniform grid, the Fourier integral is approximated by the sum $F_m \approx \frac{1}{J}\sum_{j=1}^{J} exp[-imj\Delta\theta]f(j\Delta\theta); \Delta\theta = \frac{2\pi}{J}$ This technique is known as the fast Fourier transform (FFT). Note that the predicted value for the mth Fourier component is identical to that of $m - nJ$ where n is any integer. This means that the above procedure artificially misrepresents high m-modes by their lower mode number spectrum counterparts for which $J/2 < m - nJ \leq J/2$, an effect known as "aliasing" (see also [18]). To avoid aliasing, the whole spectrum should fall inside the interval $[-J/2, J/2]$. The corresponding grid has at least 2 mesh points per wavelength for the shortest wavelength mode in the system.

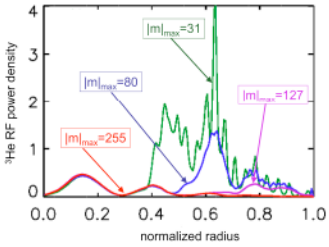

Figure 6: The importance of ensuring the full wave spectrum is sampled: power deposition profiles obtained truncating the poloidal mode spectrum at $|m| = 31$, $|m| = 80$, $|m| = 127$ and $|m| = 255$ (TORIC, Courtesy P. Bonoli).

VII. MONTE CARLO AND PARTICLE-IN-CELL TECHNIQUES

Integration in multidimensional space can be done efficiently relying on the Monte Carlo technique, which in contrast to adopting a regular grid uses a set of uniformly distributed *random* points. Adopting this procedure, the integral of a function in hyperspace is predicted up to errors of order $N^{-1/2}$, where N is the number of randomly generated positions, irrespective of the number of dimensions (while the accuracy of the prediction made on a uniform grid scales as $1/N^{1/d}$, where d is the number of dimensions). In order to simultaneously solve the wave and the Fokker-Planck equations, Hedin developed the SELFO code. He upgraded the LION wave code [15] to account for the actual drift orbits of the particles and for non-Maxwellian distribution functions by locally approximating the dielectric tensor using a series of "hat" functions [16], and interfaced the resulting code with the FIDO Monte Carlo code [17].

The FIDO Monte Carlo method advances a large number of test particles in time $\vec{\Lambda}(t_{n+1}) = \vec{\Lambda}(t_n) + \Delta\vec{\Lambda}$ and accounts for wave-particle interaction and for Coulomb collisions assuming the $\vec{\Lambda}$ are stochastic variables whose expectations E and co-variances C can be inferred from the orbit-averaged Fokker-Planck equation:

$$E[\Delta\Lambda_i] = \frac{d\mu_i}{dt}\Delta t; C[\Delta\Lambda_i, \Delta\Lambda_j] = \frac{d\sigma_{ij}}{dt}\Delta t \qquad (20)$$

in which $< ... >= \int d\vec{\Lambda} F_o ...$ is the ensemble average, $\mu_i =< \Lambda_i >$ and $\sigma_{ij} =< (\Lambda_i - \mu_i)(\Lambda_j - \mu_j) >$. The Monte-Carlo operator becomes

$$\Delta\Lambda_i = \frac{d\Lambda_i}{dt}\Delta t + \sum_k A^{ik}\xi_k(\Delta t)^{1/2} \qquad (21)$$

in which $\sum_k A^{ik}A^{jk} = d\sigma_{ij}/dt$ and where ξ_k are uncorrelated stochastic variables with zero expectation value and unity variance.

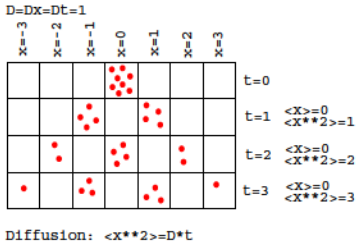

Figure 7: The principle of random walk / diffusion.

VIII. CONSERVATION LAWS

Conservation laws are often helpful when checking the precision of a computation. For Eq.(2) one readily sees that $S = Im[E * dE/dx]$ is conserved when k^2 is real i.e. in absence of damping. When damping is present the drop in "flux" S across the considered interval equals the integrated "absorbed power" $P_{abs} = Im(k^2)|E|^2$. In differential form the thus obtained conservation law is of the form $\nabla.\vec{S} + P_{abs} = 0$. Adopting a variational approach one can formulate the wave equation in such a conservative form i.e. in a form which readily yields this conservation law upon substituting the sufficiently smooth test function vector by the electric field (see e.g. [18]). The Fokker-Planck equation is written in the above conservative form from the start: rewriting it in variational form (see e.g. [23]), one can express the conservation of the total number of particles (test function $G = 1$) or of the energy ($G = mv^2/2$). When the wave and Fokker-Planck models are consistent one with the other, the

conservation laws of the 2 equations share the expression for the absorbed wave power (see e.g. [1]).

Of course, conservation laws merely allow to check the numerical accuracy of a model, but do in themselves *not* constitute a check on the correctness or on the applicability of the model $itself$. Aside from performing convergence tests to ensure the shortest scale lengths are well captured, a-posteriori checks of the assumptions underlying the derivation of an equation should be performed: it is e.g. common to adopt a truncated finite Larmor radius (FLR) expansion to include temperature effects but one rarely discards the predictions on the fate of the power carried by the short wavelength (Bernstein) modes away from the (confluence) region, notwithstanding the fact that the wave violates the starting FLR assumption ...

IX. DECIDING ON A NUMERICAL STRATEGY

The speed and memory size of present day computers allow to pursue a high degree of realism in plasma physics models. Because of this high level of sophistication, it is crucial to be able to distinguish between actual physics and numerical artefacts. Jaun and collaborators have developed a very didactic, interactive and flexible tool to highlight the perspectives and drawbacks of various numerical schemes [18]. Existing commercial or freeware software libraries such as IMSL, HSL, NAG and NetLib allow to concentrate on physics instead of on numerics. In case no ready-made subroutines can be pulled "off the shelf", softwares such as OCTAVE, MATLAB and MATHEMATICA are of great help in constructing one's own numerical schemes.

REFERENCES

1. D. VAN EESTER, Plasma Phys. Contr. Fusion **41**, L23 (1999)
2. P.U. LAMALLE Plasma Phys. Contr. Fusion **39**, 1409 (1997)
3. R. KOCH, Phys.Lett.A **157**, 399 (1991)
4. D. VAN EESTER, Plasma Phys. Contr. Fusion **35** 1309 (1993)
5. D. VAN EESTER, Journal of Plasma Physics **65** 407 (2001) and the references therein
6. C. BENDER and S. ORSZAG, Advanced mathematical methods for scientists and engineers, Mc Graw Hill, New York (1978).
7. V.P. BHATNAGAR et al., Nuclear Fusion **24**, 955 (1984)
8. M. ABRAMOWITZ, I.A. STEGUN, Handbook of Mathematical Functions, Dover, New York (1972)
9. K.W. MORTON, D.F. MAYERS, Numerical Solution of Partial Differential Equations, CUP, Cambridge (1994)
10. G. STRANG and G.J. FIX, An Analysis of the Finite Element Method, Prentice Hall, Englewood Cliffs (1973).
11. R. GRUBER and J. RAPPAZ, Finite Element Methods in Linear Ideal Magnetohydrodynamics, Springer-Verlag, New York (1985).
12. D. VAN EESTER, R. KOCH, Plasma Phys. Contr. Fusion **43**, 1 (2001)
13. O. SAUTER, Nonlocal Analyses of Electrostatic and Electromagnetic Waves in Hot, Magnetized, Nonuniform, Bounded Plasmas, LRP-457/92, Ecole Polytechnique Fédérale de Lausanne (1992).
14. G. HEBER, R. BISWAS, G.R. GAO, Self-Avoiding Walks over Two-Dimensional Adaptive Unstructured Grids, CAPSL Technical Memo 21, University of Delaware (1998)
15. D.B. BATCHELOR, Integrated Simulation of Fusion Plasmas, Physics Today, **02/05**, 35 (2005)
16. J.C. WRIGHT et al., Phys. Plasmas **11**, 2473 (2004)
17. E.F. JAEGER et al., Phys. Plasmas **13**, 056101 (2006)
18. O. JAUN, J. HEDIN, T. JOHNSON, Numerical methods for partial differential equations: an overview and applications, Report TRITA-ALF-1999-05, Royal Institute of Technology, Stockholm (1999-2000); downloadable from http://www.lifelong-learners.com/pde
19. L. VILLARD et al., Comput. Phys. Rep. **4**, 95 (1986)
20. J. HEDIN, Ion Cyclotron Heating in Toroidal Plasmas, Ph.D. thesis, Royal Institute of Technology, Stockholm (2001)
21. J. CARLSSON, ICRH Heating and Current Drive in Tokamaks, Ph.D. thesis, Royal Institute of Technology ISBN 97-7107-237-7 (1998)
22. D. VAN EESTER, R. KOCH, Plasma Phys. Contr. Fusion **40**, 1949 (1998)
23. D. VAN EESTER Proc. 7th Eur. Fus. Theory Conf., Julich **1**, 283 (1997)

ELECTRON CYCLOTRON WAVES*

Egbert Westerhof

DIFFER, Dutch Institute for Fundamental Energy Research,
De Zaale 20, 5612 AJ Eindhoven, the Netherlands, www.differ.nl

* These lecture notes are updated from those appearing under the same title in proceedings of the 10th-13th Carolus Magnus Summer School

ABSTRACT

This lecture gives an overview of heating and current drive with electron cyclotron waves. We present the main theoretical aspects of wave propagation, wave absorption, and non-inductive current drive, as well as important technical aspects for the application of high power electron cyclotron waves, and the major achievements in their experimental application.

I. INTRODUCTION

Electron cyclotron waves are electromagnetic waves with a frequency in the range of the electron cyclotron frequency. For a given magnetic field the electron cyclotron frequency is 28 B [T] GHz. This means that for a typical field of 4 T or in case of second harmonic resonance and a field of 2 T, we are dealing with frequencies of the order of 100 GHz and, consequently, wavelengths of a few mm. In this frequency range, the waves can be injected from vacuum in the form of well-focused beams with higher power densities than achieved by any of the other additional heating methods (like neutral beams, ion cyclotron or lower hybrid waves). Moreover, these beams can be injected from steerable mirrors towards different parts of the plasma. Because the coupling of the power to the plasma is the result of a resonant interaction with the electrons, the power deposition in the plasma is localized. This combination of narrow, steerable beams and localized power deposition is unique for electron cyclotron resonance heating (ECRH) and current drive (ECCD). It is also what has given ECRH and ECCD its unique tasks among the other additional heating systems, in particular, for the control of instabilities. Excellent reviews of ECRH and ECCD can be found in Refs [1-4].

II. THEORETICAL ASPECTS

II.A. Wave Propagation.

A basic impression of wave propagation in the electron cyclotron range of frequencies is obtained by analysis of the cold plasma dispersion. The relevant dispersion relation is known as the Appleton-Hartree dispersion relation and is given by

$$N^2 = 1 - \frac{\omega_p^2}{\omega^2}\frac{2(\omega^2-\omega_p^2)}{2(\omega^2-\omega_p^2)-\omega_c^2(\sin^2\theta \pm \rho)} \qquad (1)$$

with

$$\rho^2 = \sin^4\theta + 4\cos^2\theta\left(\frac{\omega^2-\omega_p^2}{\omega-\omega_c}\right)^2,$$

where ω is the wave frequency, $\omega_p \equiv (n_e e^2/\varepsilon_0 m_e)^{1/2}$ the electron plasma frequency, $\omega_c \equiv eB/m_e$ the electron cyclotron frequency (defined positive here) and θ is the angle between the wave vector and the magnetic field. The + and − signs refer to the two possible modes of propagation which are known as the extraordinary or X-mode and ordinary or O-mode, respectively.

Because of toroidal symmetry, RN_ϕ is a conserved quantity along the trajectory of wave propagation. This means that the parallel refractive index, $N_\parallel$, is an approximate constant as well, such that the accessibility of the plasma to electron cyclotron waves can be gleaned from inspection of dispersion curves for the perpendicular wave vector at constant $N_\parallel$ (see Figure 1). Wave cut-offs and resonances can be conveniently defined as cut-offs and resonances of the perpendicular refractive index, i.e. $N_\perp = 0$ and $N_\perp = \infty$, respectively. The O-mode is seen to have a single branch with a cut-off at the plasma frequency ω_p. The X-mode has a right hand, ω^+, and a left hand cut-off, ω^-, and is split into two branches by an evanescent region between the right hand cut-off and the Upper-Hybrid resonance, ω_{UH}. The right hand and left hand cut-offs are given by

$$\omega^\pm \equiv \pm\tfrac{1}{2}\omega_c + \sqrt{(\tfrac{1}{2}\omega_c)^2 + \omega_p^2/(1-N_\parallel^2)}\,, \qquad (2)$$

while the Upper Hybrid resonance is

$$\omega_{UH} \equiv \sqrt{\omega_c^2 + \omega_p^2}\,. \qquad (3)$$

The upper X-mode branch $\omega > \omega^+$, which is characterized by faster–than–light phase velocities, is known as the fast X-mode branch, while the other branch limited from above by the Upper Hybrid resonance and from below by the left hand cut-off, ω^-, is the slow X-mode.

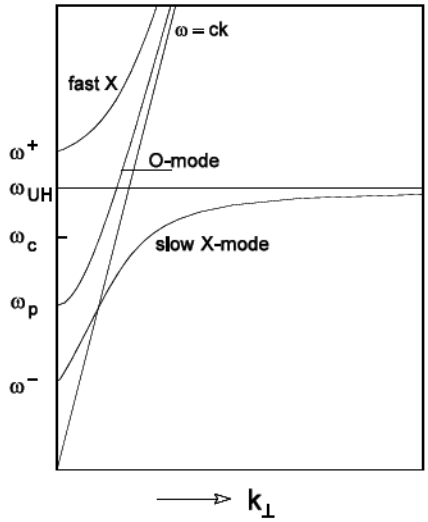

***Figure 1:**. The dispersion diagram of high frequency electromagnetic waves is sketched for an under dense plasma, i.e. $\omega_p < \omega_c$. The O-mode is seen to propagate for $\omega > \omega_p$, while the X-mode has two cut-offs $\omega^{+,-}$ and a resonance at ω_{UH}.*

These wave modes are characterized by their polarization. For perpendicular propagation, the electric field of the O-mode is parallel to the equilibrium magnetic field, and X-mode polarization is perpendicular to the magnetic field. Near the cyclotron resonance, the X-mode attains a large electrostatic contribution, which minimizes the interaction with the right handedly gyrating electrons, i.e. the perpendicular X-mode becomes left handed. Efficient absorption of X-mode at the fundamental resonance requires oblique injection of the waves or a very high plasma temperature.

Wave accessibility

In a tokamak the magnetic field is approximately inversely proportional to the major radius, $B \propto 1/R$, and the density usually rises monotonically from the edge to the magnetic axis. This leads to a picture of the wave cut-offs and resonances inside the plasma as sketched in Fig. 2. For the X-mode two cases are shown with either the fundamental or second harmonic resonance inside the plasma. The former case is characterized by the presence of an evanescent layer in between the right hand cut-off and the Upper-hybrid resonance, which shields the fundamental resonance from waves injected from the low field side. Fundamental X-mode heating is only possible with high field side (HFS) launch. The accessibility for second harmonic X-mode and fundamental O-mode is similar. They are in cut-off when either the right hand cut-off (2X) or plasma frequency (O), exceeds the wave frequency. Thus, waves injected from any direction can reach the resonance as long as the

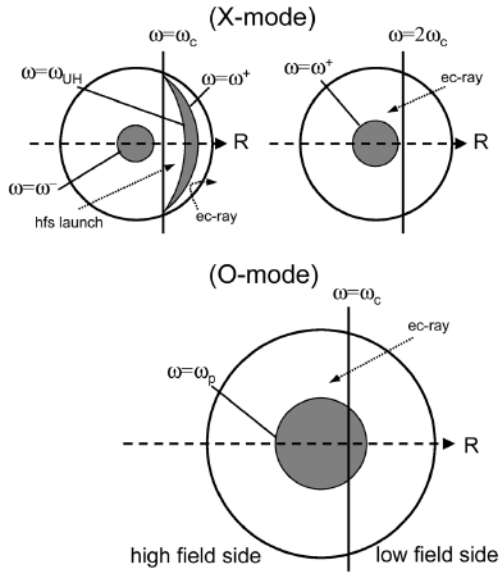

***Figure 2:** Wave cut-offs and resonances in a poloidal cross section of a tokamak plasma. The upper figure shows two X-mode cases with either the fundamental or second harmonic resonance inside the plasma. The lower figure shows the fundamental O-mode. A high central density is assumed in all cases such that all relevant cut-offs are in the plasma. Gray regions are evanescent. Dotted curves sketch possible wave trajectories. The dashed line indicates the major radius, R.*

resonance itself is not inside a cut-off region. As densities come close to cut-off, wave refraction will play an important role. Evaluation of actual wave trajectories requires detailed ray-tracing calculations.

II.B. Wave Absorption

It is straightforward to see how a right handed gyrating electron, satisfying the resonance condition

$$\omega = \omega_c / \gamma + k_{\parallel} v_{\parallel} \tag{4}$$

is continuously accelerated in the vertical direction by a right handed polarized electric field. At the same time one easily sees that for other harmonics or a parallel electric field the interaction always averages to zero unless the wave has a finite perpendicular wave number and the electron a finite Larmor radius ρ_e. We will illustrate this by the example of the equation of motion of an electron in a perpendicularly propagating O-mode, $E_{\parallel} \cos(k_{\perp} x - \omega t)$,

$$\dot{p}_{\parallel} = -eE_{\parallel} \cos\left(k_{\perp} \rho_e \sin(\omega_c t / \gamma) - \omega t + \phi\right). \tag{5}$$

With the help of the Bessel function identity

$$\cos z \sin\phi = \sum_{n=-\infty}^{n=\infty} \cos(n\phi) \mathrm{J}_n(z)$$

this is rewritten in terms of an infinite sum of cyclotron harmonics $n\omega_c$. One obtains,

$$\dot{p}_\parallel = -eE_\parallel \sum_{n=-\infty}^{n=\infty} \cos(n\omega_c t/\gamma - \omega t + \phi) \mathrm{J}_n(k_\perp \rho_e), \qquad (6)$$

which shows the possibility of resonant acceleration of electrons satisfying a (harmonic) resonance condition $n\omega_c/\gamma = \omega$. Individual particles either gain or lose energy, subject to their phase relative to the wave. Net exchange of energy between wave and plasma depends on the ensemble average over all particles. Just as in the case of Landau damping this depends on the gradient of the distribution function at the cyclotron resonance.

At this stage a side remark must be made as it may appear as if the O-mode leads to an increase of the parallel energy, whereas the wave itself carries no parallel momentum. This is because in our discussion above we have completely neglected the action of the magnetic field that is also associated with the wave. Although it cannot provide a net energy gain it does rotate the momentum vector in such a way, that the net energy gain will be in the perpendicular direction: *electron cyclotron absorption leads primarily to an increase in the perpendicular energy of resonant electrons*.

A useful quantity is the optical depth τ, which is defined as the integral of the absorption coefficient α along the trajectory s of the wave, $\tau \equiv \int \alpha ds$. The total absorbed power P_{abs} in the plasma is

$$P_{abs} = P_{inj}\left(1 - \exp(-\tau)\right). \qquad (7)$$

Optical depths of a plasma slab in which the magnetic field varies as B ~ 1/R are given in Table I. For the O-mode, the optical depth is given for perpendicular propagation and harmonics n = 1, 2, … . Similarly for the X-mode and harmonics n = 2, 3, … . The optical depth for the fundamental harmonic n = 1 of the X-mode is given for oblique propagation. In the table, N_O and N_X refer to the refractive indices of the O- and X-mode, while $v_t = (kT_e/m_e)^{1/2}$ is the thermal electron velocity. Currently, in most ECRH experiments either the fundamental O-mode or second harmonic X-mode is employed. Except near the plasma edge, optical depths of order of one or higher are generally achieved for both fundamental O- as well as second harmonic X-mode resulting in complete single pass absorption.

Table I. The optical depth of EC waves[1]

$\tau^O_{n\geq 1}(\perp)$	$\frac{\pi^2 n^{2(n-1)}}{2^{n-1}(n-1)!} N_O^{2n-1} \left(\frac{\omega_p}{\omega_c}\right)^2 \left(\frac{v_t}{c}\right)^{2n} \frac{R}{\lambda}$
$\tau^X_{n\geq 2}(\perp)$	$\frac{\pi^2 n^{2(n-1)}}{2^{n-1}(n-1)!} A_n \left(\frac{\omega_p}{\omega_c}\right)^2 \left(\frac{v_t}{c}\right)^{2(n-1)} \frac{R}{\lambda}$ with $A_n = N_X^{2n-3}\left(1 + \frac{\omega_p^2/\omega_c^2}{n(n^2-1-\omega_p^2/\omega_c^2)}\right)^2$
$\tau^X_{n=1}(\angle)$	$\pi^2 N_X^5 \left(1 + \frac{\omega_p^2}{\omega_c^2}\right)^2 \left(\frac{\omega_c}{\omega_p}\right)^2 \left(\frac{v_t}{c}\right)^2 \cos^2\theta \frac{R}{\lambda}$

II.C. Non-inductive Current Drive

As described above, EC wave absorption leads mainly to an increase in perpendicular energy of resonant electrons. Nevertheless efficient non-inductive current drive by EC waves is possible. The basic mechanism is best understood as follows. Take an electron with given parallel and perpendicular momentum. This electron will lose its parallel momentum in a typical momentum loss time defined by the collision frequency ν_m. Now, assume that after interaction with EC waves its perpendicular momentum is increased by a small amount. Again it will lose its parallel momentum in a collision time, but the collision frequency is now decreased since it is proportional to ~$1/v^3$. Oblique injection leads to a Doppler shifted resonance and selectively heats electrons moving in one direction, thus generating a net current.

This picture has been formalized by Fisch and Boozer to obtain the current drive efficiency [5]. Suppose an electron is moved from a position v_1 in velocity space to a position v_2. As a consequence it contributes an additional amount of current during its subsequent slowing down, which is estimated as

$$J \equiv \frac{1}{\Delta t}\int^{\Delta t} j(t)dt \approx \frac{-e}{\Delta t}\left(\frac{v_{\parallel 2}}{\nu_2} - \frac{v_{\parallel 1}}{\nu_1}\right) \qquad (8)$$

where ν_i are the appropriate collision frequencies for momentum slowing down. The power that has been spent to create this current is $(E_2 - E_1)/\Delta t$. Substituting differentials for the finite differences, this leads to the current drive efficiency defined as [4,5]

$$\frac{J}{P} = -e\frac{\hat{s}\cdot\nabla_{\mathbf{p}} v_\parallel/\nu_m}{\hat{s}\cdot\nabla_{\mathbf{p}} p^2/2m_e} \qquad (9)$$

where $\hat{s}$ is the unit vector in the direction of EC wave driven momentum displacement. In case of ECCD, the nominator and denominator must be integrated along the electron cyclotron resonance curve with appropriate weighting for the local (in momentum space) power absorption.

This picture is further complicated by the presence of trapped electrons. During slowing down, an electron may become trapped and, thereby, loose its remaining parallel momentum. This effect can be incorporated in the current drive efficiency (9) by substituting the correction due to trapping in the response function $v_\parallel/\nu_m$. EC waves can also directly push passing electrons over the trapping boundary thereby destroying their momentum and driving a reversed current, known as the Ohkawa current [6].

The highest current drive efficiencies are expected for deposition of the wave power on fast particles. A large Doppler shift is called for to selectively heat particles with high parallel velocities. Such a Doppler

shift, of course, requires a corresponding up- or down-shift of the wave frequency with respect to the local cyclotron frequency. On this basis, two ECCD scenarios are discerned: the down-shifted scenario with waves injected from the high-field side, and the up-shifted scenario using low-field side injection. In the down shifted scenario, the X-mode is the natural mode of choice, since it has the highest possible absorption for oblique injection. For the up-shifted scenario, either the fundamental O- or second harmonic X-mode can be used.

The down-shifted scenario is the scenario of choice in smaller tokamaks, where it is difficult to obtain sufficient absorption in the fundamental O- or second harmonic X-mode. However, in large hot tokamaks the highest ECCD efficiencies are found with up-shifted scenarios. In such devices the optical depth of the fundamental O- or second harmonic X-mode is sufficient to deposit all power in energetic particles on one side of the resonance.

II.D. Numerical Tools

Ray- and Beam-tracing codes

At higher densities and, in particular near cut-off, wave refraction plays an important role and will have to be taken into account in calculations of the power deposition profiles. This is commonly done using ray-tracing codes in which a wave beam is represented by a large set of individual rays. Each of these rays is then traced through the plasma using the geometric optics approximation [7]. The power absorbed along the ray is evaluated and linear estimates of the non-inductively driven current may be obtained as well.

In many present day experiments focused beams are being used. Near the beam focus simple ray-tracing breaks down. For these conditions, beam tracing-codes have been developed. An example of such a code is the TORBEAM code [8], which describes the propagation through the plasma of a Gaussian wave beam in terms of its central ray trajectory and the evolution of its beam width and curvature.

Most ray- and beam-tracing codes evaluate the trajectories on the basis of cold plasma dispersion only using the full warm plasma dispersion relation to evaluate the power absorbed along these trajectories. However, near electron cyclotron resonance, the warm plasma dispersion and absorption are strongly inhomogeneous in both real and wave vector space. This has important consequences for the wave beam propagation both in terms of its direction [9] as well as for the beam width. Apart from full wave analyses, a proper description of these effects requires new, quasi-optical techniques [10].

Density and magnetic field perturbations due to plasma turbulence also affect wave propagation. As the turbulence is slow compared to the time scale of wave propagation, at any instant in time the wave propagation is determined by the instantaneous plasma state. Averaged over time the net effect of the turbulence can then be obtained from an ensemble average of the different beam realizations. This idea is embodied in the recent WKBeam code [11]. In particular, edge turbulence in larger tokamaks like ITER has been found to result in a significant broadening of the wave power deposition profile [12].

Fokker-Planck codes

When the absorbed power density exceeds the limit of $p_{abs}[MW/m^3]/n_e^2[10^{19}/m^3] > 0.5$, EC waves will modify the electron momentum distribution function significantly [13]. This has consequences for the local power absorption as well as the non-inductively driven current. The kinetic evolution of the electron momentum distribution function can be described by the bounce-averaged quasi-linear Fokker-Planck equation, which symbolically can be written as [14]

$$\frac{\partial f_e}{\partial t} = \left.\frac{\partial f_e}{\partial t}\right|_{\text{collisions}} + \left.\frac{\partial f_e}{\partial t}\right|_{\text{ECRH}} + \left.\frac{\partial f_e}{\partial t}\right|_{E_\parallel}, \qquad (10)$$

where the distribution function is averaged over the fast gyro and bounce motion of the electrons. This gives an equation for the distribution function on each magnetic surface that is 2D in momentum space ($p_\parallel$,$p_\perp$). The Fokker-Planck equation describes the balance between collisions, driving the distribution function back to Maxwellian, the diffusion of resonant particles driven by the waves, as well as the convection caused by a parallel electric field. An additional term can be added to model the anomalous radial transport of electrons. This makes the model 3D and becomes necessary, when the relevant collisional timescale on which a steady state is reached, becomes similar to the time scale for radial transport. Several numerical 3D Fokker-Planck codes are available and have been used to model non-thermal electron generation and current drive under conditions of high power ECRH [14].

III. TECHNICAL ASPECTS

III.A. Wave Sources

The high power required for ECRH and ECCD experiments is provided by gyrotrons [15]. In a gyrotron the waves are generated by leading a weakly relativistic electron beam (typically ~80 kV) through a resonant cavity in a magnetic field. A magnetic field slightly in excess of ν(GHz)/28 T is required for efficient fundamental interaction. The field must be very stable and is usually generated by a superconducting magnet. The specific (wave guide) mode that is generated in the cavity depends on the magnetic field, the position in the cavity of the electron beam and the size of the cavity. Modern gyrotrons use high order modes (for example, $TE_{22,6}$) to limit dissipation in the cavity. An internal quasi optical mode converter is used to convert the radiation into a Gaussian beam, which is coupled out of the gyrotron.

One of the most critical issues for high power, long pulse gyrotrons is the handling of the power dissipation

in the various components: in particular, inside the cavity, on the collector where the power of the spent electron beam is being dumped, and in the vacuum window through which the radiation is transmitted. In the latest generation of gyrotrons the dissipation in the collector is reduced by using a depressed collector. This also improves the overall efficiency of the gyrotron to well over 50% as required by ITER specifications. The material of choice for the vacuum window these days is CVD (Chemical Vapor Deposition) diamond, which combines a very low loss for mm waves with very high heat conductivity. Long pulse, 1 MW gyrotrons in the 100 to 170 GHz range are now available and 2 MW co-axial gyrotrons are being developed. In addition, multi-frequency gyrotrons are now available providing even further flexibility to future ECRH systems.

III.B. Wave Transmission and injection

Wave transmission from the source to the plasma is commonly achieved by oversized waveguides, quasi-optical lines, or a mixture of both. Modern waveguides are now generally corrugated and employ the low loss HE_{11} mode (hybrid TE_{11}/TM_{11}). This mode couples well to a Gaussian beam and vice versa. The coupling efficiency has a sharp maximum at the appropriate wave-guide diameter. Also optical techniques like miter (mirror) bends can be used. In such cases transmission is very efficient with the losses being determined mainly by the bends (0.25% to 0.5% per bend). In case of high power wave transmission or small diameter waveguides, arcing can pose serious problems. In order to avoid arcing, evacuated waveguides have been employed.

In quasi-optical (QO) lines the free space Gaussian beam is transported between mirrors. Though achieving equally high transmission efficiency, QO systems require significantly more space to allow for the expansion of the Gaussian beam between mirrors. Typical losses on individual copper mirrors are 0.2 %.

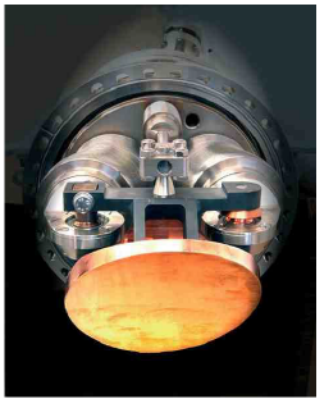

Figure 3: Picture of the launching mirror of the TEXTOR ECRH system. The focusing mirror and the push and pull rods for actuation of horizontal and vertical rotation are visible.

On most tokamaks, a focused wave beam is finally launched quasi-optically from a steerable mirror. An example of the latter is given in Fig. 3, which shows the launching mirror of the former TEXTOR ECRH system. The TEXTOR ECRH launcher was steerable in both the horizontal and vertical planes. Up to date descriptions of modern ECRH systems in use on various tokamaks can be found in Refs [16–20]. The largest ECRH system is the one at the advance stellarator Wendelstein 7-X which has recently become in operation [56]. First results from Wendelstein 7-X are reported in [57].

IV. EXPERIMENTAL RESULTS

IV.A. Validation of Propagation and Absorption

A first step in the experimental verification of theoretical predictions regarding wave propagation and absorption is the measurement of transmitted power. Such measurements have been performed in the electron cyclotron range of frequencies both at low power for diagnostic purposes as well as at high power (see Ref. [2] and references therein). Measurements generally agree well with predictions from ray-tracing as long as refraction is not too strong. It is likely that at high densities, close to cut-off, fluctuations in the plasma can give rise to time varying refraction, which on average leads to a broadening of the wave beam.

The absorption profile can be determined by the initial plasma response following switch-on of ECRH (assuming a steady state at the time of switch on):

$$p_{\mathrm{ECRH}}(r) = \frac{\partial}{\partial t}\left(\tfrac{3}{2} n_e k T_e\right)\Big|_{t=t+} \qquad (11)$$

Alternatively, it can be determined by the plasma response at switch-off or by the plasma response to modulated ECRH. The location of the power deposition is generally observed to coincide well with predictions from ray- or beam-tracing [3,21]. Several experiments report total amounts of measured power significantly below the amount of power absorbed from the beam according to transmission measurements or calculations. The 'missing power' has been ascribed to fast changes in electron transport or hidden energy reservoirs [2]. In more recent power deposition studies on ASDEX-Upgrade, the full absorbed power could be accounted for in the deposition measurements [21]. More detailed analysis methods and recent experiments as performed on DIII-D show that the EC power deposition profile can be significant broadened with respect to predictions from ray or beam tracing [22]. Edge density fluctuations, scattering the EC waves, most likely are the cause of this deposition profile broadening.

IV.B. Validation of Current Drive Predictions

Measurements of the EC driven current are usually complicated by the presence of other currents like the bootstrap current and, in most cases, the inductive current. The presence of a residual loop voltage also

affects the current drive efficiency. Bounce averaged Fokker-Planck code calculations predict significant synergy between ECCD and the loop Voltage in agreement with experiments [23]. Large differences are predicted between co- and counter current drive [24]. The most detailed comparison between experiments and simulations comes from DIII-D. In the analysis of these experiments measurements of the Motional Stark Effect are used to determine the internal poloidal magnetic field and from there the current density distribution. Comparing discharges with and without ECCD the driven current is obtained. A series of equilibrium reconstructions is required to obtain the loop voltage at the position of ECCD. That information has been used in a bounce averaged Fokker-Planck code (CQL3D [25]) to simulate the experiments. Such a complete simulation is shown to provide a good fit to the experimental results [26]. Simulations either neglecting the parallel electric field or based on a linear calculation of the driven current lead to unsatisfactory fits. The data set covers co- as well as counter-drive, and a large range of minor radii. In addition, the data covers a wide range in the non-linearity parameter $p_{abs}[MW/m^3]/n_e^2[10^{19}/m^3]$ with many points near or over the threshold [3,26]. The good correspondence of the data and the simulations provides a critical test of the bounce averaged quasi-linear Fokker-Planck model including, in particular, trapped particle effects.

Fully non-inductive current drive with ECCD has only been obtained in a limited number of tokamaks. This generally requires special conditions like low density and or low plasma current to maximize on the one hand the EC driven current and on the other hand the bootstrap current fraction. One such example comes from the T-10 tokamak [27]. However, in this case the ECCD pulse was relatively short and a steady state was not reached. More recently, fully non-inductive current drive with ECCD has been obtained in TCV. The discharge could be maintained stable over several current redistribution times provided a sufficiently broad current profile was driven by ECCD [28]. This was achieved by aiming three ECCD beams at different positions in the poloidal cross section.

IV.C. Plasma Heating and Confinement

In terms of confinement, plasmas heated by ECRH behave in very much the same way as plasmas heated by other additional heating methods such as NBI and ICRH [2]: ECR heated plasmas roughly follow the L-mode scaling. The transition to H-mode is observed at the expected power level or even below. Differences in confinement scaling can be attributed to the strong (central) localization of the ECRH power deposition and the fact that ECRH heats only electrons. The latter two effects also have consequences for the particle transport: the central density sometimes displays a strong pump-out during ECRH.

In several experiments, very high central electron temperatures of the order of 10 keV have been achieved with central power deposition. In particular, in the presence of an internal transport barrier created by a region of negative or reduced magnetic shear. For example, on TCV [29] this has been achieved by using ECCD to drive some counter-current on axis to establish the negative shear, while on ASDEX Upgrade [30] ECRH has been applied during a preexisting internal transport barrier, established through a programmed current ramp.

The localized nature of the ECRH power deposition makes it an ideal tool for detailed studies of electron transport. One such study has been performed on the RTP tokamak, where a scan of the power deposition over the minor radius revealed a complex response of the plasma with multiple internal transport barriers [31]. Modulation of the ECRH power has become a standard tool for the study of the electron heat diffusivity.

IV.D. MHD Stability Control

The localization of the power deposition also makes ECRH and ECCD ideal tools to control the plasma pressure or current density profiles, which determine the MHD stability of the plasma. Several instabilities are affected by ECRH: sawteeth, tearing modes, ELMs, etc..

Most tokamaks equipped with ECRH report a lengthening of the sawtooth period or complete sawtooth stabilization by ECRH near the sawtooth inversion radius (see, e.g. the early experiments on T-10 [32] or the more recent and more detailed results from TCV [33] and ASDEX Upgrade [34]). The sawtooth crash is triggered when the m=1, n=1 internal kink mode is destabilized [35]. The stability threshold of this mode is seen to depend on the shear at the q=1 surface. Consequently, changes to the shear at q=1 affected by localized current drive such as ECCD can strongly change the sawtooth period. This has been observed in various experiments and has been modeled in detail for TCV [36]. The dependence of the internal kink stability threshold on the local shear can also be used to derive a simple criterion for the required EC driven current to have a significant effect on the sawtooth period [37]:

$$I_{cd} \geq 2I_{q=1}(\Delta r_{cd} / r_{q=1})^2 \qquad (12)$$

where I_{cd} is the non-inductively driven current with a Gaussian width of Δr_{cd}, and $I_{q=1}$ is the plasma current inside the q=1 surface, $r_{q=1}$. Co-current drive just inside the q=1 surface is found to shorten the sawtooth period, whereas co-current driven just outside the q=1 surface will lengthen the sawtooth period. Counter-current drive will have just the opposite effect. A comprehensive review of sawtooth control in provided in Ref. [38].

The control of tearing modes by ECRH and ECCD has received a lot of attention over the years. This stems from the potential threat that these modes pose to tokamak reactors: large tearing modes not only lead to a substantial degradation of plasma confinement, they may also lead to disruption of the plasma [39]. In particular, control of neoclassical tearing modes (NTM) occurring in high β tokamak plasmas has been studied [40]. The stability of an (N)TM can be affected in two ways. First,

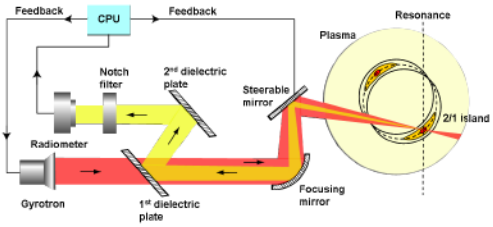

Figure 4: *The principle of inline ECE as sensor for feedback controlled EC power deposition. The dielectric plates stand for frequency selective couplers that transmit the high power ECRH waves but reflect the low power ECE at desired frequencies. When the steering mirror is adjusted such that a feature like a 2/1 magnetic island is localized in the sensor spectrum at the actuator (gyrotron) frequency, the power deposition exactly on that feature is ensured.*

through control of the equilibrium profiles which determine the stability parameter Δ' [41]. Second, by generating additional current, the failing current inside the magnetic island, responsible for its instability, can be replaced resulting in stabilization of the mode [40]. The additional current inside the island can either be generated inductively by heating the island, or driven non-inductively, for example, by ECCD [42]. The suppression of NTMs by ECCD has been demonstrated in several experiments [43-46].

In several experiments the NTM suppression was achieved by operation of the ECRH systems under full feedback control [45,46]. EC emission (ECE) is used as sensor to detect the location of the NTM with the help of the oscillations due the mode on the ECE signals, and this knowledge is then used to steer the actuator, i.e. the ECRH launcher, in the proper direction. This requires real-time knowledge of the equilibrium and real-time ray tracing to link the sensor derived location to the reference frame of the actuator. To circumvent these latter steps, inline ECE (see Figure 4) has been proposed [47]. In this case the sensing occurs along the reference frame of the actuator, i.e. the gyrotron wave beam. A proof-of-principle inline ECE system was implemented on TEXTOR [48] and used successfully to demonstrate tracking and suppression of tearing modes [49].

V. THE ITER ECRH SYSTEMS

The international experimental fusion reactor ITER will be equipped with an advanced ECRH system [50-52]. According to the ITER design requirements and guidelines this system must have the capability to perform or assist in a number of tasks: (1) heating in order to access H-mode and reach conditions for Q>10 operation, (2) on and off-axis current drive for steady state operation (achieving a current density on axis of > 20 MA/m^2 and a total driven current inside $\rho = 0.6$ in excess of 1 MA), (3) stabilization of NTMs by current drive at the q=3/2 and q=2 surfaces, (4) wall conditioning, and (5) start-up assist. To (3) should be added the control of sawteeth by current drive at the $q = 1$ surface. To perform these tasks an ECRH system has been designed consisting of a total of 24, 170 GHz gyrotrons each capable of delivering a power of 1 MW, CW. The power will be transferred to the tokamak through evacuated HE_{11} wave guide using wave guide switches to switch between the alternate upper-port or mid-plane launchers. Due to limited steering capabilities of these launchers, each of them will be used to perform specific tasks. The mid plane launcher is optimized for central heating and current drive, whereas the upper port launcher design is optimized towards the control of NTMs (cf. Fig. 5) and sawteeth. The design work is supported by extensive simulations for the various tasks and by extrapolation from current experiments to ITER [53-55]. Still uncertainties remain. For example, edge density fluctuations have been shown to potentially result in a doubling of the ECCD power deposition profile width near the q =1.5 or 2 rational surfaces, which would correspond to an equivalent increase in the required ECCD power for NTM suppression [12].

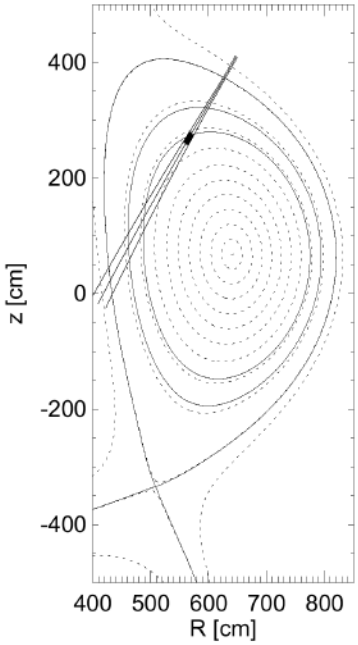

Figure 5: *Example of results from of a beam tracing calculation with the TORRBEAM code for a single wave beam coming from an upper launcher, aiming at the q=3/2 surface. The black region shows the well localized area of power deposition. The dotted curves indicate flux surfaces with some special surfaces indicated by full lines, from the outside going in: the separatrix, the q=2, and q=3/2 surface, respectively.*

ACKNOWLEDGMENTS

DIFFER is part of the institutes organisation of NWO.

REFERENCES

[1] M. BORNATICI et al. Nucl. Fusion, **23**, 1153 (1983)

[2] V. ERCKMANN and U. GASPARINO, Plasma Phys. Contr. Fusion, **36**, 1869 (1994)

[3] R. PRATER, Phys. Plasmas, **11**, 2349 (2004)

[4] N.J. FISCH, Rev. Modern Phys. **59** 175 (1987)

[5] N.J. FISCH, A.H. BOOZER, Phys. Rev. Lett. **45** 720 (1980)

[6] T. OHKAWA, Steady state operation of tokamaks by rf heating, General Atomics Report GA-A13847 (1976)

[7] R. PRATER et al., Nucl. Fusion **48** 035006 (2008)

[8] E. POLI, A.G. PEETERS, G.V. PEREVERZEV, Comput. Phys. Commun. **136,** 90 (2001)

[9] M.D. TOKMAN et al., Nucl. Fusion **43**, 1295 (2003)

[10] A.A. BALAKIN et al., Nuclear Fusion **48**, 065003 (2008)

[11] H. WEBER et al., EPJ Web of Conferences **87**, 01002 (2015)

[12] E. POLI et al., Nucl. Fusion **55** (2015) 013023.

[13] R.W. HARVEY,et al., Phys. Rev. Lett. **62**, 426 (1989).

[14] E. WESTERHOF, *Proc. of 9th Joint Workshop on ECE and ECH, Borrego Springs, California, 1995*, Ed. J. Lohr, World Scientific, Singapore, p. 3 (1995).

[15] G.S. NUSINOVICH, M.K.A. THUMM, M.I. PETELIN, J. Infrared Milli Terahz Waves **35** (2014) 325.

[16] T.P. GOODMAN et al., Proc. 19th Symp. Fusion Technology, Lisbon, 16-20 September 1996, Ed. C. Varandas, F. Serra (North-Holland, Amsterdam, 1997), Vol. 1 pp. 565 (1996).

[17] F. LEUTERER et al., Nucl. Fusion **43**, 1329 (2003)

[18] R.W. CALLIS et al., Nucl. Fusion **43**, 1501 (2003)

[19] Y. IKEDA et al., Fus. Eng. Design **53**, 351 (2001)

[20] E. WESTERHOF et al., Nucl. Fusion **43**, 1371 (2003)

[21] K.K. KIROV et al., Plasma Phys. Controlled Fusion **44**, 2583 (2002).

[22] M.W. BROOKMAN et al., Phys. Plasmas **28**, 042507 (2021)

[23] R.A. JAMES et al., Phys. Rev. A **88**, 8783 (1992)

[24] A. MERKULOV et al., Phys. Plasmas **14**, 052508 (2007)

[25] R.W. HARVEY, M.G. McCOY, *Proc. IAEA TCM Advances in simulations and modeling of thermo-nuclear plasmas*, Montreal, Canada, 1992 (IAEA, Vienna, 1993) p.498

[26] C.C. PETTY, et al., Nucl. Fusion **42**, 1366 (2002)

[27] V.V. ALIKAEV et al., Nucl. Fusion **32**, 1811 (1992)

[28] O. SAUTER et al., Phys. Rev. Lett. **84**, 3322 (2000)

[29] Z.A. PIETRZYK et al., Phys. Rev. Lett. **86**, 1530 (2001)

[30] S. GÜNTER et al., Phys. Rev. Lett. **84**, 3097 (2000)

[31] N.J. LOPES CARDOZO et al., Plasma Phys. Control. Fusion **39** B303 (1997)

[32] R.M.J.SILLEN et al., Nucl. Fusion **26**, 303 (1986)

[33] Z.A. PIETRZYK et al., Nucl. Fusion **39**, 587 (1999)

[34] A. MÜCK, et al., Plasma Phys. Control. Fusion **47** 1633 (2005)

[35] F. PORCELLI et al., Plasma Phys. Control. Fusion **38**, 2163 (1996)

[36] C. ANGIONI et al., Nucl. Fusion **43**, 455 (2003)

[37] A. MERKULOV et al., *Theory of Fusion Plasmas, Proc. Joint Varenna-Lausanne Int. Workshop, Varenna, Italy, August 30 – September 3 2004*, J.W. Connor et al. (Editors), Societa Italiana di Fisica, Bologna, 2004, p. 279

[38] I.T. CHAPMAN et al., Plasma Phys. Control. Fusion **49** (2007) B385

[39] H.R. KOSLOWSKI, 'Operational limits and limiting instabilities in tokamak machines', these proceedings

[40] R.J. LA HAYE, Phys. Plasmas **13**, 055501 (2006)

[41] E. WESTERHOF, Nucl. Fusion **30** 1143 (1990)

[42] C.C. HEGNA, J.D. CALLEN, Phys. Plasmas **4**, 2940 (1997)

[43] G. GANTENBEIN et al., Phys. Rev. Lett. **85**, 1242 (2000)

[44] C.C. PETTY et al., Nucl. Fusion **44**, 243 (2004).

[45] A. ISAYAMA et al., Nucl. Fusion **43**, 1272 (2003)

[46] F. FELICI et al., Nucl. Fusion **52** (2012) 074001

[47] E. WESTERHOF et al., 13th Joint Workshop on ECE & ECRH (17–20 May 2004), ed. A. Litvak (Nizhny Novgorod, Russia: IAP/RAS) p. 357 (2005)

[48] J.W. OOSTERBEEK et al., Rev. Sci. Instruments **79**, 093503 (2008)

[49] B.A. HENNEN et al., Plasma Phys. Controlled Fusion **52**, 104006 (2010)

[50] M.A. HENDERSON et al., Nucl. Fusion **48**, 054013 (2008)

[51] K. TAKAHASHI et al., Fusion Sci. Technol. **47**, 1 (2005)

[52] M. HENDERSON et al., Phys. Plasmas **22**, 021808 (2015)

[53] D. FARINA et al., Phys. Plasmas **21**, 061504 (2014)

[54] R.J. LA HAYE et al., Nucl. Fusion **46**, 451 (2006)

[55] I.T. CHAPMAN et al., Nucl. Fusion **53**, 066001 (2013)

[56] V. ERCKMANN et al., Fusion Science and Technology **52**:2 291 (2007)

[57] R.C. WOLF et al., Nucl. Fusion **57**, 102020 (2017)

NON-INDUCTIVE CURRENT DRIVE*

Egbert Westerhof

DIFFER, Dutch Institute for Fundamental Energy Research,
De Zaale 20, 5612 AJ Eindhoven, the Netherlands, www.differ.nl

* These lecture notes are updated from those appearing under the same title in the proceedings of the 10th-13th Carolus Magnus Summer School

ABSTRACT

This lecture addresses the various ways of non-inductive current generation. In particular, the topics covered include the bootstrap current, RF current drive, neutral beam current drive, alternative methods, and possible synergies between different ways of non-inductive current generation.

I. INTRODUCTION

Earlier lectures [1,2] have stressed the requirement of a finite poloidal magnetic field in addition to the toroidal magnetic field in order to confine charged particles in a toroidal configuration. Whereas in a stellarator the poloidal field is supplied by external coils [3], the tokamak relies on a toroidal plasma current for the generation of the poloidal field. Generally, the toroidal current in a tokamak is generated inductively by means of a transformer, in which the plasma acts as the secondary winding [1]. This immediately leads to a major limitation of tokamak operation: the finite flux swing of the transformer in combination with the finite resistivity of the plasma results in a finite pulse length of a tokamak discharge and necessarily pulsed reactor operation. For many reasons steady state operation of a fusion reactor is highly desirable. This has motivated the development of alternate ways for the generation of the toroidal plasma current. Such methods are classified as 'non-inductive current drive'. A second advantage offered by non-inductive current drive, is that it decouples the current density profile from the temperature profile, which determines the plasma conductivity and consequently defines the inductive current density profile. The freedom to shape the current density profile is particularly important for the control of plasma stability [4, 5].

An important measure is the efficiency of current drive which can be defined as the ratio of the driven current density, j, over the spent power density, p: $\gamma_{CD} \equiv j/p$. Since the total current generated scales as $I_{CD} \sim \pi a^2 j$, while the total spent power scales as $P \sim 2\pi R \pi a^2 p$, a more practical measure for the current drive efficiency is $\eta_{CD} \equiv n_e R I_{CD}/P$. Here, a and R are the minor and major radius of the tokamak, respectively. The factor n_e accounts for the fact that in many cases the non-inductively driven current is inversely proportional to the density such that the current drive efficiency η_{CD} becomes a constant which can be compared across different experiments and used for extrapolation to future devices.

Subsequent sections treat various methods of non-inductive current generation. First, the so-called bootstrap current is discussed, which in a toroidal device comes entirely for free. It is a parallel (with respect to the magnetic field) plasma current which is driven by finite pressure gradients in toroidal geometry. Next, the various methods of non-inductive current generation by radio frequency (RF) waves are treated. This is followed by a discussion of the current generated by injection of neutral particle beams and a brief overview of various alternate concepts for non-inductive current generation.

For further reading we advice the excellent early review by N.J. Fisch [6], and for later updates the relevant chapters of the ITER Physics Basis [7] and its update [8]. Very instructive is also the book by J. Wesson [9].

II. BOOTSTRAP CURRENT

Neoclassical, collisional transport [10] in high pressure toroidal plasma generates a finite parallel plasma current. This current is known as the bootstrap current and is entirely self generated by the plasma [9, 11]. Its origin can be best understood as follows. In toroidal plasma the particles do not follow the magnetic field lines exactly, but exhibit a finite drift as a consequence of the magnetic field curvature and inhomogeneity. For the trapped particles this results in banana shaped orbits with a finite width [4]

$$w_b = 2\frac{m v_{\|,m}}{q B_{p,m}}, \qquad (1)$$

where q is the charge of the particle, m its mass, and $v_{\|,m}$ and $B_{p,m}$ are the parallel velocity and poloidal magnetic field at the mid plane (i.e. the position of minimum magnetic field along the orbit). In the presence of a finite density gradient, this results at any given point on the mid plane in an imbalance between the trapped particles moving in co- and counter-current direction. This constitutes the banana current. The bootstrap current finally is generated through collisional coupling of the trapped and passing particles. Formulated in terms of the velocity distribution function at a given position on the low field side of the mid plane, one notices that a finite density gradient results in an asymmetry in the trapped

particle region. Collisions will extend this asymmetry across the trapped passing boundary into the passing particle region resulting in the bootstrap current.

In a more complete theory, not only the density gradient, but also the temperature gradient is seen to contribute to the bootstrap current. For large aspect ratio $\varepsilon^{-1} \equiv R/a$, the expression for the bootstrap current is [10]

$$j_{BS} = -\frac{\sqrt{\varepsilon} n}{B_p}\left(2.44(T_e + T_i)\frac{dn}{ndr} + 0.69\frac{dT_e}{dr} - 0.42\frac{dT_i}{dr}\right), \quad (2)$$

while for $\varepsilon \to 1$ it reduces to [10]

$$j_{BS} = -\frac{1}{B_p}\frac{dp}{dr}, \quad (3)$$

where p is the total plasma pressure.

III. PRINCIPLES OF RF CURRENT DRIVE [6]

Intuitively, the generation of a non-inductive current appears to require some method to directly impart parallel momentum to electrons. This could be done for example by means of neutral beams (see Section IV) or through resonant interaction with RF waves. In the latter case, the wave can impart its energy and momentum to electrons satisfying either the Landau resonance, $\omega - k \cdot v = 0$, or, in the case of strongly magnetized plasmas, the cyclotron resonance, $\omega - k_{\|} v_{\|} - n\Omega_e/\gamma = 0$ ($n = \pm 1, \pm 2, \ldots$).

An estimate of the theoretical current drive efficiency is obtained from the following arguments. Suppose the parallel momentum imparted to an electron is $m\Delta v_{\|}$. The incremental current carried by this electron is $\Delta j = -e\Delta v_{\|}$, while its incremental energy is $\Delta\varepsilon = mv_{\|}\Delta v_{\|}$. The fact that $\Delta\varepsilon/\Delta j$ is proportional to $v_{\|}$, shows that it is energetically favorable to accelerate low parallel velocity electrons and, consequently, first studies of RF current drive focused on waves with low phase velocity $\omega/k \ll v_{te}$ such as Alfvén waves. However, the incremental current will decay with the collision frequency $\nu(v) \sim 1/v^3$ and the power required to sustain this current consequently is $P_{RF} = \nu(v)\Delta\varepsilon$. Using the notation $J = \Delta j$, and combining the expressions for Δj, $\Delta\varepsilon$ and P_{RF}, one obtains the theoretical steady state current drive efficiency as

$$\frac{J}{P_{RF}} = \frac{-e}{mv_{\|}\nu(v)}. \quad (4)$$

Thus, maximizing the current drive efficiency requires minimizing the expression $v_{\|}\nu(v)$. Optimization is obtained in two opposite limits (see also Fig. 1): for $v_{\|} \to 0$, but $v_{\perp} \approx v_{te}$, one has $\nu(v) \approx$ constant; while for $v_{\|} \gg v_{te}$, $\nu(v) \sim 1/v_{\|}^3$. The second limit calls for the use of waves with high parallel phase velocity such as Lower Hybrid (LH) waves (lower hybrid current drive, LHCD).

It can be shown that the direct transfer of parallel momentum is not even a strict requirement for current drive. This was first realized by N.J. Fisch and A.H. Boozer [12]. The basic argument runs as follows. Take an electron with given parallel and perpendicular momentum, mv_1. This electron would lose its parallel momentum in a typical momentum loss time defined by the collision frequency ν_1. As its parallel momentum decays, it would contribute a parallel current which averaged over the time Δt can be approximated by $J_1 \approx -ev_{\|1}/\Delta t\nu_1$. Now, assume that after interaction with EC waves its momentum is changed by a small amount to mv_2. Again it will lose its parallel momentum in a collision time, but the collision frequency is now changed since it is proportional to $1/v^3$. As a result a net current is generated, which can be equated to

$$J \equiv J_2 - J_1 \approx \frac{-e}{\Delta t}\left(\frac{v_{\|2}}{\nu_2} - \frac{v_{\|1}}{\nu_1}\right). \quad (5)$$

The power that has been spent to create this current is $(E_2 - E_1)/\Delta t$. Substituting differentials for the finite differences, this leads to the Fisch-Boozer current drive efficiency given by [6, 12]

$$\frac{J}{P_{RF}} = -e\frac{\hat{s} \cdot \nabla_{\mathbf{p}}(v_{\|}/\nu)}{\hat{s} \cdot \nabla_{\mathbf{p}}(p^2/2m_e)} \quad (6)$$

where $\hat{s}$ is the unit vector in the direction of RF driven momentum displacement. As parallel momentum transfer between waves and particles no longer is a requirement, also waves which carry little or no parallel momentum can be used for effective current drive. In fact, the theoretical efficiency for current drive by perpendicular pushing of electrons reaches up to 3/4 of the efficiency for direct parallel pushing of electrons [13]. This holds, in particular, for electron cyclotron current drive (ECCD).

It has subsequently been found that 'adjoint techniques' allow to find a more precise expression for the 'current response function', $\chi = -ev_{\|}/\nu$. Starting from the steady state Fokker-Planck equation,

$$C(f_e(v)) = \nabla_p \cdot S_w, \quad (7)$$

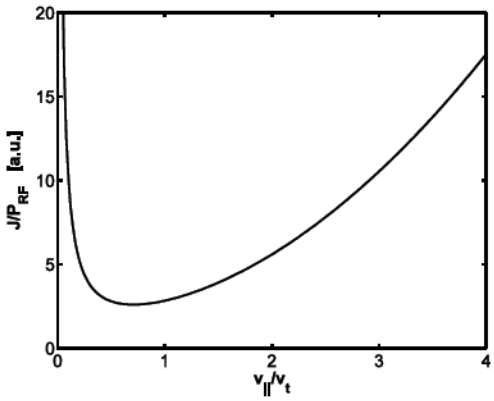

Figure 1: The theoretical current drive efficiency (in arbitrary units) for direct momentum transfer as a function of the parallel velocity.

where S_w is the quasi-linear wave driven momentum space flux, an adjoint equation for the current response function can be written as [6, 14]

$$C(f_{em}(v)\chi(v)) = ev_{\parallel}f_{em}(v), \quad (8)$$

where $f_{em}(v)$ is the Maxwellian distribution function, and $f_{em}(v)\chi(v)$ is required to have zero density and energy. Now, writing the current from the solution to the steady state Fokker-Planck equation as

$$J = -\int ev_{\parallel} f_e(v)\, d^3v = -\int (f_e/f_{em})\, C(f_{em}\chi)\, d^3v, \quad (9)$$

and using the self-adjointness of the collision operator,

$$\int \psi\, C(f_{em}\chi)\, d^3v = \int \chi\, C(f_{em}\psi)\, d^3v, \quad (10)$$

it is easily shown that

$$J = \int S_w \cdot \nabla_p \chi\, d^3v. \quad (11)$$

The current drive efficiency then becomes

$$\frac{J}{P_{RF}} = -e\frac{\int \hat{s}\cdot\nabla_{\mathbf{p}}\chi d^3v}{\int \hat{s}\cdot\nabla_{\mathbf{p}}(p^2/2m_e)d^3v} \quad (12)$$

generalizing the Fisch-Boozer efficiency (6). These adjoint techniques are limited to the regime in which the plasma response to the RF waves is almost linear. When significant quasi-linear modifications of the distribution function are induced, a proper estimate of the driven current can only be obtained from solution of the full Fokker-Planck equation.

The presence of trapped electrons further complicates the picture: in a tokamak or stellarator, all particles in the cone in velocity space given by $|v_{\parallel 0}/v_{\perp 0}| < (B_{max}/B_{min}-1)^{0.5}$ are trapped between the magnetic field maxima along a field line [2]. Trapped particles have zero average parallel velocity and cannot contribute to the parallel current. Consequently, when a passing particle crosses the trapped/ passing boundary during its slowing down, it no longer contributes any parallel current. This will reduce the current drive efficiency. As a passing particle is pushed across the trapped/passing boundary by the resonant interaction with RF waves, its contribution to the parallel current is lost and a net current is driven in the opposite direction, which is known as the Ohkawa current [15]. Furthermore, increasing a particle's perpendicular energy near the maximum in the magnetic field will increase its parallel velocity on the remainder of its trajectory. This should favor current drive by pushing particles in the perpendicular direction (in particular, ECCD) on the high field side. All these effects can be included in an adjoint calculation of the current drive efficiency by calculating the appropriate current response function for the bounce-averaged Fokker-Planck equation [16, 17, 18].

III.A. Lower Hybrid Current Drive (LHCD)

LHCD has proven to be the most successful non-inductive current drive method in tokamaks to date [19]. It makes use of the slow wave in the intermediate frequency regime between the ion and electron cyclotron frequencies: $\Omega_{ci} \ll \omega \ll |\Omega_{ce}|$. This is the realm of the lower hybrid resonance,

$$\omega_{LH} = \frac{\omega_{pi}^2}{1+\omega_{pe}^2/\Omega_{ce}^2} = \frac{|\Omega_{ci}\Omega_{ce}|}{1+\Omega_{ce}^2/\omega_{pe}^2}. \quad (13)$$

For the slow wave to have access to the high density part of the plasma in this frequency range, the parallel refractive index must satisfy the accessibility condition [20]

$$N_{\parallel} > N_c \equiv \frac{1}{1-\omega^2/|\Omega_{ci}\Omega_{ce}|}. \quad (14)$$

As a result, the waves are evanescent at the plasma edge and efficient coupling of the waves requires a close proximity of the LH wave antenna to the plasma edge. A particular property of lower hybrid waves is that the group velocity is perpendicular to the wave vector. Since also typically $k_{\perp} \gg k_{\parallel}$, the group velocity is almost parallel to the magnetic field and the wave propagates in a narrow "resonance cone" along the magnetic field. This means that the waves can only reach the centre of the plasma after traveling a number of times around the torus.

For efficient current drive, one should avoid parasitic damping of the waves by ions and, in case of a reactor, by fusion alpha particles. This requires the use of sufficiently high frequencies in order to avoid the presence of the lower hybrid resonance inside the plasma. In addition, efficient current drive is favored by high phase velocities, i.e. small $N_{\parallel}$. While one would expect such high phase velocities with $v_{ph} \gg v_{te}$ to be ill absorbed as a consequence of exponentially small numbers of resonant electrons, early experiments nevertheless showed good absorption. The reason for this is the generation of an extended tail of energetic electrons by quasi-linear interaction with lower phase velocity components not originally present in the launched wave spectrum. The generation in the plasma of these lower phase velocity components is known as the "spectral gap" problem. It is generally assumed that the multi-pass ray trajectories in these experiments are responsible for the required $N_{\parallel}$ upshift [21]. Several alternative explanations have been proposed to fill the spectral gap, including spectral broadening due to scattering off density fluctuations, wave diffraction, magnetic ripple, and parametric instabilities in the scrape-off layer in front of the launching antenna [22]. State of the art modeling employs coupled 3D ray-tracing and (2D in velocity space) Fokker-Planck codes with self-consistent absorption from the quasi-linearly modified electron distribution function [23]. This standard model of LHCD has proven very successful in explaining present experimental results [24].

LHCD has been the main tool for bulk current drive and for current profile tailoring in reversed central shear or low shear, hybrid tokamak scenarios. A record 3 hour discharge sustained by LHCD has been demonstrated on TRIAM-1M albeit at low current and density. On larger devices like JET and JT-60 fully non-inductive discharges have been sustained by LHCD at 3.0 and 3.6 MA, respectively. Current drive efficiencies obtained to date have reached values of $\eta_{LHCD} = 0.3\times10^{20}$ A/Wm^2

(JT-60U and JET), and across different experiments are found to scale roughly as $\eta_{LHCD} \approx 1.2 \times 10^{20} <T_e[keV]> / (5+Z_{eff})$ A/Wm^2 [8].

In ITER, the penetration of LH waves is limited to the outer parts as very efficient Landau damping occurs at plasma temperatures in the range of ~10 keV. Simulations confirm this limitation of LHCD to the colder outer part of the plasma. Typical efficiencies predicted for ITER are in the range of $\eta_{LHCD} = 0.2 \times 10^{20}$ A/Wm^2 [23]. The major aim of a possible LHCD system for ITER would be the achievement and sustainment of reversed shear or hybrid tokamak scenarios and the generation of discharges with fully non-inductive current drive.

Typical frequencies used for LHCD are in the range of 1 to 10 GHz, and in this frequency range fundamental wave guides can be used for an efficient transport of the waves. To generate the required spectrum grill antennae existing of multiple, appropriately phased fundamental wave guides are being used [20]. Also high power sources in this frequency range, especially klystrons, are readily available.

III.B. Electron Cyclotron Current Drive (ECCD)

Electron cyclotron waves generally carry little or no momentum, and current drive by these waves is based on the Fisch-Boozer mechanism in which electrons moving in one direction are selectively heated [25, 26]. This selective heating can be achieved by proper tailoring of the EC resonance condition,

$$\omega = n\,|\,\Omega_{ce}\,|\,/\,\gamma + k_{||}v_{||} \qquad (15)$$

in the region of power deposition. It generally requires a finite parallel refractive index, $N_{||} = k_{||}c/\omega$, and sufficient optical depth in order to guarantee almost complete absorption on one side of the resonance. One then distinguishes ECCD at downshifted ($\omega < |\Omega_{ce}|$) and at upshifted frequencies ($\omega > |\Omega_{ce}|$) as illustrated in Fig. 2. Efficient downshifted ECCD can be obtained by oblique injection of slow X-mode waves at the fundamental resonance from the high field side. However, most experiments currently affect ECCD at upshifted frequencies by low field side oblique injection of either fundamental O-mode or second harmonic fast X-mode waves. State of the art modeling of ECCD employs ray- or beam tracing codes employing adjoint techniques for the calculation of the driven current [27]. Quasi-linear modifications of the electron distribution become significant for power levels exceeding the threshold value $p_{ECCD}[MW/m^3]/n_e^2[10^{19}/m^3] > 0.5$ [28]. In such cases proper predictions of the EC driven current can only be obtained from (2D in velocity space) bounce averaged quasi-linear Fokker-Planck codes [29].

The current drive figures of merit achieved to date are typically in the range of $\eta_{ECCD} = 1 - 4 \times 10^{18}$ A/Wm^2, where the largest values have been achieved in high temperature discharges on JT-60U [30]. Extensive studies on DIII-D have shown that the experimentally measured EC driven current is in good agreement with predictions from combined ray-tracing and Fokker-Planck code calculations provided the synergy between the ECCD and a residual parallel electric field is properly accounted for [31]. Full non-inductive current drive over several current diffusion times has been demonstrated on TCV [32]. In these discharges, the EC driven current density profile had to be carefully tailored in order to avoid driving too much current near the centre of the discharge and the resulting instabilities. This is a due to the very localized EC power absorption and current drive as a consequence of the use of well focused wave beams and the cyclotron resonant character of the wave-plasma interaction. This localized character of the ECCD is in fact its main attractive feature: it allows the localized manipulation of the current density profile as required for the control of MHD instabilities like sawteeth and neoclassical tearing modes [25, 26].

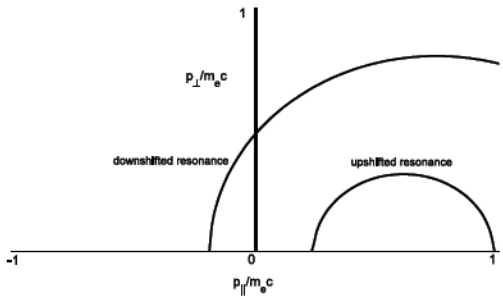

Figure 2: Illustration of the down and up shifted EC resonance in momentum space. The parallel refractive index is $N_{||} = 0.5$, and the wave frequencies are chosen as $\omega / |\Omega_{ce}| = 0.9$ and 1.1 for the down- and upshifted case, respectively.

Calculations of the expected ECCD efficiency in ITER predict a value of $\eta_{ECCD} = 0.2 \times 10^{20}$ A/Wm^2 in the high temperature centre of the discharge. Off-axis ECCD efficiencies will be significantly lower as a consequence of both trapped particle effects and lower local temperatures. Still the predicted driven current densities for the total available power of 20 MW are more than sufficient for the control of sawteeth and tearing modes [33], one of the major tasks of the ITER ECRH system.

III.C. Ion cyclotron resonance frequency (ICRF)

Current drive by ICRF waves (ICCD) is possible in a variety of scenarios [7, 8]. The wave to be injected in this range of frequencies is the fast magnetosonic wave (or fast wave FW), which has a dominant perpendicular electric field polarization [34]. Avoiding significant damping on the ions or mode conversion to ion Bernstein waves, most of the power can be deposited on electrons through multi pass absorption by electron Landau-damping and transit time magnetic pumping (TTMP). In case of the injection of an asymmetric wave spectrum, these result in fast wave current drive (FWCD). FWCD has been demonstrated on JFT-2M, DIII-D [35], and Tore-Supra [36]. Current drive efficiencies obtained scale with the central electron

temperature and have reached values up to $\eta_{FWCD} = 4 \times 10^{18}$ A/Wm^2 in agreement with theoretical modeling [7, 37]. Typical driven current density profiles are very peaked on axis due to both central peaking of the power deposition and trapped particle effects. Extrapolation of these results to ITER yield an expected current drive efficiency of $\eta_{FWCD} = 0.2 \times 10^{20}$ A/Wm^2 with a centrally peaked driven current density profile.

Alternative scenarios of ICCD make use of the generation of extended energetic ion tails, for example, through ion minority heating. In the case of asymmetric wave particle interaction, these can result in a sizeable driven ion current, which can be calculated from a trivial generalization of the Fisch-Boozer efficiency (6). As in the case of Neutral Beam current drive (see section IV) this energetic ion current J_m (with minority ion charge Z_m) results in a net plasma current $J = J_m (1 - Z_m/Z_i)$ where Z_i is the majority ion charge. The final equation for the ion minority current drive efficiency then becomes [6]

$$\frac{J}{P_{ICCD}} = eZ_m(1 - Z_m/Z_i)\frac{\hat{s}\cdot\nabla_{\mathbf{p}} v_{\|}/\nu}{\hat{s}\cdot\nabla_{\mathbf{p}} p^2/2m_e}. \qquad (16)$$

Additional energetic ion currents can arise from finite orbit widths of (trapped) resonant ions [38]. These latter currents are highly localized and due to their diamagnetic origin typically of bipolar shape. This makes these currents well suited for MHD instability control. Successful control of sawteeth has been demonstrated by ICCD on JET resulting in possible avoidance of NTM [39].

III.D. Alfvén wave Current Drive (AWCD)

At first glance, current drive by low frequency $\omega < \Omega_{ci}$, low phase velocity $v_{ph} < v_{te}$ Alfvén waves appears very attractive as the current drive efficiency increases dramatically for low phase velocities (see Fig. 1). However, as the wave momentum is imparted to electrons with very small parallel velocity, most of these electrons are likely to be trapped. For this reason efficiencies for AWCD are expected to be very low. In one of the few experiments an efficiency of $\eta_{AWCD} = 0.4 \times 10^{18}$ A/Wm^2 was achieved. However, the favorable regime with very low phase velocity $v_{ph} < v_{te}$ could not be accessed [40].

IV. NEUTRAL BEAM CURRENT DRIVE (NBCD)

The possibility of current drive by the injection of energetic beams of neutral particles was already realized in the early stages of tokamak research [41]. Following the discussion as given in Ref. [6], the principle of NBCD can be understood as follows. Consider a homogeneous, neutral plasma with two groups of counter streaming ions. It is then always possible to choose the frame of reference such that their currents cancel exactly and the net ion current vanishes. When one of the two ion populations, say the left moving bulk ions, can now be made to collide more efficiently with the electrons then the right moving beam ions, the

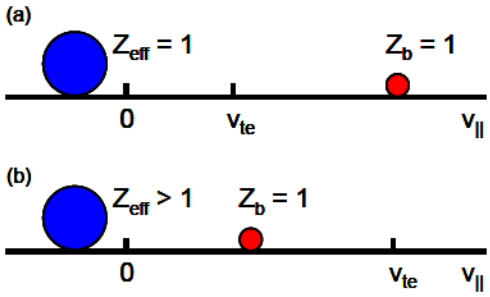

Figure 3: Illustration of the principle of neutral beam current drive. A difference in the momentum transfer rate from bulk (left) and beam (right) ions to the electrons is due to (a) a beam velocity well in excess of the electron thermal velocity or (b) a difference in charge state between bulk and beam ions.

electrons will be displaced in the direction of this left moving bulk ions and a net plasma current in the opposite direction would result. Finally, note that in neutral plasma the current is a Lorentz invariant, such that it is independent of the frame of reference in which it is derived.

Two possible ways to realize such a situation with different momentum transfer rates from the bulk and beam ion populations to the electrons are sketched in Fig. 3 (after Ref. [6]). In the first example (Fig. 3a), a beam of highly energetic ions is moving to the right at velocities v_b well above the electron thermal velocity (i.e. $v_b \gg v_{te}$). Due to the velocity dependence of the Coulomb collision frequency, the electrons would then collide much more frequently with the left moving bulk ion population, and a net current to the right would result. As said, this requires neutral beam injection with beam velocity far exceeding the electron thermal velocity, which in high temperature fusion plasmas is unpractical.

In the second example (Fig. 3b), the beam velocity maybe smaller than the electron thermal velocity (i.e. $v_b < v_{te}$). A difference in momentum transfer rates is now obtained by exploiting the dependence of the Coulomb collision frequency on the square of the ion charge state Z_i, while the current carried is only linear in Z_i. When the effective charge state of the bulk ions Z_{eff} now exceeds that of the energetic ion beam Z_b (or vice versa), the electrons again will collide more frequently with the left moving bulk ions (the beam ions), and a net current to the right (left) will arise. Neglecting trapped electron effects, this results in a current

$$J = \left(1 - \frac{Z_b}{Z_{eff}}\right) J_b, \qquad (17)$$

where J_b is the current carried by the energetic ion beam. Trapped electron effects further restrain the electron motion, resulting in a further reduction of the cancelling electron current. In the large aspect ratio approximation the net result is [9,42]

$$J = \left(1 - \frac{Z_b}{Z_{eff}}\left(1 - 1.46\sqrt{\varepsilon}A(Z_{eff})\right)\right)J_b\,, \qquad (18)$$

where $A(Z_{eff})$ is a function whose values vary from 1.67 for $Z_{eff} = 1$ to 1.18 for $Z_{eff} = 4$.

A calculation of the beam current J_b, requires a Fokker-Planck solution of the beam ion distribution. In the absence of trapping an analytical solution for this 'slowing down distribution' has been found in the form [9]

$$J_b = p_{NBCD}\frac{2\tau_s e Z_b}{m_b v_b(1+u_c^2)}\int_0^1 f_1(u)u^3 du \qquad (19)$$

where p_{NBCD} is the local density of neutral beam power deposition, m_b the mass of the beam ions, τ_s is the energetic ion slowing down time, and u is the energetic ion velocity normalized to the injection velocity v_b. The function f_1 is the first order Legendre harmonic of the energetic ion distribution function, and is given by

$$f_1(u) = u^{2\beta}\left(\frac{1+u_c^3}{u^3+u_c^3}\right)^{1+2\beta/3}, \qquad (20)$$

where

$$\beta = \frac{m_i Z_{eff}}{2m_b\overline{Z}}, \qquad u_c^3 = \frac{3\sqrt{\pi}m_e\overline{Z}v_{te}^3}{4m_i v_b^3}$$

and

$$\overline{Z} = \sum_i \frac{m_b n_i Z_i^2}{m_i n_e}$$

where the subscript i refers to the different bulk ion species.

NBCD has been applied successfully in a number of tokamaks. The maximum driven currents are in agreement with the theoretical expectations according to the model outlined above [8]. Typical beam energies in current experiments range from several 10's of keV in the smaller tokamaks up to 350 keV in the larger JT-60U tokamak. For efficient penetration into the high density ITER core, beam energies of 0.5 to 1 MeV will be required. The efficient neutralization of the accelerated beam ions before injection into the plasma at these high energies is only possible using negative ion sources. Due to the nature of the NB power deposition the NBCD profile can be relatively broad, and is most useful for driving bulk plasma current rather than current density profile tailoring. A record NBCD efficiency of $\eta_{NBCD} = 0.15 \times 10^{20}$ A/Wm^2 has been achieved on JT-60U using negative ion based NBCD at beam energies of 350 keV in $T_e(0) = 14$ keV, high beta plasmas with fully non-inductive plasma current sustainment [43]. Calculations for ITER conditions predict NBCD efficiencies up to $\eta_{NBCD} = 0.4 \times 10^{20}$ A/Wm^2 [7] for an optimized system.

V. ALTERNATIVE METHODS

Many alternative methods have been considered in the literature. However, none of these methods has achieved the experimental maturity of the RF and neutral beam based current drive methods discussed above. We will provide only a cursory sketch of these alternatives.

V.A. Helicity injection

Helicity is defined as the inner product of the vector potential and the magnetic field, $K \equiv \boldsymbol{A}\cdot\boldsymbol{B}$, where the vector potential $\boldsymbol{A}$ satisfies $\boldsymbol{B} = \nabla\times\boldsymbol{A}$. A transport equation for helicity can be written using Ohm's law as [44]

$$\frac{\partial K}{\partial t} + \nabla\cdot\boldsymbol{Q} = -2\eta\boldsymbol{J}\cdot\boldsymbol{B}, \qquad (21)$$

where the helicity flux is

$$\boldsymbol{Q} = \boldsymbol{B}\phi + \boldsymbol{E}\times\boldsymbol{A} = 2\boldsymbol{B}\phi + \boldsymbol{A}\times\partial\boldsymbol{A}/\partial t \qquad (22)$$

with ϕ being the electrostatic potential, and the total electric field $\boldsymbol{E} = -\nabla\phi - \partial\boldsymbol{A}/\partial t$. The evolution of the total magnetic helicity $K_{tot} \equiv \int \boldsymbol{A}\cdot\boldsymbol{B}\,dV$, where the integration is over a plasma volume bounded by a magnetic surface, then is given by

$$\frac{\partial K_{tot}}{\partial t} = 2V_{loop}\Phi_T - \int 2\,\eta\boldsymbol{J}\cdot\boldsymbol{B}dV. \qquad (23)$$

Here, the first term on the right hand side represents the helicity injection at the edge of the plasma given by the product of the toroidal loop voltage and the toroidal magnetic flux. The second term represents the volume integrated helicity dissipation. In the case of inductive current drive the dissipation of helicity is canceled by a DC loop voltage, which is limited by the flux swing of the primary transformer. In the concept of oscillating field current drive (OFCD) (or AC helicity injection) very low frequency, oscillating toroidal and poloidal electric fields are applied at the plasma edge, with relative phasing such that net time averaged helicity injection is obtained [45, 46]. The current generated in this way is located at the plasma surface and penetration to the plasma core must rely on Taylor relaxation: the conjecture that magnetically confined plasmas tend to relax to states with minimum magnetic energy while conserving total helicity [47]. An experimental demonstration is given in Ref. [48].

Electrostatic (or DC) helicity injection makes use of the term $2\boldsymbol{B}\phi$ in the helicity flux (22). This is only possible in case of open field lines exciting and entering the plasma volume. A simple prescription for electrostatic helicity injection then would be to cut an electric gap dividing the bounding surface into two areas where magnetic flux either enters or leaves the volume and to apply a voltage V over this electric gap. This results in an amount of helicity injection given by [44]

$$\left.\frac{\partial K_{tot}}{\partial t}\right|_{inj} = 2V\Phi_M\,, \qquad (24)$$

where

$$\Phi_M = \frac{1}{2}\int|\boldsymbol{B}\cdot\boldsymbol{n}|\,dS$$

is the net flux entering/leaving the volume. The method has been applied successfully in a number of experiments using different geometries for the applied magnetic fields and voltages [49–52], and appears

particularly useful for current start-up in solenoid-free spherical tokamaks [53].

V.B. Alpha power channeling

The basic idea of 'alpha power channeling' is to transfer energy from the energetic fusion alpha particles into waves, which may then be put to practical use. The transfer of energy from particles to waves requires the inversion of the alpha particle distribution along the wave diffusion trajectory. In the original proposal, the alpha particle energy is channeled through interaction with Lower Hybrid waves into current drive [54]. Later, alpha particle interaction with Ion Bernstein waves has been envisaged to channel alpha particle energy into heating of fuel ions with the potential of increasing the plasma reactivity [55]. A review of the main concepts and of some partial experimental tests is given in Ref. [56].

V.C. Synchrotron radiation

Fusion plasmas are a powerful source of synchrotron radiation. As the tokamak vessel walls are generally highly reflective for these waves, the radiation is continuously emitted and reabsorbed. Whereas the emitted radiation is isotropic, it has been suggested that by proper shaping of the vessel walls the reflected spectrum can be made anisotropic such that the reflected waves could effectively drive plasma current [57]. The anisotropic reflection is achieved by means of a sawtoothed or fish-scale wall in which the vertical sections are made absorbing while the slanted sections are made reflecting. Further investigations seem to indicate that only part of the current can be driven in this way in a realistic fusion reactor [58, 59].

VI. SYNERGY

So far, the different current drive schemes have been treated individually. Synergy could be expected from combinations of any of these. For example, combining LHCD and ECCD has been shown to significantly increase the ECCD efficiency as the EC waves can interact with the LHCD produced high energy tail electrons [60]. In another experiment the combination of LHCD and ion Bernstein waves (IBW) has been shown to lead to a locally increased LHCD current, which is due to the local generation of a broadened electron velocity distribution by the IBW on which the LHCD wave are damped more efficiently [61]. On JET a synergy between LHCD and the FWCD was noted [62]. An increased NBCD efficiency could be expected from ion cyclotron resonance heating of the energetic beam ions: the increase of the perpendicular velocity of the beam ions increases their slowing down time and the resulting beam current [63]. Finally, radial gradients in RF driven quasi-linear populations will affect the bootstrap current [64].

VII. PROSPECTS FOR A STEADY STATE TOKAMAK REACTOR

Even with the highest predicted current drive efficiencies quoted above, full non-inductive drive of the total plasma current in a standard high performance H-mode discharge in ITER would require a prohibitively large amount of power. As we can foresee now, the fully non-inductive, steady state operation of ITER and future tokamak fusion reactors will have to rely on the bootstrap current for supplying the major part of the plasma current. Other methods, like NBCD or ECCD, need than be used to supply sufficient core current to fill in the hollow bootstrap current profile $\sim\sqrt{\varepsilon}dp/dr$ [8]. Maximizing simultaneously bootstrap current fraction and performance is one of the goals of advanced tokamak scenario development. Integrated modeling of such scenarios illustrates the possibilities for steady state discharges in ITER [65].

ACKNOWLEDGMENTS

DIFFER is part of the institutes organisation of NWO.

REFERENCES

[1] M. VAN SCHOOR, 'Fusion Machines', these proceedings.
[2] H.J. DE BLANK, 'Guiding centre motion, these proceedings.
[3] D.A. HARTMANN, 'Stellarators', these proceedings.
[4] H.J. DE BLANK, 'MHD instabilities in tokamaks', these proceedings.
[5] H.R. KOSLOWSKI, 'Operational limits and limiting instabilities in tokamak machines', these proceedings.
[6] N.J. FISCH, Rev. Modern Phys. **59** 175 (1987).
[7] ITER Physics Basis, Chapter 6: Nucl. Fusion **39** 2495 (1999).
[8] C. GORMEZANO, et al, Nucl. Fusion **47** S285 (2007).
[9] J. WESSON, 'Tokamaks' Third Edition, (2004).
[10] P. HELANDER, 'Neoclassical transport in plasmas', these proceedings.
[11] A.G. PEETERS, Plasma Phys. Control. Fusion **42** B231 (2000).
[12] N.J. FISCH, A.H. BOOZER, Phys. Rev. Lett. **45** 720 (1980).
[13] C.F.F. KARNEY, N.J. FISCH, Nucl. Fusion **21**, 1549 (1981).
[14] C.F.F. KARNEY, Comp. Phys. Reports **4**, 183 (1986).
[15] T. OHKAWA, General Atomics Report GA-A13847 (1976).
[16] R.H. COHEN, Phys. Fluids **30**, 2442 (1987)
[17] Y.R. LIN-LIU, et al, Phys. Plasmas **10**, 4064 (2003).

[18] N.B. MARUSHCHENKO, et al, Nucl. Fusion **48**, 054002 (2008).
[19] Y. PEYSSON, in Radio Frequency Power in Plasmas, AIP Conf. Proc. **485**, 183 (1999).
[20] R.A. CAIRNS, Radiofrequency heating of plasmas, IOP Publishing, Bristol (1991).
[21] P.T. BONOLI, R.C. ENGLADE, Phys. Fluids **29**, 2937 (1986).
[22] R. CESARIO, et al, Nucl. Fusion **46**, 462 (2006).
[23] P.T. BONOLI, et al, in Radio Frequency Power in Plasmas, AIP Conf. Proc. **694**, 24 (2003).
[24] P.T. BONOLI, et al, Phys. Plasmas **15**, 056117 (2008).
[25] E. WESTERHOF, 'Electron Cyclotron Waves', these proceedings.
[26] R. PRATER, Phys. Plasmas **11**, 2349 (2004).
[27] R. PRATER, et al, Nucl. Fusion **48** 035006 (2008).
[28] R.W. HARVEY, et al, Phys. Rev. Lett. **62**, 426 (1989).
[29] E. WESTERHOF, 9th Joint Workshop on ECE and ECH, Borrego Springs, California, 1995, Ed. J. Lohr, World Scientific, Singapore, p. 3 (1995).
[30] T. SUZUKI, et al, Nucl. Fusion **44**, 699 (2004).
[31] C.C. PETTY, et al, Nucl. Fusion **42**, 1366 (2002).
[32] O. SAUTER, et al, Phys. Rev. Lett. **84**, 3322 (2000).
[33] G. RAMPONI, et al, Fusion Sci. Technol. **52** 193 (2007).
[34] F. LOUCHE, 'Coupling of EM waves to the plasma', these proceedings.
[35] R. PRATER, et al, Plasma Phys. Control. Fusion **35**, A53 (1993).
[36] EQUIPE TORE SUPRA, presented by B. Saoutic, Plasma Phys. Control. Fusion **36** B123 (1994).
[37] C.C. PETTY, et al, Plasma Phys. Control. Fusion **43** 1747 (2001).
[38] T. HELLSTEN, et al, Phys. Rev. Lett. **74** 3612 (1995).
[39] O. SAUTER, et al, Phys. Rev. Letters **88**, 105001 (2002).
[40] T. INTRATOR, et al, Phys. Plasmas **2**, 2263 (1995)
[41] T. OHKAWA, Nucl. Fusion **10**, 185 (1970).
[42] J.W. CONNER, J.G. CORDEY, Nucl. Fusion **14**, 185 (1974).
[43] T. OIKAWA, et al, Nucl. Fusion **41**, 1575 (2001).
[44] T.H. JENSSEN, M.S. CHU, Phys. Fluids **27**, 2881 (1984).
[45] P.M. BELLAN, Phys. Rev. Letters **54**, 1381 (1985).
[46] A.H. BOOZER, Phys. Fluids **29**, 4123 (1986).
[47] J.B. TAYLOR, Phys. Rev. Letters **33**, 1139 (1974).
[48] K.J. McCOLLAM, et al, Phys. Rev. Letters **96**, 035003 (2006).
[49] M. Ono, et al, Phys. Rev. Letters **59**, 2165 (1987).
[50] B.A. NELSON, et al, Phys. Plasmas **2**, 2337 (1995).
[51] A.J. REDD, et al, Phys. Plasmas **9**, 2006 (2002).
[52] R. RAMAN, et al, Nucl. Fusion **41**, 1081 (2001).
[53] R. RAMAN, et al, Nucl. Fusion **47**, 792 (2007).
[54] N.J. FISCH, J.M. RAX, Phys. Rev. Letters **69**, 612 (1992).
[55] N.J. FISCH, et al, Nucl. Fusion **34**, 1541 (1994).
[56] N.J. FISCH, Nucl. Fusion **40**, 1095 (200).
[57] J.M. DAWSON, P.K. KAW, Phys. Rev. Letters **48**, 1730 (1982).
[58] I. FIDONE, et al, Phys. Fluids **31**, 2300 (1988).
[59] W. KERNBICHLER, S.V. KASILOV, Phys. Plasmas **3**, 4128 (1996).
[60] G. GIRUZZI, et al, Phys. Rev. Letters **93**, 255002 (2004).
[61] F. PAOLETTI, et al, Phys. Plasmas **6**, 863 (1999).
[62] J. JACQUINOT, Plasma Phys. Control. Fusion **35**, A35 (1993).
[63] K. OKANO, et al, Nucl. Fusion **23**, 235 (1983).
[64] R.W. HARVEY, and G. Taylor, Phys. Plasmas **12**, 052509 (2005).
[65] W.A. HOULBERG, et al, Nucl. Fusion **45**, 1309 (2005).

MODELLING RADIATIVE POWER EXHAUST AND IMPURITY TRANSPORT

S. Wiesen[1]

[1] *Forschungszentrum Jülich GmbH, Institut für Energie- und Klimaforschung - Plasmaphysik,*

ABSTRACT

A brief introduction on power and particle exhaust is given and the concept of a radiative divertor in detached conditions is briefly described. The role of impurity radiation and transport at the plasma edge in fusion devices is highlighted especially for devices with a metallic wall. Some important aspects for future reactors are described with the focus on enhanced dissipation by plasma core radiation. The implications on the pedestal fueling and core confinement are highlighted. For extrapolations towards future electricity producing reactors robust detachment scaling criteria are required. Existing reduced semi-empirical models are described and compared to numerical models.

I. POWER & PARTICLE EXHAUST IN THE NUTSHELL: BASIC PHYSICS

For a given scrape-off layer (SOL) flux-tube of connection length $L_\parallel$ and power P_{SOL} crossing the separatrix into the SOL (c.f. fig. 1), the upstream parallel heat-flux density is defined as

$$q_\parallel^u = \frac{P_{SOL}}{A_\parallel} = \frac{P_{SOL} B}{2\pi R B_p \lambda_q} \qquad (1)$$

with $A_\parallel$ being the cross-section of the flux-tube expressed by the major radius R, the local ratio of toroidal and poloidal field B/B_p and width λ_q (heat decay parameter) of the flux-tube. At the target plate, the parallel heat-flux density can be most generally formulated by dissipation factor $(1 - f_{diss})$

$$q_\parallel^t = (1 - f_{diss})\, q_\parallel^u. \qquad (2)$$

Taking into account that the target plate can be tilted to allow for a poloidal and toroidal inclination with effective inclination angle θ_t at the plate the minimum dissipation required for a given (material dependent) maximum perpendicular heat-flux density is defined through

$$f_{diss}^{min} = 1 - \frac{q_\perp^{max}}{q_\parallel \sin\theta_t} \qquad (3)$$

For existing tokamak devices a robust wall-material independent scaling for the upstream power fall-off length has been identified[1, 2] $\lambda_q \sim 1/B_p \sim 1/I_p$ (albeit only for unseeded and attached divertor conditions) which seems to be consistent with the recent heuristic drift model scaling of Goldston[3] $\lambda_q \sim 2a\rho_p/R$. From this scaling, an upstream $q_\parallel^u \sim P_{SOL}B/R$ for ITER $\approx 5\,GW/m^2$ and for DEMO $\approx 30 > GW/m^2$ is to be expected, leading to an unmitigated $q_\perp^t$ of $50\,MW/m^2$ and $300\,MW/m^2$ for ITER and DEMO, respectively[4], clearly exceeding the tolerable material limit $q_\perp^{t,max} \approx 5 - 10\,MW/m^2$ for actively cooled W-PFCs.

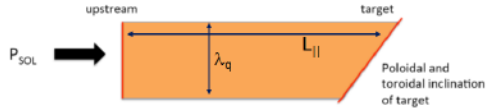

Figure 1: Sketch of a scrape-off layer (SOL) tube along the magnetic field. The power enters the SOL P_{SOL} from upstream, is transported mainly conductively along the field with cnnection length $L_\parallel$ before it hits an (inclined) target plate. A power decay length λ_q is assumed.

The so called detached divertor regime has been suggested in the 1990s (c.f. Fenstermacher et al.[5]) providing a concept to avoid excessive heat loads to the PFCs. P_{SOL} enters the SOL region from the core (mainly driven by anomalous, ballooning like convective-diffusive turbulent transport). A conducted heat-flux $q_\parallel$ is driven and altered along the field lines by collisions and impurity radiation causing a reduction in temperature. Interaction with neutrals induces a pressure loss by charge-exchange and elastic processes. With increasing density the a high-recycling regime is established in the divertor, causing the divertor to cool further down. In case of $T^{div} < 2 - 3\,eV$ an additional particle loss is induced by volumetric recombination causing a reduction of the target particle-flux Γ^t and a subsequent roll-over thereof with increasing divertor neutral pressure p_0^{div}. Energy transfer of recombining ions at the surface can thus also be minimised that may be significant in large scale fusion devices[4].

One speaks of a *fully detached* or *completely detached regime* in which the $q_\parallel^t$ is near to zero everywhere across the target plate. A *partially detached regime* assumes that $q_\parallel^t$ is reduced significantly close to the separatrix but not zero everywhere. An inter-

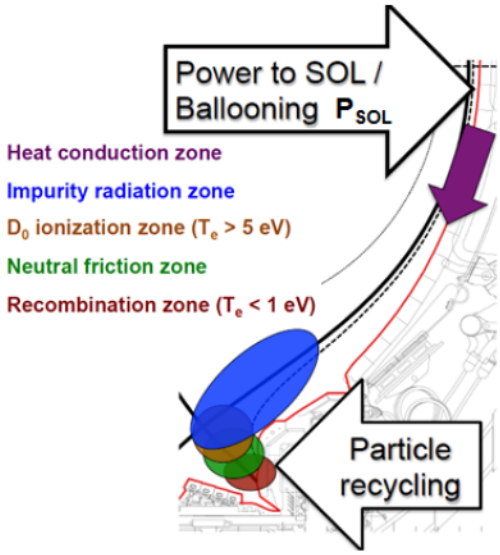

Figure 2: Concept of a detached divertor [5]

mediate regime, if stabilized, can be identified as a so-called *pronounced detached regime* [6] in which $q_{\parallel}^{t}$ is reduced across the plate but not vanishing.

In metallic devices H-mode detachment can be typically classified as follows (c.f. Asdex-Upgrade (AUG) as example[7]): without impurity seeding one identifies the onset of detachment at the inboard side of the divertor first (by observing a roll-over of the saturation current j_{sat}^{t}). With increasing density one enters a state with radiative fluctuations close to the X-point region[8]. Additionally, a so-called HFS high-density (HFSHD) region establishes being sustainable only of sufficient power reaches the inboard far-SOL region[9]. Contrary to devices with a C-wall, the radiation of metallic impurities is usually not sufficient to drive the divertor into detachment in H-mode. Hence impurity seeding (using N, Ne, Ar or even Kr or Xe) can be used to induce significant power dissipation. Nitrogen is more likely radiating in the divertor and can be used for example to feedback on the level of detachment in the LFS divertor (see also next section). In case of partial detachment induced by seeding a significant fraction of radiation takes place close to the X-point and the HFSHD region disappears as it cannot be sustained anymore. Complete detachment is achieved by even stronger seeding with the consequence of radiation condensation around the X-point (including also Blamer radiation to occur inside the confined region). As a consequence pressure is lost upstream which has some important consequences on the confinement (c.f. section below).

It is not only the radiation of impurities that controls the power dissipation process. A zoo of processes exists helping to realise the shape and locality of radiation and interaction with neutrals (recombination and friction zone). A large set of atomic and molecular data exists that can be included in state-of-the-art edge codes like SOLPS-ITER[10] or EDGE2D-EIRENE[11, 12, 13] by allowing the neutrals (from recycling and impurities) to be treated kinetically and coupling those at self-consistently to the plasma fluid for which particle, ion-momentum and energy balances (Braginskii equations) are solved. Also, the wall geometry plays an important role as neutrals are to bound to the field lines and thus at least a 2D representation of the divertor is required.[14]. Additionally, radial (anomalous) transport leads to an extra loss of particles, momentum and energy along the field. In total the parallel heat-flux arriving at the target plate is reduced by the combination of aforementioned losses:

$$q_{\parallel}^{t} = q_{\parallel}^{u} - q_{rad}^{imp} - q_{recy}^{rad} - q_{\perp} - q_{recom}. \qquad (4)$$

2D edge codes like EDGE2D-EIRENE or SOLPS-ITER nowadays have proven that they are capable to reproduce the H-mode detachment transition at least qualitatively (c.f. examples for JET[15] and AUG[16]). Further refinement of the dominant atomic processes governing the neutral dynamics have improved the credibility of the modelling of high-density discharges (c.f. examples of C-mod[17]) showing that the inclusion of molecular assisted processes, ion-molecule elastic processes, neutral-viscosity[18] is mandatory to be included in the edge models exploring into ITER or DEMO relevant divertor regimes at high densities. Other effects like the Lyman-α opacity[19] may have an indirect impact on the operational regime as it is the recombination-ionisation balance that is amended and an increase in the peak value of $q_{\parallel}$ can always be overcome by an increase in p_0^{div} (however it has also been demonstrated that for JET-C that a strong X-point MARFE can only be stabilised numerically with the SOLPS4.3 code if Lyman-radiation trapping is included in the model[20], that can be seen as a potential requirement for numerical extrapolations to DEMO using such codes). A similar argument follows for the inclusion of the sub-divertor geometry as without inclusion of neutral conductance below and behind divertor legs the experimentally observed linear dependence of pumping efficiency and p_0^{div} cannot be matched numerically for existing devices [21, 22].

II. POWER DENSITY OF RADIATION LOSSES

Normally, impurities enter the plasma as neutral particles, generated in erosion processes of the wall elements [23, 24] or deliberately seeded [25, 26]. In the process of ionization by electrons these neutrals are converted into ions of different electric charges

Z. The power density of radiation losses from all impurity charge states can be calculated as follows:

$$Q_{rad} = \sum_{Z=0}^{Z_{max}} n n_Z L_Z \tag{5}$$

Here n is the density of plasma electrons which loss their energy either by exciting electrons bounded in impurity ions or due to Bremsstrahlung radiation by Coulomb scattering; n_Z the density of impurity ions of the charge Z; L_Z the so called cooling rate, i.e., the power lost from a unit volume if one electron and one impurity ion are present there. To determine n_Z and L_Z, one has to consider the processes responsible for the transport of impurity particles and radiation from them.

If the exact spreading of each impurity charge state is non-relevant, one can express Q_{rad} through the effective impurity cooling rate $L_I = \sum_Z \zeta_Z L_Z$ and the total impurity ion density $n_I = \sum_Z n_Z$:

$$Q_{rad} = n n_I L_I \tag{6}$$

where $\zeta_Z = n_Z/n_I$ are the relative concentrations of different impurity charge states.

A. Impurity ion density

The densities of ions of different charges are described by the continuity equations:

$$\partial_t n_Z + \nabla_\parallel \left(n_Z V_\parallel^Z \right) + \nabla_\perp \Gamma_\perp^Z = S_Z - \nu_Z n_Z \tag{7}$$

where V_Z is the ion velocity along magnetic field, $\Gamma_\perp^Z$ the density of their flux in the perpendicular direction, S_Z and ν_Z are the source density and the frequency of ion disintegration, respectively. The latter include diverse processes [27], e.g., ionization by electrons, capture of free electrons by radiative and dielectronic recombination, and of electrons bounded in hydrogen atoms by charge-exchange, etc.

The parallel motion of impurity ions is of the most importance close to the sources where impurity particles are released into the plasma and obeys the momentum transfer equation:

$$\begin{aligned} &\partial_t \left(n_Z V_\parallel^Z \right) + \nabla_\perp \left(\Gamma_\perp^Z V_\parallel^Z \right) \\ &+ \nabla_\parallel \left[n_Z \left(V_\parallel^Z \right)^2 + n_Z T_Z / m_Z \right] \\ &= M_Z - \nu_Z n_Z V_\parallel^Z + Z e E_\parallel / m_Z \\ &+ \nu_{Zi} \left(V_\parallel - V_\parallel^Z \right) + \xi_Z \nabla_\parallel T / m_Z \end{aligned} \tag{8}$$

The first term on the right hand side, M_Z, is the momentum assimilated from the ion source and the second one is the loss by the ion disintegration; the third term is the acceleration due to the parallel electric field; the forth one term is due to friction of impurities with the background ions moving with the mass parallel velocity $V_\parallel$, and ν_{Zi} is the friction coefficient [28]; the last term is the so called thermal force arising also due to collisions with the background plasma particles if their temperature T has a parallel gradient; this force exists because the collision frequency decreases with increasing temperature and for the impurity ion mass m_Z significantly larger than that of the background ions[29], m_i, $\xi_Z \approx 3.3 Z^2$. Normally, the electric field arises because light electrons escape from the plasma to the limiter or divertor plate faster than ions. In such a case both electric and friction forces drag the impurity ions back to the material surface but the thermal force pulls them in the opposite direction, towards the region of higher temperature.

The perpendicular flux of impurities, averaged over the magnetic surfaces, is normally decomposed into diffusive and convective terms:

$$\Gamma_{Z\perp} = -D_\perp \nabla_\perp n_Z + V_\perp n_Z \tag{9}$$

In the diffusivity $D_\perp$ and convection velocity $V_\perp$ usually neoclassical and anomalous contributions are taken into account:

$$D_\perp = D_\perp^{neo} + D_\perp^{an} \tag{10}$$

$$V_\perp = V_\perp^{neo} + V_\perp^{an} \tag{11}$$

The former one is due to collisions with the main ions [30] and the latter one due to drift micro-instabilities in the plasma [31]. Normally $D_\perp^{neo} \ll D_\perp^{an}$ and $V_\perp^{neo} \leq V_\perp^{an}$. The convection velocities are controlled by the radial gradients of plasma parameters such as density, temperature, safety factor, etc.

The temperature T_Z of impurity species in the parallel pressure gradient on the left hand side of Eq. 8 is changing through the Coulomb collisions with the background plasma particles and is governed by the heat transfer equation:

$$\begin{aligned} &\partial_t \left(\frac{3}{2} n_Z T_Z \right) + \nabla_\perp \left(\frac{3}{2} \Gamma_\perp^Z T_Z \right) + \nabla_\parallel \left(\frac{5}{2} n_Z V_\parallel^Z T_Z \right) \\ &= Q_Z - \frac{3}{2} \nu_Z n_Z T_Z + 3 \nu_{Zi} n_Z \left(T - T_Z \right) \end{aligned} \tag{12}$$

where Q_Z is the density of heat assimilated from the ion source. It is worth to note that different impurity charge states are heated by the plasma particles to different temperatures and in the vicinity of local sources of impurity the effect of impurity heating on its parallel transport can be comparable or even higher than that from the electric field arising by impurity ionization.

B. Impurity cooling rate

There are two the most important radiation processes through which plasma electrons lose their energy in interactions with impurity particles. The first one is the line radiation arising when impurity is excited by electron impacts [32]. In hot fusion plasmas the excited particles are normally de-excited

spontaneously by radiating photons. Since tokamak plasmas are normally transparent to impurity radiation, this leads to plasma cooling. The second one is Bremsstrahlung arising due to change of electron velocity caused by the attraction towards the impurity nuclei. Normally at the plasma edge the line radiation is the main contribution to the radiation from impurities. The cross-section of the Bremsstrahlung process increases, however, as Z^2 and in the hot central plasma, where impurity particles are strongly ionized, it dominates radiation losses. The temperature dependence of the cooling rate for carbon ions of all charges is shown in Fig. 3. The low ionized B, Be, Li-like charge states with $Z = 1, 2, 3$ are easy to excite since their typical excitation energy E_{ex} is of $5 - -10\,eV$; the He, H-like ions C^{4+} and C^{5+} with $E_{ex} \sim E_{ion} \geq 300\,eV$ can be excited only at high temperatures; the nuclei C^{6+} contribute to Bremsstrahlung only.

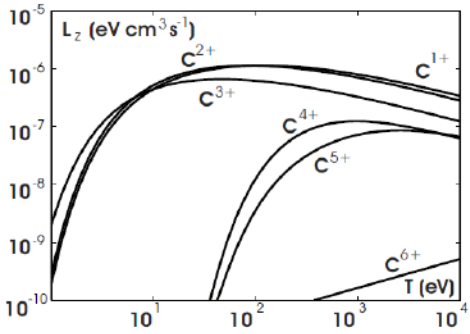

Figure 3: The temperature dependence of the cooling rates for different carbon charge states[33]

Often, e.g. in the hot central plasma, the effective impurity cooling rate L_I is assessed in the so called corona approximation [32]. It has been developed for the description of Sun corona where the processes of ionization and recombination dominate the particle balances for different charge states and their densities are governed by the relations:

$$k^{ion}_{Z-1} n_{Z-1} + k^{rec}_{Z+1} n_{Z+1} = \left(k^{ion}_{Z} + k^{rec}_{Z}\right) n_Z \qquad (13)$$

Here $k^{ion}_{Z,Z\pm1}$ and $k^{rec}_{Z,Z\pm1}$ are the ionization and recombination rate coefficients depending only on the electron temperature. In this case the relative concentrations of different impurity charge states, ζ_Z, and, thus, the effective impurity cooling rate L_I depend also on the local electron temperature only. This dependence is shown for carbon by the solid curve in Fig. 4. The increase of L_I with the temperature at low T is due to temperature behavior of L_Z for impurity ions of low charges with small excitation energies, see Fig. 3. The sharp drop of L_I at high temperatures is due to ionization of impurity particles into dim high-Z states.

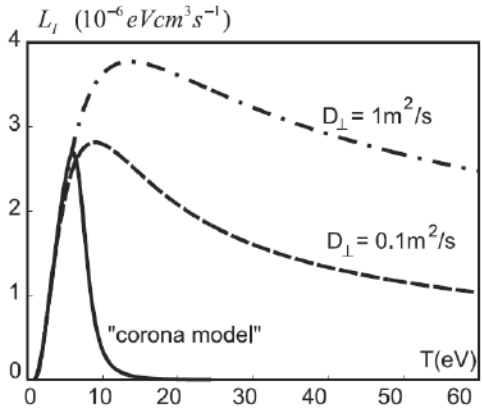

Figure 4: The effect of perpendicular diffusion of impurity ions on the effective cooling rate of carbon[33].

At the plasma edge in fusion devices the anomalous transport can be very intensive. Low-Z impurity ions, which are generated from neutrals entering the plasma, have enough time to diffuse into hot plasma regions before they are ionized into dim high-Z states. Therefore, transport processes increase effective cooling rate and make it less temperature sensitive compared to the corona approximation without transport effects; see Fig. 4 where L_I is shown by dashed and dash-dotted curves for different values of the impurity diffusivity $D_\perp$ [33]. Similarly, the charge-exchange of impurity ions with hydrogen neutrals affects L_I [35]. The effects of elementary and transport processes on the density, radiation losses and ion heat exchange from impurity are taken firmly into account in transport codes. Figure 5 shows the radial profiles of the radiation loss density for different charge states of carbon computed by the code RITM (Radiation of Impurity and Transport Model) for an Ohmic discharge in the tokamak TEXTOR [34]. One can see that the Li-like ions C^{3+} are the main contributors to the radiation losses. This is explained by the fact that, on the one hand, the characteristic excitation energy of these ions is relatively low, of $8\,eV$, and, on the other hand due to high enough ionization energy of $64\,eV$ they live long and penetrate deeply into the plasma.

In the vicinity of intense localized impurity sources, e.g. diagnostic beams, injection valves or suddenly melted parts of the wall, one has to take into account the essential time-dependence and 3-dimensionality of the impurity spreading process. During the life time $\tau^{ion}_Z \equiv 1/\left(k^{ion}_Z n\right)$ impurity ions of the charge state Z move along the magnetic field and diffuse in the direction y perpendicular to the field at distances $l_Z \approx V^Z_\parallel \tau^{ion}_Z$ and $\delta_Z \approx \sqrt{D_\perp \tau^{ion}_Z}$, respectively. On the one hand the area $A_Z = \delta_Z l_Z$

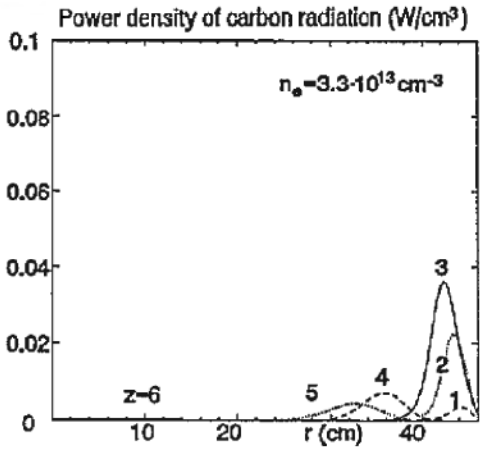

Figure 5: The radial profiles of the radiation loss density for different charge states of carbon impurity entering the plasma through the LCMS located at the minor radius $r = 46\ cm$, computed with the code RITM for an Ohmic discharge in the tokamak TEXTOR [34].

occupied by ions of low Z ions with very large k_Z^{ion} and small τ_Z^{ion} is negligible compared with the total area A_S of the magnetic surface. On the other hand, k_Z^{ion} decreases with increasing Z and, thus, A_Z grows up also. Therefore, the Z-state serves as an intensive but localized source for the next charge state. All together the regions on the magnetic surface occupied by charge states with $A_Z < A_S$ form a set of nested shells evolving in time. By using this "shell" approximation [36] one can complement transport codes, modeling the radial profiles of impurity ion densities, e.g., RITM, with a description of non-stationary spreading of impurity on magnetic surfaces.

III. THE REQUIREMENT OF ENHANCED DISSIPATION THROUGH RADIATION (CORE AND SOL) FOR FUTURE REACTORS

Tokamak devices with metallic plasma-facing components (PFCs) have demonstrated to perform successfully preserving the first wall [37]. It has been shown that long-term fuel retention can be minimised [38] and metallic PFCs do allow for fast isotope exchange [39]. However, armour materials like tungsten or W-coated CFC have significantly lower heat load limits restricted by melting, embrittlement and recrystallization effects compared to graphite/CFC PFCs. Also, W-sputtering and an unfavourable neoclassical transport of W-impurities can possibly lead to W accumulation which requires adequate avoidance techniques, at least for existing devices. Due to the lack of the intrinsic carbon radiator in present day metallic devices, discharges at high power require reliable exhaust schemes employing low-Z (Ne, N) or medium-Z (Ar, Kr, Xe) impurity seeding.

In order to mitigate the large power fluxes of a future reactor like DEMO of the order $> 300\,MW/m^2$ or more to an acceptable (material) limit $\approx 5\,MW/m^2$ a significant increase of the power dissipation in the plasma edge of more than 95% is required[4, 40]. A desired radiation pattern would consist of $f_{rad}^{core} \geq 30\%$ in SOL/divertor and $f_{rad}^{SOL} \leq 65\%$ inside the confined region close to the separatrix, concomitantly allowing only a minimal impact on the central burning plasma region.

The cause of a requirement of a finite level of f_{rad}^{core} can be understood by the actual achievable radiation fraction in the SOL, which is limited by the amount of removable pressure in the SOL through momentum loss[41]:

$$f_{rad}^{SOL,achieve} = 1 - K\frac{p^u}{q_\parallel^u}(1 - f_{mom}) \qquad (14)$$

with K being a weak function of T^t for $T^t > T_{crit}^t = 5\,eV$. The momentum loss parameter f_{mom} is defined through the ratio of up- and downstream pressures $p^t/p^u = (1 - f_{mom})$. Eq. 14 can be derived from simple 2-point model assumptions and energy/momentum balance conservation. The level of $f_{rad}^{SOL,achieve}$ decreases with p_u and increases with $q_\parallel^u$ making it difficult to increase the SOL radiation level at large plasma β and/or PB/R. This effect can be mitigated by momentum removal, i.e. pressure loss along the field, to achieve a high level of impurity radiation. The actual amount of removable momentum in the SOL (and thus radiation) is then limited by the maximum degree of detachment achievable for a given device, i.e. for complete detachment, a vanishing of

$$\Gamma^t \sim \frac{p^t}{\sqrt{T}} \sim \frac{p^u(1 - f_{mom})}{\sqrt{T}} \sim \frac{q_\parallel^u - q_{rad}^{imp}}{E_{pot}} - \Gamma_{rec} \qquad (15)$$

is required. Furthermore, significant reduction of $q_\parallel^t \sim p^t\sqrt{T} \sim p^u(1 - f_{mom})\sqrt{T}$ (c.f. eq. 4) can only be achieved through maximising momentum loss[42]. As a consequence for this state, and in case of $(1 - f_{mom}) \ll 1$ and for $T^t < T_{crit}^t$ power starvation may occur, i.e. having not enough power available to sustain a counter-balancing pressure p^t (meaning both, plasma and neutrals) in the divertor for a given upstream $q_\parallel^u$ (eq. 1). Hence, depending on the device (i.e. size) the SOL alone may or may not be capable to achieve the required f_{diss}^{min} to mitigate q^t sufficiently. It must follow that for a large scale future devices like DEMO significant radiation inside the confined region (i.e. inside the H-mode pedestal region) is required to reduce p^u and thus q^t.

Various seeding impurities are possible to dissipate energy by means of radiation. Depending on

their individual cooling function $L_z(n_e, T_e, \tau)$ and its shape (c.f. figure 6), the radiation pattern of $q_{rad}^{imp} = n_e n_z L_z l$ depends on the applied impurity species (or a combination thereof). The range consists of low-Z (N, Ne), medium-Z (Ar, Kr) and high-Z (Xe) impurities, covering the divertor (N), the SOL (Ne & Ar), the pedestal (Ar, Kr) and the core (Kr, Xe). Low-Z to medium-Z have been successfully used to induce significant divertor dissipation at AUG and JET [40]. High radiation levels with enhanced impurity seeding can be achieved and existing devices recover strong condensation of radiation close to the X-point for all selected species (N, Ne, Ar, Kr)[40] with condensation of Balmer radiation lines also inside the confined region[43, 9]. It has been shown experimentally for AUG and also numerically that with strong X-point radiation a depletion of pedestal density n_e^{ped} and temperature T_e^{ped} concomitantly occurs driven by poloidal gradients and transport into the X-point region[43]. Similar observations could be made in AUG and JET[44]. SOLPS does recover this pedestal pressure loss mechanism[43].

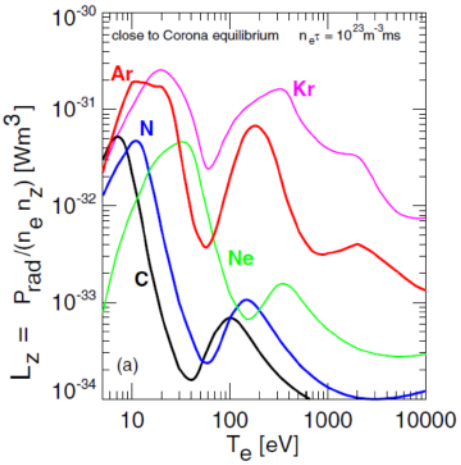

Figure 6: Radiative loss parameter L_z for seed impurities from ADAS and an electron density of $10^{20}\, m^{-3}$, as the sum of line radiation, recombination-induced radiation and Bremsstrahlung (taken from Kallenbach et al[45])

IV. IMPLICATIONS ON CORE/PEDESTAL PLASMA: FUELING & CONFINEMENT

Since the introduction of metal PFCs into existing devices like AUG, JET or C-mod, kinetic effects in neutral transport are more prominent and sustainable[14]. There exists a competition between slow moving particles (e.g. those re-emitted from the surfaces as recycling molecules) and fast ballistic neutrals (e.g. fast atoms from charge-exchange processes, surface reflections or ELMs). For a given divertor geometry (e.g. vertical vs horizontal target configurations) one expects a pronounced impact of the divertor configuration on neutral transport, pumping and the overall neutral pressure distribution, and thus on the poloidal ionisation profile. EDGE2D-EIRENE modelling confirms that the divertor geometry plays a significant role in the H-mode pedestal pressure loss mechanism in JET[46]. Especially in JET with a semi-horizontal configuration and thus with the recycling neutrals pointing away from the separatrix on the outboard side, the upstream pressure loss is induced by a combination of impurity radiation with increasing seeding and increase penetration depth of kinetic (fast) neutrals.

The previously mentioned HFSHD region which has been observed in both, JET and AUG, can also lead to spatial changes in the poloidal fuelling profile. The HFSHD spatial extent and maximum density caries with heating power, (nitrogen) seeding rate and divertor neutral pressure[47], and it can extend up to the inboard-side mid-plane and lead to strong poloidal asymmetries in density[48]. Correlations of the change in confinement with the HFSHD are observed[47, 49].

The understanding of the HFSHD region has significantly improved recently for AUG H-modes[9]. The basic requirements for such a model (inclusion of magnetic and vessel geometry, radial ballooning like transport, classical parallel transport for impurities including friction and thermal forces) are standard in SOLPS-ITER simulations nowadays[14]. Key however are the inclusion the neutral conductance within and below the divertor as well as the inclusion of cross-field drifts[9]. With the inclusion of ∇B-drift terms and radial and poloidal $E \times B$-drifts the inboard to outboard asymmetry in density and power load could be much better matched compared to the experiment. The increasing spatial extent of the HFSHD with increasing fueling up to the mid-plane could also be reproduced. As a consequence, the poloidal fuelling profile is amended with the existence of a HFSHD by diffusive fueling from the inboard region (in addition to neutral fuelling mainly from the outer X-point region and drift-driven advective flows). The model reproduces also large inverted radial density gradients at the HFS separatrix upstream (leading to the diffusive inward flux). The scaling of the HFSHD with heating power and impurity seeding (maximum density and spatial extent with increasing P_{heat} and/or decreasing seeding) up to reattachment of inner strike-point has been demonstrated by the model.

V. DETACHMENT SCALING CRITERIA

For extrapolation to large scale fusion devices like ITER or DEMO, usually the inclusion of the full physics into the numerical is mandatory but barely possible due to the complexity of physics processes. Subsequently long simulation times do occur (by the time of writing a full-blown physics model for an ITER simulation including drifts at a time-step $\Delta t \approx 10^{-8}\,s$ would take about a decade assuming $1\,s$ execution time for one time-step Δt). Even with massive parallelisation and other optimisation techniques (which would allow to increase Δt and/or computational speed within the next years) still typical simulation time of a few months would be required. To provide input to DEMO design studies which usually employ systems codes or simplified spreadsheet analysis models this is not acceptable. To mitigate this practical problem, simplified scaling laws are currently being developed which are based partly on experimental input and/or numerical results.
One of the more recent examples of such a scaling is the criteria for H-mode detachment. By using the heuristic drift-model (HD-model) approach a scaling for the divertor impurity concentration could be derived by Goldston[50]

$$c_z^{\text{Goldston}} \sim \frac{P_{SOL}}{B_p\,(1+\kappa^2)^{3/2}\,f_{GW}^2} \tag{16}$$

with f_{GW} being the Greenwald-fraction. The interpretation of this expression is as follows: how much should one vary the impurity concentration c_z in the SOL to maintain detachment if one of the r.h.s. parameters are changed (note: no dependence on major radius R in eq. 16). Goldston's detachment criteria is based on the 2-point model assuming a 100% radiated fraction and $T^t \leq 1\,eV$.

Another example takes into account a scaling for the H-mode threshold, resulting in[51]

$$c_z^{\text{Reinke}} \sim B_T^{0.88} R^{1.33} \tag{17}$$

which is suggesting a actual size-scaling of the device (as within this model P_{SOL} is expressed in terms of both f_{GW} and P_{LH} resulting in a machine size dependent scaling for $q_\parallel \sim B_T^{2.52} R^{0.16}$).

Other examples include also experimental data, as for example using data from AUG[6]

$$c_z^{\text{Kallenbach}} \sim const \cdot p_0^{div} + \frac{P_{sep}}{R\lambda_{int}} \tag{18}$$

introducing the measured (or scaled) value for the integrated heat-decay length parameter λ_{int} at the target plate[52]. In eq. 18 the constant is dependent on the selection of impurity species and no size scaling is present.

SOLPS recovers the empirical scaling law (eq. 18) in terms of P_{rad} for N-induced L-mode detachment within a factor of 2 for both AUG and JET[16].

Similarity studies on power exhaust are currently being developed as those can be ultimately helpful to identify (if any) discrepancies when scaling up a detachment model with increasing size. Such experimental benchmarks can be based on earlier work of Hutchinson & Vlases[53] which essentially derive scalings for control parameters P_{heat}, n_e^{sep}, flux expansion f_x and q_{95} to match at the divertor entrance and target T, collisionality ν^*, the width of the SOL (Δ_{SOL}) and ρ^*. Even though the effect of drifts can be included in such a matched experiment (by conserving ρ^*) the approach does not conserve the poloidal neutral mean-free path l_0. A much simpler and more straightforward approach (which conserves l_0 but not ρ^*) was suggested by Lackner[54] that matches essentially the full $q_\parallel$-profile by controlling $P_{SOL}B/R$ (i.e. λ_q upstream), T_e^{plate} and connection length L_c. Currently new JET and AUG experiments are being setup to follow this latter approach which should help in the validation of both, empirical and model based exhaust criteria.

References

[1] F. Wagner *Nucl. Fus.*, vol. 25, p. 525, 1985.

[2] T. Eich *Nucl. Fus.*, vol. 53, p. 093031, 2013.

[3] R. J. Goldston *J. Nucl. Mater.*, vol. 463, p. 397, 2015.

[4] M. Wischmeier *J. Nucl. Mater.*, vol. 463, p. 22, 2015.

[5] M. E. Fenstermacher *Plasma Phys. Control. Fusion*, vol. 41, p. A345, 1999.

[6] A. Kallenbach *Nucl. Fusion*, vol. 55, p. 053026, 2015.

[7] S. Poetzel *J. Nucl. Mater.*, vol. 438, p. S285, 2013.

[8] P. Manz *Nucl. Mater. Energy*, vol. 12, p. 1152, 2017.

[9] F. Reimold *Nucl. Mater. Energy*, vol. 12, p. 193, 2017.

[10] S. Wiesen *J. Nucl. Mater.*, vol. 463, p. 480, 2015.

[11] R. Simonini *Coontrib. Plasma Phys.*, vol. 34, p. 368, 1994.

[12] D. Reiter *J. Nucl. Mater.*, vol. 196-198, p. 80, 1992.

[13] S. Wiesen, "Itc project report." http://www.eirene.de/e2deir_report_30jun06.pdf, 2006.

[14] S. Wiesen *Nucl. Mater. Energy*, vol. 12, p. 3, 2017.

[15] A. Jaervinen *J. Nucl. Mater.*, vol. 463, p. S135, 2015.

[16] L. Aho-Mantila *J. Nucl. Mater.*, vol. 463, p. 546, 2015.

[17] S. Lisgo *J. Nucl. Mater.*, vol. 337-339, p. 139, 2005.

[18] V. Kotov *Plasma Phys. Control. Fusion*, vol. 50, p. 105012, 2008.

[19] D. Reiter and S. Wiesen *J. Nucl. Mater.*, vol. 313-316, p. 845, 2003.

[20] V. Kotov, D. Reiter, and S. Wiesen *J. Nucl. Mater.*, vol. 438, p. S449, 2013.

[21] D. Moulton *Proceedings of the 42nd EPS Conference on Plasma Physics*, 2015.

[22] S. Varoutis *Fusion Eng. Des*, vol. 121, p. 13, 2017.

[23] W. Eckstein *Suppl. Nucl. Fusion*, vol. 1, p. 51, 1991.

[24] A. A. Hasz *Suppl. Nucl. Fusion*, vol. 7A, p. 9, 1998.

[25] U. Samm *Plasma Phys. Contr. Fusion*, vol. 35, p. B167, 1993.

[26] R. S. Granetz *Nucl. Fusion*, vol. 47, p. 1086, 2007.

[27] P. C. Stangeby, *The Plasma Boundary of Magnetic FUsion Devices*. IOP Publishing, Bristol, 2000.

[28] S. I. Braginskii *Reviews of Plasma Physics*, vol. 1, p. 205, 1965.

[29] S. Chapman *Proc. Phys. Soc., London, Sect. A*, vol. 72, p. 353, 1958.

[30] S. P. Hirshman *Nucl. Fusion*, vol. 21, p. 1079, 1981.

[31] J. Weiland, *Colelctive Modes in Inhomogeneous Plasma, Kinetic and Advanced Fluid Theory*. IOP Publishing, Bristol, 2000.

[32] D. E. Post *Atomic Data and Nuclear Data Tables*, vol. 20, p. 397, 1977.

[33] M. Z. Tokar *Phys. Plasmas*, vol. 10, p. 4378, 2003.

[34] M. Z. Tokar *Plasma Phys. Control. Fusion*, vol. 36, p. 1819, 1994.

[35] D. E. Post *J. Nucl. Mater.*, vol. 220-222, p. 143, 1995.

[36] M. Koltunov *Plasma Phys. Control. Fusion*, vol. 54, p. 025003, 2012.

[37] R. Neu *IEEE 25th Symposium*, vol. 1-8, 2013.

[38] S. Brezinsek *Nucl. Fusion*, vol. 53, p. 083023, 2013.

[39] T. Loarer *J. Nucl. Mater.*, vol. 463, p. 1117, 2015.

[40] M. Bernert *NME*, vol. 12, p. 111, 2017.

[41] C. S. Pitcher and S. P. C. *Plasma Phys. Control. Fusion*, vol. 39, p. 779, 1997.

[42] S. Krashenninikov and K. A. S. *Nucl. Fusion*, vol. 57, p. 102010, 2017.

[43] F. Reimold *J. Nucl. Mater.*, vol. 463, p. 128, 2015.

[44] M. Wischmeier *IAEA-FEC, St. Petersburg, Russia*, 2014.

[45] A. Kallenbach *Plasma Phys. Control. Fusion*, vol. 55, p. 124041, 2013.

[46] A. Jaervinen *Plasma Phys. Control. Fusion*, vol. 58, p. 045011, 2016.

[47] S. Potzel *J. Nucl. Mater.*, vol. 463, p. 541, 2015.

[48] L. Guimarais *Proc. of the 42nd EPS Conference on Plasma Physics, Lisbon, Portugal, P1.111*, 2015.

[49] M. Dunne *Plasma Phys. Control. Fusion*, vol. 59, p. 014017, 2017.

[50] R. Goldston *Plasma Phys. Control. Fusion*, vol. 59, p. 055015, 2017.

[51] M. Reinke *Nucl. Fusion*, vol. 57, p. 034004, 2017.

[52] M. Makowski *Phys. Plasmas*, vol. 19, p. 056122, 2012.

[53] I. Hutchinson and G. Vlases *Nucl. Fusion*, vol. 36, p. 783, 2096.

[54] K. Lackner *Plasma Phys. Control. Fusion*, vol. 15, p. 359, 1994.

EROSION, DEPOSITION AND FUEL RETENTION MECHANISMS IN FUSION PLASMAS

D. Matveev, A. Kirschner

Forschungszentrum Jülich GmbH, Institut für Energie- und Klimaforschung – Plasmaphysik, Partner of the Trilateral Euregio Cluster (TEC), 52425 Jülich, Germany

ABSTRACT

An overview of erosion, deposition and fuel retention processes in fusion devices is presented and examples from contemporary fusion experiments are provided. The underlying physical and chemical mechanisms are discussed, as well as their impact on the lifetime of plasma-facing components and tritium retention in next step fusion devices such as ITER.

I. INTRODUCTION

Magnetic confinement fusion devices represent so far the most successful and promising concept on the way to economically feasible fusion reactors. The next major step on this way is the international experimental reactor ITER [1]. Plasma confinement in such devices is inevitably not perfect so that particles from plasma are transported across the toroidal magnetic field to surrounding vessel walls leading to plasma-material interaction (PMI). In addition to ion fluxes, also fluxes of energetic neutrals originating from charge-exchange reactions can contribute significantly to PMI, especially in remote, plasma-shadowed areas not accessible for ions. Furthermore, radiation damage by neutrons originating from fusion reactions will play an important role in wall lifetime and fuel retention aspects of future fusion reactors. PMI plays an important role in fusion energy extraction, fuel recycling and removal of the fusion product, helium (He). At the same time, PMI with its steady-state and intermittent particle and heat loads lead to material erosion, degradation of material properties, degradation of plasma performance, and fuel retention. Erosion limits the lifetime of plasma-facing components (PFCs) and, in the case of actively cooled PFCs, can lead to a component failure and related loss of coolant accidents. Transport of particles of eroded materials into the core plasma may lead to degradation of plasma performance due to fuel dilution and plasma cooling by radiation. Transport of particles of eroded materials to other locations may lead to formation of loose and/or fuel-rich deposited layers with detereorated thermal and mechanical properties. Such layers provide an additional risk of dust formation by flaking or delamination, especially during plasma ramp-up phase. Also the surface and bulk material of PFCs can suffer from strong plasma-induced modifications of their thermal and mechanical properties, morphology and structural integrity. Current estimates of wall lifetime and tritium retention in ITER are based on extrapolations from existing experimental data and modeling implying relatively large uncertainties [2, 3]. These extrapolations indicate that the cumulative plasma time before reaching the safety-imposed tritium retention limit or the maximum allowed erosion of wall components could be unacceptably low for an economical operation. In ITER with its long-pulse or even steady-state operation PMI will determine the device availability. Understanding of involved mechanisms is therefore essential for upscaling the results from contemporary devices to ITER and beyond, such as DEMO [4], in order to find possibilities to minimize the adverse effects of PMI.

From the plasma side PMI is defined by plasma particle species, their fluxes and impact energy and angle distributions, which in turn are governed by a multitude of processes in the plasma edge. From the material side, PMI naturally depends on the choice of PFC materials. The material choice for ITER consists of beryllium (Be) for the main wall cladding and tungsten (W) for the divertor. The choice of Be with its low atomic number (Z=4) for the large area of the main wall is governed by lower plasma dilution and cooling due to radiation if eroded Be is transported to the core plasma, compared to high-Z elements. In addition, Be has the advantage of being a good oxygen getter. Divertor target plates represent the most intense PMI areas where ions leaving the confined plasma region and following the magnetic field lines are transported to. High particle and heat loads require an erosion-resistant material with a high melting temperature, and W is currently considered to be the best candidate. In the initial ITER design carbon fiber composite (CFC) PFCs were supposed to be used in the divertor due to their excellent heat resistance. Carbon, however, is prone to chemical erosion by hydrogen isotopes leading to formation of volatile hydrocarbon species resulting in long-range carbon transport and re-deposition in form of hydrogen-rich surface layers. Formation of such tritium-rich carbon layers in a fusion reactor was identified as the major safety issue and the use of CFC was phased out in the actual ITER design. Another nuclear safety issue arises from the fact that fusion neutrons in a fusion reactor will lead to

activation of surrounding materials by transmutations. Therefore the material choice not only for PFCs but also for structural components is governed by the necessity to avoid production of long-living radioactive waste.

II. EROSION MECHANISMS

Wikipedia gives the general definition of erosion as the process of *"gradual removal of a substance by chemical or mechanical means"* and, in the case of earth science, specifies it as *"the action of surface processes (such as water flow or wind) that removes soil, rock, or dissolved material from one location on the Earth's crust, and then transports it to another location"* [5]. In the PMI case we can redefine erosion as the action of plasma-material interaction and related surface processes that remove atoms from one location at the plasma-facing material surface and transport them to another location within the vacuum vessel. The strength of erosion is usually characterized by the erosion yield, Y, which is defined as the ratio of the flux of outgoing eroded particles (typically atoms), Γ_{out}, to the flux of incoming projectiles (ions, atoms or molecules), Γ_{in}:

$$Y = \frac{\Gamma_{\mathrm{out}}}{\Gamma_{\mathrm{in}}}, \qquad (1)$$

where the respective fluxes are given as the number of particles per unit of surface area and per unit of time. It is important to note that erosion yield is a statistical characteristics, i.e. it describes the action of a large ensemble of projectiles and thus for a single projectile represents a mere average probability of removing some material atoms upon surface impact.

Two fundamental atomic scale mechanisms of erosion will be addressed in the following in sufficient detail: physical sputtering and chemical erosion. Besides, several other mechanisms related to material erosion and wall life time will be shortly addressed in the following sections that are related to the role of material temperature, mechanical properties and various synergistic effects leading to surface morphology changes.

For a detailed review of experimental data, theory and simulations regarding physical sputtering and chemical erosion the reader is referred to the book *"Sputtering by particle bombardment"* under the edition of Eckstein and Behrisch [6].

II.A Physical sputtering

The process of physical sputtering (or just *sputtering*) implies collisions of incoming projectiles (energetic ions or neutrals) with atoms of the target material, in which the momentum transfer to surface atoms leads to their ejection. While interaction with electrons of the target material is an inelastic energy loss mechanism leading to slowing down of the projectile, collisions between projectile and target nuclei change their momentums and thus shape the projectile trajectory in the solid. Although the first momentum transfer from projectile to target atoms is directed into the surface, momentum reversal, e.g. in the case of a close to head-on collision, can lead to momentum transfer out of the solid surface in subsequent collisions.

In the general case, projectile-target collisions should be considered as multi-body interactions. For practical reasons, however, one turns to the binary collisions approximation (BCA), within which a sequence of two-body collisions between the projectile and single atoms within the target is considered. Provided energy and momentum conservation for the system of two colliding particles, interaction potential between them defines their scattering angles and energies. Due to presence of electrons, the so-called screened Coulomb repulsive interaction potentials are generally considered. An exhaustive description of the scattering theory and interaction potentials can be found in the classical book *"Computer simulation of ion-solid interactions"* by Wolfgang Eckstein [7].

If the energy transferred to the surface atom is sufficient to overcome the collective pull of surrounding surface atoms (the surface binding energy), the target atom can leave the solid and is considered to be physically sputtered. The actual value of the surface binding energy is barely known for most of materials, therefore it is common to use the heat of sublimation as an estimate.

Different regimes of collisions can be distinguished depending on the projectile energy and mass as illustrated in figure 1:

i) Single collision regime

After a single collision of the projectile with a target atom, the projectile hits a surface target atom leading to its sputtering. This process particularly occurs for light projectile ions with high momentum reversal probability and relatively low impact energies, so that energy transfer to target atoms is limited.

ii) Linear cascade regime

In the case of moderate projectile energies (above several tens of eV, below keV range) a collision cascade is developing, in which several collisions along the projectile trajectory result in sufficient energy transfer to displace atoms of the target and set them in motion (so-called recoil atoms). In this regime collisions between two moving recoils are rare.

iii) Thermal spike regime

At high impact energies (keV – MeV) and for heavier projectiles the number of recoils and their density are increasing so that most atoms within a given region are moving, whereby collisions between simultaneously moving particles become important. This regime, in fact, can be seen as local

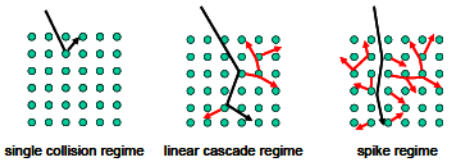

Figure 1: Collision regimes inside a solid induced by impact of a projectile atom. The trajectory of the projectile is sketched in black, while motion of recoil atoms is depicted in red.

melting and apparently cannot be described by the BCA.

In general, physical sputtering occurs for all combinations of projectile and target materials. In case of sputtering of metals, the sputtered species are mostly neutral atoms or small atomic clusters of the target material. In the following we will address sputtering of single atoms and main factors defining the physical sputtering yield, Y_{phys}.

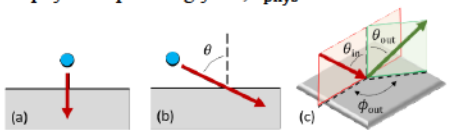

Figure 2: Illustration of normal (a) and oblique (b) incidence of a projectile on a target. Figure (c) shows the general case when a sputtered or reflected particle is emitted with a velocity vector (green) outside of the plane of incidence (red). θ_{in} is the polar angle of incidence and θ_{out} and φ_{out} are the polar and the azimuthal angles of ejection, respectively.

Energy dependence of Y_{phys}

Under the energy dependence of erosion yield the dependence on the impact energy of projectiles is understood. Let us first consider the case of normal incidence (figure 2a) and restrain ourselves to the collision regimes, for which the BCA is applicable.

Physical sputtering is a result of energy transfer from a projectile to target atoms. The maximal energy transfer in a binary collision occurs in the case of a head-on collision and is given by

$$\frac{\Delta E}{E_0} = \gamma = \frac{4M_1M_2}{(M_1+M_2)^2}, \qquad (2)$$

where E_0 is the projectile energy in the centre of mass system and M_1 and M_2 are the atomic masses of the projectile and target elements, respectively. Factor γ is maximal (= 1) for *"self-bombardment"*. If the transferred energy is below the surface binding energy, E_{sb}, sputtering cannot occur. It means that there is a minimal threshold energy for sputtering, which, as follows from equation 2, depends on the particular projectile-target combination. It is logical to assume that the higher the impact energy, the more energy can be transferred to the target and thus the larger the sputtering yield should be. However, as the

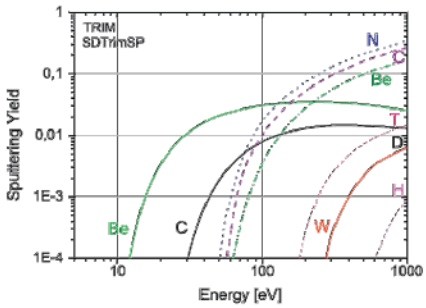

Figure 3: Energy dependence of the physical sputtering yield for Be, C, W by D and for W by Be, C, N predicted by SDTrimSP code [8] simulations. Reproduced from [9].

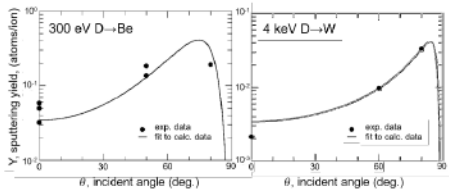

Figure 4: Angular dependence of the physical sputtering yield for Be and W by D from experiment and modelling. Reproduced from [6].

projectile energy is deposited deeper under the surface, it becomes more difficult for recoil atoms to reach the surface. In the case of impact of light ions, the sputtering yield reaches its maximum at the energy range from several hundreds of eV to several keV and then slowly decreases with energy, while for heavier projectiles and comparable masses of projectile and target atoms the sputtering yield continues increasing up to 10 keV and even 100 keV range [6]. Figure 3 shows an example of the energy dependence of the physical sputtering yield for some fusion relevant projectile-target combinations for the relevant impact energies up to 1 keV as predicted by computer simulations with the SDTrimSP code [8] that is based on the BCA.

Angular dependence of Y_{phys}

The angle of incidence of the projectile is understood to be the poloidal angle of incidence, θ (figure 2b). At oblique incidence ($\theta > 0$) the momentum reversal / backscattering is generally more probable and energy deposition is shallower, so that sputtering yield increases. At very shallow incidence with θ close to 90°, however, also the direct reflection probability increases, so that the sputter yield decreases. An example of such angular dependence observed in experiments and predicted by simulations is shown in figure 4.

Empirical fit formulae for Y_{phys}

The current understanding and description of the sputtering process, though based on the theory of scattering from central force potentials, relies extensively on and therefore is inseparable from computer simulations, especially those using the BCA. The SDTrimSP code mentioned earlier and its predecessors are among the main tools in this area. Experimental data on physical sputtering yields are mainly obtained by means of ion beam irradiation where energetic ions are focused on a target sample. The sputtering yield can then be determined by the sample weight loss measurements. At low energy bombardment, however, and especially near the threshold energy of physical sputtering ion beam intensities become very low, so that the measured data are rare and more uncertain. Other modelling approaches, in particular molecular dynamics (MD), help to close this gap.

Accumulated experimental and BCA-modelling data on sputtering together with a thorough data analysis supported by the theory of ion-solid collisions allowed developing rather universal empirical fit formulae to predict physical sputtering yields for any elementary projectile-target combination (a single projectile species on a mono-atomic target) with different impact parameters. The original expressions for the sputtering yield at normal incidence, known as the *Bohdansky formula* [10], and for the angular correction, known as *Yamamura formula* [11], have been revised and improved over time to correct for various discrepancies with experimental and modelling data, in particular the behaviour of sputtering rates at near-threshold impact energies and at very shallow angles of incidence, in particular for self-sputtering. The following expressions [12] are currently commonly accepted. Please note, however, that the same fit formulae published earlier in [6] and [13] had an error regarding the missing term $w(\varepsilon_{\mathrm{L}})$ in the equation for $Y(E_0, \theta = 0)$.

The sputtering yield at normal incidence is given by

$$Y(E_0, \theta = 0) = q s_{\mathrm{n}}^{\mathrm{KrC}}(\varepsilon_{\mathrm{L}}) \frac{\left(\frac{E_0}{E_{\mathrm{th}}} - 1\right)^{\mu}}{\lambda / w(\varepsilon_{\mathrm{L}}) + \left(\frac{E_0}{E_{\mathrm{th}}} - 1\right)^{\mu}} \quad (3)$$

with fit parameters $q, \lambda, \mu, E_{\mathrm{th}}$ (the threshold energy is also considered as a fit parameter) and the nuclear stopping power for the Kr-C interaction potential

$$s_{\mathrm{n}}^{\mathrm{KrC}}(\varepsilon_{\mathrm{L}}) = \frac{0.5 \ln(1 + 1.2288 \varepsilon_{\mathrm{L}})}{w(\varepsilon_{\mathrm{L}})}, \quad (4)$$

$$w(\varepsilon_{\mathrm{L}}) = \varepsilon_{\mathrm{L}} + 0.1728 \sqrt{\varepsilon_{\mathrm{L}}} + 0.008 \varepsilon_L^{0.1504}$$

with the Lindhard reduced energy

$$\varepsilon_{\mathrm{L}} = E_0 \frac{M_2}{M_1 + M_2} \frac{a_L}{Z_1 Z_2 e^2}, \quad (5)$$

where Z_1 and Z_2 are the atomic numbers, and M_1 and M_2 the masses of the projectile and the target atom, respectively; e is the electron charge, and the Lindhard screening length, a_{L}, is given by

$$a_L = \left(\frac{9\pi^2}{128}\right)^{1/3} a_B \left(Z_1^{2/3} + Z_2^{2/3}\right)^{-1/2} \quad (6)$$

with the Bohr radius, $a_B = 0.0529177$ nm.

The sputtering yield at oblique incidence is given by

$$\frac{Y(E, \theta)}{Y(E, \theta = 0)} = \left\{ \cos\left[\left(\frac{\theta}{\theta_0} \frac{\pi}{2} \right)^c \right] \right\}^{-f} \times \exp\left\{ b \left(1 - 1/\cos\left[\left(\frac{\theta}{\theta_0} \frac{\pi}{2} \right)^c \right] \right) \right\} \quad (7)$$

with fit parameters f, b, c and parameter θ_0 taking care that the angle of incidence of 90° cannot be reached

$$\theta_0 = \pi - \arccos \sqrt{\frac{1}{1 + E_0 / E_{\mathrm{sp}}}} \geq \frac{\pi}{2}, \quad (8)$$

where E_{sp} stands for the (chemical) binding energy of projectiles and is taken to be equal to the surface binding energy E_{sb} for self-bombardment, 0 for noble gas projectiles and 1 eV for hydrogen isotopes and nitrogen. No information regarding the choice of E_{sp} for other material combinations is provided in the original publications [6, 12, 13].

According to equations 3 and 7, the full description of the sputtering yield in terms of impact energy and angular dependence is reduced to 7 fit parameters (E_{sb} and E_{sp} not counted). Tabulated examples and illustrations for a variety of different projectile-target combinations can be found in chapter *"Sputtering yields"* by Wolfgang Eckstein in [6].

Energy and angular distributions of sputtered particles

Leaving aside some underlying theoretical concepts of energy transfer and recoil generation [6, 14], the differential sputtering yield with respect to the kinetic emission energy, E, and to the solid angle Ω around the polar emission angle θ in the linear cascade regime at normal incidence can be approximated by the general expression

$$\frac{dY}{dE d\Omega} \propto \frac{E}{(E + U)^{\alpha + 1}} \cos^y \theta, \quad (9)$$

where $U \cong E_{sb}$, $\alpha \lesssim 2$, and y are treated as fitting parameters describing the experimentally measured

spectra.

The energy part of expression 9, especially in the case of $\alpha = 2$ is often referred to as the Thompson distribution [14]. It is characterized by the high-energy fall-off proportional to E^{-2}, peak position (most probable energy of emission) at $\approx U/2$, and high energy cut-off at the projectile impact energy, E_0.

The angular part of expression 9 with $y = 1$ corresponds to the so-called cosine angular distribution. Cases with $y > 1$ are called over-cosine distributions and are rather common for impact energies in keV range. At low energies, under-cosine or "butterfly" [15] angular distributions with the most probable angle of incidence away from normal (figure 5) are observed that can be approximated e.g. by $dY/d\Omega = A\cos^{\alpha}\theta - B\cos^{\beta}\theta$. A word of caution has to be mentioned regarding the interpretation of these distributions in terms of the distribution of the polar angle of emission [16]. As can be seen from equation 9, the differential distribution is defined with respect to the solid angle Ω around the polar angle θ and not with respect to the polar angle itself. In order to recalculate the differential distribution $dY/d\theta$ one has to keep in mind the relation between angles in spherical coordinates: $d\Omega = \sin\theta d\theta d\varphi$.

The theory underlying expression 9 assumes an isotropic distribution of recoil velocities in the solid, thus isotropic collision cascades at normal incidence. More complex expressions exist that account for oblique incidence and some mutual dependencies between the energy and angular spectra [17, 18]. At oblique incidence, in particular, the emission distribution is often peaked near the specular direction. However, all the above expressions imply amorphous-like materials with a random distribution of collision partners and are not applicable to sputtering of crystalline targets, for which preferential ejection of atoms in the direction of certain crystal axes (mainly closed-packed lattice rows) is observed.

More information and excessive literature overview about various aspects related to this topic can be found in chapter *"Energy and Angular Distributions of Sputtered Species"* by Hubert Gnaser in [6].

Sputtering of rough surfaces

Figure 6 illustrates the peculiarities of sputtering of rough surfaces as compared to flat surfaces. Two apparent differences are (i) different local angles of incidence, θ_{loc}, compared to the nominal angle of incidence, θ_{nom}, resulting in respectively different probabilities for sputtering (eq. 7); and (ii) possibility of redeposition of sputtered particles inside the "valleys". One intuitive expectation regarding surface morphology evolution from these two factors would be that faster erosion

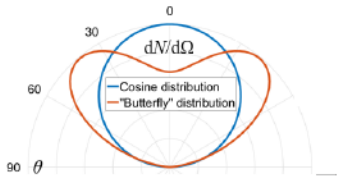

Figure 5: Examples of angular distributions of sputtered particles with respect to solid angle Ω around the polar emission angle θ. Figure courtesy of A. Eksaeva.

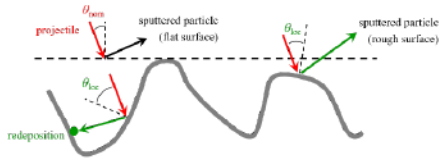

Figure 6: Illustration for sputtering of a rough surface (thick solid line) as compared to sputtering of a nominal flat surface (dashed line). Local angles of incidence, θ_{loc}, differ from the nominal angle of incidence, θ_{nom}.

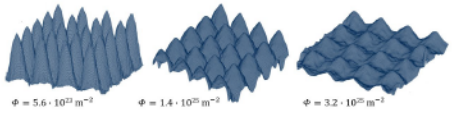

Figure 7: ERO2.0 code simulation of evolution of surface morphology with fluence under ion impact for Mo target, mono-energetic 250 eV D^+ ion flux of $1.4 \cdot 10^{21}\ \mathrm{m^{-2}s^{-1}}$ perpendicular to the nominal surface, and cosine initial surface profile with the peak height of 0.7 μm [20]. SDTrimSP code based sputtering data for local angles of incidence are used, sputtered particles are traced, and their re-deposition in "valleys" leads to surface smoothing. Figure courtesy of A. Eksaeva [20].

of "hills" due to more oblique local angles of incidence and redeposition in "valleys" should lead to smoothing of the surface with time. Such a process under certain conditions can be reproduced by modelling. Figure 7 shows an example of such modelling with the impurity transport code ERO2.0 [19, 20]. However, in most of real cases more effects are involved that lead to development of surface morphology rather than to surface smoothing. Some of these effects are discussed in the following subsections. Surface roughness expectedly affects the effective sputtering yield [21], as well as emission energies and angles of sputtered particles.

Preferential sputtering and multicomponent targets

The term preferential sputtering applies usually to the following two distinct cases. First, in polycrystalline targets, different grains are often sputtered with different rates depending on the grain orientation [22], which, in part, is explained by different planar density of surface atoms. Second, in multi-component materials, e.g. alloys, atoms of different elements have different sputtering yields

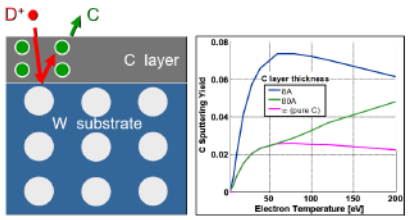

Figure 8: Sputtering of layered targets. In this example sputtering of the carbon layer is enhanced by preferential reflection of deuterium form the heavy atoms of the tungsten substrate.

[23], which, in part, is explained by different energy transfer probabilities (recall the mass dependence from eq. 2) and binding energies. In both cases, some parts of the target surface can be more prone to erosion, thus resulting in development of surface morphology, e.g. cone-like or grass-like structures [23]. In the case of multicomponent targets, gradual surface enrichment with more erosion-resistant species, normally with heavier elements, can be observed [24]. Irradiation of multicomponent targets in general is associated with changes of the surface composition and is therefore fluence dependent up to the point when an equilibrium surface composition is established. It has to be noted that surface enrichment can be compensated by diffusion of lighter constitutes from the bulk to the surface at sufficiently high temperatures [25]. This effect, as well as onset of evaporation at temperatures close to the melting point, can be responsible for the temperature dependence of the sputtering yield, which is otherwise negligible.

A specific case of multicomponent targets are layered systems. In the example shown in figure 8, a layer of light element (carbon) is deposited on the tungsten substrate. Very efficient backscattering of even lighter D atoms from heavy and large W atoms provides the momentum reversal resulting in enhanced sputtering of C atoms. For this effect to be pronounced, the thickness of the surface layer has to be less than the projected range of impinging ions. In figure 8 this is illustrated by the dependence of the sputtering yield on the plasma electron temperature, which defines the impact energies of plasma ions. Higher temperatures mean higher energies and result in deeper penetration so that the above mentioned effect becomes observable even for a thicker layer.

II.B Chemical erosion and chemical sputtering

Chemical erosion, in contrast to physical sputtering by energetic projectile, involves an action of thermal projectiles that can initiate chemical reactions with surface atoms resulting in volatile reaction products. Such chemical reactions occur only for specific combinations of projectile and target atoms (chemically reactive species). In fusion research chemical erosion of beryllium and carbon-based materials by hydrogen isotopes is of main importance. One example would be chemical erosion of graphite with thermal atomic hydrogen resulting in emission of hydrocarbon species (C_xH_y).

The term chemical sputtering refers to all the processes in which the kinetic energy of projectiles plays a catalysing role in chemical reactions leading to erosion. Collisions of energetic projectiles with surface atoms lead to breaking of chemical bonds between them and produces weakly bound surface atoms that facilitate chemical reactions and can be easier released into the gas phase. This release is normally thermally driven, thus both chemical erosion and chemical sputtering exhibit dependence on surface temperature. The energy can be provided by chemically reactive projectiles themselves or by other species in the case of combined irradiation.

Chemical erosion and chemical sputtering of carbon have been studied in great detail and an extensive review can be found in chapter *"Chemical Sputtering"* by Wolfgang Jacob and Joachim Roth in [6]. A compressed overview was published in the previous edition of this lecture [26]. The relevance of carbon in fusion research has declined in recent years, since the use of carbon-based PFCs in ITER has been abandoned, precisely because of the adverse effects of chemical erosion of carbon, namely, due to the long-range transport of erosion products and their accumulation in the form of tritium-rich layers. On the contrary, chemical erosion of beryllium is a subject of intense research, some findings of which will be briefly described in the following.

Spectroscopic observation of BeD molecules in the JET tokamak and in the PISCES-B linear plasma device sparked interest in the chemical sputtering of metals, which was believed to be not important. Dedicated experiments and molecular dynamics simulations [27, 28] confirmed that chemical effects are considerable for Be at impact energies below 100 eV and dominant at energies as low as 7-20 eV. Simulations helped to identify the mechanism of erosion, which was named *swift chemical sputtering* [29, 30], though later the term *chemically assisted physical sputtering* (CAPS) was introduced and is more often used when erosion in form of BeD in JET is addressed experimentally [31, 32] and by modelling [33]. It was observed in MD simulations that emitted BeD molecules are formed not with the incoming D ions, but rather with a D atom that is already present on the surface, bound to the Be atom. Upon examining the sputtering process in more detail, the following aspects of the CAPS mechanism were identified [27, 29]:

- if an incoming energetic D ion enters between two Be atoms, it can break the respective bond by forcing them apart;
- there is a finite energy window for the bond breaking to occur: for a too low kinetic energy ($\lesssim$ 2 eV in the case of Be), D ion will be

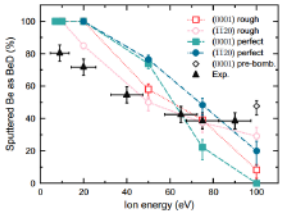

Figure 9: Fraction of Be atoms sputtered as BeD molecules after Be exposure to D plasma. Results of MD simulations for two different orientations of the Be surface and both initially rough and perfect surfaces are shown alongside with the experimental data. Reproduced from [27].

reflected without entering the region between Be atoms; for too high energy ($\gtrsim$ 40 eV for Be), D ion does not spend enough time between the Be atoms to cause bond breaking;

- if one of the Be atoms is only loosely bound to the surface, this can cause sputtering of the Be atom along with a D atom bound to it;
- the energy per bond for a surface Be atom depends on the number of neighbouring D and Be atoms (e.g. depends on surface orientation and roughness); D atoms at the surface weaken the surface binding of Be atoms, making them easier targets for sputtering;
- the observed mean release energy of BeD molecules of around 2 eV is still much higher than that corresponding to the surface temperature; the release angles form a cosine distribution around the surface normal.

It has to be noted that energy transfer in CAPS is fundamentally different from that in binary collisions. The impact energy dependence of BeD emission is illustrated in figure 9. CAPS contributes 100% to the erosion yield at low energies and reduces almost to zero at impact energies about 100 eV. Unlike purely thermally activated processes, erosion in form of BeD molecules decreases at sufficiently high surface temperatures as observed in specially designed JET experiments [31, 32]. This at first counterintuitive fact is explained by the depletion of the D content in the surface due to thermal desorption.

II.C Erosion at elevated temperatures

At high temperatures atoms can leave the surface by sublimation and evaporation. The higher is the temperature, the greater is the kinetic energy of surface atoms and thus the faster are the release rates. It could be therefore assumed that erosion of chemically inert surfaces under ion bombardment is dominated by physical sputtering (no temperature dependence) at low temperatures and by sublimation/evaporation (strong temperature dependence) at sufficiently high temperatures. This picture is, however, contradicted by experimental data for carbon and several solid and liquid metals, where a strong increase of erosion is observed for

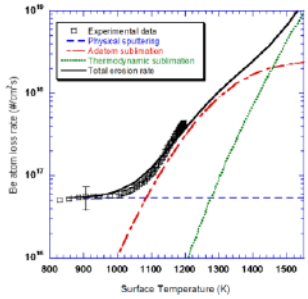

Figure 10: Be atom loss rate under exposure to He plasma as a combination of physical sputtering, thermodynamic sublimation and adatom sublimation according to the RAAS model [34]. Figure courtesy R. P. Doerner [35].

temperatures lower than expected from thermodynamic sublimation/evaporation [34]. This effect for carbon was explained by the model of radiation enhanced sublimation (RES), that involves diffusion to the surface and sublimation of interstitial carbon atoms produced in collision cascades. In [34], the authos point out several weak points of RES and, on the example of Be and liquid Li, propose the radiation activated adatom sublimation (RAAS) model, according to which enhanced erosion is caused by less strongly bound surface adatoms (isolated adsorbed atoms) with reduced sublimation activation energy. According to this model, adatoms are created at the surface layer as a result of interaction with the incoming projectiles and annihilate at surface bonding sites due to surface diffusion. Model parameters are found by fitting to the experimental data. An example for Be bombardment by He plasma in PISCES-B [34] is shown in figure 10.

II.D Erosion by plasma

It is important to realize that in plasma in general, and therefore also in any fusion experiments, the impact energies of individual ions hitting a surface and their impact angles are not all the same. Impact energy and angle distributions are determined by the plasma sheath characteristics, mainly by the ion and electron temperatures, T_i and T_e, so that the total sputtering yield becomes a convolution of the energy and angular dependence of sputtering, $Y(E,\theta)$, with the energy and angular distribution of impinging ions, $f(E,\theta) = dN(E,\theta) \,/\, dEd\theta$:

$$Y = \frac{\Gamma_{out}}{\Gamma_{in}} = \frac{\iint Y(E,\theta) f(E,\theta) dEd\theta}{\iint f(E,\theta) dEd\theta}. \qquad (10)$$

In quite many cases, however, for the sake of simplicity and relying on the fact that ions are accelerated in the electrostatic sheath and in the pre-sheath [36, 37], a constant ion impact energy

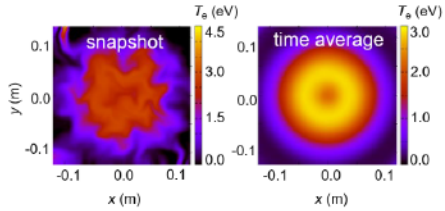

Figure 11: An example of a snapshot (left) and temporal average (right) distribution of the electron temperature for a synthetic turbulence simulation in the PSI-2 linear plasma device [39]. The figure shows a cross-section of the linear plasma perpendicular to the magnetic field in the center of the plasma column. The PSI-2 magnetic field strength is of the order of 0.1 T and (for Ar as a working gas) the electron temperatures and particle densities are of the order of $T_e \sim 2-4$ eV and $n_e \sim 10^{18}$ m^{-3}, respectively. Figure courtesy of D. Reiser [39].

$$E_0 = 2kT_i + 3ZkT_e \quad (11)$$

is assumed, where Z is the charge state of the ions, and k is the Boltzmann constant. The first term on the right-hand side of equation 11 reflects the Maxwell-distributed thermal velocity of ions and their energy gain in the pre-sheath electric field, while the second term originates from the acceleration in the sheath potential near an electrostatically isolated, thus floating, surface, at which ion and electron fluxes are equalized [36].

One further peculiarity of sputtering by plasma, which is especially inherent to fusion devices, comes from plasma fluctuations [38, 39]. Large amplitude fluctuations of plasma parameters on time scales of μs are known to be present in linear plasma and tokamak devices. These fluctuations influence ion impact energies and angles even under the assumption of equation 11. Figure 11 shows an example of a momentary and time-averaged electron temperature distributions in the PSI-2 linear plasma device [40] as obtained by synthetic turbulence simulations [39]. Since in the analysis of experimental data and in computations time averaged data is often used, the question arises whether it is justified to use e.g. the erosion rate at time average plasma parameters as a measure of the time average erosion rate:

$$\langle Y(n_e, T_e, \dots)\rangle \gtrless Y(\langle n_e\rangle, \langle T_e\rangle, \dots) \quad (12)$$

Though simulations show no significant deviations (<10%) of 'true' temporal averaged quantities from approximate averages based on mean values of background plasma parameters under conditions of the PSI-2 experiment [39], the possible contribution of plasma fluctuations and non-stationary plasma conditions in general should not be underestimated. In particular, plasma instabilities may lead to intermittent ejections of large amounts of heat and particles from the plasma and cause excessive erosion of PFCs. In tokamaks with high confinement mode of operation (H-mode), edge localized modes (ELMs) [41] are perhaps the most critical repetitive events of such kind. A detailed assessment of W sources and erosion rates in JET H-mode plasma conditions experimentally and by modelling [42] allowed separating the erosion under quasi-steady-state plasma conditions between ELMs (inter-ELM phase) and erosion during the ELM impact (intra-ELM). It was concluded that W erosion in this case is driven by intra-ELM sputtering of W with D as dominant projectile species and that this situation is expected to persist in ITER, thus stressing the importance of ELM suppression in extending the lifetime of the ITER divertor.

III. DEPOSITION, SURFACE COMPOSITION

III.A Reflection and deposition

Projectiles hitting a surface can be reflected (backscattered) from the surface with a certain probability expressed by the reflection coefficient, R, that, analogously to the erosion yield, is defined as the ratio of fluxes of backscattered and impinging particles (eq. 1). Unlike erosion, for which values $Y > 1$ are possible, the values of the reflection coefficient are limited to $0 \leq R \leq 1$. If the projectile is not reflected, it is considered to be implanted or deposited. The first term is usually used for high impact energies leading to deeper ion penetration into the solid material and pronounced radiation damage, while the latter term applies for energies typically below few eV when ion penetration and energy deposition is limited to only few nanometres. In the following we will mainly use the latter term as more applicable to PMI. The probability for a projectile to be deposited is, respectively, $1 - R$. For molecular projectiles the term sticking is often used instead of deposition. It has to be noted that for chemically reactive molecular species surface reactions may lead to formation of other types of volatile species that leave the surface. In this case, the surface loss probability, $\beta = S + \gamma$, is defined as the sum of the sticking coefficient (probability), S, and the probability of the projectile to react to a non-reactive volatile product, γ, so that the following holds: $S + \gamma + R = 1$ [43]. Interestingly, in the case of interaction of methyl radicals (CH_3) with an amorphous hydrocarbon film surface at a temperature around 600 K, due to chemical erosion effects, the surface loss probability can be even negative [44]. In the following we will address only atomic species.

Particles reflected from metals are in most cases neutrals. Similar to erosion yields reflection coefficients of atoms can be measured under well-defined conditions in ion beam experiments, however, accurate reflection data at fusion relevant low impact energies are rare. Therefore for

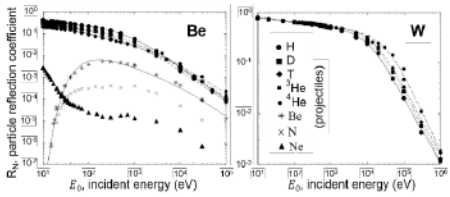

Figure 12: Energy dependence of the reflection coefficient for Be and W bombarded by different projectile species (see legend). Symbols represent calculated data by BCA codes and lines are fitted curves. Reproduced from [45].

calculation of reflection coefficients the same tools as for sputtering are applied, namely BCA based codes, such as SDTrimSP, and MD simulations. The same principles of atomic scattering as introduced for sputtering in section II apply. For example, from equation 2 it becomes clear that the reflection coefficient depends on the impact energy and masses of projectile and target atoms. Generally, the reflection coefficient increases with increasing mass ratio M_2/M_1 – reflection of light projectiles at heavy target atoms is very effective.

Energy dependence of R

At high impact energies the probability of reflection decreases due to deeper penetration (implantation) of projectiles into the target material. At low impact energies, as mentioned, no accurate experimental data is available (for ions). At energies below 10-100 eV the BCA becomes not applicable, though simulation results down to energies of 0.2 eV have been reported [46] applying a planar surface potential to account for chemical binding effects. Simulation results from BCA codes for bombardment of Be and W surfaces are shown in figure 12. MD simulations reveal additional features of hydrogen reflection at low energies [47, 48, 49]. In particular, reflection tends to be maximal close to $R = 1$ at energies between 1 eV and 10 eV, and decrease for higher as well as for sub-eV energies.

Angular dependence of R

The probability of reflection monotonously increases with the impact energy. The increase is rather moderate at very low impact energies and more pronounced at keV energy range [46] that can be to a large extent explained by less deep penetration into the material.

Empirical fit formulae for R

Similarly to physical sputtering, BCA simulations results for R can be rather well described by empirical formulae [46]. In particular, for self-bombardment:

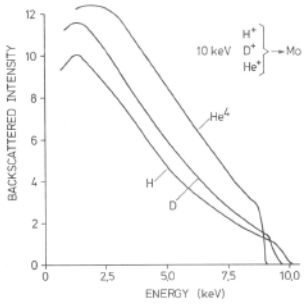

Figure 13: Energy distribution of H, D, He particles backscattered from Mo. Reproduced from [50].

$$R = \frac{\exp(a_1 \varepsilon_L^{a_2})}{1+\exp(a_3 \varepsilon_L^{a_4})}; \qquad (13)$$

for reflection of light ions (H and He isotopes):

$$R = \frac{b_1 \varepsilon_L^{b_2}}{1+b_3 \varepsilon_L^{b_4}}; \qquad (14)$$

and for the angular dependence:

$$R = c_1 + c_2 \tanh(c_3 \alpha \pi/180 - c_4), \qquad (15)$$

with a_i, b_i, c_i as fit parameters.

More details on fit formulae for R can be found in [46] and references therein.

Energy and angular distributions of reflected particles

An example of the energy distribution of reflected particles measured experimentally is shown in figure 13. BCA simulations with SDTrimSP allow to record such distributions and provide along with the particle reflection coefficient, R_N, also the energy reflection coefficient, R_E, defined as $R_E = \frac{\overline{E}}{E_0} R_N$, where $\overline{E}$ is the mean energy of reflected particles. The angular distribution of reflected particles at normal incidence is well described by a cosine distribution. At grazing incidence, specular reflection dominates.

Reflection at rough surfaces

Surface morphology leads to different local angles of incidence compared to the nominal angle of incidence and provide a non-zero probability that a reflected particle can experience a second collision with the surface (figure 6). Both factors affect the probability for backscattering.

For example, experiments with W bombardment by 950 eV $^{13}C^+$ ions at oblique incidence [51] demonstrated that for a rough surface the angular distribution of reflected and self-sputtered C atoms tends to be more cosine-like than

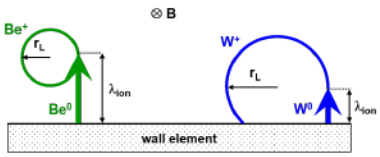

Figure 14: Schematic view of prompt re-deposition for W^+.

in the case of a flat surface at an impact angle of 30°. At 80° backscattering/emission towards the incoming flux was observed for a rough surface, contrary to predominantly specular reflection/sputtering seen for a flat surface. It has to be noted, however, that continuous deposition of C atoms on the surface of W took place throughout the experiment leading to pronounced fluence dependent changes of the surface composition and respectively of the reflection and sputtering yields. Thus, observed angular distributions combine together reflected and self-sputtered C atoms that cannot be clearly distinguished.

Prompt re-deposition

In fusion experiments magnetic fields are applied to ensure plasma confinement. Eroded particles are emitted from the surface mostly as neutrals but are ionized in plasma at some distance from the surface, which in average is characterized by the ionization length λ_{ion} that depends on the local plasma parameters. The ionized particles gyrate in the magnetic field with a certain Larmor radius r_L and, as can be seen from figure 14, if $r_L < \lambda_{ion}$, with some probability can return to the surface within the very first gyration, where they can be "promptly" re-deposited with a probability of $1 - R$. Since the Larmor radius is proportional to the ion mass, prompt re-deposition especially occurs for high-Z materials. This is also illustrated schematically in figure 14 for W (high-Z) in comparison to beryllium (low-Z). Prompt re-deposition strongly depends on plasma parameters and can reach 100% for high plasma temperature and electron density. In JET the gross W erosion measured by spectroscopy was up to factor 15 higher than the net erosion measured post-mortem. Modelling with the ERO code [51] confirmed that prompt re-deposition of W with probabilities larger than 50% is responsible for the drastic reduction of the net erosion compared to the gross erosion.

III.B Flux balance and surface composition

Large-scale devices such as tokamaks differ in many aspects form smaller laboratory devices. One of important features is a strong variation of particle fluxes impinging the PFC at different locations. Plasma-wall interactions at some locations within the device lead to material erosion, eroded material can be ionized in plasma and transported to other locations where it can be deposited, re-eroded and transported further along PFC or even across the device. Furthermore, plasma is never free from impurities. Apart from hydrogen isotopes, there is always a certain oxygen influx. Depending on the experimental conditions additional impurities such as argon or neon can be injected into the edge plasma for the purpose of radiative plasma cooling. Local plasma parameters define the amounts of neutral particles, in particular fast charge-exchange neutrals, hitting the wall. Finally, in the case of a fusion experiment with a significant amount of fusion reactions, also helium ions and neutrons will hit the surrounding walls. Obviously, compared to a laboratory experiment the situation in a tokamak is much more complex: instead of one projectile species there is a whole bunch of impinging projectiles, which in addition are not mono-energetic but have a certain impact energy and angle distribution.

Whether erosion or deposition will dominate at a given location, depends on the balance of incoming and outgoing fluxes:

$$\frac{dN}{dt} = A\sum\left(\Gamma_{dep} - \Gamma_{ero}\right), \qquad (16)$$

In equation 16, $\frac{dN}{dt}$ gives the change rate of the total number of particles in the surface element of an area A due to erosion (outgoing) and deposition (incoming) fluxes of all species present in the plasma flux and in the material surface. Similar equations can be written for each species separately. Let us consider a simple example, in which W surface is bombarded by D plasma with a fraction, $f_{Be} = \frac{\Gamma_{Be^+}}{\Gamma_{D^+}+\Gamma_{Be^+}}$, of Be^+ ions as impurity in the total plasma flux. We neglect here that Be ions with higher charge states can be present in plasma. Note that such ions would gain higher energies in the sheath electric field and thus will be characterized by higher sputtering yields of the wall material. Though dynamic computer simulations with SDTrimSP or similar would be required to assess the rates of particle deposition and removal under changing surface composition, with some simplifications we can write analytical expressions in form of equation 16 for W and Be:

$$\frac{dN_W}{dt} = -c_W(t)\left(Y_{D\to W}\Gamma_{D^+} + Y_{Be\to W}\Gamma_{Be^+}\right), \qquad (17)$$

$$\frac{dN_{Be}}{dt} = -c_{Be}(t)\left(Y_{D\to Be}\Gamma_{D^+} + Y_{Be\to Be}\Gamma_{Be^+}\right), \\ +(1 - R_{Be})\Gamma_{Be^+} \qquad (18)$$

where $c_W(t) + c_{Be}(t) = 1$ are time-dependent relative concentrations of W and Be in a surface layer of a given thickness, where particle interaction takes place, Y are respective erosion yields (keep in mind the impact energy and angle dependence and potential contribution of chemical effects for D→Be), and R_{Be} is the total Be reflection coefficient,

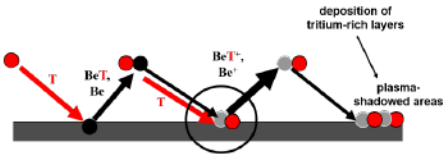

Figure 15: Illustration: formation of co-deposited layers of beryllium with tritium (T:Be).

that also depends on the surface composition, so that $(1\text{-}R_{Be})\Gamma_{Be+}$ gives the deposition rate. Similarly to erosion terms in equations 17 and 18, we can write in a simplified way

$$R_{Be} = c_W(t)R_{Be\to W} + c_{Be}(t)R_{Be\to Be} \qquad (19)$$

By making such assumptions, we assume that species are mixed in the surface layer of a given thickness (interaction layer) and that their contribution to reflection and erosion is simply proportional to their relative concentration in this layer, the so called homogenous mixing model (HMM). Provided that incoming plasma fluxes do not change, steady-state (constant in time) erosion/deposition rates will establish as soon as the equilibrium surface concentrations defined by $\frac{dc_W}{dt} = 0$ and $\frac{dc_{Be}}{dt} = 0$ will be reached. It has to be noted, that for known erosion and reflection yields, the coupled equations 17 and 18 can be solved numerically or by Monte-Carlo simulations to obtain the steady-state erosion/deposition rates and equilibrium surface concentrations. However, the calculated time, at which equilibrium is established, will depend on the selected interaction layer thickness and thus should not be considered as a true physical time.

III.C Fuel co-deposition

In the example considered above, we accounted for material erosion by D ions but neglected that D atoms are in fact implanted into the material and can remain in the surface. This effect is especially important in the case of deposition-dominated conditions, since ions of hydrogen isotopes (fuel) are incorporated into the growing deposited layer (figure 15). In the example above this would imply D co-deposition with Be, but also co-deposition with heavy elements such as W can take place. Since the layer growth is not limited under the deposition-dominated conditions, so also the build-up of fuel inventory in the co-deposited layers is not limited and represents a safety issue. Moreover, thick deposited layers can become unstable, so that flaking and dust formation cannot be excluded. Fuel containing dust particles can be mobilized during plasma operation or off-normal events, thus posing additional risks on plasma performance and hazard control.

In view of ITER, co-deposition of tritium with Be and W have to be considered. Experience from JET tokamak with the ITER-Like Be and W wall material mix suggests that thick D:Be co-deposits can be formed in the divertor. Several laboratory studies have been performed in the recent years to assess the fuel content in co-deposited layers of D with metals. Empirical scaling expressions have been proposed to describe the D/Me (Me stands for metal) ratios in such layers as a function of different parameters, mainly deposition fluxes, impact energies and surface temperature. For Be the so-called De Temmerman scaling [52] was deduced, which has been recently challenged by extending the range of experimental parameters [53]. As an alternative, a sophisticated analytical method based on reaction-diffusion rate equations has been recently developed and validated on dedicated laboratory experiments with W, Mo and Al [54] and tested against the available data for Be [55].

IV. FUEL RETENTION

Retention of the radioactive tritium fuel in the wall materials is a major concern for future fusion devices since the in-vessel amount of tritium has to be limited for safety aspects. If a certain limit is reached, plasma operation has to be stopped and the walls have to be cleaned from tritium. This limits the availability of the device and demonstrates the need to develop effective fuel retention diagnostics and cleaning methods. In particular, baking of the vessel (keeping the walls at elevated temperatures) and wall conditioning with ion-cyclotron RF plasma or glow discharge plasma are investigated as tools for reducing the tritium content in the walls [56].

Retention by co-deposition has been already addressed in the previous section. In this section we will consider fundamental mechanisms of retention. We will use the name hydrogen as collective for all hydrogen isotopes.

Figure 16 illustrates the processes of hydrogen interaction with a surface of a metal. Hydrogen atoms and molecules can adsorb on surfaces of metals. If hydrogen molecules are present in the vacuum chamber (gas phase) they can dissociate, adsorb on the surface and finally penetrate into the lattice, occupying interstitial (solute) sites. The amount of adsorbate is usually described as a function of the gas pressure at constant temperature (adsorption isotherms) [57]. In the case of ion implantation, however, ions usually have enough energy to overcome the surface energy barrier, penetrate several atomic layers into the surface and only then thermalize in the lattice, finally occupying interstitial positions. Interstitial positions are the local energy minima (figure 17) and hydrogen atoms can experience temperature dependent random walk between these positions. So hydrogen diffuses in the lattice since the random walk from the region of implantation (region of high concentration of

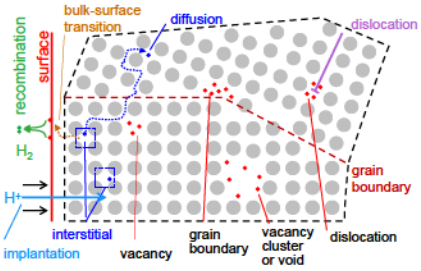

Figure 16: Illustration of hydrogen in a metal lattice.

hydrogen atoms) results in the net transport of atoms to regions with low concentration, namely towards the surface of the material and into the material bulk. Two hydrogen atoms that reach the surface of the material in this process can recombine into a molecule and desorb from the surface [58]. The overall process of hydrogen implantation, diffusion and desorption is called hydrogen recycling (also reflection has to be taken into account). In these processes hydrogen ions are absorbed by the walls and hydrogen atoms and molecules are released. Dissociation and ionization of these molecules in plasma leads to plasma cooling so that when the plasma flux to the wall increases, also the effect of cooling by interaction with neutral particles increases. For sufficiently high plasma fluxes in tokamaks, also depending on the neutral pumping capabilities in the divertor, ion-neutral interactions lead to so-called high recycling divertor conditions and finally to divertor detachment [59], which is characterized by a beneficial reduction of the heat flux to the wall due to plasma recombination.

In fusion-relevant materials, hydrogen diffusion is active at rather moderate temperatures. If materials would have ideal lattices without impurities, most of hydrogen would outgas from the walls within seconds after plasma exposure even at room temperature. This is, however, not the case, since any material has intrinsically present defects, by nature or by manufacturing, and impurities. Furthermore, ion implantation itself introduces radiation defects (via collision cascades) and stresses in the material. In future fusion devices also damage by neutron irradiation will become important. Material defects are responsible for hydrogen trapping, i.e. they act as energetically favourable sites for hydrogen binding with different degree of binding strength. In figure 17 this is illustrated by a deeper energy minimum with activation energy of de-trapping, ΔE_{trap}, compared to the activation energy of diffusion, ΔE_D, that characterizes the transitions between interstitial sites. Strongly trapped hydrogen becomes immobile and can be released only under higher material temperatures. Weaker bound hydrogen can be released over rather long time after exposure (days). Presence of traps (defects) with relatively weak binding energies

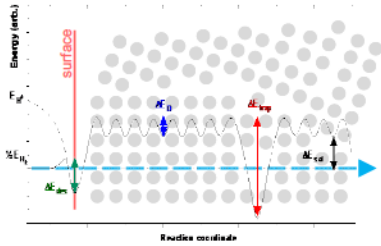

Figure 17: Energy diagram of hydrogen in the lattice. The shown processes are de-trapping from a trapping site (1), diffusion via interstitial (solute) sites (2) and desorption from the adsorption site on the surface (3) with respective energy barriers ΔE_{trap}, ΔE_D, ΔE_{des}.

slows down the diffusive hydrogen transport and thus outgassing due recurring trapping and de-trapping reactions. De-trapping, diffusion and desorption are considered to be thermally activated Arrhenius processes so that the rates of respective transitions are proportional to the Boltzmann exponent with respective activation energy, ΔE_a:

$$R \sim \exp(-\Delta E_a / kT) \qquad (20)$$

Hydrogen atoms occupying interstitial sites (solute hydrogen), empty and hydrogen-filled traps can be represented by their spatially and time dependent concentrations in the material. Evolution of these concentrations can be described by a system of coupled partial differential equations that can be solved numerically, see e.g. [60, 61] and references therein. Essential parameters for such macroscopic rate equation modelling are the energy barriers for various trapping and de-trapping reactions. Experimental determination of such parameters is rather challenging and prone to lots of uncertainties. So typically such data are obtained from first-principles calculations, mainly by the density functional theory (DFT), see e.g. [62, 63], and then tested against experimental data. As far as the experimental data is concerned, these are typically thermal-desorption spectra (TDS) and hydrogen depth-profiles from the nuclear-reaction analysis (NRA) and secondary ion mass spectrometry (SIMS).

A lot of experimental efforts have been devoted to the studies of exposure temperature, flux and fluence dependences of retention, see e.g. [64, 65]. In particular for the fluence dependence, the concentration of implantation-induced defects is assumed to saturate at high fluences, which means that for long enough exposure times the total retention will be dominated by diffusion-driven population of intrinsic traps. This fact is supported by high fluence exposures in the linear plasma device PISCES-B [66], where a square-root of time dependence of total retention was measured up to a maximum D fluence of 2×10^{28} m^{-2}. However, for shorter exposure times retention is usually strongly dominated by radiation induced effects. Figure 18

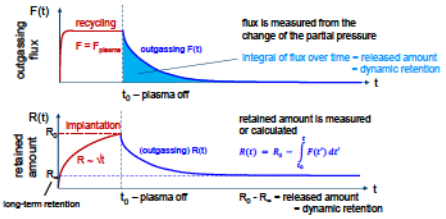

Figure 18: Illustration of evolution of the outgassing flux (upper frame) and total retention (lower frame) in the material during and after plasma exposure [67].

illustrates the evolution of the total accumulated fuel in the material and the outgassing flux as a function of time during and after exposure assuming saturation of the total retention with fluence. Experience from the JET tokamak suggests, however, that the total in-vessel retention in the Be-W wall material mix will be rather dominated by tritium co-deposition with beryllium.

In a fusion environment radiation damage by fusion neutrons has to be taken into account. Unlike ion-induced damage, it will not be located in the near-surface region, thus can be responsible for fuel accumulation in deeper bulk regions. In addition, interaction of neutrons with beryllium will lead to the production of tritium via nuclear reactions (transmutation) inside the material itself.

An important role in hydrogen retention, especially in presence of helium play surface modifications, such as formation of blisters, which will be briefly addressed in the following section.

V. SURFACE MORPHOLOGY CHANGES

Material erosion, impurity deposition and fuel retention mechanisms described in the previous sections can be considered as atomistic aspects of plasma-wall interactions. These processes, however, can lead to rather macroscopic changes of the surface morphology. Surface roughening due to preferential sputtering, prompt re-deposition and formation of deposited layers is the first example. In the following we will briefly cover some more exotic but still rather common phenomena.

V.A Blistering

Blisters are formed when implanted hydrogen or helium atoms accumulate at some material defects such as dislocation kinks, small voids or starting from clustering of single vacancies. In case of helium, clustering is energetically favourable even at interstitial sites. Accumulation of atoms eventually leads to formation of gas bubbles. Gas in the bubble exerts pressure on the surrounding material, leading to mechanical stresses. If the bubble is close to the surface, the stress field can be partly released by the deformation of the material above the bubble, e.g. by bending of the surface or by glide of the crystallographic planes. In both cases protruding elements appear on the surface that are called blisters. Blister caps can be eroded or open by cracking leading to the release of the enclosed gas. Blister caps can peel-off leading to formation of micro-flakes. Blisters are formed on most of fusion relevant materials if they are exposed to high plasma flux. Blister formation tends to reduce at elevated temperatures, however at very high fluxes (10^{24} ion/m^2/s and above) blister formation was observed at surface temperatures as high as 1100 K [65]. While blistering under high flux D plasma exposure acts as an additional retention channel, simultaneous exposure to 5% of He flux reduces hydrogen retention [66]. Laboratory experiments, in particular [68], demonstrated that defect-rich blistered surface layer from one side acts as getter for hydrogen atoms, increasing the near-surface retention but preventing their penetration deeper into the material, and from the other side promotes that ~80% of hydrogen is eventually released by opening of blisters due to continuous erosion of the surface.

V.B Fuzz formation

We will limit our description to tungsten fuzz. These are He-induced nanostructures (fibres) that form on W surface under He irradiation at elevated surface temperatures [69]. The most common explanation for W fuzz is growth and burst of He bubbles [70, 71]. He atoms diffuse and form small mobile clusters. For the critical cluster size of 7-8 He atoms, a W atoms is ejected, so that a self-interstitial W atoms and a vacancy are produced. The He cluster gets pinned to the vacancy and continues to growth by absorbing He atoms and small He clusters. In this process it continues to displace further W atoms that at certain point reorganize into a dislocation loop that detaches from the He bubble (dislocation loop punching). Loop punching and bubble bursting lead to pin holes, dips, and protrusion formation on the surface. New subsurface bubbles form propagating further surface morphological evolution. Potential issues associated with fuzz formation are the increased probability of arcing, increased erosion, and low thermal conductivity. In the absence of strong plasma fluctuations (such as ELMS), fuzz thickness increases with a square-root of time dependence [72]. W fuzz can be expected to form over a narrow region in the ITER divertor. According to recent analysis [69], W fuzz formation should not be critical for ITER operation.

V.C Melting and melt-layer motion

High heat loads to PFCs, especially in the case of transient events such as unmitigated ELMs or disruptions, can lead to melting of the material. Molten material is subject to several forces, among which the JxB force was shown to dominate in JET

[73] and ASDEX-Upgrade [74]. Here B is the toroidal magnetic field and J is the replacement current flowing through the molten layer to compensate for thermionic emission from PFC [75]. Melting causes material damage via deep material re-solidification and related propagation of macro-cracks. Gross melt motion leads to macroscopic surface modifications [76]. Melt splashing can occur, leading to ejection of liquid metal droplets into plasma. Such droplets can provide a very intensive source of impurities in the plasma that can impair the plasma performance. Finally, droplets that survive on their way through plasma are deposited elsewhere in the device and in some cases can be remobilized as dust particles, e.g. during subsequent plasma ramp-up.

V.D Thermal shock and transient heat loads

PFCs in fusion devices are exposed to rather high steady-state particle and heat loads. On top of that, transient particle and heat loads can be present, e.g. due to ELMs. Transient thermal loads induce a wide range of surface modifications such as roughening due to plastic deformation, formation of small cracks and extended crack networks on the PFC surface, impairing the PFC integrity and reducing its lifetime [77]. Furthermore, simultaneous exposure to heat and particle fluxes, especially to helium, leads to lower material plasticity and critical stress for damage/crack formation due to H/He embrittlement, promoting faster damage evolution [78].

SUMMARY

In this manuscript the most important processes affecting the life time of plasma-facing components in fusion devices have been briefly described. Material erosion under bombardment of energetic particles from plasma has been addressed both in terms of physical sputtering and in view of chemical processes. Particle reflection, implantation and deposition have been described and the role of co-deposition of fuel atoms with eroded wall materials in the in-vessel accumulation of tritium in fusion devices has been highlighted. Elementary atomistic mechanisms of fuel retention in metals have been introduced and macroscopic effects of hydrogen and helium irradiation on the surface morphology of plasma-facing components have been presented. Finally, a short overview of effects of transient high heat loads and combined particle and heat loads have been given. This manuscript in no way pretends to be an exhaustive review of plasma-wall interaction processes. The authors hope that the provided literature references will allow a deeper immersion into the topic for an interested reader.

REFERENCES

[1] *Progress in the ITER Physics Basis*, Nucl. Fusion 47 (2007), https://iopscience.iop.org/issue/0029-5515/47/6

[2] G. Councell *et al*, Plasma Phys. Control. Fusion 48 (2006) B189 https://doi.org/10.1088/0741-3335/48/12B/S18

[3] A. Kirschner *et al*, J. Nucl. Mater. 152 (2009) 390 https://doi.org/10.1016/j.jnucmat.2009.01.155

[4] F. Maviglia et al, *Nucl. Mater. Energy* 26 (2021) 100897 https://doi.org/10.1016/j.nme.2020.100897

[5] Wikipedia contributors. *Erosion [Internet]*. Wikipedia, The Free Encyclopedia (2021 Nov 2, 08:45 UTC) Available from: https://en.wikipedia.org/w/index.php?title=Erosion&oldid=1053163547

[6] R. Behrisch and W. Eckstein (Eds.), *Sputtering by Particle Bombardment*, Springer, Topics in Applied Physics 110 (2007) https://doi.org/10.1007/978-3-540-44502-9

[7] W. Eckstein, *Computer Simulation of Ion-Solid Interactions*, Springer Series in Materials Science 10 (1991) https://doi.org/10.1007/978-3-642-73513-4

[8] A. Mutzke *et al*, IPP Report 2019-02, Max-Planck-Institut für Plasmaphysik https://doi.org/10.17617/2.3026474

[9] S. Brezinsek and JET-EFDA contributors, J. Nucl. Mater. 463 (2015) 11 https://doi.org/10.1016/j.jnucmat.2014.12.007

[10] J. Bohdansky, Nucl. Instr. Meth. B 2(1984) 587 https://doi.org/10.1016/0168-583X(84)90271-4

[11] Y. Yamamura, Y. Itikawa, N. Itoh, Japan Report, IPPJ-AM-26, Nagoya University (1983) http://dpc.nifs.ac.jp/IPPJ-AM/IPPJ-AM-26.pdf

[12] W. Eckstein, Vacuum 82 (2008) 930 https://doi.org/10.1016/j.vacuum.2007.12.004

[13] W. Eckstein and R. Preuss, J. Nucl. Mater. 320 (2003) 209 https://doi.org/10.1016/S0022-3115(03)00192-2

[14] M. W. Thompson: Philos. Mag. 18 (1968) 377 https://doi.org/10.1080/14786436808227358

[15] E. Oyarzabal *et al*, J. Appl. Phys. 100 (2006) 063301 https://doi.org/10.1063/1.2336502

[16] J. Greenwood, Vacuum 67 (2002) 217 https://doi.org/10.1016/S0042-207X(02)00173-2

[17] A. Goehlich *et al*, Phys. Rev. B62 (2000) 9349 https://doi.org/10.1103/PhysRevB.62.9349

[18] G. Falcone *et al*, IL NUOVO CIMENTO D 15

(1993) 1159
https://doi.org/10.1007/BF02451724
[19] J. Romazanov *et al*, Phys. Scr. (2017) 014018
https://doi.org/10.1088/1402-4896/aa89ca
[20] A. Eksaeva *et al*, Nucl. Mater. Energy 19 (2019) 13
https://doi.org/10.1016/j.nme.2019.02.006
[21] A Eksaeva *et al*, Phys. Scr. (2020) 014057
https://doi.org/10.1088/1402-4896/ab5810
[22] M. Rasinski *et al*, Nucl. Mater. Energy 12 (2017) 302
https://doi.org/10.1016/j.nme.2016.11.001
[23] M. Rasinski *et al*, Phys. Scr. T170 (2017) 014036 https://doi.org/10.1088/1402-4896/aa8de5
[24] M. Rasinski *et al*, Phys. Scr. T167 (2016) 014013 https://doi.org/10.1088/0031-8949/2016/T167/014013
[25] H. R. Koslowski *et al*, Nucl. Mater. Energy 22 (2020) 100736
https://doi.org/10.1016/j.nme.2020.100736
[26] A. Kirschner, *Erosion and deposition mechanisms in fusion plasmas*, 12th Carolus Magnus Summer School on Plasma and Fusion Energy Physics, Forschungszentrum Jülich GmbH (2015)
https://juser.fz-juelich.de/record/283648
[27] C. Björkas *et al*, New J. Phys. 11 (2009) 123017 https://doi.org/10.1088/1367-2630/11/12/123017
[28] C. Björkas *et al*, J. Nucl. Mater. 438 (2013) S276
https://doi.org/10.1016/j.jnucmat.2013.01.039
[29] K. Nordlund *et al*, Nucl. Instr. and Meth. B 269 (2011) 1257
https://doi.org/10.1016/j.nimb.2010.12.080
[30] C Björkas *et al*, Plasma Phys. Control. Fusion 55 (2013) 074004
https://doi.org/10.1088/0741-3335/55/7/074004
[31] S. Brezinsek *et al*, Nucl. Fusion 54 (2014) 103001 https://doi.org/10.1088/0029-5515/54/10/103001
[32] S. Brezinsek *et al*, Nucl. Fusion 55 (2015) 063021 https://doi.org/10.1088/0029-5515/55/6/063021
[33] D. Borodin *et al*, Nuclear Materials and Energy 9 (2016) 604
https://doi.org/10.1016/j.nme.2016.08.013
[34] R. P. Doerner *et al*, J. Appl. Phys. 95 (2004) 4471 https://doi.org/10.1063/1.1687038
[35] R. P. Doerner, IAEA Sputtering Database Meeting, Vienna, Dec. 12 & 13, 2011
https://www-amdis.iaea.org/meetings/SputtMtg2011/SputtMtg-Doerner-2011-12-12.pdf
[36] P. C. Stangeby, *The Plasma Boundary of Magnetic Fusion Devices* (1st ed.), CRC Press (2000)
https://doi.org/10.1201/9780367801489
[37] B. Unterberg, *Transport processes in the plasma edge*, 12th Carolus Magnus Summer School on Plasma and Fusion Energy Physics, Forschungszentrum Jülich GmbH (2015)
http://hdl.handle.net/2128/10002
[38] D. Reiser, *Introduction to drift-wave turbulence*, 12th Carolus Magnus Summer School on Plasma and Fusion Energy Physics, Forschungszentrum Jülich GmbH (2015)
http://hdl.handle.net/2128/10003
[39] D. Reiser *et al*, Phys. Scr. T170 (2017) 014039
https://doi.org/10.1088/1402-4896/aa8db2
[40] A. Kreter *et al*, Fusion Science and Technology 68 (2015) 8
https://doi.org/10.13182/FST14-906
[41] H. R. Wilson, *Edge localized modes in tokamaks*, 12th Carolus Magnus Summer School on Plasma and Fusion Energy Physics, Forschungszentrum Jülich GmbH (2015)
http://hdl.handle.net/2128/10101
[42] S. Brezinsek *et al*, Nucl. Fusion 59 (2019) 096035
https://doi.org/10.1088/1741-4326/ab2aef
[43] C. Hopf *et al*, J. Appl. Phys. 87 (2000) 2719
https://doi.org/10.1063/1.372246
[44] M. Meier *et al*, Nucl. Fus. 43 (2003) 25
https://doi.org/10.1088/0029-5515/43/1/303
[45] W. Eckstein, IPP Report 17/12 (2009), Max-Planck-Institut für Plasmaphysik
http://hdl.handle.net/11858/00-001M-0000-0026-F342-A
[46] W. Eckstein and J. P. Biersack, Appl. Phys. A 38 (1985) 123
https://doi.org/10.1007/BF00620463
[47] O. V. Ogorodnikova *et al*, J. Appl. Physics 119 (2016) 054901
https://doi.org/10.1063/1.4940678
[48] P. N. Maya, J. Nucl. Mater. 480 (2016) 411
https://doi.org/10.1016/j.jnucmat.2016.08.007
[49] D. S. Meluzova *et al*, Nucl. Instr. and Meth. B 460 (2019) 4
https://doi.org/10.1016/j.nimb.2019.03.037
[50] W. Eckstein and H. Verbeek, IPP Report 9/32 (1979), Max-Planck-Institut für Plasmaphysik
http://hdl.handle.net/11858/00-001M-0000-0027-6B60-B
[51] A. Kirschner *et al*, Plasma Phys. Control. Fusion 60 (2018) 014041
https://doi.org/10.1088/1361-6587/aa8dce
[52] G. De Temmerman and R. P. Doerner, Nucl. Fusion 49 (2009) 042002
https://doi.org/10.1088/0029-5515/49/4/042002
[53] M. J. Baldwin *et al*, Phys. Scr. T171 (2020) 014014
https://doi.org/10.1088/1402-4896/ab41a3
[54] S. A. Krat *et al*, Nucl. Mater. Energy 24 (2020) 100763
https://doi.org/10.1016/j.nme.2020.100763

[55] S. A. Krat *et al*, Nucl. Mater. Energy 26 (2021) 100949 https://doi.org/10.1016/j.nme.2021.100949
[56] T. Wauters *et al*, Plasma Phys. Control. Fusion 62 (2020) 034002 https://doi.org/10.1088/1361-6587/ab5ad0
[57] K.Y. Foo, B.H. Hameed, Chem. Eng. J. 156 (2010) 2 https://doi.org/10.1016/j.cej.2009.09.013
[58] K. Schmid, M. Zibrov, Nucl. Fusion 61 (2021) 086008 https://doi.org/10.1088/1741-4326/ac07b2
[59] S. I. Krasheninnikov *et al*, Phys. Plasmas 23 (2016) 055602 https://doi.org/10.1063/1.4948273
[60] E.A. Hodille *et al*, J. Nucl. Mater. 467 (2015) 424 https://doi.org/10.1016/j.jnucmat.2015.06.041
[61] K. Schmid *et al*, J. Appl. Phys. 116 (2014) 134901 https://doi.org/10.1063/1.4896580
[62] K. Heinola *et al*, Phys. Rev. B 82 (2010) 094102 https://doi.org/10.1103/PhysRevB.82.094102
[63] N. Fernandez *et al*, Acta Materialia 94 (2015) 307 https://doi.org/10.1016/j.actamat.2015.04.052
[64] B. Lipschultz *et al*, MIT report PSFC/RR-10-4 (2010) https://library.psfc.mit.edu/catalog/reports/2010/10rr/10rr004/10rr004_full.pdf
[65] L. Buzi, PhD Thesis (2015) https://hal.univ-lorraine.fr/tel-01751975
[66] R. P. Doerner *et al*, Nucl. Mater. Energy 9 (2016) 89 https://doi.org/10.1016/j.nme.2016.04.008
[67] D. Matveev *et al*, Phys. Scr. 96 (2021) 124079 https://doi.org/10.1088/1402-4896/ac43d6
[68] J. Bauer *et al*, Nucl. Fusion 57 (2017) 086015 https://doi.org/10.1088/1741-4326/aa7212
[69] G. De Temmerman *et al*, Nucl. Mater. Energy 19 (2019) 255 https://doi.org/10.1016/j.nme.2019.01.034
[70] K. D. Hammond, Mater. Res. Express 4 (2017) 104002 https://doi.org/10.1088/2053-1591/aa8c22
[71] D. Dasgupta *et al*, Nucl. Fusion 59 (2019) 086057 https://doi.org/10.1088/1741-4326/ab22cb
[72] M. J. Baldwin *et al*, J. Nucl. Mater. 390-391 (2009) 886 https://doi.org/10.1016/j.jnucmat.2009.01.247
[73] J. W. Coenen *et al*, Nucl. Fusion 55 (2015) 023010 https://doi.org/10.1088/0029-5515/55/2/023010
[74] K. Krieger *et al*, Nucl. Fusion 58 (2018) 026024 https://doi.org/10.1088/1741-4326/aa9a05
[75] M. Komm *et al*, Nucl. Fusion 60 (2020) 054002 https://doi.org/10.1088/1741-4326/ab7c27
[76] E Thorén *et al*, Plasma Phys. Control. Fusion 63 (2021) 035021 https://doi.org/10.1088/1361-6587/abd838
[77] Th. Loewenhoff *et al*, Phys. Scr. T145 (2011) 014057 https://doi.org/10.1088/0031-8949/2011/T145/014057
[78] M. Wirtz et al, Nuc. Mater. Energy 9 (2016) 177 https://doi.org/10.1016/j.nme.2016.07.002

STOCHASTIC BOUNDARY PLASMA IN TOKAMAKS WITH RESONANT MAGNETIC PERTURBATIONS

Y. Liang

Forschungszentrum Jülich GmbH, Institut für Energie- und Klimaforschung - Plasmaphysik, 52425 Jülich, Germany

ABSTRACT

Experimental results from different devices demonstrate that magnetic topology plays a key role in plasma confinement, edge MHD stability, and interactions between the plasma and the first wall, particularly with the divertor. Recently, three-dimensional (3D) magnetic topology effects, which are associated with stochastic boundary plasma physics, form one of the hottest topics in fusion research today, and understanding them is essential for the success of future fusion devices. In this paper, an overview of the physics understanding of the formation first of 3D magnetic topology and then of a stochastic layer, and its effects on the edge and divertor transport and on MHD stability in tokamak plasmas will be presented. In addition, comparing the advantages and disadvantages of 2D and 3D magnetic topology effects in magnetic confinement fusion will be discussed.

I. INTRODUCTION

On the basis of the fusion reseach achievements of the past half century, it is foreseen that a steady state operation of ITER [1] and future fusion power plants, e.g. DEMO, will require the resolution of plasma wall interaction, in which a tolerable plasma exhaust, including steady state and transient heat and particle fluxes on plasma-facing components, is controlled reliably by one or more mechanisms at high power densities.

A. Problem of transient plasma wall interaction

The standard tokamak H-mode [2] is foreseen as the baseline operating scenario of a future fusion machine, e.g. ITER. However, the steep plasma pressure gradient and associated increased current density at the edge pedestal could exceed a threshold value for driving magnetohydrodynamic (MHD) instabilities referred to as Edge Localized Modes (ELMs). Using results from various current devices, an extrapolation of the heat and particles deposited on the wall components has been carried out for ITER. Since the exact physics and scaling is unknown, the predicted ELM energy loss ranges from $\sim$ 5 to $22MJ$[4]. It is expected that approximately half of this energy will reach the wall and be deposited over a region of $\sim 1m^2$, known as the wetted area. Thus, the surface energy density is suggested to be 2.5 to $11MJm^{-2}$ which is $\sim$ 5 to 20 times higher than acceptable for the planned first wall components, primarily made of tungsten or carbon fibre composites, which can receive a maximum of $0.5MJm^{-2}$. Therefore, it is important to find mitigation/suppression solutions for ELMs.

B. Problem of stationary plasma-wall interaction

In a fusion reactor, a significant amount of heating power, which is mainly from auxiliary heating and energetic α particles produced in the D-T burning plasmas, has to be continuously exhausted through radiation or deposited directly on the plasma facing components during long-pulse or steady-state operation. Since the transport along field lines is several orders of magnitude higher than the cross field transport, this results a very rapid decay of the profiles inside the scrape-off layer (SOL) which causes a thin power deposition width,λ_q.

$$\lambda_q \approx \pi q R \sqrt{\frac{\chi_\parallel}{\chi_\perp}}, \tag{1}$$

Here, R is the major radius of the tokamak, q is the safety factor at the edge, $\chi_\parallel$ and $\chi_\perp$ are the energy diffusion coefficients in the direction parallel and perpendicular to the field lines, respectively.

Based on the present experimental scaling[3], λ_q is expected to be less than $1mm$, and then the parallel heat flux may approach $1GWm^{-2}$ for ITER. This obviously exceeds the engineering capability for any plasma-facing component. Therefore, it is necessary both to decrease the power conducted and convected to the edge by enhancing exhaust through non-magnetically confined particles (neutral atoms or photons) and also to increase the λ_q by controlling the edge plasma transport.

C. Stochasticity in Fusion Plasmas

The success of the *stochastic ansatz* goes back to 1905, when Einstein published three fundamental papers, one of which was on Brownian motion

[5, 6], a simple continuous-time stochastic process in natural science. Nowadays, the term stochastic occurs in a wide variety of professional or academic fields to describe events or systems that are unpredictable due to the influence of a random variable. The theory of stochasticity has been further developed [7, 8, 9, 10, 11]. Recently, *stochastic transport* theory was developed for plasmas [12].

In a magnetically confined fusion device, resonant magnetic perturbations (RMPs) can tear the nested flux surfaces and generate magnetic islands. The width of the magnetic island is proportional to the square root of the perturbation field. By simply increasing the perturbation field, the island width can be increased. Due to the fixed distance between neighbouring islands, the island chains will grow and further overlap. Then, the field lines start to behave in a chaotic way and all closed flux surfaces between the two surfaces will be destroyed. A standard criterion of stochastization is the Chirikov parameter, σ_{ch}, which is the ratio of the island width to the radial distance between the neighbouring island-chains. When $\sigma_{ch} \geq 1$, the criterion indicates island overlapping [8]. The magnetic fields between these two surfaces are now called *stochastic* or *ergodic*. These two terms are used with almost the same meaning in the fusion community although there is some difference in their mathematical meanings. If the overlapping of island chains exists, the transport (radial) will be greatly enhanced and the pedestal gradient could be reduced.

Very recently, structure formation and transport in stochastic plasmas has been a topic of growing importance in many fields of plasma physics from astrophysics to fusion research. In particular, the investigation of the possibility of controlling the particle and heat transport by the formation of a stochastic boundary layer has been investigated on most large and medium-sized magnetic confinement fusion devices across the world [13]. A major result was discovering that large type-I ELMs in H-mode tokamak plasmas can be mitigated [14]or even suppressed [15] by RMPs. This discovery opens up a possible mechanism for suppressing large type-I ELMs in future fusion devices such as ITER. However, it is widely recognized that a more basic understanding of the plasma response to the RMPs is needed to extrapolate the results obtained in present experiments to future fusion devices.

D. Scope of this lecture

This lecture will address the topic of stochastic boundaries and focus on three-dimensional (3D) edge physics and applications of RMPs in tokamaks. However, this topic itself is not specific to the tokamak magnetic configuration. In both tokamaks and stellarators, stochastic magnetic fields can arise and influence the interplay between 3D magnetic topology and plasma confinement. Stellarator devices represent an inherent 3D challenge. They make use of the island divertor concept, and stochasticity and magnetic topology therefore play a fundamental role in their operation. With the extended operational regimes pioneered on the Large Helical Device (LHD), and with W7-X, attention has been directed towards the challenge of 3D plasma equlibria, transport and plasma-surface interactions.

In this lecture, the fundamental physics of the formation of a stochastic boundary layer by the application of RMPs will be described. The physics of stochastic boundary plasmas including the rotational screening effect, the plasma equilibrium effect on the magnetic topology, and stochastic plasma transport and its effects on plasma-wall interactions will be discussed. Finally, the application of RMPs for controlling pedestal profiles and stability will be presented.

II. FORMATION OF A STOCHASTIC BOUNDARY LAYER IN MAGNETICALLY CONFINED FUSION PLASMAS

A. Resonant magnetic perturbations

Magnetic perturbations which are resonant with field lines in the plasma are known as RMPs. The resonance condition is fulfilled when the inverse winding number of the field lines, in tokamak physics known as the safety-factor

$$q = \frac{1}{2\pi} \oint \frac{B_t}{RB_p ds}, \tag{2}$$

corresponds to the ratio of the applied poloidal m and toroidal n perturbation mode numbers: $q = \frac{m}{n}$. Here, R is the major radius of the torus, B_t and B_p the toroidal and poloidal magnetic field components, and ds the line element in the poloidal plane. The term RMP is mostly used if the perturbation is deliberately applied. In a magnetic confinement device, several resonance conditions are usually fulfilled due to the continuous q-profile. As will be seen below, the key resonant perturbations are those in the plasma boundary.

B. Methods of producing RMPs

A standard technique for producing such RMPs is the usage of either in-vessel or external coil systems with a certain geometry to apply the required poloidal and toroidal mode numbers. The main focus is often on low toroidal mode numbers, usually in the range of 1 to 4. Although the general idea is always the same, the design of such RMP coil systems differs greatly from device to device.

On JET, the error field correction coils (EFCCs), which are located outside of the vacuum vessel, as seen in figure 1, are used to apply RMPs. They were originally designed to correct the intrinsic error field of misaligned toroidal field coils. As a consequence of

the large distance between the coils and the plasma edge, a strong current of several tens of kA is required to achieve an adequate perturbation of the plasma edge using such EFCCs.

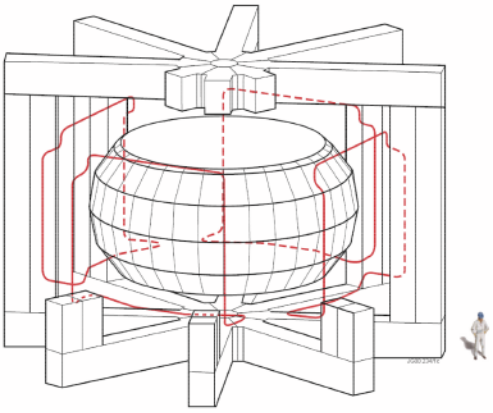

Figure 1: Perspective view of JET showing the 4 large error field correction coils mounted between the transformer limbs.

Depending on the wiring of the EFCCs, either $n = 1$ or $n = 2$ fields can be created [17]. The effective radial resonant magnetic perturbation amplitude, $|b_{res}^{r,eff}| = |B_{res}^{r,eff}/B_0|$, where $B_{res}^{r,eff}$ and B_0 are the radial resonant magnetic perturbation field and the on-axis toroidal magnetic field, respectively, calculated for $I_{EFCC} = 1kAt$ in $n = 2$ configuration, is shown in figure 2. $|b_{n=2}^{r,eff}|$ is the $n = 2$ effective radial resonant magnetic perturbation amplitude.

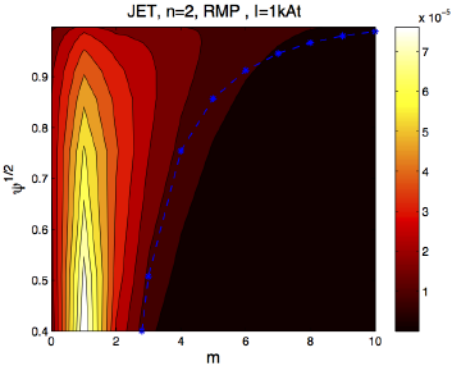

Figure 2: Radial component of the $n = 2$ helical mode spectrum with $I_{EFCC} = 1kAt$ using vacuum fields. Here, the x-axis is the poloidal mode number, m. The calculation is based on an equilibrium reconstruction for JET pulse #69557 at $20s$. Pitch resonant modes with $m = nq(\Psi)$ are shown by the blue dashed line.

Recently, the formation of helical current filaments flowing along field lines has been observed in the SOL during the application of lower hybrid waves (LHWs) on the Experimental Advanced Superconducting Tokamak (EAST) [18]. Magnetic perturbations induced by the currents flowing in these edge helical filament structures have been measured by a set of Mirnov coils during the modulation of LHWs. Because of the geometric effect of the LHW antenna, the perturbation fields induced by the HCFs are dominated by the $n = 1$ component. The magnetic perturbation spectrum calculated based on the experimental parameters indicates a good resonant feature, whereby the plasma edge resonant surfaces are well aligned on the ridge of the spectrum as seen in figure 3.

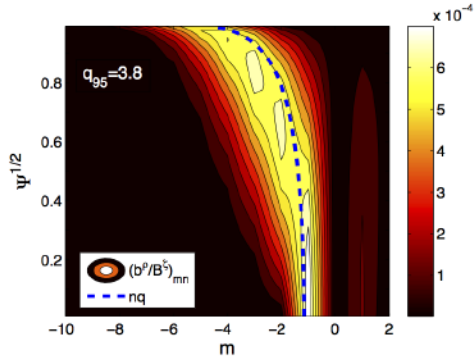

Figure 3: Radial component of the $n = 1$ helical mode spectrum calculated with $1kA$ HCF current. The calculation is based on an equilibrium reconstruction for a EAST pulse. Pitch resonant modes with $m = nq(\Psi)$ are shown by the blue dashed line.

C. 3D magnetic topology in tokamaks with RMPs

The application of RMPs results in the reorganization of the magnetic topology into a new equilibrium state. Resonances outside the plasma (in the SOL) cause an external kinking of the plasma; resonances inside the plasma lead to internal kinking and magnetic reconnection processes, also known as tearing. Due to this reconnection, magnetic islands are created on surfaces at locations where q is resonant. On these flux surfaces, groups of islands form which correspond in the number of islands in the poloidal and toroidal directions with the poloidal and toroidal mode numbers of the resonance at that location.

One method of visualizing the changes in the magnetic topology is by using a Poincaré plot. The simplest approach to modelling the effects of RMPs on the plasma is to superpose the axisymmetric equilibrium field with the additional perturbation field. This is a vacuum approach as no plasma is considered, although the field produced by the toroidal plasma current is included. Knowing the total magnetic field

$\vec{B} = (B_R, B_\phi, B_Z)$, the field lines can be traced based on the equations

$$\frac{dR}{d\Phi} = R\frac{B_R}{B_\Phi}, \frac{dZ}{d\Phi} = R\frac{B_Z}{B_\Phi}. \quad (3)$$

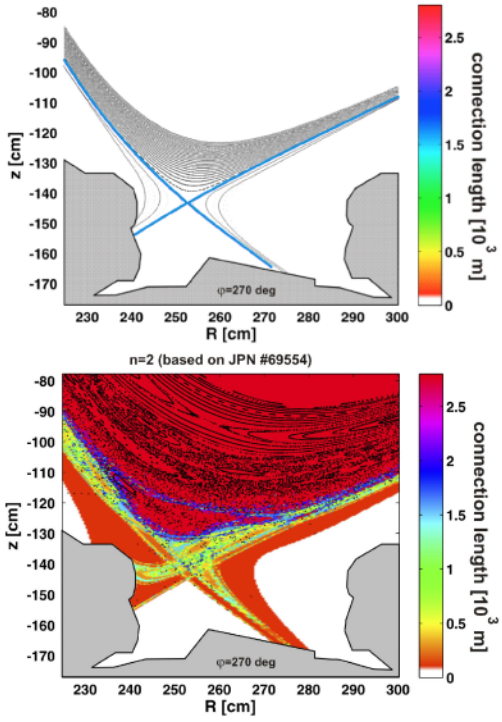

Figure 4: Poincaré plots of the separatrix topology combined with the contour plots of the connection length of the field lines with (upper) and without (lower) $n = 2$ EFCC perturbations with $I_{EFCC} = 32kAt$.

The crossing points of the field lines with the poloidal cross-section at a fixed toroidal angle Φ generate the Poincaré plot. Figure 4 (upper and lower) shows the modification of the magnetic topology when an $n = 2$ EFCC field was applied to a 2D poloidal divertor equilibrium. Here, the combined Poincaré plots of the stochastic magnetic field structures and the connection length of the perturbed field lines are calculated by the GOURDON field line tracing code [16] for an $n = 2$ EFCC configuration on JET. The calculation is based on an equilibrium reconstruction used for the calculation of the spectrum in figure 2 with the perturbation field superposed according to the vacuum approach [17]. Screening effects due to plasma rotation have been neglected. However, these initial results clearly exhibit the stochastic nature of the field line behaviour in the region around the X-point where the plasma rotation is low. The lobes of the manifolds step out, seen as a splitting of the strike point. The connection length of the perturbed field lines slightly inside the separatix is a few $100m$, which is less than ~ 20 toroidal turns.

The plasma edge of magnetic confinement devices is of great interest in RMP physics. In that region, the effective perturbation (the perturbation field normalized to the toroidal field), is aimed to be highest in order to achieve a strong stochastization. Within the stochastic region, the radial transport is enhanced, which changes the plasma parameters [19, 20, 21, 22] and may explain experimental observations like the heat redistribution [23], modification of the edge electric field [24, 25] , and the control of edge instabilities [15, 26, 27].

III. 3D BOUNDARY PLASMA PHYSICS

Within the last decade, it has become clear that the magnetic topology of a plasma in a tokamak cannot be fully described by the simple vacuum approach. In particular, during plasma operation in H-mode, additional currents exist in the plasma or are created as a response of the plasma to the applied external RMP fields. Many studies [28, 29, 30, 31, 32] have shown that this plasma response needs to be considered in order to understand the ongoing processes in a tokamak plasma in the presence of RMPs. The two main effects discussed are RMP field screening and the 3D equilibrium effect in low- or moderate-beta plasmas. Resonant field amplification has to be considered in high-beta plasmas, in which the external kink mode naturally becomes unstable. In addition, particle drifts in H-mode operation appear to have a strong influence [33]. Different ideas for improving the vacuum approach are discussed [33, 34, 35] and new methods based on kinetic [36] and fluid modelling used [37, 38, 39]. All these improved modelling approaches show an impact on the magnetic topology in the edge and core regions leading to modified plasma transport.

A. Plasma rotation screening effect on the RMPs

Depending on the plasma parameters and RMP spectrum, the actual RMP field could be very different in rotating plasmas, where the generation of current perturbations on rational surfaces could prevent reconnection and island formation, leading to the effective screening of RMPs [36, 40]. The equilibrium radial electric field produces $\vec{E} \times \vec{B}$ rotation which, together with the diamagnetic electron rotation, is particularly important for RMP screening in the pedestal region [38, 41].

Generally, the screening effect increases for lower resistivity, stronger rotation and smaller RMP amplitude. For an H-mode plasma with a steep pressure gradient at the edge pedestal, RMP penetration typically only occurs in the narrow region near

the separatrix due to the higher resistivity. However, at certain plasma parameters and/or because of the non-linear evolution of the radial electric field due to RMPs, $\vec{E} \times \vec{B}$ perpendicular rotation can be compensated by the electron diamagnetic rotation, i.e. $(V_{\theta,\vec{E}\times\vec{B}} + V^*_{\theta,e} \sim 0)$. In this case, the RMP harmonic (n, m) penetrates locally and forms islands on the corresponding resonant surface $q = m/n$ [42].

B. 3D equilibrium with a stochastic boundary

Tokamaks are often considered to be two-dimensional and consequently, their equilibrium is treated by solving the Grad-Shafranov equation. In real devices, the toroidal field ripple, error fields due to coil misalignments and the deliberate application of RMPs lead to a three-dimensional problem. The addition of RMPs to an axisymmetric equilibrium perturbs the force balance

$$\nabla p \neq \vec{J} \times (\vec{B} + \vec{B}_{pert,vac}). \quad (4)$$

Here, p, $\vec{J}$ and $\vec{B}$ are the plasma pressure, current density and magnetic field in an axisymmetric equilibrium, and $\vec{B}_{pert,vac}$ is the 3D vacuum perturbation field. To study the effect of the deviations from axisymmetry on the equilibrium the application of complex numerical tools is necessary. To re-establish the force balance, a 3D equilibrium including an equilibrium response to the 3D perturbation fields is needed.

$$\nabla p + \nabla p_{res} = (\vec{J} + \vec{J}_{res}) \times (\vec{B} + \vec{B}_{pert,vac} + \vec{B}_{res}). \quad (5)$$

Here, p_{res}, $\vec{J}_{res}$ and $\vec{B}_{res}$ are the 3D plasma responses of pressure, current density and magnetic field to the applied perturbation fields.

Nowadays, a number of numerical codes for the calculation of 3D MHD equilibria are available (VMEC, PIES, HINT2, IPEC). Some assume nested flux surfaces (VMEC, IPEC), while others allow for magnetic islands (PIES, HINT2). On TEXTOR, the HINT2 code [43] is used to compute numerical 3D equilibria. The converged 3D equilibria are compared with the simple vacuum superposition assumption for the case with a DED current of $7.5kA/coil$. While the major structures are conserved in the HINT2 calculation, an additional ergodisation around the X-points of the major islands (e.g. the 3/2 island) appears. Furthermore, secondary structures appear in the islands, a feature already observed experimentally for 2/1 islands with the DED in 3/1 configuration [44]. This effect is caused by the modified Pfirsch-Schlüter current density distribution driven by the pressure gradient around the island. In figure 5 (a) and (b), connection length plots for an enlarged edge area are shown and indicate an increased island size in the HINT2 case. Furthermore, a statistical analysis shows an increase in short ($\leq 1000m$) and very long ($\approx 16000m$) field lines (see figure 5 (c)) in the HINT2 case. This indicates a shaper transition from the confined core to the vacuum region. It should be noted

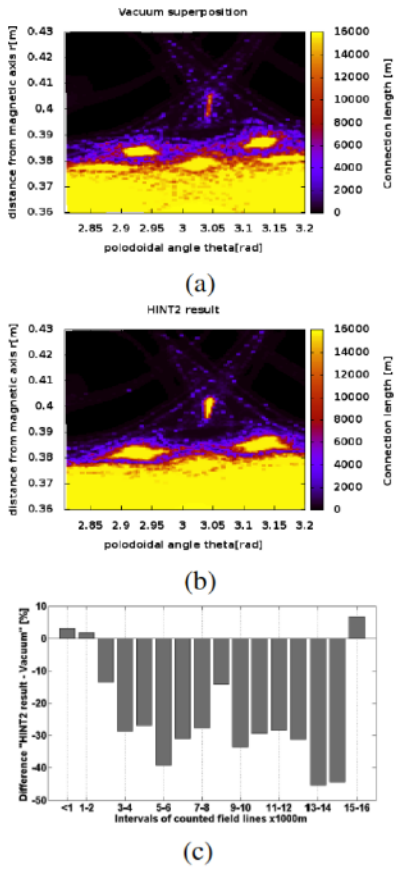

Figure 5: Connection length plots: (a) vacuum, (b) HINT2. (c) Difference in the number of field lines in specified length intervals: HINT2 result minus vacuum superposition in percent.

that the screening of the RMPs due to plasma rotation is not taken into account in the present HINT2 calculation.

C. Plasma transport in the stochastic boundary

A strong effect on the electron and thus heat transport is expected in a deep stochastic boundary layer ($\sigma_{ch} \gg 1$). The field line diffusion coefficient D_{FL}, and the electron heat diffusion coefficient can be described as :

$$\chi_e = D_{FL}\nu_{th}, D_{FL} = \sum_{m,n} \pi q R_0 |\frac{\delta B_{m,n}}{B_0}|^2. \quad (6)$$

Here, ν_{th} is the electron thermal velocity, $\delta B_{m,n}$ is the resonant component of the magnetic perturbation field. The electron heat transport in a stochastic boundary layer can be of the order of $10 - 100m^2s^{-1}$ over the perturbed edge and largely exceeds the usual anomalous transport $\sim 1m^2s^{-1}$ at the plasma edge.

Spin-up of the edge plasma rotation in the co-current direction and a change of the plasma edge electric field to a more positive value in the stochastic boundary layer have been observed in experiment [45]. This is due to the much larger electron mobility compared to the ion mobility implying an electron-retarding electric field in the plasma edge, which was previously dominated by ion losses due to their larger Larmor radius.

The effect of an additional radial diffusion on particle transport is difficult to analyse due to the coupling of the complicated transport regime to that of the physics of particle sources, namely neutral penetration. On JET, in a low- or a moderate-collisionality regime (electron collisionality at the pedestal, $\nu^*_{ped,e} \leq 1$), the electron density at the pedestal top decreased by $\sim 20\%$, the so-called density pump-out [46], during the application of an $n = 1$ field, while the pedestal electron temperature increased, keeping the pedestal pressure almost constant. However, the pedestal pressure gradient obtained from the derivative of the fitted curve shows that the maximum pressure gradient in the profile is decreased by 20% during the application of the $n = 1$ field, and the edge pressure barrier is 20% wider [47]. This is an effect mostly ascribable to the strong decrease in the n_e pedestal height with an almost unvaried width. In a high-collisionality regime ($\nu^*_{ped,e} > 1$), the effect of RMPs on the pedestal particle and heat transport is not clearly observed. [51].

Compensation of the density pump-out has been also investigated on JET using either gas fuelling or pellet injection in low-triangularity H-mode plasmas [17, 49, 50]. Although the ELM frequency stays high with $n = 1$ fields, no recovery of stored energy is observed. An optimized fuelling rate for compensating the density pump-out effect has been identified, and it depends on the plasma configuration.

D. Effects of a stochastic boundary layer on plasma-wall interaction

In the edge transport model, the transport of power in the stochastic layer has been treated as a diffusive process [55], which gives a significantly enlarged effective cross-field transport for the electron energy. As a result, a widening of the contact zone between plasma and wall has been predicted[56]. Experimental results from different devices [23, 57] have proved that the heat and particle deposition patterns are strongly structured.

The resulting heat deposition pattern reflects the complicated structure of the perturbed volume. It has been shown in [52] that the connection length and the radial penetration of the magnetic field lines defines the amount of power deposited on the target structures. The maximum of the heat flux density corresponds to the field lines with long connection length; however, those with shallow penetration seem to be strongly affected by the collisionality, in contrast to the field lines with deep penetration, which connect the outermost existing island chain to the divertor surface. For a proper analysis of such a complicated topology, inevitably one needs 3D transport codes, which could describe such a variety of magnetic field lines.

As an example, splitting of the outer strike point (SP), appearing as multiple peaks in the ELM heat flux profile along the outer divertor plate, has been measured by a fast IR camera during the application of $n = 2$ fields on JET with the ITER-like wall (ILW) as shown in figure 6. These multiple peaks in the heat flux profile are observed only during a mitigated ELM crash when a certain I_{EFCC} threshold is reached. The preliminary results indicate that this I_{EFCC} threshold for the appearance of splitting of the outer SP during the ELM crash is at a similar level to that occurring for the saturation effect of the plasma response. Similar findings of strike point splitting have been reported on DIII-D in the presence of $n = 3$ RMP fields [53].

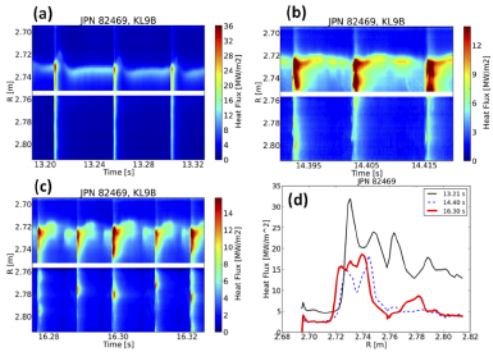

Figure 6: Extended time traces of the heat flux distribution on the outer divertor plate in the phases (upper left) without $n = 2$ field, (upper right) with $I_{EFCC} = 44$ kA and (lower left) with $I_{EFCC} = 88$ kA. (Lower right) ELM peak heat flux profiles along the outer divertor. From reference [51]

.

IV. ELM CONTROL USING RMP

Active control of ELMs by RMP fields offers an attractive method for next-generation tokamaks, e.g. ITER. The results obtained from the DIII-D, JET, MAST, KSTAR, AUG and NSTX tokamaks have shown that magnetic field perturbations can either completely suppress ELMs [15], trigger small ELMs during ELM-free periods, or affect the frequency and size of the type-I ELMs in a controllable way, preserving good global energy confinement [14].

A. Type-I ELM suppression with RMPs

The first successful demonstration of the ELM suppression technique was reported from DIII-D [15], where the in-vessel coils (I-coils) were employed. The I-coils consist of 12 single-turn loops, six above and six below the midplane (up-down symmetric) mounted on the low-field side of the vessel. For the ELM suppression experiments, the upper and lower loops are operated with either the same current polarities (even parity) or opposite current polarities (odd parity), and induce a static perturbation field with a toroidal mode number $n = 3$.

On DIII-D, the experimental results show that the effectiveness of ELM suppression with $n = 3$ fields depends on q_{95}. In low collisionality ($\nu^*_{ped,e} \leq 0.2$) H-mode plasmas, ELM suppression without small intermittent events is obtained in a narrow q_{95} window ranging from 3.5 to 3.9 with an even parity $n = 3$ field and ~ 7.2 with an odd parity $n = 3$ field. Outside this q_{95} range, type-I ELMs are mitigated (ELM frequency increased and ELM size decreased) by the applied $n = 3$ fields. These results indicate a resonant condition on the amplitude of RMPs for ELM suppression.

B. Type-I ELM mitigation with RMPs

Active control of type-I ELMs by the application of static $n = 1$ or 2 perturbation fields has been developed for more ITER-relevant configurations and parameters in a wide operational space of plasma triangularity (δ_U up to 0.45), q_{95} $(4.8 - 3.0)$ and beta (β_N up to 3.0) on JET [14, 48, 49, 17]. The first results of ELM mitigation with $n = 2$ fields on JET demonstrate that the frequency of ELMs can be increased by a factor of $\sim 4-5$, limited by the available EFCC coil current. A wide operational window of q_{95} has also been obtained for ELM mitigation with $n = 2$ fields. During the application of the $n = 1, 2$ fields, a reduction in the ELM size (ΔW_{ELM}) and ELM peak heat flux on the divertor target by roughly the same factor as the increase in the ELM frequency has been observed. The reduction in heat flux is mainly due to the drop of particle flux rather than a change of the electron temperature. A modest drop (a few per cent) in the total stored energy has been observed during the ELM control phase with the EFCCs. However, when normalized to the $IPB98(y, 2)$ scaling, the confinement time shows almost no reduction.

Recently, mitigation of type-I ELMs was observed with an $n = 2$ field on JET with the ITER-like wall (ILW) [51]. A strong mitigation of type-I ELMs was observed when an $n = 2$ field was applied in high-collisionality ($\nu^*_{ped,e} = 2.0$) H-mode plasmas. No density pump-out effect was observed in the high-collisionality case, but was observed in the low-collisionality case. In the moderate-collisionality type-I ELMy H-mode plasmas with the ILW wall, a saturation effect of ELM mitigation and clear pre-ELM structures were observed on the outer divertor plate during the application of $n = 2$ fields, depending on q_{95}[51, 54].

V. SUMMARY AND OPEN QUESTIONS

Regarding on the control of plasma transport in the boundary zones, two conflicting issues have to be balanced. On one hand, to achieve a homogenization of the power deposition on target plates and reduce the peak heat flux on the divertor or the limiter, a high cross field transport level is required in the SOL. On the other hand, to keep a high fusion gain, good confinement with the edge plasma transport barrier (H-mode), is required. One attractive idea for broadening the SOL and distributing the particle and heat fluxes more evenly and over a larger surface is to soften the edge of the magnetic cage by the formation of a stochastic boundary with the application of external magnetic perturbations.

In tokamaks, non-axisymmetric magnetic perturbations, which change the magnetic topology, have been applied on the majority of contemporary large-scale tokamaks to control plasma edge stability and transport. Recent research has highlighted the significance of the role that stochasticity and 3D magnetic topology also play in this fundamentally 2D concept. Their influence can be seen in transport and energy confinement, in the control of various MHD instabilities, most notably ELMs, which expel considerable amounts of energy from the plasma and pose a risk of damaging plasma-facing components in ITER and other next-generation fusion devices.

RMP ELM suppression/control has shown very promising results up to now, although the physics mechanism is not well understood as yet. Future joint experiments from different devices (DIII-D, JET, MAST, NSTX, AUG, TCV, KSTAR and EAST) will help us to understand ELM suppression physics and provide support for ITER.

To date, many attempts to explain ELM suppression have focused on the idea that the edge thermal and particle losses are enhanced due to the formation of an outer 'ergodic' zone with RMP fields. This 'ergodic' boundary would reduce the edge pressure gradients, and thus stabilize the peeling-ballooning modes thought to underlie ELM formation [15], [37]. This mechanism is mainly supported by two experimental results from DIII-D: *i*) splitting of the inner strike-point observed during the RMP ELM suppression phase; and *ii*) spin-up of the edge plasma rotation in the co-current direction and a change of the plasma edge electric field to a more positive value due to larger losses of electrons than ions with an ergodic boundary. However, either bulk plasma or diamagnetic rotation can screen the RMP fields from the resonant magnetic flux surfaces. Many calculations of the Chirikov parameter or overlapping of resonant magnetic islands employ a vacuum assumption, which

neglects the plasma response (rotational screening effect and equilibrium effect).

Although the mechanism of ELM control with RMPs is not yet fully understood, it has been examined in a wide operational window in many different devices. Further optimisation of the magnetic perturbation with less reduction of the plasma performance, and an understanding of the underlying physics are essential for future investigations.

In addition, the existence of these stochastic and 3D magnetic topology effects brings tokamak and stellarator physics closer together, and a holistic approach to studying them provides the most promising path to making good progress. Understanding these effects is essential for the success of future fusion devices, and they represent a hot topic in current fusion research. Furthermore, reversed field pinches offer access to these topics with unique features such as the bifurcation into self-generated 3D equilibria and multi-mode unstable plasma conditions with a high degree of magnetic field stochasticity.

REFERENCES

1. "ITER Physics Basis", *Nucl. Fusion* **39** 2137 (1999)
2. F. Wagner et al., "Regime of Improved Confinement and High Beta in Neutral-Beam-Heated Divertor Discharges of the ASDEX Tokamak", *Phys. Rev. Lett.*, **49**, 1408 (1982).
3. T. Eich, et al., "Inter-ELM Power Decay Length for JET and ASDEX Upgrade: Measurement and Comparison with Heuristic Drift-Based Model", *Phys. Rev. Lett.*, **107**, 215001 (2011).
4. Loarte A, et al., "ELM energy and particle losses and their extrapolation to burning plasma experiments", *J. Nucl. Mater.*, **313-316** 962 (2003)
5. A. Einstein, "Über die von der molekularkinetischen Theorie der Wärme geforderte Bewegung von in ruhenden Flüssigkeiten suspendierten Teilchen", *Ann. Phys.*, **17** 549-560 (1905).
6. J. Klafter and M. Sokolov, "Anomalous diffusion spreads its wings", *Physics World*, **18** 29-32 (2005).
7. R. Kubo, "Statistical-mechanical theory of irreversible processes: I. General theory and simple applications to magnetic and conduction problems", *J. Phys. Soc. Japan*, **12** 570 (1957).
8. B. V. Chirikov, "A universal instability of many-dimensional oscillator systems", *Phys. Rep.* **52** 263?379 (1979).
9. G. M. Zaslavsky, "Chaos, fractional kinetics, and anomalous transport", *Phys. Rep.* **371** 461?580 (2002).
10. G. M. Zaslavsky, "Hamiltonian Chaos and Fractional Dynamics", *Oxford: Oxford University Press* (2005)
11. S. Chandrasekhar, "Stochastic problems in physics and astronomy", *Rev. Mod. Phys.* **15** 1?89 (1943)
12. R. Balescu, "Aspects of Anomalous Transport in Plasmas" *Bristol: Institute of Physics Publishing* (2005)
13. Y. Liang, "Overview of edge-localized mode control in tokamak plasmas", *Fusion Science and Technology* **59**, 586 (2011).
14. Y. Liang, et al., "Active control of type-I edge-localized modes with n=1 perturbation fields in the JET tokamak", *Phys. Rev. Lett.*, **98** 265004 (2007)
15. T. E. Evans, et al., "Edge stability and transport control with resonant magnetic perturbations in collisionless tokamak plasmas", *Nature Phys.*, **2** 419 (2006)
16. C. Gourdon, "Programme optimise de calculs numeriques dans les configurations magnetiques toroidales", *CEN Fontenay aux Roses* (1970)
17. Y. Liang, et al., "Active control of type-I edge localized modes with n = 1 and n = 2 fields on JET", *Nuclear Fusion* **50**, 025013 (2010).
18. Y. Liang, et al., "Magnetic Topology Changes Induced by Lower Hybrid Waves and their Profound Effect on Edge-Localized Modes in the EAST Tokamak", *Phys. Rev. Lett.*, **110** 235002 (2013)
19. T. Stix. "Plasma transport across a braided magnetic field", *Nuclear Fusion*, **18**, 353?358 (1978).
20. H. Wobig and R. H. Fowler, "The effect of magnetic surface destruction on test particle diffusion in the Wendelstein VII-A stellarator", *Plasma Physics and Controlled Fusion* **30**, 721 (1988).
21. T. Eich, D. Reiser and K. Finken, "Two dimensional modelling approach to transport properties of the TEXTOR-DED laminar zone", *Nuclear Fusion* **40**, 1757 (2000).
22. A. Wingen, S. Abdullaev, K. Finken, M. Jakubowski and K. Spatschek, "Influence of stochastic magnetic fields on relativistic electrons", *Nuclear Fusion* **46**, 941 (2006).
23. M. W. Jakubowski, S. Abdullaev, K. Finken and the TEXTOR Team, "Modelling of the magnetic field structures and first measurements of heat fluxes for TEXTOR-DED operation", *Nuclear Fusion* **44**, S1 (2004).

24. S. Jachmich, P. Peleman, M. Van Schoor, Y. Xu, M. Jakubowski, M. Lehnen, B. Schweer and R. Weynants, "First Mach probe measurements of rotation, electric field and particle transport in the DED-ergodized edge plasma of TEXTOR", In: *Proceeding of the 33rd EPS Conference on Plasma Physics*, **O3.014** (2006)

25. A. Wingen and K. Spatschek, "Influence of different DED base mode configurations on the radial electric field at the plasma edge of TEXTOR", *Nuclear Fusion* **50**, 034009 (2010).

26. O. Schmitz et al., "Aspects of three dimensional transport for ELM control experiments in ITER-similar shape plasmas at low collisionality in DIII-D", *Plasma Physics and Controlled Fusion* **50**, 124029 (2008).

27. Y. Liang, C. G. Gimblett, P. K. Browning, P. Devoy, H. R. Koslowski, S. Jachmich, Y. Sun and C. Wiegmann, "Multiresonance Effect in Type-I Edge-Localized Mode Control With Low n Fields on JET", *Physical Review Letters* **105**, 065001 (2010).

28. T. E. Evans, I. Joseph, R. Moyer, M. Fenstermacher, C. Lasnier and L. Yan. "Experimental and numerical studies of separatrix splitting and magnetic footprints in DIII-D", *Journal of Nuclear Materials* **363-365**, 570-574 (2007).

29. E. Nardon et al. "Strike-point splitting induced by external magnetic perturbations: Observations on JET and MAST and associated modelling", *Journal of Nuclear Materials* **415**, S914-S917 (2011).

30. A. Kirk et al. "Magnetic perturbation experiments on MAST L- and H-mode plasmas using internal coils", *Plasma Physics and Controlled Fusion* **53**, 065011 (2011).

31. Y. Yang, Y. Liang, Y. Sun, T. Zhang, J. Pearson, Y. Xu and TEXTOR Team. "Experimental observations of plasma edge magnetic field response to resonant magnetic perturbation on the TEXTOR Tokamak." *Nuclear Fusion* **52**, 074014 (2012).

32. P. Denner, Y. Liang, Y. Yang, M. Rack, L. Zeng, J. Pearson, Y. Xu and the TEXTOR team. "Local measurements of screening currents driven by applied RMPs on TEXTOR". *Nuclear Fusion* **54** (2014).

33. A. Wingen, O. Schmitz, T. E. Evans and K. H. Spatschek. "Heat flux modeling using ion drift effects in DIII-D H-mode plasmas with resonant magnetic perturbations", *Physics of Plasmas*, **21**, 012509 (2014).

34. P. Cahyna and E. Nardon. "Model for screening of resonant magnetic perturbations by plasma in a realistic tokamak geometry and its impact on divertor strike points", *Journal of Nuclear Materials* **415**, S927 ?S931 (2011).

35. H. Frerichs, D. Reiter, O. Schmitz, P. Cahyna, T. E. Evans, Y. Feng and E. Nardon. "Impact of screening of resonant magnetic perturbations in three dimensional edge plasma transport simulations for DIII-D", *Physics of Plasmas* **19**, 052507 (2012).

36. M. F. Heyn, I. B. Ivanov, S. V. Kasilov, W. Kernbichler, I. Joseph, R. A. Moyer and A. M. Runov. "Kinetic estimate of the shielding of resonant magnetic field perturbations by the plasma in DIII-D", *Nuclear Fusion*, **48**, 024005 (2008).

37. M. Bécoulet et al. "Physics of penetration of resonant magnetic perturbations used for Type I edge localized modes suppression in tokamaks.", *Nuclear Fusion* **49**, 085011 (2009).

38. E. Nardon, P. Tamain, M. Bcoulet, G. Huysmans and F. Waelbroeck. "Quasi-linear MHD modelling of H-mode plasma response to resonant magnetic perturbations", *Nuclear Fusion* **50**, 034002 (2010).

39. A. Wingen, N. M. Ferraro, M. W. Shafer, E. A. Unterberg, T. E. Evens, D. L. Hillis and P. B. Snyder. "Impact of plasma response on plasma displacements in DIII-D during application of external 3D perturbations", *Nuclear Fusion* **54** (2014).

40. R. Fitzpatrick, "Bifurcated states of a rotating tokamak plasma in the presence of a static error-field", *Phys. Plasmas* **5** 3325 (1998)

41. D. Reiser D. and D. Chandra, "Plasma currents induced by resonant magnetic field perturbations in tokamaks", *Phys. Plasmas* **16** 042317 (2009)

42. M. Bécoulet, et al., "Screening of resonant magnetic perturbations by flows in tokamaks", *Nuclear Fusion*, **52** 054003 (2012)

43. Y. Suzuki, et al., "Development and application of HINT2 to helical system plasmas", *Nuclear Fusion*, **46** L19-L24 (2006)

44. Y. Liang, et al., "Observations of secondary structures after collapse events occurring at the q = 2 magnetic surface in the TEXTOR tokamak", *Nuclear Fusion*, **47** L21-L25 (2007)

45. K. H. Finken, et al., "Toroidal plasma rotation induced by the Dynamic Ergodic Divertor in the TEXTOR tokamak",*Phys. Rev. Lett.* **94** 015003 (2005)

46. J. C. Vallet et al., "Stabilization of tokamak Ohmic discharges at the density limit by means of the ergodic divertor", *Phys. Rev. Lett.* **67** 2662 (1991)

47. A. Alfier et al., "Edge T-e and n(e) profiles during type-I ELM mitigation experiments with perturbation fields on JET" *Nucl. Fusion* **48** 115006 (2008)

48. Y. Liang, et al., "Active control of type-I edge localized modes on JET", *Plasma Phys. Control. Fusion* **49** B581 (2007)

49. Y. Liang, et al., "Active control of edge localized modes with a low n perturbation fields in the JET tokamak", *J. Nucl. Mater.* **390-91** 733-739 (2009)

50. Y. Liang, et al., "Overview of ELM Control by Low n Magnetic Perturbations on JET", *Plasma and Fusion Research*, **5**, S2018 (2010)

51. Y. Liang, et al., "Mitigation of type-I ELMs with n=2 fields on JET with ITER-like wall", *Nucl. Fusion* **48** 115006 (2013)

52. M. W. Jakubowski, et al., "Observation of the heteroclinic tangles in the heat flux pattern of the ergodic divertor at TEXTOR", *J. Nucl. Mater.* **363** 371-376 (2007)

53. M. W. Jakubowski et al., "Overview of the results on divertor heat loads in RMP controlled H-mode plasmas on DIII-D", *Nucl. Fusion* **49**, 095013 (2009).

54. M. Rack, et al., "Findings of pre-ELM structures through the observation of divertor heat load patterns at JET with applied n=2 perturbation fields", *Nucl. Fusion* **54**, 072004 (2014).

55. A. B. Rechester and M.N. Rosenbluth, "Electron Heat Transport in a Tokamak with Destroyed Magnetic Surfaces", *Phys. Rev. Lett.* **40** 38 (1978)

56. A. V. Nedospasov and M.Z. Tokar, "Conception of divertorless tokamak reactor with turbulent plasma blanket", *J. Nucl. Mater.* **93-94** 248 (1980)

57. A. Grosman, P. Ghendrih, B. Meslin and D. Guilhem, "Power and particle flux to the neutraliser plates of the Tore Supra ergodic divertor modules", *J. Nucl. Mater.* **241-243** 532 (1997)

CLASSICAL AND NEOCLASSICAL TRANSPORT THEORY

J.H.E. Proll[1]

[1]*Eindhoven University of Technology, Eindhoven, The Netherlands*

ABSTRACT

These lecture notes are meant as an introduction to classical and neoclassical transport theory in tokamaks and stellarators. For cases when the mean-free path is shorter than typical macroscopic length scales of the plasma, classical theory is applicable. Neoclassical theory is valid when the mean-free path becomes longer than the macroscopic length scales and the geometry of the confining magnetic field has to be taken into account. Heuristic random walk arguments can be used to shed light on how the diffusivities scale with the collisionality. Additionally, kinetic theory provides insight into phenomena such as the Spitzer resistivity or the bootstrap current.

I. INTRODUCTION

How fast both heat and particles leave the plasma crucially determines how efficient our fusion reactor can be. We therefore need to understand the fluxes of heat, particles and charge, as given by Fourier's law

$$\mathbf{q} = -\chi n \nabla T \tag{1}$$

with heat flux $\mathbf{q}$, heat diffusivity χ and temperature T,
Fick's law for the particle flux $\mathbf{\Gamma}$

$$\mathbf{\Gamma} = -D\nabla n \tag{2}$$

with particle diffusivity D and density n, as well as Ohm's law for the current density $\mathbf{j}$

$$\mathbf{j} = \sigma \mathbf{E} \tag{3}$$

with conductivity σ and electric field $\mathbf{E}$. How these diffusive fluxes arise can be understood by studying classical and neoclassical theory. In both cases, collisions between particles are the drivers of transport. For classical transport, the mean free path between two collisions, λ is short compared with the macroscopic length L, $\lambda/L \ll 1$, so that the geometry of the magnetic field can be neglected. For neoclassical transport, the mean free path is considered arbitrary and can also be long compared with the macroscopic length. The geometry of the magnetic field thus needs to be taken into account.
A rigorous treatment of these transport processes requires the use of kinetic theory.

A. Fluid equations

When taking the moments of the kinetic equation

$$\frac{\partial f_a}{\partial t} + \mathbf{v}\cdot\nabla f_a + \frac{e_a}{m_a}(\mathbf{E}+\mathbf{v}\times\mathbf{B})\cdot\frac{\partial f_a}{\partial \mathbf{v}} = C_a\left(f_a\right), \tag{4}$$

we obtain the equations describing the conservation of density, momentum and energy,

$$\frac{\partial n_a}{\partial t} + \nabla\cdot\left(n_a\mathbf{V}_a\right) = 0 \tag{5}$$

$$\frac{\partial\left(m_a n_a \mathbf{V}_a\right)}{\partial t} + \nabla\cdot\mathbf{\Pi}_a = n_a e_a\left(\mathbf{E}_a + \mathbf{V}_a\times\mathbf{B}\right) + \mathbf{F}_a \tag{6}$$

$$\frac{\partial}{\partial t}\left(\frac{3n_aT_a}{2} + \frac{m_a n_a V_a^2}{2}\right) + \nabla\cdot\mathbf{Q}_a \tag{7}$$

$$= e_a n_a \mathbf{E}\cdot\mathbf{V}_a + \int \frac{m_a v^2}{2} C_a\left(f_a\right) d^3v, \tag{8}$$

where friction force

$$\mathbf{F}_a = \int m_a \mathbf{v} C_a\left(f_a\right) d^3v, \tag{9}$$

pressure tensor

$$\mathbf{\Pi}_a = \int m_a \mathbf{v}\mathbf{v} f_a d^3v \tag{10}$$

and energy flux

$$\mathbf{Q}_a = \int \frac{1}{2} m_a v^2 \mathbf{v} f_a d^3v \tag{11}$$

have to be calculated using kinetic theory. With these, the viscosity tensor

$$\boldsymbol{\pi}_a = \mathbf{\Pi}_a - p_a\mathbf{I} - m_a n_a \mathbf{V}_a\mathbf{V}_a \tag{12}$$

with the unit tensor $\mathbf{I}$ and the heat flux

$$\mathbf{q}_a = \mathbf{Q}_a - \frac{5p_a\mathbf{V}_a}{2} - \boldsymbol{\pi}_a\cdot\mathbf{V}_a - \frac{m_a n_a V_a^2 \mathbf{V}_a}{2} \tag{13}$$

can be defined. We will see later on how, using expansions in the small parameter $\delta = \rho_a/L \ll 1$ with the gyroradius ρ_a and the macroscopic length L amongst others will allow us to calculate the distribution function f_a and thus friction force, pressure tensor and energy flux.

B. Collisional processes

In the equations above we make use of the collision operator C_a. It describes all collisional processes of species a as a sum of contributions of collisions with species b (including the case $a = b$).

$$C_a = \sum_b C_{ab}\left(f_a, f_b\right). \tag{14}$$

Important properties of the collision operator are that it conserves particles,

$$\int C_{ab}\left(f_a, f_b\right) d^3v = 0, \tag{15}$$

and that

$$\int m_a \mathbf{v} C_{ab}\left(f_a, f_b\right) d^3v = -\int m_b \mathbf{v} C_{ba}\left(f_b, f_a\right) d^3v$$
$$\int \frac{m_a v^2}{2} C_{ab}\left(f_a, f_b\right) d^3v = -\int \frac{m_b v^2}{2} C_{ba}\left(f_b, f_a\right) d^3v. \tag{16}$$

On the particle level, collisions can be understood as small changes in direction of flight, when a particle's movement is altered due to the Coulomb interaction with another particle. As these changes in direction tend to be very small, the collision time is defined as the time it takes for a particle of type a to interact so often with a particle of type b that its change in direction is 90 degrees. The collision frequency (i.e. the inverse of the collision time) of electrons with velocity v_e with ions can thus be found as

$$\nu_{ei}(v_e) \sim \frac{n_i e^4}{4\pi m_e^2 \epsilon_0^2 v_e^3} \ln\Lambda \tag{17}$$

with the Coulomb logarithm

$$\ln\Lambda = \ln \frac{\text{Debye length}}{\text{minimum distance}} \sim 10 - 20.$$

For the other combinations of collisions, similar expressions can be found. Due to the disparate masses, the collisions between ions (with charge Ze) and electrons can be ordered as follows:

$$\tau_{ei} : \tau_{ee} : \tau_{ii} : \tau_{ie} \simeq \tag{18}$$
$$1 : 1 : \frac{1}{Z^3}\left(\frac{m_i}{m_e}\right)^{1/2}\left(\frac{T_i}{T_e}\right)^{3/2} : \frac{1}{2Z}\frac{m_i}{m_e} \tag{19}$$

and thus

$$\tau_{ei} \sim \tau_{ee} < \tau_{ii} < \tau_{ie}.$$

C. Random walk model

The collisions quantified above lead to a change in direction for the particles. The particle movement can thus be treated as a random walk. With a typical step length Δx and step time τ we obtain the diffusivity

$$D = \frac{(\Delta x)^2}{\tau}.$$

For both classical and neoclassical transport, we can estimate the appropriate step lengths for particles in a fusion plasma in various limits and thus obtain diffusivities that come remarkably close to those found by kinetic theory.

For the step times, we need to be aware that in order to obtain particle transport, the centre of mass of the two particles colliding must actually change. Like-particle collisions will therefore not contribute to the particle flux $\mathbf{\Gamma}$. For the heat flux, on the other hand, like-particle collisions *do* contribute, as the centre of energy moves.

II. CLASSICAL TRANSPORT

A. Random walk model of classical transport

Transport along B

Along the magnetic field, the random walk model is the same as if there were no magnetisation. The particles of species are assumed to stream along the magnetic field line with their thermal speed $v_T = (2T/m)^{1/2}$ until they are stopped in their path by a collision after a typical collision time $\tau = 1/\nu$. The step length is thus equal to the mean free path

$$\Delta x = \lambda_{mfp} = v_T \tau$$

and the parallel particle diffusivity of species a is obtained as

$$D_{\parallel,a} = \frac{\left(v_T \tau_{ab}\right)^2}{\tau_{ab}} = v_T^2 \tau_{ab}, \tag{20}$$

where only unlike-particle collisions with collision times τ_{ab} are contributing. If we utilise the ratios given by Eq. 19, we find that $D_{\parallel,i} \ll D_{\parallel,e}$, i.e. the electron transport is much stronger. For the heat diffusivities $\chi_{\parallel,a}$, like-particle collisions can also contribute. However, as $\tau_{ie} > \tau_{ii}$ and $\tau_{ee} \sim \tau_{ei}$, we find the heat diffusivities to be approximately the same as the particle diffusivities. This means that also the electron heat diffusivity is much larger than the ion heat diffusivity, $\chi_{\parallel,e} \gg \chi_{\parallel,i}$. We also note that for the transport along the magnetic field, collisions actually *hinder* the transport, very much in contrast to transport across the field, where collisions *enable* transport, as we shall see now.

Transport across B

For transport perpendicular to the magnetic field, the step size is given by the gyroradius ρ_a of species a. Collisions act to modify the velocity of the particles, therefore effectively moving the centre of the gyration and thus leading to transport. Again, for the particle diffusivity only unlike-particle collisions contribute, so that the particle diffusivity of species a is given by

$$D_{\perp,a} = \frac{\rho_a^2}{\tau_{ab}} \tag{21}$$

It is found that the perpendicular particle diffusivities of electrons and ions are equal:

$$D_{\perp,i} = \frac{\rho_i^2}{\tau_{ie}} = \frac{\rho_e^2}{\tau_{ei}} = D_{\perp,e} \equiv D_\perp. \tag{22}$$

This is also referred to as *ambipolarity*.
For the heat diffusivities, again also the like-particle collisions contribute. This time, as the collision times appear in the denominator, the smaller of the two collision times τ_{ab} and τ_{ba} will be chosen, i.e. for the ions τ_{ii} and for the electrons $\tau_{ee} \sim \tau_{ei}$. The heat diffusivities are thus

$$\chi_{\perp,i} = \frac{\rho_i^2}{\tau_{ii}} \approx \sqrt{\frac{m_i}{m_e}} D_\perp \tag{23}$$

$$\chi_{\perp,e} = \frac{\rho_e^2}{\tau_{ee}} \approx D_\perp \tag{24}$$

$$\tag{25}$$

Of the transport coefficients, the largest by far is thus the ion heat diffusivity $\chi_{\perp,i}$. In contrast to transport along the magnetic field, transport across the field is enabled by collisions.

B. Classical transport according to kinetic theory

In order to proceed with kinetic theory, we need to establish a number of assumptions. The first, as mentioned above, is that the gyroradius is small compared agains the macroscopic scale length:

$$\delta = \rho_a / L \ll 1$$

and that the time derivative is small,

$$\partial/\partial t \sim \delta^2 v_{Ta}/L, \tag{26}$$

which removes plasma waves from the equations. For classical transport in particular, we assume that the collisional mean free path λ is short, $\lambda/L \ll 1$. We further assume that the electric field is ordered large

$$E/B \sim v_{Ta}, \tag{27}$$

while for neoclassical transport, it is typically ordered small, $E/B \sim \delta v_{Ta}$.
Now, equipped with these assumptions, we can begin to investigate the classical transport theory. Because we are assuming the large-flow ordering, we transform the kinetic equation to a frame moving with that flow velocity $\mathbf{V}_a(\mathbf{r}, t)$. Introducing the definitions $\mathbf{v}'_a = \mathbf{v} - \mathbf{V}_a$, and the field in the moving frame $\mathbf{E}' = \mathbf{E} + \mathbf{V}_a \times \mathbf{B}$, as well as the convective derivative

$$\frac{d}{dt} = \frac{\partial}{\partial t} + \mathbf{V}_a \cdot \nabla$$

the kinetic equation becomes

$$\frac{df_a}{dt} + \mathbf{v}'_a \cdot \nabla f_a \tag{28}$$

$$+ \left[\frac{e_a}{m_a} (\mathbf{E}' + \mathbf{v}'_a \times \mathbf{B}) - \frac{d\mathbf{V}_a}{dt} \right] \cdot \frac{\partial f_a}{\partial \mathbf{v}'_a} \tag{29}$$

$$-v'_{aj} \frac{\partial V_{ak}}{\partial r_j} \frac{\partial f_a}{\partial v'_{ak}} = C_a(f_a) \tag{30}$$

With the assumptions of small gyroradius and short mean free path one finds that the collision term on the right hand side and the term including the magnetic field on the left hand side are the largest. If we now expand the distribution function, $f_a = f_{a0} + f_{a1} + \ldots$, we can solve the equation perturbatively. In lowest order, we will find that for the electrons (with charge $e_a = -e$) the distribution function is a Maxwellian at rest in the moving frame,

$$f_{e0} = n_e \left(\frac{m_e}{2\pi T_e} \right)^{3/2} e^{-x^2}, \tag{31}$$

where $x^2 = m_e v_e'^2 / 2T_e$. In next order, the kinetic equation becomes

$$\begin{aligned} &C_{ee}(f_{e1}) + C^0_{ei}(f_{e1}) + \frac{e}{m_e} \mathbf{v} \times \mathbf{B} \cdot \frac{\partial f_{e1}}{\partial \mathbf{v}} \\ &= \left[\frac{d \ln n_e}{dt} + \left(x^2 - \frac{3}{2} \right) \frac{d \ln T_e}{dt} + \mathbf{v} \cdot \nabla \ln n_e \right. \\ &+ \left(x^2 - \frac{3}{2} \right) \mathbf{v} \cdot \nabla \ln T_e + \frac{m_e \mathbf{v}}{T_e} \cdot \left(\frac{e}{m_e} \mathbf{E}' + \frac{d\mathbf{V}_e}{dt} \right) \\ &\left. + \frac{m_e v_j v_k}{T_e} \frac{\partial V_{ek}}{\partial r_j} + \nu_{ei} \frac{m_e \mathbf{v} \cdot \mathbf{u}}{T_e} \right] f_{e0} \end{aligned} \tag{32}$$

where we have now written $\mathbf{v}$ instead of $\mathbf{v}'_e$ and where $\mathbf{u} = \mathbf{V}_e - \mathbf{V}_i$ is the mean velocity of the electrons relative to the ions. We also wrote $C^0_{ei}(f_{e1}) = \nu_{ei} \mathcal{L}(f_{e1})$ for the scattering part of the electron-ion collision operator. To solve the equation, Chapman [1] and Eskog [2] discovered that the derivatives of the temperature and density on the right hand side can be eliminated when taking the moments of the equation. We will not go into further details here, but only present some results in the limit $\rho/\lambda = 1/\Omega_e \tau_{ei} \to 0$, which is mostly relevant in fusion plasmas. Here $\Omega_e = -eB/m_e$ is the electron gyrofrequency. Solving for the perturbed parts of ion and electron distribution function allows for the calculation of the heat fluxes of the electrons

$$\begin{aligned} \mathbf{q}_e &= \mathbf{q}^e_u + \mathbf{q}^e_T, \\ \mathbf{q}^e_u &= 0.71 n_e T_e \mathbf{u}_\parallel - \frac{3 n_e T_e}{2 \Omega_e \tau_e} \mathbf{b} \times \mathbf{u}_\perp \\ \mathbf{q}^e_T &= -\kappa^e_\parallel \nabla_\parallel T_e - \kappa^e_\wedge \mathbf{b} \times \nabla T_e - \kappa^e_\perp \nabla_\perp T_e \end{aligned}$$

where the heat conductivities are

$$\begin{aligned} \kappa^e_\parallel &= 3.16 \frac{n_e T_e \tau_e}{m_e} \\ \kappa^e_\wedge &= -\frac{5 n_e T_e}{2 m_e \Omega_e} \\ \kappa^e_\perp &= 4.66 \frac{n_e T_e}{m_e \Omega_e^2 \tau_e} \end{aligned}$$

and the ions, respectively:

$$\mathbf{q}_i = -\kappa^i_\parallel \nabla_\parallel T_i + \kappa^i_\wedge \mathbf{b} \times \nabla T_i - \kappa^i_\perp \nabla_\perp T_i$$

where

$$\kappa_{\parallel}^{i} = 3.9\frac{n_i T_i \tau_i}{m_i}$$
$$\kappa_{\wedge}^{i} = \frac{5 n_i T_i}{2 m_i \Omega_i}$$
$$\kappa_{\perp}^{i} = 2\frac{n_i T_i}{m_i \Omega_i^2 \tau_i}$$

with $\Omega_i = ZeB/m_i$ and

$$\tau_{ii} = \frac{12\pi^{3/2} m_i^{1/2} T_i^{3/2} \epsilon_0^2}{n_i Z^2 e^4 \ln\Lambda}$$

In both cases, the conductivities $\kappa_{\parallel}, \kappa_{\wedge}$ and $\kappa_{\perp}$ are separated by the factor $\Omega\tau$. Transport along the field is thus much stronger than across it, and is mostly carried by the electrons, as already found through the heuristic arguments. Similarly reproduced is that across the field, i.e. $\kappa_{\perp}$, the ion heat transport is largest. In addition to the heat fluxes, also the force acting on the species can be calculated. For the electrons, it is found that the force $\mathbf{F}_e$ acting on the electrons consists of a drag force and a thermal force

$$\mathbf{F}_e = \mathbf{F}_u + \mathbf{F}_T$$

with

$$\mathbf{F}_u = -\frac{m_e n_e}{\tau_e}\left(0.51\mathbf{u}_{\parallel} + \mathbf{u}_{\perp}\right)$$
$$\mathbf{F}_T = -0.71 n_e \nabla_{\parallel} T_e + \frac{3 n_e}{2\Omega_e \tau_e}\mathbf{b}\times\nabla T_e$$

and where $\mathbf{u} = \mathbf{V}_e - \mathbf{V}_i$ and $\mathbf{b} = \mathbf{B}/B$. From the drag force, we can also deduce the Spitzer conductivity

$$\sigma = 1.96\frac{n_e e^2 \tau_e}{m_e}$$

which determined the current

$$J_{\parallel} = -n_e e u_{\parallel} = \sigma E_{\parallel}$$

that arises in response to an applied parallel electric field [3]. We note that the Spitzer conductivity is, maybe unexpectedly so, independent of the density n_e, and also proportional to $T_e^{3/2}$, which implies the reduced efficiency of ohmic heating at high temperatures. While the classical transport is typically overpowered by neoclassical and turbulent transport, it does play an important role in the plasma edge, where the parallel electron heat conductivity governs transport to the divertor plates.

III. NEOCLASSICAL TRANSPORT

One important assumption of classical transport was that the mean-free path is short, which implies that particles don't actually travel the magnetic field long enough to experience any significant geometry effects. If we leave this regime and move towards longer mean-free path, geometry effects need to be considered, which leads us to *neoclassical* transport. While kinetic theory is necessary for a complete analysis of neoclassical transport, the heuristic random walk model again provides intuitive understanding of the most important phenomena and scalings. We will therefore only focus on those here. Readers interested in the full derivation are encouraged to consult [4].

A. Random walk model of neoclassical transport

As for classical transport, particle movement in toroidal confinement devices is still governed by the gyromotion around the field lines. However, on top of the helical movement, particle drifts due to the curvature and gradient of the magnetic field arise:

$$\mathbf{v}_d \simeq -\frac{v^2 + v_{\parallel}^2}{2\Omega R}\hat{\mathbf{z}}$$

The radial net drift that a particle experiences, and which will ultimately determine the average step length of importance for our random walk (particles also drift within the surface, but those drifts are of no consequence for radial transport), depends on the path a particle takes along the field. The calculation of that drift differs between *passing* and *trapped* particles, where the latter are reflected at a certain magnitude of the magnetic field according to their magnetic moment (and thus also their ratio of perpendicular and parallel velocity). As a reminder, the condition for a particle with parallel and total velocity $v_{\parallel}$ and v, respectively, to be trapped is

$$\frac{v_{\parallel}^2}{v^2} < 1 - \frac{B_{min}}{B_{max}}$$

where B_{min} and B_{max} are the minimum and maximum field strenghts on the flux surface, respectively.

Transport from passing particles

Let us first focus on the passing particles, whose parallel velocity is large enough so that they are not trapped in regions of low magnetic field and which thus largely follow the magnetic field lines. For a particle starting on the outboard midplane of a tokamak, the largest radial excursion is found after the particle has roughly travelled half around poloidally, until the inboard midplane. To determine the extent of that excursion Δr, we need to know the time it takes to travel there, Δt, with the known velocity $\mathbf{v}_d$. If we assume that the particle travels along the field line until it is stopped by a collision, we can again use the estimate of parallel transport as already used for classical transport, where we found an estimated parallel diffusivity

$$D_{\parallel} \sim \lambda^2/\tau \sim v_T^2/\nu$$

If we take the length along the field line for a half poloidal turn (so in the poloidal direction, the length

half around poloidally is $l_{pol} = \pi r$) to be

$$l = \frac{B}{B_{pol}} l_{pol} = \pi r \frac{B}{B_{pol}} = \pi R_0 q$$

with the safety factor

$$q = \frac{Br}{R_0 B_{pol}}$$

then the time for the particle with velocity v_T to travel this distance is of the order

$$\Delta t \sim \frac{(qR)^2}{D_\parallel} \sim \nu \left(\frac{qR}{v_T}\right)^2$$

In the same time, the particle can drift radially according to the drift given above. The drift is vertical, so a particle starting on the outboard midplane will either drift upwards or downwards depending on the direction of the parallel velocity, which can again be considered as a random walk in the radial direction. The typical step length of this random walk is then the radial distance that's covered in the time Δt:

$$\Delta r \sim v_d \Delta t \sim \frac{\rho v_T \Delta t}{R}$$

The diffusion coefficient for passing particles thus becomes

$$D^{NC}_{pass} \sim \frac{(\Delta r)^2}{\Delta t} \sim \nu_{ei} q^2 \rho_e^2 \sim q^2 D^{Cl}_\perp,$$

which is larger than the classical diffusion coefficient D^{Cl}_{perp} by a factor q^2 and where we have again assumed that only unlike particle collisions contribute to the particle transport. The neoclassical heat diffusivities are found using the same arguments but for like-particle collisions and are similarly larger than their classical counterparts by a factor of q^2:

$$\chi^{NC}_{e,pass} = \nu_{ee} q^2 \rho_e^2 \sim q^2 \chi^{Cl}_e \quad (33)$$
$$\chi^{NC}_{i,pass} = \nu_{ii} q^2 \rho_i^2 \sim q^2 \chi^{Cl}_i \quad (34)$$

Transport from trapped particles

Also trapped particles contribute to cross-field transport. The main modification compared with the passing particles is the typical step length, which can be found to be of the order of the banana width δr_b

$$\Delta r \sim \delta r_b \sim \frac{q\rho}{\sqrt{\epsilon}}$$

with $\epsilon = \frac{r}{R}$ being the inverse aspect ratio. In addition to the larger step size we also need to take into account, that typically only a small fraction—of the order of $f_t \sim \sqrt{\epsilon}$—are trapped and thus contribute to the trapped-particle transport. Finally, for a trapped particle to change its direction so that it is transported into a different banana orbit, the change in pitch angle required is decidedly below 90 degrees (for a moderately trapped particle it is around $\Delta\Theta \sim \sqrt{2\epsilon}$). As collision times are always defined to be accumulated until changes in pitch angle of 90 degrees are achieved, for the trapped particles an effective collision time is required

$$\tau_{eff} \sim \frac{r}{R} \tau_{90} = \epsilon \tau_{90}$$

which is a factor ϵ smaller than the typical collision time.

In total, we thus obtain for the particle diffusivity

$$D^{NC}_{tr} \sim f_t \frac{(\Delta r)^2}{\tau_{eff}} = \epsilon^{-3/2} \nu_{ei} q^2 \rho_e^2 \sim \epsilon^{-3/2} D^{NC}_{pass}$$

and the heat diffusivities

$$\chi^{NC}_{e,tr} = \epsilon^{-3/2} \nu_{ee} q^2 \rho_e^2 \sim \epsilon^{-3/2} \chi^{NC}_{e,pass} \quad (35)$$
$$\chi^{NC}_{i,tr} = \epsilon^{-3/2} \nu_{ii} q^2 \rho_i^2 \sim \epsilon^{-3/2} \chi^{NC}_{i,pass} \quad (36)$$

The trapped-particle contribution to transport is thus by a factor $\epsilon^{-3/2}$ larger than that of the passing particles, and one could assume that the transport by the passing particles thus only plays a minor role. This is indeed largely true when the so-called collisionality, i.e. the ratio between collision frequency and transit frequency $\omega_t = v_T/qR$, is small. In that case can the trapped particles complete their (banana) orbits and therefore contribute to transport. This regime of low collisionality is thus also called the Banana regime. Typically, the core of tokamaks is in this regime thanks to the high temperatures.

In the opposite limit of high collisionality with $\nu/(v_T/qR) \ll 1$, the so-called Pfirsch-Schlüter regime, the collisions interrupt the trapped-particle orbits and we need to consider the short-mean-free-path-approximation, where the calculation for the passing particles holds. So in both regimes the diffusivities are proportional to the collisionality, albeit with different proportionality constants. Typically, these two regimes transition directly into one another. if the inverse aspect ratio is small, $\epsilon \ll 1$, a third regime, the so-called plateau regime, emerges in between, for $\epsilon^{3/2} \ll \frac{\nu}{v_T/qR} \ll 1$, where the diffusivities remain roughly constant. Here, most circulating particle orbits are completed but trapped orbits are interrupted (see also Fig. 1 for a sketch of the different regimes of diffusivity). Note that also at fairly large aspect ratios of e.g. $R_0/r = 5$ the plateau almost vanishes.

B. The Bootstrap current

Another important result of neoclassical theory is the Bootstrap current, which is found as one part of the parallel current. When solving the drift kinetic equation for f_1 and calculating the parallel current with it, we obtain

$$J_\parallel = -\frac{f_t q n_e T_e}{\epsilon B} \left[1.66 \left(1 + \frac{T_i}{T_e}\right) \frac{d \ln n_e}{dr} + 0.47 \frac{d \ln T_e}{dr} - \frac{0.29}{T_e} \frac{dT_i}{dr}\right] + (1 - 1.31 f_t) \sigma E^{(A)}_\parallel$$

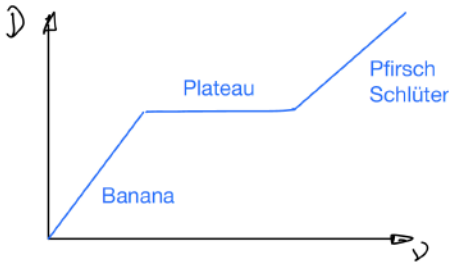

Figure 1: Sketch of how the neoclassical diffusion coefficient D depends on the collisionality ν, with the three different regimes indicated.

for a large-aspect-ratio tokamak with circular cross section. Here, $f_t \simeq 1.46\epsilon^{1/2}$ is the "effective" fraction of trapped particles, and while the second term denotes the effective reduction of parallel current by the fraction of trapped particles because they cannot contribute to it, the first term denotes the Bootstrap current that arises *because of* the trapped particles, and, as seen from the equation, due to a gradient in the density. It can be understood when considering the trajectory of the trapped particles from the birds-eye-view onto the tokamak. Then, just as with the view of the poloidal cut, the orbits are seen as bananas: If the centre of the banana orbit is found at r, then the part of the orbit with positive parallel velocity is found at roughly half a banana width $\delta r_b \sim q\rho/\epsilon^{1/2}$ away, thus at $r + 1/2\delta r_b$, and the return path with negative parallel velocity is found at $r-1/2\delta r_b$. At the same time, at $r+1/2\delta r_b$ we find the particles who have their banana centre at $r+\delta r_b$, but those are already on their return orbit and have negative parallel velocity. The net current at $r + 1/2\delta r_b$ is thus given by the difference in density between the two different banana centres:

$$J_{BS} \sim v_\parallel e_a \left(n(r) - n(r + \delta r_b)\right) \sim v_T e_a \frac{dn}{dr}\delta r_b \quad (37)$$

$$\sim -\frac{qT_a}{\epsilon^{1/2}B}\frac{dn_a}{dr} \quad (38)$$

A similar argument can be made for the passing particles, which also experience radial drifts and thus contribute to a toroidal current and which are in collisional equiilibrium with the trapped particles. The total Bootstrap current is found to scale as

$$J_{BS} \sim \frac{\epsilon^{1/2}p}{rB_p}$$

where $B_p = \epsilon B/q$ is the poloidal field. Note that especially at larger ϵ the Bootstrap current can become rather large, comparable to or even greater than the Ohmic current, and is thus highly important for economically running a tokamak.

IV. NEOCLASSICAL TRANSPORT IN STELLARATORS

So far the discussion focussed on tokamaks, with their axisymmetry and radially confined trapped particles. While the transport for high collsionality does not differ much between tokamaks and stellarators as the mean-free path is not long enough to really take any geometry effects into account, the transport at low collisionality is decidedly different.

A. The $1/\nu$ regime at low collisionality

Generally, the orbits of trapped particles (often trapped in local minima) in non-axisymmetric magnetic fields are *not* closed, and the trapped particles experience a net radial drift towards to outside of the plasma. Similar to the parallel transport, we therefore consider the transport of heat and particles as *hindered by* the collisions. A typical step length for these radially drifting particles is then

$$\Delta r \sim v_{d,r}\Delta t$$

where $v_{d,r}$ is the (bounce-averaged) radial component of the particle drift. Similar to the considerations before, the step time for trapped particles is shorter than the typical collision time because full 90 degrees collisions are not necessary, so that the step time becomes

$$\Delta t \sim \epsilon_h/\nu,$$

where $\epsilon_h \sim \delta B/B$ is the so-called *helical ripple*, which denotes the local variation of the magnetic field.
The particle diffusivity then becomes

$$D_{1/\nu} \sim \epsilon_h^{1/2}\frac{\Delta r^2}{\Delta t} \sim \frac{\epsilon_h^{3/2}v_d^2}{\nu},$$

which is proportional to $1/\nu$. This low-collisionality regime is therefore also referred to as the $1/\nu$ regime. Note that the diffusivity scales as

$$D_{1/\nu} \sim \frac{m^{1/2}T^{7/2}}{nB^2R^2}$$

which means that especially for reactor conditions with very high temperature the transport can become very large, which poses a severe problem for stellarators.
The $1/\nu$ transport can be reduced significantly if the bounce-averaged drift of the trapped particles is minimised. Fields where the bounce-averaged drift is exactly zero are called omnigeneous, and several routes to achieve this at least approximately exist, e.g. those of quasi-symmetry (realised in the Helically symmetric stellarator HSX in Madison, Wisconsin, USA),or those of quasi-isodynamicity (realised in Wendelstein 7-X in Greifswald, Germany). Often the zero net drift is only achieved on one flux surface and minimised on the others, but the total transport can still

be reduced significantly. A comparison of the diffusion coefficients computed for different stellarators is found in [6].
An important difference between tokamaks and stellarators is the so-calledf intrinsic ambipolarity: While the electron and ion particle fluxes are automatically equal in axisymmetric devices, this is not the case in stellarators. The particle flux for a species a is given by

$$\Gamma_a - = -n_a \left[D_{1a} \left(\frac{d \ln n_a}{dr} - \frac{e_a E_r}{T_a} \right) + D_{2a} \frac{d \ln T_a}{dr} \right]$$

where the diffusion coefficients (the Ds) are larger for the ions than for the electrons, so that the fluxes can be of different magnitude and ions and electrons are transported at different rates outside of the plasma. A radial electric field E_r builds up until both fluxes are equal. Depending on the sign of this field, we speak of an *electron root* or an *ion root*. The former is commonly found in plasmas where the electron temperature is significantly above the ion temperature, and is characterised by a rather strong field, which can in turn lead to a strong reduction of the transport, as we will see in the next section. If electron and ion temperature are very similar, the plasma will more frequently be in ion root, where the electric field is smaller.

B. The influence of the radial electric field

If the electric field is sufficiently strong, the $E \times B$ drift that arises and which is within the surface can detrap the helical particles. The frequency associated with this poloidal movement is

$$\omega_e \sim \frac{v_{E \times B}}{2\pi r} \sim E/rB,$$

and will dominate the distance the particle can travel radially (once the $E \times B$ drift has moved the particle out of the trapping well it becomes a passing particle with a vanishing net drift):

$$\Delta r \sim v_d / \omega_e$$

For the effective collision frequency, we again take into account that the scattering in and out of trapping regions is important, and we therefore use

$$\nu_{eff} \sim \frac{\nu}{\epsilon_h} \sim \frac{\nu}{f^2}$$

where f is again the fraction of trapped particles. The estimate for the diffusivity now becomes

$$D \sim f (\Delta r)^2 \nu_{eff} \sim \frac{\nu}{f} \frac{v_d^2}{\omega_e^2},$$

which diverges as $f \to 0$. However, the assumption was that the frequency responsible for stopping the particle from drifting and therefore the dominant one was that associated by the electric field. We can thus

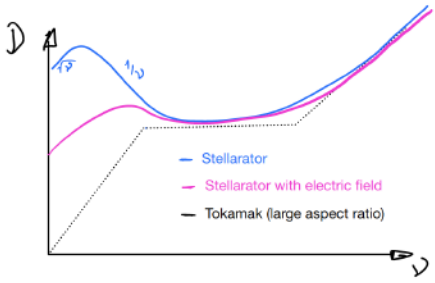

Figure 2: Sketch of how the neoclassical diffusion coefficient D depends on the collisionality ν in a typical stellarator. At low collisionality, both the typical $1/\nu$ regime and the $\sqrt{\nu}$ regime (the result of a radial electric field) are indicated. For higher collisionality, the transport in stellarators and tokamaks barely differs.

create an upper limit for the effective collision frequency

$$\nu_{eff} \leq \omega_e$$

and thus it follows that

$$f \geq \frac{\nu}{\omega_e} \to \nu_{eff}^{max} \sim \omega_e$$

and

$$D \sim \frac{\nu^{1/2} v_d^2}{\omega_e^{3/2}}.$$

In this regime, the transport thus scales with $\sqrt{\nu}$ and decreases with an increasing electric field due to $E^{-3/2}$ [7].

V. SUMMARY

Classical and neoclassical transport theory lead to several important findings: Classical transport, while usually overwhelmed by turbulent transport, is suited to describe transport in the edge. Neoclassical transport often is applicable to describe transport of impurities and, in unoptimised stellarators, also the transport of the bulk species. The neoclassical reduction of the conductivity are predicted, so is the Bootstrap current, without which economically running tokamaks would be unimaginable.

VI. FURTHER READING

The heuristic arguments presented here are described in more detail in Freidberg's excellent textbook [8], which is generally highly recommended for learning about fusion. For collisional transport in particular, the text book by Helander and Sigmar [4] provides thorough derivations, while still being paedagogical and understandable. For classical transport,

the review by Braginskii [9] must of course be mentioned.

REFERENCES

1. S. Chapman, *Phil. Trans. R. London Ser. A* **98**, 1 (1916).

2. D. Enskog, "Kinetische Theorie der Vorgänge in mässig verdünnten Gasen" *Almqvist & Wiksell* Uppsala, 1917

3. L. Spitzer and R. Härm, *Phys. Rev.* **89**, 977 (1953).

4. P. Helander and D.J. Sigmar, "Collisional transport in magnetized plasmas" *Cambridge University Press* (2002).

5. M.N. Rosenbluth, R.D. Hazeltine and F.L. Hinton, *Phys. Fluids* **15(1)**, 116 (1972).

6. C.D. Beidler, K. Allmeier, M.Yu. Isaev, S.V. Kasilov, W. Kernbichler, G.O. Leitold, H. Maaßberg, D.R. Mikkelsen, S. Murakami, M. Schmidt, S.A. Spong, V. Tribaldos and A. Wakasa, *Nucl. Fusion* **51**, 076001 (2011).

7. P. Helander, C.D. Beidler, T.M. Bird, M. Drevlak, Y. Feng, R. Hatzky, F. Jenko, R. Kleiber, J.H.E. Proll, Yu. Turkin and P. Xanthopoulos, *Plasma, Phys. Control. Fusion* **54**, 124009 (2012).

8. J.P. Freidberg, "Plasma Physics and Fusion Energy", *Cambridge University Press* (2007).

9. S.I. Braginskii in "Reviews of Plasma Physics" edited by M.A. Leontovich, *Consultants Bureau* Vol. 1, p. 205 (1965).

NEOCLASSICAL TEARING MODES

H.R.Wilson

York Plasma Institute, Department of Physics, University of York, Heslington, York, YO10 5DQ U.K.
howard.wilson@york.ac.uk

ABSTRACT

Tearing modes often limit the performance of tokamak plasmas, because the magnetic islands which they generate lead to a loss of confinement, or even a disruption. A particularly dangerous instability is the neoclassical tearing mode, which can grow to a large amplitude because of the amplification effect that the bootstrap current has on an initial 'seed' magnetic island. This paper will address the mechanisms which dominate the neoclassical tearing mode evolution, and thereby identify possible control techniques.

I. INTRODUCTION

The good confinement of the tokamak is achieved because to leading order the ions and electrons follow the magnetic field lines, which in turn lie on toroidally symmetric, nested magnetic flux surfaces. However, there are a number of plasma instabilities which can modify the magnetic geometry and so lead to a reduction in confinement and a loss of plasma stored energy. In this paper we shall concentrate on a particular type of instability, the tearing mode, and explore its consequences for tokamak performance. One consequence of the tearing mode instability is that the plasma adopts a new, non-symmetric equilibrium (or, if the instability is particularly violent, the plasma can be lost altogether in a disruption). This new equilibrium is characterised by a chain of magnetic islands, and field lines can migrate radially around these over a distance comparable to the island width. The result is that the radial particle and energy flux is enhanced in the regions where the magnetic islands form, and the overall confinement is degraded (eg the central plasma temperature is reduced). For this reason, understanding the causes of tearing modes is an important part of tokamak physics research, and this paper provides a brief review of the progress made in our understanding, and the gaps that remain.

We shall begin in Section II with a brief summary of the basic properties of tearing modes, and provide a simple derivation of the 'classical' (Rutherford) tearing mode evolution equation[1]. Then in Section III we shall address a number of other mechanisms which can contribute to the tearing mode evolution in toroidal plasmas to derive, heuristically, the so-called modified Rutherford equation for neoclassical tearing modes (NTMs). In Section IV we shall explore the experimental evidence for neoclassical tearing modes and make comparisons with the theory. Finally, in Section V, we shall consider some of the control methods which have been proposed, largely motivated by our theoretical understanding of these instabilities.

II. CLASSICAL TEARING MODE PHYSICS

Let us begin by introducing some of the terminology associated with tearing mode physics, broadly following Ref [2]. To simplify the geometry, let us take an annulus of toroidal plasma with major radius R (say between minor radii $r=r_1$ and $r=r_2$), and cut this open in the toroidal and poloidal directions to form the plasma slab shown in Fig 1. We have placed an island chain at the radial position $r=r_s$ and indicated the positions of the so-called X-points and O-points of the island. It is conventional to define the mode structure in terms of the dominant Fourier components of the island; the case shown in Fig 1 has poloidal mode number $m=2$ and toroidal mode number $n=1$. Note that the dashed line connecting the island O-points is approximately a line of symmetry in the large aspect ratio approximation of the tokamak. Thus the island magnetic geometry can be defined in terms of three coordinates: the radial variable, r, the poloidal angle, θ, and a new helical angle, ξ, which is directed along a line perpendicular to

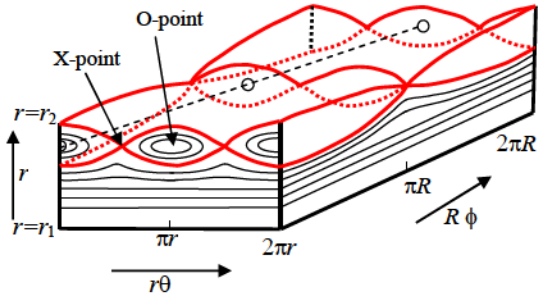

Fig. 1. A toroidal annulus of plasma showing flux surfaces forming magnetic islands. The annulus has been cut along the poloidal (θ) and toroidal (ϕ) directions and opened out.

that connecting the island O-points

$$\xi = \theta - \frac{n}{m}\phi \tag{1}$$

Again adopting a large aspect ratio approximation, we see that the component of magnetic field in the helical direction is given by

$$B_h = B_\theta\left(1 - \frac{n}{m}q(r)\right) \tag{2}$$

where B_θ is the poloidal component of the magnetic field and $q(r)$ is the safety factor. The role of the tearing mode instability is to provide the radial component of magnetic field required to generate a magnetic island. Denoting this by $\delta B = B_r \sin m\xi$, and noting that a field line will follow a trajectory given by

$$\frac{dr}{r_s d\xi} = \frac{\delta B}{B_h} \tag{3}$$

we see that the radial excursion of field lines is negligible unless B_h is small (we consider that the radial field generated by the tearing mode is typically much smaller than the equilibrium magnetic fields imposed in the tokamak by the machine operator). Thus the largest radial excursions are experienced at the radial position where $q=m/n$; that is, island chains form on rational surfaces. Taylor expanding q about the rational surface $r=r_s$, then we can use Eq (2) in Eq (3) to derive the following equation for the field lines:

$$\Omega = \frac{2x^2}{w^2} - \cos m\xi \tag{4}$$

where $x=r-r_s$, Ω is a flux surface label (a constant of the integration) and

$$w = 2\left(\frac{rqB_r}{mB_\theta dq/dr}\right)^{1/2} \tag{5}$$

is the island half-width. Note that $\Omega=1$ defines the island separatrix, $-1<\Omega<1$ defines flux surfaces inside the island and $\Omega>1$ defines flux surfaces outside the island.

Having described the geometry and introduced the essential terminology, we are now in a position to describe some of the basic theoretical principles behind tearing modes. The theory can be broadly categorised into linear and non-linear theory. We shall be concerned with larger magnetic islands, so that the non-linear theory is the appropriate one to adopt here. Above, we characterised the perturbation in terms of the radial magnetic field it produced; in fact we shall find it more convenient to instead use the flux function, ψ. Thus we define the perturbed flux

$$\psi = \tilde{\psi}\cos m\xi \qquad B_r = \frac{m\tilde{\psi}}{rR} \tag{6}$$

where $\tilde{\psi}$ is related to B_r and is assumed to vary only slowly with radius over the island width length scale. In terms of ψ, the total magnetic field is given by

$$\mathbf{B} = f(r)\nabla\phi + \nabla\phi\times\nabla(\Psi+\psi)\ , \tag{7}$$

where $f(r)=RB_\phi$ and $\Psi(r)$ is the poloidal magnetic flux. Let us restrict consideration to small magnetic islands whose width is much less than the tokamak minor radius. Then the current perturbation is small, and we are justified in assuming that ψ varies only slowly with r. For islands whose width is much less than their length, Ampere's law relates ψ to the current density perturbation parallel to the magnetic field, $J_\parallel$:

$$\frac{1}{R}\frac{d^2\psi}{dr^2} = \mu_0 J_\parallel\ , \tag{8}$$

Another condition on the validity of this expression is that the perturbed current is localised about the island region so that, although $d\psi/dr$ is small, it changes rapidly in a narrow region in the vicinity of the island so that its second derivative need not be small. Making use of this we integrate across the island region from $r=-l$ to $r=l$, where $r_s>>l>>w$ is assumed. In addition we define a parameter which characterises the jump in $d\psi/dr$ across the island, conventionally denoted by the symbol Δ':

$$\Delta' = \lim_{l\to\infty}\frac{1}{\psi}\left[\left.\frac{d\psi}{dr}\right|_{r=l} - \left.\frac{d\psi}{dr}\right|_{r=-l}\right] \tag{9}$$

As a result we arrive at the following basic equation for tearing mode evolution:

$$\Delta'\tilde{\psi} = 2\mu_0 R\int_{-\infty}^{\infty}dx\oint d\xi\, J_\parallel\cos m\xi \tag{10}$$

The next task is to determine the perturbed current. Note that it is only the current parallel to the magnetic field that contributes to the island evolution equation. The simplest model is that considered by Rutherford[1], in which the only contribution to $J_\parallel$ comes from the induced current associated with island growth. Thus, for an island which is evolving, so that ψ has a time-dependence, an electric field proportional to $d\psi/dt$ is generated parallel to the magnetic field (note that ψ is proportional to the component of the

perturbed vector potential in the magnetic field direction). This gives rise to a current via Ohm's law:

$$\eta J_{\parallel} = \frac{\partial \tilde{\psi}}{\partial t}\cos m\xi - \nabla_{\parallel}\varphi \qquad (11)$$

where η is the plasma resistivity, φ is the electrostatic potential and $\nabla_{\parallel}$ is the derivative along the perturbed magnetic field lines of the island.

It is worthwhile spending a little time considering the $\nabla_{\parallel}$ operator, which is defined as

$$\nabla_{\parallel} \equiv \frac{\mathbf{B}\cdot\nabla}{B} = \frac{1}{Rq}\frac{\partial}{\partial\theta}\bigg|_{\Omega,\xi} + k_{\parallel}\frac{\partial}{\partial\xi}\bigg|_{\theta,\Omega} \qquad (12)$$

where $k_{\parallel}=-mx/rL_s$ and $L_s=Rq/s$, with $s=(r/q)(dq/dr)$ being the magnetic shear. A useful procedure is to define an average over the two angles, θ and ξ, which annihilates the $\nabla_{\parallel}$ operator. We shall indicate this averaging procedure by angled brackets, defined as

$$\langle\cdots\rangle \equiv \begin{cases} \dfrac{\oint d\theta \oint d\xi \dfrac{\cdots}{\sqrt{\Omega+\cos\xi}}}{\oint d\theta \oint d\xi \dfrac{1}{\sqrt{\Omega+\cos\xi}}} & \Omega > 1 \\ \\ \displaystyle\sum_{\sigma} \sigma \dfrac{\oint d\theta \displaystyle\int_{-\xi_b}^{\xi_b} d\xi \dfrac{\cdots}{\sqrt{\Omega+\cos\xi}}}{\oint d\theta \displaystyle\int_{-\xi_b}^{\xi_b} d\xi \dfrac{1}{\sqrt{\Omega+\cos\xi}}} & -1 < \Omega < 1 \end{cases} \qquad (13)$$

where $\cos\xi_b=-\Omega$ and $\sigma=x/|x|$. We can now use this averaging operator to eliminate φ from Eq (11) as follows. First we note that we expect $J_{\parallel}$ to be a function only of Ω, due to the fact that we neglect particle drifts perpendicular to the magnetic field for the present (so that perpendicular currents must also be absent), and therefore we must satisfy $\nabla\cdot\mathbf{J}=\nabla_{\parallel}J_{\parallel}=0$. Thus, we arrive at the result

$$J_{\parallel} = \frac{1}{\eta}\frac{\partial\tilde{\psi}}{\partial t}\langle\cos m\xi\rangle \qquad (14)$$

and substitution of this into Eq (10), together with Eq (5), yields the classical Rutherford tearing mode evolution equation:

$$a_1\tau_r\frac{dw}{dt} = r_s^2\Delta' \ , \qquad (15)$$

where $\tau_r=\mu_0 r_s^2/\eta$ is the current diffusion time and $a_1=0.82$ is associated with the island geometry. Note that this equation predicts that an island will grow linearly in time provided $\Delta'>0$, at least initially when the island is sufficiently small that Δ' is independent of w. Clearly the parameter Δ' is important for the stability of tearing modes, and it is therefore useful to say a few more words about its physical significance, and how it is determined.

Recall that we have assumed that ψ is approximately independent of r in the vicinity of the island, and so far we have only solved for ψ, or equivalently w, in that region. Away from the island region, two simplifying approximations can be made: (1) the plasma response is linear, and (2) resistivity is unimportant. Thus, away from the island region the equations of linear ideal magnetohydrodynamics (MHD) can be used to evaluate $\psi(r)$ (note that over the longer length scales across the plasma minor radius, the r dependence of ψ cannot be neglected, and indeed is calculated from the ideal MHD equations). Applying appropriate boundary conditions at the plasma edge and centre, and integrating the MHD equations from the centre out to the rational surface, and from the edge into the rational surface, one can calculate $\psi(r)$ over the full plasma region, taking ψ to be continuous at the island rational surface. In general, one will find that this solution will have a discontinuous gradient at the rational surface, and from this one can calculate Δ' from the ideal region using Eq (9), but replacing $-l$ with the limit as $r\to r_s$ from below, and $+l$ with the limit as $r\to r_s$ from above. This is basically a matching condition between the solution for ψ in the ideal MHD region and that in the island region. Thus we see that Δ' is a property of the *global* plasma equilibrium, and in the limit of small islands ($w\ll r_s$) is not influenced by the presence of the island itself. Indeed, it can be shown that Δ' represents the free energy available in the plasma current density distribution to drive the tearing mode. In the following sections we will see how other effects can modify the evolution of tearing modes, but these are different from the Δ' drive in that they originate from the island region itself.

III. THE MODIFIED RUTHERFORD EQUATION

In the previous section we considered only the inductive contribution (due to island growth) to the perturbed current, $J_{\parallel}$. In this section we consider a number of other contributions, which together constitute the ingredients of the so-called neoclassical tearing mode (NTM).

Let us begin by considering the most important element: the perturbed bootstrap current[3,4]. The bootstrap current is a current which flows along the tokamak magnetic field lines due to the combined effect of the trapped particles and the density and temperature gradients which exist. We do not go into the details of this current here, but it suffices to know that the bootstrap current is proportional to a linear combination of density and temperature gra-

dients, and requires the plasma to be in a low (so-called 'banana' or 'plateau') collisionality regime so that trapped particles can perform a complete orbit before being de-trapped by collisions. For our purposes it is sufficient to use a simple model for the bootstrap current, which we express in the form:

$$J_{bs} = -2.44 \frac{\sqrt{\varepsilon}}{B_\theta} \frac{dp}{dr} \tag{16}$$

This expression is accurate in the limit of small inverse aspect ratio, ε, and zero temperature gradient (p denotes the plasma pressure).

The main reason for a perturbation in the bootstrap current in the vicinity of the island is due to the island's effect on the plasma pressure there. Suppose that at some initial time there exists a magnetic island. There is rapid parallel transport along field lines so that the pressure is approximately a flux surface quantity; this means that in the absence of heat and particle sources inside the island, the pressure gradient tends to be removed from inside the island. From Eq (16) we therefore see that the bootstrap current is removed from inside the island, whilst outside (where a pressure gradient is still maintained across the flux surfaces) the bootstrap current remains. Thus there is a 'hole' in the bootstrap current which exists around the island O-points; ie there is an additional contribution to $J_\parallel$ which has the required $\cos m\xi$ component to contribute to the island evolution in Eq (10). Thus, if we now combine this contribution with the inductive contribution, Eq (14), and substitute the total $J_\parallel$ into Eq (10) (using Eq (5) for the island width in place of ψ), we find:

$$a_1 \frac{\tau_r}{r_s^2} \frac{dw}{dt} = \Delta' + a_2 \sqrt{\varepsilon} \frac{\beta_\theta}{w} \frac{L_q}{L_p} \tag{17}$$

We have introduced a new numerical factor a_2, which originates from the integral over space, the poloidal beta, $\beta_\theta = 2\mu_0 p/B_\theta^2$, $L_q^{-1} = d\ln q/dr$ and $L_p^{-1} = -d\ln p/dr$. Note that in normal tokamak situations $L_q/L_p > 0$ and therefore the bootstrap current term usually contributes a *drive* for the tearing mode (a notable exception is the case of reverse shear discharges, where $L_q < 0$). Indeed, for sufficiently small island widths the bootstrap term is the dominant one, so that even in situations when the plasma is stable to the classical tearing mode, the effect of the bootstrap current is to drive it unstable. In such cases the instability is called a *neoclassical tearing mode*.

Let us suppose that we are in this neoclassical tearing mode instability regime, so that $\Delta' < 0$. It is useful to plot dw/dt as a function of w, and this is shown in Fig 2. There

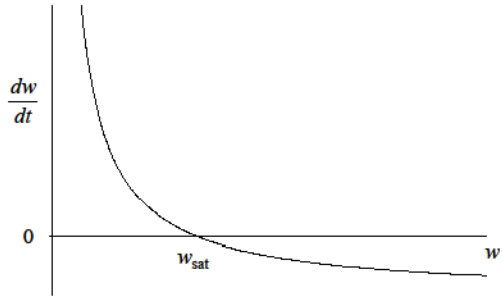

Fig. 2. The island growth as a function of the width, from Eq (17) indicating the saturated island width solution at $w = w_{sat}$.

is an important value of $w = w_{sat}$ for which $dw/dt = 0$: for $w < w_{sat}$, $dw/dt > 0$, so the island will grow until $w = w_{sat}$; for $w > w_{sat}$, $dw/dt < 0$, so the island will shrink until $w = w_{sat}$. Thus we see that $w = w_{sat}$ is a stable point, corresponding to the saturated island width that the neoclassical tearing mode will evolve towards. We can use Eq (17) to derive:

$$\frac{w_{sat}}{r_s} = a_2 \sqrt{\varepsilon} \frac{\beta_\theta}{(-r_s \Delta')} \frac{L_q}{L_p} \tag{18}$$

In order to gain an order of magnitude estimate of the effect, let us further suppose that $L_q \sim L_p$ and that $r_s\Delta' \sim -2m$ (which is correct in the asymptotic limit of large m); then we find that

$$\frac{w_{sat}}{r_s} \sim \frac{\beta_\theta}{2m} \tag{19}$$

Equation (19) illustrates why these modes are so dangerous: as we increase β_θ the island will grow, leading to an ever increasing degradation in confinement; eventually a situation would be reached where all the heating power which is put into the plasma is immediately flushed out by the island, and it will be impossible to increase β_θ further. In this sense, the NTM provides a 'soft' β-limit. However, particularly for low m modes, we see that Eq (19) predicts that island sizes can become comparable to the minor radius of the tokamak: then we would expect the plasma to respond violently, and terminate in a disruption.

If Eq (17) represented the full story, then the future of the tokamak would be exceedingly bleak, and indeed it would not have enjoyed the success it has had, particularly in recent years. The point is that, according to Eq (17), all neoclassical tearing modes which have a rational surface in the plasma would be unstable and the confinement would be completely wrecked. This clearly is not the case,

and so there must be more to the story. Indeed there are additional effects which are important when the island size is very small. For such small islands the theory is seriously complicated by both finite particle orbit width effects and finite radial transport effects. To illustrate this, note that the theory used to calculate the bootstrap current expression given in Eq (16) is based on an expansion in the ratio of ion banana width to the equilibrium length scales, assumed small. Clearly, then, for islands whose width is of order the ion banana width, Eq (17) may be flawed. Indeed, all rigorous analytic calculations of the modified Rutherford equation to date rely on an expansion in the ratio of the ion banana width to the island width: this therefore sets the scale at which the theory must be questioned. Let us now look briefly at two additional effects which may be important for such small islands.

We begin with the effects of radial diffusion[5,6]. Recall that we made the statement that the pressure gradients would be removed from inside the island region. This is a statement that the parallel transport effects dominate the radial diffusion. For arguments sake, let us consider a model for the electron heat transport (the particle transport is further complicated by the requirement that we expect quasi-neutrality to be maintained and the parallel transport would be dominated by sound waves). In steady state, and in the absence of any heat sources, we expect $\nabla\cdot\mathbf{Q}=0$, where $\mathbf{Q}$ is the heat flux. Suppose the heat flux parallel to the field lines is given by $Q_\parallel=-n\chi_\parallel\nabla_\parallel T$ and that perpendicular to the field lines is $Q_\perp=-n\chi_\perp\nabla_\perp T$ where $\chi_\parallel$ and $\chi_\perp$ are the thermal diffusivities parallel and perpendicular to the magnetic field, respectively, n is the density and T is the temperature. Taking these diffusivities to be approximately constant over the island width length scale of interest, we deduce

$$\nabla\cdot\mathbf{Q}=n\chi_\parallel\nabla_\parallel^2 T+n\chi_\perp\nabla_\perp^2 T=0 \qquad (20)$$

Now if the perpendicular transport can be neglected, then Eq (20) clearly provides the result that the temperature is constant on a field line (and it then follows that it must be constant inside the island). Suppose we now consider the conditions under which the perpendicular transport effects cannot be neglected. It is easiest to assume that T is independent of θ, ie $T=T(\Omega,\xi)$, and then the parallel operator can be taken to be of order $mw/(RqL_q)$ (see Eq (12) and note that the relevant length scale in $k_\parallel$ is $x\sim w$). For the perpendicular gradients, the relevant length scale is again w, and so we deduce that the radial transport term will compete with the parallel transport term when

$$\frac{m^2w^2}{R^2q^2L_q^2}\chi_\parallel\sim\frac{\chi_\perp}{w^2} \qquad (21)$$

that is, for a sufficiently small magnetic island. Rearranging Eq (21) we can therefore deduce a critical island width, w_χ, below which the pressure is not flattened across the island, and therefore the drive for the NTM is reduced:

$$w_\chi=\sqrt{\frac{RqL_q}{m}}\left(\frac{\chi_\perp}{\chi_\parallel}\right)^{1/4} \qquad (22)$$

[Note that in hot, collisionless plasmas, free streaming dominates the parallel transport, resulting in a balance $k_\parallel v_\parallel\sim\chi_\perp\nabla_\perp^2$, and a different scaling for w_χ]. To estimate the size of w_χ and how it scales with plasma parameters is difficult because this needs knowledge of the perpendicular heat diffusivity in the plasma, and this is not well-understood. If one puts in neoclassical heat diffusivity, then one obtains a very small value of the order 1mm: clearly the NTM model we have described is not appropriate at such small scale lengths, when finite Larmor radius effects will inevitably play a role. However, we know that in tokamaks the perpendicular heat flux is larger than the neoclassical prediction because of the plasma turbulence. As one possible model for this, let us assume that the transport has a gyro-Bohm scaling, ie $\chi_\perp\sim\rho_i^2 v_{thi}/r$, where ρ_j is the Larmor radius and v_{thj} is the thermal velocity (j labels ions or electrons). Taking a collisional model for the parallel diffusivity, $\chi_\parallel\sim v_{the}^2/\nu_e$, where ν_e is the electron collision frequency, we then have the estimate:

$$w_\chi\sim\sqrt{\frac{L_q\rho_i}{m}}\nu_{*e}^{1/4}q^{1/4}\left(\frac{\varepsilon m_e}{m_i}\right)^{1/8} \qquad (23)$$

where m_j and ν_{*j} are the mass and collisionality of species j, respectively. If we take typical tokamak parameters, then we find that this predicts a value in the region $w_\chi\sim$1cm. This value puts us above the length scales where Larmor radius effects are important, but is typical of the ion banana width in a tokamak, and therefore we remain in a regime where finite orbit width effects need to be taken into account. [Note that the parallel transport of density and ion heat is slower that that of the electron heat, and thus w_χ would be somewhat larger for these quantities.]

Let us now consider finite orbit width effects. There is no simple model to describe these, and therefore we will not attempt to reproduce the analysis here, but instead restrict ourselves to a discussion of the origin of the effect. Interested readers can consult the reference list for the more detailed theory, which is an evolving subject[7-14]. For small magnetic islands with width comparable to the ion banana width, the ions and electrons respond differently to the perturbed magnetic surfaces. For the electrons, the

parallel streaming (ie the $v_\parallel \nabla_\parallel$ term in the kinetic equation) dominates their response, and the electron distribution function will adjust so that, to leading order, it will be constant along the perturbed field lines. In contrast, for the ions the $\boldsymbol{E}\times\boldsymbol{B}$ drift dominates their response. Clearly the ion density must be a flux surface quantity if the electron density is (to satisfy quasi-neutrality) and therefore the $\boldsymbol{E}\times\boldsymbol{B}$ drift must be strongest along the perturbed flux surfaces. This, in turn, means that an electrostatic potential must be generated which is constant on the island flux surfaces. Away from the island (ie a few island widths away) both the electron and ion distribution functions are unaffected by the island, and therefore this electrostatic potential is localised around the island.

Having established that an electrostatic potential is an essential feature of any small scale island, let us now consider the more detailed consequences of this. The trapped ions will execute their banana orbits, and in doing so will experience an average of the potential over these orbits. The electrons, on the other hand, have a much narrower banana orbit, and they will experience the local potential. The consequence of this is that the $\boldsymbol{E}\times\boldsymbol{B}$ drifts of the two species will differ, and therefore a current perpendicular to the magnetic field will be generated. This is the neoclassical polarisation current. We noted below Eq (10) that only a current parallel to the magnetic field can affect the island evolution. However, one finds that the divergence of this perpendicular current is not zero and therefore a small electric field is generated, directed along magnetic field lines. This accelerates the electrons to generate a parallel current (the sum of this parallel current and the perpendicular current is divergence-free), and this does contribute to the island evolution. An additional feature of the neoclassical polarisation current is that when the ion collision frequency is sufficiently high, ie $\nu_i/\varepsilon\omega>1$ (ω is the island propagation frequency in the frame where the electric field far from the island is zero), the drift information carried by the trapped ions is communicated to the passing ions, leading to a large amplification of the polarisation current[9,10].

If one works through the algebra, one finds that this polarisation current contributes an additional term to the modified Rutherford equation, known as the polarisation term. A final point to note is that this polarisation term depends on the island propagation frequency ω, and can be either stabilising or destabilising. This complicates matters because additional, uncertain, physics related to plasma dissipation processes (eg viscosity or Landau damping) needs to be introduced in order to determine ω, and here the theory is as yet incomplete[15]. What is generally assumed, and this will suffice for our purpose, is that the mode frequency is such that the polarisation current provides a stabilising effect (without this assumption it is difficult to interpret the experimental data, which we come to in the next section). The result is our final expression for the modified Rutherford equation, which becomes:

$$a_1 \frac{\tau_r}{r_s^2}\frac{dw}{dt} = \Delta' + a_2\sqrt{\varepsilon}\frac{\beta_\theta}{w}\frac{L_q}{L_p}\frac{w^2}{w^2+w_\chi^2} - a_3 g(\varepsilon,\nu_i)\left(\frac{\rho_{bi}}{w}\right)^2\left(\frac{L_q}{L_p}\right)^2\frac{\beta_\theta}{w} \tag{24}$$

$$g(\varepsilon,\nu_i) = \begin{cases} 1.64\varepsilon^{1/2} & \nu_i/\varepsilon\omega \ll 1 \\ \varepsilon^{-1} & \nu_i/\varepsilon\omega \gg 1 \end{cases} \tag{25}$$

ρ_{bi} is the ion banana width and a_3 is a third numerical coefficient associated with the spatial integral (which appears in Eq (10)) and the value of ω. Equation (24) can be derived using drift-kinetic theory, provided the island width is larger than the ion banana width and $w_\chi \to 0$[9]. We shall assume that the expression actually holds for island widths down to the ion banana width, but stress that as yet there is no theoretical justification for this assumption. Such a justification is a challenging task, which can probably only be addressed through large scale computational modelling[12].

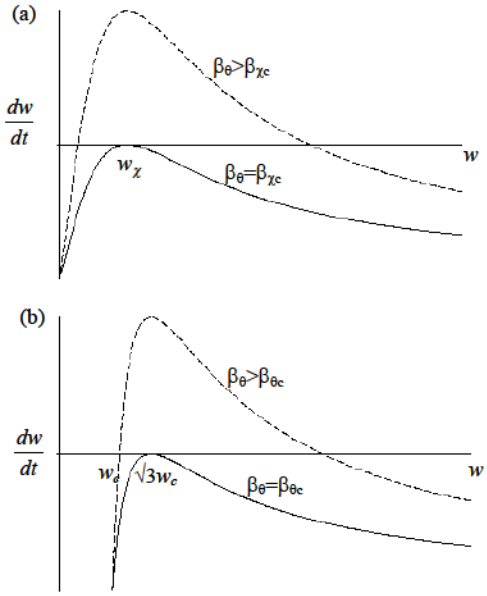

Fig. 3. Plots of *dw/dt* versus *w* for (a) the transport threshold model, and (b) the polarisation current model. Curves for β_θ equal to its critical value and exceeding this value are shown.

Note that we have taken account of the effect of the radial transport through a modification of the bootstrap current term: this modification is an interpolation formula, which reproduces Eq (17) for $w \gg w_\chi$ and also reproduces the results of linear theory in the opposite limit $w \ll w_\chi$[5]. Equation (24) thus provides a model which includes all the essential ingredients of neoclassical tearing modes. [There is an additional, so-called 'Glasser' stabilising term[16,17], which we have not discussed here due to space limitations; this may be particularly important for spherical tokamaks[18].]

Both the radial transport effects and the polarisation current can provide a threshold for NTMs. Let us first take $a_3=0$ and consider finite w_χ: this is shown in Fig 3a (to be compared with Fig 2, where no threshold effects were included). We see that for $\beta_\theta<\beta_{\chi c}$ $dw/dt<0$ for all w, so any initial 'seed' perturbation which led to a magnetic island would always decay away. However, for $\beta_\theta>\beta_{\chi c}$ the situation is particularly interesting: there are now *two* values of w for which $dw/dt=0$. For $w<w_{\chi c}$, $dw/dt<0$ and the island will tend to shrink, while for $w>w_{\chi c}$, $dw/dt>0$ and the island will grow; indeed it will continue to grow until w reaches w_{sat}, when $dw/dt=0$ again. For $w>w_{sat}$, $dw/dt<0$ and islands will decay. Thus we note that $w=w_{sat}$ again corresponds to a stable point, corresponding to a saturated island. On the other hand, the point $w=w_{\chi c}$ is an unstable point: it corresponds to a threshold in that an initial 'seed' island width must exceed this value for the island to grow to the large width $w=w_{sat}$. Thus, for this model, two conditions are required for growth of the NTM: both β_θ *and* the 'seed' island width must exceed critical values. These critical values, which can be deduced from Eq (24), are

$$\beta_{\chi c} = -\frac{2\Delta' w_\chi}{a_2\sqrt{\varepsilon}}\frac{L_p}{L_q} \qquad w_{\chi c} = \frac{w_\chi \beta_{\theta c}}{2\beta_\theta} \tag{26}$$

where the expression for $w_{\chi c}$ is given for β_θ far above threshold (at threshold $w_{\chi c}=w_\chi$).

We turn to the polarisation term ($a_3\neq 0$) and set $w_\chi=0$. Fig 3b shows dw/dt as a function of w; we see that it is essentially of the same form as that obtained from the transport effects, described above. Again we see that thresholds in *both* β_θ and w need to be exceeded for island growth, and they can be deduced from Eq (24):

$$\beta_{\theta c} = \frac{3\sqrt{3}}{2a_2\sqrt{\varepsilon}}\frac{L_p}{L_q}\left(-w_c\Delta'\right)$$
$$w_c = \sqrt{\frac{a_3}{3a_2}}\frac{\sqrt{g(\varepsilon,\nu_i)}}{\varepsilon^{1/4}}\sqrt{\frac{L_p}{L_q}}\rho_{bi} \tag{27}$$

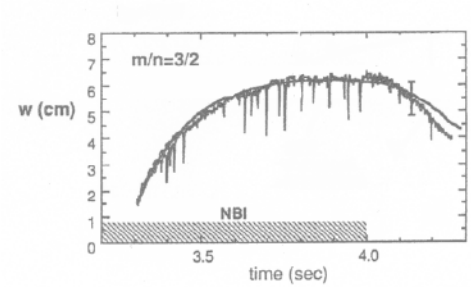

Fig. 4: Trace comparing the experimentally determined island width in TFTR with the result obtained by integrating Eq (17); 'NBI' indicates the time for which neutral beam injection heating was applied [Reprinted with permission from Z Chang et al, *Phys Rev Lett* 74 4663 (1995). Copyright (1995) by the American Physical Society.].

The expression for w_c is given for β_θ far above threshold (at threshold w_c is simply a factor $\sqrt{3}$ larger). There are two important points to note about this result: (1) the threshold is predicted to be significantly larger in the collisional regime (through the variable g, see Eq (25)) and (2) the thresholds are proportional to the ion banana width.

IV. EXPERIMENTAL EVIDENCE

The first evidence for neoclassical tearing modes in a tokamak came from measurements on the TFTR tokamak[19]. In Fig 4 we show a comparison between the measured magnetic signal and the prediction of Eq (17), and we see that in general the comparison is rather encouraging. However, two features are evident: (1) at the beginning of the trace, we see that the mode is initiated at finite amplitude, suggesting that a threshold ~1cm needs to be exceeded for island growth, and (2) the fit is not so good when the island starts to decay. Both of these point towards a

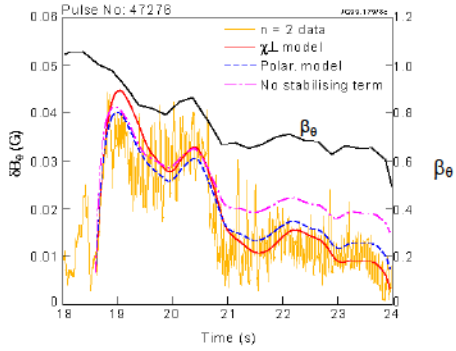

Fig. 5. Tracking the island evolution as the heating power is reduced on JET, we see that inclusion of either of the threshold effects improves the agreement with the measured amplitude of the magnetic perturbation, δB (from Ref 20)

threshold mechanism which is important for small island widths, but has little influence on the evolution of larger islands. Indeed, this is a property of both of the threshold effects we have discussed above. Careful experiments on JET have shown that the agreement between the data and experiment is much better when the threshold effects are taken into account[20], and this can be seen in Fig 5, where the predicted evolution is plotted (1) neglecting threshold effects, (2) including only the transport effect and (3) including only the polarisation effect. Recent high resolution temperature profile measurements in the vicinity of NTMs on MAST indicate that the transport effects are likely to play a role in the threshold physics[21].

The theory we have described suggests that very small islands cannot grow (at least if $\Delta'<0$); ie, island growth cannot occur unless an initial 'seed' island is generated by some other mechanism to excite it above the threshold. This does indeed seem to be the case experimentally, and in many cases NTM growth follows immediately after a sawtooth crash[22,23,24]. One model is that the sawtooth is predominantly an instability associated with the q=1 surface, but that as this instability grows, it induces magnetic island chains at other rational surfaces through toroidal coupling, for example. If these so-called 'sideband' islands exceed the thresholds for NTM growth, then as the sawtooth crash occurs, and the associated q=1 instability disappears, the NTM is free to grow. Other types of instability have also been observed to seed NTMs[24].

Experiments have probed the conditions for NTM onset rather deeply[21,25,26]. In particular, roles have been deduced for both collisionality and ρ_* (which is the ratio of ion Larmor radius to minor radius). While there seems no general consensus between the different devices for the dependence on collisionality, it is generally observed that NTMs are only observed at lower values of collisionality. One feature of the polarisation threshold model is that it is a much stronger effect at higher collisionality (through $g(\varepsilon,\nu_i)$), and the transport model can also provide a collisionality dependence. In addition, experiments on ASDEX-Upgrade seemed to confirm a role for ρ_* in the threshold[25], as predicted by the polarisation model, but could also originate from the transport model if one adopts a gyro-Bohm scaling for the perpendicular diffusivity (see Eq(23)). A particular concern for ITER is that a multi-machine database appears to indicate that the threshold β_θ is linearly proportional to ρ_*, a parameter which is rather small on ITER[20,26]. On the other hand, there is also some evidence that the seed island size reduces as ρ_* gets smaller[26], and then whether or not NTMs will be an issue on ITER will depend on which gets smaller faster: the threshold, or the seed islands from the sawteeth. So far we do not have sufficiently accurate data in the correct regimes to be confident in the predictions, and therefore it is prudent to assume NTMs will be an issue for ITER, and we must guard against them.

The key to avoiding or controlling NTMs is current drive. One can envisage two schemes: (1) to reduce the free energy available in the equilibrium current profile so that Δ' becomes more negative, and (2) to drive current directly at the island O-point (to replace the missing bootstrap current). Both of these have been tried, with success. In COMPASS-D, radio-frequency waves in the lower hybrid frequency range have been used to drive current close to the rational surface where the island forms[23]. In these experiments, the radial width of the current deposition was typically much wider than the island width, and then it can be shown that there is little contribution to the right hand side of Eq (10). However, calculations of Δ' showed that the additional current that was being driven by the lower hybrid waves did make Δ' more negative, and then both expressions (26) and (27) predict that the threshold for NTMs is increased. Fig 6 shows the experimental results.

The second technique is to drive current directly at the island O-point, highly localised within the magnetic island. Here the stabilisation is achieved through an additional contribution to $J_\parallel$ on the right hand side of Eq (10). This has been achieved using radio-frequency waves at the electron-cyclotron resonance, which drives current in a much narrower radial region than the lower hybrid waves used on COMPASS-D. In particular, successful experiments have been performed on ASDEX-Upgrade[24] and DIII-D[25], and this is the method envisaged for ITER.

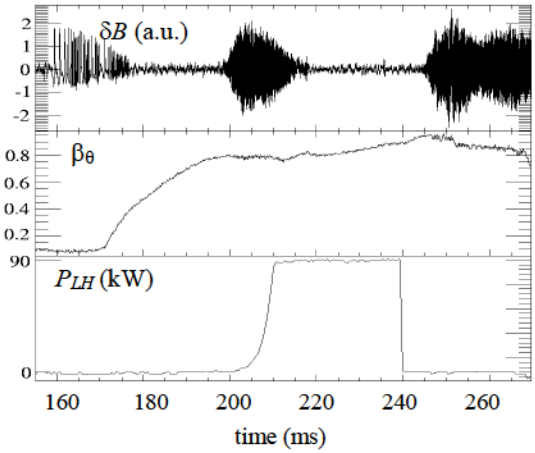

Fig. 6. The magnetic signal (δB) shows the growth of a NTM on COMPASS-D after 190ms, with a corresponding saturation in β_θ. 90kW of lower hybrid power (P_{LH}) is switched on just after 200ms, the NTM decays, and β_θ again rises.

V. SUMMARY

In summary, understanding the physics of the NTM is one of the success stories of fusion. The instability was predicted 10 years before it was identified experimentally, and since then theories have been refined, and broadly confirmed, by more detailed experiments. Nevertheless, the theory is still some way short of being truly predictive: it needs to address the seed island formation, as well as provide more accurate, quantitative models of the threshold effects, both of which require improved models to describe the relevant situation when the island width is comparable to the ion banana width. This will inevitably require the development of large scale numerical models for the situation. The neoclassical tearing mode is likely to be an issue for ITER, but the prospects for controlling them using radio-frequency waves to drive current close to the rational surface, or perhaps by controlling the seeding mechanism[26], look promising. This remains an evolving topic of research, both theoretically and experimentally.

ACKNOWLEDGMENTS

I should like to thank Richard Buttery, Jack Connor and Anthony Webster for their helpful comments.

REFERENCES

1. P H Rutherford "Nonlinear growth of the tearing mode", *Phys Fluids* 16 1903 (1973)
2. J Wesson, *Tokamaks, first edition* (Clarendon Press, 1987), p168
3. R Carrera, R D Hazeltine and M Kotschenreuther "Island bootstrap current modification of the non-linear dynamics of the tearing mode", *Phys Fluids* 29 899 (1986)
4. W X Qu and J D Callen "Nonlinear growth of a single neoclassical MHD tearing mode in a tokamak", University of Wisconsin report UWPR 85-5 (1985)
5. R Fitzpatrick "Helical temperature perturbations associated with tearing modes in tokamak plasmas", *Phys Plasmas* 2 825 (1995)
6. R D Hazeltine, P Helander and P J Catto "Plasma transport near the separatrix of a magnetic island", *Phys Plasmas* 4 2920 (1997)
7. A I Smolyakov "Nonlinear evolution of tearing modes in inhomogeneous plasmas" *Plasma Phys Control Fusion* 35 657 (1993), and references therein.
8. J W Connor, F L Waelbroeck and H R Wilson "The role of polarization current in magnetic island evolution", *Phys Plasmas* 8 2835 (2001), and references therein
9. H R Wilson, J W Connor, R J Hastie and C C Hegna "Threshold for neoclassical magnetic islands in a low collision frequency tokamak", *Phys Plasmas* 3 248 (1996)
10. H R Wilson et al "The collisionality dependence of tokamak β-limits", *Plas Phys Control Fusion* 38 A149 (1996)
11. F L Waelbroeck, J W Connor and H R Wilson, "*Finite Larmor radius theory of magnetic island evolution*", Phys Rev Lett **87** (2001) 215003-1
12. A Bergman, E Poli and A G Peeters, *"Collisionality dependence of the polarisation current"*, Phys Plasmas **12** 072501 (2005)
13. R. Fitzpatrick and F.L. Waelbroeck, "Drift-tearing magnetic islands in tokamak plasmas" *Phys Plasmas* 15 (2008) 012502
14. M James, H.R. Wilson and J.W. Connor "Modelling the effect of cross-field diffusion on tearing mode stability", *Plas. Phys. Cont. Fusion* **52** (2010) 075008
15. A B Mikhailovskii, et al "An approach to calculation of magnetic island rotation frequency", *Phys Plasmas* 7 2530 (2000)
16. M Kotschenreuther, R D Hazeltine and P J Morrison "Nonlinear dynamics of magnetic islands with curvature and pressure", *Phys Fluids* 28 294 (1985)
17. H.Lutjens, et al "Curvature effects on the dynamics of tearing modes in tokamaks, *Phys Plasmas* **8** (2001) 4267
18. C C Hegna "Nonlinear dynamics of pressure driven magnetic islands in low aspect ratio tokamaks", *Phys Plasmas* 6 3980 (1999)
19. Z Chang et al, "Observation of nonlinear neoclassical pressure-gradient-driven tearing modes in TFTR", *Phys Rev Lett* 74 4663 (1995)
20. R J Buttery et al "Neoclassical tearing modes", *Plasma Phys Control Fusion* 42 B61 (2000)
21. J. Snape, et al, "The influence of finite radial diffusion on the structure and evolution of m/n=2/1 neoclassical tearing modes on MAST", Plas. Phys. Control. Fusion **54** (2011) 085001
22. R J la Haye and O Sauter "Threshold for metastable tearing modes in DIII-D", *Nucl Fusion* 38 987 (1998)
23. R J Buttery et al "Onset and control of neoclassical tearing modes on JET", *Proceedings of the 26th EPS Conference on Controlled Fusion and Plasma Physics (Maastricht)* 121 (1999)
24. A Gude et al "Seed island of neoclassical tearing modes at ASDEX Upgrade", *Nucl Fusion* 39 127 (1999)
25. S Günter et al "β scaling for the onset of neoclassical tearing modes at ASDEX-Upgrade", *Nucl Fusion* 38 1431 (1998)
26. R J la Haye et al "Dimensionless scaling of the critical beta for onset of a neoclassical tearing mode", *Phys Plasmas* 7 3349 (2000)
27. C D Warrick et al "Complete stabilization of neoclassical tearing modes with lower hybrid current drive on COMPASS-D", *Phys Rev Lett* 85 574 (2000)
28. H Zohm et al "Experiments on neoclassical tearing mode stabilization by ECCD in ASDEX Upgrade", *Nucl Fusion* 39 577 (1999)
29. R J la Haye et al "Control of neoclassical tearing modes in DIII-D, *Phys Plasmas* 9 2051 (2001)
30. O Sauter et al "Control of neoclassical tearing modes by sawtooth control", Phys Rev Lett 88 105001-1 (2002)

EDGE LOCALIZED MODES IN TOKAMAKS

Howard Wilson

York Plasma Institute, Department of Physics, University of York, Heslington, York YO10 5DQ UK
Email: howard.wilson@york.ac.uk

ABSTRACT

As one increases the heating power in a tokamak beyond a threshold, the confinement undergoes a bifurcation, with a dramatic increase in the confinement time by a factor ~2. This improved confinement regime, or H-mode, is primarily due to the formation of an insulating region at the plasma edge, where steep pressure gradients can form. A feature of H-mode operation is a series of explosive plasma eruptions, called Edge Localised Modes, or ELMs. They repeatedly expel large amounts of energy and particles from the plasma, with serious consequences for the heat loads that plasma facing components must be designed to handle. The present understanding of these ELMs in terms of ideal magneto-hydrodynamic instabilities will be reviewed in this paper.

I. INTRODUCTION

In the early 1980's an exciting new discovery was made in tokamaks: the H-mode[1]. This mode of operation is achieved by increasing the plasma heating power above a threshold. The plasma then undergoes a bifurcation to a new state called the H-mode, in which the confinement is typically a factor of two greater than that in the standard L-mode discharges. The discovery of the H-mode is exceedingly important for fusion. In particular, ITER relies on achieving H-mode in order to meet its objectives.

There has been much activity to understand why the plasma suddenly jumps to this high confinement state. It is known, for example, that the reason for the high confinement is that a transport barrier forms at the plasma edge. A transport barrier is a region where heat and/or particle transport across the magnetic flux surfaces is suppressed. The pressure gradient is therefore typically high there. While this is good for confinement, instabilities called edge localized modes, or ELMs, can be triggered[2,3,4] in this high pressure gradient region (which is also sometimes called the pedestal region). These ELMs are repetitive events, which eject a large amount of heat and particles from the plasma. In a large tokamak, like ITER, the energy expelled could cause excessive erosion[5]. It is therefore essential that this phenomenon is understood so that steps can be taken to ameliorate the effect of ELMs, or perhaps eliminate them altogether. This paper describes the progress that has been made in our understanding of ELMs in terms of magneto-hydrodynamic (MHD) instabilities. In particular, we shall explore some of the characteristic features of ELMs, and how they can be understood in terms of this model. In Section 2, we discuss some of the experimental signatures for ELMs, before introducing the so-called peeling-ballooning model in Section 3. This linear ideal magneto-hydrodynamic (MHD) model is widely believed to explain at least the largest ELMs, and some of the experimental evidence for this is described in Section 4. In Section 5 we consider non-linear aspects of the model, and again compare with experimental observations. We conclude in Section 6, including a brief discussion on ELM control techniques.

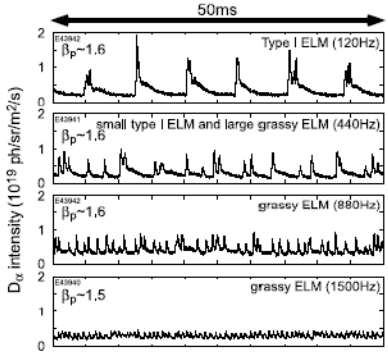

Fig. 1. D_α light emission, showing a sequence of ELMs on the JT-60U tokamak as bursts in the intensity; time traces for 4 discharges are shown giving examples of large, Type I ELMs (top) down to small, high frequency, "grassy" ELMs (bottom). [reproduced from Ref 6]

II. EXPERIMENTAL SIGNATURE OF ELMS

IIA. D_α light

An ELM is typically detected by observing the emission of D_α light near the divertor target plates, for example (see Fig 1). It is worthwhile considering the origin of the D_α light. The largest cross section for emission results from the interaction of electrons with neutral particles. Thus D_α light which is emitted from the divertor target plate region arises due to the electrons which are ejected from the core plasma during the ELM and then rapidly travel along the scrape-off layer towards the target plates where they interact with neutral particles. Ions are also ejected during the ELM, and these travel down to the target plate on a longer time-scale. They also increase the level of D_α light there by either (i) releasing more neutral particles from the target plate, which then interact with the electrons, or (ii) become neutralized themselves, again increasing the number of neutral particles for the electrons to interact with. After rapidly reaching a peak, the D_α light decays away more slowly as the ELM event finishes and the number of electrons arriving at the target plates decays to zero.

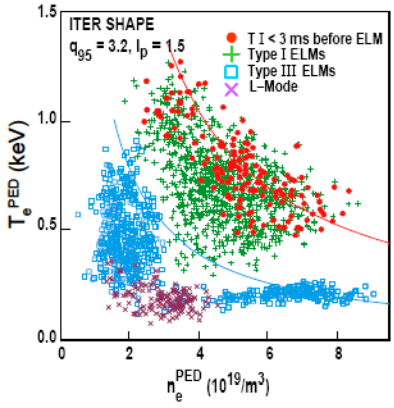

Fig. 2. Plot of temperature pedestal versus density pedestal for a range of different ELM types on DIII-D [figure reproduced from Ref 8]

IIB. ELM types

Experimentalists have managed to group the range of different ELM types into a number of different categories. Most ELMs fall into the category of Type I or Type III. The way these are typically distinguished is by measuring how the frequency of ELM events (ie the "ELM frequency") varies with heating power. For Type I ELMs, the frequency increases with power, while for Type III ELMs the frequency decreases. Perhaps a more useful distinction between the ELM types is obtained by comparing the temperatures and densities of discharges[7]. These are measured at the inner edge of the transport barrier: the so-called pedestal values. Figure 2 shows an example of how a set of discharges from DIII-D are distributed in the space of temperature pedestal, T_{ped}, versus density pedestal, n_{ped}[8]. Note that the Type I ELMs are clustered around a line of constant pressure. This provides some evidence that these are instabilities that are driven by the plasma pressure. There are two clusters of Type III ELMs: one at high density, low temperature, and one at low density, high temperature. Both of these clusters are positioned at a pedestal pressure significantly below that where Type I ELMs occur. Note also that the Type III ELMs occur in a similar region to where the transition from the L-mode to the H-mode occurs.

It is found that regimes with Type I ELMs tend to have better confinement than those with Type III, but that the energy expelled in a Type I ELM event is much greater than for a Type III. Indeed, Type I ELMs would likely be too damaging on ITER, and therefore cannot be tolerated. The confinement degradation caused by Type III ELMs, on the other hand, is likely to be unacceptable. From Fig 2, it is clear that the pressure pedestal in Type III-ELMing discharges is significantly less than that in Type I discharges. This lower pedestal pressure is presumably the cause of the reduced confinement. This therefore raises the question "can we operate with a pressure pedestal characteristic of Type I ELM regimes, but with ELMs that release a much smaller amount of energy"? The answer is "yes": but it is not easy and the parameter space required to achieve this is presently rather restrictive. Nevertheless, a range of small ELM regimes exist which seem to have good confinement[9]. These include Type II ELMs, grassy ELMs, Type V ELMs, etc. An example of grassy ELMs from the Japanese tokamak, JT-60U, is shown in the lower D_α trace of Fig 1, and compared to that for Type I ELMs. No clear definition of these regimes exists, and we will not attempt to refine our definition beyond that of small ELMs with good confinement. There is as yet no complete theoretical understanding for these ELM-types, but they do seem to be associated with strong plasma shaping and/or high edge safety factor. In addition, the grassy ELMs shown in Fig 1 appear to be associated with higher plasma rotation[6]. Without a rigorous understanding, it remains unclear whether ITER will be able to operate with any of these small ELMs. The subject therefore remains an active area of tokamak research.

III. PEELING-BALLOONING MODEL OF ELMS

Over the past decade the peeling-ballooning model[10,11,12,13] has emerged as the strongest contender to explain the characteristics of the largest ELMs: Type I. In

addition, there is scope within the model to explain the origin of smaller ELM types, although the models here are much more qualitative and not universally accepted.

As the name suggests, the model derives from two particular instabilities: the ballooning mode and the peeling mode. The ballooning mode has a short wavelength perpendicular to the magnetic field lines, and a long wavelength parallel to them. It is destabilized when the pressure gradient exceeds a critical value, but tends to be stabilized by current density. In particular, sufficiently high current density completely stabilizes the ballooning mode, allowing the pressure gradient to be increased indefinitely (neglecting the effect of other types of instability). This is known as "second stability access". These features are illustrated in Fig 3a. Actually, this second stability access strictly only occurs in the limit that the toroidal mode number, n, tends to infinity. As we shall see later, intermediate n modes (the peeling-ballooning modes) also have a drive due to the current density gradient, and these typically close off the second stability access. A final point to note is that the instability typically affects the whole of the plasma in the transport barrier region, and would therefore be expected to have a significant impact on it.

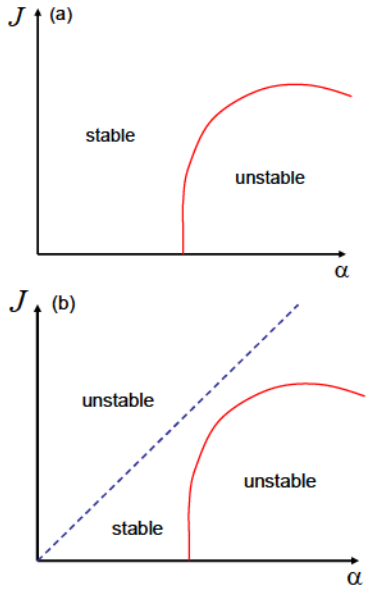

Fig. 3. Stability diagrams for (a) the ballooning mode and (b) the ballooning (full) and peeling mode (dashed). J is the current density at the plasma edge, α is the normalized pressure gradient.

The second type of instability, the peeling mode, is destabilized by the current density at the plasma edge, but stabilized by pressure gradient there. It is strongly related to the external kink instability, but is not limited to finite n. The schematic stability diagram for a limited plasma is illustrated in Fig 3b. This peeling mode is highly localized, and only affects a very small region of the transport barrier, exceedingly close to the plasma edge. At high pressure gradient, the peeling and ballooning modes couple[10,14], providing a strong instability with both current and pressure gradient drives that affects the whole transport barrier region. It is this coupled instability that is thought to be responsible for driving Type I ELMs.

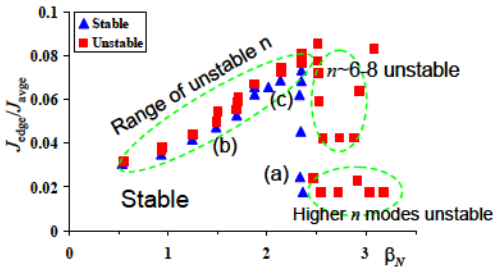

Fig. 4. Stability diagram for a JET-like plasma. The edge current density, J_{edge}, and normalized pressure, β_N, for each equilibrium are plotted as a square if unstable, and a triangle if stable.

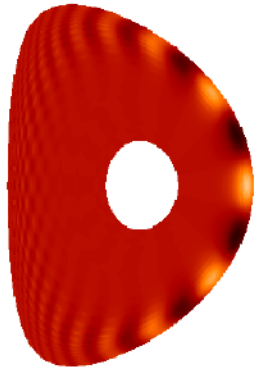

Fig. 5. ELITE calculation for the mode structure in the poloidal plane for a coupled peeling-ballooning mode. Orange represents zero perturbation, while dark and light colours correspond to positive and negative perturbations, respectively.

In Fig 4 we show the stability diagram for a (JET-like) model tokamak equilibrium. This has been produced using the ELITE code[12,15], which is a very efficient code for calculating the stability of the plasma edge to ideal MHD instabilities with intermediate to high toroidal mode numbers, n. For each point, the current density in the pedestal region is assumed to be a combination of the bootstrap current and Ohmic current. The stability boundary (between square and triangle symbols) is qualitatively similar to what one would expect, combining the peeling and ballooning stability boundaries of Figs 3b. Using ELITE, we can also evaluate the mode structures. Figure 5 shows the mode structure for a peeling-ballooning mode, which extends right across the pedestal region. Note that the amplitude is maximum on the outboard (low field) side. This characteristic is referred to as "ballooning". The pure ballooning mode has a similar structure, but the pure peeling mode differs in two respects. First, the peeling mode has a similar amplitude on the inboard side to that on the outboard side (ie no ballooning nature). Second, it is extremely edge localized, typically well within the last 1% of poloidal flux (unless the toroidal mode number is low, ie n~1,2); we do not plot it here as it would not even be visible. The pure ballooning modes, from the region of Fig 4 labeled (a), have very high toroidal mode numbers (several 10's); the pure peeling modes, from the region labeled (b) have a range of toroidal mode numbers, the most unstable having their external rational surface closest to the plasma edge; the peeling-ballooning modes, from the region labeled (c), have intermediate toroidal mode number n~10.

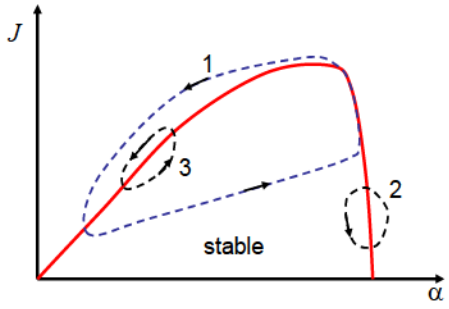

Fig. 6. Possible trajectories (dashed curves) of edge current density, J, and normalized pressure gradient, α, during ELMs. The stability boundary is indicated by the full curve. See text for descriptions and suggested links to ELM types.

Stability diagrams such as Fig. 4 are a simplification of the actual situation, as the stability diagram typically depends on the width of the pedestal region, as well as the pressure gradient within it (narrower pedestals tend to be more stable that wider ones at fixed pressure gradient).

The linear stability calculations shown in Figs 4 and 5 motivate the peeling-ballooning model for ELMs. Figure 6 shows a number of possible trajectories for the edge pressure gradient and current density in an ELMing discharge. These could correspond to different ELM types as follows. Starting with the trajectory labeled 1 in Fig 6, this is proposed as the trajectory of edge plasma parameters during a Type I ELM. Thus, while the plasma is stable between ELMs, the edge pressure gradient increases up to the ballooning boundary. The bootstrap current, which is proportional to the pressure gradient, would also increase until the peeling-ballooning mode is destabilized. Recall that this mode extends right across the transport barrier, so affects the whole pedestal region. As the instability develops, the expected increase of transport causes the pressure gradient to fall, further destabilizing the mode and triggering a large crash in the pressure (and consequent large energy loss). The discharge parameters eventually re-enter the stable region, and the cycle repeats. The trajectory labeled 2 is somewhat different. The plasma achieves a similar pressure gradient (and hence confinement) to the trajectory labeled 1, but now only the ballooning mode is destabilized. In this regime, which has reduced current compared to trajectory 1, the drop in pressure gradient stabilizes the ballooning mode, switching off the instability without a dramatic loss in pressure. This could provide an explanation of some of the small ELM regimes. Finally, the trajectory labeled 3 could provide a substantial loss of pressure gradient but, because the instability is so extremely edge-localized, the total loss of energy might be small (no rigorous theory for this speculative statement exists as yet). Note that the pressure gradient for this trajectory is significantly below that for trajectory 1, and this might therefore provide a model for Type III ELMs where the confinement is reduced (at least the class with low density and high temperature, where the edge current density is expected to be high).

Of the three models, the trajectory describing the Type I ELM behavior is the most accepted. The others are more speculative. Indeed, we shall see later that there is additional important physics that has been deduced from non-linear theories. This should be taken into account for a full understanding of ELM behavior. Before we address this non-linear physics, let us first consider some of the experimental evidence that supports some of the features predicted by this linear MHD model for Type I ELMs.

IV. EXPERIMENTAL EVIDENCE FOR THE PEELING-BALLOONING MODEL

The best way to test the peeling-ballooning model for ELMs is to carefully reconstruct the equilibrium using detailed measurements of the current density and pressure

gradient in the transport barrier, and compare with the predicted stability boundaries. The pressure increases by an order of magnitude over the ~few cm width of the transport barrier so that high resolution, high accuracy measurements of the density and temperature are required. Note that the error in the pressure gradient is significantly larger than the error in the pressure. Nevertheless, there are several tokamak experiments around the world that can now make this measurement with a reasonable accuracy (though not always for both the electrons and ions, so that often some form of approximation must be made). The other key requirement is the current density. In the core plasma, this is usually inferred from a measurement of the magnetic field using a technique such as motional Stark effect (MSE). This type of measurement is significantly complicated in the transport barrier for two reasons. First, the magnetic field structure in this region is determined largely by the geometry produced by the magnetic coils, and is less sensitive to the current density in the plasma. Second, there is a strong electric field in the transport barrier (indeed, this is widely thought to be responsible for the formation of the transport barrier). This electric field must be taken into account when interpreting the Stark splitting of the spectra. On DIII-D significant progress has been made in the measurement of current density using a lithium beam[16], but this is not a routine measurement, and interpretation of the data is difficult. Generally, then, the current density in the transport barrier is not known, and one must resort to modeling.

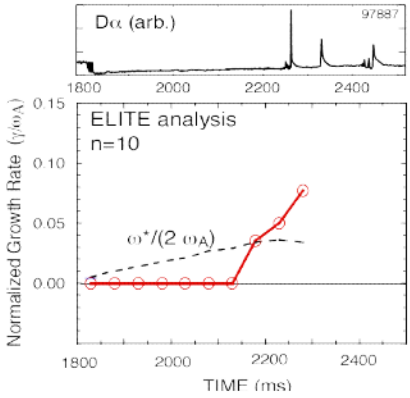

Fig. 7. The D_α trace of a DIII-D discharge and the ideal MHD growth rate (full curve) from an ELITE stability analysis [12]

The bootstrap current is driven in a tokamak through a combination of the trapped particles and the pressure gradient. Although it is suppressed to some extent in the transport barrier through collisional effects, it is nevertheless typically the largest contribution because of the high pressure gradient that exists there. Therefore most stability analyses of the plasma edge region simply use the bootstrap current expression rather than a direct measurement of the current density.

We consider two examples of how the peeling-ballooning model is typically tested against experimental data. The first is a comparison with data from DIII-D. The upper trace in Fig 7 shows the D_α light as a function of time. The drop in the signal at the beginning indicates the transition from L mode to H-mode, at which time the steep pressure gradient begins to form in the transport barrier region. A sequence of stability analyses using the ELITE code (setting n=10, which is typically the most unstable mode number) indicates that the plasma is stable to peeling-ballooning modes up to the time 2150ms, at which point the plasma becomes unstable, and the growth rate begins to rise until the first ELM appears at a time of around 2300ms. Thus, there is a reasonable correspondence between the predicted onset of instability and the onset of the ELM (particularly when diamagnetic effects are taken into account, in which case the growth rate must exceed half of the diamagnetic frequency, $\omega_*/2$, for instability).

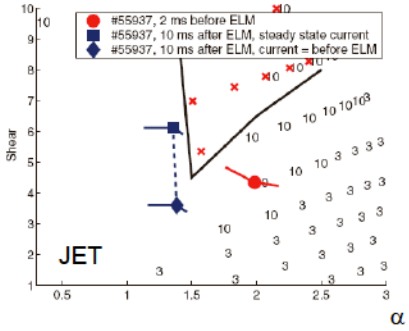

Fig. 8. Stability diagram for a JET discharge. See text for description. [Reproduced from ref 17]

The second type of stability analysis that we show is more typical of the analyses that have been performed on tokamaks like JET[17], DIII-D[12],, MAST[18] and ASDEX-Upgrade[19], for example. The specific case shown in Fig 8 corresponds to a study on JET[17]. The diagram shows the magnetic shear (which increases for decreasing current density) and normalised pressure gradient, α, for a range of equilibria. Each unstable equilibrium is represented by a single number, which indicates the most unstable toroidal mode number. The solid curve denotes the n=∞ ballooning mode stability boundary. The areas with no numbers, not bound by the solid curve are stable. Also shown on the figure are three points representing the

actual experimental values of shear and α for this JET discharge (55937). The circle shows the parameters immediately (2ms) before an ELM, indicating that the discharge is indeed close to the stability boundary. It is therefore reasonable to assume that the instability is the cause of the ELM. Just after the ELM event (10ms after), the pressure gradient is lower, and the discharge moves away from the stability boundary. There are two points indicated at this later time, and these correspond to two assumptions about the plasma current which, as stated earlier, cannot be measured. The point at higher magnetic shear has a lower plasma current, given by the steady bootstrap current associated with the lower pressure gradient at this later time. The point at lower magnetic shear has a higher current density: in this case it is assumed that in the brief period between the ELM onset and the end of the ELM event, the current has not had time to relax. The current is therefore assumed to be the same as that immediately before the ELM (and given by the steady state bootstrap current at that time).

V. NON-LINEAR MODELS

VA. The theory

While linear models provide quantitative information about the onset of instability, they tell us relatively little about the consequences. In particular, it is unlikely that we shall be able to construct a predictive model for the energy ejected during an ELM on ITER based purely on linear theory. Having said that, we have already suggested that there might be a link between the radial extent of the linear eigenmode structure and the energy lost during the ELM. There is certainly some evidence to support this, at least qualitatively[20,21], but also quantitatively in some cases (eg from DIII-D[12]). However, in general there does not seem to be a one-to-one correspondence between the radial width of the linear eigenmode and the ELM-affected volume[22]. This does not exclude some form of correlation between the radial eigenmode width and the ELM-affected region, but the two do not appear to be the same in general.

Thus it seems unlikely that we can address the key question of how much energy is ejected during an ELM from a model based purely on the linear theory. This has motivated recent studies that address non-linear models. One of the first was an analytic calculation during the early non-linear phase of the ballooning mode in a tokamak plasma[23]. This has recently been extended deeper into the non-linear regime[24]. There were two key predictions from this first model[23]: that the ballooning mode grows explosively during the non-linear phase, and that the instability would eject hot filaments of plasma. The explosive nature is an important point. One might expect from linear theory that a pure ballooning mode would grow relatively slowly as the pressure gradient builds on a transport timescale through the marginally stable value. However, the non-linear theory suggests there is much more to the story. As the mode amplitude grows to a level where the non-linear terms first become important, the growth is accelerated much above the linear growth rate. In addition, the spatial structure of the mode is also altered during the non-linear phase to form filament-like structures that are predicted to be aligned with the magnetic field lines.

In Section 3 we described a model based on linear theory which suggests that the crash is a consequence of a coupling between the peeling and ballooning modes. The explosive growth predicted by the non-linear model suggests that it is possible to trigger a crash event just by considering the ballooning mode. However, there is another twist. The equation that describes the non-linear evolution of the ballooning mode has a key term that causes the explosive behavior. If the coefficient of this term is positive, the filaments erupt outwards towards the scrape-off layer, otherwise they erupt inwards towards the core. It has been found theoretically that filaments only erupt outwards when there is sufficient current density in the plasma edge[25]. If one assumes that an outward-erupting filament is more dangerous than an inward one, then this could provide another reason why the ELM size might depend on the edge current density and provide an ingredient to understanding the differences between the mechanisms for large and small ELMs.

There are other types of models that predict filamentary structures. These are related to so-called "blob" theories, and predict that if a filament of plasma should break off from the core plasma, then it will propagate radially outwards due to an ExB drift[26,27]. This is different to the non-linear ballooning mechanism, where the filament is only ejected from the outboard side, and remains connected into the core plasma on the inboard side. Thus the filaments due to a non-linear ballooning mode can continue to tap the free energy of the pressure gradient in the transport barrier, and accelerate rapidly away from the core plasma. In addition, because they remain connected to the core plasma, they can act as a conduit (or hose-pipe), linking the transport barrier region to the scrape-off layer, siphoning hot plasma from the barrier region into the exhaust region. If this is the mechanism, it raises a new concern: what if the filaments should strike the vessel wall on the outboard side while still connected to the core plasma on the inboard side? This would place very high heat loads on the vessel walls, where there is relatively little protection. If, on the other hand, the filaments break off from the core plasma before striking the wall they would have a reduced impact on it. If this is the case, there is scope for both mechanisms to play a role: the non-linear ballooning theory may be

relevant for the early phase of the ELM, while the "blob" theories may be relevant later, after the filament has detached.

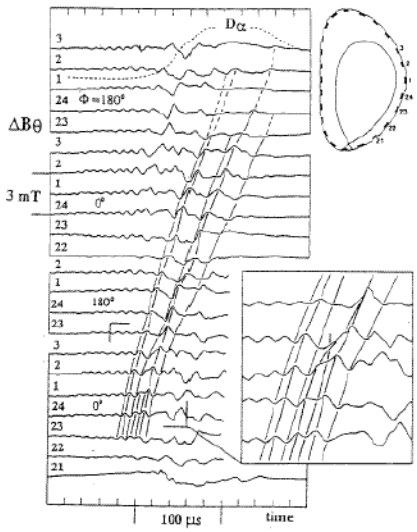

Fig. 9. Mirnov signals from a series of coils positioned at various toroidal and poloidal positions around the COMPASS-D tokamak[28].

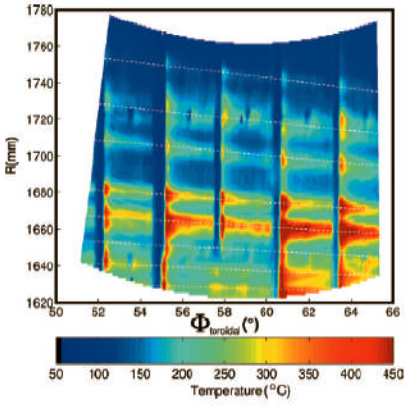

Fig. 10. Filamentary structures evident in the infra-red emission from the outer sections of the ASDEX-Upgrade divertor target [Figure reproduced from Ref 30]

VB. Experimental evidence for filaments

Some of the first data that suggested that filamentary structures might be associated with ELMs comes from COMPASS-D[28]. A poloidal and toroidal array of Mirnov coils allowed the magnetic signal associated with the ELM to be tracked in time in the two directions. The results, reproduced in Fig 9, indicate a field-aligned structure. More recently, a series of stripes have been observed in the infra-red emission from the outer sections of the divertor in ASDEX-Upgrade (see Fig 10)[29,30]. These stripes are also consistent with ELMs ejecting field-aligned filamentary structures. The most dramatic evidence, where the filaments were first observed directly, comes from the MAST tokamak[31,32,33]. A unique feature of a spherical tokamak is that one can view the whole plasma surface through a port. Such a view is shown in Fig 11 where the filamentary structures are clearly visible. These filaments are aligned with the magnetic field lines, as theory would predict[33], and are ejected far into the scrape-off layer, and beyond. They are observed to accelerate radially, qualitatively consistent with the prediction of non-linear ballooning theory, and decelerate in the toroidal direction[33].

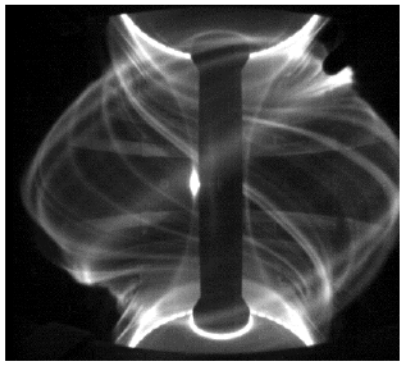

Fig. 11. Filamentary structures observed during ELMs on the MAST tokamak[32]

Another interesting observation, made on both MAST and DIII-D, is that the rotation shear (that is the differential rotation between different flux surfaces) is eliminated during the ELM event[34,35] (see Fig 12). Within the ideal MHD model of the non-linear ballooning mode, this must happen: the filament could not erupt out of the plasma if there is differential rotation. So again there is a nice consistency here. It does, however, raise an interesting question: Is the eruption of the filament causing a locking of the flow profile in the outer regions of the plasma, or is there some other event which removes

the flow shear, which then allows the filaments to erupt? In other words, is the filament a cause or consequence of the ELM? The consensus is that the filaments are the cause, but conclusive proof remains elusive.

VC. Heat loss mechanisms

Let us close this section with a discussion of the possible heat loss mechanisms. We simply state the possible mechanisms which might be operating here, and do not attempt to rule any of the models out or in. More details are provided in Ref 36.

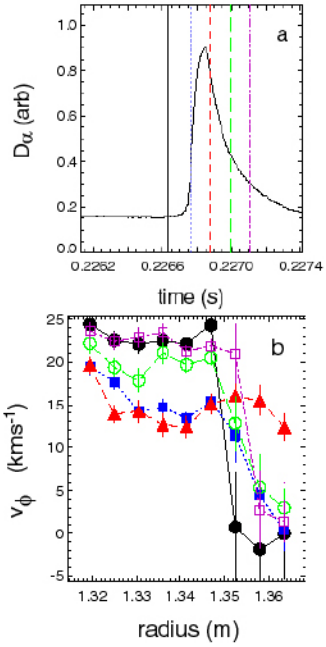

Fig. 12. Flow shear suppression during ELMs on the MAST tokamak. The full circles are the earliest time indicated by the vertical lines in the D_α trace of a single ELM (top), followed by the full squares, full triangles, open squares and open triangles. [Fig reproduced from Ref 34]

A key point to note is that within ideal MHD there can be no loss of heat or particles: everything that flows out along the filament into the scrape-off layer would flow back into the confinement region while the filament remained attached to the core plasma on the inboard side. It is necessary to introduce some additional physics. Three mechanisms are proposed for how the filaments might lead to enhanced transport. (1) The hot filaments "leak", so that hot plasma flows across field lines from the filament as it pushes out into the scrape-layer. (2) There is a reconnection process, probably in the vicinity of the X-point, in which the magnetic field lines contained in the hot filament break and then reconnect with the magnetic field lines of the scrape-off layer on the outboard side. Because the filament is relatively unperturbed on the inboard side, it remains inside the transport barrier there. Thus, following the reconnection event, there would be a continuous path along the filament from the pedestal region to the divertor target plates, and therefore a rapid loss of heat and particles. (3) The transport barrier is thought to be sustained by a sheared plasma flow within it. As the filament pushes out, it suppresses the flow shear and the barrier collapses with a significant, temporary confinement degradation. There is much experimental activity, and increasing efforts to simulate ELMs computationally, to identify the dominant mechanism. Both are exceedingly difficult, and are high priority areas of research for ITER.

VI. CONCLUSIONS

The importance of understanding ELMs and developing control scenarios for ITER is now well-established. Considerable progress has been made in our understanding, with the majority of the community accepting the peeling-ballooning model for at least the largest, Type I ELMs. There is also scope within the model to explain some of the other ELM regimes, but there is more uncertainty here. Non-linear theories have been developed and, together with experiment, have established that filamentary structures are likely to be an important part of the process of energy and particle loss during ELM events.

So, after all of this work, what are the consequences for ITER? ELMs remain one of the biggest concerns for ITER, which cannot operate for more than a few discharges at full power if large Type I ELMs are triggered. Small ELM regimes do exist, but the operating space for these is generally small, and it is not even clear that they will extrapolate to ITER. For this reason, there has been an increased focus on ELM control. We do not go into the details here, but instead refer the interested reader to the references. One method involves applying small magnetic perturbations to the plasma edge, thus degrading the confinement. The mechanism is not completely understood, but ELMs are then generally suppressed, probably because the pressure gradient in the transport barrier is maintained below the critical value for instability. Experiments on DIII-D validated and then perfected this form of ELM control[37,38], which has recently been repeated in ASDEX-Upgrade[39]. A second technique, pioneered on ASDEX-Upgrade, is complementary to this. Rather than suppress ELMs, they are instead triggered more frequently by firing small

pellets of frozen deuterium into the transport barrier. Each time a pellet is fired into the plasma edge, an ELM is triggered[40]. By triggering frequent ELMs, the energy released in a single event is smaller, and the impact on the divertor target is much reduced. A physical understanding of the mechanism is emerging from nonlinear MHD simulations[41].

To summarize, there is still much to do for a complete understanding of the ELM event, although much progress has been made in the last decade. As well as being an issue that we must address for ITER, it is an area that is rich in physics. Here we have focused on the plasma physics issues, but there is also a range of issues related to plasma-surface interactions that must be brought into the model to develop a complete understanding of the ELM cycle: a formidable, but rewarding, task.

ACKNOWLEDGMENTS

I am grateful to Andrew Kirk, for many enlightening discussions regarding the experimental data and its interpretation.

REFERENCES

1. F. WAGNER, et al, *Phys Rev Lett* **53**, 1453 (1984)
2. H. ZOHM *Plasma. Phys. Control. Fusion* **38**, 105 (1996)
3. J. W. CONNOR, *Plasma. Phys. Control. Fusion* **40**, 531 (1998)
4. W. SUTTROP, *Plasma. Phys. Control. Fusion* **42**, A1 (2000)
5. A. LOARTE, et al, *Phys Scri* **T128**, 222 (2007)
6. N. OYAMA, et al, Nucl Fusion **45**, 871 (2005)
7. W. SUTTROP, et al *Plasma Phys. Control. Fusion* **39**, 2051 (1997)
8. T. OSBORNE, et al, *Proceedings of the 24th EPS Conference on Controlled Fusion and Plasma Physics, Berchtesgaden* Part III, 1101 (1997)
9. N. OYAMA, et al, *Plasma Phys. Control. Fusion* **48**, (2006) A171
10. J.W. CONNOR, et al, *Phys. Plasmas* **5**, 2687 (1998)
11. H.R. WILSON, et al, *Phys. Plasmas* **6**, 1925 (1999)
12. P.B. SNYDER, et al, *Phys. Plasmas* **9**, 2037 (2002); Figure reprinted with permission from reference. Copyright (2002), American Institute of Physics.
13. P.B. SNYDER, et al, *Nucl Fusion* **44**, 320 (2004)
14. C.C. HEGNA, et al, Phys Plasmas **3**, 584 (1996)
15. H.R. WILSON et al, *Phys. Plasmas* **9**, 1277 (2002)
16. D. THOMAS, et al *Phys. Rev. Lett.* **93**, 065003 (2004)
17. S. SAARELMA, et al, *Plasma Phys. Control. Fusion* **47**, 713 (2005)
18. S SAARELMA et al, *Plasma Phys. Control. Fusion* **49**, 31 (2007)
19. C. KONZ, et al, to appear in *Proceedings of the 34th EPS Conference on Controlled Fusion and Plasma Physics, Warsaw* (2007)
20. L.L. LAO, et al, *Nucl. Fusion* **41**, 295 (2001)
21. S. SAARELMA et al, *Nucl. Fusion* **43**, 262 (2003)
22. A. LOARTE, et al *Plasma Phys. Control. Fusion* **44**, 1815 (2002)
23. H.R. WILSON and S.C. COWLEY, *Phys Rev Letts* 92 175006 (2004)
24. P. ZHU, C.C. HEGNA and C.R. SOVINEC, Phys Plasmas **14**, 055903 (2007)
25. H.R. WILSON, et al *Proceedings of the 21st IAEA Fusion Energy Conference, Chengdu, on CD-ROM: IAEA-CN-149,* paperTH/4-1Rb (2006)
26. S.I. KRASHANINNIKOV, Phys Lett A **283**, 368 (2001)
27. W. FUNDAMENSKI, et al *Plasma. Phys. Control. Fusion* **48**, 109 (2006)
28. M. VALOVIC, et al, *Proceedings of 21st EPS Conference on Controlled Fusion and Plasma Physics, Montpelier* Part I, 318 (1994)
29. T. EICH, et al, *Phys Rev Lett* **91**, 195003 (2003)
30. T. EICH, et al, *Plasma. Phys. Control. Fusion* **47**, 815 (2005)
31. A. KIRK, et al, *Phys Rev Lett* **92**, 245002 (2004)
32. A. KIRK, et al *Proceedings of the 21st IAEA Fusion Energy Conference, Chengdu, on CD-ROM: IAEA-CN-149,* paper EX/9-1 (2006)
33. A. KIRK, et al *Plasma. Phys. Control. Fusion* **48**, B433 (2006)
34. A. KIRK, et al *Plasma. Phys. Control. Fusion* **47**, 315 (2005)
35. J.A. BOEDO, et al, *Phys. Plasmas* **12**, 072516 (2005)
36. H.R. WILSON, et al, *Plasma Phys. Control. Fusion* **48** A71 (2006)
37. R.A. MOYER, et al, *Phys. Plasmas* **12** (2005) 056119
38. T. E. EVANS, R.A. Moyer et al. *Phys. Rev. Lett.* **92** (2004) 235003
39. W. SUTTROP et al, *Phys. Rev. Lett.* **106** (2011) 225004
40. P.T. LANG, et al, *Nucl. Fusion* **44** 665 (2004)
41. G.T.A. HUYSMANS, et al, *Plasma Phys. Control. Fusion* **51** (2009) 124012

INTRODUCTION TO KINETIC PLASMA THEORY WITH APPLICATIONS TO THE SOLAR WIND

Stefaan Poedts

CmPA / Dept. of Mathematics, KU Leuven, Leuven, Belgium
Institute of Physics, University of Maria Curie-Skłodowska, Lublin, Poland

Abstract

First, the place of kinetic theory among other mathematical models to describe plasma physics is discussed. Next, some basic kinetic concepts are introduced and the kinetic plasma equations are described. The use of these equations is then demonstrated considering electron plasma oscillations, a simple example of collective behaviour, and deriving a fundamental plasma parameter, viz. the plasma frequency, a fundamental plasma parameter. The a surprising fundamental phenomenon Landau damping is briefly discussed.

1 Introduction: theoretical models in plasma physics

Different mathematical models exist for different kinds of plasma processes. The model to be used or applied depends on the kind of phenomenon to be studied. Three kinds of theoretical description can be distinguished on the basis of the chosen approach [2]:

1. the theory of the motion of *individual charged particles* in given magnetic and electric fields; e.g. the motion of a charged, non-relativistic particle is described by

$$m\frac{d\mathbf{v}}{dt} = q(\mathbf{E} + \mathbf{v} \times \mathbf{B})\,, \qquad (1)$$

where $\mathbf{E}(\mathbf{r}, t)$ and $\mathbf{B}(\mathbf{r}, t)$ are given solutions of the Maxwell's equations, and one has to solve for the particle velocity $\mathbf{v}(\mathbf{r}, t)$. This model is useful to describe gyration of particles in a magnetic field and adiabatic invariants of this cyclotron motion, the magnetic mirror effect, drifts, etc. But plasmas usually contain a lot of particles, e.g. a large Corona Mass Ejection on the Sun involves up to 10^{30} particles, requiring a different model approach;

2. the *kinetic theory* of a such collections of charged particles, describing plasma behavior on a *microscopic scale* by means of particle distribution functions $f_{e,i}(\mathbf{r}, \mathbf{v}, t)$, the evolution of which is most generally described by the Boltzmann dissipative equation (see below). There exists an alternative Particle-In-Cell (PIC) approach, however, in which the particles are modelled as 'super particles' or 'particle clouds' which are accelerated by the forces (Lorentz, gravitational, etc.). This alternative approach will described in module KT-2;

3. the *fluid theory* (MHD), describing plasma behavior on a *macroscopic scale* in terms of averaged (over $\mathbf{v}$) functions of only $\mathbf{r}$ and t. The three basic steps to get from kinetic theory to the plasma model are discussed in the last section of this contribution.

Clearly, this is a rough division of model approaches and there exist combinations, like hybrid models with one or more species described in the fluid theory and other species described in kinetic theory. Here, we will focus on the kinetic plasma theory.

Why kinetic theory?

In the single particle orbit theory mentioned above, the interactions between the particles is ignored. This is a valid

assumption only when the density of the charged particles is low enough. Plasmas, however, exhibit *collective behaviour* because of the large amount of *interacting* particles involved. As a result, a statistical approach can be used to analyse its dynamics and this is precisely what kinetic plasma theory does. In this sense, the kinetic description of plasma is fundamental. The position of particles is known in phase space, the space of all possible values of position and momentum variables, making even the electron scale accessible.

Of particular importance are kinetic or micro-instabilities. These are short wavelength - high frequency modes of the system that may grow in amplitude when the charged particle species in a collisionless plasma posses a non-Maxwellian velocity distribution. In other words, these modes are driven unstable by the kinetic anisotropy of the plasma particles which provides a source of free energy. The velocity distributions (microstates) measured in-situ in space plasmas, for instance, often show departures from thermodynamic (Maxwellian) equilibrium in the form of temperature anisotropy, plasma flows or beams ('strahls'), suprathermal tails, etc. *These deviations from thermal equilibrium and the micro-instabilities they induce can be described only with a kinetic approach.*

Here, we will not elaborate on the derivation of the equation(s) describing the evolution of the plasma, which was introduced by Ludwig Boltzmann in 1872 and constitutes a vast amount of theoretical analysis (See, e.g. the comprehensive treatise by Balescu [3]), but merely exploit *the Boltzmann equation*, one of the end results of this work.

Closely following Goedbloed, Keppens, and Poedts [2], we will first introduce some basic kinetic concepts (Section 4) and consider a simple example of collective behaviour (Section 5), viz. electron plasma oscillations, and derive *the plasma frequency*, a fundamental plasma parameter. The (Landau) damping of these oscillations through kinetic effects is then discussed briefly in Section 5. It will also be discussed in modules KW-1 and KW-2 in this school. In module KT-2, numerical simulation models based on kinetic theory will be discussed and some of the impressive results will be demonstrated there.

2 Some basic plasma parameters

In Eq. (1) we did not specify the mass m and the charge q of the particles. Clearly, they correspond to either electrons ($m = m_e$, $q = -e$) or ions with mass number A and charge number Z (i.e. multiples of the proton mass and charge: $m = m_i = Am_p$, $q = Ze$). When we consider such a charged particle in a constant magnetic field in the z-direction, in the absence of an electric field: $\mathbf{B} = B\mathbf{e}_z$, $\mathbf{E} = 0$, we can get some insight by performing two simple vector operations on Eq. (1). First project this equation $\mathbf{B}$ and using vector identities, we get that $v_\parallel = \text{const}$ because

$$m\frac{dv_\parallel}{dt} = 0\,. \tag{2}$$

When we project the same equation on $\mathbf{v}$, we get

$$\frac{d}{dt}(\tfrac{1}{2}mv^2) = 0 \;\rightarrow\; \tfrac{1}{2}mv^2 = \text{const}\,, \tag{3}$$

which in combination with (2) yields that also $v_\perp = \text{const}$. because

$$\tfrac{1}{2}mv_\perp^2 = \text{const}. \tag{4}$$

Solving Eq. (1) more systematically, using $\mathbf{v} = d\mathbf{r}/dt = (\dot{x}, \dot{y}, \dot{z})$, we get two coupled differential equations describing the motion in the perpendicular plane:

$$\begin{aligned} \ddot{x} - \Omega\,\dot{y} &= 0\,, \\ \ddot{y} + \Omega\,\dot{x} &= 0\,, \end{aligned} \tag{5}$$

where

$$\Omega \equiv \frac{|q|B}{m}\,, \tag{6}$$

is *the gyro-* or *cyclotron frequency.*

We here do not elaborate on the derivation (see [2]), but the helical orbit consists of gyration (a periodic circular motion) $\perp$ $\mathbf{B}$ about a *the guiding centre* and with a *the gyro-* or *cyclotron radius*

$$R \equiv \frac{v_\perp}{\Omega} = \text{const}\,, \tag{7}$$

and inertial motion $\parallel \mathbf{B}$. The magnetic field $\mathbf{B}$ thus determines the geometry of the plasma.

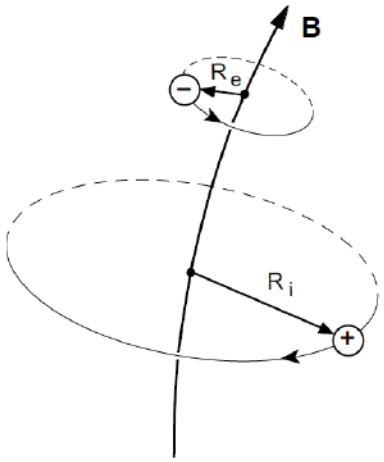

Figure 1: Gyration of electrons and ions in a magnetic field (source: [2]).

Remark that electrons and ions gyrate in opposite directions (Fig. 1). Due to their mass difference, their gyro-frequencies and gyro-radii are quite different:

$$\begin{aligned} \Omega_e \equiv \frac{eB}{m_e} \quad &\gg \quad \Omega_i \equiv \frac{ZeB}{m_i}\,, \\ R_e \equiv \frac{v_{\perp,e}}{\Omega_e} \quad &\ll \quad R_i \equiv \frac{v_{\perp,i}}{\Omega_i} \quad (\text{assuming } T_e \sim T_i)\,. \end{aligned} \tag{8}$$

Inserting a magnetic field $B = 3\,\mathrm{T}$ (= 30 kgauss), typical for tokamaks, and the values for e, m_e, and m_p, we find for the angular frequencies of protons and electrons

$$\begin{aligned} \Omega_e &= 5.3 \times 10^{11}\,\mathrm{rad\,s^{-1}} \quad (\text{i.e., a freq. of } 84\,\mathrm{GHz})\,, \\ \Omega_i &= 2.9 \times 10^{8}\,\mathrm{rad\,s^{-1}} \quad (\text{i.e., a freq. of } 46\,\mathrm{MHz})\,. \end{aligned} \tag{9}$$

Considering particles with thermal speed $v_\perp = v_{\mathrm{th}} \equiv \sqrt{2kT/m}$ we can estimate the gyro-radii. For electrons and protons at $\widetilde{T} = 10\,\mathrm{keV}$, i.e. $T_e = T_i = 1.16 \times 10^8\,\mathrm{K}$, we obtain

$$\begin{aligned} v_{\mathrm{th},e} &= 5.9 \times 10^{7}\,\mathrm{m\,s^{-1}} \quad \Rightarrow \quad R_e \approx 0.1\,\mathrm{mm}\,, \\ v_{\mathrm{th},i} &= 1.4 \times 10^{6}\,\mathrm{m\,s^{-1}} \quad \Rightarrow \quad R_i \approx 5\,\mathrm{mm}\,. \end{aligned} \tag{10}$$

Adding a constant background electric field perpendicular to the magnetic field, i.e. $\mathbf{B} = B\mathbf{e}_z$, $\mathbf{E} = E\mathbf{e}_y$, only slightly complicates the analysis. However, in this case the gyration is superposed with a constant 'drift' in $x-$direction. Hence, the perpendicular electric field results in the so-called $\mathbf{E} \times \mathbf{B}$ drift (see [2]).

3 Kinetic model equations

The equations of the kinetic model consist of equations for the particle distribution functions combined with Maxwell's equations (13) which determine the electric and magnetic fields $\mathbf{E}(\mathbf{r}, t)$ and $\mathbf{B}(\mathbf{r}, t)$.

3.1 The Boltzmann equation

Let us consider a plasma that consists of electrons and one kind of ions. Clearly, the information on the individuality of the particles is lost in the statistical description. However, the time-dependent *distribution functions* $f_\alpha(\mathbf{r}, \mathbf{v}, t)$ for the electrons and ions ($\alpha =$ e, i) contain relevant physical information on the plasma as a whole. The distribution functions express the density of the representation points of particles of type α in the six-dimensional *phase space* which is formed by the three position coordinates (x, y, z) and the three velocity coordinates (v_x, v_y, v_z) (see, e.g., Bittencourt [4]). In other words, $f_\alpha(\mathbf{r}, \mathbf{v}, t)\, d^3r\, d^3v$ represents the probable number of particles of type α in the six-dimensional volume element $d^3r\, d^3v$ centred at $(\mathbf{r}, \mathbf{v})$. We here assume that the total number of particles, $N_\alpha \equiv \iint f_\alpha d^3r\, d^3v$, is constant. This is, of course, not valid for plasmas that are in thermal and/or chemical non-equilibrium, like the partially-ionized plasmas in the lower solar atmosphere (photosphere and lower chromosphere) and thermonuclear plasmas in which fusion reactions create and annihilate particles. In such cases, more than two distribution functions are needed, e.g. also one for neutrals in the case of the solar photosphere, and the respective total number of particles will not be constant.

We now make a distinction between the motion of individual particles and the motion of a collection of their representative points in phase space, which is somehow similar to the motion of a swarm of bees (versus the motion of a particular bee in the swarm). The 'swarm' of representative points is described by the the distribution

function $f_\alpha(\mathbf{r},\mathbf{v},t)$, and its motion is given the *total* time derivative of f_α, using the chain rule we get:

$$\begin{aligned}\frac{\mathrm{d}f_\alpha}{\mathrm{d}t} &\equiv \frac{\partial f_\alpha}{\partial t}+\frac{\partial f_\alpha}{\partial \mathbf{r}}\cdot\frac{d\mathbf{r}}{dt}+\frac{\partial f_\alpha}{\partial \mathbf{v}}\cdot\frac{d\mathbf{v}}{dt}\\ &= \frac{\partial f_\alpha}{\partial t}+\mathbf{v}\cdot\frac{\partial f_\alpha}{\partial \mathbf{r}}+\frac{q_\alpha}{m_\alpha}\left(\mathbf{E}+\mathbf{v}\times\mathbf{B}\right)\cdot\frac{\partial f_\alpha}{\partial \mathbf{v}}, \end{aligned} \quad (11)$$

where Eq. (1) has been used inserted in the second line.

Here, the scalar products involving derivatives with respect to the vectors $\mathbf{r}$ and $\mathbf{v}$ simply denote sums over the products of the vector components, i.e. $\mathbf{v}\cdot\partial/\partial\mathbf{r} \equiv v_x\,\partial/\partial x + v_y\,\partial/\partial y + v_z\,\partial/\partial z$, and idem for the term with $\partial/\partial\mathbf{v}$. Notice also the subtle difference between $\mathrm{d}/\mathrm{d}t$ for the total time derivative and d/dt for ordinary time derivatives. Liouville's theorem ([6])states that, in the absence of binary interactions between particles, $\mathrm{d}f_\alpha/\mathrm{d}t = 0$, i.e. the density of representative points in phase space remains constant.

Clearly, the behaviour of a collection of particles only becomes interesting when these particles collide with each other, i.e. interact. In 1872, Ludwig Boltzmann derived an equation describing the time variation of the distribution functions of electrons and ions. This kinetic equation, called *the Boltzmann equation* reads:

$$\frac{\partial f_\alpha}{\partial t}+\mathbf{v}\cdot\frac{\partial f_\alpha}{\partial \mathbf{r}}+\frac{q_\alpha}{m_\alpha}\left(\mathbf{E}+\mathbf{v}\times\mathbf{B}\right)\cdot\frac{\partial f_\alpha}{\partial \mathbf{v}} = \left(\frac{\partial f_\alpha}{\partial t}\right)_{\text{coll}}. \quad (12)$$

Note that here $\mathbf{E}(\mathbf{r},t)$ and $\mathbf{B}(\mathbf{r},t)$ consist of the contributions of the external fields plus that of the averaged internal fields originating from the long-range inter-particle interactions. The right-hand side represents the effect of an unspecified collision term which should model the short-range inter-particle interactions, or 'collisions'. These are the large-angle Coulomb collisions resulting from the cumulation of the many small-angle velocity changes. A first important objective of kinetic theory is to distinguish between different (long- and short-range) interactions and binary collisions and to determine on what ranges they are valid, yielding different forms of this collision term. One choice leads to the Landau collision integral (1936) [8]. And when only the accumulated effects of the small-angle collisions are taken into account, the above equation leads to the *Fokker–Planck equation*; and neglecting all collisions, i.e. setting the RHS equal to zero, leads to the *Vlasov equation* (1938) [20].

3.2 Maxwell's equations

In order to obtain a closed system of equations the Boltzmann equation (12) (or the Vlasov equation in case collisions can be ignored) for the distribution functions $f_\alpha(\mathbf{r},\mathbf{v},t)$, are combined with Maxwell's equations (13), determining the electric and magnetic fields $\mathbf{E}(\mathbf{r},t)$ and $\mathbf{B}(\mathbf{r},t)$, and providing expressions (14) for the charge and current density source terms $\tau(\mathbf{r},t)$ and $\mathbf{j}(\mathbf{r},t)$. In mksA units these equations are given by:

$$\begin{cases} \nabla\times\mathbf{E} = -\dfrac{\partial\mathbf{B}}{\partial t} & \text{(Faraday)}, \\ \nabla\times\mathbf{B} = \mu_0\mathbf{j}+\dfrac{1}{c^2}\dfrac{\partial\mathbf{E}}{\partial t} & \text{('Ampère')}, c^2=(\epsilon_0\mu_0)^{-1}, \\ \nabla\cdot\mathbf{E} = \dfrac{\tau}{\epsilon_0} & \text{(Poisson)}, \\ \nabla\cdot\mathbf{B} = 0 & \text{(no magnetic monopoles)}. \end{cases} \quad (13)$$

We have ignored polarisation and magnetisation effects, i.e. $\epsilon = \epsilon_0$ and $\mu = \mu_0$ so that $\mathbf{D} = \epsilon_0\mathbf{E}$ and $\mathbf{H} = (\mu_0)^{-1}\mathbf{B}$, since these effects are absorbed in the definitions of charge and current density:

$$\begin{cases} \tau = \sum_\alpha q_\alpha n_\alpha \\ \mathbf{j} = \sum_\alpha q_\alpha n_\alpha \mathbf{u}_\alpha \end{cases} \quad (\alpha = \mathrm{e},\,\mathrm{i}). \quad (14)$$

Here, n_α and $\mathbf{u}_\alpha$ are the particle density and the macroscopic velocity of particles of type α.

The charge and current density source terms $\tau(\mathbf{r},t)$ and $\mathbf{j}(\mathbf{r},t)$ are related to the particle densities and the average velocities:

$$\begin{aligned} n_\alpha(\mathbf{r},t) &\equiv \int f_\alpha(\mathbf{r},\mathbf{v},t)\,d^3v\,, \\ \text{and}\quad \tau(\mathbf{r},t) &\equiv \sum q_\alpha n_\alpha\,, \end{aligned} \quad (15)$$

$$\begin{aligned} \mathbf{u}_\alpha(\mathbf{r},t) &\equiv \frac{1}{n_\alpha(\mathbf{r},t)}\int \mathbf{v} f_\alpha(\mathbf{r},\mathbf{v},t)\,d^3v\,, \\ \text{and}\quad \mathbf{j}(\mathbf{r},t) &\equiv \sum q_\alpha n_\alpha \mathbf{u}_\alpha\,. \end{aligned} \quad (16)$$

This completes the microscopic equations.

Solving these kinetic equations in seven dimensions (with the details of the single particle motions entering the collision integrals) is a formidable task, even with the help

of present-day supercomputers. Hence, whenever possible, i.e. when the physical phenomenon that is studied allows it, modelers will look for a macroscopic reduction. Here, however, we will stick to the kinetic equations and take up the challenge of solving them.

4 Moment reduction

Macroscopic equations, i.e. equations that do not involve details of velocity space any more can be obtained by expanding in a finite number of moments of the Boltzmann equation (12). These moments are obtained by first multiplying the equation with a function $\chi(\mathbf{v})$ and then integrating over velocity space. The function χ consists of powers of the velocity:

$$\chi(\mathbf{v}) = \begin{cases} 1, & \text{zeroth moment;} \\ \mathbf{v}, & \text{first moment;} \\ v^2, & \text{second moment;} \\ \dots & , \end{cases} \tag{17}$$

and the procedure is truncated after a finite number (5, 10, 20...) of such moments. Clearly, taking moments of the Boltsmann equation involves the moments of the distribution function itself. For instance, the zeroth moment is associated with the particle density $n_\alpha(\mathbf{r},t)$ and the first moment is associated with the average velocity $\langle \mathbf{v} \rangle_\alpha \equiv \mathbf{u}_\alpha(\mathbf{r},t)$, defined above. This expansion in moments clearly needs to be truncated in order to be practical. A popular truncation occurs already after the five moments (one scalar + one vector + one scalar) indicated explicitly in Eq. (17). This truncation is justified in the transport theory. Macroscopic variables $\langle g \rangle_\alpha(\mathbf{r},t)$ generally appear as averages of some phase space function $g(\mathbf{r},\mathbf{v},t)$ over the velocity space, i.e.

$$\langle g \rangle_\alpha(\mathbf{r},t) \equiv \frac{1}{n_\alpha(\mathbf{r},t)} \int g(\mathbf{r},\mathbf{v},t)\, f_\alpha(\mathbf{r},\mathbf{v},t)\, d^3v\,. \tag{18}$$

Clearly, this definition assumes or requires that the distribution functions f_α decrease fast enough with $v \to \infty$ in order to yield a finite answer.

The systematic procedure of taking moments of the Boltzmann equations also involves the determination of the different moments of the collision term in the RHS. The collision operator

$$\left(\frac{\partial f_\alpha}{\partial t}\right)_{\text{coll}} \equiv C_\alpha\,, \tag{19}$$

represents evolution of f_α due to local collisions. It can be decomposed in contributions $C_{\alpha\beta}$ due to collisions of particles α (e.g. electrons) with particles β (i.e. electrons as well as ions):

$$C_\alpha = \sum_\beta C_{\alpha\beta}\,. \tag{20}$$

So, e.g. C_i is the sum of the intraspecies collision operator C_{ii}, which represents the effect of ion-ion collisions, and the interspecies collision operator C_{ie}, which represents the effect on the ions of ion-electron collisions. C_α is thus an operator which maps functions of velocity space, $f_i(\mathbf{v})$ and $f_e(\mathbf{v})$, to a function of velocity space, $C_\alpha(\mathbf{v})$.

The collision of course respect some constraints. For instance, in the absence of fusion reactions, there is *conservation of mass*, i.e. the total number of particles α at a certain position does not change by collisions with particles β:

$$\int C_{\alpha\beta}\, d^3v = 0\,. \tag{21}$$

In a similar way, *conservation of momentum* yields

$$\int \mathbf{v} C_{ii}\, d^3v = 0\,, \tag{22}$$

and

$$\int ||\mathbf{v}||^2 (C_i + C_e)\, d^3v = 0\,; \tag{23}$$

while *conservation of energy* yields

$$\int \mathbf{v} C_{ii}\, d^3v = 0\,, \tag{24}$$

and

$$\int ||\mathbf{v}||^2 (C_i + C_e)\, d^3v = 0\,. \tag{25}$$

More details of the derivation of these expressions and on the procedure in general can be found in Goedbloed, Keppens, and Poedts [2]. In order to give an idea of the procedure, we will here only derive the lowest moment equation, which describes mass conservation.

As mentioned above, the *zeroth moment* is obtained by integrating the Boltzmann equation (Eq. (12)) over velocity space. Doing this term by term, we get subsequently:

$$\int \frac{\partial f_\alpha}{\partial t}\, d^3v = \frac{\partial n_\alpha}{\partial t} \quad \text{(def. (15))},$$

$$\int \mathbf{v}\cdot\frac{\partial f_\alpha}{\partial \mathbf{r}}\, d^3v = \nabla\cdot(n_\alpha \mathbf{u}_\alpha) \text{ (def. (16))},$$

$$\int \frac{q_\alpha}{m_\alpha}(\mathbf{E}+\mathbf{v}\times\mathbf{B})\cdot\frac{\partial f_\alpha}{\partial \mathbf{v}}\, d^3v = 0 \quad \text{(int. by parts)},$$

$$\int C_\alpha\, d^3v = 0 \quad \text{(summing Eq. (21))}.$$

The continuity equation for particles of species α is obtained by adding these four expressions, yielding

$$\frac{\partial n_\alpha}{\partial t} + \nabla\cdot(n_\alpha \mathbf{u}_\alpha) = 0\,. \tag{26}$$

Similarly, the *first moment* of the Boltzmann equation is obtained by multiplying it with $m_\alpha \mathbf{v}$ and integrating this expression over the velocities. This yields *the momentum equation*:

$$\frac{\partial}{\partial t}(n_\alpha m_\alpha \mathbf{u}_\alpha) + \nabla\cdot\Big(n_\alpha m_\alpha \langle \mathbf{v}\mathbf{v}\rangle_\alpha\Big) - q_\alpha n_\alpha(\mathbf{E}+\mathbf{u}_\alpha\times\mathbf{B}) = \int C_{\alpha\beta}\, m_\alpha \mathbf{v}\, d^3v\,. \tag{27}$$

The *scalar second moment* of Eq. (12) is then obtained by multiplying with $\frac{1}{2}m_\alpha v^2$ and integrating over velocity space. This yields *the energy equation*:

$$\frac{\partial}{\partial t}\Big(n_\alpha \tfrac{1}{2} m_\alpha \langle v^2\rangle_\alpha\Big) + \nabla\cdot\Big(n_\alpha \tfrac{1}{2} m_\alpha \langle v^2 \mathbf{v}\rangle_\alpha\Big) - q_\alpha n_\alpha \mathbf{E}\cdot\mathbf{u}_\alpha = \int C_{\alpha\beta}\tfrac{1}{2} m_\alpha v^2\, d^3v\,. \tag{28}$$

See [2] for the explicit steps in the derivation of these equations.

This chain of moment equations can be continued indefinitely. Notice that each moment introduces a new unknown whose temporal evolution is described by the next moment of the Boltzmann equation. However, the infinite chain must be truncated to be useful. In fluid theories truncation is just after the above five moments: the continuity equation (26) (scalar), the momentum equation (27) (vector), and the energy equation (28) (scalar), by making additional assumptions. In (very) broad outlines, the procedure can be summarized as follows:

(a) First, split the particle velocity $\mathbf{v}$ into an average part $\mathbf{u}_\alpha$ and a random part $\tilde{\mathbf{v}}_\alpha$, i.e.

$$\tilde{\mathbf{v}}_\alpha \equiv \mathbf{v} - \mathbf{u}_\alpha\,, \quad \text{where } \langle \tilde{\mathbf{v}}_\alpha\rangle = 0\,. \tag{29}$$

In this way *thermal quantities* can be defined, like

$$T_\alpha(\mathbf{r},t) \equiv \frac{m_\alpha}{3k}\langle \tilde{v}_\alpha^2\rangle \quad \textit{(temperature)}\,, \tag{30}$$

$$\mathbf{P}_\alpha(\mathbf{r},t) \equiv n_\alpha m_\alpha \langle \tilde{\mathbf{v}}_\alpha \tilde{\mathbf{v}}_\alpha\rangle = p_\alpha \mathbf{I} + \boldsymbol{\pi}_\alpha\,, \quad p_\alpha \equiv n_\alpha k T_\alpha \quad \textit{(stress tensor)}, \tag{31}$$

$$\mathbf{h}_\alpha(\mathbf{r},t) \equiv \tfrac{1}{2} n_\alpha m_\alpha \langle \tilde{v}_\alpha^2 \tilde{\mathbf{v}}_\alpha\rangle \quad \textit{(heat flow)}\,, \tag{32}$$

$$\mathbf{R}_\alpha(\mathbf{r},t) \equiv m_\alpha \int C_{\alpha\beta}\tilde{\mathbf{v}}_\alpha d^3v \quad \textit{(momentum transfer)}, \tag{33}$$

$$Q_\alpha(\mathbf{r},t) \equiv \tfrac{1}{2} m_\alpha \int C_{\alpha\beta}\, \tilde{v}_\alpha^2\, d^3v \quad \textit{(heat transfer)}\,. \tag{34}$$

Note that in this notation $\mathbf{I}$ is the unit tensor, i.e. $\boldsymbol{\pi}_\alpha$ represents the off-diagonal terms of the pressure tensor $\mathbf{P}$. For instance, the *Maxwell distribution* for thermal equilibrium:

$$f_\alpha^0(\mathbf{r},\mathbf{v},t) = n_\alpha \left(\frac{m_\alpha}{2\pi k T_\alpha}\right)^{3/2} \exp\left(-\frac{m_\alpha \tilde{v}_\alpha^2}{2kT_\alpha}\right), \tag{35}$$

is consistent with these definitions and makes the LHS of the Boltzmann equation (12) vanish. This means that the collision term on the RHS should vanish too, i.e. when the two distributions have equal average velocities ($\mathbf{u}_e = \mathbf{u}_i$) and temperatures ($T_e = T_i$). The deviations from this thermal equilibrium and the way in which collisions cause relaxation to thermal equilibrium, is what plasma kinetic theory is concerned with (Braginskii [5]).

(b) The temperature evolution equation is then transformed into a pressure evolution equation by introducing the ratio of specific heats, $\gamma \equiv C_p/C_v = 5/3$. The resulting equations for n_α, $\mathbf{u}_\alpha$, and p_α then appear rather macroscopic, but still hide unsolved kinetic dependencies involving higher order moments and variables which involve the unspecified collision operator.

(c) The obtained truncated set of moment equations is then finally closed by exploiting the transport coefficients derived by *transport theory* (Braginskii [5], Balescu [3]), which concerns the deviations from local thermodynamic equilibrium, expressed by Eq. (35). In this theory the distribution functions are developed in powers of a small parameter measuring these deviations. This results in *transport coefficients*, determining relations between the thermal quantities defined in Eqs. (30)–(34) and the gradients of the macroscopic quantities. The second objective of kinetic theory is to provide these coefficients, which is again a formidable task.

Following [2], we will now present an application of the two-fluid description (Section 5). It will be highly simplified in the sense that most of the complicated terms discussed above do not occur. Yet, this simple application illustrates a very important basic physical mechanism at work, namely collective electrostatic oscillations. After that, we will return to the kinetic description in terms of distribution functions and discuss how velocity space effects lead to Landau damping, a surprising kinetic phenomenon (Section 6).

5 Collective phenomena: plasma oscillations

Chen [7] defines a plasma as *a quasi-neutral gas of charged and neutral particles which exhibits collective behaviour*. The typical size of a region in the plasma over which charge imbalance due to thermal fluctuations may occur, is the *Debye length*. In the present section, we will extend these electric field concepts. We will first study perturbations of quasi-neutrality in a cold plasma by typical *plasma oscillations* which are called Langmuir waves (1929) [1]. We then study how these oscillations are affected by finite temperatures; first by including a finite pressure, next by taking into account velocity space effects by applying the kinetic equations, which will lead to the concept of *Landau damping*.

[1] named after the author who also introduced the term 'plasma' in 1923

5.1 Cold plasma oscillations

We start by considering a highly simplified case, viz. that of a cold plasma in the absence of a magnetic field ($\mathbf{B} = 0$). In other words, all thermal effects are neglected ($\mathbf{P}_\alpha$, $\mathbf{h}_\alpha$, $\mathbf{R}_\alpha$, and Q_α vanish). As a result, all the complicated terms in the equations of motion vanish and the energy equations can be dropped. For cold plasma oscillations we thus just need to consider the continuity equations,

$$\frac{\partial n_\alpha}{\partial t} + \nabla \cdot (n_\alpha \mathbf{u}_\alpha) = 0 \qquad (\alpha = e, i)\,, \tag{36}$$

and the simplified ($\mathbf{B} = 0$) momentum equations,

$$m_\alpha \Big(\frac{\partial \mathbf{u}_\alpha}{\partial t} + \mathbf{u}_\alpha \cdot \nabla \mathbf{u}_\alpha \Big) = q_\alpha \, \mathbf{E} \qquad (\alpha = e, i)\,. \tag{37}$$

The *Poisson equation* (13)(c) then enables us to determine the electric field in a self-consist manner, where *the charge density* is obtained from Eq. (14)(a):

$$\nabla \cdot \mathbf{E} = \frac{\tau}{\epsilon_0} = \frac{e}{\epsilon_0} \left(Z n_i - n_e \right). \tag{38}$$

Remark that these equations form a complete set for the variables $n_{e,i}(\mathbf{r}, t)$, $\mathbf{u}_{e,i}(\mathbf{r}, t)$, and $\mathbf{E}(\mathbf{r}, t)$ which describe the problem of electrostatic oscillations.

One of the most fundamental properties of plasmas is that they maintain approximate charge neutrality. As a matter of fact, charge imbalances on a macroscopic scale L would create huge electric fields ($E \sim \tau L/\epsilon_0$) which would accelerate the electrons and thus neutralise these imbalances extremely fast. As a result, the plasma maintains almost perfect charge neutrality.

Charge imbalances do occur, however, on a finer time and length scale, viz. in the form of typical oscillations. For these plasma oscillations, we can consider the heavy ions ($m_i \gg m_e$) as a fixed ($\mathbf{u}_i = 0$) neutralising background in which only the light electrons move ($\mathbf{u}_e \neq 0$). When a small region inside the plasma is then perturbed, by displacing the electrons in that region, the charge neutrality is disturbed ($n_e \neq Z n_i$). The problem is then completely determined by the electron variables (the two ion equations (36) and (37) for $\alpha = i$ may be dropped):

$$\begin{aligned} n_e &\approx n_0 + n_1(\mathbf{r}, t)\,, \\ \mathbf{u}_e &\approx \qquad \mathbf{u}_1(\mathbf{r}, t)\,, \end{aligned} \tag{39}$$

whereas the ion variables simplify to

$$n_i \approx n_0/Z = \text{const}\,, \qquad \mathbf{u}_i \approx 0\,. \tag{40}$$

Here, the subscripts 0 and 1 refer to the constant background and the (small) perturbations, respectively. The small density perturbation $|n_1(\mathbf{r},t)| \ll n_0$ occurs in a small region of the plasma. We can thus *linearize* the equations, i.e. we can neglect terms involving products of perturbations since these are much smaller than the linear terms. As a result, the small electric field $\mathbf{E}_1$ that is created is proportional to n_1 and creates a small electron flow velocity $\mathbf{u}_1$, which is also proportional to n_1.

A complete set of equations is thus obtained, consisting of the linearized electron density equation (36), the momentum equation (37) (both with $\alpha = e$), and the Poisson equation (38):

$$\begin{aligned} &\frac{\partial n_1}{\partial t} + n_0 \nabla\cdot\mathbf{u}_1 = 0\,,\\ &m_e \frac{\partial \mathbf{u}_1}{\partial t} = -e\mathbf{E}_1\,,\\ &\nabla\cdot\mathbf{E}_1 = \frac{\tau_1}{\epsilon_0} = -\frac{e}{\epsilon_0}\,n_1\,. \end{aligned} \tag{41}$$

Eliminating $\mathbf{u}_1$ and $\mathbf{E}_1$ then yields a single wave equation for n_1:

$$\frac{\partial^2 n_1}{\partial t^2} = -n_0\nabla\cdot\frac{\partial \mathbf{u}_1}{\partial t} = \frac{n_0 e}{m_e}\nabla\cdot\mathbf{E}_1 = -\frac{n_0 e^2}{\epsilon_0 m_e}\,n_1\,. \tag{42}$$

5.2 Plasma frequency and Debye length

The solutions of the wave equation (42) can be written in the form $n_1(\mathbf{r},t) = \hat{n}_1(\mathbf{r})\exp(-\mathrm{i}\omega t)$. They represent *plasma oscillations*, which are electron density oscillations with a characteristic frequency, called *the electron plasma frequency*:

$$\omega = \pm\omega_{pe}\,, \quad \omega_{pe} \equiv \sqrt{\frac{n_0 e^2}{\epsilon_0 m_e}}\,. \tag{43}$$

This frequency is one of the fundamental parameters of a plasma and is usually very high (because m_e is very small). It provides a diagnostic for the determination of the plasma density since it depends only the plasma density. In tokamak plasmas, a typical density $n_0 = 10^{20}\,\mathrm{m}^{-3}$ gives

$$\omega_{pe} = 5.7\times10^{11}\,\mathrm{rad\,s^{-1}} \quad (\text{i.e. } 91\,\mathrm{GHz})\,,$$

which is of the same order of magnitude as the electron cyclotron frequency for tokamaks with very strong magnetic fields ($B \sim 3\,\mathrm{T}$).

Remark that in cold plasma theory the spatial form of the amplitude $\hat{n}_1(\mathbf{r})$ of the plasma oscillations is not determined. This is different for 'warm' plasmas, where deviations from charge neutrality due to thermal fluctuations occur in small regions of a size of the order of the *Debye length*

$$\lambda_\mathrm{D} \equiv \sqrt{\frac{\epsilon_0 k_\mathrm{B} T_e}{n_0 e^2}} = \frac{v_{\mathrm{th},e}}{\sqrt{2}\,\omega_{pe}}\,. \tag{44}$$

Note that we here indicate the Boltzmann constant with a subscript, k_B, to distinguish it from the wave number k of the waves that now enters the analysis. For thermonuclear plasmas, with $T = 10\,\mathrm{keV}$, $v_{\mathrm{th},e} = 5.9\times10^7\,\mathrm{m\,s^{-1}}$, $\omega_{pe} = 5.7\times10^{11}\,\mathrm{rad\,s^{-1}}$ gives

$$\lambda_\mathrm{D} = 7.4\times10^{-5}\,\mathrm{m} \approx 0.07\,\mathrm{mm}\,,$$

i.e. the Debye length is of the order of the electron gyroradius R_e.

5.3 (Finite pressure) Plasma oscillations

In warm plasmas, the frequency of the plasma oscillations becomes dependent on the wavelength because of the above-mentioned thermal fluctuations. The thermal contributions may be computed by means of the two-fluid equations for an unmagnetised plasma ($\mathbf{B} = 0$), assuming an isotropic pressure and neglecting heat transport and collisions. Assuming immobile ions again and linearising these equations for the electrons, like we did before for a cold plasma, we now get a modified eigenvalue problem where the pressure $p_0 = n_0 k_\mathrm{B} T_0$, i.e. the temperature, of the background plasma enters:

$$\frac{\partial n_1}{\partial t} + n_0\nabla\cdot\mathbf{u}_1 = 0\,, \tag{45}$$

$$n_0 m_e \frac{\partial \mathbf{u}_1}{\partial t} + \nabla p_1 = -e n_0 \mathbf{E}_1\,, \tag{46}$$

$$\frac{\partial p_1}{\partial t} + \gamma p_0 \nabla\cdot\mathbf{u}_1 = 0\,, \tag{47}$$

$$\nabla\cdot\mathbf{E}_1 = -\frac{e}{\epsilon_0}\,n_1\,. \tag{48}$$

Assuming plane waves in the x-direction, and ignoring spatial dependencies in the y- and z-directions,

$$n_1(x,t) = \hat{n}_1 \mathrm{e}^{\mathrm{i}(kx-\omega t)}, \tag{49}$$

(and similar expressions for $\mathbf{u}_1$, p_1, $\mathbf{E}_1$), the gradients $\nabla \to \mathrm{i}k\mathbf{e}_x$ and the time derivatives $\partial/\partial t \to -\mathrm{i}\omega$, so that Eqs. (45)–(48) become an algebraic system of equations for the amplitudes $\hat{n}_1$, $\hat{\mathbf{u}}_1$, $\hat{p}_1$, and $\hat{\mathbf{E}}_1$. The dispersion equation is obtained from the determinant and reads

$$\omega^2 = \omega_{pe}^2(1+\gamma k^2\lambda_{\mathrm{D}}^2)\,. \tag{50}$$

Notice that here, since the oscillations are one-dimensional, we should exploit the value $\gamma = 3$ (see Chen [7], Chapter 4). Remark that the (c)old result (43) is recovered for long wavelengths, where $k^2\lambda_{\mathrm{D}}^2 \ll 1$, but there is a large effect now on the oscillations for wavelengths of the order of or smaller than the Debye length. However, this thermal correction of the dependence of ω on k turns out to be incomplete as misses the damping obtained in the proper kinetic derivation. We will discuss this briefly in the next section.

6 Collective phenomena: Landau damping

Following Goedbloed, Keppens, and Poedts [2], we remark that a more refined analysis of longitudinal plasma oscillations for 'warm' plasmas should take velocity space effects into account, exploiting the Vlasov, or *collisionless* Boltzmann, equation (12) (with vanishing RHS) for the perturbations $f_1(\mathbf{r},\mathbf{v},t)$ of the electron distribution function. Considering again plane wave solutions $\sim \exp \mathrm{i}(\mathbf{k}\cdot\mathbf{r}-\omega t)$, one immediately runs into a mathematical problem:

$$\frac{\partial f_1}{\partial t} + \mathbf{v}\cdot\frac{\partial f_1}{\partial \mathbf{r}} = -\mathrm{i}(\omega - \mathbf{k}\cdot\mathbf{v})\, f_1 = \frac{e}{m_e}\mathbf{E}_1\cdot\frac{\partial f_0}{\partial \mathbf{v}}\,, \tag{51}$$

so that inversion of the operator $\partial/\partial t + \mathbf{v}\cdot\partial/\partial\mathbf{r}$, to express f_1 in terms of $\mathbf{E}_1$, leads to singularities for every $\omega - \mathbf{k}\cdot\mathbf{v} = 0$. Landau (1946) [9] performed a proper treatment of the related initial value problem, and showed that these singularities give rise to damping of the plasma oscillations, now called *Landau damping*. Since there is no dissipation as we are considering a purely collisionless medium here, this is a surprising phenomenon! Twenty years later, Malmberg and Wharton [12] verified the phenomenon of Landau damping experimentally. In fact, later (1968) these authors also demonstrated that the information contained in the initial signal may be recovered by means of plasma wave echos, i.e. it is not lost [13].

Van Kampen (1955) [18, 19] considered a complementary approach to the electrostatic plasma oscillations by means of a normal mode analysis. In this approach, the singularities $\omega - \mathbf{k}\cdot\mathbf{v} = 0$ lead to a continuous spectrum of singular, δ-function type, modes (the Van Kampen modes), which constitute a complete set of 'improper' eigenmodes for this system. Damping occurs because of *phase mixing*, a package of those modes rapidly loses its spatial phase coherence.

6.1 Landau's solution of the initial value problem

For a more careful analysis, which is beyond the level of this introductory chapter, we refer to Goedbloed, Keppens, and Poedts [2].

Landau's careful study of the initial value problem of electrostatic plasma oscillations shows that there is an important contribution of the singularities $v = v_{\mathrm{ph}} \equiv \omega/k$ where the particles are in resonance with the phase velocity of the waves. For a Maxwell distribution, the solution of the dispersion equation (obtained by Landau) for long wavelengths ($k\lambda_{\mathrm{D}} \ll 1$) is given by

$$\omega \approx \omega_{pe}\Big\{1+\tfrac{3}{2}k^2\lambda_{\mathrm{D}}^2 - \mathrm{i}\sqrt{\tfrac{\pi}{8}}\,(k\lambda_{\mathrm{D}})^{-3}\, e^{-\frac{1}{2}(k\lambda_{\mathrm{D}})^{-2}-\frac{3}{2}}\Big\}, \tag{52}$$

where the imaginary part represents *damping of the waves*. For long wavelengths, this damping is exponentially small. For short wavelengths ($k\lambda_{\mathrm{D}} \sim 1$), the damping becomes very strong so that wave motion with wavelengths smaller than the Debye length becomes impossible.

7 Kinetic processes in the solar wind

7.1 Proton and electron distribution data

Kinetic theory is necessary to explain observations of the velocity distribution functions of protons and electrons at 1 au (about the average distance from the Sun to the Earth, 149 597 871 kilometers). Old Helios observations[14] of proton distributions show a variety of temperature anisotropies. Some examples are given in Fig. 2 which shows cuts through the velocity distribution functions (VDFs) in the ecliptic plane. The left column shows the proton distribution in the slow wind (with typical velocity of 300-350 km/s) at different distances from the Sun. Helios went all the way to 0.3 au[2]. The right column shows the same for the fast solar wind (typically 700 km/s) and the middle column corresponds to the intermediate wind. The dashed lines represent the local magnetic field.

The coloured isocontours of the VDFs displayed in Fig. 2 show that they come in a variety of shapes. The proton distribution is highly anisotropic: the perpendicular temperature $T_\perp$ is higher than the parallel temperature $T_\parallel$, which is most apparent in the proton distributions at low heliospheric distances and in the intermediate and fast solar wind (middle and RHS bottom plots in Fig. 2. Moreover, the proton distribution has a core part (red and orange contours) and a slightly drifting suprathermal 'halo' part (the blue contours). Some distributions are deformed by the asymmetric (magnetic field aligned) beam or 'strahl', which is also suprathermal and most apparent in the intermediate wind distribution at 0.39 au. The electron distributions (not shown here) are similar although they have a less anisotropic core. They also have a suprathermal halo and the electron distribution s are also deformed by an asymmetric (field aligned) strahl.

These features of the observed proton and electron distribution functions in the solar wind can be described with combinations non-Maxwellian and kappa distribution functions and explained by kinetic theory. In fact, the observed temperature anisotropy is much higher than theory predicts, so there must be some additional perpendicular heating going on to explain this.

[2]Actually, Helios A (launched in December 1974) went as close to the Sun as 0.31 au and Helios B (launched in January 1976) even to 0.29 au (= 43 432 million km).

7.2 Modelling the velocity distribution functions

The complicated VDFs shown in Fig. 2 are modelled in (linear) theory using distribution functions with a (bi-)Maxwellian quasi-thermal core, like

$$f_{\rm core}(v_\parallel, v_\perp) = n_c C_M \exp\left[-\frac{v_\parallel^2}{w_\parallel^2} - \frac{v_\perp^2}{w_\perp^2}\right], \qquad (53)$$

while the non-thermal component is described by different Kappa distribution functions. The suprathermal halo, for instance, can be modelled by a bi-Kappa distribution function:

$$f_{\rm halo}(v_\parallel, v_\perp) = n_h C_\kappa \left[-\frac{v_\parallel^2}{\kappa\theta_\parallel^2} - \frac{v_\perp^2}{\kappa\theta_\perp^2}\right]^{-\kappa-1}, \qquad (54)$$

while the suprathermal, asymmetric (magnetically field-aligned) strahl or beam can be modelled by a drifting Kappa distribution function:

$$f_{\rm strahl}(v_\parallel, v_\perp) = n_s C'_\kappa \left[-\frac{(v_\parallel - V_0)^2}{\kappa'\theta^2} - \frac{v_\perp^2}{\kappa'\theta^2}\right]^{-\kappa'-1}. \qquad (55)$$

An example of such a complicated VDF with a bi-Maxwellian core, a bi-kappa halo, and a drifting Kappa strahl, is shown in Fig. 3. So the non-thermal part is split in a halo and a strahl both modelled by kappa distributions.

7.3 Occurrence rates of the temperature anisotropy

A summary of the solar wind distribution at 1 au (Earth orbit) is given in Figures 4 (core + halo protons) and 5 (core electrons). These figures contain millions of data points from different spacecraft (mostly WIND) over decades summarised in 2D plots. They have been produced by Peter Yoon who combined data from different sources[17, 1, 15, 10, 11]. At 1 au most protons are broadly distributed near quasi-isotropic conditions (the red dot in the meddle). The proton data distribution boundaries have a strange shape. It turns out that this outer boundary can be explained by kinetic processes, namely instabilities and collisions.

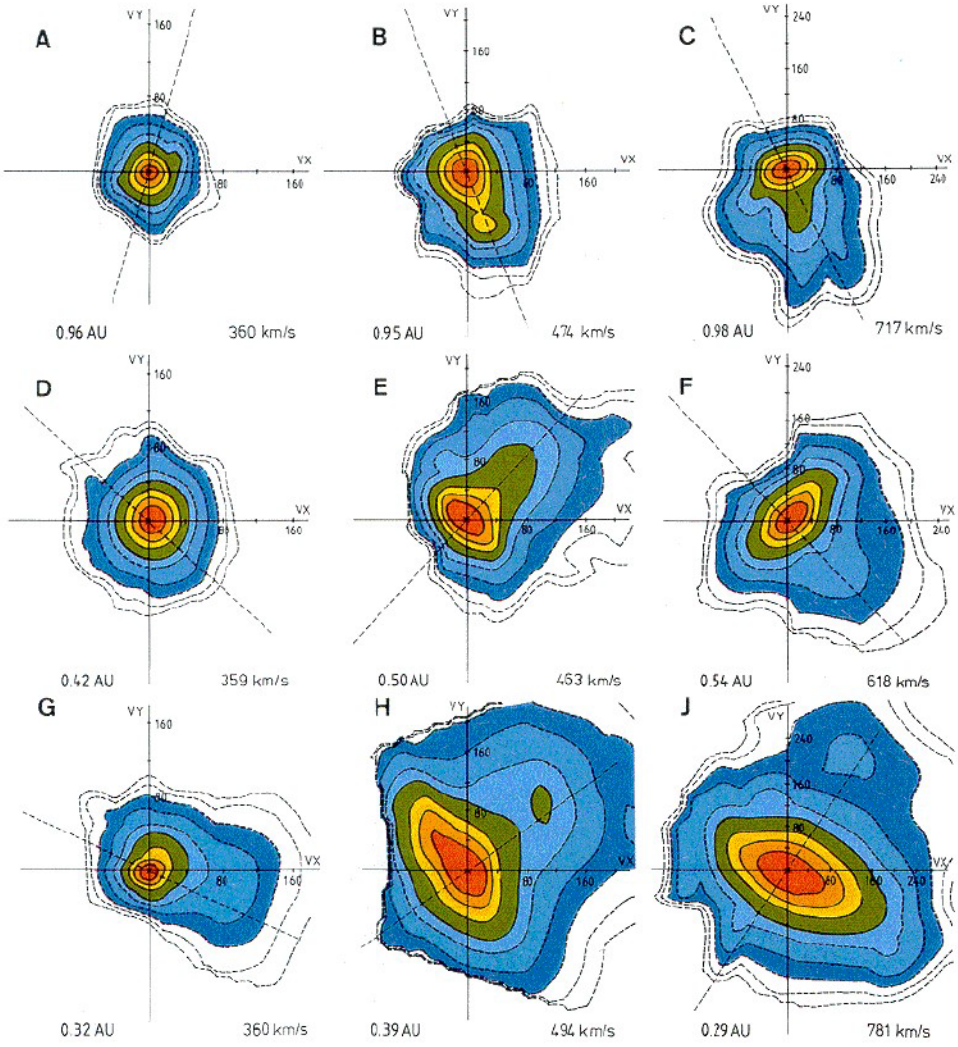

Figure 2: Proton velocity distribution functions in the solar wind near the perihelion of the Helios spacecraft and farther out. The VDFs have different shapes. Some are isotropic, others are anisotropic in perpendicular temperature and some are asymmetric, showing a magnetic field-aligned beam of 'strahl'. From Marsch[14]

11

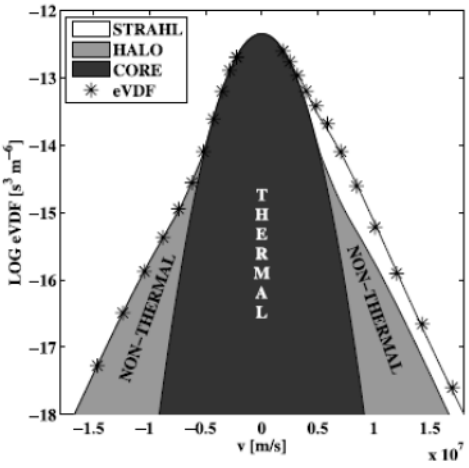

Figure 3: The modified model used for electron distributions by Štverák et al.[17] contains a thermal core and a non-thermal part consisting of a halo and a strahl, which gives a better estimate of their relative densities.

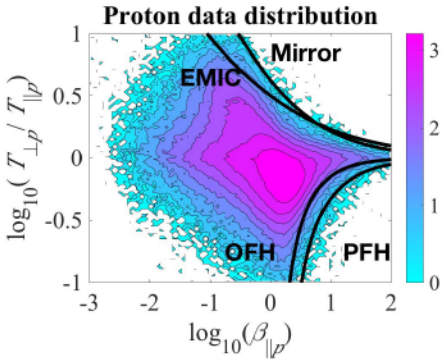

Figure 4: Log-log plot of the occurrence rates of the proton temperature anisotropy $T_{\perp p}/T_{\parallel p}$ versus the parallel plasma beta $\beta_{\parallel p}$ for the entire (core + halo) proton population in the solar wind at 1 au (Earth orbit). The over-plotted curves represent the marginal stability threshold for the indicated instabilities. Credit: Peter Yoon.

The core of the electron data distribution shown in Fig. 5 shows a similar behaviour. The halo electron data distribution, not shown here, is somewhat less anisotropic.

7.4 Kinetic processes behind the temperature anisotropy

The proton and electron data distributions shown in Figs. 4 and 5 show strange outer boundaries to the right. These can be explained by a number of marginal kinetic instability thresholds. When $T_\perp > T_\parallel$, there are electromagnetic electron cyclotron (whistler) instability (EMEC) and electromagnetic ion (proton) cyclotron instability (EMIC) and mirror instabilities with their marginal thresholds indicated in Figs. 4 and 5 (black lines at upper right boundaries). And when $T_\parallel > T_\perp$, there are the parallel proton (PFH) and electron (EFH) firehose and oblique proton firehose (OFH) instability thresholds, all indicated in Figs. 4 and 5 (black lines in lower right boundaries). The firehose modes and mirror modes are basically fluid modes, but kinetic theory provides a better

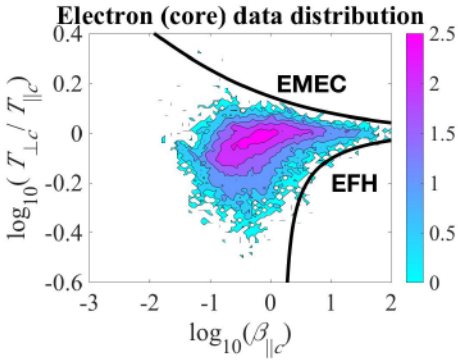

Figure 5: Log-log plot of the occurrence rates of the electron temperature anisotropy $T_{\perp e}/T_{\parallel e}$ versus the parallel plasma beta $\beta_{\parallel e}$ for the core electron population in the solar wind at 1 au. The over-plotted curves represent the marginal stability threshold for the EMEC nd EFH instabilities. Credit: Peter Yoon.

description of these instabilities. EMIC is clearly a kinetic instability.

The same EMEC/whistler and EFH marginal stability thresholds define the right outer boundaries of the hot (halo) component of the electron data distribution. So the thresholds of these instabilities determine the right outer boundaries of the distributions mentioned before from marginal stability conditions, which is linear theory.

7.5 Quasi-linear theory

However, linear theory does not take into account the dynamics, the changes of the background inhomogeneity, as it assumes it is in equilibrium. To take the background dynamics into account a nonlinear theory is needed. Quasi-linear theory describes the slow evolution of the distribution functions and their relaxation back to a marginally stable state. Quasi-linear theory is limited solely to determining how the distribution functions relax and, therefore, the simplest nonlinear theory. But it partially explains the observed outer boundaries. According to quasi-linear theory, $T_\parallel$ and $T_\perp$ evolve due to these instabilities and so do the magnetic field perturbations. Quasi-linear theory yields a dispersion relation for parallel propagation, so EMIC [16].

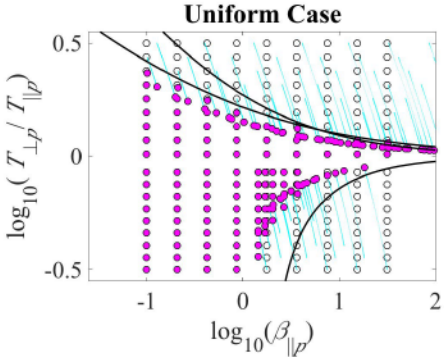

Figure 6: Log-log plot of the proton temperature anisotropy $T_{\perp p}/T_{\parallel p}$ versus the parallel plasma beta $\beta_{\parallel p}$ of the results obtained by solving the equations from quasi-linear theory. Credit: Peter Yoon.

Solving the equations of quasi-linear theory[16], results in the plot shown in Fig. 6 created by Peter Yoon. The open white dots are some hypothetical initial conditions. When unstable, they move to the marginal stability threshold and are coloured when they reach their final, marginally stable position. When the initial conditions are stable, they stay in place and are coloured too. The outer boundaries on the RHS are more or less reproduced like this, which you can see on the right and by comparing this figure with Fig. 4.

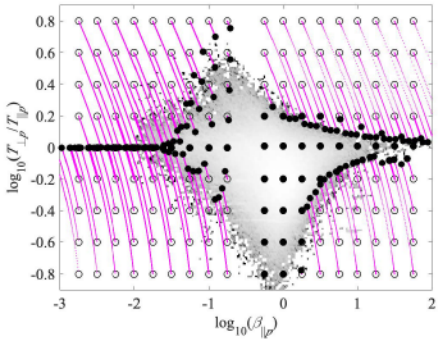

Figure 7: $T_{\perp p}/T_{\parallel p}$ versus $\beta_{\parallel p}$ log-log plot of the results obtained by solving the relaxation equations for binary collisions combined with the equations from quasi-linear theory from Fig. 6. Credit: Peter Yoon.

For explaining the boundaries to the left another kinetic process is needed. Indeed, when there are no instabilities operative, one has to bring in some other kinetic relaxation process, namely binary collisions. The relaxation equations for binary collisions[16] can be solved/relaxed as before. The result is seen in Fig. 7, which is again created by Peter Yoon and which is a combined figure showing the effect of collisions and instabilities at the same time. The white dots (representing initial conditions) move along the magenta lines and all settle down, according to the collision relaxation equations, and they are coloured black when they do. Hence, combining the quasi-linear equations with the relaxation equations results in Fig. 7 which can be directly compared to Fig. 4.

The points to the upper right are EMIC unstable and move down close to EMIC marginal stability threshold. Points to the lower RHS are firehose unstable and move up, lining up along the firehose marginal stability threshold. All the points to the left, on the other hand, are not unstable but they respond to collisions. They also move and line up. The result nicely fits the outer boundaries of the proton data distribution on the left as seen by comparing this figure to the data (Fig. 4): a nice example of how you can involve kinetic processes to explain observations.

8 From kinetic theory to fluid description

In this section we come back to the text of Goedbloed, Keppens, and Poedts [2]. We have seen that kinetic theory involves the detailed evolution of the distribution functions on very short length and time scales, such as the Debye length $\lambda_{\rm D}$ and the plasma frequency ω_{pe}. The development of the fluid picture of plasmas from the kinetic theory involves three major steps, illustrated in Fig. 8:

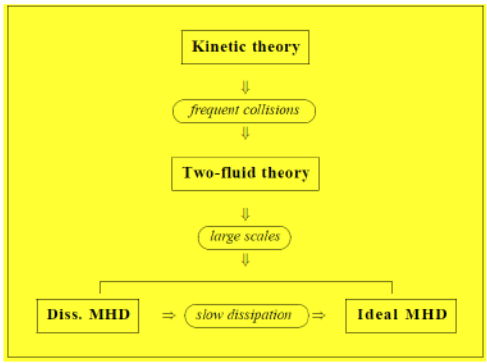

Figure 8: Different theoretical plasma models and their connections. Source Goedbloed, Keppens and Poedts[2].

(a) Collisionality The formulation of the lowest moments (26)–(28) of the Boltzmann equation in Section 4 and the transport closure relations mentioned there, was the first step, yielding a system of *two-fluid equations* in terms of the ten variables $n_{e,i}$, $\mathbf{u}_{e,i}$, $T_{e,i}$. To establish the two fluids, the electrons and ions must undergo frequent collisions:

$$\tau_{\rm H} \gg \tau_i \quad \left[\gg \tau_e \right], \tag{56}$$

with $\tau_{\rm H}$ the time scale on which the hydrodynamic description is valid, while τ_e and τ_i indicate the collisional relaxation times of the electrons and ions respectively.

(b) Macroscopic scales Since the two-fluid equations still involves the small length and time scales of the fundamental phenomena we have encountered, viz. the plasma frequency ω_{pe}, the cyclotron frequencies $\Omega_{e,i}$, the Debye length $\lambda_{\rm D}$, and the cyclotron radii $R_{e,i}$, the essential second step towards the *magnetohydrodynamics* (MHD) description of plasmas is to consider *large length and time scales*:

$$\lambda_{\rm MHD} \sim a \gg R_i\,, \qquad \tau_{\rm MHD} \sim a/v_{\rm A} \gg \Omega_i^{-1}\,. \tag{57}$$

Hence,the larger the magnetic field strength, the more easy these conditions are satisfied. On these scales, the plasma is considered as a *single* conducting fluid without distinguishing its individual species.

(c) Ideal fluids The third and final step is to consider the plasma dynamics on time scales *faster* than the *slow dissipation* connected with the decay of the macroscopic variables, in particular the resistive decay of the magnetic field:

$$\tau_{\rm MHD} \ll \tau_{\rm R} \sim a^2/\eta\,. \tag{58}$$

This condition is well satisfied for the relatively small sizes of fusion machines, and very easily for the huge sizes of astrophysical plasmas, and leads to the model of *ideal MHD*, which provides a solid macroscopic description of magnetised plasmas.

Acknowledgments

I thank Peter Yoon for kindly providing Figures 4, 5, 6, and 7. These results were obtained in the framework of the projects C14/19/089 (C1 project Internal Funds KU Leuven), G.0D07.19N (FWO-Vlaanderen), SIDC Data Exploitation (ESA Prodex-12), and Belspo projects

BR/165/A2/CCSOM and B2/191/P1/SWiM. For the computations we used the infrastructure of the VSC – Flemish Supercomputer Center, funded by the Hercules foundation and the Flemish Government – department EWI.

References

[1] S.D. Bale, J.C. Kasper, G.G. Howes, E. Quataert, C. Salem, D. Sundkvist, *Phys. Rev. Lett.* **103**, 211101 (2009).

[2] J.P. Goedbloed, R. Keppens and S. Poedts: "Magnetohydrodynamics of laboratory and astrophysical plasmas", Cambridge University Press, 2019. ISBN: 9781107123922

[3] R. Balescu, *Transport Processes in Plasmas; Vol. 1: Classical Transport Theory, Vol. 2: Neoclassical Transport* (Amsterdam, North Holland, 1988).

[4] J. A. Bittencourt, *Fundamentals of Plasma Physics* (New York, Pergamon Press, 1986); 2nd edition (Brazil, Foundation of the State of São Paulo for the Support of Research, 1995).

[5] S. I. Braginskii, 'Transport processes in a plasma', in *Reviews of Plasma Physics, Vol. 1*, ed. M. A. Leontovich (New York, Consultants Bureau, 1965), pp. 205–311.

[6] H. Goldstein, *Classical Mechanics*, 2nd edition (Reading, Addison Wesley, 1980).

[7] F. C. Chen, *Introduction to Plasma Physics and Controlled Fusion, Vol. I: Plasma Physics*, 2nd edition (New York, Plenum Press, 1984).

[8] L. D. Landau, 'The transport equation in the case of Coulomb interactions', *J. Exp. Theor. Phys. USSR* **7** (1937), 203. [Transl.: *Phys. Z. Sowjet.* **10** (1936), 154; or *Collected Papers of L. D. Landau*, ed. D. ter Haar (Oxford, Pergamom Press, 1965) pp. 163–170.]

[9] L. D. Landau, 'On the vibrations of the electronic plasma', *J. Phys. USSR* **10** (1946), 25. [Transl.: *JETP* **16** (1946), 574; or *Collected Papers of L.D. Landau*, ed. D. ter Haar (Oxford, Pergamom Press, 1965) pp. 445–460.]

[10] M. Lazar, V. Pierrard, S.M. Shaaban, H. Fichtner, S. Poedts, 'Dual Maxwellian-Kappa modelling of the solar wind electrons: new clues on the temperature of Kappa populations', *Astron. Astrophys.* **602** (2017), A44.

[11] M. Lazar, S.M. Shaaban, S. Poedts, Š. Štverák, 'Firehose constraints of the bi-Kappa distributed electrons: a zero-order approach for the suprathermal electrons in the solar wind', *Monthly Not. Roy. Astron. Soc.* **464**, 564-571 (2017).

[12] J. H. Malmberg and C. B. Wharton, 'Dispersion of electron plasma waves', *Phys. Rev. Lett.* **17**, 175–178 (1966).

[13] J. H. Malmberg, C. B. Wharton, R. W. Gould and T. M. O'Neil, 'Observation of plasma wave echos', *Phys. Fluids* **11** (1968), 1147–1153.

[14] E. Marsch, R. Schwenn, H. Rosenbauer, K.-H. Muehlhaeuser, W. Pilipp, F.-M. Neubauer, 'Solar wind protons: Three-dimensional velocity distributions and derived plasma parameters measured between 0.3 and 1 AU', *J. Geophys. Res.* **87** (1982), 52-72.

[15] M.J. Michno, M. Lazar, P.H. Yoon, R. Schlickeiser, *Astrophys. J.* **781**, 49 (5pp), 2014.

[16] S.M. Shaaban, M. Lazar, P.H. Yoon, S.Poedts, *Astrophys. J.* **871**, 237 (11pp), 2019.

[17] Š. Štverák, P. Trávníček, M. Maksimovic, E. Marsch, A.N. Fazakerley, E.E. Scime, Journal of Geophysical Research (Space Physics), **113**, A03103 (2008).

[18] N. G. van Kampen, 'On the theory of stationary waves in plasmas', *Physica* **21** (1955), 949–963.

[19] N. G. van Kampen and B. U. Felderhof, *Theoretical Methods in Plasma Physics* (Amsterdam, North-Holland Publishing Company, 1967).

[20] A. A. Vlasov, 'The oscillation properties of an electron gas', *Zhur. Eksp. Teor. Fiz.* **8** (1938), 291–318; 'Vibrational poperties, crystal structure, non-dissipated counterdirected currents and spontaneous origin of these properties in a "gas" ', *J. Phys. USSR* **9** (1945), 25–40.

KINETIC PLASMA SIMULATIONS: PARTICLE IN CELL METHOD

G. Lapenta[1] and F. Pucci[2,1]

[1] *Centre for mathematical Plasma Astrophysics, Department of Mathematics, Katholieke Universiteit Leuven, Celestijnenlaan 200B, B-3001 Leuven, Belgium*

[2] *Istituto per la Scienza e Teconologia dei Plasmi, Consiglio Nazionale delle Ricerche (ISTP-CNR), Via Amendola 122/D, 70126 Bari, Italy*

ABSTRACT

In this paper, we present a brief introduction to the Particle in Cell (PIC) method for solving the Vlasov-Maxwell system of equations for a multi-species plasma. First, we recall the basic equations of electromagnetism and the physical difference between strongly and weakly coupled systems (sec. I-III). Second, the different numerical treatments for these two types of system are presented (sec. IV-V). Third, the mathematical derivation of the PIC method is presented in the one-dimensional electrostatic regime (sec. VI-X). Finally, a recapitulation of the PIC method is given (sec. XI).

I. INTRODUCTION

The classical or relativistic description of the natural world is based on describing the interaction of elements of matter via force fields. The example that will guide the discussion is that of a plasma composed of charged particles but the discussion would be similar and easily replicated for the case of gravitational forces. In the case of a plasma, the system is composed by charged particles (for example negative electrons and positive ions) interacting via electric and magnetic fields.

If we identify each particle with a label p and their charge with q_p, position with $\mathbf{x}_p$, position with $\mathbf{v}_p$, the force acting on the particles is the combination of the electric and magnetic (Lorentz) force:

$$\mathbf{F}_p = q_p \mathbf{E}(\mathbf{x}_p) + \mathbf{v}_p \times \mathbf{B}_p(\mathbf{x}_p) \tag{1}$$

The force acting on the particles is computed from the electric and magnetic fields evaluated at the particle position.

The electric and magnetic fields are themselves created by the particles in the system and by additional sources outside the system (for example magnets around the plasma or external electrodes). The fields are computed by solving the Maxwell's equations:

$$\begin{aligned} \nabla \cdot \mathbf{E} &= \frac{\rho}{\epsilon_0} & \nabla \times \mathbf{E} &= -\frac{\partial \mathbf{B}}{\partial t} \\ \nabla \cdot \mathbf{B} &= 0 & \nabla \times \mathbf{B} &= \mu_0 \mathbf{J} + \mu_0 \epsilon_0 \frac{\partial \mathbf{E}}{\partial t} \end{aligned} \tag{2}$$

II. TYPES OF INTERACTING SYSTEMS

A key point in the derivation of the particle in cell method is the consideration of how the sources in the Maxwell's equations ought to be computed. In principle since the system is made of a collection of particles of infinitesimal size, the sources of the Maxwell's equations are distributions of contributions one for each particle.

Figure 1 summarises visually the situation. Let us consider a system made by a collection of particles, each carrying a charge situated in a box with the side of the Debye length, λ_D (the box is 3D but is depicted as 2D for convenience). We choose the Debye length because a basic property of plasmas is to shield the effects of localized charges over distances exceeding the Debye length. Of course the shielding is exponential and the effect is not totally cancelled over one Debye length, but such a length provides a conventional reasonable choice for the interaction range. The electric field in each point of the box is computed by the superposition of the contribution of each particle.

Let us conduct an ideal thought experiment based on using a experimental device able to detect the local electric field in one spatial position. Such an experimental device exists, but the determination of the local electric field remains a difficult but not impossible task. At any rate we try to conduct a thought experiment where in no step any law of physics is violated but where the difficulties of experimental work are eliminated.

If we consider the configuration in Fig. 1, we note that within the domain there are few particles and the measurement obtained by our fantastic electric field meter would be very jumpy. The particles in the box move constantly, interacting with each other and agitated by their thermal motion. As a particle

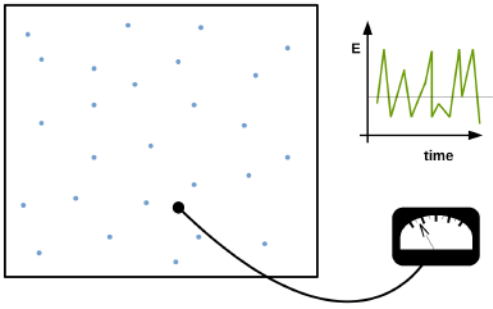

Figure 1: A strongly coupled system.

passes by the detector, the measurement detects a jump up and when a particle moves away it detects a jump down. On average at any given time very few particles are near the detector and their specific positions are key in determining the value measured. The effect of a given particle on the electric field at the location of measurement decays very rapidly with the distance and only when the particle is nearby the effect is strong.

The same effect is detected by each of the particles in the system. The electric field each particle feels is a the sum of the contributions of all others but only when another particle passes by the electric field would register a jump: in common term this event is called a collision. The particle trajectories would then be affected by a series of close encounters registered as jumps in the trajectory.

The system described goes in the language of kinetic theory as a *strongly coupled system*, a system where the evolution is determined by the close encounters and by the relative configuration of any two pairs of particles. The condition just described is characterised by the presence of few particles in the box: $N_D = n\lambda_D^3$ is small.

The opposite situation is that of a weakly coupled system. The corresponding configuration is described in Fig. 2.

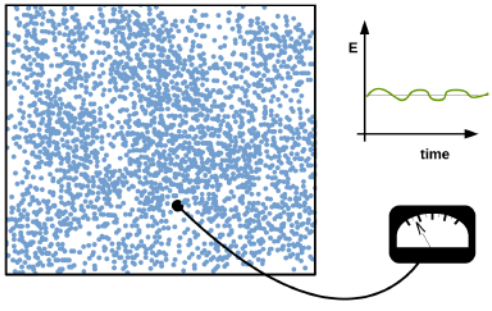

Figure 2: A weakly coupled system.

Now the system is characterised by being composed by an extremely large number of particles. In any given point, the number of particles contributing to the electric field is very large. Regardless of the particle motion, the field is given by the superposition of many contributions. As a consequence, by simple averaging of the effects of all the particles contributing to the measurement, the measurement is smooth and does not jump in time. Similarly the trajectory of a particle is at any time affected by a large number of other particles. The trajectory is smooth and without jumps. These systems are called *weakly coupled*. If in the strongly coupled system, the characteristic feature was the presence of a succession of collisions, in the weakly coupled system, the characteristic feature is the mean field produced by the superposition of contributions from a large number of particles.

III. DESCRIPTION OF INTERACTING SYSTEMS

The discriminant factor in the previous discussion was the number of particles present in the box under consideration. If we choose the conventional box with side equal to the Debye length, the number of particles present is

$$N_D = n\lambda_D^3 \tag{3}$$

where n is the plasma density.

A system is considered weakly coupled when N_D is large and strongly coupled when N_D is small.

This concept can be further elaborated by considering the energies of the particles in the system. The particles in the box are distributed in a non-uniform, random way, but on average, the volume associated with each particle is simply the volume of the box, λ_D^3, divided by the number of particles in the box, N_D. This volume, $V_p = n^{-1}$, can be used to determine the average interparticle distance, $a = V_p^{1/3} \equiv n^{-1/3}$. This relation provides an average statistical distance. The particles are distributed randomly and their distances are also random, but on average the interparticle distance is a.

The electrostatic potential energy between two particles with separation a is

$$E_{pot} = \frac{q^2}{4\pi\epsilon_0 a} \tag{4}$$

where we have assumed equal charge q for the two particles. Conversely, from statistical physics, the kinetic energy of the particles can be computed to be of the order of

$$E_{th} = kT \tag{5}$$

where k is the Boltzmann constant.

A useful measure of the plasma coupling is given by the so-called *plasma coupling parameter*, Λ, defined as:

$$\Lambda = \frac{E_{th}}{E_{pot}} = \frac{4\pi\epsilon_0 akT}{q^2} \tag{6}$$

Recalling the definition of Debye length ($\lambda_D = (\epsilon_0 kT/ne^2)^{1/2}$) and the value of a obtained above, it follows that:

$$\Lambda = \frac{4\pi\epsilon_0 kT}{q^2 n^{1/3}} \equiv 4\pi N_D^{2/3} \tag{7}$$

The plasma parameter gives a new physical meaning to the number of particles per Debye cube. When many particles are present in the Debye cube the thermal energy far exceed the potential energy, making the trajectory of each particle little influenced by the interactions with the other particles: this is the condition outlined above for the weakly coupled systems. Conversely, when the coupling parameter is small, the potential energy dominates and the trajectories are strongly affected by the near neighbour interactions: this is the condition typical of strongly coupled systems.

IV. COMPUTER SIMULATION

A computer simulation of a system of interacting particles can be conducted in principle by simply following each particle in the system. The so-called *particle-particle (PP)* approach describes the motion of N particles by evolving the equations of Newton for each of the N particles taking as a force acting on the particle the combined effect of all the other particles in the system.

The evolution is discretized in many temporal steps Δt, each chosen so that the particles move only a small distance, and after each move the force is recomputed and a new move is made for all the particles. If we identify the particle position and velocity as, respectively, $\mathbf{x}_p$ and $\mathbf{v}_p$, the equations of motion can be written as:

$$\begin{aligned} \mathbf{x}_p^{new} &= \mathbf{x}_p^{old} + \Delta t \mathbf{v}_p^{old} \\ \mathbf{v}_p^{new} &= \mathbf{v}_p^{old} + \Delta t \mathbf{F}_p \end{aligned} \tag{8}$$

The main cost of the effort is the computation of the force which requires to sum over all the particles in the system,

$$\mathbf{F}_p = \sum_{p'} \mathbf{F}_{pp'} \tag{9}$$

where $F_{pp'}$ is the interaction force between two particles p and p'. For example in the case of the electrostatic force,

$$\mathbf{F}_{pp'} = \frac{q_p q_{p'}}{4\pi\epsilon_0 |\mathbf{x}_p - \mathbf{x}_{p'}|^2} \cdot \frac{\mathbf{x}_p - \mathbf{x}_{p'}}{|\mathbf{x}_p - \mathbf{x}_{p'}|} \tag{10}$$

where in practice all forces are computed with the old values of the particle positions available at a given time. Once the force is computed the new velocities can be computed. Then the new positions can be computed and the cycle can be repeated indefinitely.

For each particle, the number of terms to sum to compute the force is $N-1$, and considering that there are N particles, but that each pair needs to be computed only once, the total number of force computations is $N(N-1)/2$.

For strongly coupled systems, where the number of particles per Debye cube is small, the PP approach is feasible and forms the basis of the very successful molecular dynamics method used in condensed matter and in biomolecular studies. We refer the reader to a specific text on molecular dynamics to investigate the approach more in depth [4]. The approach is also used in the study of gravitational interactions, for example in the cosmological studies of the formation and distribution of galaxies. In that case, specifically the dark matter is studied with a PP approach. The PP approach can be made more efficient by using the *Barnes-Hut* or *tree algorithm* [1] that can reduce the cost (but not without loss of information) to $O(N \log N)$.

Even with the reduced cost of the tree algorithm, PP methods cannot be practical for weakly coupled systems where the number of particles is very large. As the number of particles increases, the cost scales quadratically (or as $N \log N$) and makes the computational effort unmanageable. In that case, one cannot simply describe every particles in the system and a method must be devised to reduce the description to just a statistical sample of the particles. This is the approach described in the next section.

V. FINITE SIZE PARTICLES

The key idea behind the simulation of weakly coupled systems is to use as building block of the model not single particles but rather collective clouds of them: each computational particle (referred to sometimes as superparticle) represents a group of particles and can be visualised as a small piece of phase space. The concept is visualized in Fig. 3.

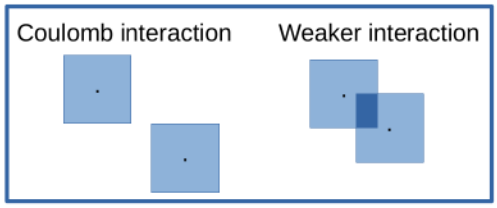

Figure 3: Interaction of finite size particles. When the particles do not overlap they interact as point particles (left), instead, when they overlap, their interaction becomes weaker because the overlap area in dark blue is neutralized (right).

The fundamental advantage of the finite-size particle approach is that the computational particles, be-

ing of finite size, interact more weakly than point particles. When two point particles interact, for example via coulombian force, the repulsive or attractive force grows as the particles approach, reaching a singularity at zero separation. Finite size particles instead, behave as point particles until their respective surfaces start to overlap. Once overlap occurs the overlap area is neutralized, not contributing to the force between the particles. At zero distances when the particles fully overlap (assuming here that all particles have the same surface) the force become zero. Figure 4 shows the force between two spherical charged particles as a function of their distance. At large distances the force is identical to the Coulomb force, but as the distance becomes smaller than the particle diameter, the overlap occurs and the force starts to become weaker than the corresponding Coulomb force, until it becomes zero at zero separation.

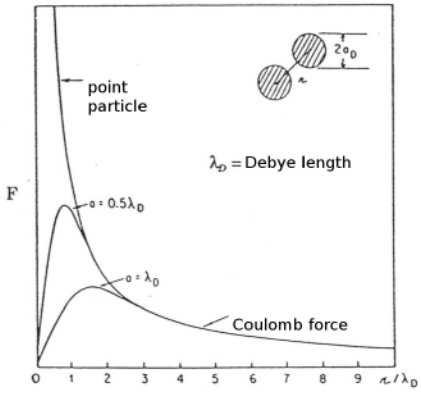

Figure 4: Interactions between finite size particles. Reproduced from [3].

The use of finite-size computational particles allows to reduce the interaction among particles. Recalling the definition of plasma parameter, the use of finite-size particles results in reducing the potential energy for the same kinetic energy. The beneficial consequence is that the correct plasma parameter can be achieved by using fewer particles than in the physical system. The conclusion is that the correct coupling parameter is achieved by fewer particles interacting more weakly. The realistic condition is recovered.

VI. PARTICLE IN CELL METHOD

The idea of the particle in cell (PIC, also referred to as particle-mesh, PM) method is summarised in Fig. 5. The system is represented by a small number of finite-size particles all interacting via the correct potential at distances beyond the overlap distance, but correcting the effect of fewer particles at small distances by the reduced interaction potential.

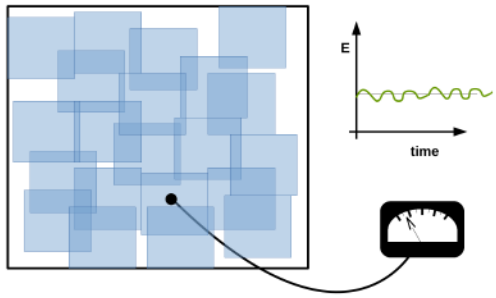

Figure 5: A system of finite size particles.

The end result is that the electric field fluctuations in the system are correctly smooth as they should be in a weakly coupled system. The reason now is not that at any time a very large number of particles average each other but rather that the effect of the few particles close to the measure point is weak.

Similarly the trajectory of particles are smooth as in the real system but not because each particle is surrounded by a very large number of near neighbours. Rather the few near neighbours produce weak interactions.

The collective effect is still correct as the long range interaction is unmodified and reproduces correctly the physical system.

VII. MATHEMATICAL DERIVATION OF THE PIC METHOD

We consider there the procedure for deriving the PIC method. Two classic textbooks [5, 2] and a review paper [3] report a heuristic derivation based on the physical properties of a plasma. We consider here a different approach aimed at making a clear mathematical link between the mathematical model of the plasma and its numerical solution. To make the derivation as easy as possible, while retaining all its fundamental steps we consider the following 1D electrostatic and classical plasma. The extension to 3D electromagnetic plasmas is no more difficult but clouded by the more complicated notation.

The phase space distribution function $f_s(x, v, t)$ for a given species s (electrons or ions), defined as the number density per unit element of the phase space (or the probability of finding a particle in a dx and dv around a certain phase space point (x, v)), is governed by the Vlasov equation:

$$\frac{\partial f_s}{\partial t} + v\frac{\partial f_s}{\partial x} + \frac{q_s E}{m_s}\frac{\partial f_s}{\partial v} = 0 \qquad (11)$$

where q_s and m_s are the charge and mass of the species, respectively.

The electric field in the electrostatic limit is described by the Poisson's equation for the scalar potential:

$$\epsilon_0 \frac{\partial^2 \varphi}{\partial x^2} = -\rho \tag{12}$$

where the net charge density is computed from the distribution functions as:

$$\rho(x,t) = \sum_s q_s \int f_s(x,v,t) dv \tag{13}$$

A. Numerical Approach

The PIC method can be regarded as a *finite element approach* but with finite elements that are themselves moving and overlapping. The mathematical formulation of the PIC method is obtained by assuming that the distribution function of each species is given by the superposition of several elements (called computational particles or superparticles):

$$f_s(x,v,t) = \sum_p f_p(x,v,t) \tag{14}$$

Each element represents a large number of physical particles that are near each other in the phase space. For this reason, the choice of the elements is made in order to be at the same time physically meaningful (i.e. to represent a bunch of particles near each other) and mathematically convenient (i.e. it allows the derivation of a manageable set of equations).

The PIC method is based upon assigning to each computational particle a specific functional form for its distribution, a functional form with a number of free parameters whose time evolution will determine the numerical solution of the Vlasov equation. The choice is usually made to have two free parameters in the functional shape for each spatial dimension. The free parameters will acquire the physical meaning of position and velocity of the computational particle. The functional dependence is further assumed to be the tensor product of the shape in each direction of the phase space:

$$f_p(x,v,t) = N_p S_x(x - x_p(t)) S_v(v - v_p(t)) \tag{15}$$

where S_x and S_v are the *shape functions* for the computational particles and N_p is the number of physical particles that are present in the element of phase space represented by the computational particle.

A number of properties of the shape functions come from their definition:

1. The support of the shape functions is compact, to describe a small portion of phase space, (i.e. it is zero outside a small range).
2. Their integral is unitary:

$$\int_{-\infty}^{\infty} S_\xi(\xi - \xi_p) d\xi = 1 \tag{16}$$

where ξ stands for any coordinate of phase space.

3. While not strictly necessary, Occam's razor suggests to choose symmetric shapes:

$$S_\xi(\xi - \xi_p) = S_\xi(\xi_p - \xi) \tag{17}$$

While these definitions still leave very broad freedom in choosing the shape functions, traditionally the choices actually used in practice are very few.

B. Selection of the particle shape

The standard PIC method is essentially determined by the choice of S_v, the shape in the velocity direction as a Dirac's delta:

$$S_v(v - v_p) = \delta(v - v_p) \tag{18}$$

This choice has the fundamental advantage that if all particles within the element of phase space described by one computational particle have the same speed, they remain closer in phase space during the subsequent evolution.

The original PIC methods developed in the 50's were based on using a Dirac's delta also as the shape function in space. But now for the spatial shape functions, all commonly used PIC methods are based on the use of the so-called b-splines. The b-spline functions are a series of consecutively higher order functions obtained from each other by integration. The first b-spline is the flat-top function $b_0(\xi)$ defined as:

$$b_0(\xi) = \begin{cases} 1 & if\ |\xi| < 1/2 \\ 0 & otherwise \end{cases} \tag{19}$$

The subsequent b-splines, b_l, are obtained by successive integration via the following generating formula:

$$b_l(\xi) = \int_{-\infty}^{\infty} d\xi' b_0(\xi - \xi') b_{l-1}(\xi') \tag{20}$$

Figure 6 shows the first three b-splines.

Based on the b-splines, the spatial shape function of PIC methods is chosen as:

$$S_x(x - x_p) = \frac{1}{\Delta_p} b_l\left(\frac{x - x_p}{\Delta_p}\right) \tag{21}$$

where Δ_p is the scale-length of the support of the computational particles (i.e. its size). A few PIC codes use splines of order 1 but the vast majority uses b-splines of order 0, a choice referred to as cloud in cell because the particle is a uniform square cloud in phase space with infinitesimal span in the velocity direction and a finite size in space.

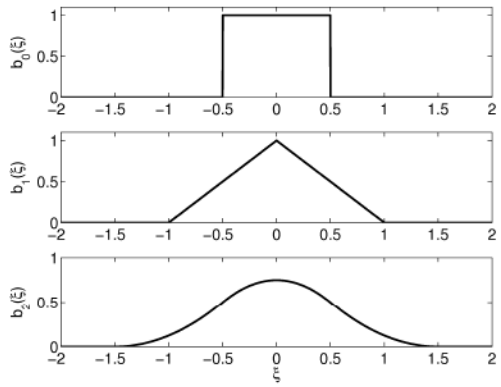

Figure 6: First three b-spline functions.

VIII. DERIVATION OF THE EQUATIONS OF MOTION

To derive the evolution equations for the free parameters x_p and v_p, we require that the first moments of the Vlasov equation to be exactly satisfied by the functional forms chosen for the elements. This procedure require some explanations:

1. The Vlasov equation is formally linear in f_s and the equation satisfied by each element is still the same Vlasov equation. The linear superposition of the elements gives the total distribution function and if each element satisfies the Vlasov equation, the superposition does too. A caveat, the electric field really depends on f_s making the Vlasov equation non-linear. As a consequence the electric field used in each Vlasov equation for each element must be the total electric field due to all elements, the same entering the complete Vlasov equation for f_s:

$$\frac{\partial f_p}{\partial t} + v\frac{\partial f_p}{\partial x} + \frac{q_s E}{m_s}\frac{\partial f_p}{\partial v} = 0 \qquad (22)$$

2. The arbitrary functional form chosen for the elements does not satisfy exactly the Vlasov equation. The usual procedure of the finite element method is to require that the moments of the equations be satisfied.

We indicate the integration over the spatial and velocity domain by the symbol $< \ldots >\equiv \int dx \int dv$.

A. Moment 0

The zeroth order moment ($< Vlasov >$) gives:

$$\frac{\partial < f_p >}{\partial t} + \left\langle v\frac{\partial f_p}{\partial x}\right\rangle + \left\langle \frac{q_s E}{m_s}\frac{\partial f_p}{\partial v}\right\rangle = 0 \qquad (23)$$

where we used the interchangeability of the integration in $dxdv$ and of the derivation over time. The second and third term are zero, as:

$$\int \frac{\partial f_p}{\partial x} dx = f_p(x = +\infty) - f_p(x = -\infty) = 0$$

where the last equality follows from the compact support of f_p, assumed in the definition of the elements. A similar calculation holds for the term with the derivative over v. Recalling that $< f_p >= N_p$, it follows:

$$\frac{dN_p}{dt} = 0 \qquad (24)$$

The application of the first zeroth order moment leads to the establishment of the conservation of the number of physical particles per computational particle.

B. Moment $\mathbf{1_x}$

The application of the first order moment in x, ($< x \cdot Vlasov >$) gives:

$$\frac{\partial < f_p x >}{\partial t} + \left\langle vx\frac{\partial f_p}{\partial x}\right\rangle + \left\langle x\frac{q_s E}{m_s}\frac{\partial f_p}{\partial v}\right\rangle = 0 \qquad (25)$$

The last term is still zero by virtue of integration over v, the other terms, instead, are new. The first term is:

$$< f_p x >= N_p \int S_v(v - v_p)dv \int xS(x - x_p)dx$$

where the first integral is 1 by definition of S_v as a function of unitary integral and the second expresses the first order moment of S_x. Recalling the assumption of symmetry of S_x, that moment equals x_p:

$$< f_p x >= N_p x_p$$

The third term requires the integration of:

$$\int vdv \int x\frac{\partial f_p}{\partial x}dx =$$

$$\int v\left[f_p(x = +\infty) - f_p(x = -\infty)\right] xdv - \int vf dxdv =$$

$$- < f_p v >$$

where integration by part has been used. The integral can be computed as above, reversing the roles of x and v:

$$< f_p v >= N_p \int vS_v(v - v_p)dv \int S(x - x_p)dx = N_p v_p$$

using the parity of S_v. The end result of applying the first order moment in x is:

$$\frac{dx_p}{dt} = v_p \qquad (26)$$

C. Moment $\mathbf{1_v}$

The application of the first order moment in v, ($< v \cdot Vlasov >$) gives:

$$\frac{\partial < f_p v >}{\partial t} + \left\langle v^2 \frac{\partial f_p}{\partial x} \right\rangle + \left\langle v \frac{q_s E}{m_s} \frac{\partial f_p}{\partial v} \right\rangle = 0 \quad (27)$$

The second term is still zero by virtue of integration over x, as in the case of the zeroth order moment. The first term has already been computed above. The remaining term must be computed:

$$\int \frac{q_s E}{m_s} dx \int v \frac{\partial f_p}{\partial v} dv = -\int \frac{q_s E}{m_s} dx \int f_s dv = \\ = \left\langle \frac{q_s E}{m_s} f_s \right\rangle$$

using again integration by part and the finite support of the elements.

The remaining integral defines a new important quantity, the average electric field acting on a computational particle, E_p:

$$\left\langle \frac{q_s E}{m_s} f_s \right\rangle = -N_p \frac{q_s}{m_s} E_p$$

where the electric field on a computational particle is:

$$E_p = \int S_v(v - v_p) dv \int S_x(x - x_p) E(x) dx \quad (28)$$

Recalling the property of S_v, the formula for E_p simplifies to:

$$E_p = \int S_x(x - x_p) E(x) dx \quad (29)$$

The first order moment in v gives the final equation:

$$\frac{dv_p}{dt} = \frac{q_s}{m_s} E_p \quad (30)$$

D. Equations of motion for the computational particles

The equations above give the following complete set of evolution equations for the parameters defining the functional dependence of the distribution within each element:

$$\frac{dN_p}{dt} = 0$$

$$\frac{dx_p}{dt} = v_p \quad (31)$$

$$\frac{dv_p}{dt} = \frac{q_s}{m_s} E_p$$

It is a crucial advantage of the PIC method that its evolution equations resemble the same Newton equation as followed by the regular physical particles. The key difference is that the field is computed as the average over the particles based on the definition of E_p.

Naturally, the electric field is itself given by Maxwell's equations which in turn need the charge density (and for complete models also the current density). The particle in cell approach described above provides immediately the charge density as the integral over the velocity variable of the distribution function:

$$\rho_s(x,t) = q_s \sum_p \int f_p(x,v,t) dv \quad (32)$$

Using the functional form for the distribution function of each computational element, the charge density becomes:

$$\rho_s(x,t) = \sum_p q_s N_p S_x(x - x_p) \quad (33)$$

The set of equations above provide a closed description for the Vlasov equation. Once accompanied by an algorithm to solve Maxwell's equations the full Vlasov-Maxwell system can be solved.

IX. FIELD EQUATIONS

The solution of the field equations can be done with a wide variety of methods. The majority of the existing PIC methods relies on finite difference or finite volume, a choice we follow here to provide an example of the interfacing with the numerical solution of the Poisson and Vlasov equations.

Assuming the finite volume approach, a grid of equal cells of size Δx is introduced with cell centres x_i and cell vertices $x_{i+1/2}$. The scalar potential is discretized by introducing the cell-averaged values φ_i. The discrete form of the field equation is obtained by replacing the Laplacian operator (i.e. the simple second derivative in 1D) with a corresponding discretized operator.

In the simplest form, the Poisson's equation can be discretized in 1D using the classic three point formula:

$$\epsilon_0 \frac{\varphi_{i+1} - 2\varphi_i + \varphi_{i-1}}{\Delta x^2} = -\rho_i \quad (34)$$

where the densities ρ_i are similarly defined as average over the cells:

$$\rho_i = \frac{1}{x_{i+1/2} - x_{i-1/2}} \int_{x_{i-1/2}}^{x_{i+1/2}} \rho(x) dx \quad (35)$$

A most convenient formulation of the density averaged over each cell can be obtained recalling the definition of the b-spline of order 0

$$\int_{x_{i-1/2}}^{x_{i+1/2}} \rho(x) dx = \int_{-\infty}^{\infty} b_0 \left(\frac{x - x_i}{\Delta x} \right) \rho(x) dx \quad (36)$$

and recalling the expression of the density:

$$\int_{x_{i-1/2}}^{x_{i+1/2}} \rho(x)dx = \sum_p \int_{-\infty}^{\infty} b_0\left(\frac{x-x_i}{\Delta x}\right) S(x-x_p)dx \tag{37}$$

The standard nomenclature of the PIC method defines the *interpolation function* as:

$$W(x_i - x_p) = \int S_x(x-x_p) b_0\left(\frac{x-x_i}{\Delta x}\right) \tag{38}$$

It is crucial to remember the distinction between the shape function and the interpolation function. The interpolation function is the convolution of the shape function with the top hat function of span equal to the cell. The usefulness of the interpolation functions is that they allow a direct computation of the cell density without the need for integration. Defining the average cell density as, $\rho_i = \int_{x_{i-1/2}}^{x_{i+1/2}} \rho(x)dx/\Delta x$, it follows that:

$$\rho_i = \sum_p \frac{q_p}{\Delta x} W(x_i - x_p) \tag{39}$$

where $q_p = q_s N_p$.

From the definition of the shape functions based on the b-spline of order l, it follows that if the shape function $S_x = \frac{1}{\Delta_p} b_l\left(\frac{x-x_p}{\Delta_p}\right)$ a very simple expression can be derived when the particle size equals the cell size, $\Delta p = \Delta x$:

$$W(x_i - x_p) = b_{l+1}\left(\frac{x_i - x_p}{\Delta_p}\right) \tag{40}$$

that follows trivially from the generating definition of the b-splines.

The solution of the Poisson equation can be conducted with the Thomas algorithm given appropriate boundary conditions. Once the solution is obtained, the potential is known in each cell, but in the form of the discrete values of the cell-averaged potentials φ_i. To compute the fields acting on the particles, the field is needed in the continuum. A procedure is needed to reconstruct it.

First, the electric field is computed in the cell centres from the discrete potentials as:

$$E_i = -\frac{\varphi_{i+1} - \varphi_{i-1}}{2\Delta x} \tag{41}$$

where centred difference are used. Then the continuum electric field is reconstructed using the assumption that the field is constant in each cell and equal to its cell-averaged value

$$E(x) = \sum_i E_i b_0\left(\frac{x-x_i}{\Delta x}\right) \tag{42}$$

From the definition of E_p it follows that:

$$E_p = \sum_i E_i \int b_0\left(\frac{x-x_i}{\Delta x}\right) S_x(x-x_p) \tag{43}$$

and recalling the definition of interpolation function,

$$E_p = \sum_i E_i W(x_i - x_p) \tag{44}$$

X. DISCRETIZATION OF THE EQUATIONS OF MOTION

The equations of motion derived in paragraph 1.3.4 are simple ordinary differential equations with the same form as the regular Newton equations. Of course, in the literature there are many algorithms to achieve the goal of solving the Newton equations. For the PIC algorithm a efficient choice is to use simple schemes: given the very large number of particles used (billions are now common in published works), the use of complex schemes may result in prohibitively long simulations. However, if more advanced schemes allow one to use large time steps, the additional cost per time step may be compensated by taking longer time steps.

The simplest algorithm and by far the most used in the so-called *leap-frog algorithm* based on staggering the time levels of the velocity and position by half time step: $x_p(t = n\Delta t) \equiv x_p^n$ and $v_p(t = (n+1/2)\Delta t) \equiv v_p^{n+1/2}$. The advancement of position from time level n to time level $n+1$ uses the velocity at mid-point $v_p^{n+1/2}$, and similarly the advancement of the velocity from time level $n-1/2$ to $n+1/2$ uses the mid point position x_p^n. This stepping of velocity over position and position over velocity recalled some of the early users of the children's game bearing also the name leap-frog (see Fig. 7).

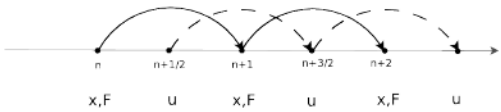

Figure 7: Visual representation of the leap-frog algorithm.

The scheme is summarised by:

$$\begin{aligned} x_p^{n+1} &= x_p^n + \Delta t v_p^{n+1/2} \\ v_p^{n+3/2} &= v_p^{n+1/2} + \Delta t \frac{q_s}{m_s} E_p(x_p^{n+1}) \end{aligned} \tag{45}$$

where E_p is computed solving the Poisson equation from the particle positions given at time level n.

Note that technically the leap-frog algorithm is second order accurate, when instead the regular explicit Euler-scheme is only first order. Nevertheless, the two differ in practice only for the fact that the velocity is staggered by half time step. This staggering is achieved by moving the initial velocity of the

first time cycle by half a time step using an explicit method:

$$v_p^{1/2} = v_p^0 + \Delta t \frac{q_s}{m_s} E_p(x_p^0)$$

XI. RECAPITULATION

Collecting the steps gathered so far, the PIC algorithm is summarised by the series of operations depicted in Fig. 8.

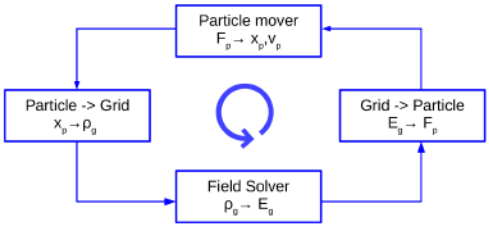

Figure 8: Summary of a computational cycle of the PIC method.

A. Algorithm of the PIC method, electrostatic case in 1D

i The plasma is described by a number of computational particles having position x_p, velocity v_p and each representing a fixed number N_p of physical particles.

ii The equations of motion for the particles are advanced by one time step using,

$$x_p^{n+1} = x_p^n + \Delta t v_p^{n+1/2}$$

$$v_p^{n+3/2} = v_p^{n+1/2} + \Delta t \frac{q_s}{m_s} E_p^{n+1}$$

using the particle electric field from the previous time step.

iii The charge densities are computed in each cell using:

$$\rho_i = \sum_p \frac{q_p}{\Delta x} W(x_i - x_p)$$

iv The Poisson equation is solved:

$$\epsilon_0 \frac{\varphi_{i+1} - 2\varphi_i + \varphi_{i-1}}{\Delta x^2} = -\rho_i$$

and the electric field E_i in each cell is computed:

$$E_i = -\frac{\varphi_{i+1} - \varphi_{i-1}}{2\Delta x}$$

v From the field known in the cells, the field acting on the particles is computed as

$$E_p^{n+1} = \sum_i E_i W(x_i - x_p^{n+1})$$

which is used in the next cycle

vi The cycle restarts.

REFERENCES

[1] J. Barnes and P. Hut.,"A hierarchical O(N log N) force-calculation algorithm", *Nature*, **324**:4446–449, 1986.

[2] C.K. Birdsall and A.B. Langdon, "Plasma Physics Via Computer Simulation", *CRC Press*, Boca Raton, 2004.

[3] J. M. Dawson. "Particle simulation of plasmas", *Rev. Mod. Phys.*, **55**:403–447, 1983.

[4] D. Frenkel and B. Smit, "Understanding Molecular Simulation", *Academic Press*, San Diego, 2002.

[5] R. W. Hockney and J. W. Eastwood, "Computer Simulation Using Particles", *McGraw-Hill*, New York, 1981.

[6] Giovanni Lapenta, "Particle simulations of space weather", *Journal of Computational Physics*, **231**(3):795–821, 2012.

[7] G. Lapenta, J. U. Brackbill, and P. Ricci, "Kinetic approach to microscopic-macroscopic coupling in space and laboratory plasmas", *Physics of Plasmas*, **13**:5904, May 2006.

ACKNOWLEDGMENTS

F.P. was partially supported by the PostDoctoral Fellowship 12X0319N and the Research Grant 1507820N from Research Foundation – Flanders (FWO).

Band / Volume 554
Characterisation of the effect of redox potential on the emission of greenhouse gases using wireless sensing techniques
J. Wang (2021), XIV, 104 pp
ISBN: 978-3-95806-581-9

Band / Volume 555
Stability assessment of variably saturated hillslopes using coupled hydromechanical models
S. Moradi (2021), xxxii, 123 pp
ISBN: 978-3-95806-583-3

Band / Volume 556
Catalytic-doping of Silicon Alloys for the Use in Silicon Heterojunction Solar Cells
Y. Liu (2021), 126 pp
ISBN: 978-3-95806-591-8

Band / Volume 557
Formation of highly oxygenated organic molecules from α-pinene photochemistry
S. Kang (2021), xvii, 156 pp
ISBN: 978-3-95806-596-3

Band / Volume 558
Synthese von Cr_2AlC MAX-Phasen Kompositen und Bestimmung ihrer oxidativen Eigenschaften
T. Go (2021), ii, 119 pp
ISBN: 978-3-95806-598-7

Band / Volume 559
Distribution of Relaxation Times for Analysis of Solid Oxide Fuel Cell Stacks
K. Fitzek (2021), 237 pp
ISBN: 978-3-95806-599-4

Band / Volume 560
Machine Learning in Modeling of the Dynamics of Polymer Electrolyte Fuel Cells
W. Zou (2021), vii, 139 pp
ISBN: 978-3-95806-601-4

Band / Volume 561
Introduction Strategies for Hydrogen Infrastructure
S. Cerniauskas (2021), viii, 179 pp
ISBN: 978-3-95806-602-1

Schriften des Forschungszentrums Jülich
Reihe Energie & Umwelt / Energy & Environment

Band / Volume 562
Noble Metal Coated Porous Transport Layers for Polymer Electrolyte Membrane Water Electrolysis
C. Liu (2021), 139 pp
ISBN: 978-3-95806-603-8

Band / Volume 563
Modeling and Diagnosis of the Stratospheric Circulation
E. J. Charlesworth (2021), v, 103, A2 pp
ISBN: 978-3-95806-605-2

Band / Volume 564
Potentialfeldmessungen zur Qualitätsbewertung von Bipolarplatten
M. Sietmann (2021), ix, 160 pp
ISBN: 978-3-95806-606-9

Band / Volume 565
Sequential and coupled inversion of time-lapse borehole GPR measurements for vadose zone model parameterization
Y. Yu (2022), XX, 121 pp
ISBN: 978-3-95806-607-6

Band / Volume 566
Cirrus clouds in the extratropical tropopause and lowermost stratosphere region
I. Bartolomé García (2022), iii, 155 pp
ISBN: 978-3-95806-610-6

Band / Volume 567
Stationary and Transient Behaviour of Polymer Electrolyte Fuel Cells
Y. Shi (2022), viii, 172 pp
ISBN: 978-3-95806-611-3

Band / Volume 568
14th Carolus Magnus Summer School on Plasma and Fusion Energy Physics
D. Reiser (Ed.), (2022), 207 pp
ISBN: 978-3-95806-613-7

Weitere ***Schriften des Verlags im Forschungszentrum Jülich*** unter
http://wwwzb1.fz-juelich.de/verlagextern1/index.asp

Energie & Umwelt / Energy & Environment
Band / Volume 568
ISBN 978-3-95806-613-7

Mitglied der Helmholtz-Gemeinschaft

JÜLICH
Forschungszentrum